UNIVERSITÀ DEGLI STUDI DI PADOVA

Dipartimento di Geoscienze

Sede Amministrativa: Università degli Studi di Padova

Scuola di Dottorato di Ricerca in Scienze della Terra

Indirizzo Unico

Ciclo: XXI

CAMP VOLCANISM: AGE, VOLCANIC STRATIGRAPHY AND ORIGIN OF THE MAGMAS. CASES STUDIES FROM MOROCCO AND THE U.S.A.

Direttore della Scuola: Ch.mo Prof. Gilberto Artioli

Supervisore: Prof. Andrea Marzoli

Dottorando

Tiberio Cuppone

Contents

1 INTRODUCTION

During Triassic time, in the proto-North Atlantic area, the late Palaeozoic fracture system, inherited from the building of Pangea supercontinent, was reactivated. Rifting and breakup of Pangea, initiated during the early Triassic, continued and intensified at the beginning of the Norian. After few million years later, a massive magmatic event, namely CAMP (Central Atlantic Magmatic Province), occurred in the rifted and inside the cratonic areas, covering more than 10 millions kilometers square, leaving its products on 4 continents: North and South America, southwest Europe and west Africa. The main magmatic event occurred at ca 199-200 Ma near the Triassic-Jurassic boundary (Tr-J) with two minor secondary pulses al ca. 195 Ma and 192 Ma. The time spanned by the main magmatic event is very short, probably less than 1 Ma (ca. 610 Ka based on Milankovitch cyclostratigraphy), and the tight occurrence with one of great extinctions events in the Phanerozoic time and the climatic crisis and biotic turnover demarcating the Tr-J, led to the intriguing hypothesis that CAMP magmatism triggered these global events. At present the CAMP magmatism is represented by tholeiitic dikes, sills and minor amounts of lava flows, deeply eroded and in few places well preserved, being due to the subtropical palaeogeographic position of the basaltic outcrops which led to heavy weathering. Most of the CAMP basalts throughout circum-Atlantic domain have quite homogeneous compositions, with low-Ti (TiO_2 <2wt.%) except for high-Ti dyke storms documented in Liberia, French Guyana and northern Brazil, strong Nb-Ta$_{PM}$ negative anomaly, enriched in light earth rare elements (LREE) and large ion lithophile elements (LILE) respect to the common normal mid-ocean ridge basalts. The purpose of this work is to describe and correlate 6 CAMP volcanic sequences in three different Morocco regions (three in the Central High Atlas, two in the Middle Atlas and one in the Western Meseta) on the base of a petrographic-mineralogic-geochemical-magneto-stratigraphic study in order to highlight similarities between the four basaltic units which made up the lava piles. Phase relationships, their major, minor and trace element compositions will be investigated to constrain crystallization order and conditions (T, P, H_2O content and

fO_2) of basalts while the accurate chemo-magneto-stratigraphic correlation of five lava sequence allow to do new suppositions about feeding system of the Moroccan CAMP basalts. Finally new and accurate $^{40}Ar/^{39}Ar$ dating on plagioclase and biotite separates from 11 basaltic sample of the Eastern North America (Newark and Culpeper basins) will be presented, discussed and compared to both previous dating of the same province and a overall CAMP ages dataset.

2 INTRODUZIONE

Durante il Triassico, nell'area circostante l'Oceano atlantico, furono riattivati sistemi di fratture Paleozoiche ereditate dall'assemblamento del supercontinente Pangea. Il processo di distensione (*rifting*) e frattura della Pangea, iniziato durante il Triassico inferiore, continuò e si intensificò al'inizio del Norico (Triassico superiore). A cavallo del limite tra il Triassico e il Giurassico (e precedendo di pochi milioni di anni la rottura definitiva della Pangea e l'allontanamento delle nuove placche continentali formatesi), ebbe luogo su una superficie di oltre 10 milioni di chilometri quadrati un massiccio evento magmatico, conosciuto con il nome di CAMP (*Central Atlantic Magmatic Province*, Provincia Magmatica dell'Atlantico Centrale), con un volume stimato di almeno 2 milioni di chilometri cubi di prodotti sia intrusivi (*sills* e *dikes*) che effusivi (colate laviche). Attualmente, questi prodotti vulcanici sono ritrovati in quattro continenti: nella costa orientale del Nord America (dalla Nuova Scozia in Canada fino alla Florida), Sud America (dalla Guinea Francese fino alle province centrali del Brasile e alla Bolivia), Sud-Ovest Europa (penisola Iberica e Francia nord occidentale) e Africa occidentale (dall'Algeria, passando per il Marocco e giù fino alla Sierra Leone). Il picco di attività magmatica principale si sviluppo ca. 199-200 milioni di anni fa (*Ma*) con due picchi secondari di minore importanza (per quanto riguarda il volume di prodotti vulcanici) a 195 e 192 *Ma*. Secondo le più recenti ricerche, il picco magmatico principale fu veramente breve (su scala geologica), probabilmente meno di un milione di anni (circa 610.000 anni, sulla base di studi ciclostratigrafici). La stretta vicinanza temporale dell'evento CAMP con uno dei più grossi eventi di estinzione di massa del Fanerozoico che demarca il limite Triassico-Giurassico, ha portato gli studiosi del settore ad ipotizzare che la CAMP possa avere innescato l'evento estintivo, anche se con modalità ancora non completamente chiarite.

La maggioranza dei prodotti vulcanici della CAMP oggi preservati è costituita da rocce intrusive (dicchi e sills), poichè gli enormi espandimenti lavici hanno subito un lungo processo di alterazione, a causa della loro posizione paleogeografica subtropicali. La maggior parte dei rocce vulcaniche della CAMP

è rappresentata da basalti e basalti andesitici. Le composizioni di queste rocce sono abbastanza omogenee, con contenuti di SiO_2, TiO_2 e K_2O piu alti rispetto ai piu comuni basalti di dorsale oceanica (N-MORB). I basalti hanno contenuti di TiO_2 <2 wt.%, eccetto che per pochi e geograficamente circoscritti prodotti intrusivi (dicchi alti in Ti, fino al 4 wt% in Liberia, Guyana Francese e Brazil del nord), mostrano una forte anomalia negativa di Nb-Ta_{PM} e un arricchimento in terre rare leggere (LREE) e elementi litofili (LILE) rispetto alle terre rare pesanti (HREE) ed elementi ad alta forza di campo (HFSE).

L'obiettivo di questo lavoro è descrivere e correlare sei sequenze di colate laviche in the differenti regioni del Marocco: tre sequenze nella catena dell'Alto Atlante centrale, due sequenze nel Medio Atlante e una nella Meseta occidentale marocchina. Operando uno studio su base petrografica, mineralogica, geochimica e magnetostratigrafica, si evidenzieranno similarità e differenze tra le quattro unità di colate basaltiche, riconoscibili sulla base di criteri composizionali e in cui le sequenze laviche sono suddivise. Le relazioni tra le fasi minerali e le composizioni in elementi maggiori, minori e tracce permetteranno di investigare sulle condizioni (T, P, contenuto di H_2O e fO_2) e ordine di cristallizzazione a cui sono stati sottoposti i basalti marocchini prima e durante la messa in posto in superficie. Inoltre un'accurata correlazione geochimica e magnetostratigrafica di cinque delle sei sequenze laviche, permetterà di fare nuove supposizioni sulle modalità temporale e geografica di messa in posto dei basalti marocchini

Infine, verrano proposte e discusse nuove e accurate età $^{40}Ar/^{39}Ar$ ottenute su separati di plagioclasi e biotiti, provenienti da basalti dei bacini sedimentari di Newark e Culpeper della provincia orientale nord americana (Eastern North America) della CAMP, in relazione alle poche età $^{40}Ar/^{39}Ar$ disponibili nella stessa provincia e in relazione ad un più ampio database di età disponibile per l'intera provincia magmatica.

Ringrazio il supporto da parte della Fondazione della Cassa di Risparmio di Padova e Rovigo (CaRiPaRo) che ha garantito la mia borsa di dottorato e mi ha permesso di svolgere un proficuo stage di analisi presso il Western Australian Argon Isotope Facility (Department of Applied Geology & JdL Centre Curtin University of Technology, Perth, Australia).

3 GEODYNAMIC EVOLUTION OF PERI-ATLANTIC DOMAIN

3.1 OPENING OF PROTO-ATLANTIC: IAPETUS AND RHEIC OCEAN

Although many details remain obscure, it is almost universally accepted that the continents ride across the face of the Earth on tectonic plates which have been in constant movement since the formation of the crust. The continents we recognise today have not always existed: great blocks of crust have united in many configurations over the planet's history. And all (or at least the most of them) of the Earth's crust has been united into a single supercontinent. The most recent and best known supercontinent was Pangea. Otherwise the oldest one which history is already well known is the Precambrian supercontinent Rodinia. The existence of this supercontinent was proposed in the 1970s, largely motivated by the evidence of contemporaneous (1.3 to 1.0 Ga) "Grenville" mountain belts on the actual different continents, and broadly supported by paleomagnetic studies **(Dalziel, 1991)**. The Rodinia supercontinent was ripped apart during the Early Neoproterozoic (Tonian), ca 750 Ma. Fragmentation of Rodinia led to the opening of the Iapetus Ocean **(Torsvik, 2003)**. Towards the end of the Proterozoic, this supercontinent fragmented, giving rise to the late Ediacaran supercontinent of Pannotia, which was very short-lived, and in turn from its disruption were created new continents: Laurentia (N America), Gondwana (Africa, S. America, Antarctica, Australia and India), Baltica (NE Europe) and Siberia. Laurentia and Baltica, according to **Torsvik *et al.* (1996)** drifted apart from Gondwana during the late Neoproterozoic. The early Ordovician (ca. 490 Ma) was the time of maximum dispersion of continents of the Palaeozoic (Fig. 3.1). A plate reorganization occurred just prior the Middle Ordovician. Successive arc-continent collisions occurred along the margins of the Iapetus-Tornquist oceanic system in Baltica and Avalonia caused the Penobscottian, Grampian, Finnmarkian and Athollian orogenies which might have been related to the transformation of a passive margin into a convergent one, due to the development of a subduction

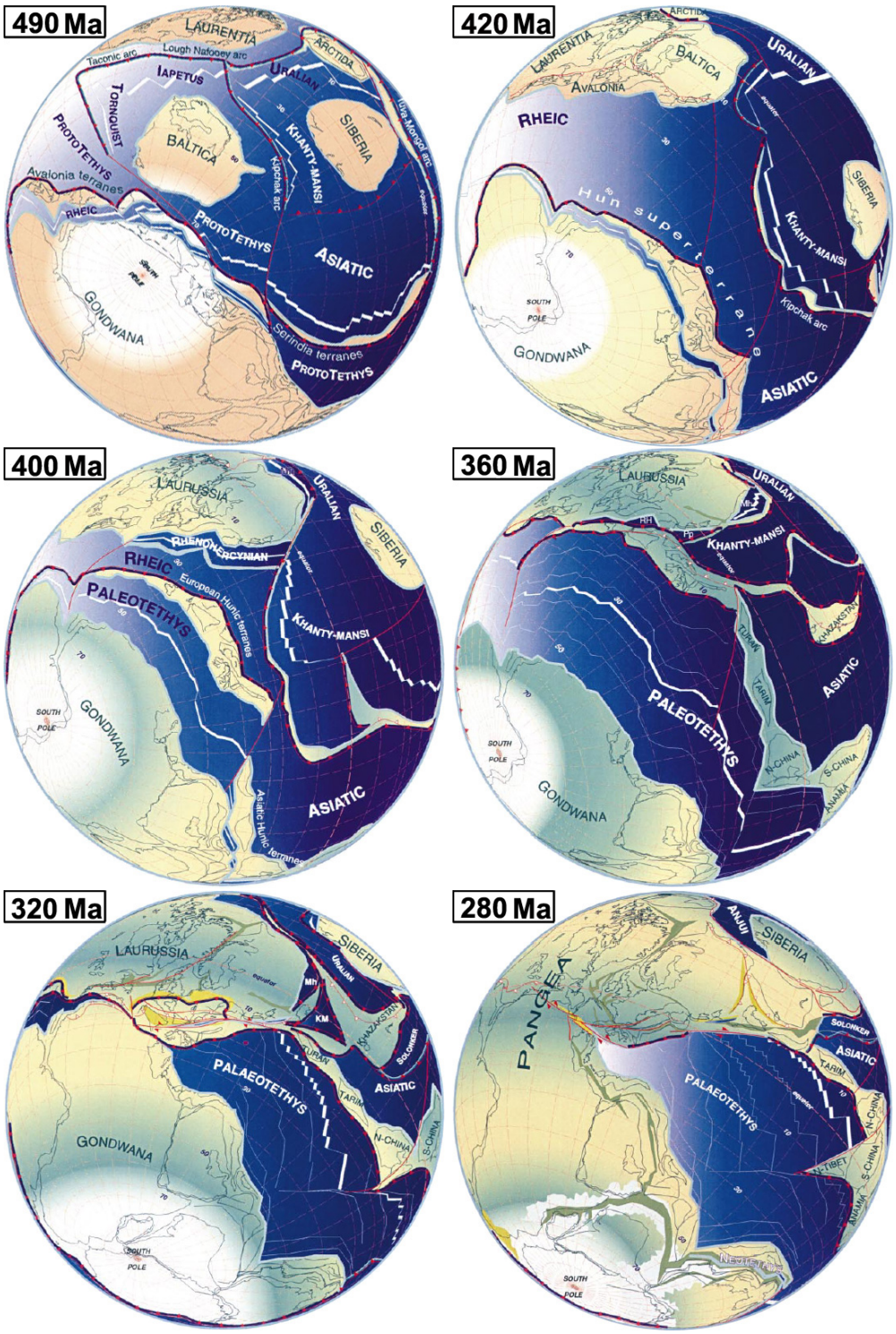

Figure 3.1: Paleogeographic reconstructions at Early Ordovician ca. 490 Ma, Late Silurian ca. 420 Ma, Middle Devonian ca. 400 Ma, Early Carboniferous ca. 360 Ma, Late Carboniferous ca. 320 Ma and at Early Permian ca. 280Ma. Modified after **Stampfli & Borel (2002)**.

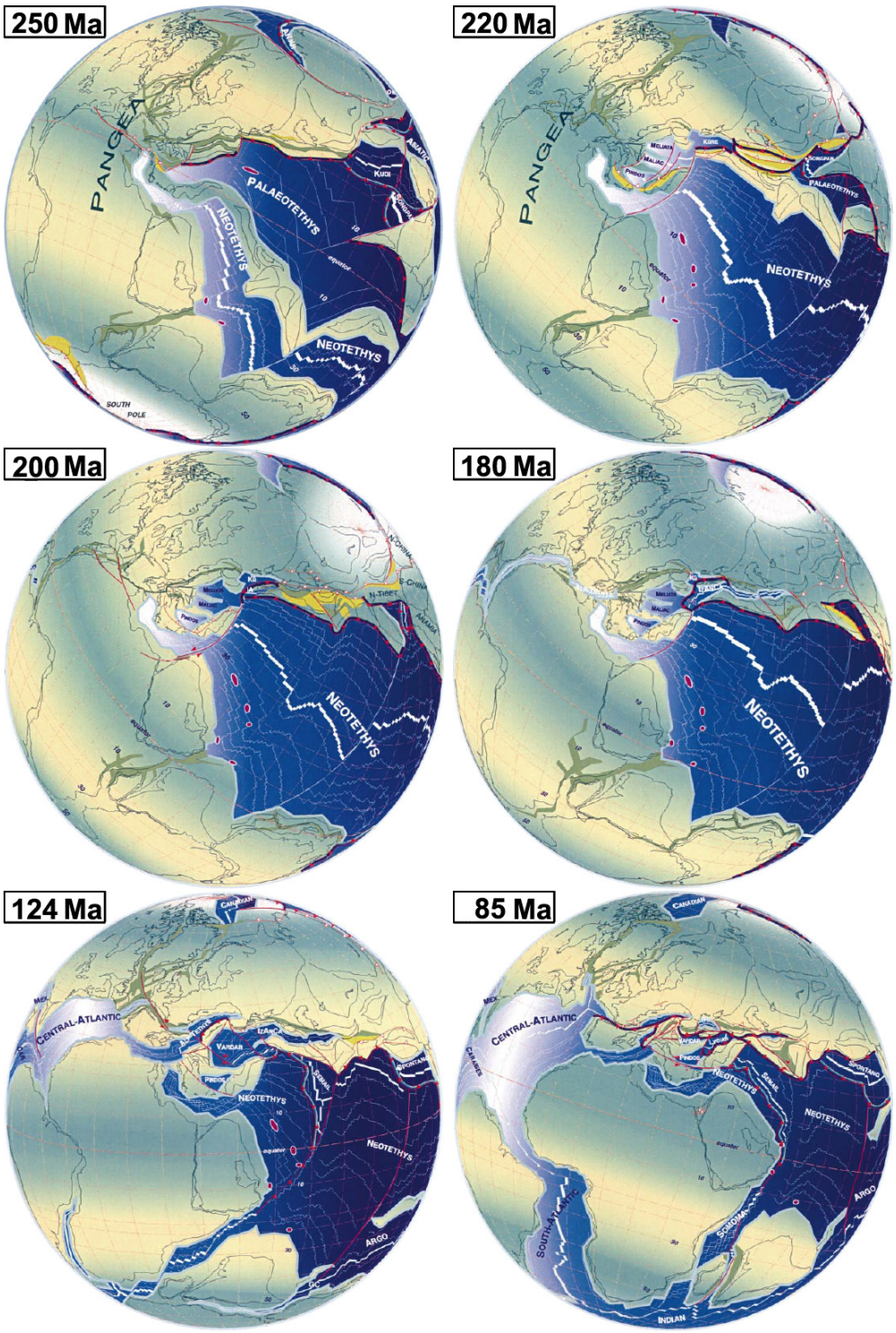

Figure 3.2: Paleogeographic reconstructions at Permian-Triassic boundary ca. 250 Ma, Early Norian ca. 220 Ma, Triassic-Jurassic boundary ca. 200 Ma, Early Middle Jurassic ca. 180 Ma, Aptian ca. 124 Ma and at Santonian ca. 85Ma. Modified after **Stampfli & Borel (2002)**.

zone. The Iapetus Ocean and the Tornquist Sea, this being situated between Baltica and Avalonia (part of Gondwana) at that time, begun to narrow. Avalonia drifted away from Gondwana towards Baltica. Between Gondwana, Baltica, Avalonia and Laurentia, a large longitudinal oceanic unit known as Rheic Ocean was formed (Fig. 3.1).

3.2 CLOSING OF IAPETUS OCEAN

This period is mainly characterized by the widening of the Rheic Ocean between Gondwana and Avalonia-Baltica and the formation of a large longitudinal ocean bounded by two large subduction zones (Fig. 3.1). The Caledonian orogeny during the Silurian and early Devonian was the result of the collision of Baltica, Laurentia and Avalonia terranes. These plates were sutured together to form the large Laurussia continent, after the complete closure of the Iapetus Ocean (Fig. 3.1).

3.3 CLOSING OF RHEIC OCEAN

The final stage of Caledonian orogeny was marked by a change in the strain field in the upper crust from contraction to extension. Sinistral displacement in Scandinavia and Greenland was a result of transtensional orogenic collapse and the western part of the Rheic Ocean begun to narrow. During the Devonian, Gondwana moved northward and rotated clockwise. At the same time, Laurussia was rotating clockwise at a faster rate. This led to collision with Gondwana and the closure of the southwest part of Rheic Ocean (Fig. 3.1). The Hercynian orogeny was the consequence of the collision of several mini-plates of Gondwana with Laurussia ones. The same happened in N. America, named here Alleghenian orogeny.

3.4 PANGEA BUILDING

The collision between Gondwana and Laurussia continued to develop. The intercontinental collision led to the building of the West African orogenies: Mauritanides, Bassarides and Rokelides **(Lécorché *et al.*, 1989)**. The Alleghenian and Ercynian orogeny in N. America and Europe, respectively, continued (**Ziegler, 1989**; **Rast, 1990**). The clockwise rotation of Gondwana resulted in the deformation in Europe and a NE-SW stress direction was added the northern

one. The early stage of formation and suture of the Urals marked the formation of the supercontinent Pangea (Fig. 3.2). The progressive closure between Gondwanan and Laurussian elements of Pangea eliminated the equatorial seaway between the Paleotethys and the western oceans. According to **Beauchamp (1997)**, a very large stress-release event, probably associated with a plate reorganization shift from convergent to divergent tectonics, occurred at the Permian-Triassic boundary (Fig. 3.2). In north-western Africa, western Europe and the proto-North Atlantic area, the late Palaeozoic fracture system was reactivated (**Ziegler, 1982, 1989**; **Doré (1991)**). Rifting of Pangea, initiated during the early Triassic, continued and intensified at the beginning of the Norian (Fig. 3.2) (**Veevers, 1994**; **Manspeizer, 1994**; **Withjack *et al.*, 1998**). The separation of North America and Gondwana, which was initiated by the Triassic stretching and rifting phase, started during the Early-Middle Jurassic. According to **Withjack *et al.* (1998)**, the transition from rifting to drifting was diachronous in the eastern North America, beginning earlier in the south-eastern, where the exposed strata within the synrift basins are Late Triassic age, with respect to the north-eastern where the rift basins are Middle Triassic to Early Jurassic in age. The final rifting phase of the Central Atlantic Ocean is marked by the massive outcrop basaltic products, both intrusive (sills and dikes) and effusive (lava flows), with the emplacement of the latter in synrift sedimentary basin. This large magmatic province, named CAMP (Central Atlantic Magmatic Province, **Marzoli *et al.*, 1999**) is one of the biggest LIPs (Large Igneous Provinces) known and it is supposed to have triggered the biotic crisis at the Triassic-Jurassic boundary, one of the most important of the Phanerozoic time **(Sepkowski, 1996)**. The start of seafloor spreading in the Central Atlantic is dated as 195 Ma (Fig. 3.2, **Sahabi *et al.* (2005)**). In maritime Canada, the drift-rift transition occurred at about 185 Ma (Fig. 3.2) **(Withjack *et al.*, 1998)**.

3.5 PANGEA BREAK-UP

In this period the newly formed central portion of Atlantic Ocean was in advanced drift stage. Extension of the Neotheys to the northwest, through the proto-Mediterranenan, produced a connection with the Central Atlantic. A connection between the Gulf of Mexico, the Central Atlantic and the Tethyan branch of the proto-Pacific Ocean was established. Rifting continued in the North Sea and in the northern proto-Atlantic **(Ziegler, 1989)**. At the end of the Jurassic also rifts developed in West and Central Africa. Initial rifting occurred be-

tween Canada and Greenland. Seafloor spreading developed in the Caribbean region, while narrow seaway developed across Europe and the North Atlantic. The initial oceanic opening of the South Atlantic took place during the early Aptian, being 124.6 Ma in age the oldest South Atlantic seafloor (Fig. 3.2) **(Bird *et al.*, 2005)** which is connected to the Paranà-Etendeka continental flood basalt **(Peate, 1997)**. The opening of South Atlantic Ocean caused the drift and counterclock rotation of Africa, which will led to Alpine orogeny in the peri-Mediterranean domain between Middle-Late Cretaceous and Miocene (Fig. 3.2).

4 GEODYNAMIC EVOLUTION OF MOROCCO

The Moroccan tectonic fabric, before the beginning of Africa/Eurasia convergence, was characterized by the building of the Tethyan margin to the north and the Atlantic margin to the west. The correlation between these two margins are not well constrained as they coexist and interfere. It is possible to recognize three main structural domains from the North to the South: the Mediterranean domain, the Alpine domain, i.e. the paleo-Tethyan margin, remodelled by thrust tectonics and local inversions during the Alpine orogeny from Cretaceous to present, and the Saharian platform, essentially Palaeozoic terrains affected by Pan-african orogeny. In Morocco, the CAMP volcanism occurred in the Alpine domain as emplacement of basaltic lava flows, mainly because of the particular tectonic configuration which led to the formation of the Alpine domain, from Triassic to recent, while the Saharian platform was interested by an essentially intrusive magmatism, mainly sills and dikes **(Ellouz *et al.*, 2003)**.

The Alpine domain includes several tectonic units. From the North to the South :

- the Rif: an asymmetric fold-and-thrust belt of classical Alpine-type, dominated in its frontal area by a thick skinned tectonic style, with numerous well-mapped thrusts and nappes, and its associated foredeep, the pre-Rif unit;

- the Meseta and its basins: this consists of two large tabular plateaux, separated by the structured Middle Atlas domain, and bordered to the South by the High Atlas. The Meseta domain is mainly composed by Paleozoic series, strongly deformed by the Hercynian orogeny, which created a heterogeneous basement prior to the Triassic rifting. The western Meseta, is located on the atlantic side and consists mainly of three Mesozoic basins: the Essaouira, Tadla and Doukkala basins. The eastern Meseta, connected to Algerian Meseta, consists of two Palaeogene basins: the Missour and High Plateaux basins. Both the western and eastern Meseta are composed of mega-blocks, which were slightly subsiding during Mesozoic times and

weakly reactivated during the Alpine compression;

- the Atlas mountains: this domain, composed by the main ENE-WSW High Atlas branch and the minor NE-SW branch of the Middle Atlas, recorded the highest deformation due to the Alpine orogeny. We will focus our attention on the Atlas domain hereafter, speaking about the geophysical tectonic units where the CAMP lava flows are located;

- the Anti-Atlas: south of the High Atlas and its associated flexural basins, the Souss and Ouarzazate basins, the Anti-Atlas chain records the strong deformation during the Hercynian orogeny **(?)**. Separated from the High Atlas by the South Atlasic Fault **(Russo & Russo, 1934)** or South Atlas Front **(de Lamotte *et al.*, 2000)** that marks the boundary between the African plate and the Euroasiatic ones, the Anti-Atlas chain is composed by Precambrian and Paleozoic rocks exposed to more than 2000 meters above sea level. Its structure suggests a large scale deformation, linked with Cenozoic compression, propagated along deep intra-crustal detachment levels. Finally, the Anti-Atlas marks the transition with the Precambrian West African craton.

4.1 THE ATLAS MOUNTAINS

The High Atlas and its Middle Atlas NE-trending branch are intracontinental mountains, a classical example of in plate-boundary orogenic belts, formed during the Cenozoic from inversion of Triassic-Jurassic transtensional troughs in the African plate (**Giese & Jacobshagen, 1992**; **de Lamotte *et al.*, 2000**; **Piqué *et al.*, 2002**; **Arboleya *et al.*, 2004**). This intraplate belt extends for more than 2000 km in a E-W direction and 100 km wide, from Morocco into Algeria and Tunisia, where it is named Saharan Atlas and Tunisian Atlas, respectively. The Atlas chain rises to 4165 m, one of the highest peaks of the Mediterranean alpine domain **(Beauchamp *et al.*, 1999)**. In the atlasic domain it is possible to recognize three tectonic phases related to well defined tectonic domains and lithostratigraphic units: a prerift phase (Paleozoic and Precambrian basement), a synrift phase (Triassic and Jurassic), a postrift phase (Cretaceous to present).

- **PRERIFT PHASE**: It's mainly represented by the Anti-Atlas domain, south of the High Atlas, in which Paleozoic and Precambrian rocks are exposed up to 2000 m, in response to the marginal up-doming of the West African craton occurred as the African plate impacted with the Eurasian

one. The late Proterozoic rocks were affected by the Pan-African orogeny and by a Hercynian deformation along a NNE-SSW strike **(Piqué & Laville, 1996)**. In the late Palaeozoic, dislocation of the Pangean plate by extensional crustal field stress led to the development of extensive episodes recorded in late Triassic to early Jurassic synrift basins striking older Hercynian-Alleghenian thrusts **(Laville *et al.*, 2004)**;

- **SYNRIFT PHASE**: From the Mid-Late Triassic to Early Jurassic, the Atlantic Moroccan rifting developed in successive phases recorded in synrift deposits. During Ladinian-Carnian times, the early extension is marked by presence on the continental fluviatile sandy silico-clastic deposits. In the Norian-Rhaetian times emplacement of basaltic lava flows is roughly contemporaneous to the depositions of silty sediments, evaporates (anhydrite and salt) in a shallow water environment in connection with the Tethyan domain, while Jurassic time is marked by deposition of marine carbonate and shales capped by continental red beds (**Roy & Piqué, 2001**; **Ellouz *et al.*, 2003**; **Davison, 2005**);

- **POSTRIFT PHASE**: At the end of the Jurassic, and during the Cretaceous, large parts of North Africa were flooded by shallow epicontinental seas that connected the Central Atlantic Ocean with the Tethys Ocean. Postrift sedimentary rocks are composed of transgressive shallow marine clastic, carbonate and continental sedimentary rocks. In the upper Eocene, the geodynamic evolution of the Atlasic domain changed back way, being related to convergence between Africa and Europe. The previous grabens and hemigrabens underwent compressional/transpressional deformations and, subsequently, a strong uplift happened, which is documented by the frequent appearance of Atlas pebbles within the foreland basins along the southern **(Harfi *et al.*, 2001)** and the northern rims of the High Atlas.

Another consequence of the Cenozoic compression and subsequent building of the Atlasic orogenic belt is the present crustal structure of the Atlas mountains. Recent studies (**Teixell *et al.*, 2003**; **Arboleya *et al.*, 2004**; **Ayarza *et al.*, 2005**; **Harfi *et al.*, 2006**) showed that the shortening related to convergence between Africa and Europe was achieved by thick-skinned thrusting and folding tectonics, which affected the pre-Mesozoic basement and the Mesozoic-Cenozoic cover. According to the work of **Teixell *et al.* (2003)** the total shortening, based on sections restoration, varies between 15% and 24% from west to east along the High Atlas while **Gomez *et al.* (1998)** estimated it in 15% for the Middle

Atlas. Nevertheless, geophysical evidences suggest that the high topography of the Atlas, up to 4000 m in the High Atlas and up to 3000 m in the Middle Atlas, can not be supported by the crustal thickening alone, requiring so some buoyancy contribution from subcrustal levels. In fact, based mainly on gravity and seismic refraction analyses (**Makris *et al.*, 1985**; **Tadili *et al.*, 1986**; **Wigger *et al.*, 1992**; **Ayarza *et al.*, 2005**), the crust in the areas adjacent to the High and Middle Atlas is 33-36 km thick, only. Near Midelt, a punctual value of 36 and 39 km (**Sandvol *et al.*, 1998**; **der Meijde *et al.*, 2003**), has been interpreted by **Ayarza *et al.* (2005)** as a Moho duplication. The crust beneath the Middle Atlas has similar thickness (35 km). A little greater value beneath the High Atlas in the range of 35-38 km, with localized maxima up to 40 km based only on gravity analyses (**Tadili *et al.*, 1986**; **Ayarza *et al.*, 2005**). A gravity model at low resolution over North Africa and the Middle Atlas by **Seber *et al.* (2001)** indicates that the crust underneath the High Atlas is about 5 km thinner than expected if topography was to be compensated at Moho levels. Moreover, seismic tomography seems to indicate a hot, low velocity mantle below the High Atlas **Seber *et al.* (1996)**, this being supported by heat flow data which yield a value of 54 mW/m^2 for the High Atlas and 85 mW/m^2 in the Middle Atlas **(Rimi, 1999)**. If it is taken into account that in the same area a widespread alkaline magmatism occurred in Cenozoic times, a contribution from a hot and shallow asthenosphere beneath a thin lithosphere could be possible, even if an arching of the lower crust, which helped maintaining the topography can not be ruled out **(Ayarza *et al.*, 2005)**.

5 CAMP OVERVIEW

Continental rifting in Central Pangea started during the Middle-Late Triassic along the trend of Late-Paleozoic Alleghenian-Hercynian sutures. After a few million years, a widespread magmatic event, straddling the Triassic-Jurassic boundary occurred near and far away from both sides of the Atlantic rift. Covering a not yet well defined surface, estimated in more than 10 million square kilometres **(McHone, 2000)**, the volcanic products of the Central Atlantic Magmatic Province (CAMP, **Marzoli *et al.* 1999**), are present on four continents and make it one of the largest igneous provinces known on Earth (Fig. 5.1). Its products are mainly giant sills, large dike swarms, some of the dikes being hundred kilometres long, few stratified intrusions, and lava flow piles preserved in Paleozoic-Mesozoic (i.e. in Brazil) and Mesozoic basins. Moreover, two longitudinally wide (up to 70-90 km) and thick (up to 25 km) basaltic wedge bodies run 2000 km along the eastern continental margin of North America (ECMA, East Coast Magnetic Anomaly) and the western continental margin of Africa (WACMA, West African Coast Magnetic Anomaly plus S1 anomaly) (**Holbrook & Keleman 1993**; **Oh *et al.* 1995**; **Sahabi *et al.* 2005**), revealed as seaward dipping reflectors (SDRs) by their magnetic anomaly and seismic reflections. The plutonic or volcanic nature of these magmatic bodies is not known, but it is supposed to belong to the CAMP event even if it has never been sampled, marking the continental to oceanic crust transition (COB, Continental-Oceanic Boundary) and the onset of the Atlantic seafloor spreading at 195 Ma (**Benson, 2003**; **Sahabi *et al.*, 2005**; **Maillard *et al.*, 2006**).The total volume of emitted products of the CAMP is not well constrained, but is estimated in at least in 2 million cubic kilometres (**Marzoli *et al.*, 1999**; **McHone, 2003**). In the last years the available ages ($^{40}Ar/^{39}Ar$, mainly) of the samples from all areas of the province are strongly increasing and suggest a rapid magmatic event. The results indicate that the whole magmatic event spanned ca. 10 Ma, commencing as early as 202 Ma. Extrusive activity initiated at ca. 200 Ma with a main peak at ca. 199 Ma (199.1±1.0 Ma, $^{40}Ar/^{39}Ar$ ages, **Marzoli *et al.*, 1999**), in which ca. 90% of the volcanic products were emitted in 1 Ma or less (**Sebai *et al.*, 1991**; **Deckart, 1996**; **Baksi &**

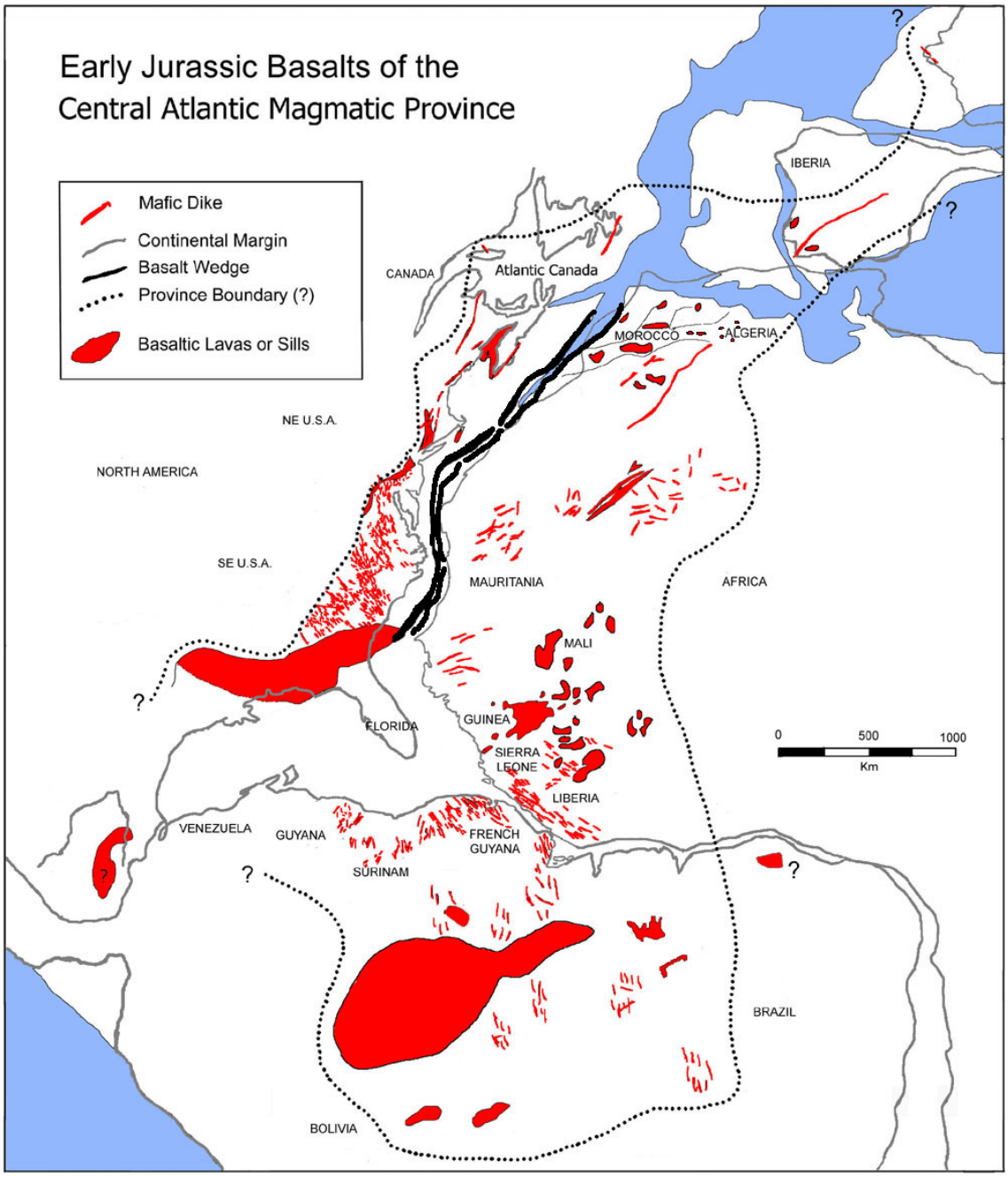

Figure 5.1: Distribution of the main CAMP provinces. Modified after McHone (2003). See text for each sub-provinces descriptions.

Archibald, 1997; **Hames *et al.*, 2000**; **DeMin *et al.*, 2003**; **Marzoli *et al.*, 1999, 2004**; **Knight *et al.*, 2004**; **Beutel *et al.*, 2005**; **Nomade *et al.*, 2007**; **Verati *et al.*, 2005, 2007**). Consistently cyclostratigraphic studies by **Olsen *et al.* (1996, 2003)** and **Whiteside *et al.* (2007)** suggest that the duration of the CAMP extrusive event in the USA basins lasted ca. 600 Ka. Moreover, paleomagnetic data from 6 section in the High Atlas, Morocco, provide a tight constrain for a brief volcanic event since the occurrence of five short volcanic pulses , each possibly less than 450 years long, could led to an estimate on the duration of the entire volcanic activity in Morocco of ca. 20 Ka or less (**Knight *et al.* 2004**). Two volumetrically minor, but distinct magmatic peaks are centred at 195 and 192 Ma (**Nomade *et al.* 2007**). The age of the main peak is very close to the age of the Triassic-Jurassic boundary proposed by **Schaltegger *et al.* (2008)** obtained by ID-TIMS U-Pb dating of single chemical-abrated zircons from volcanic ash layer in a deep marine sedimentary section in northern Perù (201.58±0.28 Ma, **Schaltegger *et al.*, 2008**). Since numerous studies have highlighted that $^{40}Ar/^{39}Ar$ ages are systematically younger than U-Pb ages by ca. 1% (**Renne *et al.*, 1998**; **Renne, 2000**; **Villeneuve *et al.*, 2000**; **Min *et al.*, 2000, 2001**; **Nomade *et al.*, 2004**; **Schoene *et al.*, 2006**; **Schaltegger *et al.*, 2008**), synchrony between the 199 Ma Ar age for CAMP basalts may correspond to the 201.6 Ma U/Pb age of the T-J boundary. The possible occurrence of the CAMP main peak at the same time as the Triassic-Jurassic biotic crises, one of the largest of the Phanerozoic (**Sepkowski, 1996**), rises the intriguing hypothesis that CAMP volcanism could have triggered the extinction event and the biotic turnover which characterized the boundary (**Tanner *et al.*, 2004**) marked also by shifts of C and Os isotopes in marine sediments (**Hesselbo *et al.*, 2002**; **Cohen & Coe, 2002**). The compositions of CAMP magmatic products are quite homogeneous and no substantial differences are in general evident between the different regions of the magmatic province. They are mostly basic in composition, ranging between basalts and basaltic andesites, with a tholeiitic affinity. Alkaline and silicic rocks are absent. Most basalts are low in TiO_2 (<2 wt%) and display in multi-elementary mantle-normalized diagrams a negative Nb and Ti anomaly coupled with a moderate enrichment in LREE (Light Rare Earth Elements) and LILE (Large Ion Lithophile Elements) over the HREE (Heavy REE). Notable exception are dikes and basaltic lava flows in French Guyana, Liberia and Brazil, high in TiO_2 (up to 4.41 wt%, **Deckart *et al.*, 1997, 2005**; **DeMin *et al.*, 2003**; **Merle *et al.*, submit.**), moderate Nb anomaly and slight positive Ti anomaly. The origin of the CAMP, like other

magmatic provinces, is still debated. Traditionally the origin of large igneous provinces and its relationships with continental break-up has been regarded as the consequence of melting of a mantle plume head impinging at the base of the lithosphere, so pointing to a deep mantle origin (**Morgan, 1983**; **Richards *et al.*, 1989**; **Hill, 1991; Hill *et al.*, 1992**; **Courtillot *et al.*, 1999**). More recently, an alternative non-plume class of models has been pointed out to explain the occurrence of these igneous provinces, relating the continental break-up and rifting to lithospheric processes and to the dynamics of the upper mantle. The plume incubation hypothesis, for example, postulates that beneath stable supercontinents with thick thermal (perisphere) or chemical (tectosphere) roots the upper mantle warms up over time, resulting in thermally driven uplift, rifting and magmatism (**Anderson, 1994**). Another model by **King & Anderson (1995, 1998)** is the Edge Driven Convection (EDC), that is an instability in the convective rolls in the upper mantle that occurs at the boundary between thick stable lithosphere (for example, an Archean craton) and thinner lithosphere. One of the more recent model is the mantle incubation under a large and stable supercontinent (like Pangea), where the subcontinental heating is generated by an increase of the flow wavelength in the convective mantle, caused by continental aggregation and leading to a less efficient heat removal (**Coltice *et al.*, 2007**).

In the following paragraphs I will briefly describe the occurrence of CAMP magmatic products across the four continents in which these are preserved.

5.1 CAMP SUBPROVINCES

5.1.1 Southwest Europe

- **FRANCE**: the Kerforne dike in West Brittany, France, is the northernmost occurrence of CAMP (**Jourdan *et al.*, 2003**). It is an intrusive body, 100 km long with a variable thickness up to 30 meters which splits into two branches in its northern part. This tholeiitic dike intrudes reactivated NW-SE Hercynian faults, crosscutting igneous and metamorphic rocks of the Armorican Massif. $^{40}Ar/^{39}Ar$ geochronology gives ages ranging from 193.4±3.7 to 174.3±3.3 Ma (isochrones ages), being the oldest age the closest to the magmatic event and falling in the range of other $^{40}Ar/^{39}Ar$ ages of the CAMP basalts, while the youngest probably record a hydrothermal event. Geochemical and isotopic data confirm that the Kerforne dike is similar in composition to most low-TiO_2 CAMP tholeiites;

- **PORTUGAL and SPAIN**: CAMP products are represented by sills, dikes, and lava flows occurring in localized areas. The sills outcrop across most of the Pyrenean chain both in France and Spain, in the southern Aquitania basin (France) and in the Cantabrian range (Spain). The 550 km long and up to 300 m thick Messajena-Plasencia dike trending NE-SW across the central-western Iberia is the most impressive outcrop of this domain (**Cebriá *et al.*, 2003**; **Youbi *et al.*, 2003**). Smaller dikes occur along the coast of SW Portugal. In the Pyrenean basin, tholeiitic doleritic (ophites) sills from the Bedous region (Aspe Valley in south Aquitania) have been dated by the U-Pb method on zircon, by ion micro-probe (**Rossi *et al.*, 2003**) revealing an age of 198.7±2.1 Ma and displaying a composition of continental tholeiitic basalts comparable with that of other rocks from Pyrenees, the Messajena-Plasencia dike and other CAMP products. Extrusive products are represented by lava flows and pyroclastic deposits (generally associated in the most complete sequence). In the Bosmediette area (from Ariège to Basque country), "Ségalas Tuffs" are supposed to be the eruptive equivalent of the Bedous ophites (**Rossi *et al.*, 2003**). In the Algarve and Santiago do Cacém basins of southern Portugal (**Verati *et al.*, 2007**; **Martins *et al.*, 2008**), the basins are filled by lava piles with maximum thickness of about 100 m, composed by no more than about 10 lava flows interstratified with sedimentary layers and volcanocalstic products (**Martins *et al.*, 2008**). Tholeiitic affinity, low TiO_2 (up to 1.2 wt%) and incompatible element patterns (LILE and LREE enrichments relative to HFSE and HREE) show the affinity of these magmatic rocks to the other CAMP continental tholeiites. A weighted mean $^{40}Ar/^{39}Ar$ age of 198.1±0.4 Ma (**Sebai *et al.*, 1991**; **Verati *et al.*, 2007**) represents the best estimate of the age of CAMP in this region, highlighting that the Iberian Mesozoic magmatism belongs to the main peak of CAMP.

5.1.2 West Africa

- **ALGERIA**: basaltic magmatism occurs in the Saharian platform (southwest Algeria) and in the Saharan Atlas, the eastern continuation of the Moroccan High Atlas. In the southwest Algeria CAMP magmatism occurs as NE-SW to ENE-WSW trending dikes, some of them hundred kilometres long (up to 800 km, Ksi-Ksou dike), sills intruding Neoproterozoic to Paleozoic terrains in three contiguous basins and two small and few meters thick lava flows (**Chabou *et al.*, 2007**). Sparse geochemical data of

the doleritic dikes and tholeiitic lava flows show a low TiO_2 content, similar to the low-Ti CAMP basalts. $^{40}Ar/^{39}Ar$ weighted mean minimum ages range from 192.7±3.0 to 197.9±2.0 Ma (on plagioclase separates by incremental step-heating technique) for the less altered samples. In the Ksour Mountains of the Saharian Atlas volcanic outcrops are represented by thin metric lava piles, where are recognizable three basaltic units, geochemically similar to the Moroccan CAMP low-Ti tholeiites, interbedded with metric silico-clastic and evaporitic strata (**Meddah *et al.*, 2007**).

- **MALI**: in northern Mali, the CAMP is represented by one of the densest dike swarms (with some sills) outcropping in the Taoudenni basin, located about 1000 km from the western African margin, just in the middle of the West African Craton (**Sebai *et al.*, 1991**; **Verati *et al.*, 2005**). Unlike the other known swarms (North America, Liberia, French Guyana) no univocal preferential trend in the dike directions is evident. However, it is possible to recognize two prevailing trends (N-S and E-W), where the former predominates in number of dikes on the latter. Geochemical analyses allow distinguishing two differentiation trends on the base of the TiO_2 content and La/Yb and Th/Y enrichments, being the N-S trending group more enriched in highly incompatible elements than the E-W trend one. These incompatible element variations are comparable to those described for the Moroccan CAMP lava flows (**Bertrand *et al.*, 1982**; **Marzoli *et al.*, 2004**). $^{40}Ar/^{39}Ar$ geochronology (plateau ages on plagioclase separates) confirms the relation to the CAMP magmatic event with a main peak at 198.1 Ma. Notable is also the presence of the 7000 km^2 large Kaarta sill (**Bertrand & Coffrant, 1986**).

- **GUINEA**: here the CAMP tholeiites are represented by enormous volumes of magma intruded in Archean and Paleozoic basement mainly as sills, namely on the Fouta Djalon plateau, spanning an area larger than 1000 km^2 and reaching a thickness of up to 500 m of doleritic/gabbro norite. A voluminous mafic to ultramafic laccolithic layered intrusion, the Kakoulima complex, extends on the coast for 50 km and up to 1000 m in thickness (**Diallo *et al.*, 1992**). Both sills and laccolith intruded along old NW-SE lineaments reactivated during the Mesozoic (**Bertrand & Villeneuve, 1989**). Also a minor N-S trending dike swarm occurs in Guinea, West of Fouta Djalon. Geochemical analyses show that Guinea intrusions are low-Ti and are characterized by negative Nb-Ta anomaly and LILE enrichments

(**Deckart *et al.*, 2005**), while $^{40}Ar/^{39}Ar$ dating by **Deckart *et al.* (1997)** gave for the magmatic event an age spanning between 200 and 195 Ma.

- **SIERRA LEONE**: the Freetown Layered Complex is a 65 km long, 14 km wide and 7 km thick, rift related tholeiitic intrusion formed by mafic-ultramafic cumulate rocks (**Hattori & Chalokwu, 1995**; **Chalokwu *et al.*, 1999**; **Chalokwu, 2001**) intruded above a Paleozoic metamorphic basement. The age of the Freetown Complex is 193±3 Ma (**Beckinsale *et al.*, 1977**) based on a Rb/Sr whole rock isochron of a composite gabbro-granophyre.

- **LIBERIA**: high-Ti (TiO_2 up to 4 wt%) and low-Ti tholeiitic dikes have been documented in Liberia (together with French Guyana and the north-east Brazil) by **Dupuy *et al.* (1988)** and **Mauche R. (1989)**. The NE-SW trending dikes intrude Precambrian basement and K-Ar dating by **Dalrymple *et al.* (1975)** gave ages between 177±4 and 197±6 Ma, while a more tight interval by **Mauche R. (1989)** gave ages ranging between 186±4 and 201±2 Ma.

5.1.3 Northeastern North America

- **CANADA**: the Fundy Basin, Nova Scotia, in the Canadian Atlantic region is the northern part of the Newark Supergroup, a series of Mesozoic extensional sedimentary basins which follow the Appalachian Orogen, coincident with the Appalachian gradient anomaly and considered to approximate the edge of the Precambrian-Early Paleozoic basement. In the Fundy Basin, the CAMP magmatism is represented by the North Mountain Basalt, composed by three lava units exposed for a length of 200 km and an average thickness of 250 m (**Greenough & Papezik, 1987**; **Dostal & Greenough, 1992**, **Kontak D. J., 2003**; **Kontak, 2008**) where very recent $^{40}Ar/^{39}Ar$ ages determination ranged from 198.9±0.7 to 201.0±1.4 Ma (**?**) . In addition, basalts from Grand Manan Island, New Brunswick (**McHone, 2005**) are correlated with the North Mountain Basalt. Also prominent NE-SW trending dikes are present: the Avalon dike in Newfoundland, the Shelburne dike in Nova Scotia, the Caraquet dike in New Brunswick and Minster Island (**Pe-Piper *et al.*, 1992**; **Dostal & Durning, 1998**). U/Pb (**Hodych & Dunning, 1992**; **Schoene *et al.*, 2006**) and $^{40}Ar/^{39}Ar$ (**Kontak D. J., 2003**) ages for the North Mountain Basalt gave respectively 202±1 and 201.0±2.5 Ma. The rocks of the Shelburne ($^{40}Ar/^{39}Ar$ plateau ages, **Dunn**

et al.), Avalon and Caraquet dikes (whole rock K-Ar, **Hodych & Hayatsu, 1988**) yielded similar ages.

- **UNITED STATES**: as said before the Newark Supergroup consists of a series of extensional Mesozoic basins between the Appalachian Mountains and the Atlantic coast from Newfoundland in Canada to South Carolina in U.S.A., while elsewhere the CAMP products are found in far land until Georgia and Alabama (**King, 1961, 1971**) and to the South in Florida (**Heatherington & Muller, 1999**). In the United States these basins are, from North to South the Deerfield, Hartford, Pomperaug, Newark, Gettysburg, Culpeper and Richmond basins. In these basins occur tholeiitic basalts (lava flows) and doleritic intrusions (sills and dikes). On the base of sedimentary strata below and interbedded with basalt lava flows it is possible to correlate these among distinct basins (**Olsen *et al.*, 2003**). Moreover drilling and seismic reflection revealed the presence of high-Ti basaltic rocks more south beneath the Cretaceous-Cenozoic cover in the Florida Coastal Plain (**Heatherington & Muller, 1999**), partly similar to high-Ti CAMP basalts from Liberia and French Guyana basalt. Whole rock K/Ar and $^{40}Ar/^{39}Ar$ ages on dikes and lava flows yielded early Jurassic ages (**Dooley & Wampler, 1983**; **Lanphere, 1983**) between 185-195 Ma. U/Pb ages from Palisades and Gettysburg sills yielded ages of 200.9±1.0 and 201.3±1.0 Ma, respectively (**Dunning & Hodych, 1990**). More recently, $^{40}Ar/^{39}Ar$ dating on plagioclase separetes by **Hames *et al.* (2000)** gave ages for the Orange Mountain and Hook Mountain basalt flows in the Newark basin of 201.0±2.1 (mini-plateaux age) and 198.8±2.0 Ma (plateaux age) and a mean age of 199.5±2.0 Ma for three dike samples from South Carolina. Dikes from Northern Carolina yielded $^{40}Ar/^{39}Ar$ plateau ages on plagioclase separates ranging between 198±1.8 and 197±1.7 Ma (**Beutel *et al.*, 2005**), while plateau ages from six Carolinas dikes range from 200.9±1.5 to 198.8±2.3 Ma (**Nomade *et al.*, 2007**). Very recent $^{40}Ar/^{39}Ar$ plateau ages have been obtained on ultra-sericitizied plagioclase selections from basalts of the Hartford-Deerfield basins, yielding ages from 198.6±2.0 to 199.8±1.1 Ma (**?**).

5.1.4 South America

- **BRAZIL**: the Brazilian CAMP magmatism is represented by low- and minor high-TiO_2 tholeiites as dike swarms (Roraima and Cassiporé dikes)

intruding Archean and Proterozoic basement, sills intruding Paleozoic sediments (Amazonia basin) and lava flow sequences overlying Paleozoic and Triassic sedimentary basins (Maranhao basin, Lavras da Mangabeira, Anarì and Tapirapuà). The tholeiitic dike swarms studied by **DeMin *et al.* (2003)** are present near the coast in North-eastern Brazil extending toward French Guyana and Surinam (**Nomade *et al.*, 2000, 2002**; **Deckart *et al.*, 1997, 2005**) with length of up to 300 km and thickness up to 100 m with prevailing NE-SW to NNE-SSW trends, which are the main orientations of Proterozoic dikes and fault systems occurring in the same regions. The Cassiporé dike swarms (like the French Guyana ones) probably continue in the contiguous regions of Western Africa, where they are represented by coeval Early Jurassic tholeiitic dikes of Liberia (**Dupuy *et al.*, 1988**). The Amazonia sill is the most extensive magmatic body in the northern part of South America, covering an area of more than 106 km2 and a variable thickness from 100 to 800 m being contiguous in three sedimentary basins. Lava outcrops occur in the western Maranhao basin, at present covering about 40.000 km^2 (Mosquito Formation; **Bellieni *et al.*, 1990**) and with a thickness of up to 175m (**Almeida, 1986**) and further east with the Lavras da Mangabeira flows. Finally, the southernmost Brazilian outcrop are represented by the Anarì and Tapirapuà lava flows, with a present surface of about 1000 km^2 each and thicknesses of 80 and 315 m, respectively. The Brazilian CAMP magmatism is dominated by low-TiO_2 basalts (<2 wt%) displaying a strong negative Nb and Ti anomaly, while few high-TiO_2 (up to 4 wt%) dikes in the Cassiporé and Maranhao region show no significant Nb and Ti anomaly (**DeMin *et al.*, 2003**, **Merle *et al.*, submit.**). In general, the Brazilian CAMP yielded $^{40}Ar/^{39}Ar$ ages of 199.0±2.4 Ma (**Baksi & Archibald, 1997**; **Marzoli *et al.*, 1999**, **DeMin *et al.*, 2003**), indistinguishable from those of other CAMP basalts. Nevertheless, a younger age of 192.7±1.8 Ma from a Cassiporé dike sample is well consistent with $^{40}Ar/^{39}Ar$ ages for French Guyana dikes and similar to those of some samples from the West Africa margin in Guinea (189.8±1.9 Ma; **Deckart *et al.*, 1997**). Moreover, paleomagnetic data, over a wide area of the South American CAMP provide further evidence for a coeval magmatic event with West Africa, North America and SW Europe ones (**Marzoli *et al.*, 1999**; **Besse & Courtillot, 2002**; **Ernesto *et al.*, 2003**).

- **BOLIVIA**: the Tarabuco-Entre Rìos sill in Bolivia intrudes Triassic sediments in a Permian to Middle Jurassic rift system (**Sempere *et al.*, 2002**).

In the same area more than 3000 km away from the Atlantic margin, occur also lava flow piles, which cover a surface of ca. 30.000 km^2 and reach a maximum thickness of 150m, being at present the southernmost basaltic occurrence of the entire CAMP (**Bertrand *et al.*, 2005**).

- **FRENCH GUYANA and SURINAM**: In French Guyana/Surinam the CAMP basalts occur mainly as dikes intruding the northern and eastern part of the Palaeoproterozoic Guyana Shield (**Deckart *et al.*, 1997, 2005**; **Nomade *et al.*, 2002**) with a NNW-SSE main trend and minor horizontal sill-like structures forming the Devil's Island NE of Kourou. The doleritic dikes, tens of meters thick and up to 100 km long, show both low and high TiO_2 contents (1.85-3.56 wt%), weak LREE enrichment over HREE, no LILE enrichment and no significant Nb anomalies with a positive Ti anomaly (**Bertrand *et al.*, 1999**; **Nomade *et al.*, 2002**). Anisotropy of magnetic susceptibility (AMS) data indicate that dikes have horizontal flow direction indicating lateral injection of the magma during two major magma pulses (**Nomade *et al.*, 2000**). $^{40}Ar/^{39}Ar$ ages for these dikes range from 198.3±2.0 to 188.7±1.9 Ma (**Deckart *et al.*, 1997**).

6 CAMP IN MOROCCO

As described previously, it is possible to recognize from North to South three tectonic units in the Morocco region: the fold-and-thrust Rif-Tell chain, the Atlas

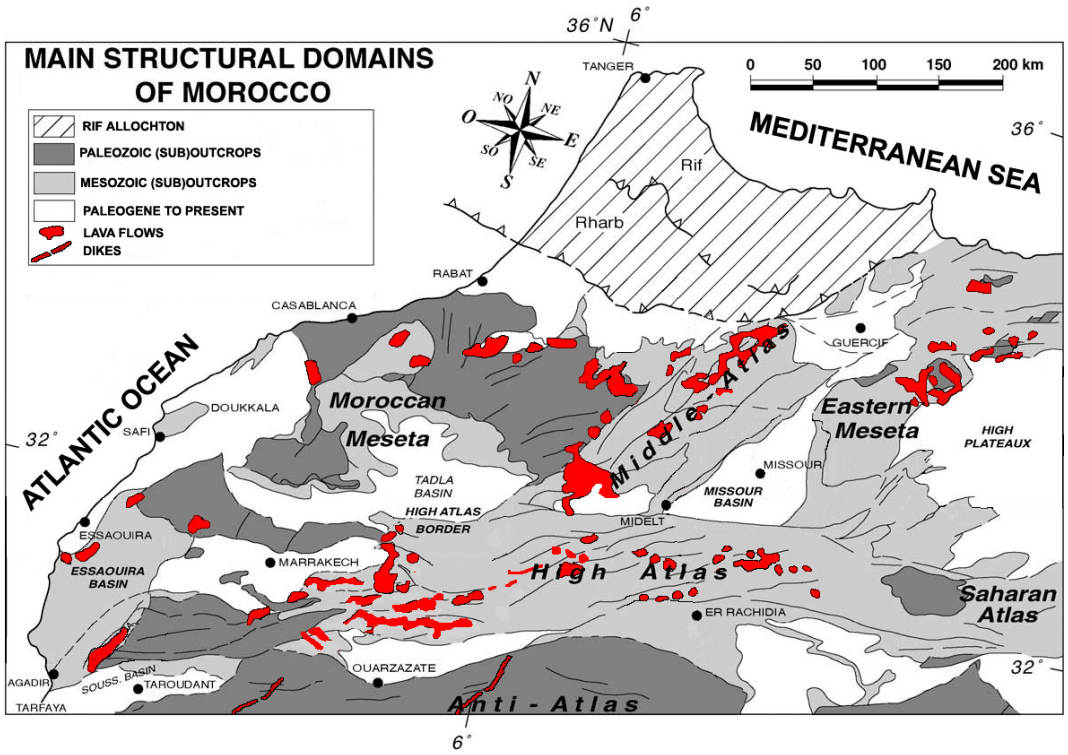

Figure 6.1: Simplified geological map of Morocco with highlighted the main CAMP outcrops (modified after **Ellouz *et al.*, 2003** and **Youbi *et al.*, 2003**).

mountains and its western and eastern Mesetas and finally the Anti-Atlas chain, separated from the Atlas system by South Atlasic fault and marking the transition with the southern Precambrian West African craton. The CAMP magmatic products outcrop as dykes and sills, lava flows and rare pyroclastic sequences in the Atlasic domain (lava flows and pyroclastic sequences in wide syn-rift Triassic sedimentary basins) and in the Anti-Atlas chain (dikes and sills intruding Precambrian to Paleozoic terranes) (Fig. 6.1). Strongly tectonized lava flow sequences

belonging to the CAMP are recognized in the Rif-Tell domain (**Mahmoudi, pers. comm.. 2007**). The formation of the Triassic sedimentary basins in the High Atlas was greatly influenced by the pre-existing ENE-WSW trending late Hercynian basement fabric (**Laville, 1991**). The present day outcrops of the rocks deposited within these basins are primarily controlled by the Alpine reverse faults associated with the Tertiary Alpine orogeny (**Michard, 1976**). This resulted in a number of ENE-WSW elongated narrow basins bound by Tertiary faults and filled with silicoclastic continental red beds and basalts, capped by Jurassic carbonates. It is possible to recognize fifteen individual basins, showing ill-defined limits, were the Triassic-Jurassic boundary is present (**Youbi *et al.*, 2003**). Overlying the Hercynian basement it is possible to find in stratigraphic order two lithologic sequences: coarse detrital rocks made of sandstones and conglomerates, and felsic lava flows both of them of Permian age (**Wartiti, 1990**). Above there is a sequence of sedimentary rocks comprising conglomerates and marine to fluvial sandstones (Oukaimeden sandstone, **Beauchamp, 1987**), dated as Carnian by palynomorphs (**Cousminer & Manspeizer, 1976**). Above this there is a sequence made up of finer grained sandstones, siltstone, pelites and evaporites (**Piqué & Laville**; **Roy *et al.*, 1997**). Within the upper part of this sequence occur the successions of CAMP lava flows, straddling the Triassic-Jurassic boundary, which ages are supported not only by determinations on palynomorphs on siltstone layers, but also by $^{40}Ar/^{39}Ar$ dating of the tholeiitic basalts (**Knight *et al.*, 2004**, **Marzoli *et al.*, 2004**, **Verati *et al.*, 2007**, **Nomade *et al.*, 2007**).

6.1 DIKES AND SILLS

The Foum Zguid dyke is one of the major dykes of the Anti-Atlas domain, extending with a NE-SW trend for more than 200 km, with a thickness of 100-150 m. It cuts Precambrian and Paleozoic terrains affect by Hercynic orogeny (**Leblanc, 1973**; **Hollard, 1973**). Locally, a system of small parallel and perpendicular dykes, a few meter thick, forms a dense swarm accompanying the Foum Zguid dyke (**Youbi *et al.*, 2003**). Another important dyke, rarely mapped on CAMP maps, is the NE-SW trend Asdrem dyke, ca. 100 km westward the Foum Zguid dyke. The Asdrem dyke extends for 200 km, with a variable thickness up to 150 m, crossing Precambrian and Paleozoic formations and intruding along late-Hercynian fractures (**Youbi *et al.*, 2003**). In the Drâ plain, the sills, which present variable extension and thickness, are intruded in the folded sedimentary

sequences closely following all structures (**Hollard, 1973**), occurring preferentially along folding between layers of contrasting competence. However, neither the sill dolerites nor the dykes that fed them and link sills at different stratigraphic levels show any deformation (**Youbi *et al.*, 2003**).

6.2 PYROCLASTIC DEPOSITS

The "Oued Defali Formation" is a volcano-sedimentary complex in the El Hajeb region, with a kilometric length and a thickness of 10 to 50 m, overlying the latest basalt flows, following **Ouorhache (1987)** and **Baudelot *et al.* (1990)**. The volcano-sedimentary sequence comprises red siltstones, tuffaceous siltstones and lapilli or lapilli-breccia tuffites. The sequence is covered by marly sediments of lagoonal character resembling the Hettangian-Sinemurian "Harira Formation" (**Baudelot *et al.*, 1990**). The stratigraphic series continues with Liassic dolomites.

6.3 LAVA FLOWS

Lava flows can be found in the both branches of the Atlas belt (Middle and High Atlas), as in the Western and Eastern Meseta, well exposed in Triassic sedimentary basins and subsurface (in this case their knowledge comes from well data). In most basins, the thickness of the lava piles is 100 to 200 m. The greatest thickness is reached on the southern flank of the Central High Atlas (as high as 350 m) while in the inter-basin area the thickness of the lava piles is not more than 50 m. The basaltic sequence is composed of one to several lava flows (up to 34 flows at Tiourjdal in the southern flank of Central High Atlas for a total section thickness of ca. 300 m, **Knight *et al.*, 2004**) with or without inter-bedded red-clastic, evaporitic or carbonated sedimentary layers, testifying brief periods of volcanic quiescence. The variations in thickness between the lava piles can be explained either by differential subsidence of the basement in the different parts of the Atlasic domain during the emplacement of the lava flows, or by the emplacement of the volcanic flows on an irregular paleotopography or on a horst and graben structure (**Youbi *et al.*, 2003**). In the Eastern Meseta (Oujda Mountains) the basaltic outcrops are sometimes associated with a system of dolerite dykes trending NE-SW to E-W, and NW-SE in the Zekkara Massif and in Jbel Ez Zidour near Jerrada (**Oujidi, 1996**). Interbedded with the lava flows are limestone intercalations, up to 13 m thick, dated as Upper

Ladinian-Lower Carnian (**Crasquin-Soleau *et al.*, 1997**), witnesses a shallow epicontinental sea open to Tethys reflecting an important time interval between the two eruptive events. Unfortunately for the present work no data of complete lava pile sections are available, mainly because of the paucity of outcrops and the general bad preservation of basalts in this part of Morocco. So only some samples from 3 localities around Oujda/Jerada zone will be described for the sake of completion. In the NE-SW trending chain of the Middle Atlas (MA) it is possible to recognize two structural domains where the basaltic lava flows outcrop: a tabular plateau, made of red beds and basaltic lava flows capped by dolomites unconformable on the Paleozoic basement and an eastern folded part, which consist of anticlinal ridges separated by synclines filled with mid-Jurassic sediments (**Mahmoudi & Bertrand, 2007**). The ridge axes consist of Triassic red beds and discontinuous magmatic formations, dismembered by faults. Two complete lava flow sections placed in the MA will be described, the Agourai section (ca. 30 km S from Meknes) and the Oum R'RBia section (ca. 90 km S from Meknes). In the High Atlas (HA), we recognize basal conglomerates characterized by coarse and immature detrital facies, usually unconformably lying over deformed Paleozoic rocks and sometimes Lower Permian red beds. Above them there are siltstones ("Ramuntcho siltstones") whose sedimentary facies and faunas suggest a marine coastal environment, followed by the Oukaimaden sandstones, up to 600 m in thickness, composed of Carnian sandstones, deposed in marine to fluviatile environments. Finally, there are the upper fine-grained pink to red siltstones with thin beds of gypsum and salt (**Beauchamp, 1988**; **Roy & Piqué, 2001**). This last part of the continental sequence contains the CAMP tholeiitic basalt overlying, not only in the HA but also in other localities (Argana basin as well as in the MA) a sequence of alternating gray and black siltstone, which yield a Late Triassic palynological assemblage (**Marzoli *et al.*, 2004**). Belonging to the Central High Atlas (CHA), three complete lava flow sections will be described in this work: the Oued Lahr section (ca. 60 km E from Marrakech) on the northern flank of CHA and the Tiourjdal and Telouet sections (both of them ca. 80 km SE from Marrakech) on its southern flank, ca. 50 km S from the Oued Lahr section. These sections are the most complete and thick (up to 34 lava flows with a total thickness of 350 m at Tiourjdal) of the HA, and of Morocco in general. Moreover, in the CHA all four lava units are preserved and are subdivided on the base of chemostratigraphic criteria (**Bertrand *et al.*, 1982**; **Patchtère, 1983**), from the base to the top: the Lower, Intermediate, Upper and Recurrent Unit. In the Western Meseta (WM), where the Triassic-Liassic deposits crop out, the

stratigraphic sequence is similar to that described for the HA. However, the lower part of Carnian age is not preserved and only the upper part unconformably lying on top of the Hercynian basement represented by few meter thick pebbles conglomerate, with thickness varying from 100 to 3000 m (**Roy & Piqué, 2001**). A complete lava flows section near the Maaziz locality (ca. 55 km SE from Rabat) placed in the northern part of WM will be described.

7 MOROCCAN LAVA PILES

The oldest lava flows in the HA, MA and WM occur on a sequence of alternating grey and black siltstone layers, constituting the uppermost part of the

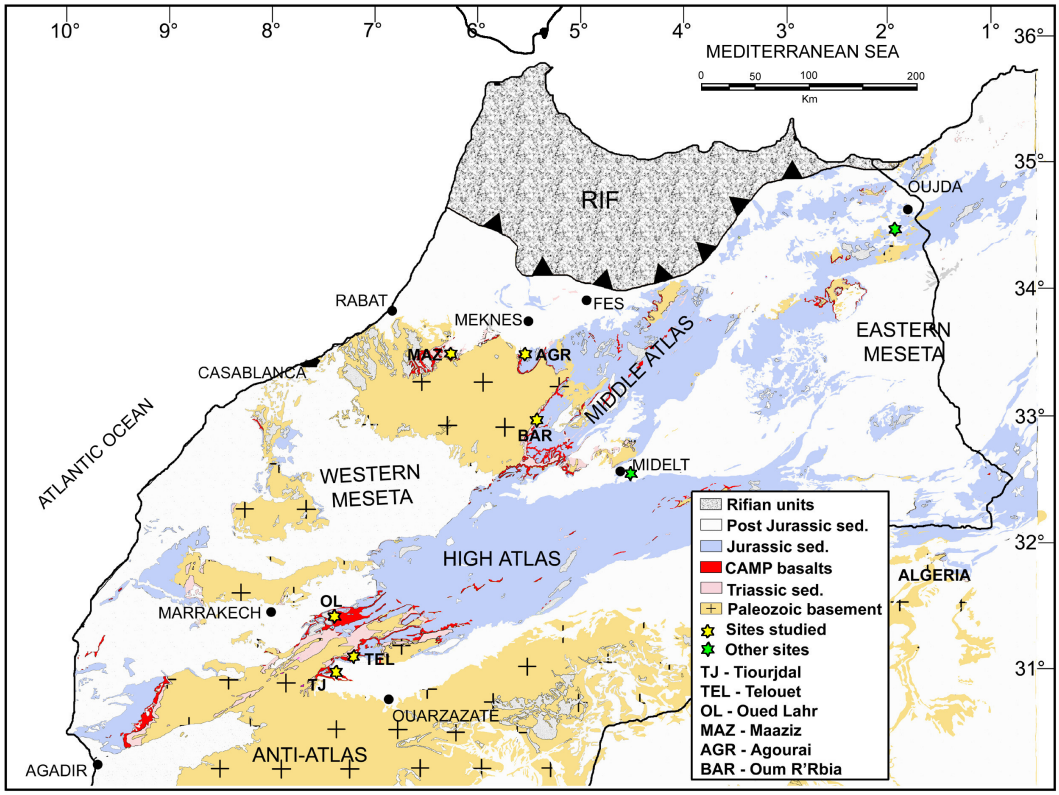

Figure 7.1: Simplified geological map of Morocco with indicated the six lava sequences studied (yellow stars) .

Upper siltstones of **Beauchamp (1988)**, which are well preserved in several localities of the Atlas chain and of the Mesetas. The contact between the black and grey siltstones appears to be tectonically undisturbed below the oldest lava flows in the MA and CHA (**Marzoli *et al.*, 2004**), being the sediments sometimes mingled with the basalts or plastically deformed by loading deformation structures and showing no hardground or paleosol, suggesting that no prolonged

depositional hiatus occurred before the volcanism. In the CHA analyses of the siltstone palynological assemblage yield a typical Late Triassic association of *Patinasporites densus*, *Corollina murphyae*, *Gliscopollis meyeriana*, *Classopollis torosus* and other sporomorphs (**Warrington, 1996**), similar to that observed in mudstone layers sampled just below the oldest basaltic flow in Argana basin lava sequences (**Marzoli *et al.*, 2004**). In the CHA, the studied sections are: Tiourjdal and Telouet (on the southern side of the CHA) and Oued Lahr (on the northern side of the CHA) (Fig. 7.1). Here, the basaltic lava piles are the thickest of Morocco, composed by up to 33 lava flows at the Tiourjdal locality (with one more stratigraphically successive flows at the Agouim locality, few kilometers NW of Tiourjdal) and a total thickness up to ca. 350 m, taking in account the thick sedimentary layer between the top of the Tiourjdal lava flow section and the ca. 15 meters massive lava flow at Agouim. The MA, WM, are represented by 3 complete sections: Maaziz (North WM), Agourai and Oum R-Rbia (also named "Barrage" due to the dam under construction where the section crops out) in the MA (Fig. 7.1). In these locations the lava piles are less thick (up to 150-170 m) and made up of no more than 18/20 flows. From the base to the top, it is possible to recognized on the basis of field observation, petrography, mineral chemistry and geochemistry (**Bertrand *et al.*, 1982**; **Marzoli *et al.*, 2004**) four distinct basaltic units, even if each of these does not outcrop everywhere: the Lower, Intermediate, Upper and Recurrent Unit. From EM few samples from three different locations around the Oujda's Mountain. The three locations sampled lack of complete volcanic sections and sometimes the outcrops are deeply altered. Five of the seven samples collected belongs to the Lower Unit and notably two of them appear to be quite evolved compared to the other studied basalts, because of the presence in the paragenesis of biotite, micrographic quartz and alkali feldspar. The absence of vitreous ground-mass and the holocrystalline texture led to think to an intrusive product, even if the field evidences do not allow to confirm this hypothesis. The two remaining samples seem to have an Intermediate Unit compositions, on the base of preliminary XRF analyses. A brief petrographic description will be done in the 11.

7.1 LAVA PILES OF THE CENTRAL HIGH ATLAS

The Tiourjdal section is placed on the southern flank of the CHA, ca. 80 km SE from Marrakech. The outcrop is characterized by sub-horizontal (12°-15° dip) massive basaltic flows. With a height of ca. 300 m of exposed flows this

is the thickest known lava pile of the Moroccan CAMP (**Knight *et al.*, 2004**) (Fig. 7.2). At its base there are the black and grey siltstones mentioned above, although the contact is not locally visible but outcropping slightly to the south. On the top, the last basaltic lava flow is covered by Liassic dolomitic limestones, Cretaceous limestones and sandstones. From the base to the top, the thickness of

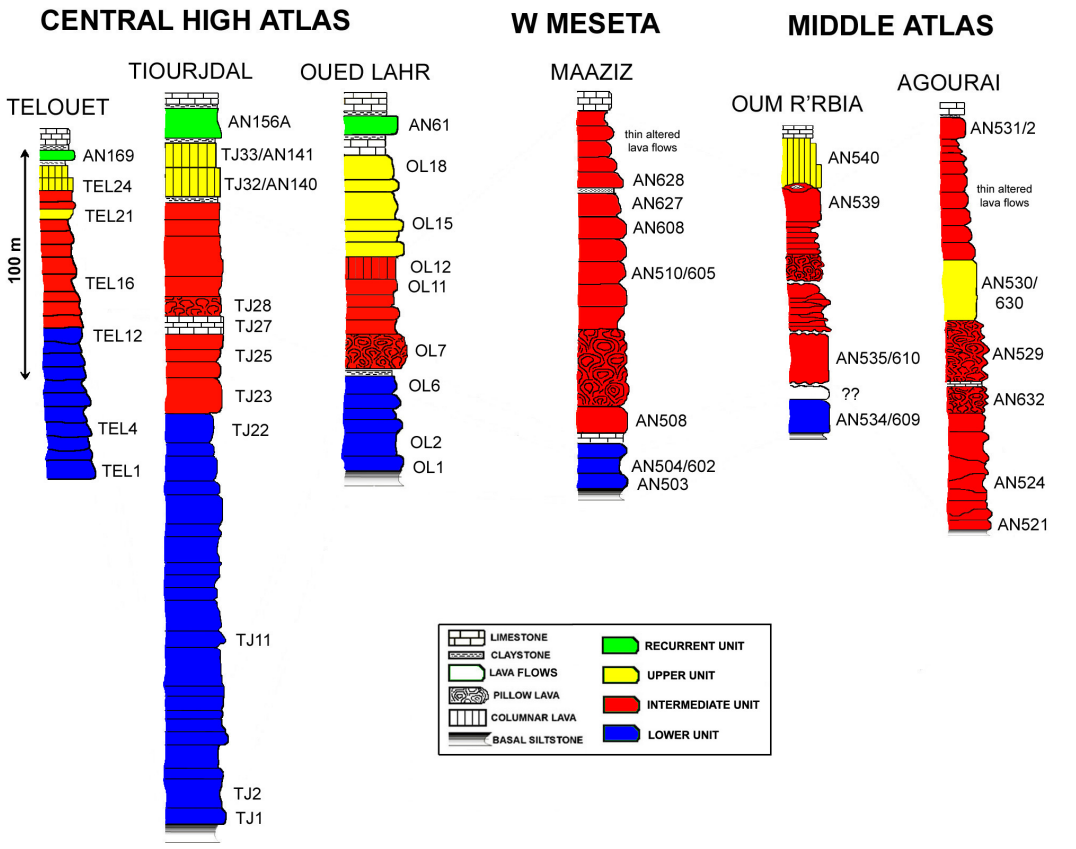

Figure 7.2: Simplified stratigraphy of the CHA, MA and WM lava sequences with indicated the stratigraphic positions of samples analysed. Chemostratigraphic unit after **Bertrand *et al.* (1982)**.

the lava flows generally increases. It is possible to recognize, on the basis of field evidences, at least 33 lava flow, partitioned on the basis of chemostratigraphic data in 22 lava flows belonging the Lower Unit, 9 lava flows for the Intermediate and 2 lava flows for Upper Unit. The Recurrent Unit is not present at Tiourjdal section, but it does few kilometers NW at Agouim locality as a single well exposed 15 or more meters thick lava flow. Even here at Agouim the sedimentary layers below (baked limestone) and above (Liassic red clays) the single massive lava flow are well visible. While the Lower and Intermediate Units are composed of multiple 1 to 10 meters thick lava flows, which present well preserved volcanic

features like pillow lavas and interdigitated flow lobes, the Upper and Recurrent Unit are made up of two and one massive decametric lava flows respectively, showing a columnar jointing, often characteristic of this units. The succession of lava flows is continuous with just one important sedimentary layer, a limestone bed ca. 1 meter thick in the middle of the Intermediate Unit. Paleomagnetic analyses showed that this layer is characterized by a magnetic inversion (**Knight *et al.*, 2004**), making this sedimentary bed a fundamental marker, first of all for the stratigraphic inter-correlations between the lava piles in the Moroccan area but also with the counterpart lava flows in the sedimentary basins of the Newark Supergroup, Eastern North America (**Olsen *et al.*, 2003**; **Whiteside *et al.*, 2007**). This brief magnetic reversal recorded in this sedimentary layer is also crucial for global correlations as it can be correlated with reversals recorded in very Late Triassic or T-J boundary strata from a marine section in England (**Hounslow M. W., 2004**) and in the continental Newark basin of Eastern North America where it occurs just below the oldest CAMP basalt flow (Orange Mountain basalt; **Kent & Olsen, 2006**). According to the different possible correlations, the reversal within the Tiourjdal section would in fact define the T-J boundary (**Knight *et al.*, 2004**) or be correlative with an Early Jurassic reversal (**Whiteside *et al.*, 2007**) as observed in the Paris basin strata (**Yang *et al.*, 1996**). Data relative to petro-mineralogic descriptions and compositions used in this work refer to 33 samples sampled for paleomagnetic studies (Tiourjdal sequence, **Knight *et al.*, 2004**) and from 7 other samples collected for geochemical analyses (Agouim sequence). In the following petrographic description I will include samples from the Agouim section because of its close position to the Tiourjdal section, hereafter I will speak about this two sections as one, referring them as Tiourjdal section.

The Telouet section is located ca 17 km NE from the Tiourjdal section. Here there are 24 lava flows preserved with a thickness of the exposed lava pile of ca 120 m (Fig. 7.2). The base of the Telouet section is not exposed, leading to an underestimation of the total number of lava flows. The top of the lava pile is the same of the Tiourjdal section capped by Early Jurassic limestones. Even if it is problematic to recognize the real number of lava flows, it is possible to assign, by chemostratigraphic analyses, the sampled lava flows to the four volcanic units as: at least 12 lava flows belonging to the Lower Unit, 10 lava flows belonging to the Intermediate Unit, three lava flows to the Upper Unit and again after about 30 meters thick sediments one single massive lava flow belonging the Recurrent Unit. An interesting point is that the first occurrence of a lava flow with an

Upper Unit geochemistry fingerprint happens between the two uppermost Intermediate lava flows. This point will be discussed further on. As for Tiourjdal sequence, the petro-mineralogic analyses have been done on 23 samples collected for paleomagnetic studies (**Knight *et al.*, 2004**) and 1 for geochemical analyses.

The third section studied in the CHA is at the Oued Lahr locality. Placed on the northern flank of the CHA, it is ca. 50 km NNE from Tiourjdal. All four CAMP units are preserved here with a total thickness of the lava pile of at least 210 m (Knight et al., 2004) (Fig. 7.2). Like at Telouet the contact with the black and grey siltstone is not directly observed, but is outcropping nearby. The lowermost unit is the thickest of the site, containing at least nine lava flows, with variable thickness from less than 1 meter to more than 20 meters. Sometimes the flow contacts are baked and show a vesiculated flow top thus marking the distinction between two contiguous lava flows. Overlying the Lower Unit flows and marking the onset of the Intermediate Unit is a well preserved pillow lava which grades into an aerial lava flow. In the pillow lava, paleomagnetic analyses have identified a magnetic reversal (**Knight *et al.*, 2004**). Notably, it is not clear if the two magnetic reversal discovered in the Tiourjdal and Oued Lahr lava piles record the same magnetic inversion event, because of its different stratigraphic position within the Intermediate Unit, just in the middle at Tiourjdal and at the base of the unit at Oued Lahr. Overlying the pillow lava flow, at least five more Intermediate flows are recognizable with the uppermost of these showing a prismatic columnar jointing. A thin limestone layer separates the Intermediate from the Upper Unit. The lowermost flow of this unit is represented by pillow lavas grading into sub-aerial lava at the top. Altogether it is possible to recognize at least six lava flow belonging the Upper Unit. Finally, overlying a ca. 50 m thick sedimentary layer (red clays and limestones), there is the Recurrent Unit lava flow. Even for Oued Lahr, like for Tiourjdal and Telouet sequences, I will describe 18 samples collected for paleomagnetic studies (**Knight *et al.*, 2004**).

7.2 LAVA PILES OF THE WESTERN MESETA

The Maaziz section is placed in the North WM, ca. 60 km SE from Rabat (Fig. 7.1). Here, outcrop only the Lower and Intermediate Units, for a estimated lava pile thickness of 100-110 m (Fig. 7.2). The lava flows are quite tilted (ca. 30°). The section overlies red clays, which at the top have at least a 1-1.5 meter of black and grey siltstones in undisturbed contact with the first lava flow. Only

three flows, each with a constant thickness of 2-3 meter build up the Lower Unit. Above there is a less than 1 meter thick deeply stratified carbonate-evaporite layer. The Intermediate Unit builds up the remaining section, consisting of at least 13 lava flows easily identifiable due the good exposure of the section. The Intermediate Unit lava pile is composed by two flow groups separated by a thin (few centimeters) baked red siltstone layer. The lower group is made up of a 15 meter thick pillow lava flow (almost at the base of Intermediate Unit) and 7 massive lava flows with thickness decreasing upward. Only one of these flows has not been sampled due its dangerous accessibility. Above the thin sedimentary layer, at least 5 thin (less than 1 meter) lava flows are recognizable. Only the first one has been sampled, being the others almost completely altered and difficult to distinguish. Finally a carbonate layer caps the volcanic sequence. Samples collected in the Western Meseta, Middle Atlas and Eastern Meseta come from two field work in 2007. The first sampling campaign had the purpose to individuate new complete lava sequences, to gain some basaltic samples for geochemical analyses, to understand how many units are preserved, and siltstone samples for palynological analyses. The second campaign was aimed at a complete flow by flow (where possible) geochemical and paleomagnetic sampling with more siltstone samples for palynological studies. On the whole, at the Maaziz sequence have been collected 5 basaltic samples belonging the Lower Unit and 11 for the Intermediate Unit. 10 samples for paleomagnetic analyses have been collected (9 from lava flows and 1 from the carbonate-evaporite sedimentary layer).

7.3 LAVA PILES OF THE MIDDLE ATLAS

The Agourai volcanic pile, placed 30 km S from Meknes, has a thickness of ca. 140 m in which is preserved only the Intermediate Unit (Fig. 7.2). The stratigraphy at the base and at the top of the lava pile is nearly the same as for the other sections: below the lava flows we found the black and grey siltstone in undisturbed contact with the lowermost flow, while the whole section is capped by red siltstones and carbonates. This sample has been found in an anomalous stratigraphic position, at the base of a 10-12 m thick lava flow overlying a 10 m thick pillow lava flow, apparently between flows belonging the Intermediate Unit. More in general, the stratigraphy of Agourai section is quite complex because of the terrigenous and debris cover, lacking only in the steepest part of the volcanic section, which hides the flow contacts. Moreover the presence of faults cutting the volcanic pile and displacing the lava flows led to a difficult reconstruction

of the volcano-stratigraphic section and the correct numeration of lava flows. In general the thickness of the flows decrease upward, with fresher massive columnar jointing with interdigitated lava lobes and thick pillow lavas flows at the base of the Intermediate Unit while thin lava flows at the top of the section are mostly weathered. At least 14-15 flows are recognizable, even if the number is probably underestimate especially in the uppermost part of the section, where the flows are thinner, more altered and partially covered by debris. At the top we found red siltstones and thick limestone layers. 15 samples belonging the Intermediate Unit have been collected, while only 2 represent the Upper Unit at Agourai. The Lower Unit has not been detected. For paleomagnetic studies have been collected 11 samples (10 from lava flows and 1 from a limestone layer in the middle of the sequence).

The Oum R-Rbia (Le Barrage) section is placed ca. 90 km S of Meknes (Fig. 7.1), outcrops with a thickness of ca. 120-130 m on a hill where recently works for a dam have exposed a section with the Lower to Upper units are outcropping (Fig. 7.2). The section is well visible along a service-road used for the construction of the dam, even if sometimes interrupted by debris build-up. Like in other sections the lowermost flow overlies a thin black siltstones layer and lower red siltstones. Also here the Lower Unit is represented by few lava flows (no more than 3), with only one massive 10-12 m thick lava flow sampled, being the overlying flow (or 2?) unattainable and unsampled due to the bad section orientation and the debris and vegetation cover. The Intermediate Unit is well represented by numerous lava flows, with more or less the same features of the Agourai and Maaziz sections: thickness of lava flows decreasing upward, numerous thin (1-1.5 m thick) highly vesicular lava flows in the uppermost part of the unit frequently displaying interdigitated lava lobes and presence of syn-volcanic faults. Also the Intermediate Unit has not been sampled completely (flow by flow) because of the bad preservation of the thin lava flows and the difficulties in reconstructing a precise volcanic stratigraphy. Altogether, it is possible to recognize about 14-15 lava flows, of which only 8 sampled. The uppermost 8-10 m thick pillow lava flow of the Intermediate Unit, with fragments of baked red siltstones well visible between the pillows ("peperites"), mark the onset of the massive columnar jointed lava flow, at least 10 meters thick, belonging the Upper Unit. The presence of pillow lavas with mingled clay-siltstone records the emplacement of lava flows in an subaqueous, maybe lagoon ambient. Moreover, the interdigitation between the columnar flow with a more vesicular one is visible and above this another thick columnar lava layer, even if it is not clear if it records a second Upper Unit

flow or not. Finally red siltstones cap the top of volcanic section. As a whole, 2 basaltic samples belong the Lower Unit, 10 basalts have an Intermediate Unit composition while only one records the Upper Unit. Globally, 9 samples have been collected for paleomagnetic analyses.

8 SAMPLING AND METHODOLOGIES

8.1 TYPES OF SAMPLING

During the field works have been sampled, where it was possible, the more massive, unfractured and non vesiculated lava flows to obtain the freshest samples as possible in order to avoid as best as possible contamination effects by secondary deposition minerals (siliceous/carbonate veins and/or vesicle). Nevertheless, there have been sampled the black siltstones at the base of the lava piles and the sedimentary layers interbedded with lava flow, for a complete interdisciplinary study allowing a better comprehension about the genesis of basaltic lava flows. There have been collected three kind of samples:

- massive basaltic chunks for XRF, EMP, ICP-MS, LA-ICP-MS, isotopic and geochronology analyses;
- basaltic and limestone (from the interbedded sedimentary layers) cylindrical cores (Ø=2.5 cm, 10-12 cm long) sampled with a special driller for paleomagnetic analyses;
- samples of black and grey siltstone at the base of the lava piles for palynological studies to constrain a lower age for the inset of CAMP event.

8.2 PROCEDURE FOR SAMPLE PREPARATIONS

The procedure for sample preparations consisted of cutting off from the basaltic rocks the outer and less fresh parts, recognizable for their brownish halo and then cm-thick slices from the inner and freshest parts. From the cm-thick slice have been cut a pair of rectangular bricks, from which have been obtained 30 μm thin sections for mineralogical-petrographic analyses under polarized microscope and successive EMP analyses (major and minor element compositions on plagioclases and augitic and pigeonitic pyroxenes) and 100 μm thin sections for LA-ICP-MS analyses (trace element spot compositions on plagioclases and augitic pyroxenes). The remaining parts of the slices have been crushed, using an agate

mortar to minimize contamination effects, to obtain a very fine powder (<10 μm) for successive XRF analyses for determination of bulk major and minor element compositions. An aliquot of this powder has been used for ICP-MS analyses for determination of bulk trace element contents. Subsequently some of the basaltic rocks, after careful inspection under the optical microscope of the freshest samples which displayed fresh mineral with no alteration in the groundmass, were selected for crushing and to obtain granulates of different sizes. The coarsest granulates (800<Ø<2000 μm and 2000<Ø<3000 μm) have been analyzed under binocular microscope to pick-up the freshest grains used for isotopic analyses on whole rock (Sr-Nd-Pb-Os systematics; performed by R. Merle). Like the coarsest, also the finest granulates (315<Ø<200 μm, 200<Ø<160 μm and 160<Ø<100 μm) have been carefully inspected under binocular microscope to separate, by hand picking, a granulate of the freshest, unfracturated and inclusion-free plagioclases, used for $^{40}Ar/^{39}Ar$ dating.

8.3 ANALYSES ON WHOLE ROCK

8.3.1 XRF (X-Ray Fluorescence)

Mineral major element whole rock compositions have been analyzed at the Dipartimento di Geoscienze, Università di Padova (Italy) by X-ray fluorescence methodology (XRF). After the preparation of a ca. 5 mm granulate, the sample is grinded in a milling machine RETSCH RS100, using an agatha mortar to obtain a fine powder (<10 μm). After loss on ignition determination (L.O.I.), the sample is mixed with $Li_2B_4O_7$ powder (1:10 ratio) and then melted at 1150°C in a Pt-Au-Rh crucible with a melting-machine CLASSIE FLUXY. The glassy disk obtained is highly homogeneous and ready to be analysed. The instrument used is a sequential spectrometer WDS Philips PW2400, using the SuperQ program for quantitative and qualitative analyses. The analyzed major elements are Si, Ti, Al, Fe, Mn, Mg, Ca, Na, K e P (as oxides weight per cent), while the trace elements are Sc, V, Cr, Co, Ni, Cu, Zn, Ga, Rb, Sr, Y, Zr, Nb, Ba, La, Ce, Nd, Pb, Th e U (as ppm). Detection limit for major elements are 0.01% for Al, Mg and Na, 0.2% for Si and 0.005% for Ti, Fe, Mn, Ca, K and P. Detection limits for trace elements vary from 3 ppm (i.e. U and Th) to 10 ppm (for LREE).

8.3.2 ICP-MS (Inductively Coupled Plasma - Mass Spectrometry)

Inductively coupled plasma-mass spectrometry (ICP-MS) is well established as a rapid and precise method for the determination of the rare earth elements (REEs) and trace elements in geologic samples (**Jenner *et al.*, 1990**; **Longerich *et al.*, 1990**) Unfortunately analyses have been performed on three different laboratories: for Tiourjdal sequence (series AN100 and TJ) samples have been analysed at Grenoble. Samples from Telouet (series TEL) and Oued Lahr (series OL) have been analysed at Acme Analytical Laboratories in Vancouver (Canada), while samples from WM/MA (Maaziz, Agourai and Oum R'Rbia, all series AN500 and AN600) have been analysed at WSU GeoAnalytical Laboratory, Washington State University (United States). Unfortunately, only for the last one laboratory are available the analytical procedure. In the Chap. 14, I'll try to compare ICP data from different laboratories, in order to find out eventual analytical bias among different ICP data-set.

At WSU GEOANALYTICAL laboratory (United States) samples have been prepared with an combination fusion-dissolution home-developed method which consists of a low-dilution fusion with Lithiun-tetraborate followed by an open-vial mixed acid digestion. This method allows to analyze 14 REEs and 13 additional trace elements in a wide range of geologic samples without having to make assumptions as to the presence or absence of resistant mineral phases. The dissolution with HF after the Lithium-tetraborate fusion quantitatively removes silica and more than 90% of the flux as gaseous fluorides, leaving clear, stable solutions for analysis. The Flux used for the fusion is Lithium-tetraborate (Spectromelt® A-10, EM Science, Gibbstown, NJ). Reagents are HNO_3 69-70% (Fisher ACS plus grade), HF 48-52% (Baker ACS reagent grade), $HClO_4$ 67-71% (Fisher Trace Metal Grade), and H_2O_2 (Baker ACS Reagent). The HF is further purified before use by sub-boiling distillation in a teflon still. All water used is > 18 MΩ deionized water from a Nanopure analytical grade water system (Barnstead/Thermolyne). Powdered samples are mixed with an equal amount of lithium tetraborate flux (typically 2g), placed in a carbon crucible and fused at 1000° C in a muffle furnace for 30 minutes. After cooling, the resultant fusion bead is briefly ground in a carbon-steel shatterbox and a 250 mg portion is weighed into a 30 ml, screw-top Teflon PFA vial for dissolution. The acid dissolution consists of a first evaporation with HNO_3 (2 ml), HF (6 ml), and $HClO_4$ (2 ml) at 110° C. After evaporating to dryness, the sample is wetted and the sides of the vial are rinsed with a small amount of water before a second evaporation with $HClO_4$ (2 ml) at 160° C. After the second evaporation, samples

are brought into solution by adding approximately 10 ml of water, 3 ml HNO_3, 5 drops H_2O_2, 2 drops of HF and warmed on a hot plate until a clear solution is obtained. The sample is then transferred to a clean 60 ml HDPE bottle diluted up to a final weight of 60 g with deionized water. Solutions are analyzed on an Agilent model 4500 ICP-MS and are diluted an additional 10X at the time of analysis using Agilent's Integrated Sample Introduction System (ISIS). This yields a final dilution factor of 1:4800 relative to the amount of sample fused. Instrumental drift is corrected using Ru, In, and Re as internal standards. Internal standardization for the REEs uses a linear interpolation between In and Re after **Doherty, 1989**) to compensate for mass-dependant differences in the rate and degree of instrumental drift. Isobaric interference of light rare earth oxides on the mid-heavy REEs can be a significant source of error in ICP-MS analysis, so tuning is optimized to keep the CeO/Ce ratio below 0.5%. Correction factors used to compensate for the remaining oxide interferences are estimated using two mixed-element solutions. The mixed element solutions contain. Standardization is accomplished by processing duplicates of three in-house rock standards with interspersed within each batch of 18 unknowns. Concentrations, oxide and drift corrections are then calculated offline using a spreadsheet.

8.3.3 Sr and Nd isotopic systematics

Twelve samples for $^{87}Sr/^{86}Sr$ and $^{143}Nd/^{144}Nd$ isotopic measurements have been analysed at Instituto de Geocências Universidade de São Paulo, Brazil by Thermal Ionization Mass Spectrometry (TIMS). After the preparation of a ca. 5 mm granulate, the samples were grinded in a milling machine RETSCH RS100, using an agata mortar to obtain a fine powder (¡10 micron). In the chemical separation has been used a separation column with ionic exchange AG50WX8 resin for Sr bulk separation from REE. A second column loaded with LN Spec for Nd and Sm separation has been used. A Finnegan Mat Mass Spectrometer Model 262 has been used for Sr and Nd ratios determinations up to 200 analyses for each sample in order to minimize standard deviation. During analyses have been used $^{146}Nd/^{144}Nd = 0.7219$ and $^{86}Sr/^{88}Sr = 0.1194$ to correct mass fractionation (**Steiger & Jäger, 1977**). NBS487 was analysed as external standard yielding, during laboratory runs (13/8/06 - 17/9/06), $^{143}Nd/^{144}Nd = 0.511838 \pm 0.000015$ and $^{87}Sr/^{86}Sr = 0.710254 \pm 0.000015$ value. Blank measurements yielded a mean value of 0.3 ng for Nd and 1 ng for Sr. All errors reported are quoted at 2σ level.

8.3.4 Paleomagnetism

Approximately 2.5 cm diameter, 5-10 cm length, specimen cores were collected using an ASC Scientific Pomeroy Model D026-C gasoline powered drill. The cores were oriented using an ASC Scientific Pomeroy Model OR-2 precision orienting fixture and a Brunton compass. When possible, approximately 6-8 cores from each flow were collected. Cores were cut into 1.5 cm long specimens using a rock saw. At least 2 specimens from each core were cut, when possible. The specimens were sanded after cutting in order to remove any stray metal that may have been left by the rock saw. All measurements were conducted in a lab shielded from the earth's magnetic field. Each specimens natural remanence magnetization (NRM) was measured on a 2-G Enterprises superconducting DC SQUID magnetometer. Every specimen was then put through alternating field demagnetization in 2 mT intervals up to 10 mT to remove any viscous remagnetization. At this point one specimen from each core was put through thermal demagnetization in an ASC Model TD-48 thermal demagnetizing furnace in 15-25°C steps up to 650°C. The number of steps varies due to different behavior of the specimens during demagnetization, in order to obtain the most measurements when the sample is losing the most magnetization, so we watch, and do smaller steps when the magnetization is changing the most). When a second specimen from a core was available, (∼90% of our cores had 2 specimens) the second specimen was demagnetized in an alternating field in 21 steps up to 100 mT. Specimen directions were calculated as a Fisher mean of measurements of the last remaining component of magnetization as determined by analysis of a Zijderfeld diagram (typically used step 20-80 mT for AF samples, and 300-500°C for thermal samples). Flow means were calculated as a Fisher mean of the specimen directions from each flow.

8.4 ANALYSES ON MINERAL PHASES

8.4.1 EMPA (Electron Micro Probe Analyses)

Mineral major element compositions have been analyzed at the Dipartimento di Geoscienze, Università di Padova (Italy) on a microprobe CAMECA SX50 of the IGG-CNR laboratory using ZAF on-line data reduction and matrix correction procedures. At constant acceleration voltage of 15 kV, the beam current was varied between 15 nA (for plagioclase) and 20 nA (for clinopyroxenes and pigeonites). It was used counting times of 2 minutes both for plagioclase and

pyroxenes with analytical uncertainties of 2% for major elements and about 5% for minor elements.

8.4.2 LA-ICP-MS (Laser Ablation ICP-MS)

In situ trace element analyses of clinopyroxenes and plagioclases were carried out using laser-ablation inductively-coupled-plasma mass-spectrometry (LA-ICP-MS) at IGG-CNR, Unit of Pavia, Italy. The laser probe consists of a Q-switched Nd:YAG laser, model Quantel (Brilliant), whose fundamental emission in the near-IR region (1064 nm) was converted into 266 nm wavelengths using two harmonic generators. The laser power was varied in the range of 0.8-4.2 mW, whereas the spot diameter was in the range of 20-100 μm (mostly 50 μm, 40 μm in the analyses done). The ablated material was analysed by using an Elan DRC-e quadrupole mass spectrometer. Helium was used as carrier gas and mixed with Ar downstream of the ablation cell. Data Reduction was carried out using the Glitter Software. NIST SRM 610 was analysed as external standard (reference values from **Pearce et al., 1997**), while ^{44}Ca has been used as internal standard. Precision and accuracy were assessed from repeated analyses of the BCR-2 or NIST SRM 612 standards and resulted usually better than 10%. Detection limits were typically in the range of 100-500 ppb for Sc, 10-100 ppb for Sr, Zr, Ba, Gd and Pb, 1-10 ppb for Y, Nb, La, Ce, Nd, Sm, Eu, Dy, Er, Yb, Hf and Ta, and usually <1 ppb for Pr, Th and U.

9 PETROGRAPHY AND MINERALOGY OF CENTRAL HIGH ATLAS PILES

Broadly, the Moroccan lava flows have quite homogeneous compositions, ranging from basalts to andesitic basalts with tholeiitic affinity. No evolved rocks (andesites-rhyolites) are present. Nevertheless, the lava flows belonging to the four units are well distinguishable not only on the base of differences of whole rock compositions (major, minor, trace elements and isotopic ratios) but also based on textures, mineral assemblage and mineral compositions which allow us to infer about affinities and differences between volcanic sections situated in different places of Morocco. The textures and mineralogical assemblages have been observed under polarized microscope, while the mineral chemistry are obtained by EMP analyses (on 30 and 100 μm thin sections) and by LA-ICP-MS analyses (on 100 μm thin sections). The proportions between different phases, their occurrences in the different units and their compositional variations will be investigated and discussed in order to establish a petrogenetic grid and allow a better comprehension of the processes occurred during the shallow-level differentiation of the magmas starting from a near primitive parental magma.

9.1 TEXTURES AND PARAGENESIS

As said previously, the samples from the Central High Atlas come from cylindrical basaltic rock cores drilled for paleomagnetic investigation (**Knight *et al.*, 2004**) and they are labelled TJ (for the Tiourjdal section), TEL (for the Telouet section) and OL (for the Oued Lahr section). These samples were used for whole rock chemical analyses (major and minor elements by XRF, trace elements by ICP-MS, isotopes by TIMS) and to obtain 30 and 100 μm thin sections for mineral chemistry by microprobe and LA-ICP-MS analyses. For this study, samples labelled AN were also used, some of them coming from the same (e.g., Tiourjdal) or other sections (for example the Agouim section). These latter are massive samples collected for geochemical and geochronologic analyses and they were used to obtain 100 μm thin sections for trace elements content determinations on pla-

gioclases and clinopyroxenes by LA-ICP-MS analyses (except one sample, OL14, coming from the Oued Lahr section). The mineral assemblage mainly consists of olivine (always altered), plagioclase, clinopyroxenes (both augitic and pigeonitic) and oxides (magnetite±ilmenite). No hydrated primary minerals (like biotite or amphibole) do occur.

9.1.1 Tiourjdal sequence

- **The Lower Unit**: it is composed by 22 lava flows sampled at Tiourjdal (samples from TJ1, at the base, to TJ22, hereafter the samples numeration will be done in stratigraphic order, i.e. from the base to the top of the unit) with 2 more samples AN49 and AN134 sampled nearby. Samples TJ1, TJ2, TJ11, AN49 and AN134, after a mineralogical-petrographic study under the polarized microscope, were selected for detailed EMP chemical analyses of the main mineral phases (see next paragraph), and sample AN134 was further selected for trace element LA-ICP-MS analyses on clinopyroxene and plagioclase. Lava flows belonging to the Lower Unit have a hypocrystalline intergranular to sub-ophitic texture, with a mineralogy dominated by almost equigranular euhedral plagioclases, with normal progressive zoning, and sub-euhedral to euhedral clinopyroxenes, sometimes zoned. Olivine occurs sometimes included in clinopyroxenes or grouped in little clusters, showing their typical shape with an euhedral habitus despite almost complete alteration into hiddingsite. In the samples TJ2, TJ3, TJ22 and AN49 occur also abundant and fresh pigeonite, a low-Ca pyroxene, recognizable for its high relief (higher than the augitic clinopyroxenes one) and rounded fractures. Sparse oxides, represented by magnetite with ilmenite exsolutions, are rarely euhedral, being more frequently in allotriomorphic plagues between the plagioclases and clinopyroxenes or rarely as micro-phenocrysts in the glassy ground-mass. In some flows the oxides are present only in the glassy ground-mass as tiny euhedral crystals or with a dendritic shape. The glassy ground-mass shows spherulitic devitrification and rare to abundant vesicles are filled with secondary minerals, like zeolites, chalcedony and more rarely quartz. These features are more or less constant along the whole unit, with few exceptions regarding the presence and abundance of olivines, vesicles or glassy ground-mass.

- **The Intermediate Unit**: it is composed of 9 lava flows (samples TJ23 to TJ26, TJ28 to TJ32) and 2 others sampled nearby (AN137A and AN138).

Samples TJ23, TJ25, TJ32 (30 μm thin sections), AN137A and AN138 (100 μm thin sections) were analyzed by EMP for mineral chemistry, while trace element analyses by LA-ICP-MS were performed on samples AN137A and AN138. The Intermediate Unit samples show an intersertal ophitic to sub-ophitic texture with abundant euhedral to sub-euhedral zoned clinopyroxenes. Elongated idiomorphic laths of plagioclase show multiple inverse rhythmic zoning, with rare rounded core and frequent glassy brownish patches of melt included within the crystals. Altogether plagioclases and clinopyroxenes are surrounded by a network of little euhedral plagioclase showing an acicular shape and normal zoning. Olivines are completely absent (except for one sample, TJ23, where they are altered), while abundant pigeonite is present as big euhedral to sub-euhedral phenocrystals, or with rounded shapes, in most of the samples (TJ25, TJ26, TJ29, TJ30, TJ31). The oxides show a euhedral habitus, are isolated or grouped to mimic a dendritic shape, and are present exclusively in the glassy brownish ground-mass. More rarely, they are large and euhedral (sample TJ25 and TJ26). The abundant glassy ground-mass, showing spherulitic devitrification, is more abundant than in the Lower Unit, as the vesicles filled with secondary minerals.

- **The Upper Unit**: it is composed by 2 samples from Tiourjdal (TJ33 and TJ34) and 1 more sampled nearby (AN141). All three samples were analyzed by EMPA for mineral chemistry (TJ33 and TJ34 on 30 μm thin sections and AN141 on 100 μm thin sections) while AN141 was used for trace element determinations by LA-ICP-MS. The texture of the flows belonging to the Upper Unit is porphyric with a microlithic ground-mass of plagioclase, clinopyroxenes and oxides, dominated by euhedral phenocrysts of fresh augitic clinopyroxene, frequently showing typical sector zoning (hourglass), and euhedral plagioclases often showing multiple inverse rhythmic zoning with cores with rounded borders and glassy brownish patches of melt included within them. Rare sparse olivines, preserving a euhedral to sub-euhedral shape, occur completely altered in the ground-mass.

- **The Recurrent Unit**: one lava flow sampled at the Tazgaoute section (sample AN156A) few kilometers from Tiourjdal. This sample was analyzed both for EMPA and LA-ICP-MS analyses on 100 μm thin section. It has a porphyric microlithic texture dominated by big euhedral phenocrysts of plagioclase, rare augitic clinopyroxenes with a very fine ground-mass of

plagioclases, clinopyroxenes and rare euhedral oxides. The plagioclase crystals show rounded core and inverse rhythmic zoning.

9.1.2 Telouet sequence

- **The Lower Unit**: it is composed by 10 lava flows (samples TEL1 to TEL4, TEL6, TEL7, TEL9 to TEL12). Samples TEL1 and TEL4 were analyzed by EMPA for mineral chemistry on 30 ±m thin sections, while no sample was used for LA-ICP-MS analyses. In general the samples coming from Telouet show a stronger alteration with respect to the Tiourjdal samples, thus limiting the microprobe analyses. The flows belonging to the Lower Unit show an intergranular intersertal texture with equigranular euhedral laths of plagioclase and poikilitic clinopyroxenes. The plagioclases have rarely large size and show progressive zoning. In one sample (TEL1) it has not been possible to analyze the plagioclases due to their deep alteration in sericite. Even the clinopyroxenes are often altered, showing large patches of chlorite, making the microprobe analyses difficult especially in the rare large phenocrysts. Olivines are well recognizable for their shape even if they are always altered like in the other sections. Apparently no pigeonite is detectable in these samples, even if the pervasive alteration could obliterate the presence of this mineral. Oxides have always micrometric size in the abundant glassy ground-mass, showing an euhedral shape. The brownish glassy ground-mass show abundant spherulitic devitrification and vesicles filled with zeolite minerals, calcite, chlorite and quartz.

- **The Intermediate Unit**: it is composed by 10 lava flows (samples TEL13, TEL15 to TEL18, TEL19a, TEL19b, TEL20, TEL22, TEL23). TEL16 and TEL 23 were analysed by EMP for mineral chemistry, no samples was analysed by LA-ICP-MS. Also the Intermediate Unit shows a deep alteration, thus making the mineralogic-petrographic description in thin section difficult. The textures of these samples range from intergranular intersertal, with abundant glassy ground-mass, to intergranular to sub-ophitic from the base to the top of the Intermediate Unit. At the same time, plagioclase shows acicular to euhedral habitus in laths with rhythmic zoning. Clinopyroxenes increase their size upward in the unit, from poikilitic to euhedral habitus sometimes enclosing acicular plagioclase, and showing the typical sector zoning of augitic clinopyroxenes. Pigeonite is present only in two flows TEL22 and TEL23, being more abundant in the latter than

the former. Olivine, differently from Tiourjdal and Oued Lahr, is present, being recognizable because of its euhedral shape, often grouped in clusters, and is totally replaced by secondary minerals. Apparently, it does not appear in the sample TEL22 and TEL23, where pigeonite occurs. Even the oxides change their habitus upward in the unit from dendritic, in the glassy ground-mass, to euhedral to sub euhedral large phenocrysts. The glassy ground-mass shows abundant spherulitic devitrification and presence of vesicles filled with secondary minerals.

- **The Upper Unit**: it is composed by 3 lava flows (samples TEL21, TEL24, TEL25). Only TEL24 was analysed by EMP. Except for TEL21, that even if deeply altered shows an intergranular textures, TEL24 and TEL25 have the typical porphyric microlithic texture of the Upper Unit. Few euhedral clinopyroxene and plagioclase phenocrysts and rare agglomerates of these minerals are interspersed in a quite fine ground-mass of acicular plagioclase, clinopyroxenes and oxides. Large euhedral olivines are completely altered. No vesicles are detectable.

- **The Recurrent Unit**: it consists of only one lava flow occurs at Telouet (sample AN169). This sample was used both for EMP and LA-ICP-MS analyses and it comes from a massive rock sampled for geochemical analyses. It has a porphyric microlithic texture dominated by big euhedral phenocrysts of plagioclases, rare augitic clinopyroxenes with a very fine ground-mass of plagioclases, clinopyroxenes and abundant big-size sub-euhedral skeletal oxides. The plagioclase crystals show rounded core with resorption features, inverse zoning with rare clinopyroxene micro-phenocrysts included within and frequent brownish glassy patches of melt. Olivines display their typical habitus but are completely altered.

9.1.3 Oued Lahr sequence

- **The Lower Unit**: it is composed by 6 lava flows (samples from OL1 to OL6). Only sample OL2 was analyzed by EMPA for mineral chemistry, while no sample from this unit was used for LA-ICP-MS analyses. The samples have an intergranular to sub-ophitic texture, dominated by rare fresh euhedral laths of plagioclases with normal progressive zoning, from poikilitic to rare big euhedral clinopyroxenes and from allotriomorphic to sub-euhedral or skeletal oxides, which show ilmenite exsolutions. Olivines are present but always altered. Pigeonite is present in two samples, OL1 and

OL2. Altogether the samples are quite altered, being plagioclases frequently altered into sericite and calcite and the clinopyroxenes altered into chlorite. The glassy ground-mass shows spherulitic devitrification and abundant vesicles filled with zeolite minerals, calcite, hematite and quartz.

- **The Intermediate Unit**: it is composed by 6 lava flows (samples OL8 to OL12). Samples OL10 and OL11 were analyzed by EMPA, while no sample from this unit was used for LA-ICP-MS analyses. Textures vary from intergranular to ophitic intersertal with normal zoned plagioclase laths and poikilitic clinopyroxenes passing to acicular plagioclase and big euhedral sector-zoned clinopyroxene phenocrysts. No olivines are detected. Pigeonite is present only in two samples, OL10 and OL11. Oxides are present only in the glassy ground-mass as little euhedral phenocrysts or showing a dendritic shape. The ground-mass shows partial spherulitic devitrification and rare vesicles filled with secondary minerals.

- **The Upper Unit**: it is composed by 6 lavas flows (samples from OL13 to OL18). The samples OL14 and OL15 were used for EMP analyses, while OL14 was analysed first by EMPA then by LA-ICP-MS. These samples have a porphyric microlithic texture dominated by big euhedral phenocrysts of plagioclase, rare augitic clinopyroxenes with a very fine ground-mass of plagioclase, clinopyroxenes and rare euhedral oxides with a dendritic shape. The plagioclase crystals show rounded core with resorption features, rhythmic zoning with rare clinopyroxene micro-phenocrysts included within and frequent brownish glassy patches of melt. Clinopyroxenes are present in big euhedral phenocrysts, showing sector zoning. Rare euhedral olivines are always altered and replaced by secondary minerals.

- **The Recurrent Unit**: it consists of only one lava flow (AN61) not analysed in this work.

9.2 MINERAL COMPOSITIONS

9.2.1 Olivine

No fresh olivine was detected in all thin sections from the three localities of the Central High Atlas and so it was not possible to analyse them by EMP or LA-ICP-MS. As described previously, the olivine is always present in the Lower and Recurrent Unit in all three sections. Only rarely olivine appears in the

Intermediate and Upper Unit at Tiourjdal and Oued Lahr, nevertheless it is present in all lava flows of the Intermediate Unit at Telouet except for a few flows.

9.2.2 Plagioclase

Plagioclase was investigated by electronic microprobe (EMPA) to study the compositional variation in major and minor elements (see details in methodologies chapter) along some traverses, from the core to the rim, and in some case

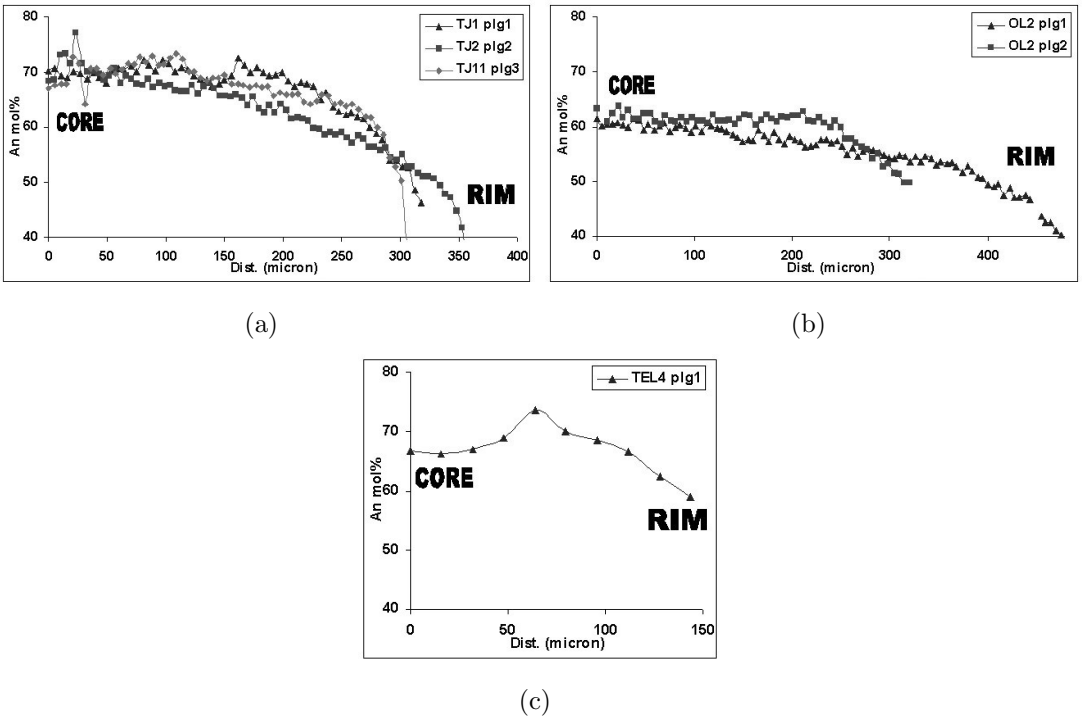

Figure 9.1: Variation of An mol% along core to rim (transects distance in microns) of plagioclase from the Lower Unit at Tiourjdal (9.1(a)), Oued Lahr (9.1(b)) and Telouet (9.1(c)) (EMP analyses). The normal progressive zoning from the core to the rim of phenocrysts is clearly observed. Moderate inverse zoning does occur in a few plagioclase crystals (TJ11 plg3 and TEL4 plg1).

from rim to rim, of the freshest minerals. A narrow spacing between each analysis point (in most cases 5-6 μm) was applied, especially on the minerals which present interesting features (multiple and inverse rhythmic zoning) useful to understand what happened during the crystallization of the magma. In other few cases, a more spaced analysis (ca. 10 μm) was applied, where crystal do not present interesting features (monotonous progressive zoning). Together with augitic clinopyroxenes (and in some cases pigeonite), plagioclase is the predominant phase which

composes about 45-50 vol.% of the basalts. EMP analyses highlight quite high

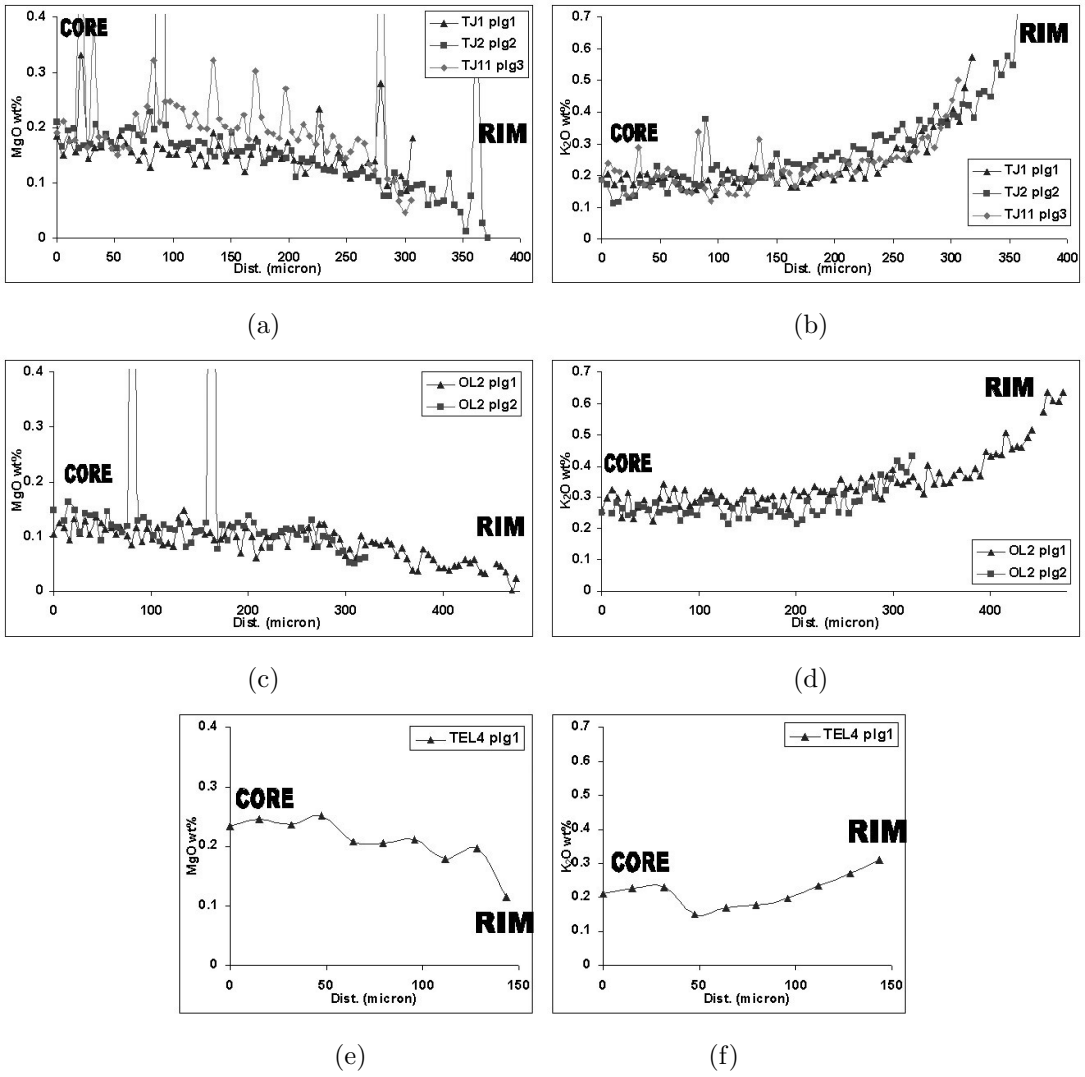

Figure 9.2: Variation of MgO and K_2O wt% along core to rim (transects distance in microns) of plagioclases from the Lower Unit at Tiourjdal (Fig. 7.2a and 7.2b), Oued Lahr (Fig. 7.2c and 7.2d) and Telouet (Fig. 7.2e and 7.2f) (EMP analyses). It is well visible the positive and negative correlation with An content, respectively for MgO and K_2O, as described in the text.

plagioclase compositional homogeneity or similar zoning within each unit and between the same units of different sections. The plagioclase phenocrysts from the Lower Unit range from bytownite to andesine compositions ($An_76Ab_{23}Or_1$ to $An_{38}Ab_{60}Or_3$ with An=100×Ca/(Ca+Na+K), Ab=100×Na/(Ca+Na+K) and Or=100×K/(Ca+Na+K); Ca, Na and K are expressed in atoms). Their most striking feature is the normal progressive zoning in all the lava flows, displayed by a monotonous decrease of anorthite (An) content from core to rim of the

phenocrysts. Inverse zoning is rare, with moderate increase of An of up to 5-7

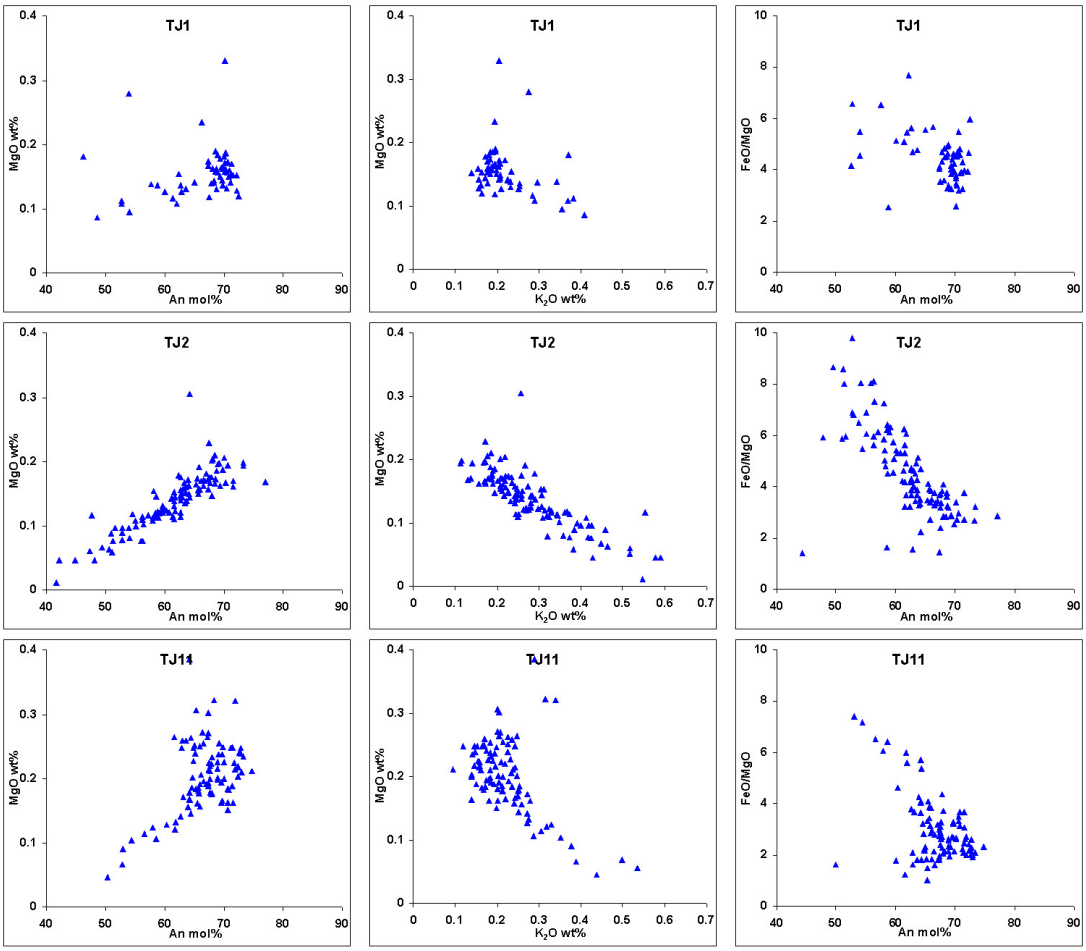

Figure 9.3: Compositional trend in the Lower Unit at Tiourjdal section. It is visible the increasing content of An, of the MgO for the same content of K_2O and the decreasing of FeO/MgO ratio.

mol% (Fig. 9.1). At the same time the MgO and K_2O content are positively and negatively correlated, respectively, with the An content, as expected for a normal crystallization of phenocryst from a progressively evolving magma. The K_2O content tends to increase towards the rim (Fig. 9.2) passing from ca 0.1-0.2 wt% in the core to ca. 0.6-0.7 wt% at the more albitic rims. By contrast, MgO varies from about 0.3 wt% in the core to 0.1 wt% at the rim (Fig. 9.2). While the compositional variation in An and K_2O is well defined, those of MgO variation are less pronounced, maybe depending of slightly faster diffusivity of Mg^{2+} compared to K^+ in the plagioclase lattice (**Costa *et al.*, 2003**), so leading to a less marked zoning in MgO composition of the crystal. In the most complete Lower Unit of Tiourjdal, 7 plagioclases from four lava flows were analysed by

EMPA (one plagioclase for TJ1, 2 for TJ2, 2 for TJ11 and 2 for AN134). On the base of data it is possible to recognize a compositional trend (Fig. 9.3) from the base to the top of the unit: the An and MgO content increase in the core, respectively from 72.50 to 76.40 mol% and from 0.19 to 0.27-0.30 wt%. Also the K_2O decreases slightly in the plagioclase core from 0.13-0.15 wt% to 0.09 wt% from the lowest to the highest sample of the Tiourjdal Lower Unit. Moreover,

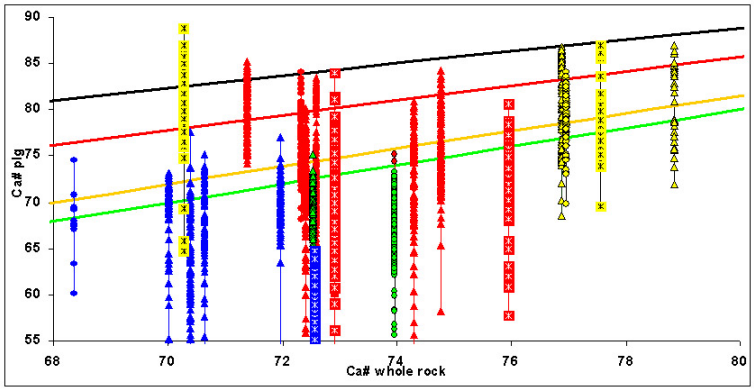

Figure 9.4: $Ca\#_{whole-rock}$ (XRF analyses) vs $Ca\#_{plagio}$ of all analysed plagioclases (EMP analyses) in the Central High Atlas. Curves represent plagioclase compositions in equilibrium with melt for different K_D^{Ca-Na}: green line K_D =1, orange line K_D =1.1, red line K_D =1.5, black line K_D =2. Blue for the Lower Unit, red for the Intermediate Unit, yellow for the Upper Unit and green for the Recurrent Unit. Triangles for Tiourjdal, circles for Telouet and squares with star for Oued Lahr. Explanations in the text.

the FeO/MgO ratio, which on the whole has a large range (from nearly 1.0 up to 9.3) from the base to the top of the unit it decreases from the lower value of ca. 2.5 to 1.0. It is not already clear if this trend is linked to the particular choice of the analysed samples, so being an analytical bias, or if it is real having in this way a petrogenetic meaning. Nevertheless all these data could be compatible with crystallization from slightly less evolved magmas, with higher Ca/Na and MgO and lower K_2O and FeO. Both at Oued Lahr and Telouet, only 1 lava flow belonging to the Lower Unit was analysed, so it is not possible to infer about a possible trend. At Telouet (few analysis points on one plagioclase, sample TEL4) the compositions in An, MgO, K_2O and FeO/MgO fit well those of Tiourjdal plagioclases. At Oued Lahr the three analysed plagioclases (sample OL2) show a systematic lower An, ranging from 63.6 mol% in the core to 40.3 mol% at the rim, lower MgO (no more than 0.16 wt%) and higher K2O (between 0.2 and 0.4 wt%). FeO/MgO also shows higher values from 4 to 9 (see Fig. 9.5, 9.6 and 9.7). In a $Ca\#_{whole-rock}$-$Ca\#_{plagio}$ diagram (Ca#=100*Ca/(Ca + Na)),

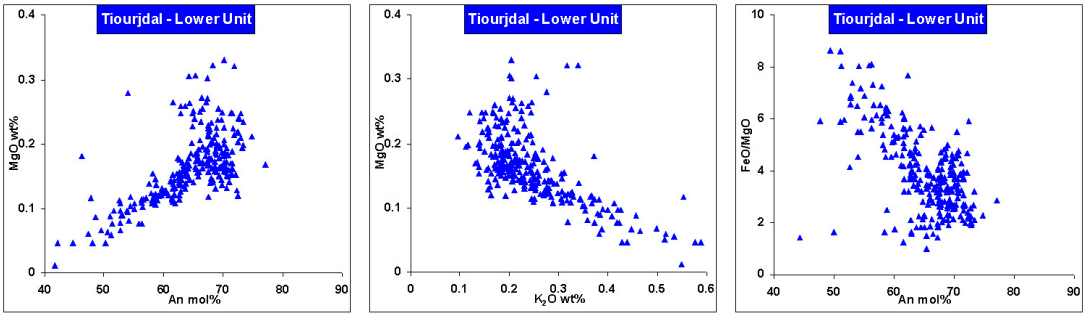

Figure 9.5: Anorthite mol% and K_2O wt% vs MgO wt% and FeO/MgO variations of plagioclase crystals from the Lower Unit at Tiourjdal (EMP analyses).

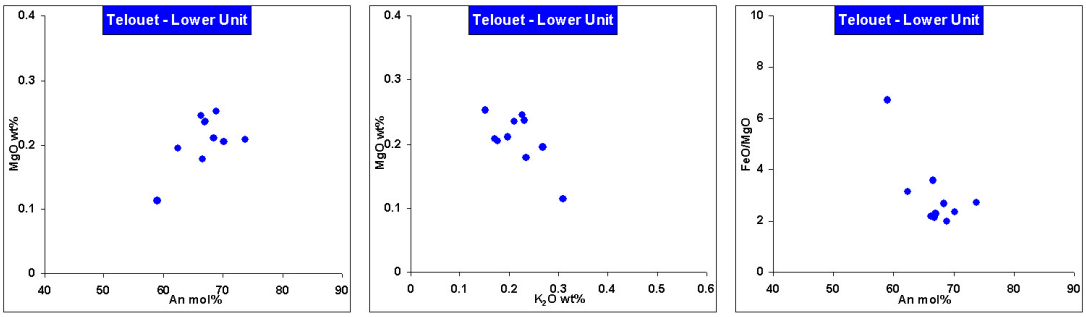

Figure 9.6: Plagioclase Anorthite mol% and K_2O wt% vs MgO wt% and FeO/MgO variations of plagioclase crystals from the Lower Unit at Telouet (EMP analyses).

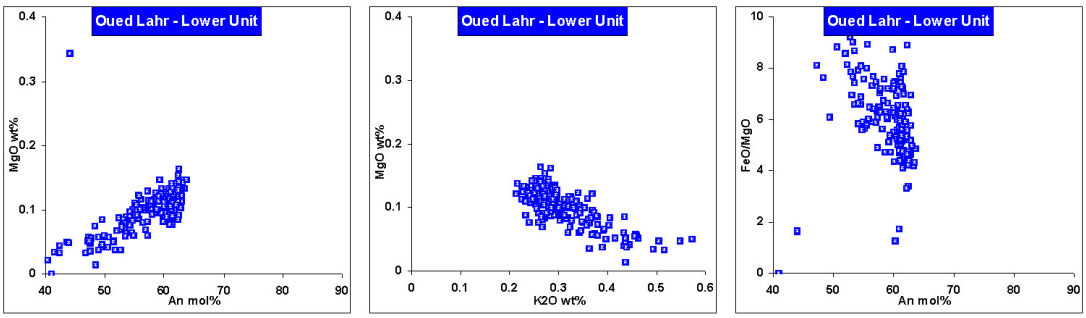

Figure 9.7: Anorthite mol% and K_2O wt% vs MgO wt% and FeO/MgO variations of plagioclase crystals from the Lower Unit at Oued Lahr (EMP analyses).

the cores of plagioclases belonging to the Lower Unit have a composition that is nearly in equilibrium with the whole-rock (mineral/melt K_D^{Ca-Na} between 1 and 1.1, green and orange lines in Fig. 9.4). The plagioclase from the Intermediate Unit show both normal progressive and reverse rhythmic zoning (Fig. 9.5) with rare rounded core and brownish glassy inclusions, which could reflect disequilibrium and resorption phenomena during the crystallization of plagioclase (probably melt generated and trapped during the dissolution of the plagioclase edge when the phenocryst entered in contact with new compositionally different magma). However, the high An variations recorded in reverse rhythmic zoning (up to 10-14 mol%) could be due to decompression phenomena, i.e. variations in the plagioclase crystallization pressure which in turn would led to high An content or to an increased water content. The crystals show higher An (84-47) and MgO (0.05-0.30 wt%), and lower K_2O (0.05 and 0.30 wt%) and more restricted FeO/MgO (1.0 and 8.0) with respect to the Lower Unit plagioclases (Fig. 9.11, 9.12 and 9.13). Compositions vary from bytownite to andesine ($An_{84.5}Ab_{15.2}Or_{0.3}$ to $An_{47.8}Ab_{50.0}Or_{2.2}$) with frequent abrupt jumps in An from the core toward the rim, always occurring in few microns (10-15 μm) (Fig. 9.9(a),9.9(b),9.9(c)). This high An variation are accompanied by other low amplitude variations of the order of 3-5 mol% which result in a saw-tooth pattern. Only at Oued Lahr (Fig. 9.9(d)) and rarely at Tiourjdal (not shown here) the plagioclase crystals display at the rims normal progressive zoning with decreasing An. An content displays the largest variation (almost 20 mol%) at the same MgO content and FeO/MgO. MgO, K_2O and FeO/MgO correlate broadly with An which has a lower variation range with respect to that of Lower Unit crystals (Fig. 9.11, 9.12 and 9.13). While at Oued Lahr is well visible the positive and negative correlation between the MgO and K_2O content with An, at Tiourjdal and Telouet, this correlation is less evident, especially for MgO (Fig. 9.10). The Intermediate Unit at Tiourjdal is the most complete, with 5 lava flows and 15 plagioclases analysed (3 for TJ23, 2 for TJ25, 3 for TJ32, 4 for AN137A and 3 for AN138). At Telouet, it is represented by two samples, TEL16 (1 plagioclase and few analysis points on a plagioclase aggregates) and TEL23 (2 plagioclases), has the lowest analysis point number which are quite scattered on compositional diagrams. Nevertheless the plagioclase compositions at Telouet fit quite well with those of Tiourjdal, displaying the same compositional variability. Differently, the Oued Lahr plagioclases (4 phenocrystals for OL10 and 2 for OL11) display quite narrow compositional ranges, with An varying from $An_{83.7}Ab_{15.8}Or_{0.5}$ to $An_{56.7}Ab_{41.5}Or_{1.8}$ and MgO slightly higher than for Tiourjdal and Telouet. FeO/MgO ranges between 1.3

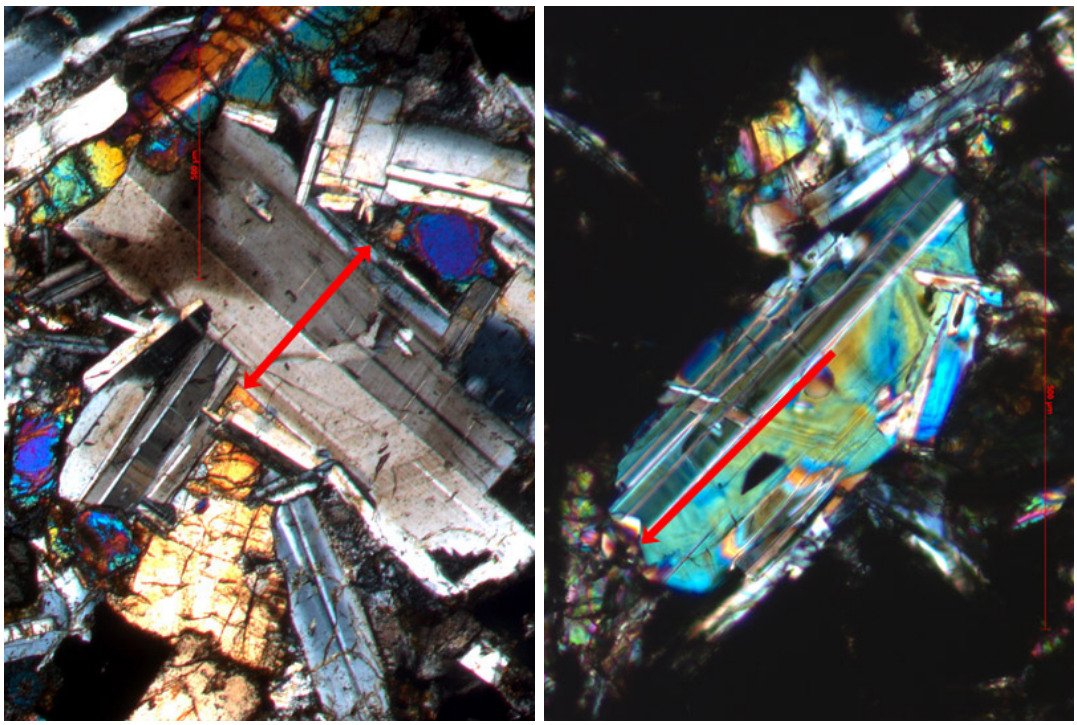

Figure 9.8: Microphotographs showing the complex zoning pattern in plagioclases from the Intermediate Unit at Tiourjdal (TJ25 plg2, on the left and AN137A plg2 on the right). Red arrows represent EMP transects.

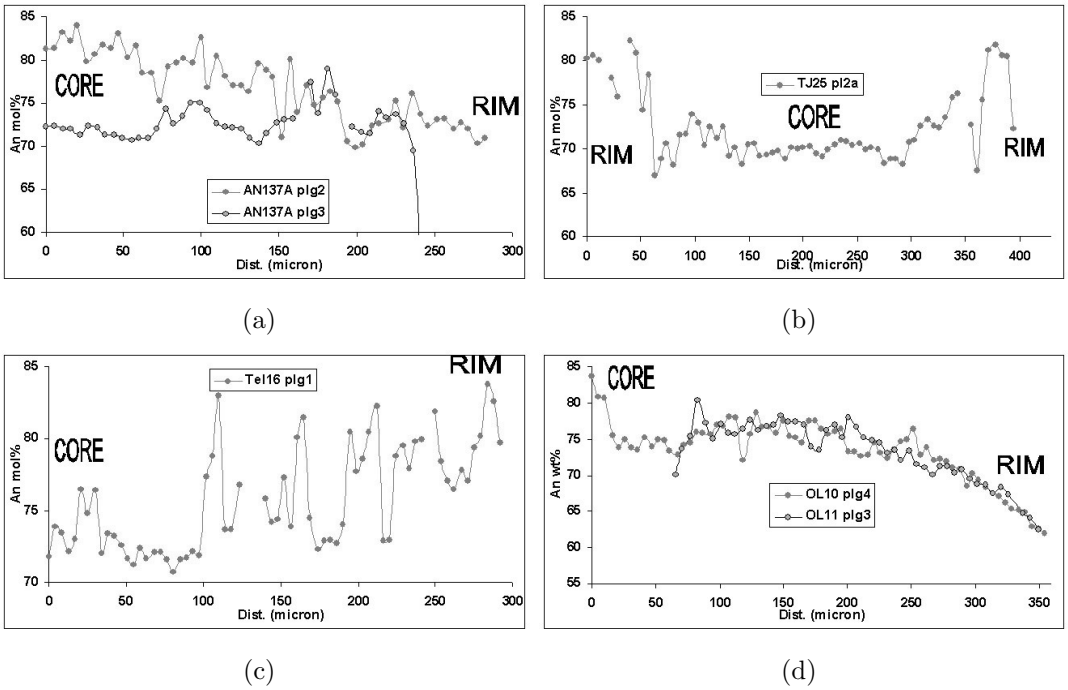

Figure 9.9: Variation of An mol% along core to rim (transects distance in microns) of plagioclase from the Intermediate at Tiourjdal (9.9(a),9.9(b)), Telouet (9.9(c)) and Oued Lahr (9.9(d)) (EMP analyses). Description in the text.

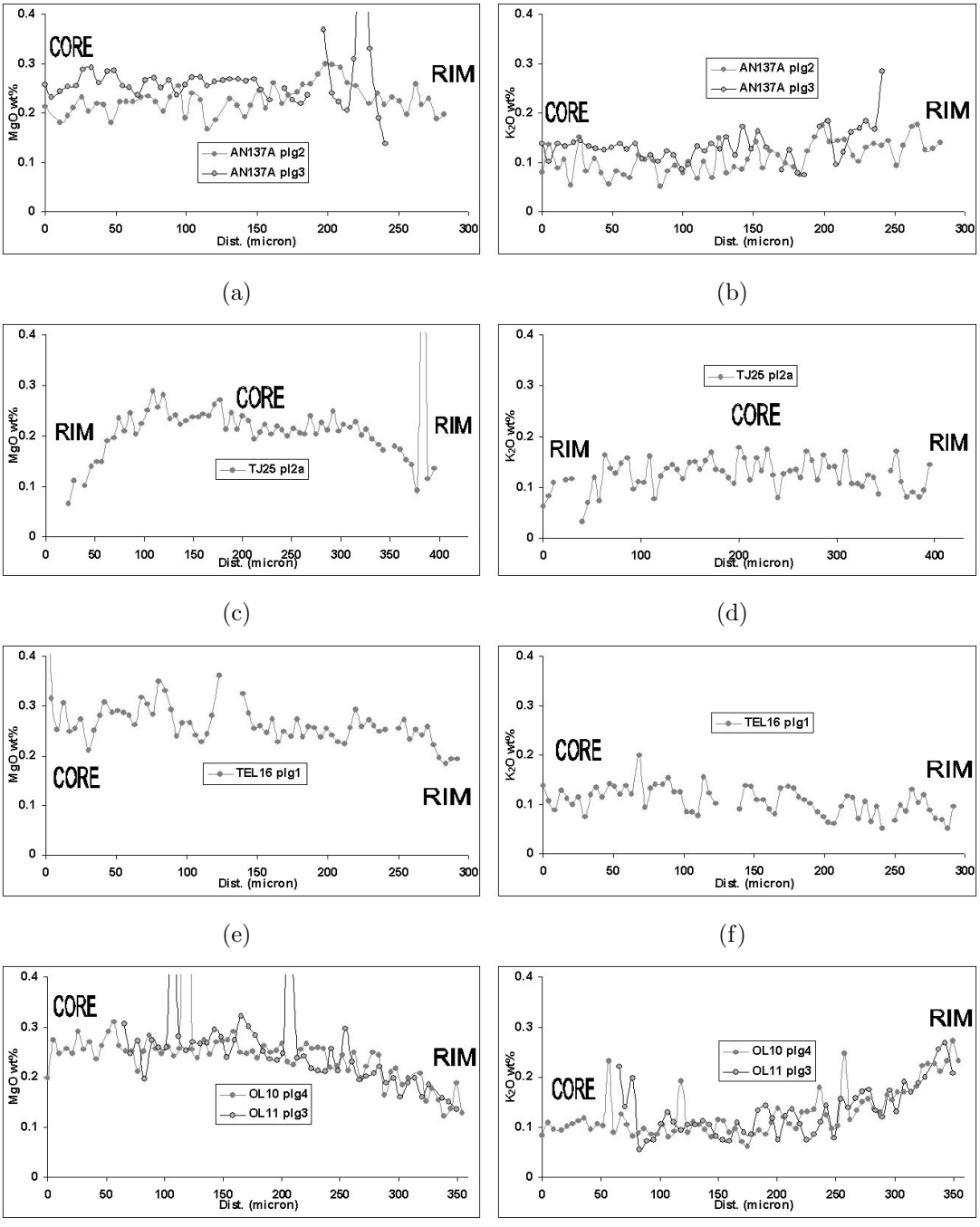

Figure 9.10: Variation of MgO and K_2O wt% along core to rim (transects distance in microns) of plagioclases from the Intermediate Unit at Tiourjdal (Fig. 9.10(a),9.10(b),9.10(c),9.10(d)), Telouet (Fig. 9.10(e),9.10(f)) and Oued Lahr (Fig. 9.10(g),9.10(h)) (EMP analyses). Descriptions in the text.

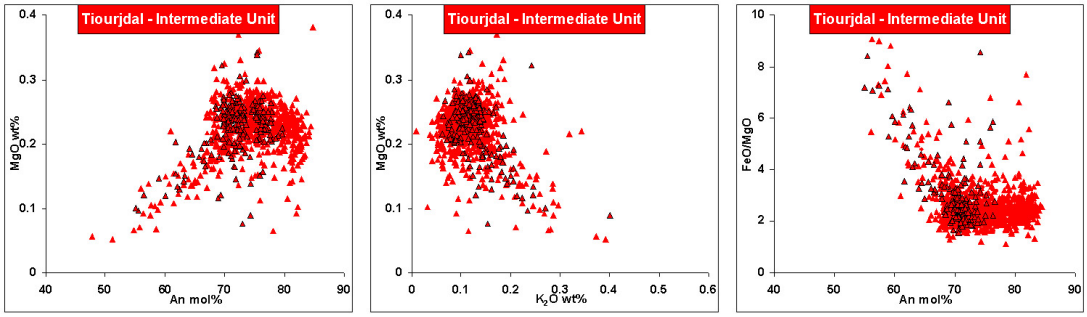

Figure 9.11: Anorthite mol% and K_2O wt% vs MgO wt% and FeO/MgO variations of plagioclase crystals from the Intermediate Unit at Tiourjdal (EMP analyses).

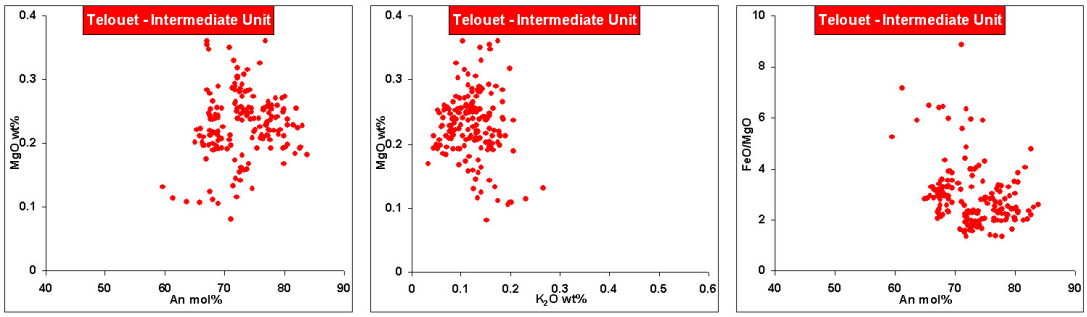

Figure 9.12: Anorthite mol% and K_2O wt% vs MgO wt% and FeO/MgO variations of plagioclase crystals from the Intermediate Unit at Telouet (EMP analyses).

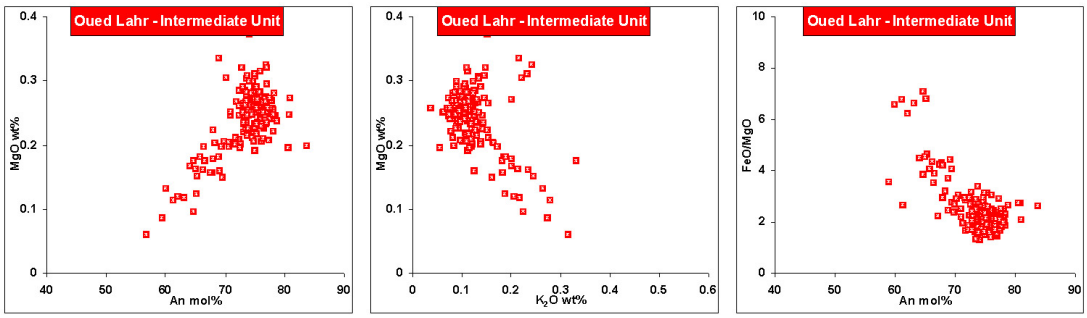

Figure 9.13: Anorthite mol% and K_2O wt% vs MgO wt% and FeO/MgO variations of plagioclase crystals from the Intermediate Unit at Oued Lahr (EMP analyses).

and 3.5 for most plagioclases and up to 7.1 in the most evolved ones. Differently from the plagioclases of the Lower Unit, the Intermediate ones have a higher Ca# than the whole-rock, i.e. they would be in equilibrium with the host basalt for Ca/Na K_D between 1.1 and 2.0 (Fig. 9.4). We will try to investigate what could affect this higher K_D, thus leading to high Ca/Na of the plagioclase cores. In all three sections of the Central High Atlas, plagioclase crystals belonging to

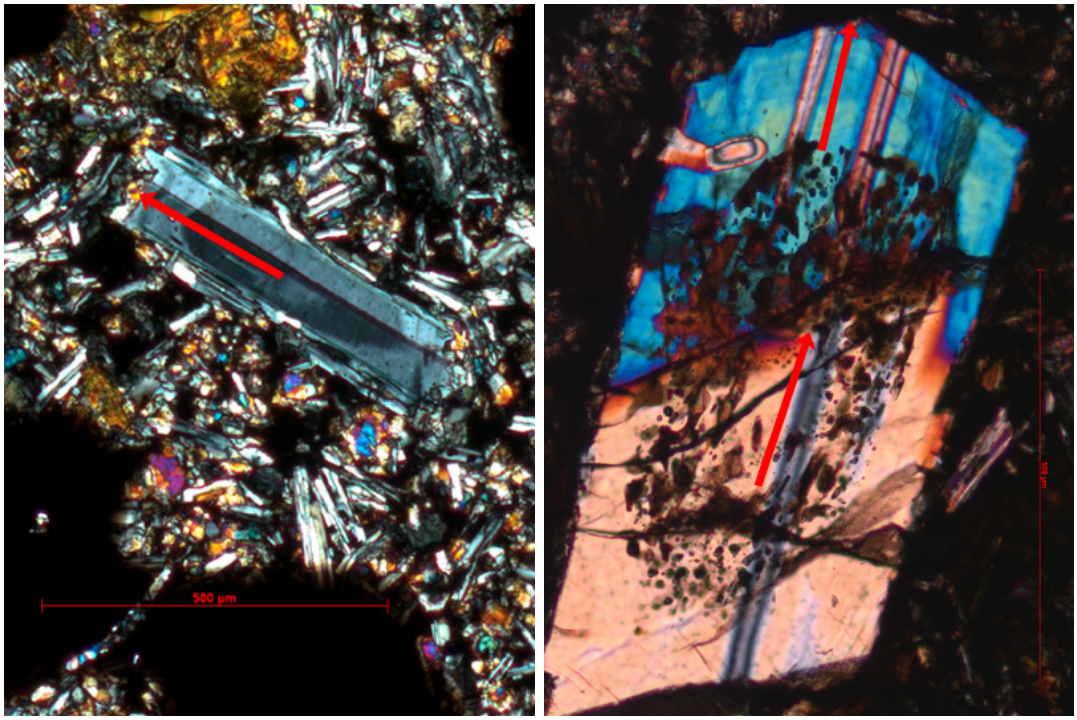

Figure 9.14: Microphotographs showing the complex zoning pattern and rounded cores in plagioclases from the recurrent Unit at Tiourjdal (TJ33 plg4, on the left) and at Oued Lahr (OL14 plg1, on the right). Red arrows represent EMP transects.

the Upper Unit have lower compositional ranges but show the highest An (up to An_{89}; Fig. 9.16, 9.17 and 9.18). In particular Tiourjdal (TJ33, 1 plagioclase and AN141, 3 plagioclases) and Oued Lahr samples (OL14, 4 plagioclases and OL15 with 2 plagioclases) have the highest An content. Telouet is represented by only one analysed rock (TEL24, 2 plagioclases), that could lead to an under-sampling and underestimation of the An variation in this lava unit. The plagioclase crystals show frequent reverse rhythmic zoning with rounded core and frequent brownish glassy inclusion. The compositions range from bytownite to labradorite ($An_{88.6}Ab_{11.1}Or_{0.3}$ to $An_{63.3}Ab_{32.9}Or_{3.8}$) and in all samples, most phenocrysts show resorbed, rounded and relatively homogeneous high-An cores (An_{81-89}), followed by an abrupt drop (few analysis points, i.e. 10-15 μm, Fig.

9.15) to An_{75-78} and multiple oscillatory zoning in the An_{70-80} range (Fig. 9.14).

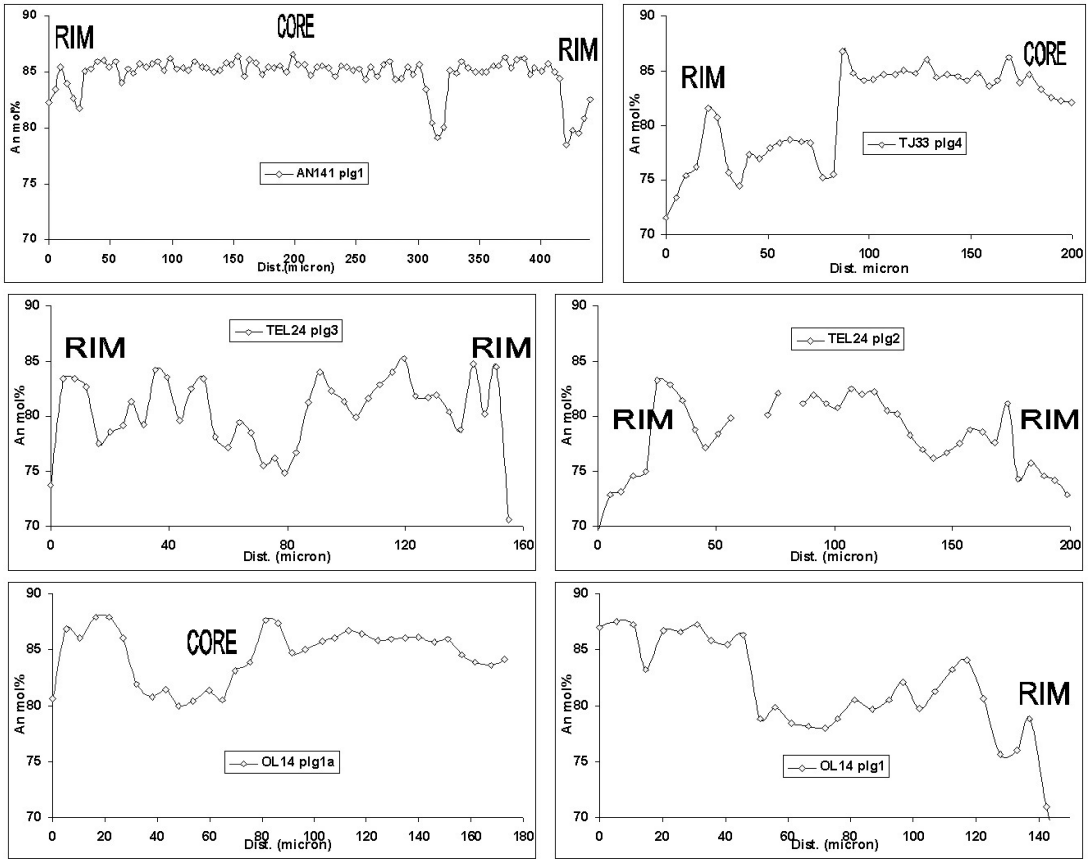

Figure 9.15: Variation of Anorthite mol% along core to rim (transects distance in microns) of plagioclases from the Upper Unit at Tiourjdal (AN141 plg1 and TJ33 plg4, above), Telouet (TEL24 plg3 and plg4, in the middle) and Oued Lahr (OL14 plg1 and plg1a, below) (EMP analyses).

The MgO content is lower than in plagioclase of the Intermediate Unit and similar to those of the Lower Unit (generally from 0.10 to 0.25-0.30 wt%, rarely exceeding the last value). The K_2O content in the plagioclases of the Upper unit is lower than in those of the Intermediate and Lower units, rarely exceeding 0.1 wt%, whereas FeO/MgO ranges from 2 to 4 and in few cases reaches up to 8. The high Ca/Na ratio of the plagioclase cores imply equilibrium with the host basalts for a K_D between 1.5 and 2 or even higher (note that the Ca# of some whole-rock may be slightly lowered by alteration) (Fig. 9.4). Plagioclases from the Recurrent Unit have the most homogeneous compositions compared to the other units (Fig. 9.16, 9.17 and 9.18). Only 2 samples were analysed: AN156A (3 plagioclases) from Tiourjdal and AN169 (4 plagioclases) from Telouet (Fig. 9.20). As said in the petrographic description (previous section) analyses of

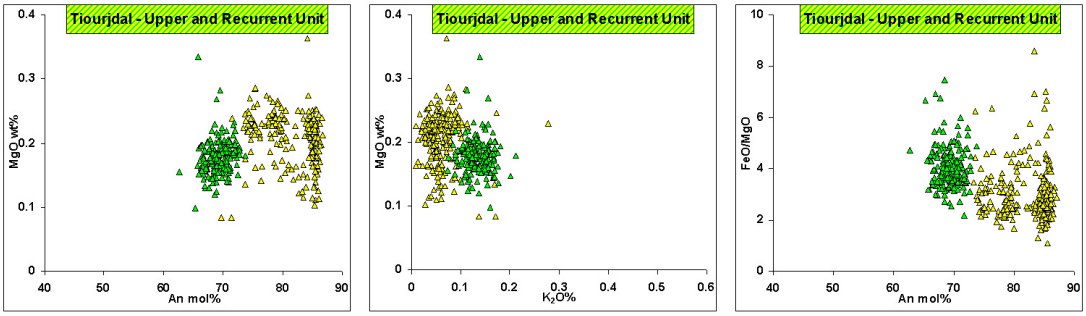

Figure 9.16: Anorthite mol% and K_2O wt% vs MgO wt% and FeO/MgO variations of plagioclase crystals from the Upper (yellow diamonds) and Recurrent (green squares) Unit at Tiourjdal (EMP analyses).

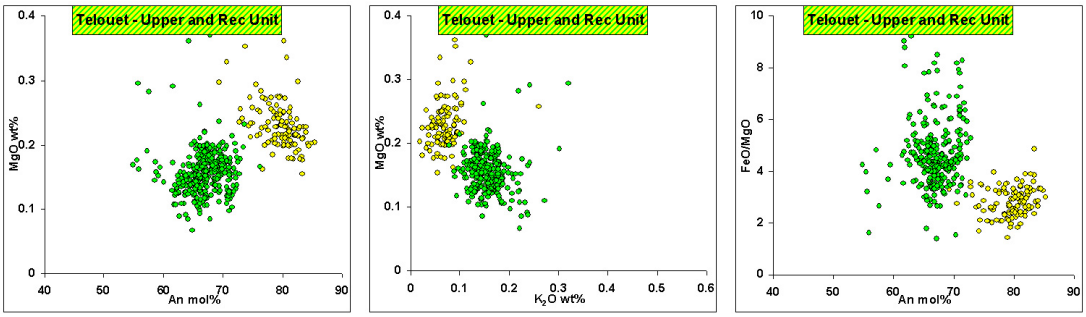

Figure 9.17: Anorthite mol% and K_2O wt% vs MgO wt% and FeO/MgO variations of plagioclase crystals from the Upper (yellow diamonds) and Recurrent (green squares) Unit at Telouet (EMP analyses).

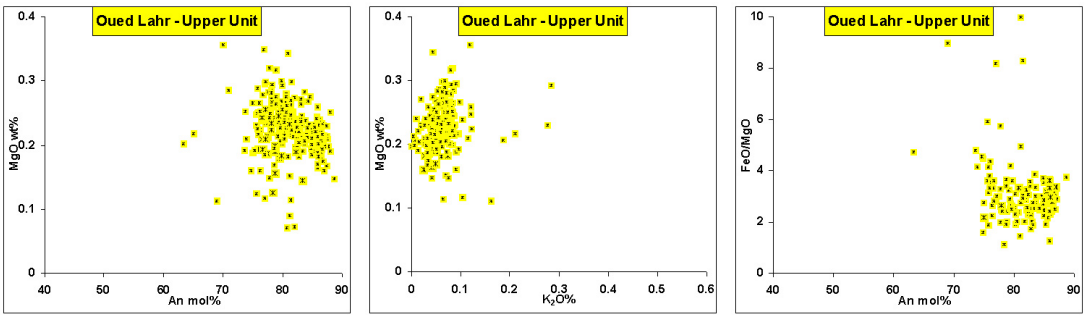

Figure 9.18: Anorthite mol% and K_2O wt% vs MgO wt% and FeO/MgO variations of plagioclase crystals from the Upper Unit at Oued Lahr (EMP analyses).

the Recurrent Unit from Oued Lahr are missing in this work. They show rare normal progressive and frequent reverse rhythmic zoning with frequent rounded cores which could register disequilibrium and resorption phenomena during the crystallization of the plagioclase (Fig. 9.19). Globally, they have the lowest An and MgO content. The compositions range from bytownite to labradorite ($An_{76.1}Ab_{23.1}Or_{0.8}$ to $An_{54.8}Ab_{43.7}Or_{21.5}$). The MgO content is the lowest between

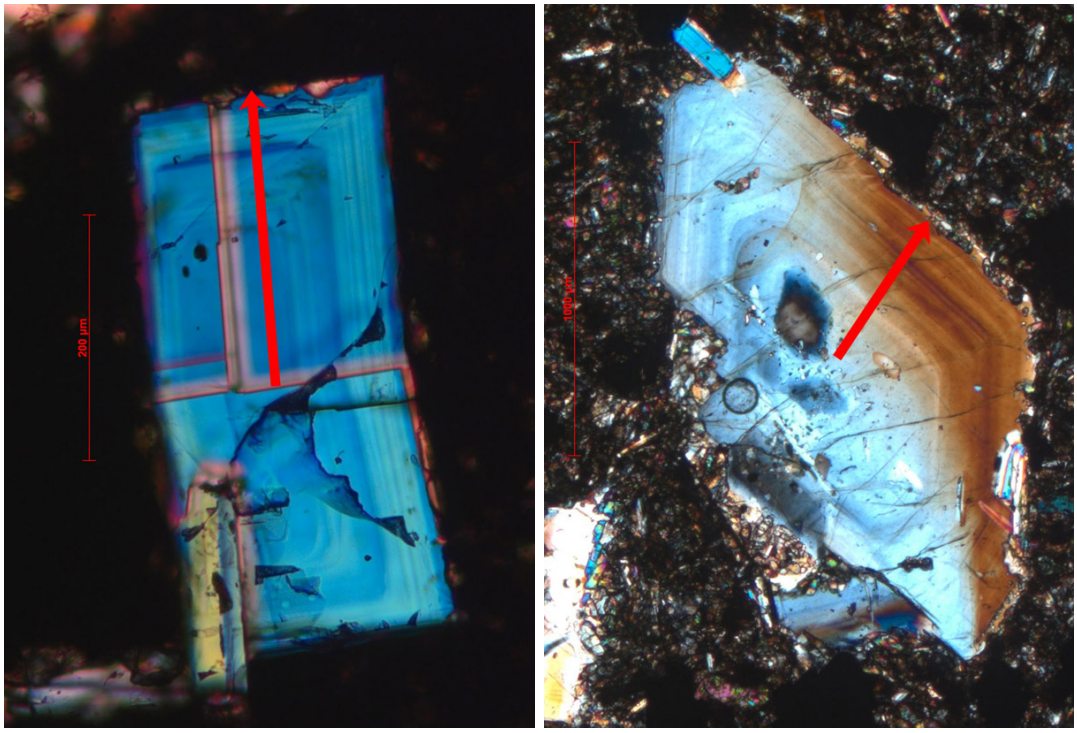

Figure 9.19: Microphotographs showing the complex zoning pattern and rounded cores in plagioclases from the Recurrent Unit at Tiourjdal (AN156A plg3, on the left) and at Telouet (AN169 plg1, on the right). Red arrows represent EMP transects.

the four units, except for the Lower Unit at Oued Lahr (compare with Fig. 9.7), being in the range between 0.10 and 0.20 wt% with few analysis points exceeding 0.22 wt% (Fig 7.21, on the left). The K_2O content is quite higher compared to the Upper Unit (mostly between 0.1 and 0.2 wt%, Fig. 7.21, on the right). FeO/MgO has a higher compositional range with respect to the Upper Unit (between 2.5 and 6.0) with few analysis points up to 9. Finally, the equilibrium Ca/Na K_D with the host basalts is about 1.0, i.e. comparable to those for the Lower Unit samples (Fig. 9.4).

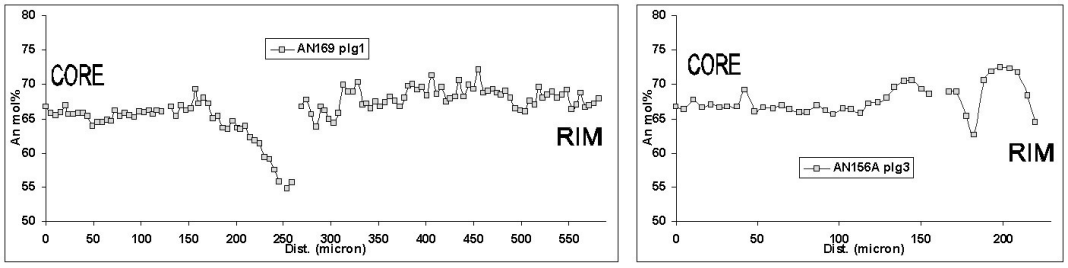

Figure 9.20: Diagrams showing the composition variation in An mol% along transect (EMP analyses)from the core to the rim of plagioclases from the Recurrent Unit at Telouet (AN169 plg1, left) and Tiourjdal (AN156A plg3, right).

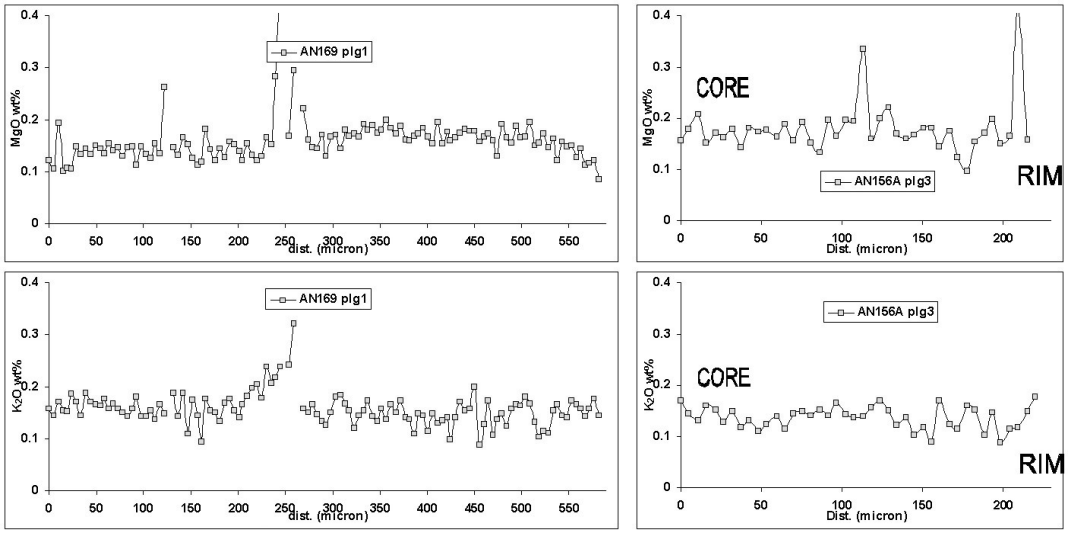

Figure 9.21: Diagrams showing the composition variation in MgO and K_2O wt% along transect (EMP analyses)from the core to the rim of plagioclases from the Recurrent Unit at Telouet (AN169 plg1, left) and Tiourjdal (AN156A plg3, right)

9.2.3 Augite (high-Ca pyroxene)

Like plagioclase, also clinopyroxenes (both high-Ca and low-Ca) were investigated by electron microprobe to study the compositional variation of major and minor elements (see details in methodologies chapter) along some traverses, both from the core to the rim and from rim to rim of the freshest and in some cases of the most zoned crystals. EMP analyses show the occurrence of augite (high-Ca clinopyroxenes) and pigeonite (low-Ca clinopyroxenes). Neither orthopyroxenes nor other clinopyroxenes have been detected. As for plagioclase analysis, a narrow spacing between each analysis point was applied (in most cases 5-6 μm). Differently from plagioclase, in general clinopyroxenes do not show optically visible rhythmic or progressive zoning. Nevertheless the augites display in the properly oriented crystals the typical sector zoning (hourglass zoning, Fig. 9.22). In

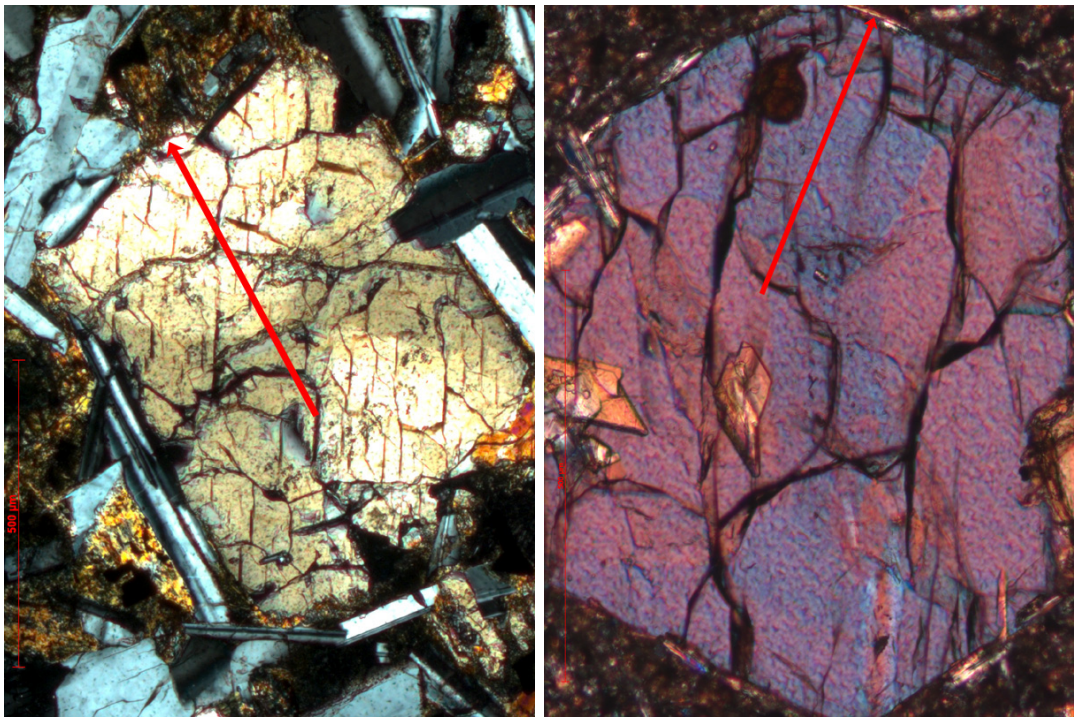

Figure 9.22: Sector zoning in fresh euhedral augitic clinopyroxenes, samples TJ11 cpx5 (left, Lower Unit) and AN141 cpx1 (right, Upper Unit). Red arrows represent EMP transects.

general pyroxenes display a less fresh aspect than plagioclase, sometimes being altered into a pale greenish fibrous mineral (probably chlorite). Like plagioclases, they have a quite wide compositional range and it is possible to recognize similar composition characteristics for clinopyroxenes from each of investigated lava piles and for the four lava flow units (Fig. 9.23). Like plagioclase, clinopyroxenes

(both augitic and pigeonitic) compose about 45-50 vol.% of the basalts. The occurrence in some samples of augite together with pigeonite, like the presence or not of pigeonite together with olivine, is indicative of particular T-P-H_2O-fO_2 conditions that we will try to investigate in order to gather information on the differentiation process of the CAMP magmas.

In all the lava flows of the Lower Unit occur augitic clinopyroxenes princi-

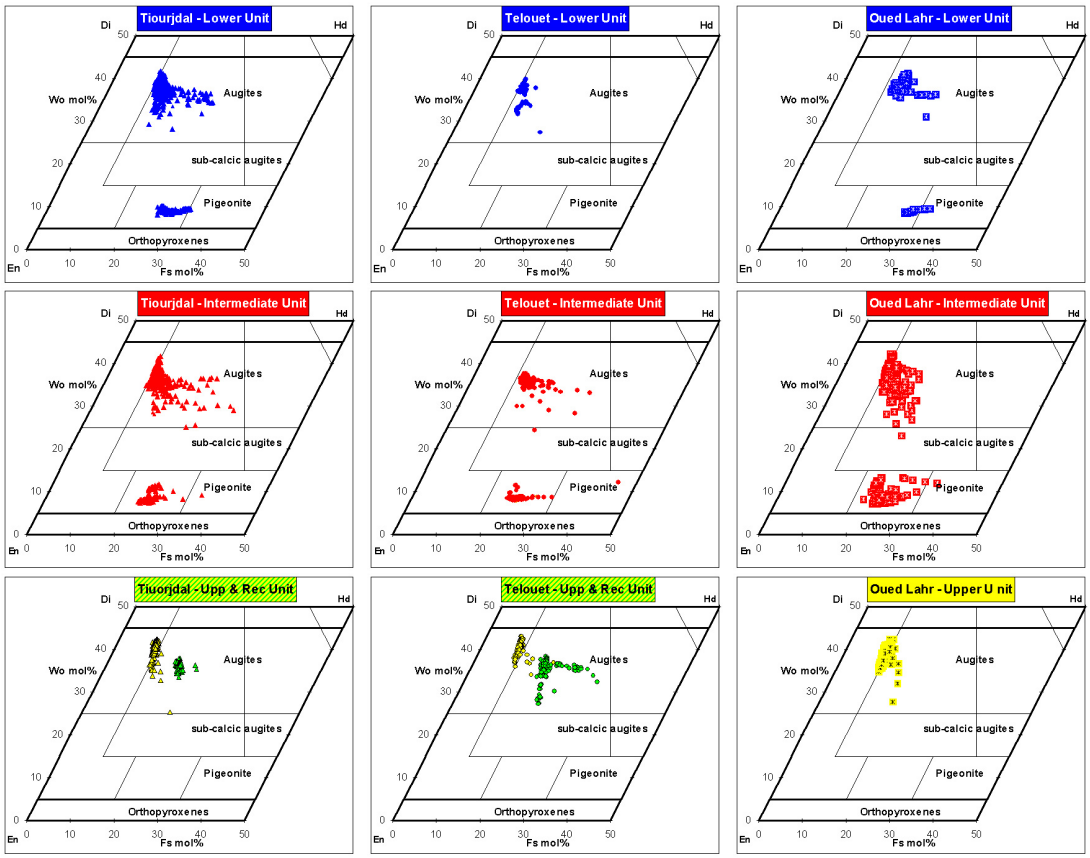

Figure 9.23: Compositions of all analysed pyroxenes plotted in a partial Wo-En-Fs ternary diagram for the three sections (TJ on the left, TEL in the middle, OL on the right) and for the all units (EMP analyses).

pally, except for a few flows at the base (TJ2, TJ3 and AN49) and at the top (TJ22) of the unit, just before the onset of Intermediate Unit, where it appears together with pigeonite (see next paragraph). As for plagioclases of the Lower Unit, the pyroxenes are best represented in the Tiourjdal section, with 4 samples analysed: TJ1, TJ2, TJ11 and AN134. Sample AN49 was analysed only for pigeonite. At Telouet and Oued Lahr, the general bad preservation and the few lava flows of the Lower Unit hinder analyses a large number of pyroxenes. However the few available data concord with the more complete dataset from

Tiourjdal. Along the whole unit clinopyroxenes plot within the augite field yet display a wide compositional variation range in the ternary diagram Wo (wollastonite, $Ca_2Si_2O_6$ mol%), En (enstatite, $Mg_2Si_2O_6$ mol%) and Fs (ferrosilite, $Fe_2Si_2O_6$ mol%): $Wo_{29-48}En_{39-57}Fs_{9-25}$ (Fig. 9.23). Even at Telouet and Oued Lahr the augite compositions, as visible from the Wo-En-Fs diagrams, overlap very well those from Tiourjdal. All augite crystals tend to evolve toward more Fs-enriched composition, decreasing their Wo and En content. Minerals have a

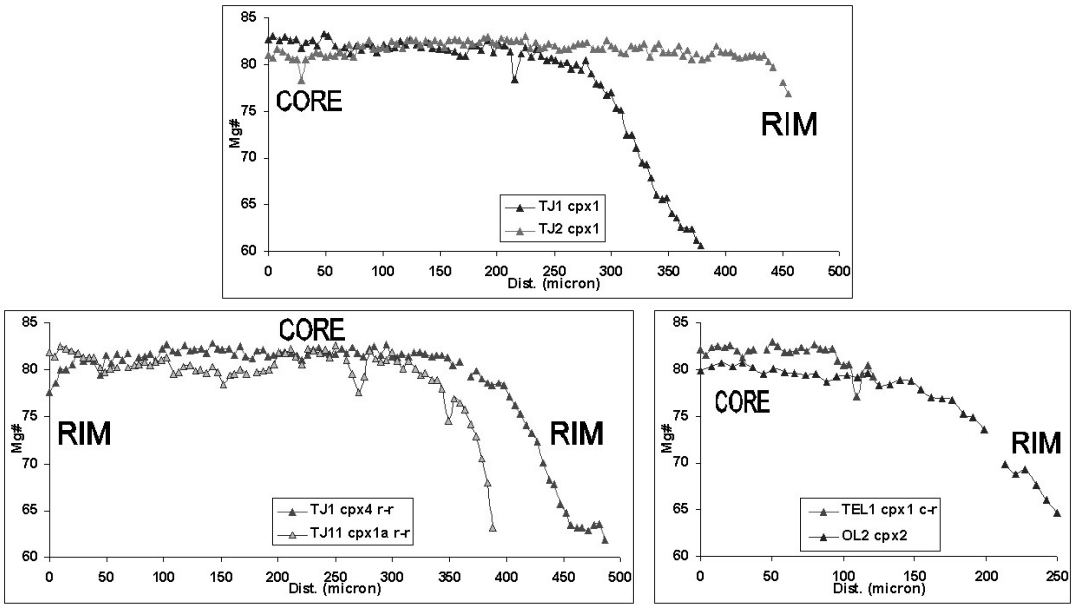

Figure 9.24: Core-rim compositional (Mg#) traverses of augites from the Lower Unit (EMP analyses).

quite wide Mg# range (Mg# = 100*atomic Mg/(Mg + Fe^{2+}), where Fe^{2+} has been calculated after **Papike *et al.* (1974)** varying from 83.6 to 60.5, in general with the highest value in the core and the lowest towards the rims of the crystals (Fig. 7.24). Cr_2O_3 ranges between 1.2 and 0 wt% and its variations are correlated with Mg#, with the higher values in the core and a progressive depletion of this element towards the rims of the phenocrysts (Fig. 9.25). TiO_2 contents (0.27 and 1.12 wt%) are the highest among those of the four units, reflecting the high bulk TiO_2 concentration of the samples of the Lower Unit. In the augites, TiO_2 increases at decreasing Mg#, thus leading to an enrichment towards the rims as clinopyroxene crystallize from more evolved magma (Fig. 9.25). In some augites, it is possible to see a change of trend of TiO_2 vs Mg# variations, probably reflecting the initial crystallization of oxides leading to Ti depletion in the melt. Nevertheless, the high TiO_2 measured in some sector zoned augites reflects

higher Ti partition coefficient for particular crystallographic orientation of the augite (**Shimizu, 1981**)(Fig. 9.22). Some augites display inverse zoning with

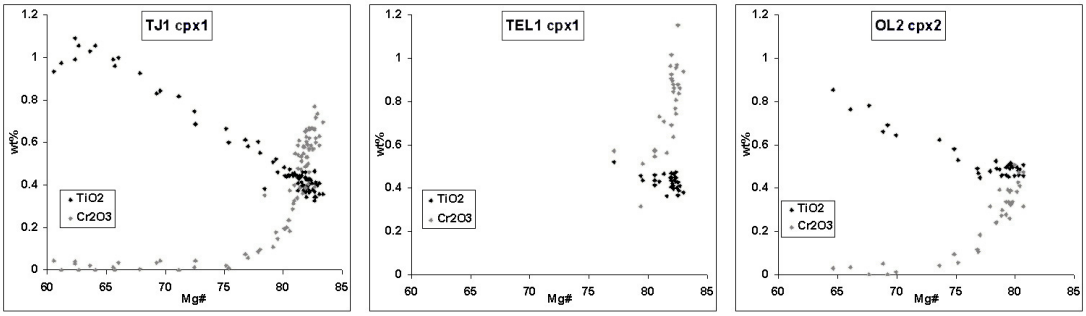

Figure 9.25: Cr_2O_3 and TiO_2 variations (EMP analyses) of augites from the Lower Unit showing the positive and negative correlation respectively with Mg#.

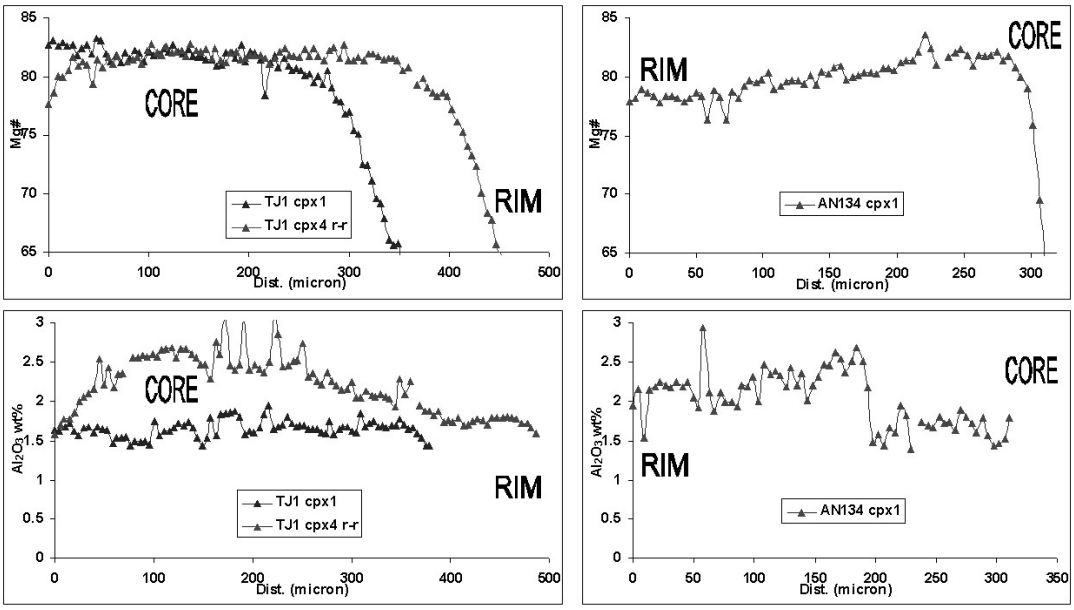

Figure 9.26: Core-rim compositional traverses (EMP analyses) of some augites from the Lower Unit showing as the Al_2O_3 content is not directly correlated with Mg#.

rim-ward increase of Mg and Cr_2O_3 and decrease of TiO_2. Mg#, Cr_2O_3 and TiO_2 variations are not continuous, but display numerous little jumps, up to 20-25% of the relative concentration of the element. This inverse zoning and its saw-tooth pattern probably reflects mixing phenomena between with possible recharge of less differentiated magma from which the augite rims crystallized (Fig. 9.27).

Also Al_2O_3 varies from the core toward the rim of augites, but its behaviour

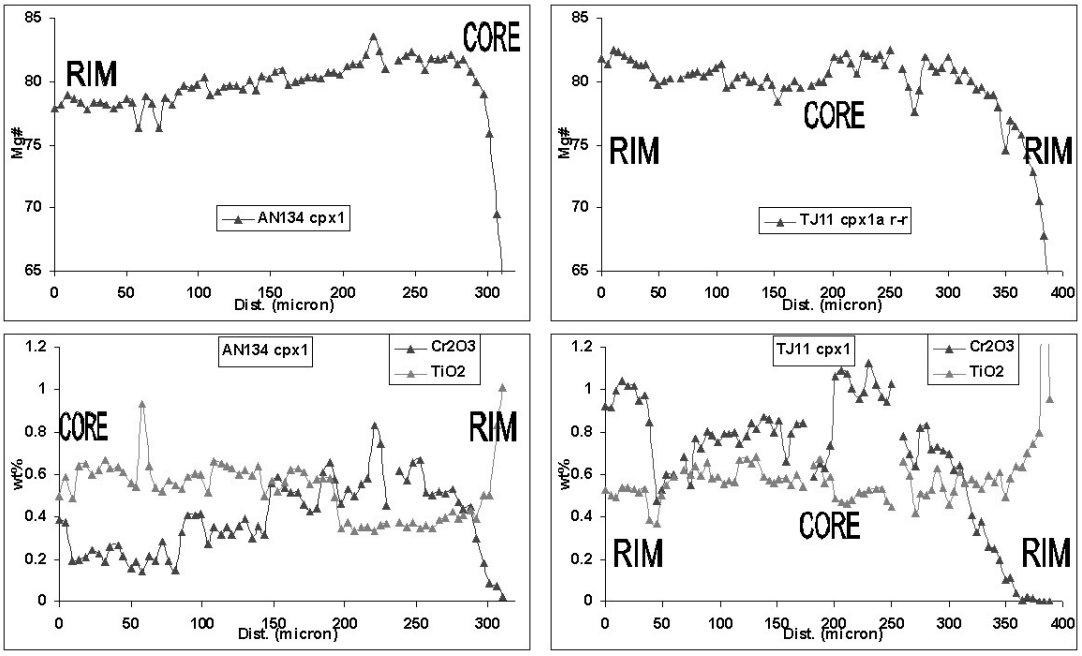

Figure 9.27: Core-rim and rim-rim compositional traverses of some inverse zoned augites from the Lower Unit (EMP analyses) showing the correlation between Cr_2O_3 and TiO_2 with Mg#.

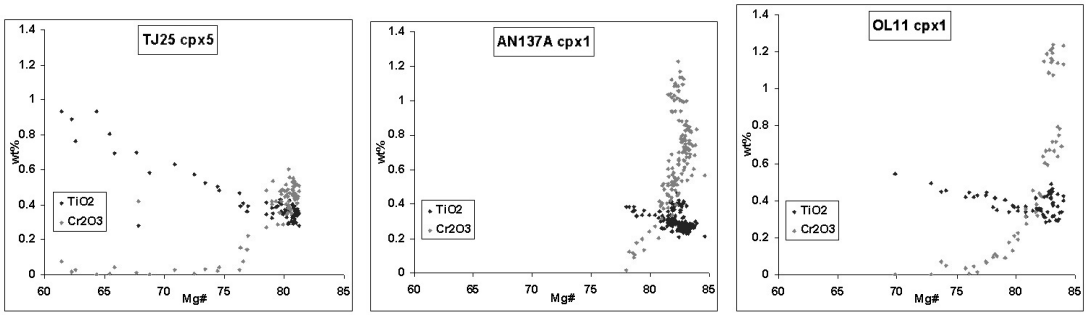

Figure 9.28: Cr_2O_3 and TiO_2 variations (EMP analyses) of augites from the Intermediate Unit showing the positive and negative correlation, respectively, with the Mg#.

seems not to be directly correlated with Mg#, probably being affected by magma evolution driven by plagioclase crystallization as well as by pressure effects (Fig. 9.26). Like in the Lower Unit, in the Intermediate Unit the predominant pyroxene is an augite, but it is often joined by pigeonite. Augites display the widest compositional variation ranges ($Wo_{24-42}En_{37-56}Fs_{9-33}$ Fig. 9.23) among the four units, with an Mg# spanning from 84 to 53. Cr_2O_3 has a slightly higher content (up to 1.24 wt%) and it is positively correlated with Mg# (Fig. 9.27). On the contrary, TiO_2 is slightly lower, both in the core and at the rims of phenocrysts (0.13 to 0.6 wt%, in few cases up to 0.9 wt%), in accordance with the lower bulk concentration of the lava flows belonging the Intermediate Unit compared to those of the Lower Unit. Also for Intermediate Unit augites, TiO2 is negatively correlated with Mg# (Fig. 9.27). Differently from the more evolved clinopyroxenes of the Lower Unit, in those of the Intermediate Unit (AN138 cpx1 and TJ25 cpx5, Fig. 9.27) it is not visible the change of TiO_2 vs Mg# variation trend. Thus could mean that augite stopped to crystallize before that oxides begun or that magma was not enough saturated in TiO_2 to start the oxides crystallization before the eruption event. The second hypothesis could be supported by the presence of tiny dendritic oxides in the glassy ground-mass in most of the Intermediate lava flows. The Upper Unit is characterized by the occurrence of large euhedral, often sector zoned augites interspersed in the fine microlithic ground-mass. Pigeonite phenocrysts are detected as microphenocryst in the groundmass, but has not been analysed. The augites belonging the Upper Unit have the highest and most homogeneous compositions among the four units, with composition spanning in the range $Wo_{27-43}En_{44-57}Fs_{8-18}$ (Fig. 9.23), with the highest and most restricted Mg# range (varying from 86.0 and 70.4). Augites from the Upper Unit have a nearly constant Wo CaO content compared to those of the Intermediate Unit but with a slightly higher En component (Fig. 9.23) and higher Cr2O3 (up to 1.28 wt%). TiO_2 concentration is the lowest observed between the four unit (from the core to the rim 0.18 to 0.54 wt%, rarely exceeding 0.70 wt%, Fig. 9.29), again consistent with the low TiO_2 of the Upper Unit basalts. An important feature of Upper Unit augites is that they are strongly zoned in terms of Cr_2O_3, Al_2O_3 and TiO_2. Large phenocryst cores often present high concentration of Cr, Al and Ti (Fig. 9.29). Like in the Upper Unit, the only detectable pyroxene phenocryst in the Recurrent Unit is augite. The minerals are compositionally homogeneous ($Wo_{27-38}En_{36-52}Fs_{15-30}$, Fig. 9.23), low in CaO and MgO, and enriched in ferrosilitic component. Mg# values are the lowest among the four unit (75 to 54, Fig. 9.29), coupled with the lowest Cr_2O_3 (0.6 wt% in the core to 0 wt% at the

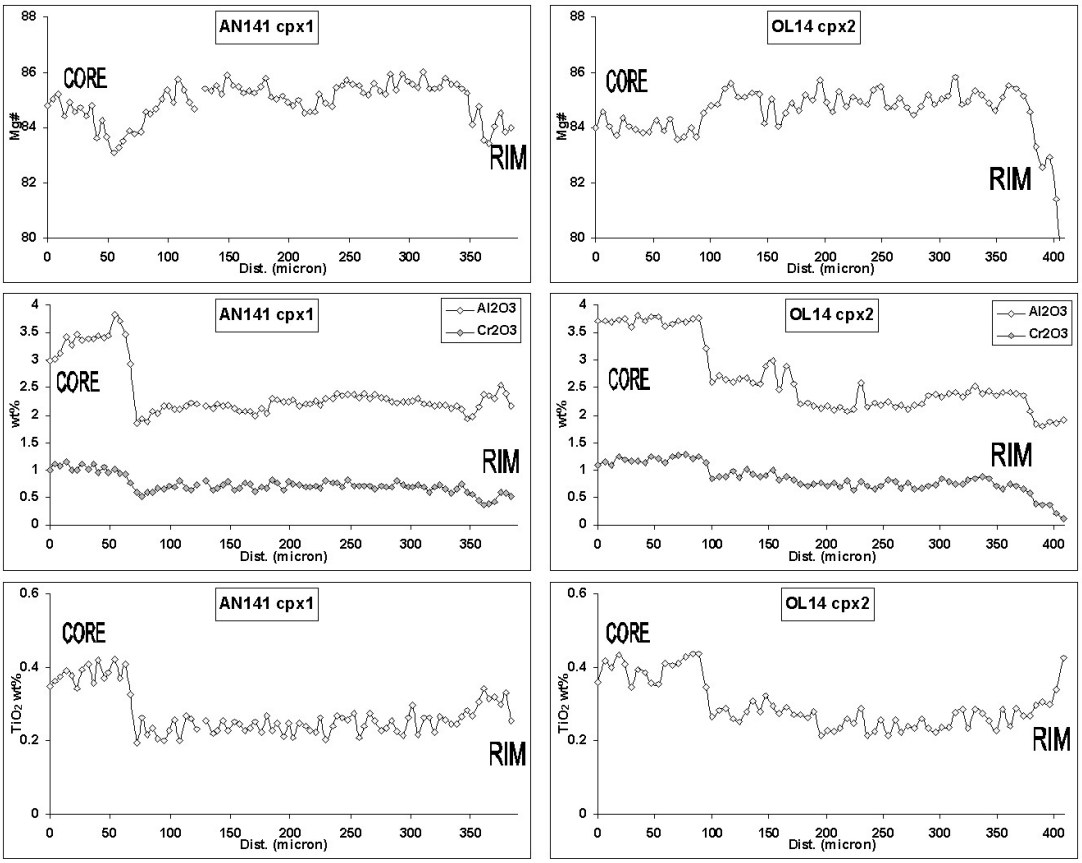

Figure 9.29: Core-rim compositional (Mg#, TiO_2, Al_2O_3 and Cr_2O_3) traverses of augites AN141 cpx1 and OL14 cpx2 from the Upper Unit (EMP analyses).

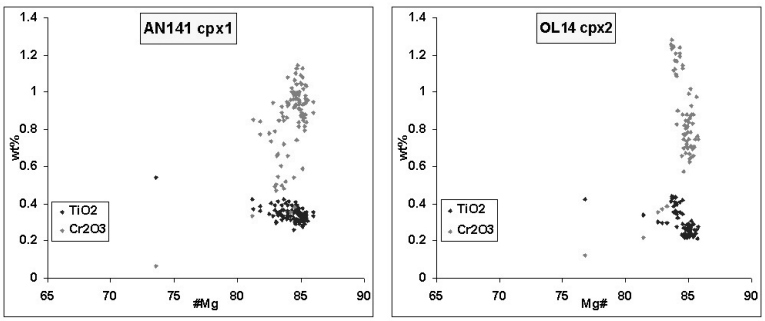

Figure 9.30: Cr_2O_3 and TiO_2 vs Mg# variations (EMP analyses) of augites AN141 cpx1 and OL14 cpx2 from the Upper Unit.

rims), while TiO_2 has higher concentrations, similar to those of the Intermediate Unit (Fig. 9.31, 9.32).

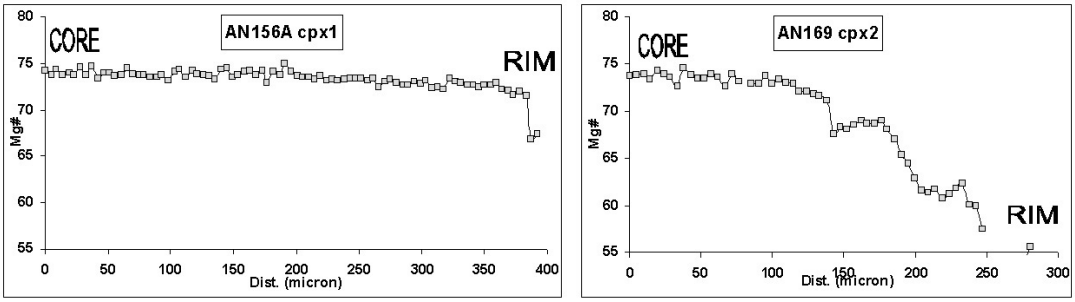

Figure 9.31: Core-rim and rim-rim compositional (Mg#) traverses of augites AN156A cpx1 and AN169 cpx2 from the Recurrent Unit (EMP analyses).

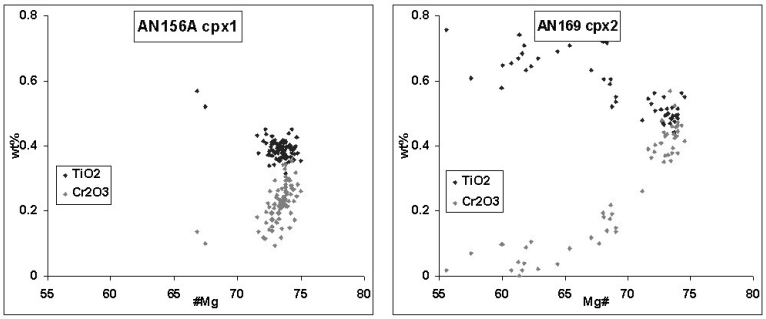

Figure 9.32: Cr_2O_3 and TiO_2 vs Mg# variations (EMP analyses) of augites AN156A cpx1, AN169 cpx2 from the Recurrent Unit (EMP analyses).

9.2.4 Pigeonite (Low-Ca pyroxene)

Pigeonite is restricted to few lava flows of the Lower Unit and quite diffuse in most of the lava flows of Intermediate Unit. Pigeonite in the Upper and Recurrent Unit is limited to the ground-mass. While in the Lower Unit pigeonite occurs together with olivine, that is a constant presence of this unit in all three sequences of the Central High Atlas, in the Intermediate Unit pigeonite occurs only when olivine is not present, and vice-versa. In general, pigeonite is recognizable as small rounded phenocrysts or microphenocrysts and only in a few samples it occurs as large euhedral phenocryst, larger than augites which are sometimes rimmed by pigeonite (Fig. 9.33). In the Lower Unit, pigeonite is present at Tiourjdal at the base (TJ2, TJ3, AN49) and at the top (TJ22) of the unit. At Oued Lahr it is

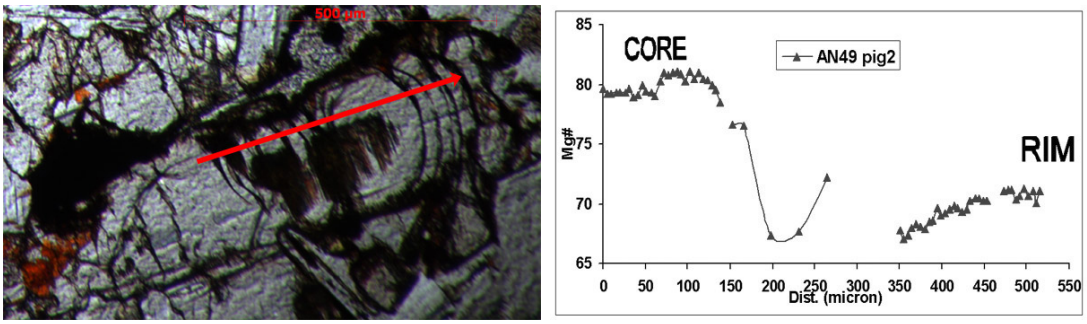

Figure 9.33: Large augite phenocryst bordered by pigeonite (sample AN49 pigeo2, Lower Unit of Tiourjdal) and relative EMP transect showing the Mg# variation from the core to the rim.

present in the first two lava flows (OL1 and OL2), while no pigeonite is detected at Telouet. The lack of pigeonite in the Lower Unit at Telouet could be due possibly to the bad preservation of the samples of this unit or may be a systematic primary characteristic of this section. In the Wo-En-Fs diagram pigeonites of the Lower

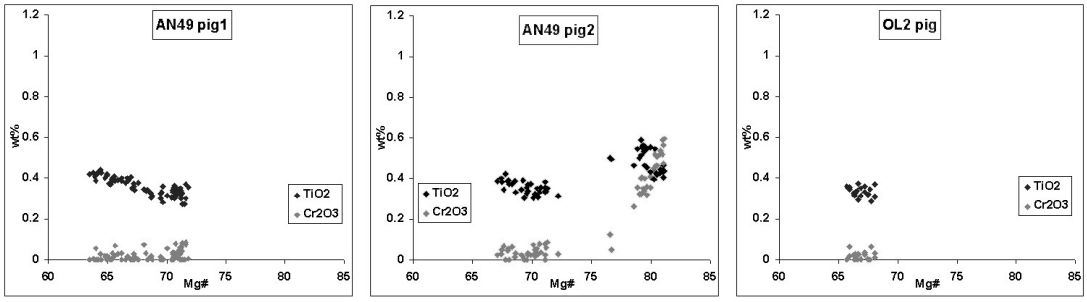

Figure 9.34: Cr_2O_3 and TiO_2 variations vs Mg# (EMP analyses) of pigeonites AN49 pig1, pig2 and OL2 pig of the Lower Unit.

Unit have a $Wo_{8-39}En_{47-65}Fs_{11-34}$ composition, displaying a strong enrichment toward Fs-rich member during the crystallization (Fig. 9.23). They display a quite wide Mg# variation (from 83.1 to 61.6), being in general the highest value in the core and the lowest toward the rim of crystal.However, in the pigeonite AN49 pigeo2 (Fig. 9.33), Mg# tends to increase towards the rim. This feature is recorded only in this phenocryst among those analyzed. Cr_2O_3 is lower than in the augites of the same samples. It varies positively with Mg# from 0.6 and 0 wt% with the higher values in the core (Fig. 9.34). Like for augites, TiO_2 (0.6 and 0.3 wt%) increases at decreasing Mg# but in general has a lower concentration than in the augites of the same sample (Fig. 9.34), implying that probably pigeonites begun to crystallize after the augites, but before the oxides

(see previous section, Fig. 9.25). The pigeonites of the Intermediate Unit are present at Tiourjdal, in almost all flows of this unit (TJ25, TJ26, TJ29, TJ30, TJ31), while at Telouet and Oued Lahr it is present only in two lava flows of the uppermost part of the unit: TEL22 and TEL23 at Telouet and OL10 and OL11 at Oued Lahr. Pigeonites of the Intermediate Unit have the widest compositional variation range both in Wo-En-Fs composition ($Wo_{7-12}En_{41-70}Fs_{21-45}$) and in Mg# (between 76.3 to 47.6). Cr_2O_3 concentration is lower than pigeonite of the

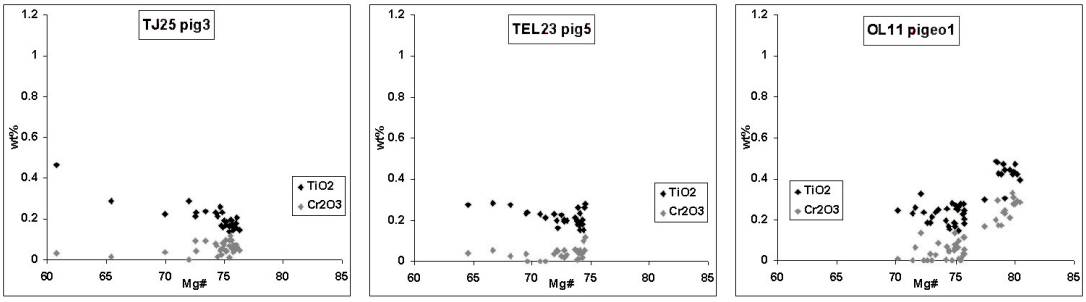

Figure 9.35: Cr_2O_3 and TiO_2 variations vs Mg# (EMP analyses) of pigeonites TJ25 pig3, TEL23 pig5 and OL11 pig1 of the Intermediate Unit.

Lower Unit. It varies positively with Mg#, between 0.18 and 0 wt% with the higher values in the cores (Fig. 9.35). TiO_2 concentration varies negatively with the Mg# between 0.13 and 0.49 wt%. Again, it has a lower concentration than in pigeonites of the Lower Unit (Fig. 9.35). As stressed before, pigeonites have been detected in some flows of the Upper Unit, occurring as microphenocrysts in the porphyric ground-mass, but have not been analysed. However, EMP analyses for pigeonites of the Upper Unit flows are available in sample AN540 from the Oum R'Rbia sequence (Chap. 12)

10 WHOLE-ROCK GEOCHEMISTRY OF CENTRAL HIGH ATLAS PILES

10.1 MAJOR, MINOR AND TRACE ELEMENT COMPOSITIONS

Major and trace elements analyses on whole-rocks have been determinated by XRF and ICP-MS analyses (Chap. **??**). In total 34 samples from Tiourjdal (TJ), 23 samples from Telouet (TEL) and 18 samples from Oued Lahr section (OL) have been analysed by XRF, while 23 samples from Tiourjdal, 10 samples from Telouet and 9 from Oued Lahr have been analysed by ICP-MS. Together with the Tiourjdal set we will take in account the data whole-rock compositions of the samples AN49, AN134 (belonging the Lower Unit), AN137A, AN138 (Intermediate Unit) and AN156A (Recurrent Unit) and AN169 (Recurrent Unit) for the Telouet section since these samples, as described in previous chapters, have been analysed by EMPA and LA-ICP-MS (during this work, Laser Ablation not performed on AN49), ICP-MS (analyses already done). For the sake of completeness I will include also the sample AN61 belonging the Recurrent Unit at Oued Lahr. XRF and ICP-MS whole rock analyses allow to recognize four units in which the basaltic lava piles of each locality can be grouped, on the basis of some element contents. From the base to the top of the lava piles (i.e., from the oldest to the youngest unit) there are: the Lower, Intermediate, Upper and the Recurrent Unit. Moreover this chemo-stratigraphy allows to correlate the different sections over an area of 10^4 Km^2 in the Central High Atlas (CHA). In a TAS diagram (Total Alkali Silica, SiO_2 wt% vs $Na_2O + K_2O$ wt%, **Bas *et al.*, 1992**, Fig. 10.1, triangles for Tiourjdal section, circles for Telouet section and squares with star for Oued Lahr section. Blue for the Lower Unit, red for the Intermediate Unit, yellow for the Upper Unit and green for the Recurrent Unit) CHA rocks plot in the sub-alkaline rocks field (**Irvine & Baragar, 1971**), being mostly basaltic andesites with few basalts. In particular both the Lower and Intermediate Unit are principally represented by basaltic andesites with minor basalts, the Upper Unit is represented by basalts with few slightly evolved basaltic andesites while

rocks belonging the Recurrent Unit are only basalts. Some rocks show very low and high SiO_2 plotting off from the rest of the rocks, i.e. one sample belonging to the Intermediate Unit at Telouet classifies as andesite. If we compare the TAS diagram with that of SiO_2 vs L.O.I.$_{tot}$ (total Loss On Ignition defined as the volatile loss from 0°C to 1000°C), it is possible to note that rocks with the highest and lowest SiO_2 are among those which have the highest L.O.I.$_{tot}$ (Fig. 10.2), so it is possible that alteration could have affected the whole rock composition towards more basic and acid compositions, remobilizing some elements. In an AFM dia-

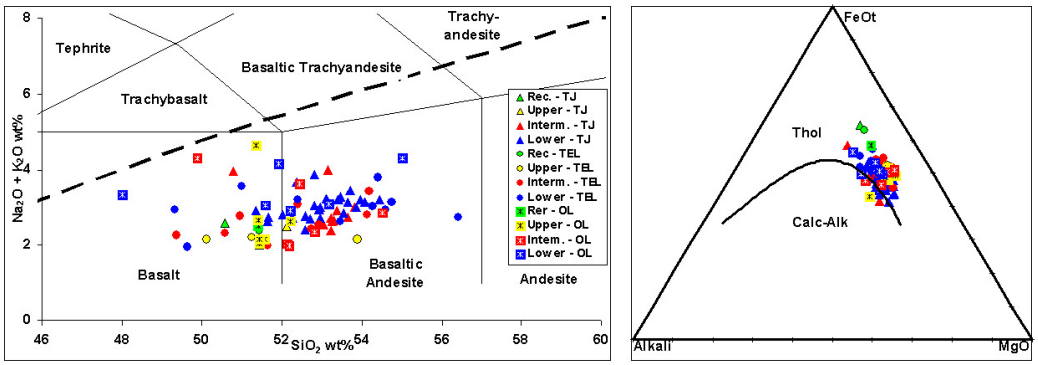

Figure 10.1: TAS and AFM classification diagram of all basalts from CHA analysed by XRF.

gram (A = Alkali, Na_2O + K_2O wt%, F = FeO_{tot} wt% and M = MgO wt% all recalculated to 100, Fig. 10.1, curved line separating tholeiitic and calc-alkaline rocks after **Irvine & Baragar (1971)**) CHA rocks define a tholeiitic evolution trend with the typical increase of Fe (and/or Fe/Mg) for the most differentiated rocks. The alkali enrichment in not visible, indicating the low differentiation degree of the CHA rocks. Major elements (wt%) vs L.O.I.$_{tot}$ (wt%) diagrams show that some elements are affected by remobilization due to weathering and/or hydrothermal fluids. In particular, as previously highlighted for SiO_2, some major element contents are correlated (both positively and negatively) with L.O.I.$_{tot}$. MgO, Alkali (Na_2O + K_2O) are positively correlated with L.O.I.$_{tot}$. TiO_2 and P_2O_5 are nearly constant, with no apparent correlation with L.O.I.$_{tot}$. CaO is negatively correlated, while Al_2O_3 and FeO_{tot} seem to be unaffected even if at high L.O.I.$_{tot}$ (4-5 wt% or higher) concentrations of these elements are more scattered (Fig. 10.2). Noteworthy, in TiO_2 and P_2O_5 vs L.O.I.$_{tot}$ diagrams the four units are well recognizable and the Telouet and Oued Lahr section have higher L.O.I.$_{tot}$ than the Tiourjdal section. Globally, CHA rocks are slightly to moderately evolved, with Mg# (Mg# = 100 x molar Mg/(Mg + Fe), $Fe^{3+}/Fe^{2+} = 0.13$) varying from 68.4 to 44.0. It is possible to note that Mg# increases from the

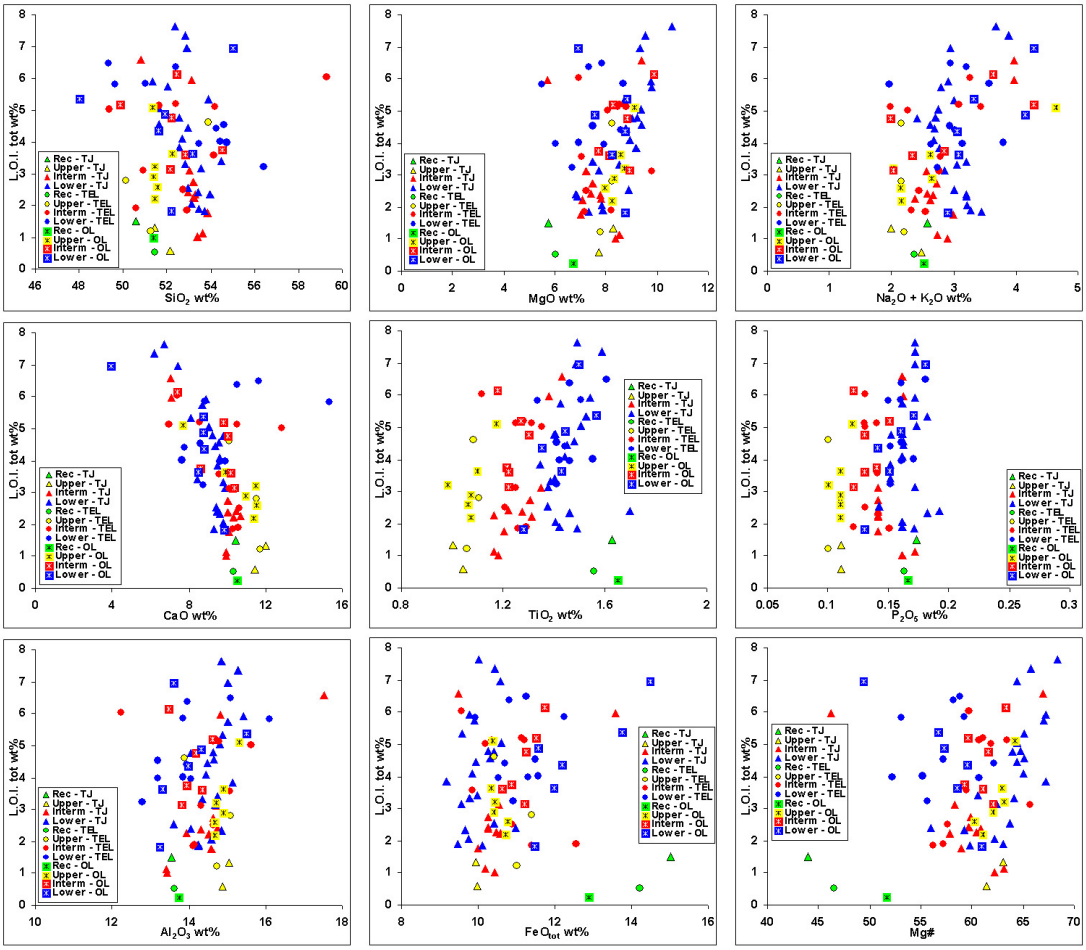

Figure 10.2: Major elements and Mg# vs L.O.I.$_{tot}$ diagrams of all basalts from CHA analysed by XRF.

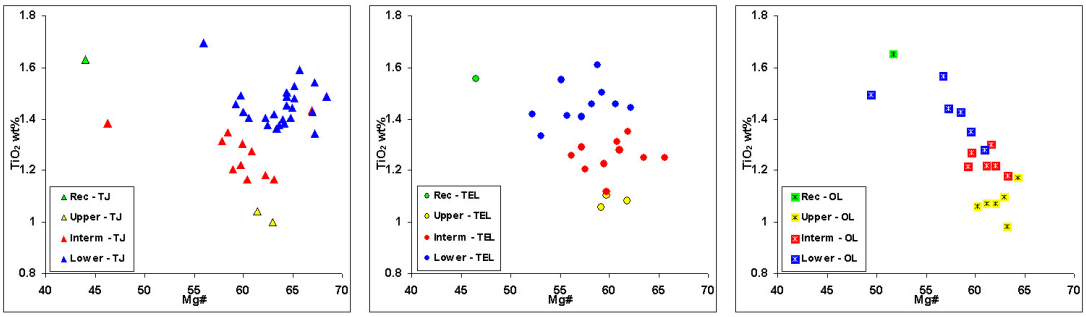

Figure 10.3: Mg# vs TiO_2 for Tiourjdal, Telouet (CHA southern flank) and Oued Lahr (CHA northern flank).

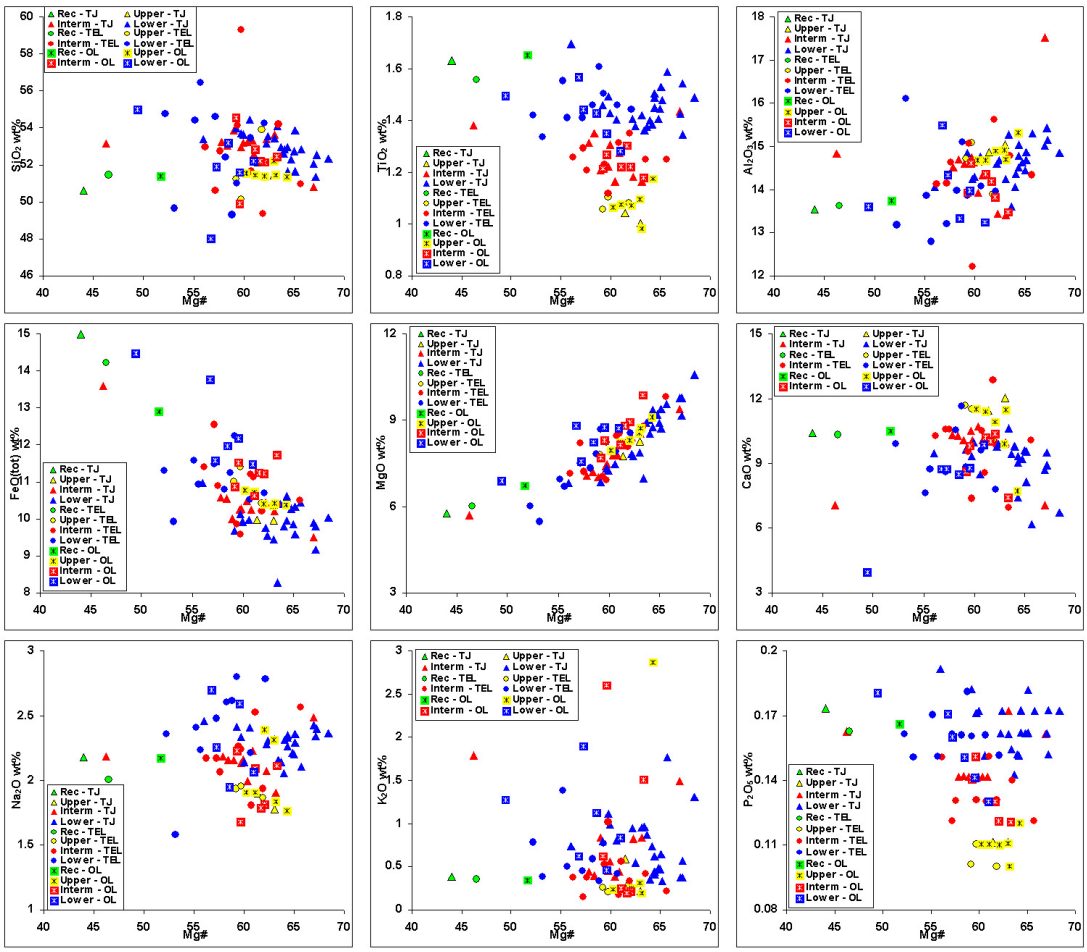

Figure 10.4: Major elements and Mg# vs L.O.I.$_{tot}$ diagrams of all basalts from CHA analysed by XRF.

Lower to the Upper Unit in all CHA sections, except than at Tiourjdal where the highest Mg# of the Lower Unit could be affected by the high L.O.I.$_{tot}$ of the samples (Fig. 10.2) as for two Intermediate samples, with the highest and the lowest Mg# (Fig. 10.3), which display high L.O.I.$_{tot}$ (¿ 6 wt%). Mg# of the Lower Unit varies from 49.4 to 68.4, from 46.2 to 66.9 for the Intermediate Unit, from 59.1 to 64.2 for the Upper Unit. On the other side the Recurrent Unit shows the lowest Mg# both at Tiourjdal and Telouet. In general Mg# is poorly correlated with major elements. Alkalies (Na_2O + K_2O) are too scattered, as said before due to secondary alteration. TiO_2 and P_2O_5 are almost constant within each unit and both of them allow to identify one unit from the others. The Lower Unit has the highest TiO_2 with contents varying from 1.30 and 1.70 wt%, progressively decreasing in the Intermediate (1.12-1.43 wt%) and in the Upper Unit (0.98-1.17 wt%). In the Recurrent Unit TiO_2 increases again (1.56-1.65 wt%). However globally the Recurrent Unit has a mean TiO_2 content higher than the Lower Unit. Also P_2O_5 displays the same behaviour with contents decreasing from the Lower to the Upper Unit and again high concentrations for the Recurrent Unit (Fig. 10.4). SiO_2 and CaO show a negative correlation with Mg#, even if the values are very scattered. MgO and FeO_{tot} are well correlated with Mg# while Al_2O_3 shows a global positive correlation. The high L.O.I.$_{tot}$ measured in most samples (up to 7.6 wt%, Fig. 10.2) hides possible differentiation trend within each unit in all sections. Compatible minor elements are slightly better correlated with Mg#, being less sensible to secondary alteration (Fig. 10.5). Cr and Ni are roughly positively correlated probably indicating olivine and clinopyroxene fractionation during the differentiation of the parental magmas. Globally the Lower Unit has the highest Cr and Ni contents (508 and 142 ppm, respectively), even if at Telouet the Lower, Intermediate and Upper Unit have similar Cr and Ni content so being not distinguishable. Also at Tiourjdal, Cr and Ni compositional field of the Upper Unit is overlapped to that of the Intermediate Unit. Notably, at Oued Lahr even if the Lower, Intermediate and Upper Unit are quite well distinct and Cr and Ni are positively correlated with Mg# within each unit, these elements tend to decrease from the Lower to the Upper at increasing Mg#. The Recurrent Unit has low Cr and Ni at Telouet (118 and 67 ppm, respectively) while at Tiourjdal Cr and Ni of the Recurrent flow are comparable with the Intermediate and Upper Unit (235 and 90 ppm, respectively). V and Sc show a quite restricted range (generally from 242 to 315 ppm and from 13 to 25 ppm respectively). The compositional fields of the Lower, Intermediate and Upper Unit are largely overlapped for V (which increases slightly up-section) and for Sc (Fig. 10.6). V of

the Recurrent Unit has the same concentration of the other units at Tiourjdal, but it is very high at Telouet (422 ppm). On the contrary, Sc has very high values in the Recurrent Unit both at Tiourjdal (39 ppm) and Telouet (50 ppm). LILE (Large Ion Lithophile Elements) are probably the elements which are worst correlated with Mg#, also due to their high affinity with aqueous fluids, leading to a great mobility during weathering and hydrothermal alteration. Only Sr and Ba allow to recognize partially the first three units even if with no obvious trend, except for a decreasing Sr content in the Lower Unit at Tiourjdal. Ba seems to be more affected by secondary alteration compared to Sr, as visible from its negative correlation with L.O.I.$_{tot}$ (Fig. 10.8). Sr and Ba compositions of the Recurrent Unit are well distinct. Rb and Cs (not shown) are too scattered and except for the Recurrent Unit, the Lower, Intermediate and Upper Unit compositional fields are completely overlapped (Fig 10.7). The Lower Unit has the highest Sr and Ba contents (up to 306 and 290 ppm, respectively), while the Intermediate and Upper Unit have progressively lower concentrations. Sr and Ba seem not to be affected by alteration, since their concentrations remain constant at increasing L.O.I.$_{tot}$ (Fig. 10.8) within each unit, even if for Ba it is possible to see a decrease in the Lower Unit at Tiourjdal. No apparent correlation between Sr and Ba/Sr with CaO within each unit, indicative of plagioclase fractionation, it is visible (Fig. 10.10), even if from the Lower to the Upper Unit there is an apparent Sr and Ba/Sr decrease at increasing CaO. However in the Ba vs Ba/Sr diagram (also seen in a similar diagram based on Sr and Ba content in plagioclase, CHAP. **??**), the Lower Unit, the Intermediate and Upper Unit define three fractional crystallization trends (Fig. 10.10), while the Recurrent Unit shows much higher Ba/Sr with respect to the older units, probably indicating a very important contribution of plagioclase fractionation to the genesis of the Recurrent Unit basalts. We will see in the Chap. 15, relative to the basalts petrogenesis as these whole-rock geochemistry informations and compositional variations of mineral phases (plagioclases and augites), are confirmed by computer modelization performed with PETROLOG (Danyushevsky, 2001). HFSE (High Field Strength Elements) are better correlated with Mg# with respect to LILE. All elements, except for Pb, allow to recognize the four units with a general increase of concentration towards lower Mg#. In particular, the Lower Unit is the most enriched in HFSE, while the Intermediate and the Upper Unit have decreasing concentrations. The Recurrent Unit has a more depleted composition plotting at lower HFSE contents for low Mg# (Fig. 10.11). The four units are well distinct in the Zr vs Zr/Nb and Th vs Th/Nb diagrams. In the first it is visible an increasing trend from

the Lower to the Upper Unit for an almost constant Zr and Nb composition of the source. In the second, the Th and Nb composition decreases from the Lower to the Upper Unit (Fig. 10.11). The Recurrent Unit displays depleted compositional field compared to those of the younger units for the most incompatible elements. Also REEs (Rare Earth Elements) show a good negative correlation with Mg#, generally being enriched in the most evolved samples (Fig. 10.12). In general the four units are well recognizable, with REE concentrations decreasing from the Lower to the Upper Unit. However, two particular features are visible in the Mg# vs LREE, MREE and HREE diagrams. The first is the progressive overlapping of the Lower, Intermediate and Upper Unit compositional fields from the LREE to HREE.

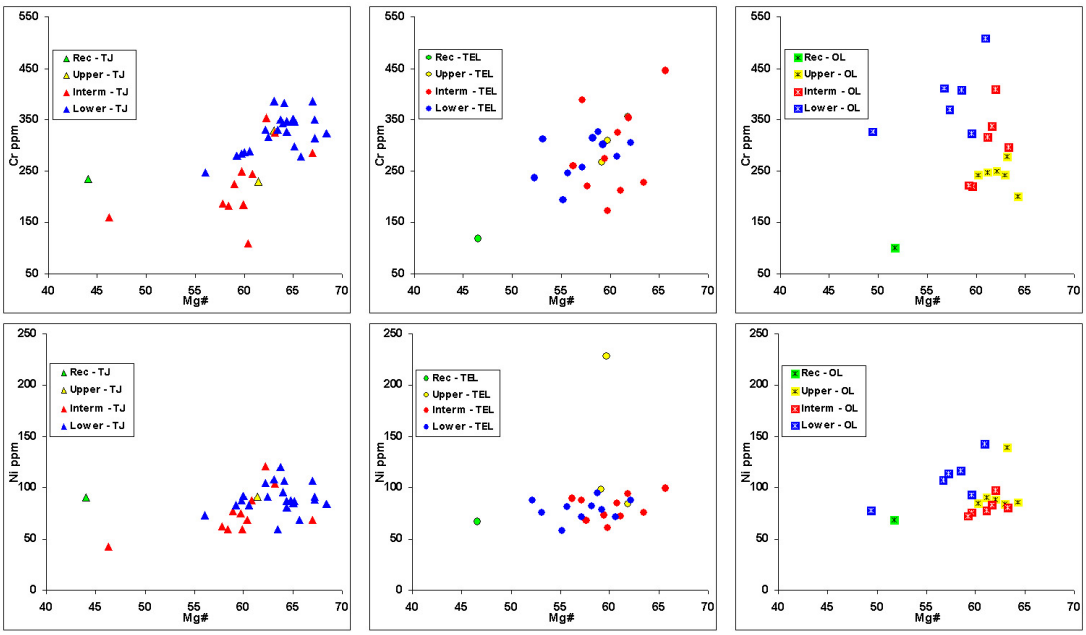

Figure 10.5: Mg# vs Cr, Ni, V, Sc and Cr vs Ni diagram for all CHA basalts analysed by XRF.

This is probably related not to a change in the REE-source composition of the basalts, but to its different partial melting degree (i.e., increasing from the Lower to the Upper Unit) which affect mostly the LREE content with respect to that of the HREE. The second important feature is the increase of HREE relative to LREE in the Recurrent Unit, this probably related to a change in the composition and/or source mineralogy, relative to the older units. A similar behaviour is visible in the Mg# vs Ce/Yb, Sm/Nd and Lu/Hf (not shown), where the ratios remain almost constant within each unit and vary progressively from

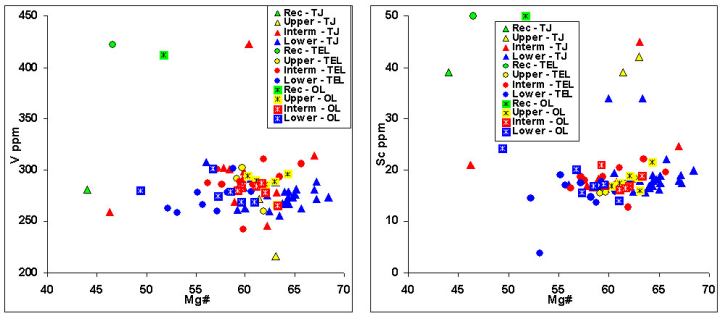

Figure 10.6: Mg# vs V, Sc diagram for all CHA basalts analysed by XRF.

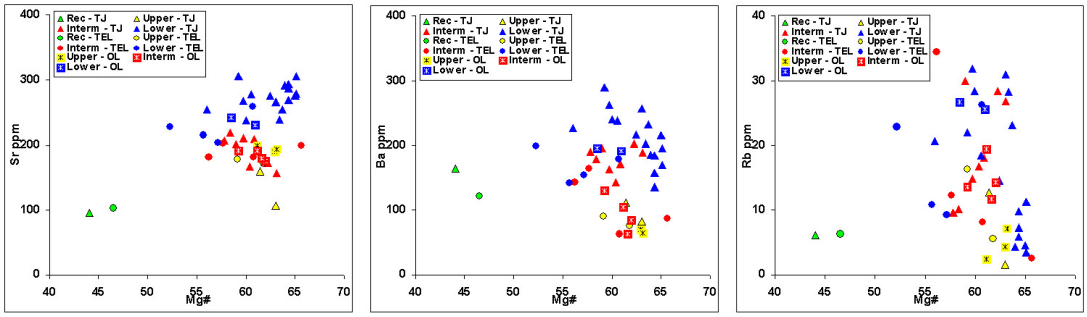

Figure 10.7: Mg# vs LILE diagram for all CHA basalts analysed by ICP-MS.

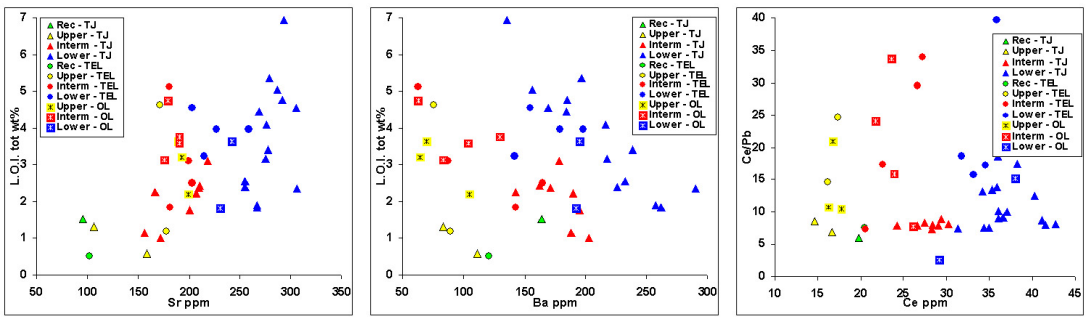

Figure 10.8: Sr and Ba vs L.O.I.$_{tot}$ and Ce vs Ce/Pb diagrams for all CHA basalts analysed.

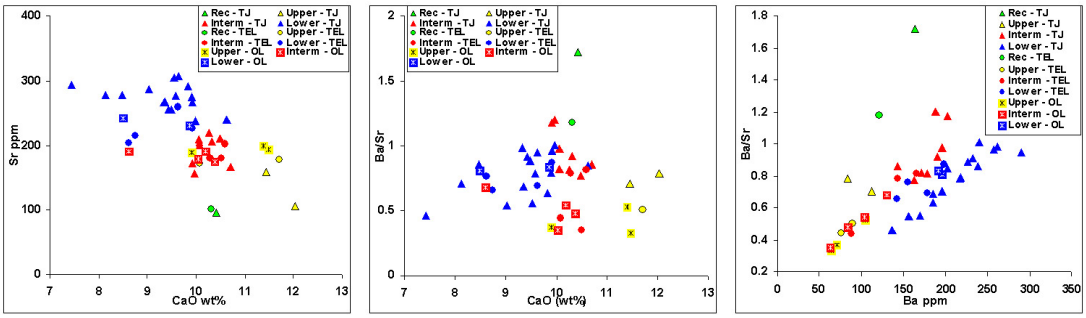

Figure 10.9: Sr vs L.O.I.$_{tot}$, CaO vs Sr and Ba vs Ba/Sr diagrams for all CHA basalts analysed by ICP-MS.

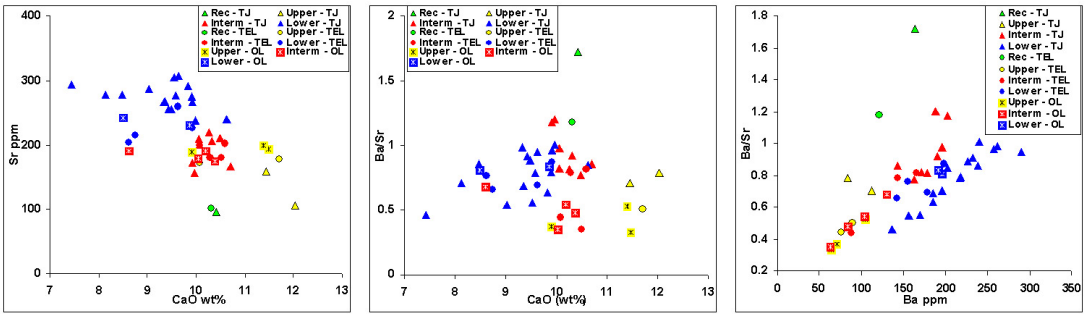

Figure 10.10: Sr vs L.O.I.$_{tot}$, CaO vs Sr and Ba vs Ba/Sr diagrams for all CHA basalts analysed by ICP-MS.

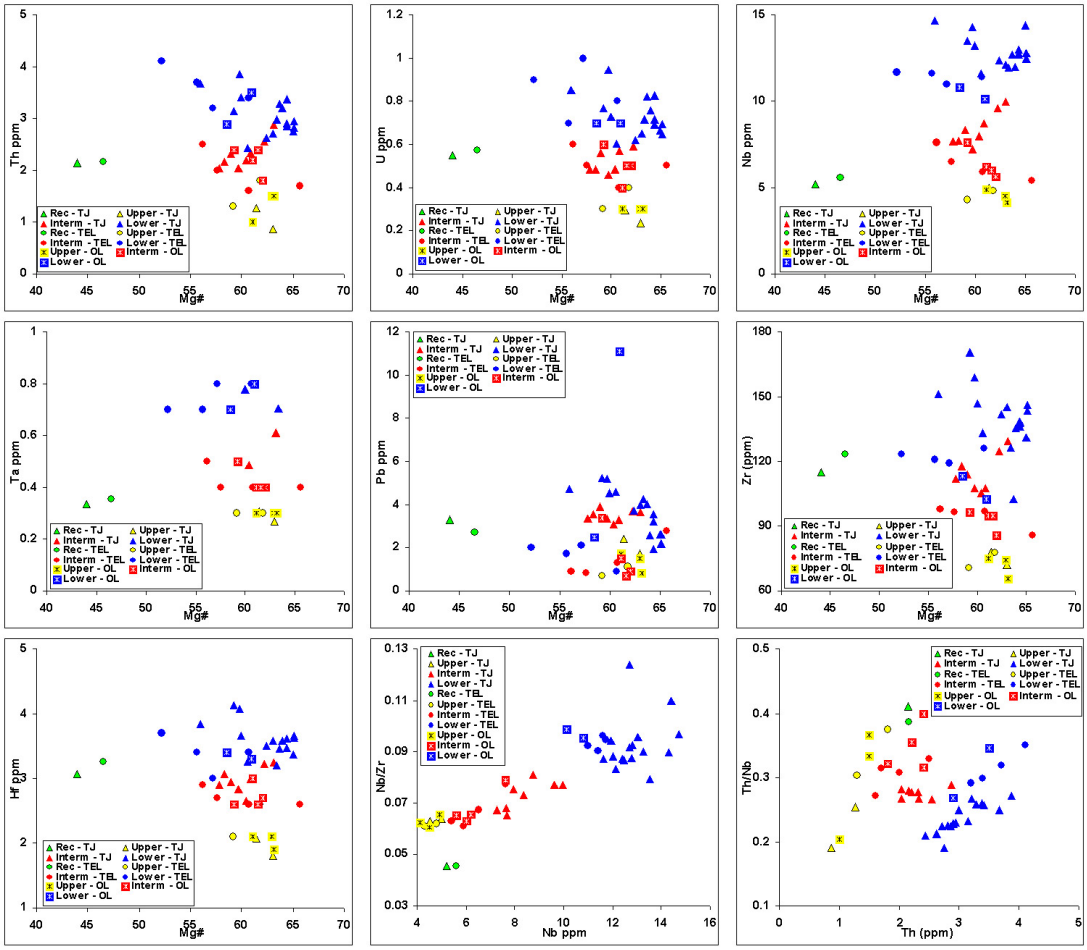

Figure 10.11: Mg# vs HFSE, Nb vs Nb/Zr and Th vs Th/Nb diagrams for all CHA basalts analysed by ICP-MS.

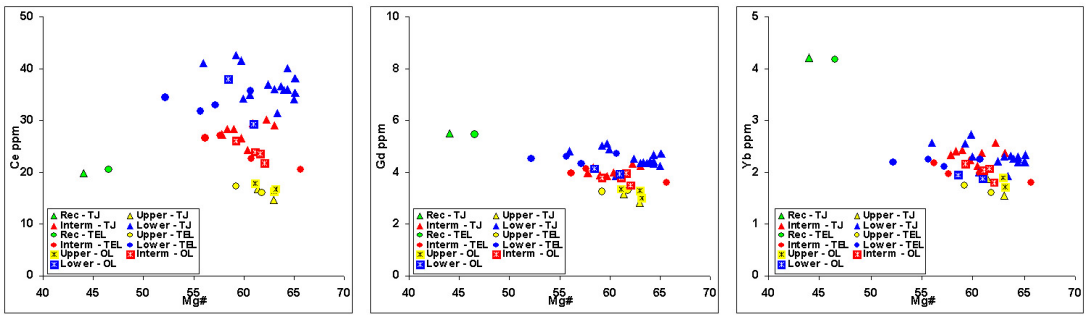

Figure 10.12: Mg# vs Ce (LREE), Gd (MREE) and Yb (HREE) diagrams for all CHA basalts analysed by ICP-MS.

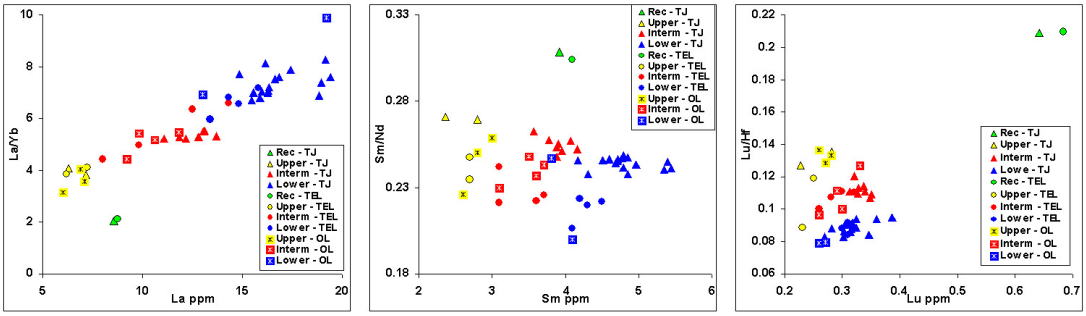

Figure 10.13: La vs La/Yb, Sm vs Sm/Nd and Lu vs Lu/Hf diagrams for all CHA basalts analysed by ICP-MS.

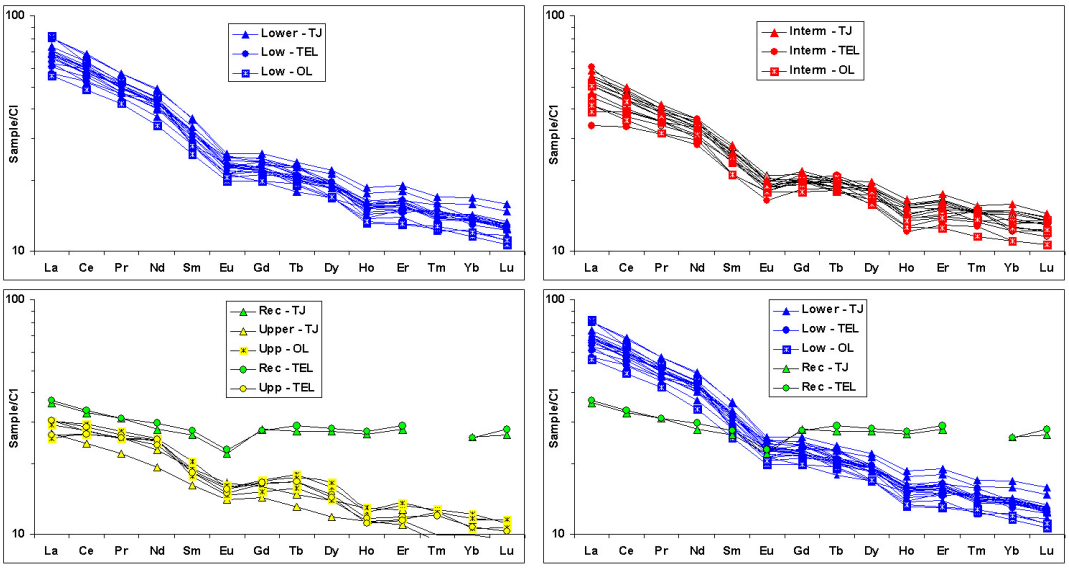

Figure 10.14: REE spider-diagrams C1 chondrite normalized (**Andres & Grevesse, 1989**) for all CHA basalts analysed by ICP-MS.

the Lower to the Upper Unit, but they are completely different in the Recurrent Unit. In chondrite normalized diagrams (**Andres & Grevesse, 1989**), the analysed basalts display REE sub-parallel patterns with a monotonous decrease from the La to Lu (LREE to HREE). LREE enrichment over HREE decreases from the Lower (La/Yb_{Ch} = 4.8-5.2) to Upper Unit (La/Yb_{Ch} = 2.8-2.2), while the Recurrent Unit is characterized by a nearly flat REE pattern (La/Yb_{Ch} = 1.4) with a LREE depletion and a HREE enrichment with respect to the older units (Fig. 10.14). The negative Eu anomaly, well visible in the REE pattern of the Recurrent Unit, is less marked in the other units, which probably means that plagioclase fractionation played an important role in the genesis of the Recurrent Unit basalts. This information supports the plagioclase fractionation hypothesis brought forward on the base of Ba vs Ba/Sr diagram (Fig. 10.10). The Primitive Mantle (PM) normalized multi-element diagram (**McDonough & s. Sun, 1995**), shows most of the features described before. First of all the common scattering of Rb and Cs, more susceptible to secondary alteration. The strong Sr_{PM} and, less evident, Eu_{PM} negative anomaly, maybe sign of plagioclase fractionation. Nb_{PM} and Ta_{PM} show a clear negative anomaly, which together the decreasing $LREE/HREE_{PM}$ from the Lower to the Upper Unit and an almost REE_{PM} flat pattern for the Recurrent Unit are characteristic of CAMP basalts (Fig. 10.14). Some flows show a Pb_{PM} anomaly: in the Lower Unit at Tiourjdal both positive and negative Pb_{PM} anomaly is present, while the Intermediate, Upper and Recurrent Unit basalts have positive Pb_{PM} anomaly (Fig. 10.15). If this feature is compared with the Ce vs Ce/Pb diagram (Fig. 10.8) the Pb_{PM} negative anomaly could be related to its remobilization by aqueous fluids which in turn led to high Ce/Pb values. A similar behaviour is visible for Telouet samples where almost all the flows have a Pb_{PM} negative anomaly (and high Ce/Pb), except for one flow of the Intermediate Unit and for the flow belonging the Recurrent Unit. Even at Oued Lahr most of the flows have a negative Pb_{PM} anomaly, few with positive or no Pb_{PM} anomaly. Finally the Recurrent Unit is characterized by a little negative Ti_{PM} anomaly, not present in the oldest units.

10.2 Sr-Nd ISOTOPIC COMPOSITIONS

Only samples from the Tiourjdal section have been analysed for Sr and Nd isotopic compositions by TIMS (Thermal Ionization Mass Spectrometry). No isotopic analyses are available for Oued Lahr while for Telouet we will use Sr and Nd isotopic compositions of sample AN169. In total 12 samples from the

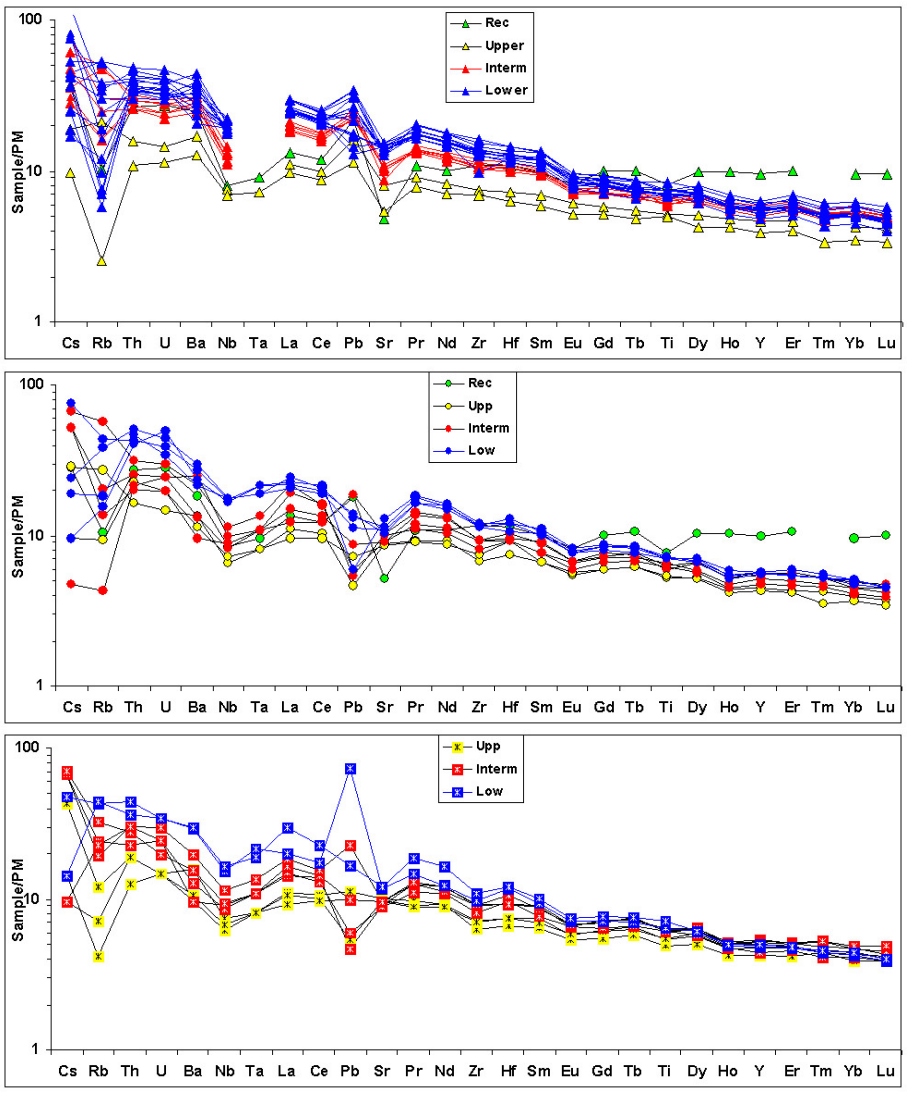

Figure 10.15: Primitive mantle normalized spider-diagrams (**McDonough & s. Sun, 1995**) for all CHA basalts analysed by ICP-MS.

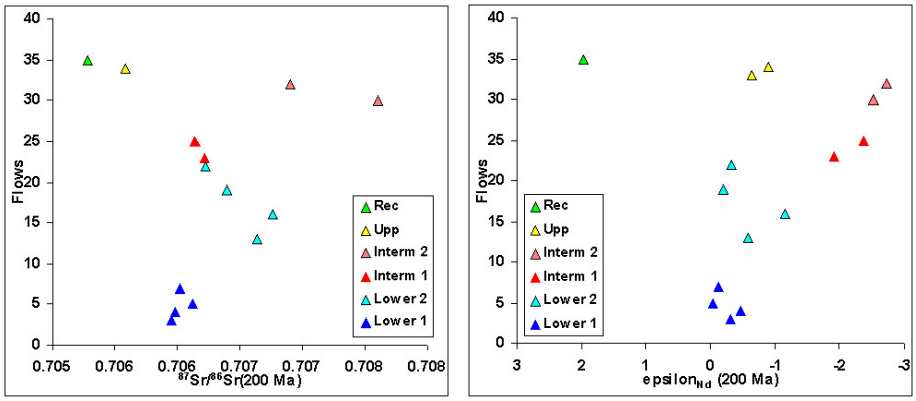

Figure 10.16: Tiourjdal up-section variations of Sr and Nd isotopic compositions, expressed as $^{87}Sr/^{86}Sr$ and εNd calculated at 200 Ma. Blue and cyan triangles for the Lower Unit, red and orange circles for the Intermediate Unit, yellow diamonds for the Upper Unit and green square for the Recurrent Unit.

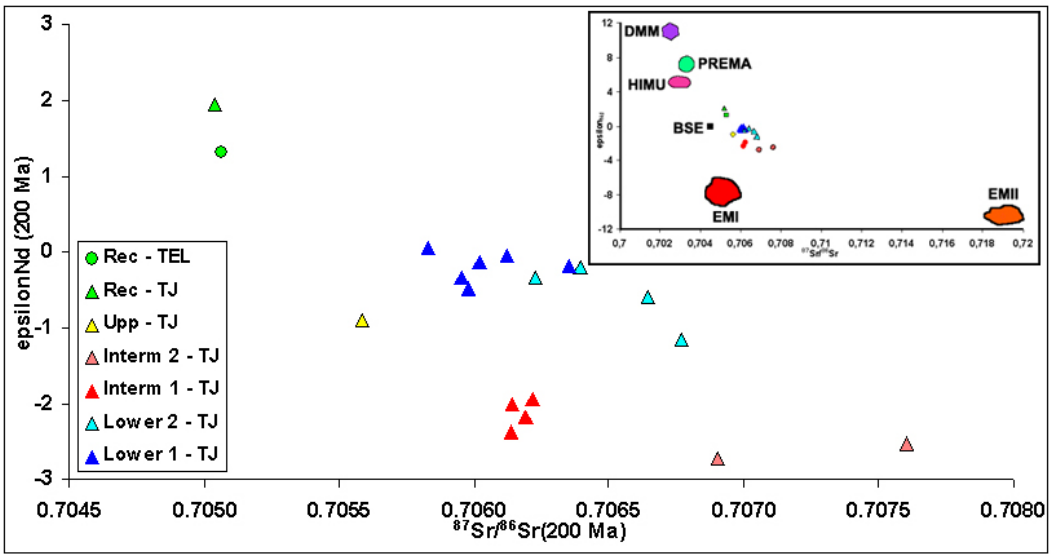

Figure 10.17: $^{87}Sr/^{86}Sr$ vs εNd diagram (calculated at 200 Ma). In the diagram are plotted samples AN49 and AN134 for the Lower Unit, AN137A and AN138 for the Intermediate Unit at Tiourjdal and AN169 for the Recurrent Unit at Telouet. Triangles for Tiourjdal section and circle for Telouet sequence. In the inset are shown the main oceanic mantle reservoirs of **Zindler & Hart (1986)**.

Tiourjdal lava piles 8 for the Lower Unit (TJ3, TJ4, TJ5, TJ7, TJ13, TJ16, TJ19, TJ22) and 4 for the Intermediate Unit (TJ23, TJ25, TJ30, TJ32) have been analysed both for Sr and Nd isotopes. From the Upper Unit two samples have been analysed, one (AN140) for Nd, while another (AN141) both for Sr and Nd. Finally for the Recurrent Unit, one sample from the Tazgaoute section (few km from Tiourjdal) has been analysed for Sr and Nd isotopes (Fig. 10.16). Like for minor and trace elements, the four units are well recognizable having distinct Sr and Nd isotopic compositions, as visible in a εNdi vs $^{87}Sr/^{86}Sr_i$ diagram (Fig. 10.17). As a whole, the Lower and the Intermediate Unit show a quite to strong enriched initial (calculated at 200 Ma) $^{87}Sr/^{86}Sr$ (0.70595-0.70677 for the Lower Unit and 0.70614-0.70761 for the Intermediate Unit) isotopic compositions and from nearly chondritic to fairly depleted for $^{143}Nd/^{144}Nd$ compositions (0.512321-0.512383, i.e., -0.04¡εNd¡-1.15 for the Lower Unit and 0.512240-0.512281, -1.92¡εNd¡-2.72 for the Intermediate Unit). The Upper Unit has lower radiogenic Sr composition (0.705587, one sample) compared with the Lower and Intermediate Unit and almost chondritic Nd composition (0.512333-0.512346, i.e., -0.65¡εNd¡-0.90). The Recurrent Unit shows the lowest initial Sr isotopic composition (0.705040-0.705061) and a marked enriched Nd composition (0.512448-0.512479, i.e. 1.33¡εNd¡1.95). In the chapter relative to CHA and MA/WM lava pile correlations (Chap. 14), I will show as using geochemical (REE and HFSE) and paleomagnetic data, it is possible to correlate the volcanic units belonging different Moroccan sequences and as some geochemical units, i.e. lava flow groups with a well define trace elements composition, do not outcrop in all studied sites. Moreover the combined use of geochemical and paleomagnetic data allows to recognize the existence of two sub-units within the Lower and Intermediate Unit, namely the Lower 1, Lower 2, Intermediate 1 and Intermediate 2 sub-units, in the Tiourjdal sequence supposedly the most complete (Fig. 14.3 and 14.5). Although isotopic data are scarce, the four sub-units defined by the incompatible element diagrams have distinct Sr and Nd isotopic compositions. In particular, within each unit, the youngest sub-unit (Lower 2 and Interm 2) have respectively higher and lower Sr and Nd isotopic compositions with respect to the older ones (Lower 1 and Interm 1), i.e. the two youngest sub-units have more enriched Sr and depleted Nd compositions. $^{87}Sr/^{86}Sr_i$ and $^{143}Nd/^{144}Nd_i$ plotted together with the relative parent-daughter ratios (Fig. 10.18), have a distinct negative correlation for the Lower and Intermediate Unit. More in detail, the Rb/Sr vs $^{87}Sr/^{86}Sr_i$ diagram shows that the youngest sub-units (Lower 2 and Interm 2) have lower Rb/Sr and higher $8^{87}Sr/^{86}Sr_i$ compared to the relative

older sub-units (Lower 1 and Interm 1), so giving a roughly negative correlation across the Lower and Intermediate Unit. Such trends would mean that the high $^{87}Sr/^{86}Sr_i$ of the youngest sub-units are not due to higher amounts of crustal contamination, since this should be produce also higher Rb/Sr. On the other side, a similar negative trend is present in the Sm/Nd vs $^{143}Nd/^{144}Nd_i$ diagram, where a time-related (from the Lower 1 to Interm 2 sub-unit) increase of Sm/Nd coupled with a decreasing $^{143}Nd/^{144}Nd_i$ is clearly visible. Also here, crustal contamination could be excluded, as it would produce a positive correlation between Sm/Nd and $^{143}Nd/^{144}Nd_i$. The Upper Unit has Sr isotopic composition lower than the Lower and Intermediate Unit, but Nd isotopic compositions similar to those of the Lower Unit (in particular to that of the Lower 1 sub-unit) coupled with a slightly higher Sm/Nd. Finally the Recurrent Unit displays the lowest $^{87}Sr/^{86}Sr_i$ and low Rb/Sr coupled with the highest $^{143}Nd/^{144}Nd_i$ compositions and Sm/Nd. One possible explanation, at least for the negative correlation in the Rb/Sr vs $^{87}Sr/^{86}Sr_i$ diagram, could be the remobilization of Rb with respect to Sr by secondary alteration, as visible in the Rb/Sr vs L.O.I.$_{tot}$ diagram where the negative correlation for the samples of the Lower and Intermediate Unit is clear (Fig. 10.19). In fact, the samples with the highest L.O.I.$_{tot}$ have the highest $^{87}Sr/^{86}Sr_i$ and the lowest Rb/Sr, even if this effect is more pronounced for Lower 1 sub-unit samples (Fig. 10.19). The effects of alteration could be highlighted also by the Ce vs Ce/Pb diagram where it is possible to see that samples from the Lower 1 sub-unit show very high Ce/Pb for a nearly constant Ce while the other units show almost Ce/Pb for decreasing Ce. On the other side, the Interm 2 sub-unit displays the highest $^{87}Sr/^{86}Sr_i$ coupled with only moderately high L.O.I.$_{tot}$, this probably indicating that these samples have been affected in lesser amount by alteration and, even if some secondary alteration occurred, this could have not hide the negative correlation visible in Fig. 10.19. By contrast, the Sm/Nd system is not affected by fluid remobilization which suggests that the negative trend shown by the Lower and Intermediate samples in Fig. 10.18 (diagram on the right) reflects magmatic and not post-magmatic effects. No clear evolution is shown by the samples of each unit (and sub-unit) if $^{87}Sr/^{86}Sr_i$ and $^{143}Nd/^{144}Nd_i$ are plotted versus SiO_2 or Mg#, even if in the SiO_2 vs $^{87}Sr/^{86}Sr_i$ diagram the two youngest sub-units (Lower 2 and Interm 2) show a negative trend with respect to the oldest one (Fig. 10.19). More clear is the positive correlation with Ce/Yb, where the units are progressively enriched in LREE over HREE from the youngest to the oldest one. Again, within the Lower and Intermediate Unit, the two sub-unit are well defined, having the youngest sub-units higher $^{87}Sr/^{86}Sr_i$

than the oldest one for constant Ce/Yb (Fig. 10.20). The same sub-units show

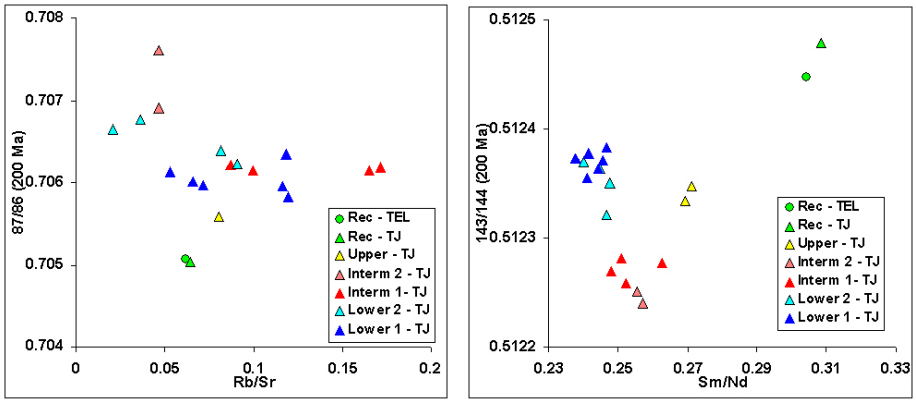

Figure 10.18: Rb/Sr vs $^{87}Sr/^{86}Sr_i$ and Sm/Nd vs $^{143}Nd/^{144}Nd_i$ diagrams (calculated at 200 Ma) of Tiourjdal and Telouet basalts analysed by TIMS.

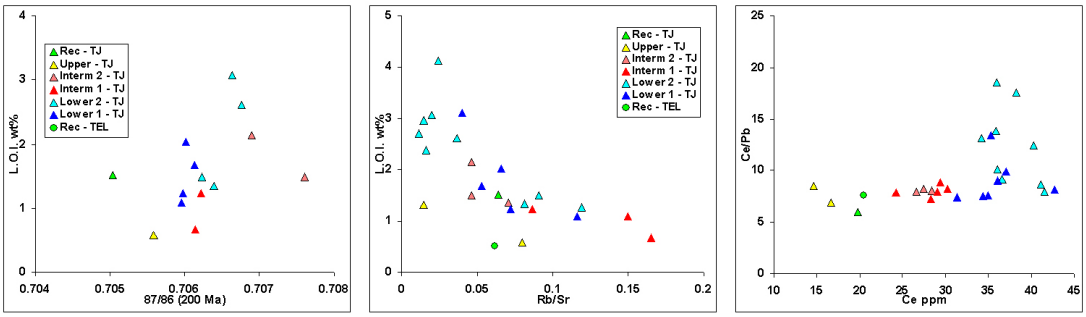

Figure 10.19: $^{87}Sr/^{86}Sr_i$ and Rb/Sr vs L.O.I.$_{tot}$ and Ce vs Ce/Pb diagrams of Tiourjdal and Telouet basalts analysed by TIMS.

progressively enriched Nd compositions, with no obvious correlation with Mg# nor SiO_2, while $^{143}Nd/^{144}Nd_i$ shows a negative correlation with Ce/Yb from the Recurrent, through the Upper to the Intermediate Unit. In the Lower Unit the Nd isotopic composition increases again at Ce/Yb higher than the other units. As for Ce/Yb vs $^{87}Sr/^{86}Sr_i$ diagram, the youngest Lower and Intermediate sub-units show an lower Nd isotopic composition for constant Ce/Yb (Fig. 10.21). Also for HFSE vs $^{87}Sr/^{86}Sr_i$ and $^{143}Nd/^{144}Nd_i$ there is no clear correlation within the Lower and Intermediate Unit, since samples with the most enriched isotopic compositions do not have the highest HFSE concentration (Fig. 10.22). The same happens if isotopic ratios are plotted versus HFSE ratios (i.e., Th/Nb and Nb/Zr, not shown).

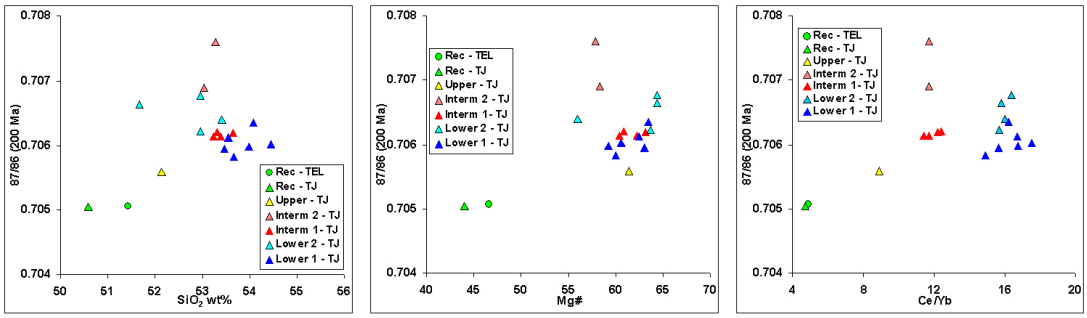

Figure 10.20: SiO_2, Mg# and Ce/Yb vs $^{87}Sr/^{86}Sr_i$ (calculated at 200 Ma) of Tiourjdal and Telouet basalts analysed by TIMS.

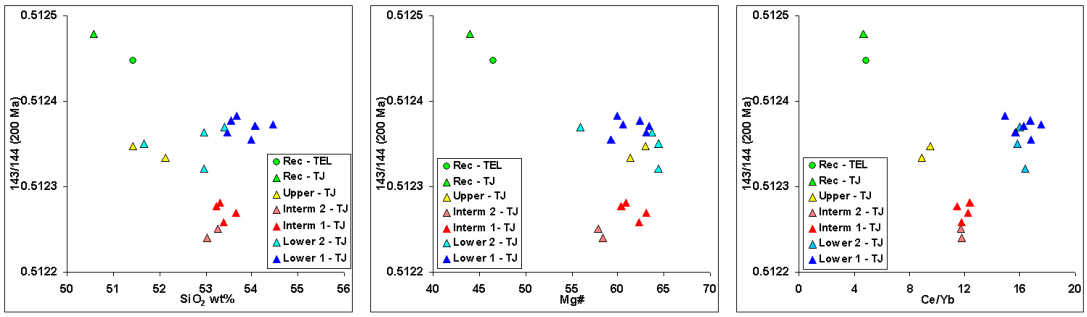

Figure 10.21: SiO_2, Mg# and Ce/Yb vs $^{143}Nd/^{144}Nd_i$ (calculated at 200 Ma) of Tiourjdal and Telouet basalts analysed by TIMS.

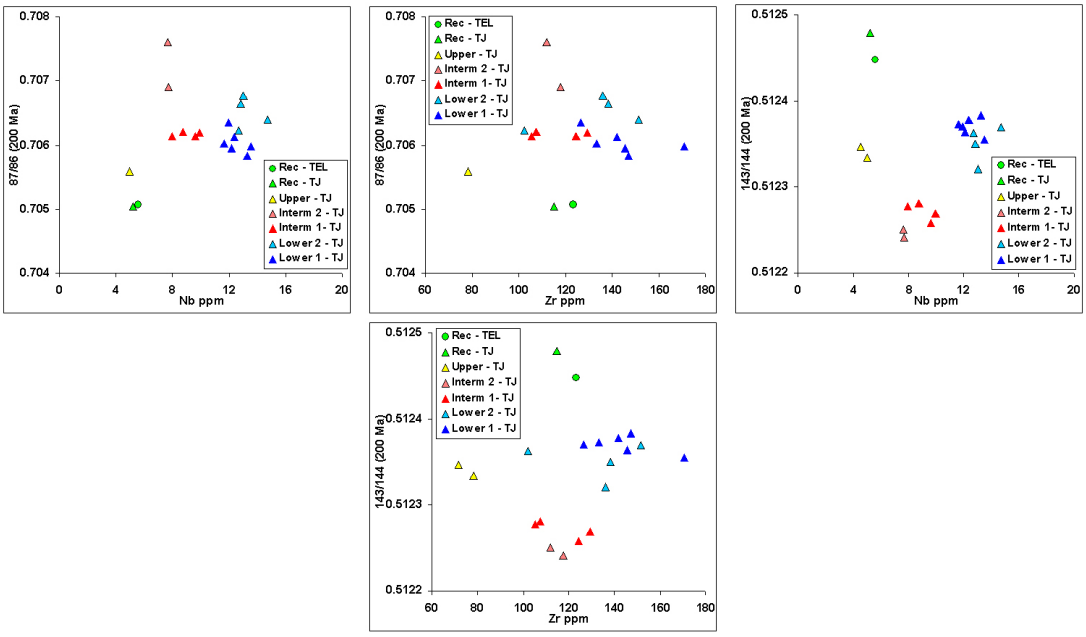

Figure 10.22: Nb and Zr vs $^{87}Sr/^{86}Sr_i$ and $^{143}Nd/^{144}Nd_i$ (calculated at 200 Ma) of Tiourjdal and Telouet basalts analysed by TIMS.

11 MINERAL PHASE TRACE ELEMENT COMPOSITIONS

In situ trace element analyses of augites and plagioclases were carried out using laser-ablation inductively-coupled-plasma mass-spectrometry (LA-ICP-MS) at IGG-CNR, Unit of Pavia, Italy (see details in the 8). No pigeonite have been analyzed for trace element contents. As previously said all the samples labelled AN have been collected for geochemical analyses and come from a big rock chunk (see details in the Chap. 8). The only one sample analysed for trace element contents coming from basaltic cores drilled for paleomagnetic investigation is OL14, from the Oued Lahr sequence. The samples analysed are AN134 (Lower Unit at Tiourjdal), AN137A and AN138 (Intermediate Unit at Tiourjdal), AN141 and OL14 (Upper Unit, respectively at Tiourjdal and Oued Lahr), AN156A and AN169 (Recurrent Unit, respectively at Tiourjdal and Telouet). The LA analyses have been performed on 100 μm thin sections, allowing to collect more material ablated as possible for a better determination of trace element contents. Before the LA-ICP-MS analyses, EMP analyses have been performed, as described in the previous paragraph, to determine major and minor element compositions for comparison. Where possible, the LA analysis points have been done as near as possible to the EMPA transect, in order to compare the major and minor element composition with the trace elements contents, performing analysis points (40 μm pit size) near the core, the rim and sometimes, if the crystal was big enough, in the middle of the phenocryst. Often we have operated a double analysis point, in order to obtain a better sensibility for detection of trace elements. For double analysis points the concentration results have been mediated, even if this would lead to a bad data interpretation, since many data are quite different, so having different meaning. In the table A.23, A.24, A.25, A.26, A.27, A.28, mean plagioclase and augite compositions are shown (EMP and LA-ICP-MS data).

11.1 PLAGIOCLASE

11.1.1 Titanium

For the Lower Unit only one phenocryst was analysed: AN134 plg1 (Fig. A.30). Only 2 analysis points have been performed near the core of the phenocryst. Titanium is the only minor element analysed in plagioclases both with EMP and LA-ICP-MS analyses. Concentrations obtained with both techniques are roughly correlated. In fact there is a quite large scatter of the data. In the sample AN134 plg1 Ti concentration in the core vary from 295 to 359 ppm (321 to 389 ppm for EMP analyses, A.23). However, EMP analyses are probably more reliable than laser ablation ones. In fact, differently from the punctual EMP analysis, laser ablation analyses mediate the composition on a 40 μm spot, moreover digging a deep pit on 100 μm thin sections, so possibly analysing included micrometric size oxides or glassy melt patches, undetectable below the surface of the thin section (Fig. 11.1, blue triangles for the Lower Unit, red circles for the Intermediate Unit, yellow diamonds for the Upper Unit and green squares for the Recurrent Unit). Using the more realistic EMP Ti concentrations, a constant $K_D^{plg-melt}$= 0.034 (**Aigner-Torres *et al.*, 2007**), and using equation:

$$C^i_{melt} = \frac{C^i_{ph}}{K^i_D} \tag{11.1}$$

this yields a TiO_2 concentration between ca. 1.45 and 1.75 wt% for the melt in equilibrium with the plagioclase core is obtained, which is just slightly higher than the TiO_2 whole rock concentration (1.43 wt

In the Intermediate Unit 4 phenocrysts have been analysed: 2 from sample AN137A (labels AN137A plg2 and AN137A plg3, Fig. A.32) and 2 from AN138 (labels AN138 plg1 and AN138 plg3, Fig. A.34). Ti content is lower than in plagioclases of the Lower Unit (Fig. 11.1), thus confirming the lower TiO_2 contents of the Intermediate Unit measured by EMPA (Chap. 9), but the analysis points, compared to those obtained by LA, are very scattered and poorly correlated. For each sample analysed, two analysis points have been taken in the core of the plagioclase (AN137A plg2 C,C1, AN137A plg3 C,C1, AN138 plg1 C,C1 and AN138 plg3 C,C1), one point at the rim of the AN137A plg2 and plg3 and two points at the rim of AN138 plg3 (A.23). No analyses are available for the rim of AN138 plg1. In general Ti data points obtained with both methodologies are poorly correlated. Ti concentrations at the plagioclase cores, obtained both with LA and EMPA, are partially concordant with values around 200±50 ppm.

Only one point analysed in the core of AN137A plg3 has a quite higher Ti con-

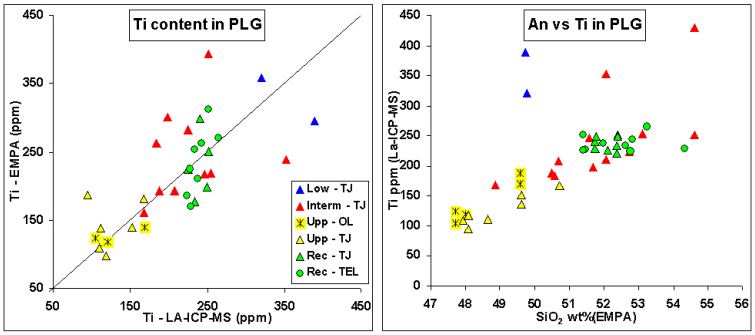

Figure 11.1: Correlation between Ti analysed by EMPA and LA-ICP-MS (left) and SiO_2 vs Ti diagram (right) for all plagioclases analysed.

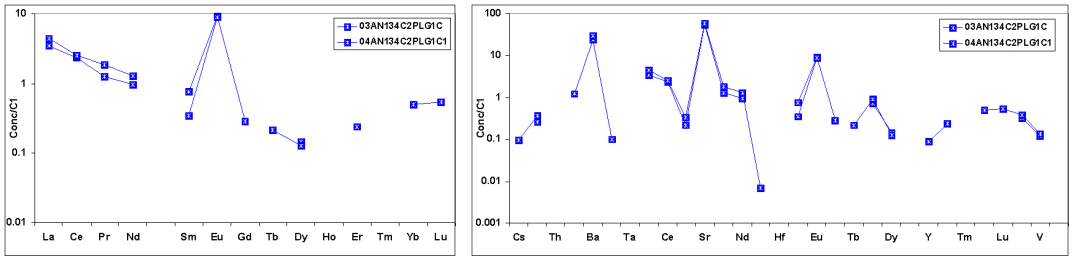

Figure 11.2: REE (left) and all trace elements (right) spidergrams of the plagioclase AN134 plg1 of the Lower Unit, normalized to CI carbonaceous chondrite of **Andres & Grevesse (1989)**.

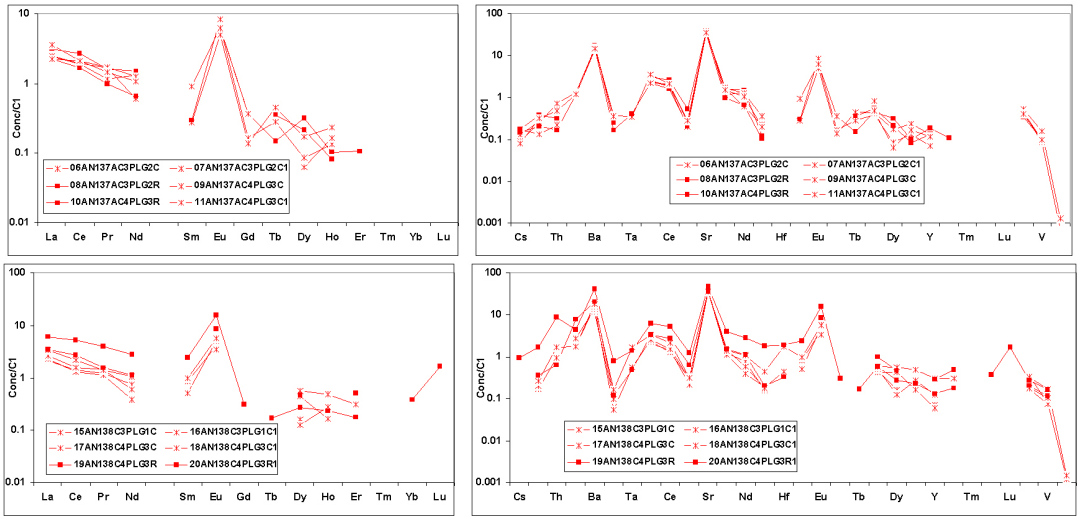

Figure 11.3: REE (on the left) and all trace elements (on the right) spidergrams of the plagioclase AN137A plg2 and plg3 (above) and AN138 plg1 and plg3 (below) of the Intermediate Unit, normalized to CI carbonaceous chondrite of **Andres & Grevesse (1989)**.

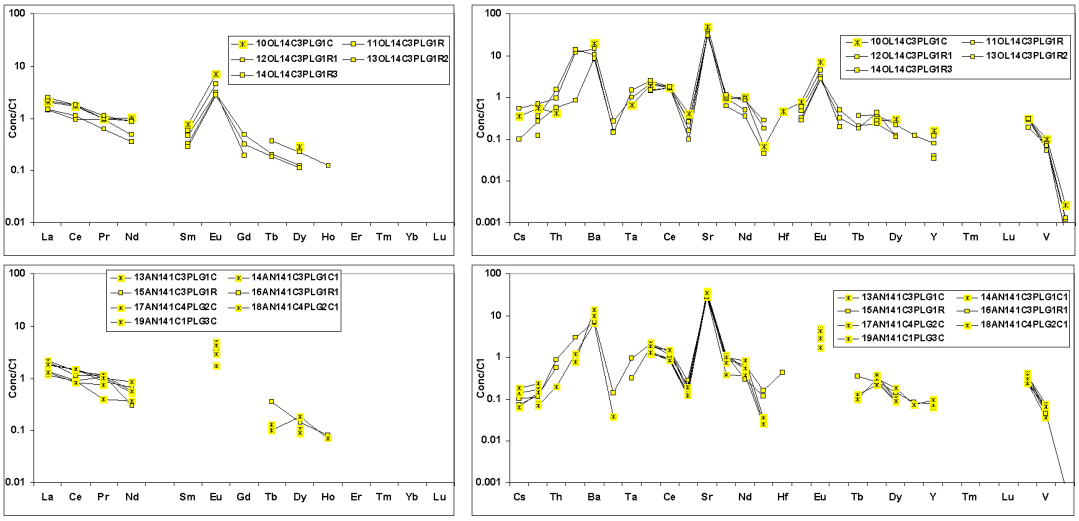

Figure 11.4: REE (on the left) and all trace elements (right) spidergrams of the plagioclases OL14 plg1 (above) and AN141 plg1, plg2 and plg3 (below) of the Upper Unit, normalized to CI carbonaceous chondrite of **Andres & Grevesse (1989)**.

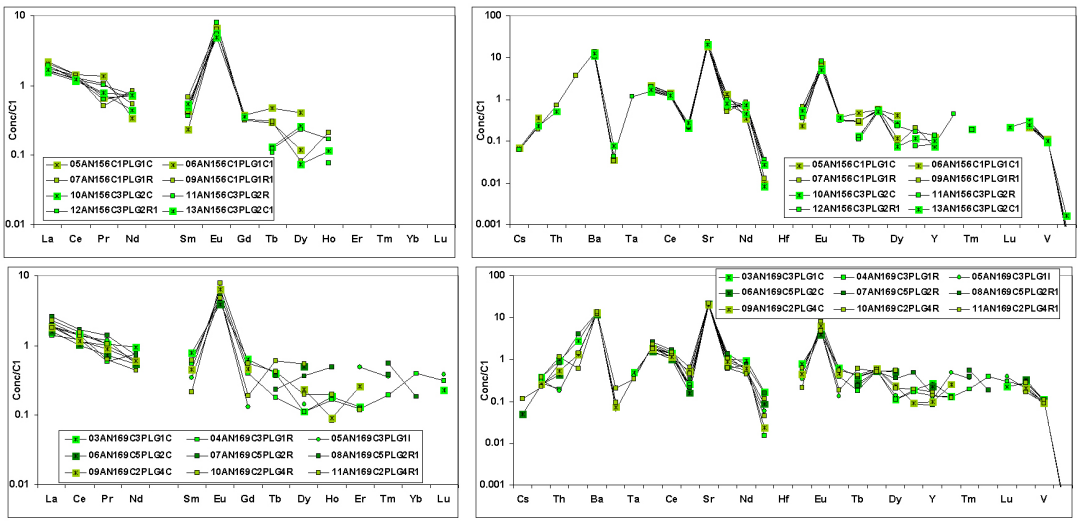

Figure 11.5: REE (on the left) and all trace elements (on the right) spidergrams of the plagioclases AN156A plg1 and plg2 (above) and AN169 plg1, plg2 and plg4 (below) of the Recurrent Unit, normalized to CI carbonaceous chondrite of **Andres & Grevesse (1989)**.

centration up to ca. 350 ppm. In all rims analysed, Ti content is always higher than in the core (up to ca. 430 ppm), except for AN137A plg3 (ca. 200 ppm). Nevertheless, EMP analyses of the AN137A plg3 gave higher Ti content at the rim than the core (ca. 300 and 240 ppm respectively). Again, taking in account the TiO_2 EMP concentrations, the Ti composition of melt in equilibrium with the plagioclase ($K_D^{plg-melt}$= 0.034, **Aigner-Torres *et al.*, 2007**) AN137A plg2 would be in the 0.78-1.06 wt% range, 1.16-1.46 wt% for AN137A plg3, 0.93-1.28 wt% for AN138 plg1 (only the core analysed) and 1.06-1.91 wt% for AN138 plg3. All of these values, except for AN138 plg1, are quite different respect to the whole rock for both AN137A and AN138 (TiO_2 1.16 wt

In the Upper Unit 4 phenocrysts have been analysed: 1 from sample OL14 (label OL14 plg1, Fig. A.39) and 3 for AN141 (labels AN141 plg1, AN141 plg2 and AN141 plg3, Figs. A.35 and A.37) Ti in the Upper Unit plagioclases, like Ti content of augites, has the lowest content among the four units, confirming the whole rock data (Fig. 11.1). Concentration data from EMP and LA analyses are fairly correlated. On the sample OL14 plg1 5 analysis points have been performed (Fig. A.39): one in the core (C), two in the middle on the rim-side (R, R1) and two at the rim (R2, R3). Ti concentrations of LA-ICP-MS confirm those of EMP analyses for the core and the middle point: respectively ca. 119 (C) and 118 ppm, ca. 105-124 (R-R1) and 124 ppm. For the rim, LA analyses are higher than those of the EMPA: ca. 170-190 (R2-R3) and 140 ppm, respectively. On sample AN141 4 analysis points for plg1 have been performed, 2 for the core (C, C1) and 2 for the rim (R, R1), 2 points in the core (C, C1) of plg2 and one point in the core (C) of plg3. Ti concentrations in all analysis points are, respectively for LA and EMPA: ca. 110 and 109 ppm (plg1 C), ca. 94 and 186 ppm (plg1 C1), ca. 118 and 97 ppm (plg1 R), ca. 111 and 138 ppm (plg1 R1), ca. 152 and 139 ppm (plg2 C), ca. 136 ppm (plg2 C1, only LA analysis), ca. 167 and 181 ppm (plg3 C). Ti compositions calculated, using EMPA data, for melt in equilibrium with plagioclase ($K_D^{plg-melt}$= 0.034, **Aigner-Torres *et al.*, 2007**), give for OL14 plg1 TiO_2 content between 0.58 and 0.68 wt%, quite lower respect to the whole rock concentration (TiO_2 1.10 wt%). For AN141, which has a TiO_2 whole rock content of 1.03 wt%, the melt in equilibrium with plg1 has TiO_2 0.46-0.90 wt%, with plg2 has TiO_2 0.68 wt% and with plg3 has TiO_2 0.88 wt

In the Recurrent Unit, 5 phenocrysts have been analysed: 3 from sample AN169 (labels AN169 plg1, AN169 plg2 and AN169 plg4, PHOTOS) and 2 from sample AN156A (labels AN156A plg1 and AN156A plg2, Fig. A.41) Ti contents of the Recurrent Unit plagioclases are similar to those of the Intermediate Unit

(Fig. 11.1). Nevertheless, while EMPA data span a wide compositional range, from ca. 170 to 310 ppm, LA data cover a more tight range, from ca. 190 to 270 ppm. Here we will take in account only EMPA data. Both the plagioclases of sample AN156A have been analysed with two analysis points at the core and at the rim, while the three plagioclases of sample AN169 have been analysed with three points each one, at the core, middle and rim for plg1, one at the core and two points at the rim for plg2 and plg4 (Figs. A.42 and A.43). In both samples AN156A plg1 and plg2 Ti concentration increases from the core towards the rim: from ca. 250 to 300 ppm for plg1 and from ca. 180 to 200-220 ppm for plg2. In the plagioclases of the sample AN169, Ti has a different behaviour for each crystal analysed. In the plg1, Ti decreases from the core toward the middle point from ca. 260 to 170 ppm, then increases at the rim to ca. 210 ppm. In the plg2 Ti decreases from the core toward the rim, from ca. 250 ppm to 220-180 ppm (R-R1). LA data confirm these trends, but display different value, sometimes higher some other lower. Finally in the plg4 Ti increases from the core towards the rim from ca. 270 up to 310 ppm. No data for plg4 R1are available. Differently from EMPA data, LA analyses show a decreasing Ti content from the core toward the rim with overall lower values. Ti compositions of the calculated melt in equilibrium with plagioclases ($K_D^{plg-melt}$= 0.034, **Aigner-Torres *et al.*, 2007**) give content for AN156A plg1 in the 1.21-1.46 wt% range (C-R) and 0.86-1.08 wt% (C-R) for AN156A plg2. For sample AN169, the calculated melt for plg1 has TiO_2 varying from ca. 1.28 through 0.83 to 1.03 wt% (C-I-R), for plg2 from 1.23 to 0.90 wt% (C-R) and for plg4 from 1.31 to 1.53 wt% (C-R). If we take in account for AN156A and AN169 a TiO_2 whole rock concentration of 1.63 wt% and 1.56 wt% respectively, probably only the rim of AN169 plg4 was in equilibrium with the bulk rock, being the others plagioclases crystallized from a melt with lower Ti.

11.1.2 LILE

The large ion lithophile elements (LILE) analysed in plagioclase phenocrysts are Cs, Rb, Ba, Sr, Pb, Li. In a trace elements spidergram Ba, Sr (together with Eu) show positive anomaly, due to their great compatibility leading to their high concentrations in plagioclases. Nevertheless also Pb and Li present have a sufficient concentration (Fig. 11.2, 11.3, 11.4 and 11.5), due to their discrete compatibility in the plagioclase (**Bindeman *et al.*, 1998; Bindeman & Davies, 2000**; **Bedard, 2006**Bedard, 2006, **Aigner-Torres *et al.*, 2007**). Rb and Cs are incompatible in plagioclase and display very low concentrations. Sr and

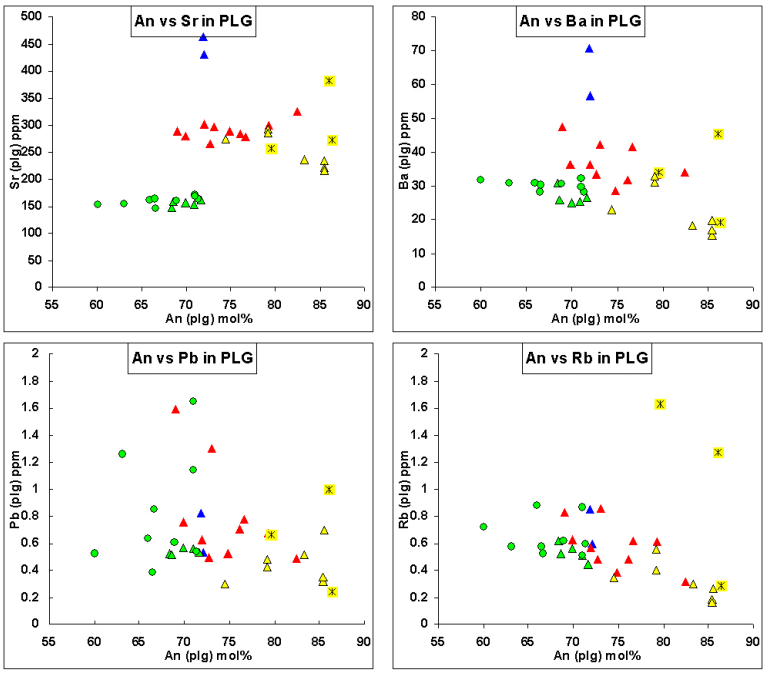

Figure 11.6: An mol% vs Sr, Ba, Pb and Rb for all plagioclases analysed by LA-ICP-MS. Li and Cs not showed. Symbols as above.

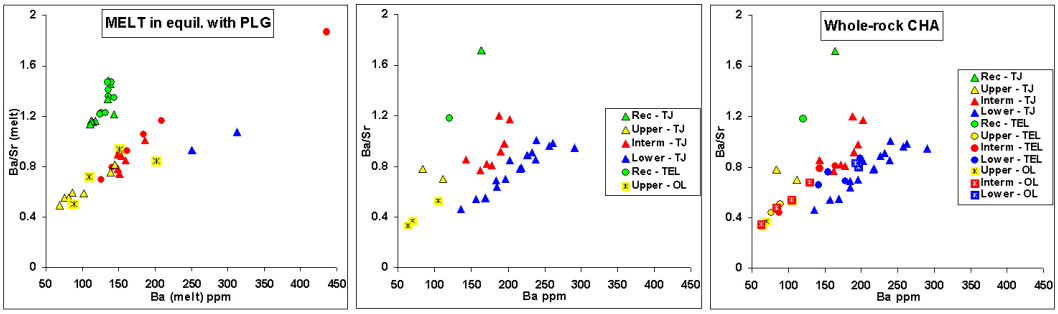

Figure 11.7: Ba/Sr ratios vs Ba diagrams of melt in equilibrium with all plagioclases analysed by LA-ICP-MS (on the left), for whole rock of the Tiourjdal sequence (plus the Upper Unit at Oued Lahr and the Recurrent Unit at Telouet)(in the middle) and for all whole rock compositions of the Central High Atlas (on the right).

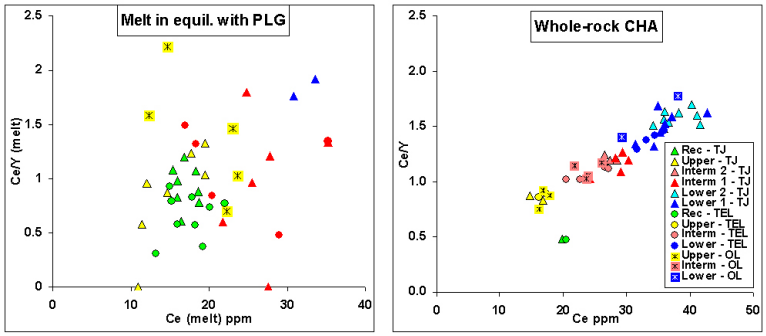

Figure 11.8: Ce/Y vs Ce diagrams of the melt in equilibrium with all plagioclases analysed by LA-ICP-MS (left) and for whole rock compositions of the Central High Atlas (right).

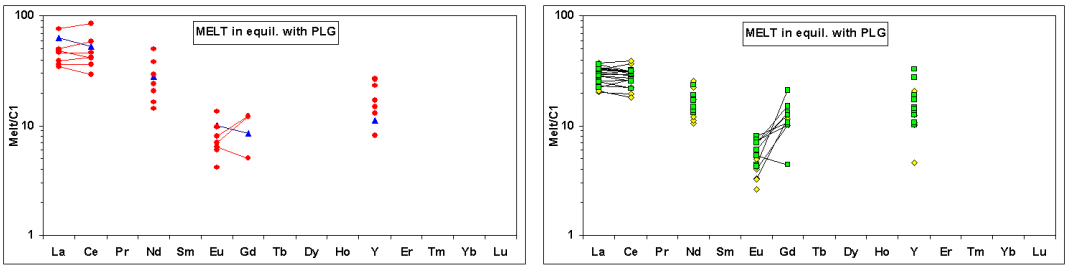

Figure 11.9: REE (plus Y) spidergrams C1 normalized of calculated melt in equilibrium with plagioclases analysed by LA-ICP-MS (**Andres & Grevesse, 1989**). Lower (blue triangles) and Intermediate Unit (red circles) on the left, Upper (yellow diamonds) and Recurrent Unit (green squares) on the right. Spidergrams are poorly defined because the lack of data in many analysis points. Explanations in the text.

Ba in the Lower Unit plagioclases display the highest content among the four units (Fig. 11.6). Since LILE have an overall incompatible character, as expected these elements are more concentrated as plagioclases are more evolved (lower An content). Nevertheless, while Sr, Ba and Rb are well correlated with An, Pb and Li (not showed) are less correlated presenting more scattered data. Cs is not shown because of its low concentration, close to detection limit of laser ablation analysis, which in turn gave no results for most of the analyses (Tables A.23, A.24, A.25). The Lower Unit is well distinct in a Ba/Sr vs Ba content diagram calculated for a melt in equilibrium with plagioclases ($K_{Ba}^{plg-melt}$= 0.226, $K_{Sr}^{plg-melt}$=1.6, **Aigner-Torres *et al.*, 2007**). In a such diagram the Lower Unit has the highest Ba content (except for an anomalous analysis in a sample of the Intermediate Unit, see below) and a Ba/Sr ratios near 1 (Fig. 11.7). This diagram resembles the Ba/Sr vs Ba of whole rock of the Tiourjdal sequence (and more in general of the Central High Atlas samples, Fig. 11.7). In particular, the calculated Ba/Sr ratio of the melt in equilibrium with plagioclase of the Lower Unit is slightly higher than the same whole rock ratio at the same Ba content. The correlation between An and Sr content is well visible in the Intermediate Unit plagioclases (Fig. 11.6). This correlation is also quite visible for Ba but it is less evident for Pb, which displays more scattered data, while in the An vs Rb the unit fields are poorly defined and partially overlapped. The Pb and Rb features are probably due to a remobilisation of these elements by aqueous fluids. Sr and Ba contents of the Intermediate Unit are lower compared to those of the Lower Unit plagioclases, except for one analysis point at the rim of sample AN137 plg3 in which Ba is much higher (not showed in Fig. 11.6). Pb and Rb have nearly the same concentration of those of the Lower Unit plagioclases but tend to increase their concentration with An content. In a Ba/Sr vs Ba diagram of the calculated melt in equilibrium with plagioclases, the Intermediate Unit plot from the same to lower Ba/Sr ratios, but with a much lower Ba content, again resembling the relative whole rock diagram, with an almost parallel trend (Fig. 11.7). The Upper Unit show comparable or slightly lower Sr, Ba and Pb values respect to those of the Intermediate Unit at much higher An contents of the plagioclases. LILE values are more scattered for the sample OL14 (yellow squares with black star in the diagram), which show a strong zonation from the core toward the rim. Ba/Sr and Ba of the calculate melt of the Upper Unit are slightly lower compared to the Intermediate Unit showing a parallel trend with the latter. Finally the Sr concentration of the Recurrent Unit plagioclases is the lowest among the four units (Fig. 11.6), moreover remaining almost constant with the An plagioclase

content. Ba and Rb seem to increase with An content with compositional fields well distinct for Ba and partially overlapped for Rb, respectively, with those of the Intermediate Unit. Ba/Sr of the calculated melt in equilibrium with plagioclases is the highest among the four units while Ba content is similar to that of the Upper Unit even if with a more restricted variation range.

11.1.3 HFSE

The high field strength elements (HFSE) analysed are U, Th, Nb, Ta, Zr, Hf. In general HFSE are to incompatible and therefore poorly concentrated in plagioclase (Fig. 11.2). In fact Hf, Th and Ta have not been detected in most of the plagioclases analysed. U, Nb and Zr have been easily detected but with at very low concentrations. For example in the sample AN134 plg1 U, Nb and Zr concentrations are 0.010, 0.025 and 0.027 ppm, respectively. In the other units, the HFSE contents in plagioclases are very low with Zr, Nb, Hf, Ta, Th and U respectively up to 1.75, 0.091, 0.181, 0.024, 0.049 and 0.114 ppm (if we exclude an anomalous analysis point in the rim of the sample AN138 plg3 enriched in the most incompatible elements, which has 9.18 ppm Zr, 0.197 ppm Nb, 0.199 ppm Hf and 0.265 ppm Th). Being the HFSE concentrations so low and not available for all analysis points, it is difficult to extract useful and reliable information about the melt composition in equilibrium with plagioclase. Therefore, we will not discuss about HFSE in plagioclases.

11.1.4 REE

Rare Earth elements (REE) are a 14 elements group which displays a highly homogeneous geochemical behaviour. This group is divided in LREE (Light REE, La, Ce, Pr, Nd), MREE (Middle REE, Sm, Eu, Gd, Tb, Dy, Ho) and HREE (Heavy REE, Er, Tm, Yb, Lu). Together with this group we will describe the behaviour of Y, which displays a geochemical behaviour very similar to that of HREE. The plagioclases analysed present, in all analysis points (Fig. 11.2), the typical enrichment in LREE (Light REE, i.e. La, Ce, Pr, Nd) with respect to other REE, a decreasing concentration (C1 normalized after **Andres & Grevesse, 1989**) with a monotonous pattern from La to Dy (except for Eu) and a marked Eu positive anomaly. The LREE enrichment is explained by the lower incompatibility of the LREE with respect to MREE and HREE in the plagioclase lattice. The high positive Eu anomaly (Eu_N/Eu_{N*}=19.8, where $Eu_{N*} = \sqrt{Sm_N \times Gd_N}$, **Taylor & McLennan, 1985**) reflect the higher concen-

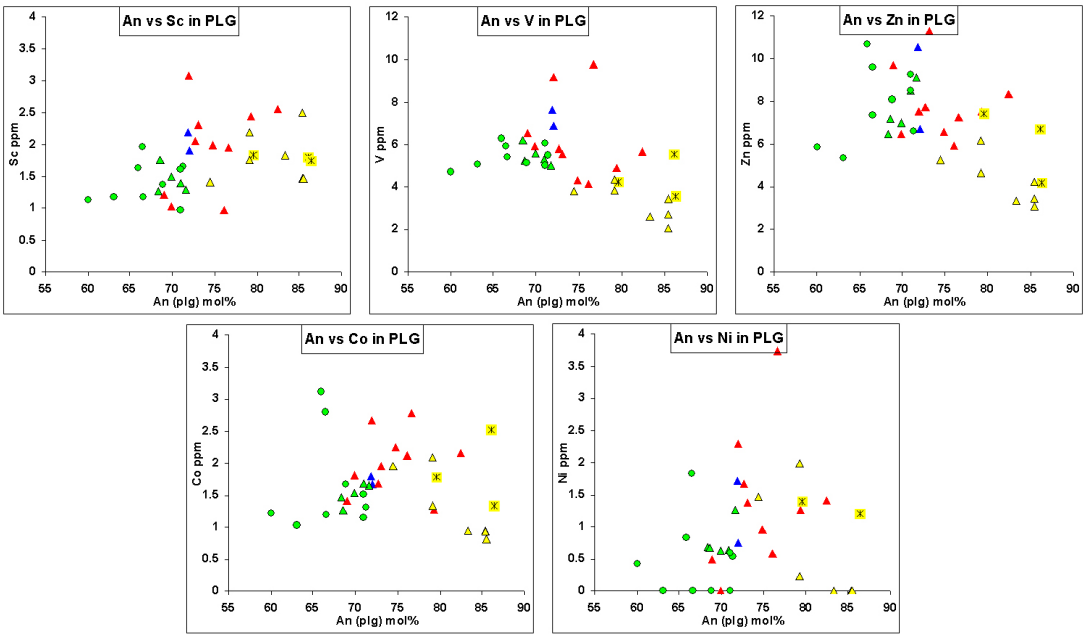

Figure 11.10: An mol% vs Sc, Zn, V, Co and Ni for all plagioclases analysed by LA-ICP-MS. Cr not showed. Symbols as above.

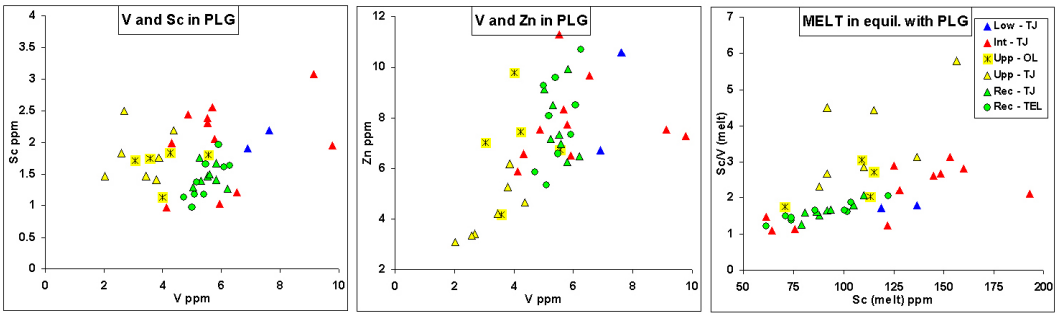

Figure 11.11: V vs Sc and Zn diagram for plagioclases and Sc/V vs Sc for melt in equilibrium with plagioclases analysed by LA-ICP-MS. Symbols as above.

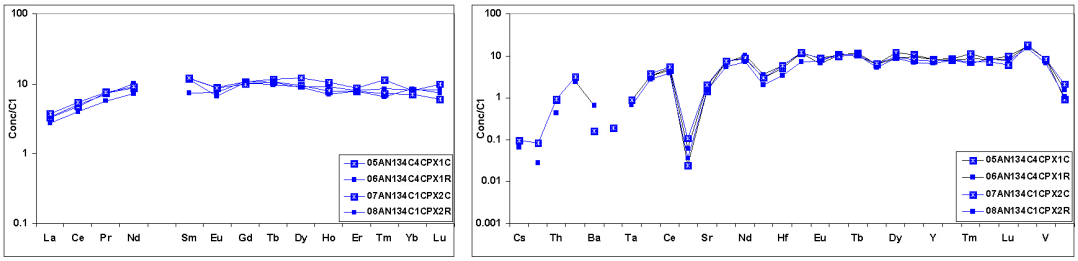

Figure 11.12: REE (on the left) and all trace elements (on the right) spidergrams of the clinopyroxenes AN134 cpx1 and cpx2 of the Lower Unit, normalized to CI carbonaceous chondrite of **Andres & Grevesse (1989)**.

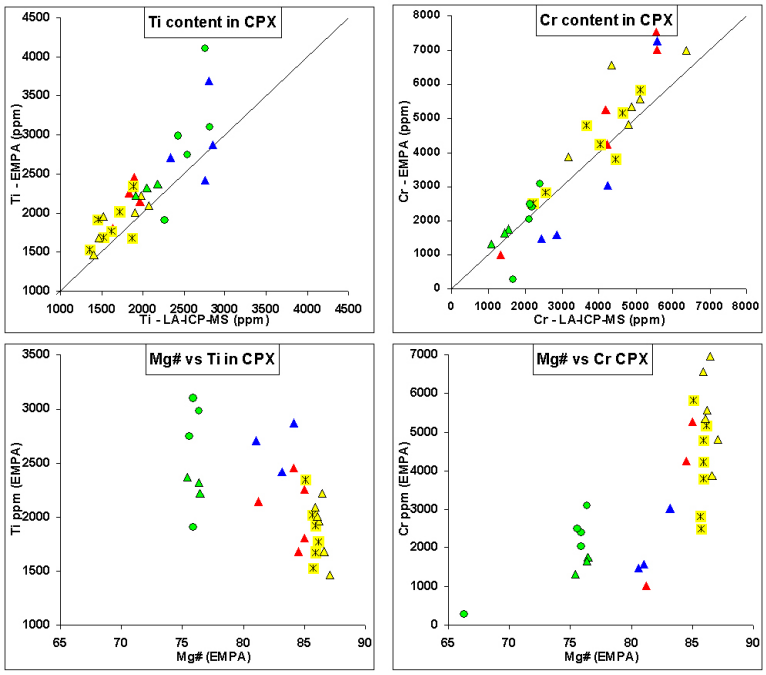

Figure 11.13: Ti and Cr content correlations between EMP and LA-ICP-MS analyses (above) and Mg# vs Ti and Cr contents in augites analysed by LA-ICP-MS.

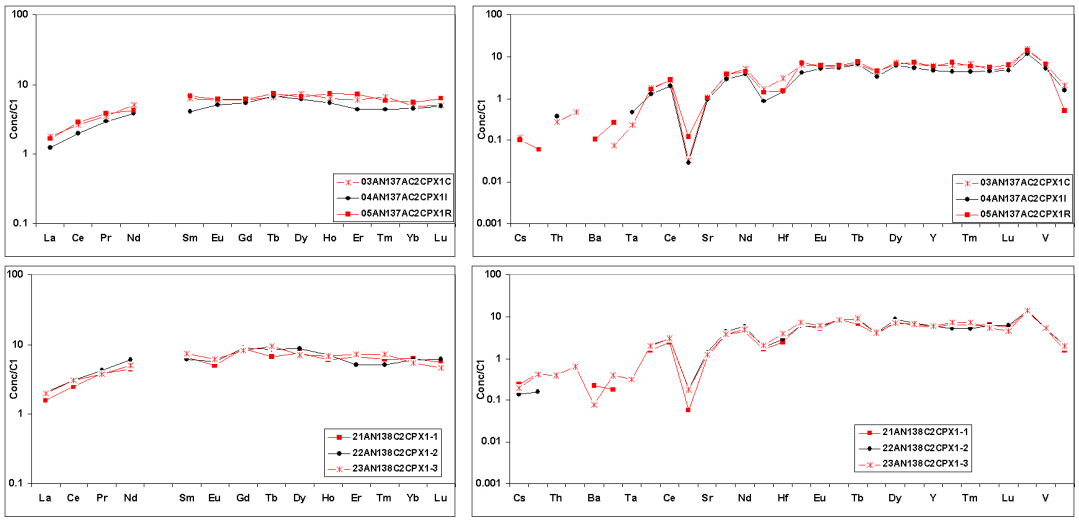

Figure 11.14: REE (on the left) and all trace elements (on the right) spidergrams of the augites AN137A cpx1 (above) and AN138 cpx1 (below) of the Intermediate Unit, normalized to CI carbonaceous chondrite of **Andres & Grevesse (1989)**.

tration of Eu^{2+} which is more compatible in the plagioclase with respect to Eu^{3+}. This feature could lead to think to quite reducing conditions of the magma when plagioclase was crystallizing. HREE behaviours are not easily explainable. As expected from the decreasing compatibility of HREE in plagioclase, the concentration of these elements should decrease instead of increasing as visible in the spidergram in Fig. 11.2, 11.3, 11.4 and 11.5. However the natural low HREE concentrations in the plagioclase, close to the detection limit of the laser ablation analyses hinders a reliable constraint of HREE content. Hereafter we will not discuss about HREE in plagioclases anymore but we will use Y as proxy for HREE (Fig. 11.8). The only plagioclase analysed belonging to the Lower Unit displays the highest LREE/Y ratio and LREE concentrations among the units (excluding few data points with anomalous compositions). Ce/Y vs Ce of the calculated melt in equilibrium with plagioclase ($K_{Ce}^{plg-melt}$= 0.046, $K_{Y}^{plg-melt}$=0.008, **Aigner-Torres *et al.*, 2007**) resembles quite well, even if data are scattered especially for Intermediate and Upper Unit, the corresponding of the whole rock with Ce/Y and Ce decreasing from the Lower to the Recurrent Unit (Fig. 11.8). The REE spidergram of the melt in equilibrium with AN134 plg1 does not allow to recognize the LREE enrichment because of the lack of data for most of these elements. However the high La/Gd_N (9.5) lead to think to a possible LREE enrichment (Fig. 11.9). The REE spidergram of the melt in equilibrium with the Intermediate, Upper and Recurrent Unit plagioclases ($K_{REE}^{plg-melt}$ after **Aigner-Torres *et al.*, 2007**) are more complete and it is possible to see features like the LREE enrichment, decreasing from the Intermediate to Recurrent Unit, the decreasing Y concentration from the Intermediate to Upper Unit and its increase in the Recurrent Unit. Light Rare Earth elements in the Recurrent Unit have the lowest concentration among all the units (Fig. 11.9). For the Upper and Recurrent Unit it is possible to note the much lower value of Eu concentrations in the calculated melt, compared to the Lower and Intermediate Unit. This negative Eu anomaly (only respect to Gd, no data are available for Sm) could be representative of a previous plagioclase fractionation (Fig. 11.9).

11.1.5 Transition metals

Other elements analysed in plagioclases (like in augites) by LA-ICP-MS are some transition metals: Cr, Ni, Zn, Co, V, Sc. In general transition metals have a low concentration in plagioclase. In general, Cr is nearly undetectable in almost all the samples analysed so no data will be presented. Co, Ni and Sc have a few ppm concentration (some data points are lacking for Ni), while Zn and V are well

detected with concentrations up to 10 ppm. As a whole transition metals are bad correlated with An content, taken as differentiation index. Only for V and less for Zn it is possible to see a negative correlation, even if with some values scattering, while Sc seems to show a slightly positive correlation with An content. V and Zn concentrations tend to increase as plagioclases become more albitic, from the Upper, through the Intermediate and Lower Unit to the Recurrent Unit. Co and Ni values are too scattered values to infer about any correlation with An content. V content of AN134 plg1 are the highest among all the samples like for augites of the same unit (Fig. 11.21), if we excluded two anomalous points in the samples AN137 plg3 and An138 plg3, belonging the Intermediate Unit. The Intermediate and Upper Unit have progressively lower V contents as plagioclase SiO_2 content decreases, while the Recurrent Unit has nearly the same mean V concentration the Intermediate Unit partially overlapping on it, being shifted toward higher SiO_2 contents. In a V vs Sc diagram the Lower, Upper and Recurrent Unit are quite well distinct, while the Intermediate Unit present more scattered data (Fig. 11.11). In this diagram V contents seem to decrease for an almost constant Sc contents (even these result quite scattered) from the Lower to the Upper Unit, while the Recurrent Unit presents V concentration comparable with those of the Intermediate Unit but with lower Sc contents. V and Zn seem to be positively correlated with decreasing contents from the Lower to the Upper Unit. The Recurrent Unit overlaps the Intermediate Unit field (Fig. 11.11). In a Sc/V vs Sc diagram of the melt in equilibrium with plagioclases the four units are well recognizable even if partially overlapped. The Lower Unit has low Sc/V ratio respect to the Intermediate and Upper Unit (Fig. 11.11) with quite high Sc content (ca. 130 ppm). The Intermediate and the Upper Unit display a wide compositional variation range both for Sc/V ratio and Sc content, while the Recurrent Unit show a restricted Sc/V ratio range (comparable or slight lower than that of the Lower Unit) but a wide Sc range with lower concentrations respect to the Lower Unit and the mean of the Intermediate and Upper Unit. This diagram compared to its similar calculated for augites (Fig. 11.22) shows as Sc variation range is wider than that of augites, especially for Intermediate and Recurrent Unit. While Sc/V ratios are much higher (up to 6 compared to the highest value for melt in equilibrium with augites, Sc/V = ca. 1). Moreover while the Lower, Intermediate and Upper Unit decrease drastically both Sc/V ratios and Sc contents, the Recurrent Unit display a minor decreasing of Sc/V ratio for an almost constant Sc concentration.

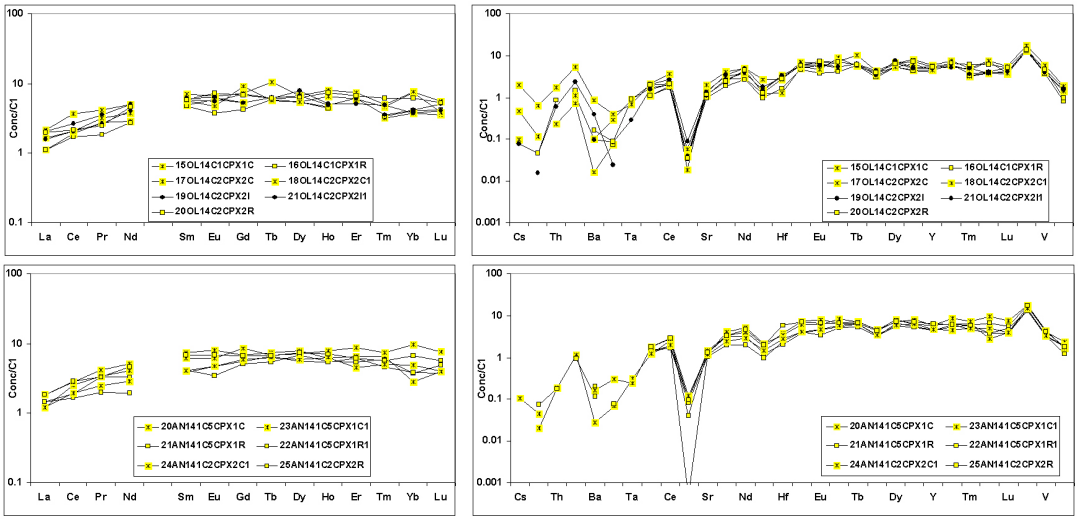

Figure 11.15: REE (on the left) and all trace elements (on the right) spidergrams of the augites OL14 cpx1 and cpx2 (above) and AN141 cpx1 and cpx2 (below) of the Upper Unit, normalized to CI carbonaceous chondrite of **Andres & Grevesse (1989)**.

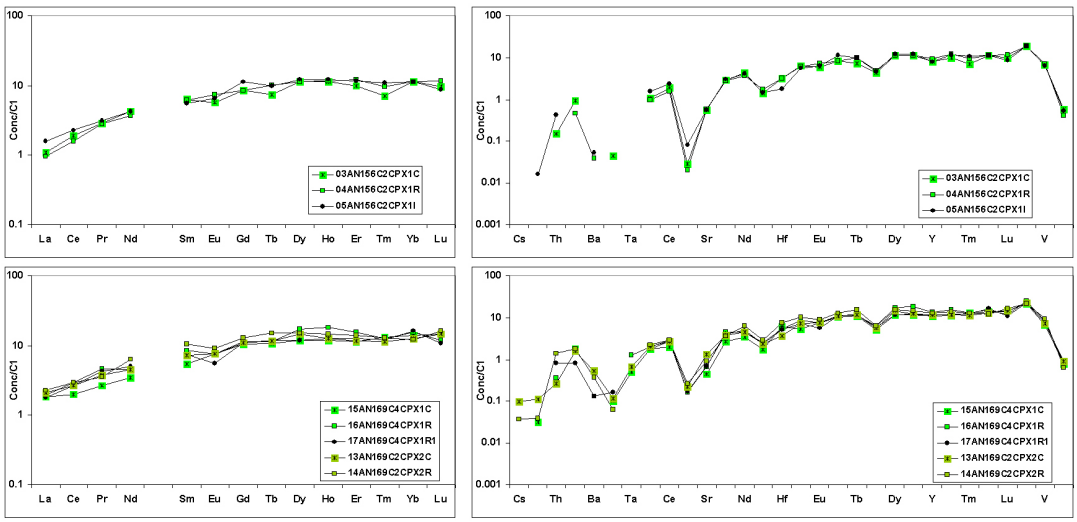

Figure 11.16: REE (on the left) and all trace elements (on the right) spidergrams of the augites AN156A cpx1 (above) and AN169 cpx1 and cpx2 (below) of the Recurrent Unit, normalized to CI carbonaceous chondrite of **Andres & Grevesse (1989)**.

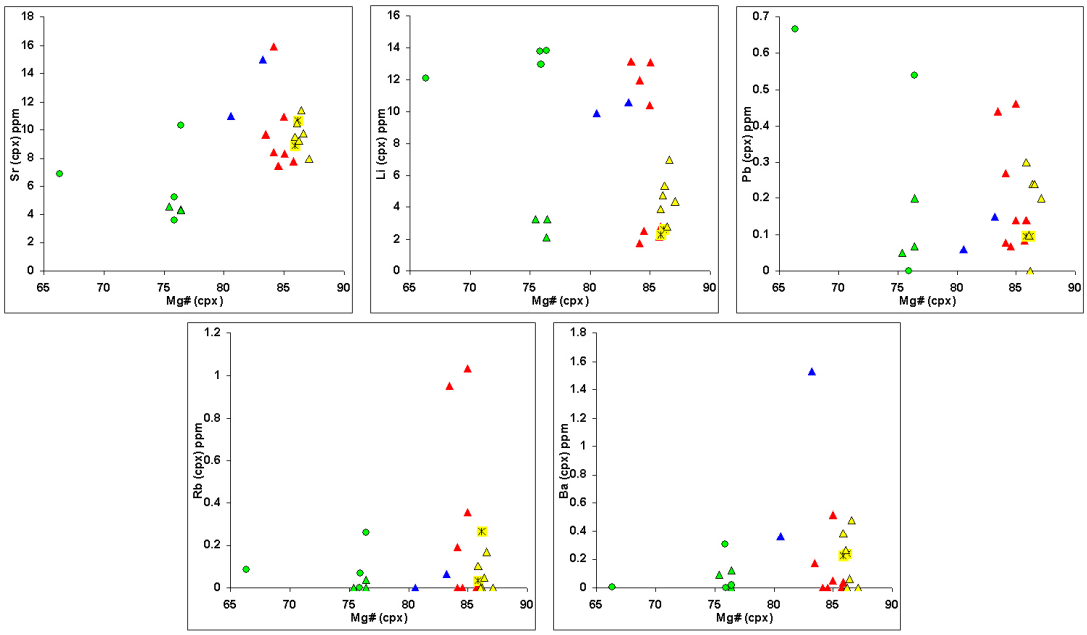

Figure 11.17: Correlations of Sr, Li, Pb, Rb and Ba with Mg# contents for all LA-ICP-MS analysis points on augites belonging the four units. As visible, many analysis points are lacking for Rb and Ba. Symbols as above.

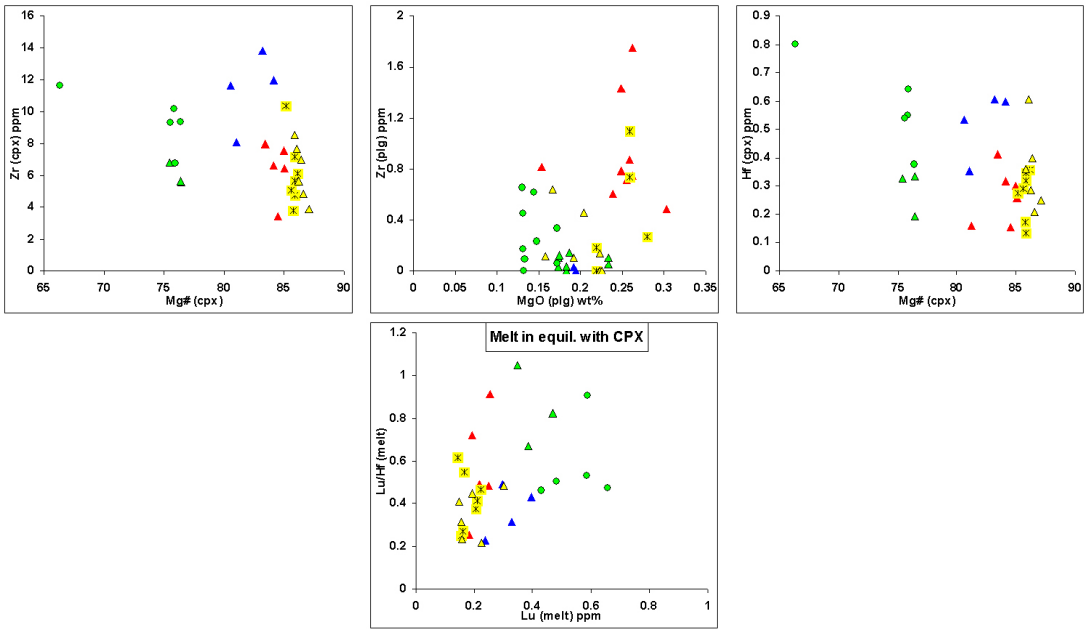

Figure 11.18: Mg# (top on the left) and MgO wt% (top on the right) vs Zr concentration, respectively for all augites and plagioclases analysed by LA-ICP-MS. Mg# vs Hf concentration (bottom on the left) and Lu/Hf ratio vs Lu content for a melt in equilibrium with all augites (bottom on the right)(LA-ICP-MS). Symbols as above.

11.2 AUGITE

11.2.1 Titanium and chromium

The minor element analysed in augites both with EMP and LA-ICP-MS analyses are Ti and Cr (Fig. 11.13). In the Lower Unit 2 phenocrysts have been analysed: AN134 cpx1 and AN134 cpx2 (Fig. A.29). Both of phenocrysts have been analysed with two analysis points, one at the core and one near the rim. Concentration obtained with both techniques, for some analyses, differ largely for both augites analysed and in general LA analyses tend to underestimate the concentrations respect to the EMPA ones. Ti content in the AN134 cpx1 core is lower for LA-ICP-MS analyses compared to the EMP one (ca. 2810 vs 3690 ppm) while at the rim it is slightly higher (ca. 2760 vs 2420 ppm)(Tables A.26, A.27 and A.28). Ti content in the AN134 cpx2 core is nearly the same both for La and EMP analyses (ca. 2870 and 2840 ppm) while at the rim it is slightly lower (ca. 2340 vs 2710 ppm). For Cr content LA compositions of AN134 cpx1 gave higher values both for the core and the rim, from ca. 2450 to 4240 ppm, with respect to the EMP ones (from 1430 to 3000 ppm, Fig. 11.13). For AN134 cpx2 the Cr content in the core is lower for laser ablation analysis compared to the EMP one (ca. 5580 vs 7280 ppm), while at the rim Cr is higher (ca. 2850 vs 1580 ppm). The calculated TiO_2 compositions of melt in equilibrium with augites ($K_{Ti}^{cpx-melt}$ = 0.384, **Hill *et al.*, 2000**) give a concentration for AN134 cpx1 from 1.60 to 1.05 wt% (C-R) and for AN134 cpx2 from 1.23 to 1.16 wt% (C-R), someway comparable with whole rock (TiO_2= 1.43 wt%). For Cr, again using the more reliable EMP analyses, we obtain for the melt in equilibrium with augites ($K_{Cr}^{cpx-melt}$ = 8.3, **Hill *et al.*, 2000**) a concentration for AN134 cpx1 between ca. 177 and 360 ppm (C-R), while for AN134 cpx2 between ca. 870 and 190 ppm (C-R), both of these around to the Cr bulk rock of 288 ppm. These seem to be reasonable estimates for Ti and Cr content, since for a $K_D^{cpx-melt}$ lower than those here used for calculations, it would result in a higher Ti and Cr melt content.

Two phenocrysts have been analysed for the Intermediate Unit: 1 from sample AN137A (AN137A cpx1, Fig. A.31) and 1 from AN138 (AN138 cpx1, Fig. A.33)Ti contents in both analysed samples are always underestimated by LA-ICP-MS analyses compared to those of EMPA (Fig. 11.1). Like for plagioclase Ti contents are lower than those of the Lower Unit augites and show a more restricted variation range. Both the augites have been analysed with three analysis points: one in the core (C), one in the middle (I) and one towards the rim

(R). AN137A cpx1 shows a decreasing Ti content from the core (ca. 2460 ppm, EMPA data) toward the middle point (ca 1680 ppm). At the rim Ti increases to ca. 2140 ppm. LA-ICP-MS analyses, even if lower than EMPA one, confirm this trend (ca. 1900 ppm at the core, ca. 1680 ppm for the middle point and ca 1960 ppm at the rim). Differently, AN138 cpx1 has a Ti content almost constant from the core to the middle point (from ca. 2190 to 2250 ppm), then decreasing at the rim (ca. 1810 ppm). Also here, LA-ICP-MS analyses confirm this trend showing lower values (ca. 1800, 1840 and 1630 ppm respectively). EMPA data of the Cr content for sample AN137A show a monotonous decrease from the core towards the rim, with ca. 7540 (C), 4250 (I) and 1010 ppm (R), confirmed by LA-ICP-MS analyses even if with quite different values, i.e. ca. 5550 (C), 4200 (I) and 1330 ppm (R). A different pattern for Cr content of sample AN138 cpx1 is confirmed by both kind of analyses: a middle point with higher Cr respect to both the core and the rim: ca. 4700 (C), 7020 (I), 5260 ppm (R) for EMP analyses and ca. 5140 (C), 5580 (I), 4180 ppm (R) for LA analyses. TiO_2 and Cr contents calculated for a melt in equilibrium with both augites give for AN137A cpx1 compositions with Ti 1.06-0.73-0.93 wt% (C-I-R) and Cr ca. 910-510-120 ppm (C-I-R) (whole rock with 1.16 wt% TiO_2 and 110 ppm Cr) while for sample AN138 compositions with Ti slightly lower, 0.95-0.98-0.78 wt% (C-I-R), and Cr ca. 570-840-630 ppm (C-I-R) (whole rock with 1.16 wt% TiO_2 and 326 ppm Cr).

For the Upper Unit, 4 phenocrysts have been analysed: 2 from sample OL14 (OL14 cpx1 and OL14 cpx2, Fig. A.38) and 2 from sample AN141 (AN141 cpx1 and AN141 cpx2, Figs. A.35 and A.37) Ti and Cr contents, measured by both LA and EMP analyses, are better correlated than the other units (Fig. 9.1). Also here LA tends to underestimate the concentration of the two elements. On sample OL14 have been done 2 analysis points on cpx1 (C, R), while 5 for cpx2: two at the core, two at the middle of augite and one at the rim (C, C1, I, I1, R). AN141 has been analysed with 6 analysis points: 4 for cpx1, 2 at the core (C, C1) and 2 at the rim (R, R1), 2 for cpx2, 1 at the core and one at the rim (C, R respectively). Like for plagioclases of the same unit, Ti concentrations are the lowest among the four units (Fig. 11.1), while Cr data, even if spanning a wide variation range, are the highest among all units, if we exclude few points with unusual high Cr in AN134 cpx2 and AN137A cpx1. Ti concentration in the sample OL14 cpx1 decreases slightly from core to rim, (1920-1530 ppm, EMPA). Sample OL14 cpx2 has very different value in the core, ca. 1770 (C) and 2350 (C1) ppm, lower but almost identical for the two middle points, 1681$\pm$5 ppm, and higher value for the rim, ca. 2010 ppm. On the contrary, this strong Ti zoning is not visible in

the LA data, which show Ti concentrations variable between ca. 1520 and 1890 ppm. AN141 cpx1 has a core with Ti content of ca. 2150±60 ppm (LA data

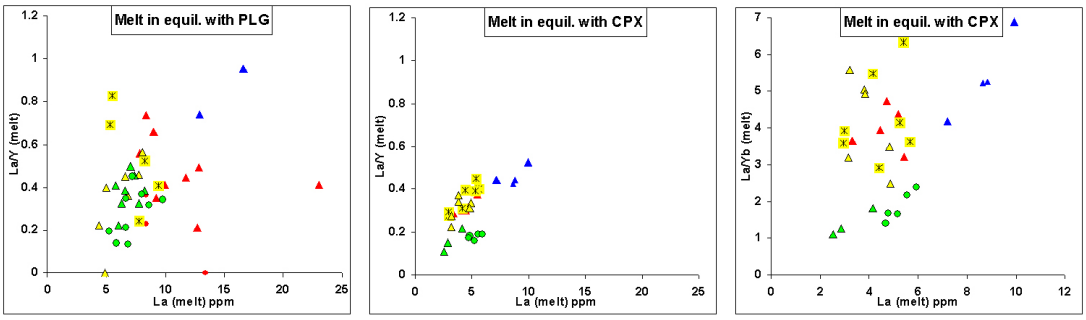

Figure 11.19: La/Y vs La diagrams of the melt in equilibrium with all plagioclases (on the left) and augites (in the middle) analysed by LA-ICP-MS and La/Yb vs La of the melt in equilibrium with augites (on the right). Symbols as above.

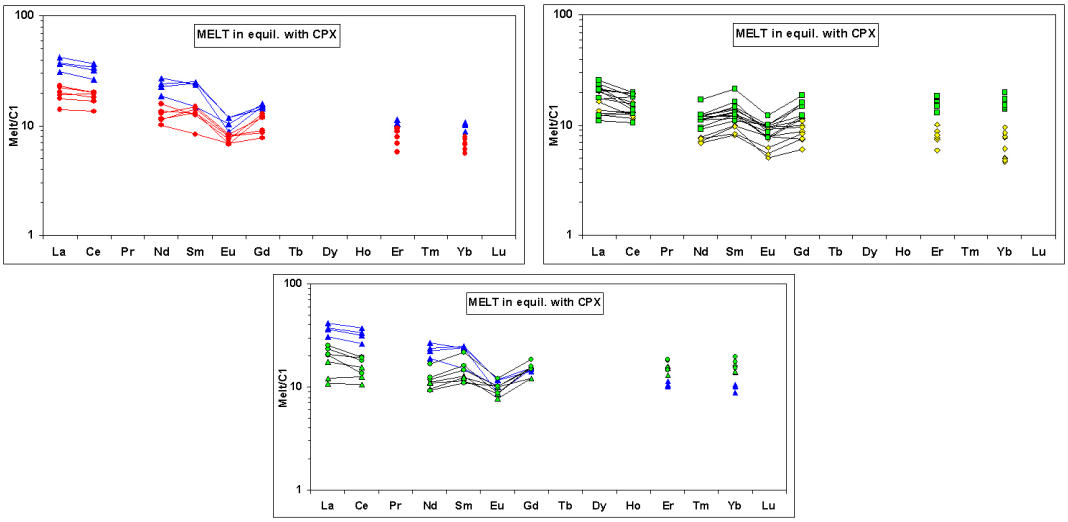

Figure 11.20: REE spidergrams of calculated melt in equilibrium with augites analysed by LA-ICP-MS (C1 normalized after **Andres & Grevesse, 1989**). Lower and Intermediate Unit (above on the left), Upper and Recurrent Unit (above on the right), Lower and Recurrent Unit (below).

ca. 2020±50 ppm) and lower Ti in the rim with ca. 1570±100 ppm (LA data ca. 1430±30 ppm). Finally both EMPA and LA data confirm a lower Ti content in the core with respect to the rim: ca. 1960 (C) and 2030 (R) ppm, ca. 1520 (C) and 1900 (R) ppm respectively. As previously said Cr displays the highest concentrations, but also the widest compositional range, this probably due to the sector zoning of the Upper Unit augites. In the sample OL14 cpx1 Cr decreases

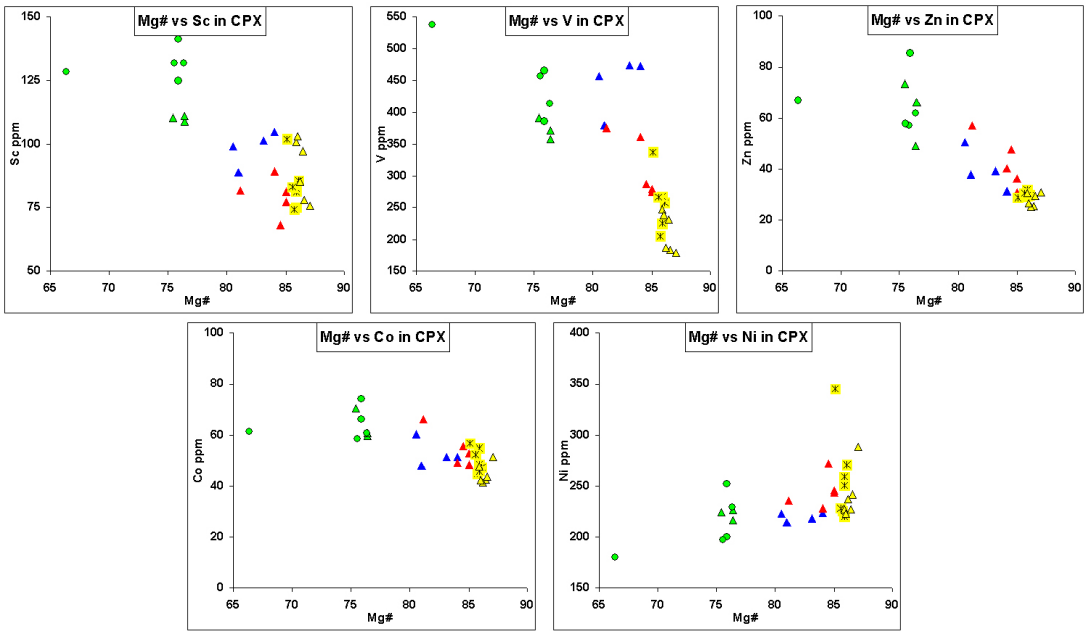

Figure 11.21: Mg# vs Sc, V, Zn, Co and Ni concentrations for augites analysed by LA-ICP-MS. Symbols as above.

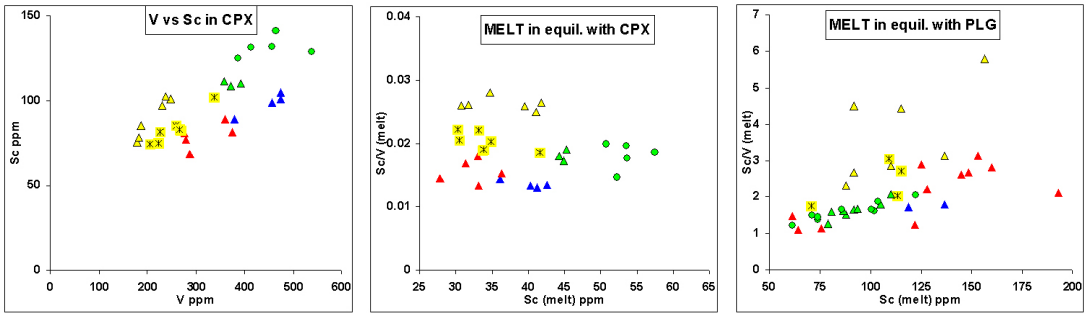

Figure 11.22: V vs Sc diagrams of all augites analysed by LA-ICP-MS, and Sc Sc/V ratio of the melt in equilibrium with augites and plagioclases. Symbols as above.

from the core to the rim, from ca. 4800 to 2500 ppm, in the sample OL14 cpx2 progressively decreases from the core, through the middle points to the rim, with ca. 5180, 5830, 4230, 3800 and 2830 ppm. In the core of sample AN141 cpx1, Cr reaches its highest value (ca. 6700±200 ppm), then decreasing towards the rim at ca. 4820 and 3880 ppm. Finally AN141 cpx2 displays only a smooth decrease in Cr from the core towards the rim (from ca. 5560 to 5360 ppm). TiO_2 and Cr compositions of the calculated melt in equilibrium with the augites ($K_{Ti}^{cpx-melt}$ = 0.384 and $K_{Cr}^{cpx-melt}$ = 8.3 , **Hill *et al.*, 2000**) vary, respectively for TiO_2 and Cr, for OL14 cpx1 0.83-0.66 wt% and ca. 580-300 ppm (C-R), for OL14 cpx2 1.01-0.73-0.98 wt% and ca. 700-480-340 ppm (C-I-R), for AN141 cpx1 0.93-0.68 wt% and ca. 810-520 ppm (C-R) and for AN141 cpx2 0.85-0.86 wt% and 670-645 ppm (C-R). These values must be compared with whole rock data: for OL14 1.10 wt% and 242 ppm, for AN141 1.04 wt% and 229 ppm. These results indicate that augites of the Upper Unit could have crystallized from a less evolved melt (or with different composition), with higher Cr and lower Ti, than the melt that generated the samples OL14 and AN141.

For the Recurrent Unit 3 phenocrysts have been analysed: 2 from sample AN169 (AN169 cpx1 and AN169 cpx2, Fig. A.42) and 1 from sample AN156A (AN156A cpx1, Fig. A.40) Ti concentrations of the Recurrent Unit augites are comparable with those of the Lower Unit and in some cases are higher, resembling the whole rock composition behaviour of the two units (Chap. **??**). On the contrary, Cr displays the lowest concentration among the four units (Fig. 11.1). Ti and Cr from both EMPA and LA-ICP-MS are well correlated, even if LA analyses tend again to underestimate concentrations with respect to EMPA. It is interesting that augites of sample AN169 are more enriched in Ti and Cr compared to the augite of AN156A. In the sample AN156A cpx1 three analysis points have been performed: one in the core (C), one in the middle (I) and one in the rim (R). In the augites of sample AN169 three (cpx1 C, R and R1) and two (cpx2 C and R) analyses points have been analysed. In AN156A cpx1, Ti content slightly increases from the core toward the rim, from ca. 2220 to 2380 ppm (EMP analyses). The same happens in AN169 cpx2 (ca. 2980 to 4110 ppm), while in AN169 cpx1 both the rim analyses are higher than the core one, but the repeated one (R1) gave a quite lower value, i.e. ca, 1910 (C), 3100 (R) and 2750 ppm (R1). Cr content tends to decrease from the core towards the rim (ca. 1760 to 1330 ppm for AN156A cpx1, ca. 3090 to 280 ppm for AN169 cpx2), while for AN169 cpx1 Cr increases from ca. 2040 to 2500 ppm. The melt in equilibrium with augites ($K_{Ti}^{cpx-melt}$ = 0.384 and $K_{Cr}^{cpx-melt}$ = 8.3, **Hill *et al.*, 2000**) has a composition,

respectively for TiO_2 and Cr, for AN156A cpx1 of 0.95-1.01 wt% and ca. 210-160 ppm (C-R), for AN169 cpx1 of 0.81-1.33 wt% and ca. 246-300 ppm (C-R), for AN169 cpx2 of 1.28-1.78 wt% and ca. 370-34 ppm (C-R). Compared to Ti and Cr whole rock composition, 1.63 wt% and 235 ppm for AN156, 1.56 wt% and 118 ppm for AN169, it results that AN156A augite crystallized from a melt with lower TiO_2 and Cr content, while AN169 augites crystallized from a melt with lower Ti but higher Cr content. Obviously melt compositions calculated for all parental magma in equilibrium with each analysis points vary accordingly with $K_D{}^{cpx-melt}$ that, if different from those used here it lead to a misleading petrologic interpretations.

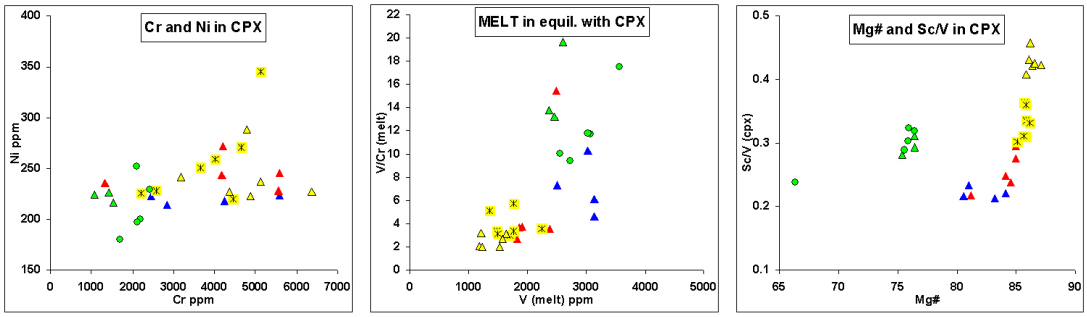

Figure 11.23: Cr vs Ni, V vs V/Cr and Mg# vs Sc/V diagrams for all augites analysed by LA-ICP-MS. Symbols as above.

11.2.2 LILE

In general, augites have a very different trace element compositions with respect to plagioclases as visible from their REE and trace elements spidergrams (Fig. 11.12). LILE concentrations are very low (Fig. 11.12, 11.14, 11.15 and 11.16). Sr has quite high concentrations, while Rb, Ba and Pb are much lower. In fact, many analysis points gave no data for these elements (Fig. 11.17). The Sr compositions plotted vs Mg# are well clustered and do not show any particular trend. So it does Pb even if the values are more scattered even due to the its low concentration in augites. Rb and Ba have very sparse values.

11.2.3 HFSE

HFSE concentrations in augites, even if slightly higher than in plagioclases, are very low and close to the detection limit for LA-ICP-MS analyses. Again Zr is the more abundant among HFSE, reaching 14 ppm in the sample of the

Lower Unit. Fig. 11.18 shows Zr variations vs Mg# in augites compared to those of plagioclases, plotted vs MgO content. Among the others elements only Hf has been always detected, with concentration varying from 0.134 and 0.803 ppm (Fig. 11.18). The other HFSE, in most analyses have not been detected with overall very low concentrations, respectively up to 0.0429 ppm for U, 0.051 ppm for Th, 0.098 ppm for Nb and 0.0178 ppm for Ta. Both in a Mg# vs Zr and Hf diagram the four units are well recognizable. Zr from the Lower to the Upper Unit decreases as Mg# increases, but it increases again at much lower Mg# for the samples of the Recurrent Unit. This diagram results completely different if compared with the similar MgO vs Zr for plagioclases, due to their low Zr concentration. Hf displays roughly the same behaviour as Zr, decreasing from the Lower to the Upper Unit as Mg# increases and again increasing its concentration at much lower Mg# values for Recurrent augites. Nevertheless the Hf ranges of each unit are quite larger than the Zr ones. Finally the Lu/Hf vs Lu diagram (Fig. 11.18) calculated for a melt in equilibrium with augites shows different but well defined compositional fields for all units. Since Lu and Hf have very similar K_D for augites ($K_{Lu}^{cpx-melt}$ =0.61 and $K_{Hf}^{cpx-melt}$ = 0.58, **Hill *et al.*, 2000**), these compositional differences probably indicate heterogeneous Lu and Hf compositions and/or processes which generated the parental magma of augites.

11.2.4 REE

Differently from plagioclase, Rare Earth elements are more concentrated in clinopyroxenes, especially the HREE, with the typical increasing monotonous pattern and no Eu anomaly, as visible from Fig. 11.3. As for plagioclase, augites belonging to the Lower Unit display the highest LREE/HREE and LREE/Y and LREE concentrations among the four units (excluding few data with anomalous compositions, Fig. 11.19), as visible in La/Y vs La diagram of the calculated melt in equilibrium with augites ($K_D^{cpx-melt}$ from **Hill *et al.*, 2000**; Fig. 11.19). In this diagram, the distinction between the four units is much more visible than in the same diagram relative to plagioclases (Fig. 11.11). In general, the higher La/Y and La for melt in equilibrium with plagioclases than with augites (Fig. 11.11) probably indicate that plagioclase begun to crystallize before augites, even if the low La and Y concentrations in plagioclases could lead to a wrong interpretation. The REE spidergrams of augites are more complete compared to those calculated for plagioclases. It is possible to see a trend, in which passing from the Lower to the Upper Unit the REE concentrations decrease with a progressive flattening of the REE pattern (i.e., La/Yb ratio from 4.7 tend to approach 1 or even lower).

11.2.5 Transition metals

The transition metals are much more compatible in augites, so their concentrations are much higher than in plagioclases, and also are better correlated with an differentiation index like Mg# (Fig. 11.13). Sc, V, Zn have positive and Co fairly negative correlation with Mg#, i.e. their concentration increase as augites have less mafic compositions. In general, Sc and V are higher in the Lower Unit compared to the Intermediate Unit. The Upper Unit displays a strong variation of these two elements for an almost constant Mg#, with Sc being similar to those of the Intermediate Unit and V being much lower. Probably, the parental magma of the Upper Unit basalts fractionated a phase like oxide, which retains preferentially V with respect to Sc, before the crystallization of analysed augite. The Recurrent Unit augites are the most enriched in Sc among the four units, while V has the same or slightly higher concentration than the Lower Unit. On the contrary Ni seems to be constant for the Lower and Intermediate Unit while in the Upper and Recurrent Unit it varies strongly for almost constant Mg#. Moreover Ni has quite lower concentration in the Lower, Intermediate and Recurrent Unit compared to the Upper Unit, probably indicating olivine fractionation before the augite crystallization while in the Upper and Recurrent Unit olivine and augite could have crystallized together. V and Sc are well correlated, allowing to recognize very well not only the four units but even the single samples (Fig. 11.22). In particular, they seem to be two parallel trends with V and Sc concentrations decreasing from the Lower to the Intermediate Unit in the first and from the Recurrent to the Upper Unit in the second, being the Recurrent and the Upper Unit more enriched in V with respect to the Lower and the Intermediate Unit respectively. Also the Sc vs Sc/V diagram calculated for a melt in equilibrium with augites ($K_{Sc}^{cpx-melt}$ =2.46 and $K_{V}^{cpx-melt}$ = 0.151, **Hill *et al.*, 2000**) allow to recognize the four units. Here Sc remains almost constant at increasing Sc/V from the Lower, through Intermediate to the Upper Unit, while the Recurrent Unit augites display higher Sc at Sc/V comparable with those of the Intermediate Unit. Compared with that for plagioclases (Fig. 11.22), this diagram shows as the Lower, Intermediate and Upper Unit have much lower both Sc/V and Sc compared to the same diagram calculated for augites, but the Recurrent Unit displays a minor decrease of Sc/V at almost constant Sc. This could mean that phases like clinopyroxenes and/or oxides could have fractionated Sc and V before the crystallization of the analysed augite. Ni and Cr concentrations are not well correlated (Fig. 11.23), as data are quite scattered and the four units have not well defined compositional fields. Anyway the Recurrent Unit seems to have the

lowest Ni and Cr value probably indicating a higher olivine and pyroxene crystallization compared to the other three units. The Intermediate and Upper Unit have a highest Ni and Cr concentration accordingly with the EMP analyses on plagioclases and augites. Also in a V vs V/Cr and a Mg# vs Sc/V diagrams the four units are well recognizable (Fig. 11.23). As visible in Fig. 11.22 and 11.23, melt V and Sc/V contents are irrealistically too high and too low, respectively, thus leading to think that $K_V^{cpx-melt}$ from **Hill *et al.* (2000)** is highly underestimated.

12 PETROGRAPHY AND MINERALOGY OF WESTERN MESETA PILES

As said in the previous chapter the Maaziz lava pile is composed by the Lower and the Intermediate Units. The volcanic sections, as previously described, were sampled flow by flow when possible, collecting two kinds of samples. A basaltic rock core drilled for paleomagnetic investigation, and a massive and possibly unfractured and fresh chunk, being the freshness of the samples is more important or geochemical rather than for paleomagnetic analyses. The samples from the Western Meseta like for the Middle Atlas were collected during two sampling campaigns, so some lava flows were sampled two times. The first in April/May 2007 (samples series AN500) pointed to a general sampling of the studied section, to understand the state of conservation and stratigraphy of lava pile and which volcanic units are preserved. After a preliminary geochemical study by XRF analysis for major, minor and some trace elements (i.e., Zr and Nb), it was possible to recognize the presence of two units. The second sampling campaign, in September/October 2007 (samples series AN600), pointed to a flow by flow sampling (where possible) to exactly determine the number of flows belonging to each unit and collect samples not only for geochemical but also for magneto-stratigraphic analyses, to further constrain the magneto-chemo-stratigraphic correlations from the Central High Atlas to Western Meseta and Middle Atlas. Both the campaigns also yielded sedimentary rock samples, mainly black and gray siltstones, for palynological investigation in order to constrain the stratigraphic relationship between lava flows (and more in general of the Moroccan CAMP volcanism) and the T-J boundary in Morocco.

12.1 TEXTURES AND PARAGENESIS

Like in volcanic sections of the CHA (Central High Atlas) the mineral assemblage of lava flows mainly consists of olivine (always altered), plagioclase, clinopyroxenes (both augitic and pigeonitic), oxides. No hydrated primary minerals (like biotite or amphibole) and no K-feldspar or quartz is observed.

12.1.1 Maaziz sequence

- **The Lower Unit**: it is composed by 3 sampled lava flows (samples AN503, AN504 (double sample with AN602), AN506[603]. Only AN504 was analysed by EMP for mineral chemistry. This sample has been analysed also in order to have a reference composition for ongoing Ar-Ar analyses on plagioclases (see chapter about methodology). These samples have an intergranular intersertal texture, dominated by fresh euhedral plagioclase laths, surrounding poikolitic clinopyroxenes, rarely big in size. Olivines are abundant, grouped in clusters, well recognizable from their habitus but are completely altered and replaced by reddish-greenish fibrous mineral. No pigeonites are recognizable in thin section. Little euhedral oxides are present in the ground-mass, often showing a dendritic shape. Frequent vesicles in the glassy ground-mass are filled with calcite, zeolite minerals and quartz.

- **The Intermediate Unit**: it is composed by 9 lava flows sampled (samples AN508[604], AN509, AN510[605], AN606, AN511, AN607, AN608, AN627, AN628). Samples AN510 and AN627 have been analysed by EMP. The samples have a texture from intergranular intersertal to porphyric with acicular plagioclase with rare euhedral plagioclase laths with inverse rhythmic zoning. The plagioclases surround little poikolitic clinopyroxenes. Like at Telouet, olivines are present, yet also here always altered and replaced by reddish-greenish fibrous mineral. Olivines are no more present in the last two samples, AN627 and AN628. Pigeonite is probably present in one sample, AN628, which has a texture from intergranular to sub-ophitic but its detection is quite ambiguous because of the little size of clinopyroxenes in these samples. Oxides are always present in the glassy ground-mass as little euhedral phenocrysts of micrometric size with sometimes a dendritic shape. Only in the sample AN628, big oxides have euhedral to sub-euhedral or skeletal habitus.

12.2 MINERAL COMPOSITIONS

12.2.1 Olivine

Like in the CHA and Middle Atlas, no fresh olivine was detected in the thin sections of the Maaziz lava pile, so it hasn't been possible to analyse them by EMP for mineral chemistry or LA-ICP-MS for trace element contents.

12.2.2 Plagioclase

As previously said (in this chapter and in the lava pile descriptions, Chap. ??) the Lower Unit in the Western Meseta and Middle Atlas is poorly represented. In particular at Maaziz, the Lower Unit is represented by 3 thin,

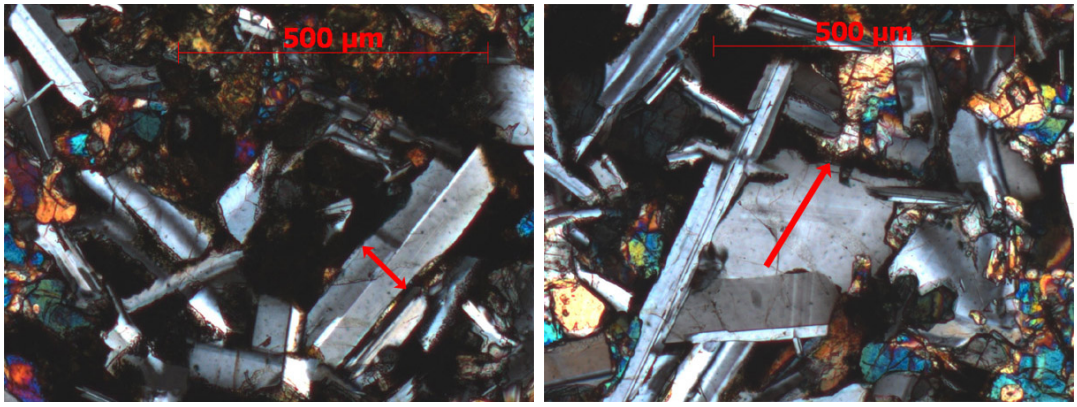

Figure 12.1: Microphotographs showing the plagioclases AN504 plg1 (on the left) and AN504 plg2 (on the right) from the Lower Unit at Maaziz. Red arrows represent EMP transects.

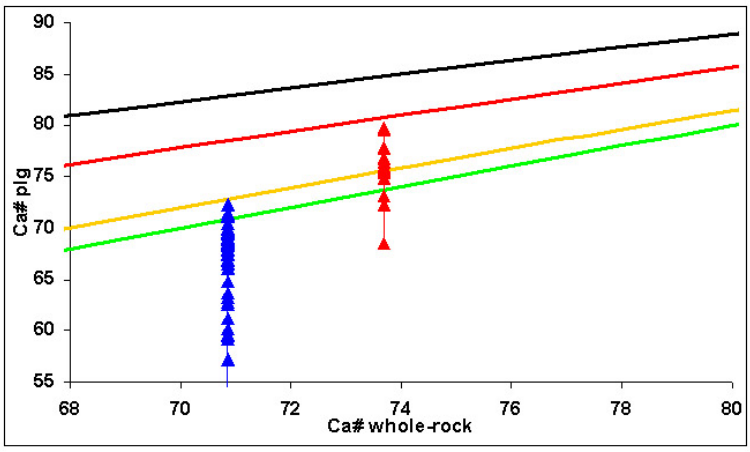

Figure 12.2: Ca# of whole-rock (XRF analyses) vs Ca# of all analysed plagioclases (EMP analyses) in the Maaziz section (Western Meseta). Blue triangles for Lower Unit, red circles for Intermediate Unit. Curves represent plagioclase compositions in equilibrium with melt for different $K_{Ca-Na}^{plg-melt}$: green line K_D =1, yellow line K_D =1.1, red line K_D =1.5, black line K_D =2.

similar lava flows. Only one sample, AN504, has been analysed by EMPA. In this thin section two plagioclase crystals have been analysed (AN504 plg1 and AN504 plg2; Fig. 12.1). Plagioclases of the Lower Unit at Maaziz are gener-

ally equigranular with smaller size (few hundred micron) with respect to those of the same unit of the CHA (compare EMPA transects) and with compositional normal zoning. Very few bigger phenocrysts show optical and compositional reverse zoning (Fig. 12.1, 12.3), features uncommon in the Lower Unit of the CHA. The plagioclases phenocrysts display a more restricted variation range

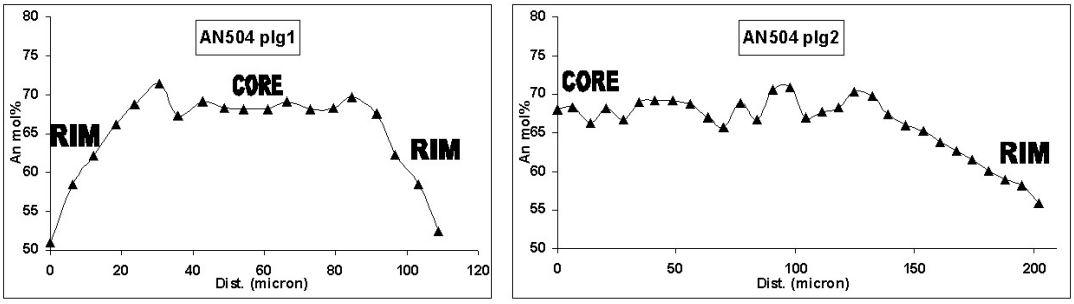

Figure 12.3: Variation of An mol% along transects (distance in microns) of plagioclases from the Lower Unit at Maaziz (EMP analyses). The slight reverse zoning from the core to the rim of phenocrysts is clearly observed.

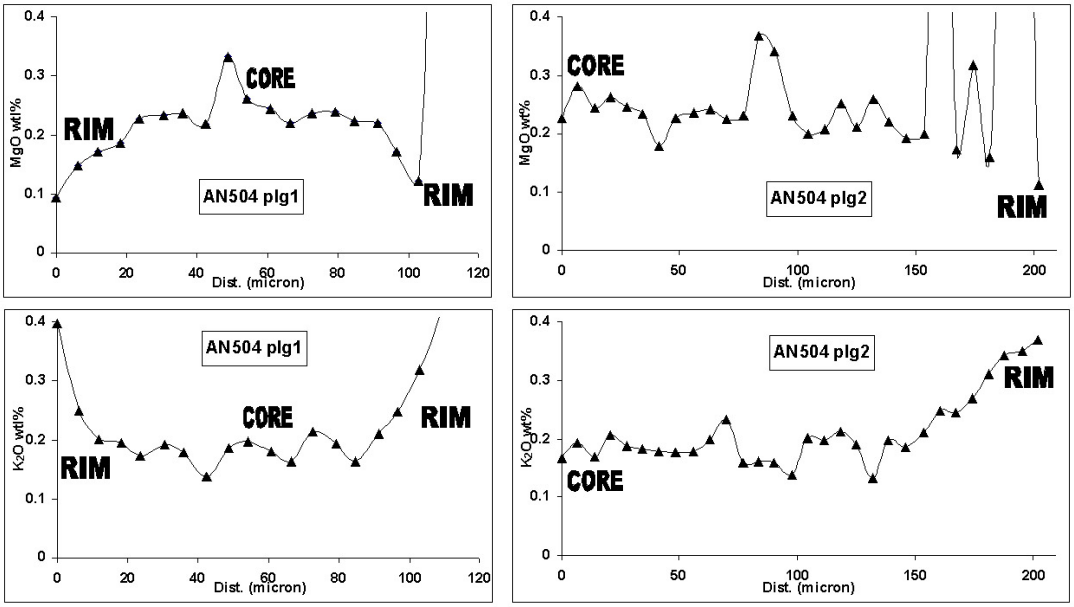

Figure 12.4: Variation of MgO and K_2O wt% along transects (distance in microns) of plagioclases from the Lower Unit at Maaziz (EMP analyses). It is well visible the positive and negative correlation with An content, respectively for MgO and K_2O.

compared to the CHA plagioclases, from bytownite to labradorite compositions ($An_{71.5}Ab_{27.5}Or_{1.0}$ to $An_{51.0}Ab_{46.5}Or_{2.5}$, Fig. 10.2) with an An- composition of

the core almost constant at An_{66-69} followed by a little An-jump up to 71-71.5 and finally by progressive monotonous decrease in An content towards the rim. MgO and K_2O contents follow quite well the An behaviour, being respectively positively and negatively correlated (Fig. 12.4, 12.5). MgO varies from 0.22-0.25

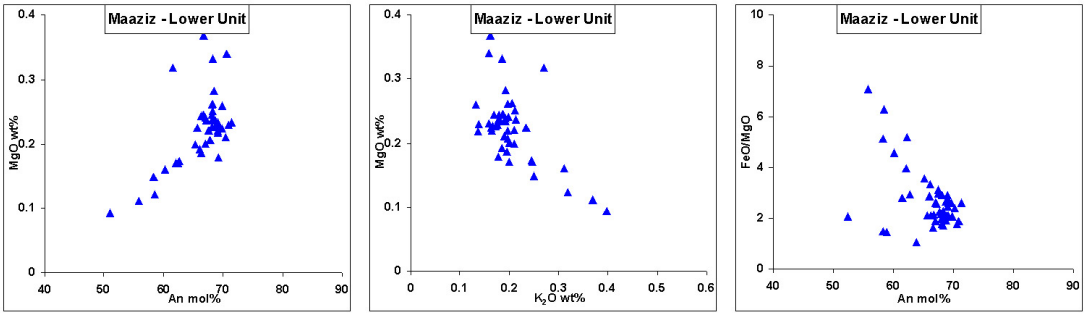

Figure 12.5: Anorthite mol% and K_2O wt% vs MgO wt% and FeO/MgO variations of plagioclase crystals from the Lower Unit at Maaziz (EMP analyses).

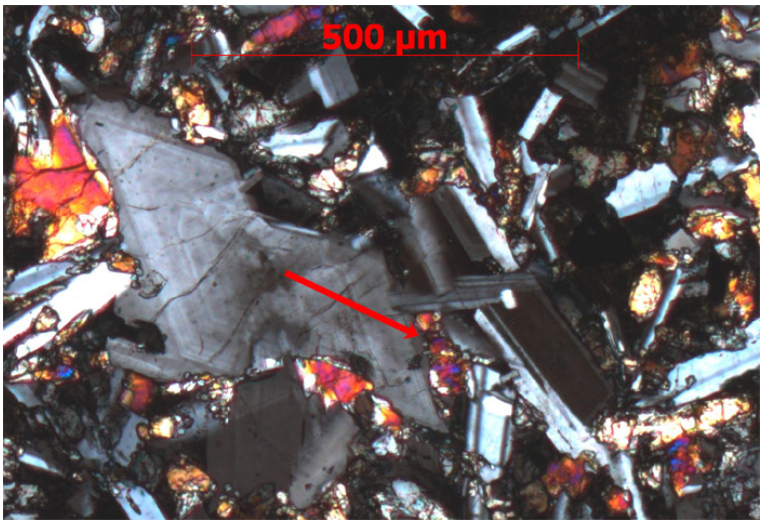

Figure 12.6: Microphotograph showing the plagioclase AN627 plg2 from the Intermediate Unit at Maaziz. Red arrows represent EMP transects.

wt% (or slightly higher) in the core to 0.10 wt% at the rim with values up to 0.36 wt% corresponding to the highest An contents in the reverse zoning. Conversely K_2O contents varies from 0.13-0.19 wt% of the core up to about 0.40 wt% at the rim. Compositional variation diagrams in Fig. 12.5 show the positive and negative correlation of MgO and K_2O (and FeO/MgO) respectively with An content. Compared with the same diagrams of the Lower Unit of the CHA, it is possible to see that the composition fields of plagioclases from Maaziz overlap well

with those of the CHA, especially with the those from Tiourjdal. No particular compositional differences are visible, except for a quite evident shift of the MgO contents towards higher values and an overall lower An content. Nevertheless it can be kept in mind that only two plagioclase crystals, with few tens of EMPA data points, are taken here as representative of the Lower Unit in the Western Meseta. So it is possible that this little higher and lower values of MgO and An contents could be due to analytical bias. The only difference between Maaziz and the CHA Lower units is that the plagioclases from the Maaziz section are somewhat less differentiated respect to those of the CHA, which reach An contents down to 40 or less. Finally in a $Ca\#_{whole-rock}$ - $Ca\#_{plagio}$ diagram, the cores of plagioclases belonging to the Lower Unit have a composition that is nearly in equilibrium with the whole-rock ($K_{Ca-Na}^{plg-melt}$ between 1 and 1.1, green and yellow lines in Fig. 12.2), again being this comparable with the plagioclases of the Lower Unit from the CHA.

Only one plagioclase belonging to the Intermediate Unit, AN627 plg2, has been analysed by EMPA (Fig. 12.6), so only few data points are available for the Intermediate Unit. The obtained informations confirm the main features characteristic of the Intermediate Unit, even if with some differences. First of all, the plagioclase analysed has the same complex optical and compositional zoning pattern found in the Intermediate Unit plagioclases from the CHA (Fig. 12.6, 12.7). AN627 plg2 has a narrow compositional range, from $An_{79.4}Ab_{20.1}Or_{0.5}$ and $An_{67.7}Ab_{31.0}Or_{1.3}$, but higher than for plagioclases of the Lower Unit at Maaziz even if not as high as in the same unit of the CHA. The EMPA transect from the core to the rim show a quite regular reverse An-zoning, with An content around 75-76 in the core, oscillating from 71.8 up to 79.4 along the transect and reaching the lowest value of 67.7 at the rim. The same complex zoning is visible in the MgO and K_2O compositional transects (Fig. 12.7). MgO contents are nearly the same of those of the sample AN504, belonging the Lower Unit (Fig. 12.8), but tend to increase towards the rim and do not follow the An content variation as it does in the Lower Unit. Probably, like in the CHA, the An content of plagioclase is affected not only by compositional variations of the parental melt but also by other factors like H2O content and decompression phenomena. The K_2O concentration is oscillating from 0.06 to 0.22 wt%. While this is in line with what found in the Intermediate Unit of the CHA (Chap. 9), the MgO contents are different from what we see in the CHA where MgO reaches up to 0.30 wt%. This influences the FeO/MgO ratio which is slightly higher (Fig. 12.8) in AN627 plg2 than in the plagioclases of the CHA. Even here, like for the Lower Unit, we

need to keep in mind the few available data. Differently from the plagioclases of

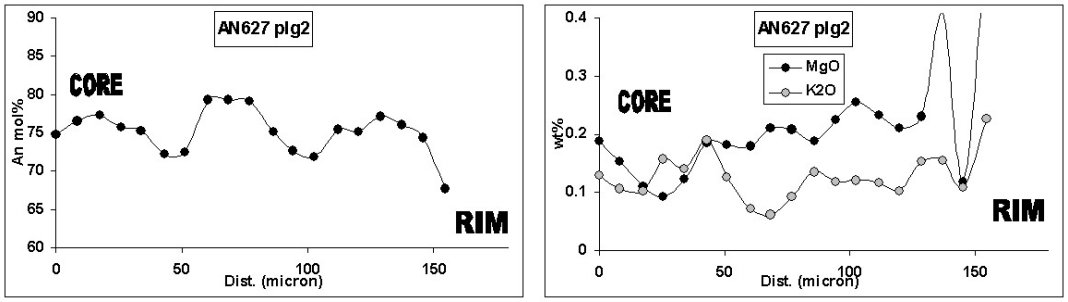

Figure 12.7: Variation of An mol% (on the left), MgO and K_2O wt% (on the right) along transects (distance in microns) of AN627 plg2 from the Intermediate Unit at Maaziz (EMP analyses). The complex zoning pattern from the core to the rim of phenocrysts is clearly observed

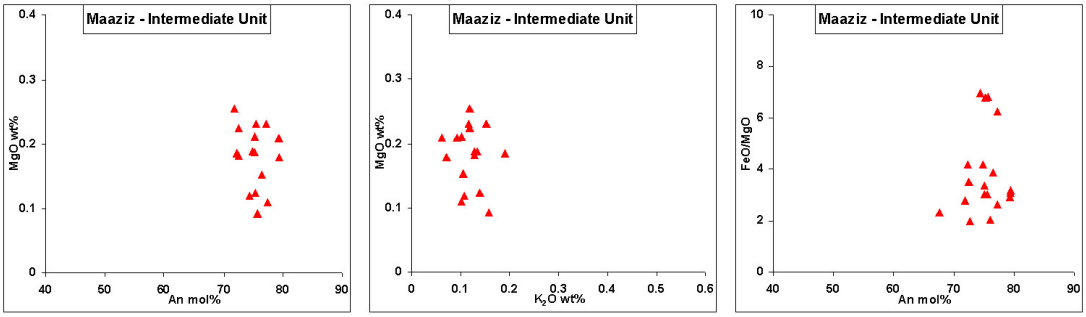

Figure 12.8: Anorthite mol% and K_2O wt% vs MgO wt% and FeO/MgO variations of AN627 plg2 from the Intermediate Unit at Maaziz (EMP analyses).

the Lower Unit, AN627 plg2 has a higher Ca# than the whole-rock, i.e. it would be in equilibrium with the host basalt for $K_{Ca-Na}^{plg-melt}$ around 1.5 (Fig. 12.2), this feature being the same of the plagioclases of the Intermediate Unit of the CHA.

12.2.3 Augite (high-Ca pyroxene)

In the lava flows of the Maaziz section only augitic clinopyroxenes have been observed (yet pigeonite may be present in the groundmass of some Intermediate units flows, AN510, AN627 and AN511; Fig. 12.14). Hereafter, we will describe only two augite phenocrysts from sample AN504 (Lower Unit, Fig. 12.9, on the left) and three from the sample AN510 (Intermediate Unit, Fig. 12.9, on the right). Augites from the Lower Unit have small size (few hundred microns) and

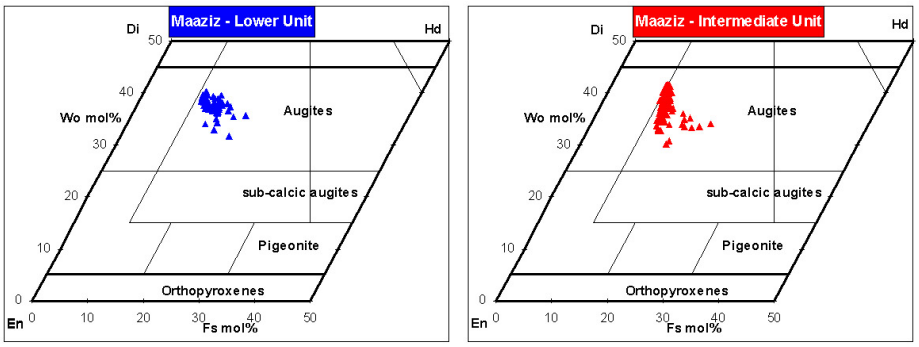

Figure 12.9: Compositions of all analysed augites plotted in a partial Wo-En-Fs ternary diagram for the Maaziz sections for the Lower Unit (on the left) and the Intermediate Unit (on the right) (EMP analyses).

rarely show an euhedral habitus (Fig. 12.10), being more frequently grown between plagioclase lathes. Phenocrysts plot within the augite field in a ternary diagram Wo-En-Fs with a fairly wide compositional range (Fig. 12.9) which, although more restricted, resembles that of the augites of the Lower Unit in the CHA (Chap. 9): $Wo_{31.7-40.2}En_{43.9-51.9}Fs_{10.9-20.5}$. The general trend is an enrichment toward the Fs apex and the depletion in the Wo and En components. At the

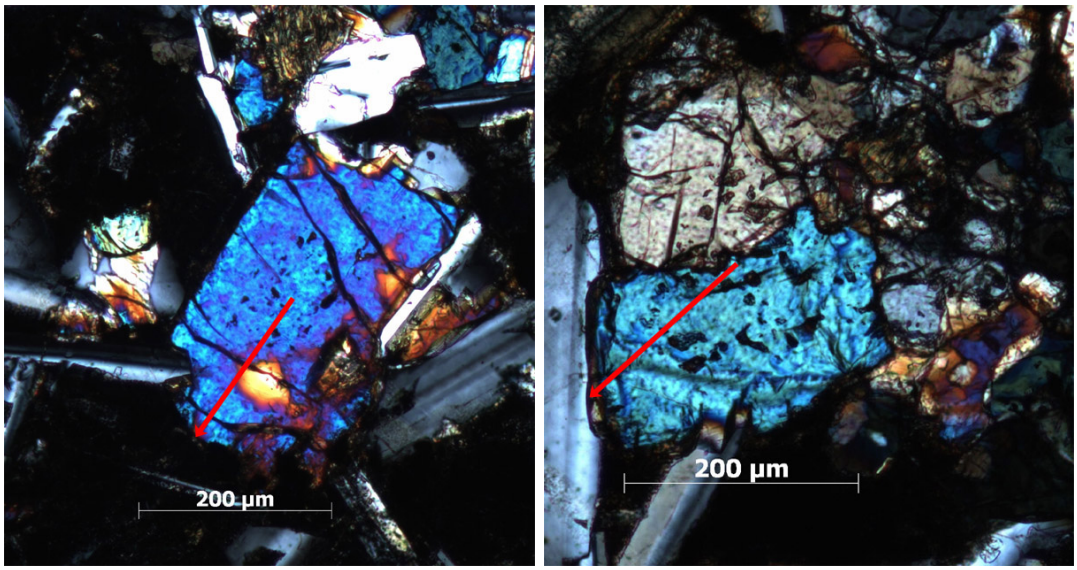

Figure 12.10: Microphotographs showing the augites AN504 cpx2 (on the left) and AN504 cpx3 (on the right) from the Lower Unit at Maaziz. Red arrows represent EMP transects.

same time, the Mg# range (83.9 to 68.6) is more restricted than corresponding augites of the CHA. Unlike those from the CHA, augites of the Maaziz Lower Unit

do not show a normal Mg# zoning, but an overall complex Mg# zoning pattern (Fig. 12.11). Cr_2O_3 concentrations vary positively with Mg#, from 0.20-0.50

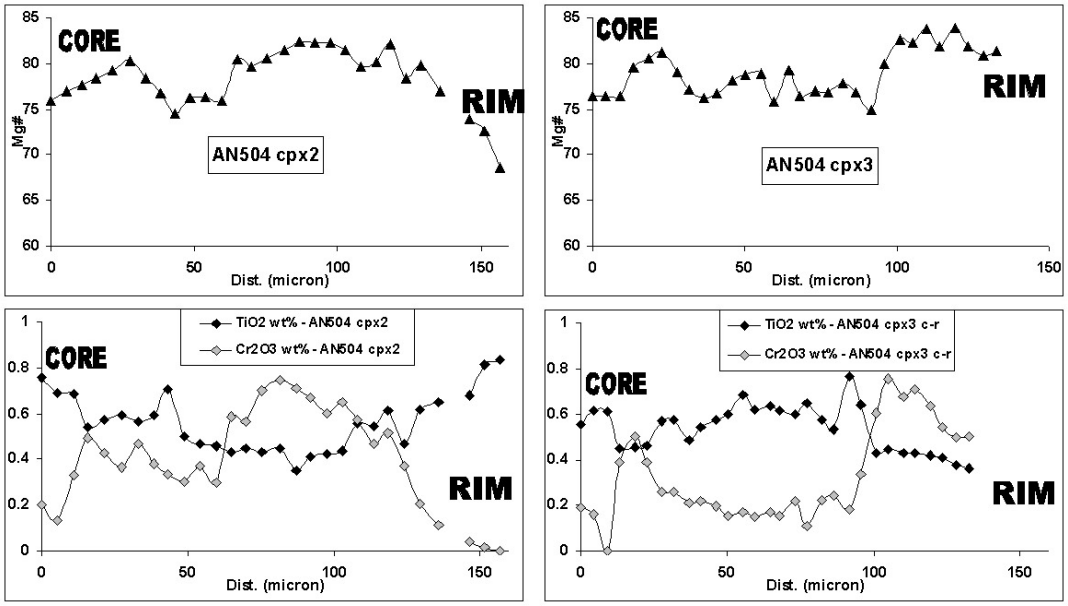

Figure 12.11: Core-rim compositional (Mg#, Cr_2O_3 and TiO_2) traverses of augites from the Lower Unit at Maaziz (EMP analyses).

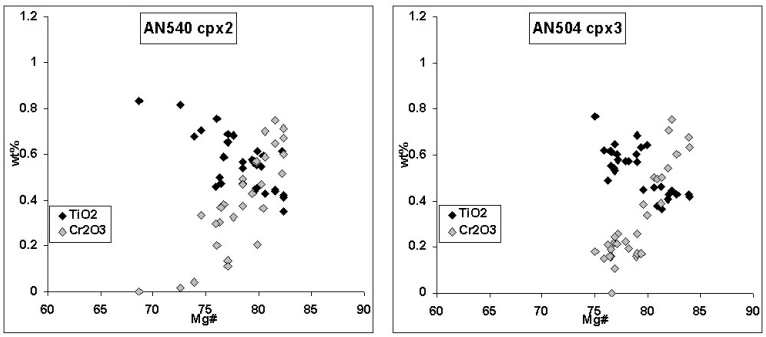

Figure 12.12: Cr_2O_3 and TiO_2 variations (EMP analyses) of augites from the Lower Unit showing the positive and negative correlation, respectively, with the Mg# even if values are quite scattered.

wt% in the core up to 0.75 wt% in the crystal zone where Mg# is highest and finally decrease at the rim. On the contrary TiO_2, which is negatively correlated with Mg#, has core concentrations in the 0.44-0.75 wt% range, which increase up to 0.80 wt% at the rim (Fig. 12.11). Even if Cr_2O_3 and TiO_2 are broadly correlated with the Mg# pattern, their compositional variations are not perfectly

anti-correlated one to each other as would be expected, probably due to oxide co-crystallization. Finally the $Mg\#_{whole-rock}$-$Mg\#_{cpx}$ diagram shows that augites of the Lower Unit are in equilibrium with the whole-rock for a $K_{Fe-Mg}^{cpx-melt} = 0.30$-$0.33$, like that found for the Lower Unit augites of the CHA (Fig. 12.13). Augites

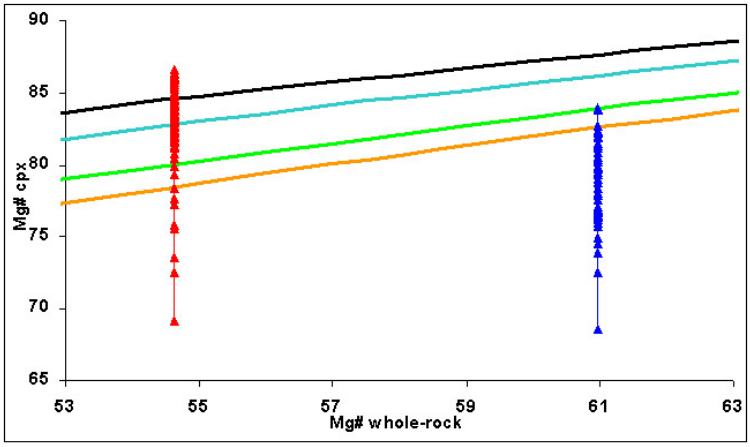

Figure 12.13: Mg# of whole-rock (XRF analyses) vs Mg# of all analysed augites (EMP analyses) in the Maaziz section (Western Meseta). Blue for the Lower Unit, red for the Intermediate Unit. Curves represent augite compositions in equilibrium with melt for different $K_{Fe-Mg}^{cpx-melt}$: orange line $K_D = 0.33$, green line $K_D = 0.30$, blue line $K_D = 0.25$ and black line $K_D = 0.22$.

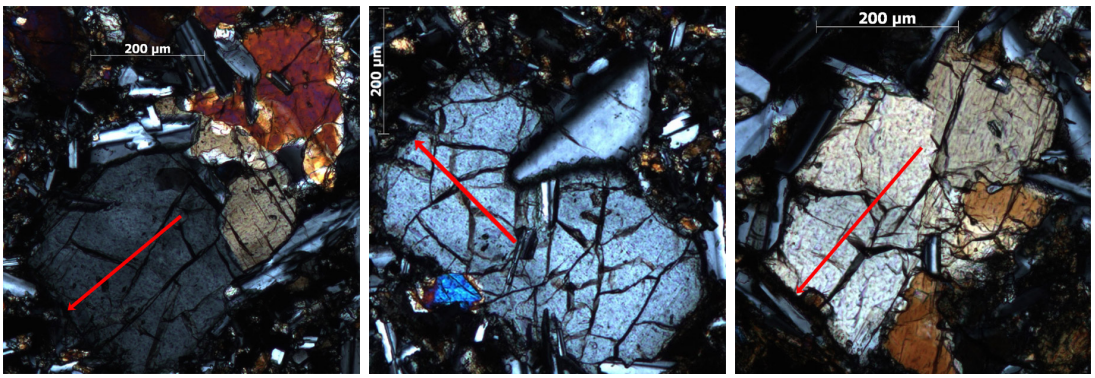

Figure 12.14: Microphotographs showing the augites AN510 cpx1 (on the left), AN510 cpx2 (on the middle) and AN510 cpx3 (on the right) from the Intermediate Unit at Maaziz. Red arrows represent EMP transects.

from the Intermediate Unit have larger size with respect to those of the Lower Unit, present an euhedral habitus (Fig. 12.14), with some little acicular enclosed plagioclase crystals. Phenocrysts plot within the augite field in the Wo-En-Fs diagram with a wider compositional range than that of the Lower Unit (Fig. 12.9),

resembling that of the augites of the intermediate Unit in the CHA even if with a more restricted range: $Wo_{30.2-41.5}En_{44.5-54.5}Fs_{9.8-21.5}$. The evolution trend is a general depletion in Wo for an almost constant En/Fs ratio and a final marked Fs/En enrichment. Augites from the Intermediate Unit have peculiar features if compared with the homologues from the CHA. First of all, the high Mg# values resemble those of the Upper rather than of the Intermediate Unit (Mg# of the CHA Intermediate Unit augites never exceed 85, being more frequently in the 82-84 range). At Maaziz, all three analysed augites have a mean Mg# around 82-83 with values up to 87, remaining nearly constantly above 80 except at the rim of most phenocrysts (Fig. 12.15). Even Cr_2O_3 and TiO_2 contents are similar to those of the CHA Upper Unit augites. Cr_2O_3 reaches 1.27 wt% decreasing toward the rim (even at constant Mg#). On the other side, TiO_2 remains quite constant, oscillating in the 0.25-0.45 wt% range and only increasing its concentration at the rim up to no more than 0.61 wt%. Another feature which resembles the augites

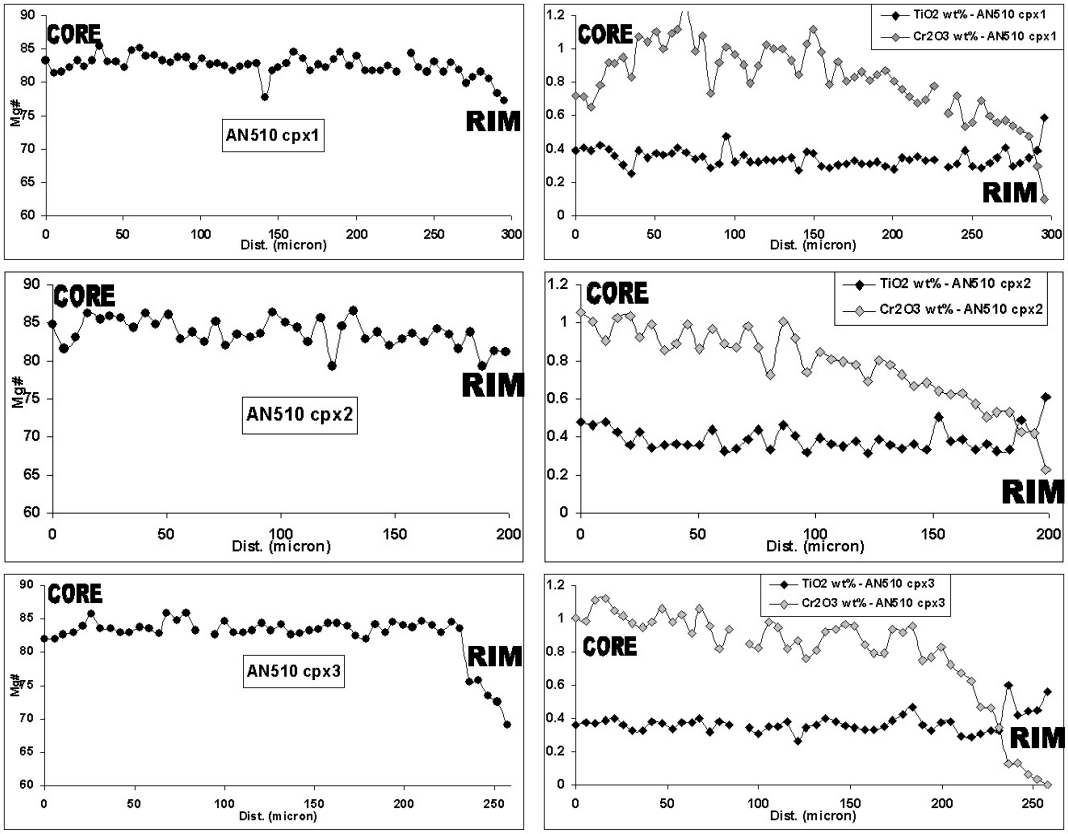

Figure 12.15: Core-rim compositional (Mg#, Cr_2O_3 and TiO_2) traverses of the three augites from the Intermediate Unit at Maaziz (EMP analyses).

of the CHA Upper Unit is the low calculated $K_{Fe-Mg}^{cpx-melt}$, 0.20-0.25 or less (Fig.

12.13). These low values are typical of the augites of Upper Unit and probably related to high H_2O concentrations of the magma during the crystallization at mid-crustal level (**Sisson & Grove, 1993**).

12.3 EASTERN MESETA SAMPLES

Due to the paucity of outcrops and bad preservation of the basalts, few samples were collected from mountains in the Oujda/Jerada zone. Moreover during the field work was collected only massive sample for geochemical analyses. No rock cores were drilled for paleomagnetic studies. The mineral assemblage, like elsewhere, consist of plagioclases, clinopyroxenes (both augitic and pigeonitic), oxides (magnetite±ilmenite), olivines (always altered) and in some samples there is the occurrence of biotite, alkali feldspar and micrographic quartz, which together with glassy groundmass absence led to think to intrusive rock even if from the field investigation it does not result clear the stratigraphic relationship of these samples with terrains aside. All these samples have been analysed only by XRF and in this work we will described them only briefly. No more analyses have been performed on these samples (EMPA, LA-ICP-MS, isotopic, Ar-Ar dating, paleomagnetism) and probably these samples will be object of further more detailed studies in the future, since there is the possibility of presence of feeder dike (or more in general intrusive rock belonging the CAMP) in this part of Morocco.

12.3.1 Col de Tizi Nmeur

These samples collected on a little mountain (Col de Tizi Nmeur), between Tanacherfi and Dada Ali villages (mean GPS coordinates 34°19′40″ N, 2°34′50″ W). The outcrop consists of a discontinuous volcanic succession ca. 40 m thick with frequent sedimentary calcareous layers interbedded, overlying red siltstones and limestones with Ba and Mn mineralizations. The three samples collected show a typical Lower Unit composition:

- **AN512**: the sample has an intergranular to ophitic texture with euhedral laths of plagioclase, rarely big in size, surrounding poikilitic augitic clinopyroxenes often altered in chlorite. Plagioclases present a progressive zoning and are often altered in sericite. The predominant femic phase is a pigeonitic clinopyroxene showing an euhedral habitus. Olivines are abundant and recognizable from their habitus, but are always altered in a reddish-brownish material (probably hiddingsite). Oxides are present as big euhedral to sub-

euhedral or as elongated phenocrysts or with skeletal shape. Little glassy ground-mass with spherulitic devetrification is present.

- **AN513 and AN514**: both the samples have a holocrystalline intergranular to ophitic texture like the previous samples with some granophyric patches. Plagioclases show together with normal zoning also inverse rhythmic zoning. The femic phases are more altered in chlorite. Olivines are not present. Oxides present the same features of the previous sample. Notable is presence of biotite well recognizable by its reddish-brownish colour and pleochroism, even if slightly altered, and small patches of micrographic quartz and alkali feldspar filling the interstices between plagioclases, clinopyroxenes and biotites. The presence of mineral evolved as biotite, K-feldspar and quarzt together with the holocrystalline texture could do to think to an intrusive rock.

12.3.2 Jbel Lamquam

These samples have been collected in the Jbel Lamquam locality (GPS coordinates 34°2′55.5″ N, 2°22′21.4″ W). The outcrop consists of a ca. 30 m thick lava pile, overlying black and red siltstones. The basal contact shows mingling structures, with baked siltstone enclaves within basalts. On the top, the basaltic sequence is covered by Liassic limestones. Like previous samples, these have a Lower Unit compositions:

- **AN516 and AN517**: both the samples show a fairly cumulitic textures with mega-phenocrysts of fresh plagioclases, with normal progressive zoning, mega-phenocrysts of augitic clinopyroxenes with olivines enclosed within, often altered in serpentine. Oxides have big size and present from euhedral to sub-euhedral shapes. Little glassy ground-mass is present between plagioclases and clinopyroxenes.

12.3.3 Oued Berkane

These samples have been collected in the Oued Berkane river bed, near the Aïn Merini locality (GPS coordinates 34°5′51.6″ N, 2°22′21.4″ W), ca. 20 Km to the west of Merija. The outcrop where the samples have been collected consists of ca. 10 m of basaltic lava flows overlied by 1 m thick limestone layer, 2-3 m thick of red claystone and siltstone and finally by several meters thick Liassic limestones. The basal contact between the lava piles and underlying sediments is

not visible, as basalts made the river bed. Based on preliminary XRF analyses, these two samples have an Intermediate Unit compositions, even if this should be confirmed by more precise analyses (i.e. ICP-MS measures):

- **AN518 and AN519**: both samples show ophitic intersertal texture with few big pyroxene and plagioclase phenocrysts (>500-600 micron) sparsed in a groundmass made by little elongated idiomorph plagioclases and pecilitic pyroxenes. Oxides have big size and present from euhedral to subeuhedral shapes. Little glassy ground-mass is present between plagioclases and clinopyroxenes. Overally quite altered samples.

13 PETROGRAPHY AND MINERALOGY OF MIDDLE ATLAS PILES

13.1 TEXTURES AND PARAGENESIS

The main features of the sampling procedure are the same for those of Western Meseta samples. Unlike at Maaziz, at the Agourai section only the Intermediate Unit is preserved. At the Oum R'Rbia section, the lava pile is more complete, comprising also the Upper Unit, but both the Lower and the Upper Unit are represented by (at least) 1 lava flow. Again the mineral assemblage consists mainly of altered olivine, plagioclase, clinopyroxenes (both augitic and pigeonitic), and oxides (magnetite). No biotite or other hydrous minerals are present.

13.1.1 Agourai sequence

- **The Intermediate Unit**: it is composed by 12 lava flows sampled (in stratigraphic order AN521, AN629, AN522, AN523, AN524, AN525[630], AN525B, AN631, AN632, AN529, AN531, AN532). As previously said, the Intermediate Unit only is preserved at Agourai, even if a couple of samples (AN525[630] and AN525B)have a high TiO_2 content up to 2 wt% (see Chap. 14) which would suggest Lower Unit-like compositions. In general, the textures of the samples vary from intergranular to sub-ophitic with few exceptions: AN525[AN630], the sample with the highest TiO_2 content (up to 2.2 wt% in the sample AN630), having a cumulitic-like structure with plagioclase megacrysts (>1000 μm) with enclosed clinopyroxenes plus oxide crystals and AN526, globally very altered with a porphyric texture. The main feature of the whole section, is the pervasive presence of pigeonite, detected in almost all the lava flows and in particular in two of them, AN523 and AN524, where this mineral is present in well shaped big elongated phenocrysts (> 1000μm) (Fig. XXX) modally representing the first femic phase of the paragenesis.

- **The Upper Unit**: is represented by only one lava flow (sample AN530[633]).

Similarly to the sample TEL21 (Telouet sequence in the CHA, Chap. 9), sample AN530[633] has been collected in the middle of the Intermediate lava flows, stratigraphically above AN529 and prior to numerous not sampled thin lava flows (maybe more than six for a lacking stratigraphy thick at least 20-30 meters) in the upper part of the volcanic sequence. AN530[633] has a nearly porphyric texture, dominated by big augitic phenocrysts (up to 900-1000μm) interspersed in a roughly microgralular ground-mass of acicular plagioclase, clinopyroxenes and oxides.

13.1.2 Oum R'Rbia sequence

- **The Lower Unit**: it is composed by one lava flow (sample AN534 [AN609]) and analysed by EMP. As described in the stratigraphy chapter, the lower part of this section has not been sampled completely due to its bad section orientation and debris and vegetation cover. Above the first sampled and lowermost lava flow belonging to the Lower Unit, there is *at least* one other lava flow (maybe 2) before the successive belonging to the Intermediate Unit. The collected sample has an intergranular to intersertal texture, with a network of little laths and aciculae of fresh plagioclases, which show normal progressive zoning. Big euhedral plagioclase phenocrysts with multiple inverse rhythmic zoning are rare. Little fresh poikilitic clinopyroxenes are enclosed between the plagioclase network and rarely display big dimensions and euhedral shape. Olivines are abundant, always altered in a red-greenish fibrous aggregate and grouped in clusters. Little euhedral oxides are sparse in the glassy ground-mass together with frequent vesicles filled with zeolites and calcite.

- **The Intermediate Unit**: it is composed by 8 lava flows (sampled in stratigraphic order: AN535 [double sample with AN610], AN536, AN537, AN538, AN611, AN612, AN539 [double sample with AN613], AN614). Only sample AN539 was analysed by EMP. The textures vary from intergranular to ophitic intersertal, in the lower part of the unit, passing to a porphyric-like structure, in the upper part where the lava flows are thinner, with sparse plagioclase/clinopyroxene aggregates and abundant devitrified glassy ground-mass. Olivines are always present, even with big size, but like other sections/units similarly altered like in the Lower Unit. Plagioclases show multiple inverse rhythmic zoning and rare brownish glassy inclusion. Oxides display big size in the more massive lava flows at the base of the unit, while

their size is micrometric and their habitus dendritic in the porphyric lava flows.

- **The Upper Unit**: it is composed by one lava flow (sample AN540) with the typical porphyric texture characterizing these unit. Few big plagioclase and clinopyroxene phenocrysts are sparse in a coarse micro-crystalline ground-mass, in which we observe pigeonite micro-phenocrysts together with acicular plagioclase and augite. Only in this sample of the Oum R'Rbia lava pile pigeonite has been detected. Olivines are absent while oxides are observed only in the ground-mass as tiny phenocrysts.

13.2 MINERAL COMPOSITIONS

13.2.1 Olivine

Like in the CHA and in the Meseta no fresh olivine has been analysed in the MA samples.

13.2.2 Plagioclase

Hereafter, I will describe only the EMPA compositional variations of plagioclases of the Oum R'Rbia sequence, since no analyses are available for the Agourai sequence. As described above, only one Lower Unit lava flow has been detected (and analysed) at Oum R'Rbia. Three plagioclases belonging the AN534 sample (AN534 plg1, plg2 and plg3 not shown, Fig. 13.1), representing this flow, have been analysed by electronic microprobe (EMPA). The three plagioclases analysed have big size (>500-600 μm), show inverse zoning and are surrounded by ground-mass network of little plagioclase laths (>200-300 μm) normal zoned. Plagioclase compositions range from bytownite to andesine compositions ($An_{75}Ab_{24}Or_1$ to $An_{44}Ab_{53}Or_3$) with moderate core An content (65-66 mol%) followed by strong increase An content (up to 10 mol%) and its subsequent rimward decreasing (Fig. 13.3). MgO and K_2O content are positively and negatively correlated, respectively with An, thus probably indicating mixing phenomena with less differentiated magma batches (Fig. 13.3) and their compositional fields are nearly the same of those of the CHA plagioclases (Fig. 13.4, cf. Chap 9). Also FeO/MgO which varies from ca. 1.5 up to 8.6 cover the same range of the CHA and WM sequences. In the $Ca\#_{whole-rock}$-$Ca\#_{plagio}$ diagram, the cores of plagioclases belonging to the Lower Unit have a composition that is nearly in equilibrium with the whole-rock ($K_{Ca-Na}^{plagio-melt} = 1$ or less, green lines in Fig.

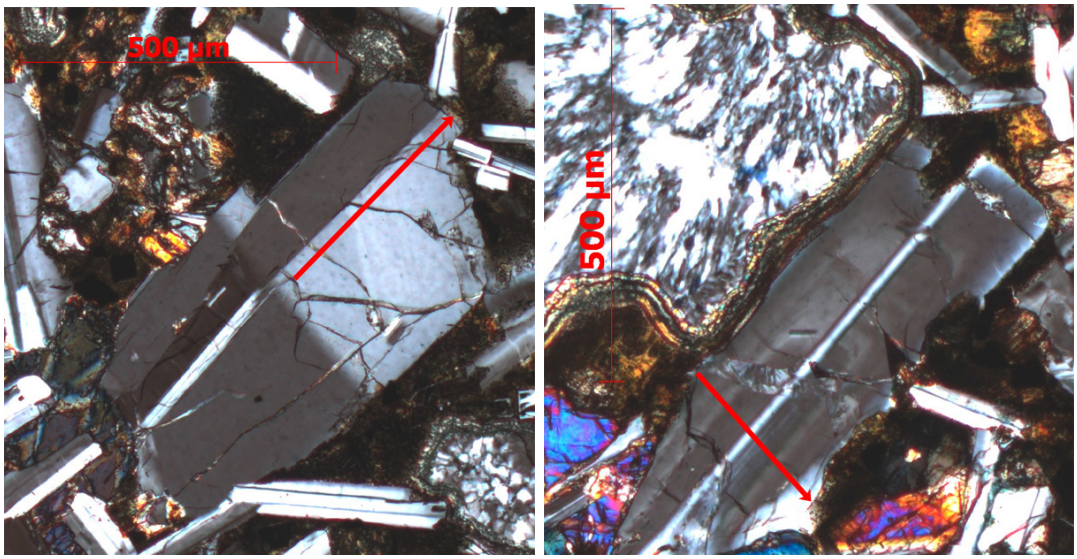

Figure 13.1: Microphotographs showing the augites AN534 plg1 (on the left) and AN534 plg2 (on the right) from the Lower Unit at Oum R'Rbia. Red arrows represent EMP transects.

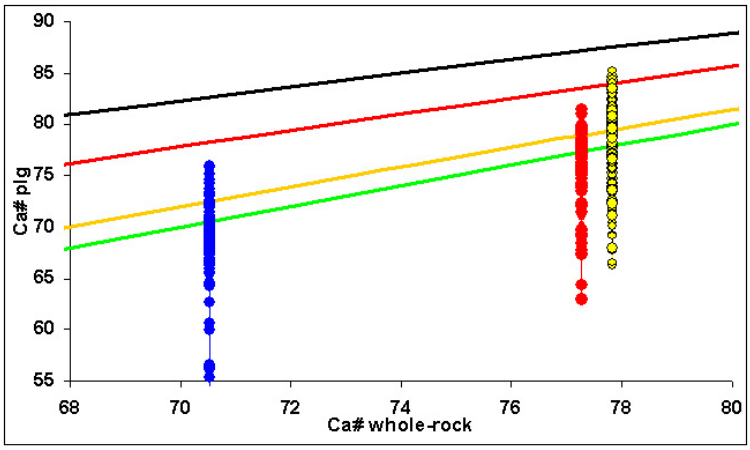

Figure 13.2: Ca# of whole-rock (XRF analyses) vs Ca# of all analysed plagioclases (EMP analyses) in the Oum R'Rbia section (Middle Atlas). Blue triangles for AN534 (Lower Unit), red circles for AN539 (Intermediate Unit), yellow diamonds for AN540 (Upper Unit). Curves represent plagioclase compositions in equilibrium with melt for different $K_{Ca-Na}^{plagio-melt}$: green line K_D= 1, yellow line K_D = 1.1, red line K_D = 1.5, black line K_D = 2.

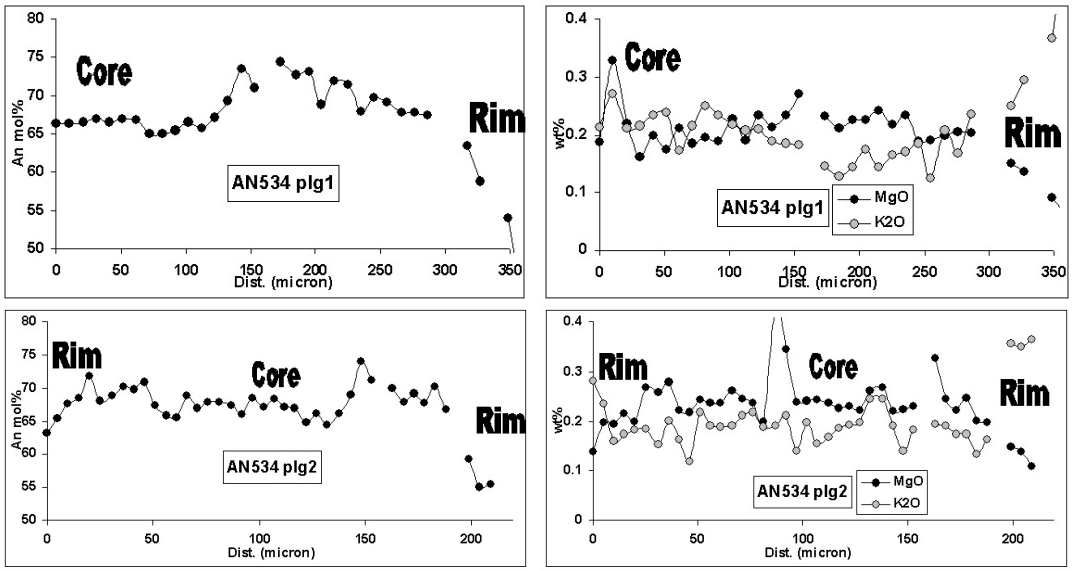

Figure 13.3: Variation of An (mol%), MgO and K_2O (wt%) along core to rim of plagioclases from the Lower Unit at Oum R'Rbia (EMP analyses).

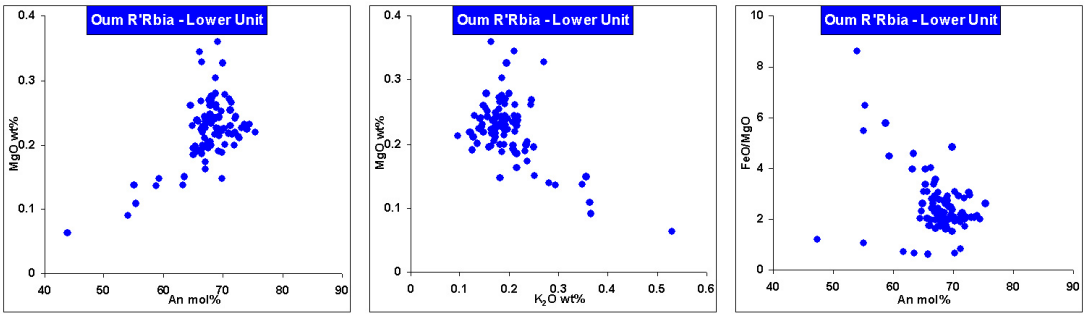

Figure 13.4: Anorthite mol% and K_2O wt% vs MgO wt% and FeO/MgO variations of plagioclase crystals from the Lower Unit at Oum R'Rbia (EMP analyses).

13.2), almost comparable with the plagioclases of the Lower Unit from the CHA. Only three plagioclases belonging one sample, AN539, of the Intermediate Unit

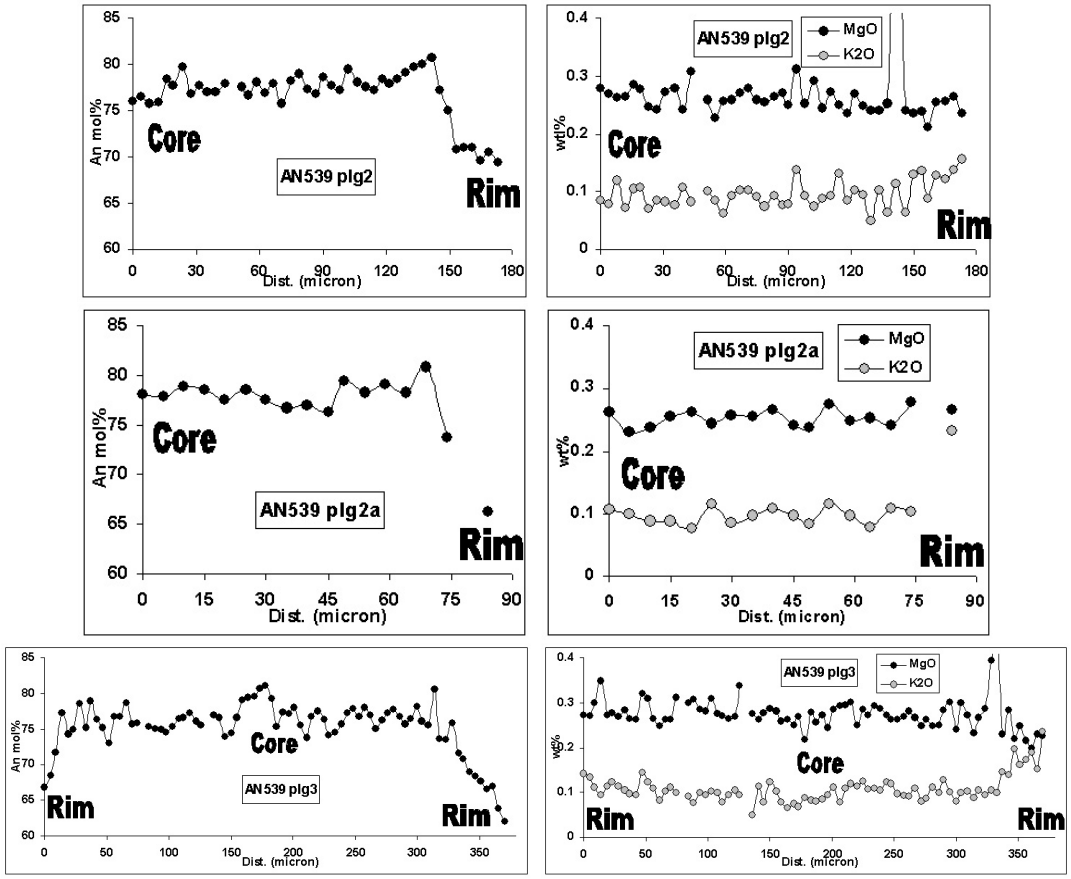

Figure 13.5: Variation of An (mol%, on the left) and MgO and K_2O (wt%, on the right), along transects (distance in microns) of plagioclases from the Intermediate Unit at Oum R'Rbia (EMP analyses).

have been analysed (AN539 plg2, plg2a and plg3, Fig. 13.6). Plagioclase with big size (>500-600 μm) have inverse multiple zoning with compositions ranging from bytownite to labradorite ($An_{81.1}Ab_{18.4}Or_{0.5}$ to $An_{62.1}Ab_{36.5}Or_{1.4}$) with a narrower compositional range compared to that of CHA plagioclase of the same unit (Chap. 9). Differently from CHA Intermediate Unit plagioclases, phenocrysts of Oum R'Rbia sequences (and Agourai) have rare glassy brownish inclusions, thus indicating that mixing and disequilibrium compositional phenomena are less common. This hypothesis is somewhat corroborated by the EMPA compositional transects, that do not show any appreciable MgO and K_2O variations together with An content (cf. below Fig. 13.5). As typical of the Intermediate Unit, plagioclase core An contents is much higher compared to the same phenocrysts

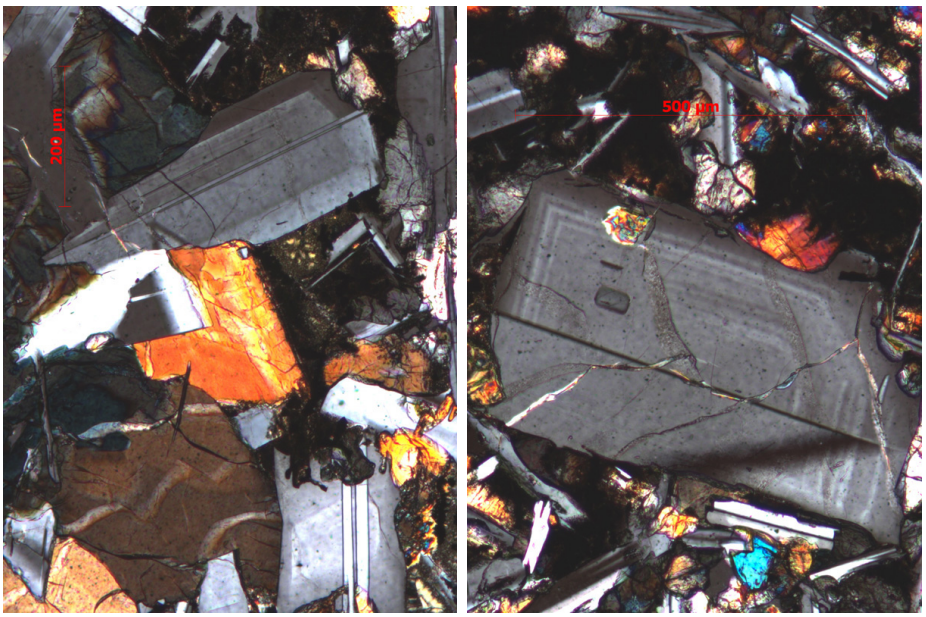

Figure 13.6: Microphotographs showing the augites AN539 plg2 and plg2a (on the left) and AN539 plg3 (on the right) from the Intermediate Unit at Oum R'Rbia. Red arrows represent EMP transects.

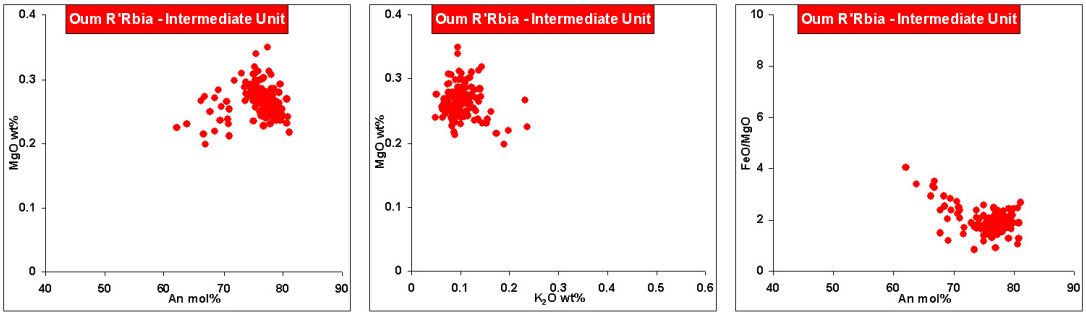

Figure 13.7: Anorthite (mol%) and K_2O vs MgO (wt%) and FeO/MgO variations of plagioclase crystals from the Intermediate Unit at Oum R'Rbia (EMP analyses).

of the Lower Unit. In the cores An varies from 75 to 80-82, increasing slightly rimward with a saw-tooth pattern up to ca. 80 and then decreasing abruptly in few tens of micron down to 65-70 (Fig. 13.5). MgO and K_2O follow nearly parallel trends (Fig. 13.5) in all three plagioclases analysed, except at the rim of the biggest (AN539 plg3) where display anti-correlated behaviours, i.e. while MgO decreases, K_2O increases. Moreover is well visible in the AN539 plg3 (the crystal that the plagioclases analysed probably records the longest differentiation history) EMPA transect that MgO and K_2O tend to increase rimward, then decrease at one of the two rims phenocryst (the opposite rim insist on cpx phenocrysts thus not recording the latest differentiation stage, Fig. 13.6). This unusual behaviour (rarely or not observed in none of analysed plagioclases) could be explained if it was that plagioclase AN539 plg3 start to crystallize before augites. In fact, Mg and K are highly incompatible in plagioclase and would tend to increase as the latter evolve. However, I described as generally MgO tend to decrease rimward (except when increase together with An, i.e. magma mixing phenomena) and this feature is well explained if together with plagioclase crystallize a femic phase (like augite and/or olivine) which fractionate MgO. Since in AN539 plg3 MgO and K_2O increase rimward, probably no augite and olivine crystallization occur prior to its rim crystallization onset. Also FeO/MgO in Fig. 13.7 could validate this hypothesis, since it remains nearly constant (ca. 1.7-2.5) from An = 82 to ca. 72, then increase as usually seen in all plagioclases previously analysed. The same behaviour is well visible in the most complete Tiourjdal Intermediate Unit plagioclase dataset, where An decrease from ca. 84 to 68-69 for nearly (even with a larger variation range of 1.3-3.5) constant FeO/MgO (Fig. 9.11). Like for the Lower Unit, the Upper Unit is represented by only one sample, AN540, where four plagioclases have been analysed (AN540 plg1, plg1a, plg2 and plg3 not shown, Fig. 13.10). The Upper Unit plagioclases show strong similarities with those of the same unit in other lava sequences: big sizes (>600-700 μm), euhedral shapes, glassy brownish inclusions, multiple inverse zoning with strong An variations and again the highest An content. Phenocrysts vary their composition from bytownite to labradorite ($An_{85.1}Ab_{14.7}Or_{0.1}$ to $An_{65.6}Ab_{33.2}Or_{1.1}$) with the highest An contents near the rim in some phenocrysts (AN540 plg1, plg1a and plg3 not shown Fig. 13.8) and An decreasing rimward in other (AN540 plg2). Like for Upper Unit plagioclases of the other sequences, An-content variations are not correlated with MgO and K_2O content and in the two phenocrysts with the high-An rim, MgO and K_2O display parallel trend (along the compositional transect) with the highest and lowest concentration, respectively. In AN540 plg2,

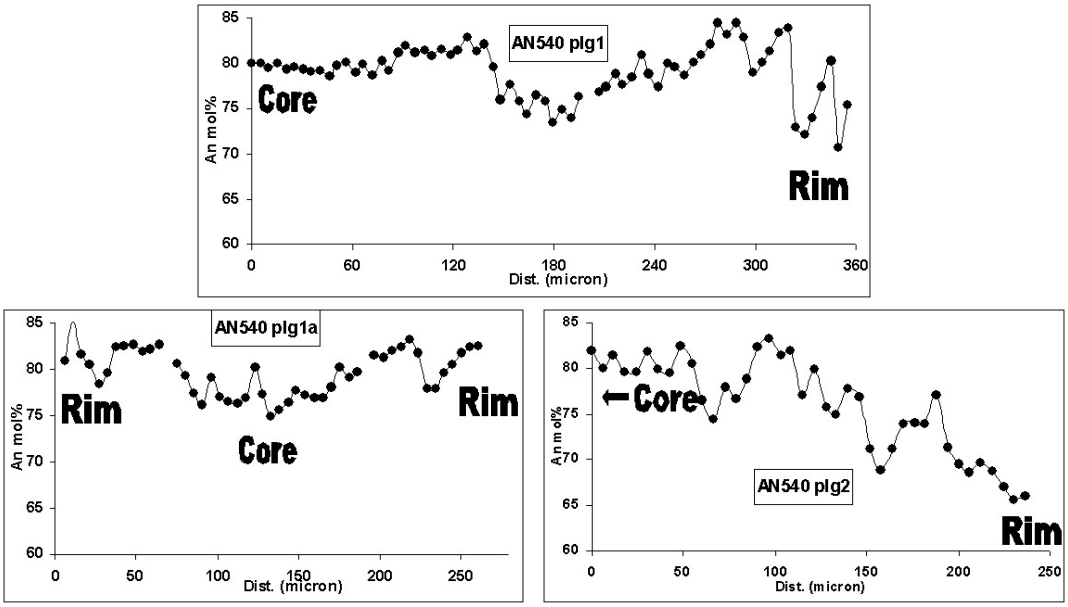

Figure 13.8: Variation of An (mol%), along transects (distance in microns) of plagioclases AN540 plg1, plg1a and plg2 (one transect only) from the Upper Unit at Oum R'Rbia (EMP analyses).

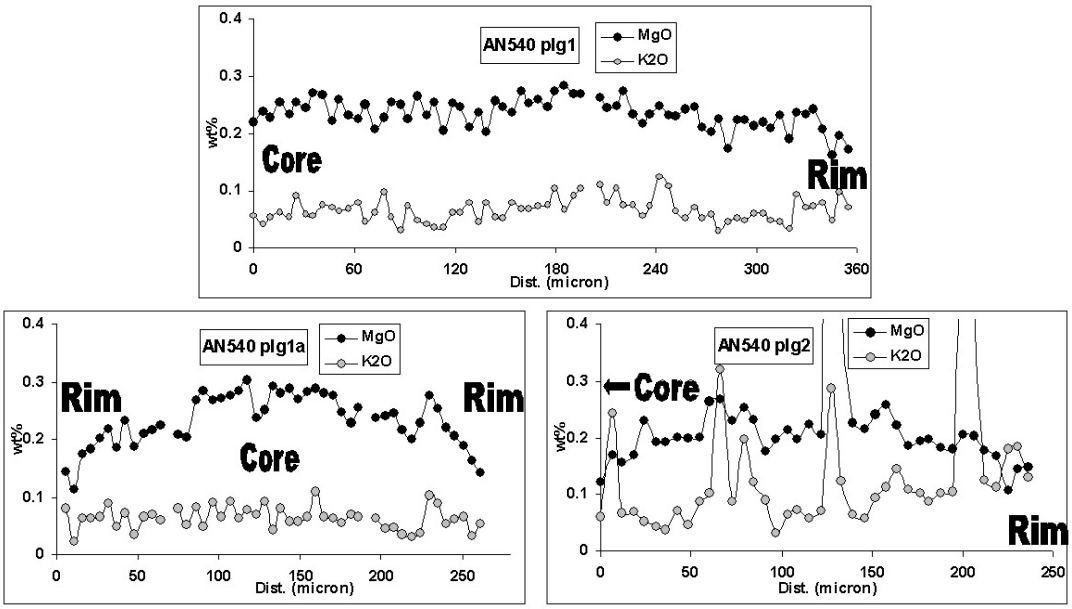

Figure 13.9: Variation of MgO and K_2O (wt%), along transects (distance in microns) of plagioclases AN540 plg1, plg1a and plg2 (one transect only) from the Upper Unit at Oum R'Rbia (EMP analyses).

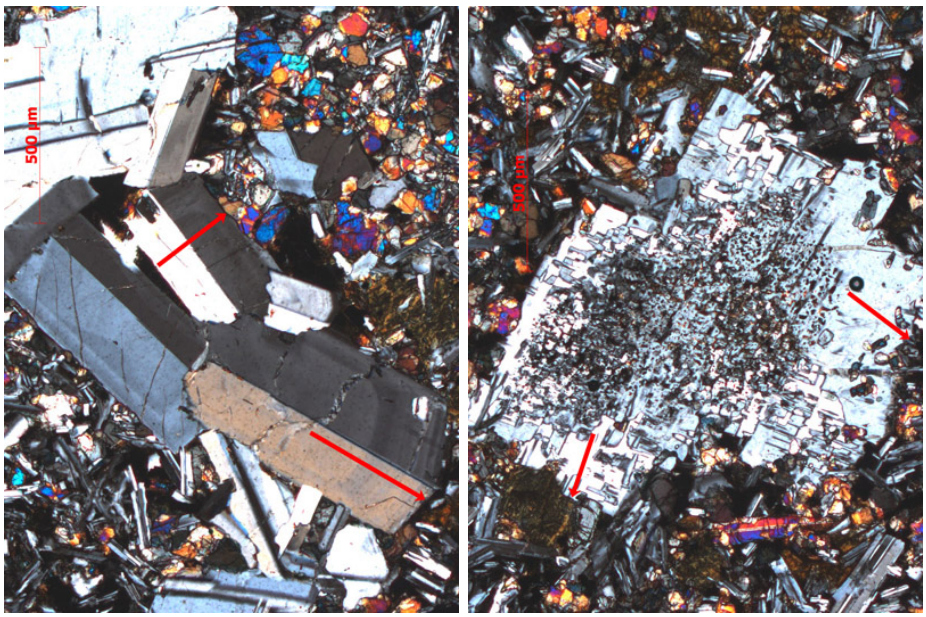

Figure 13.10: Microphotographs showing the augites AN540 plg1 and plg1a (on the left) and AN540 plg2 (on the right) from the Upper Unit at Oum R'Rbia. Red arrows represent EMP transects

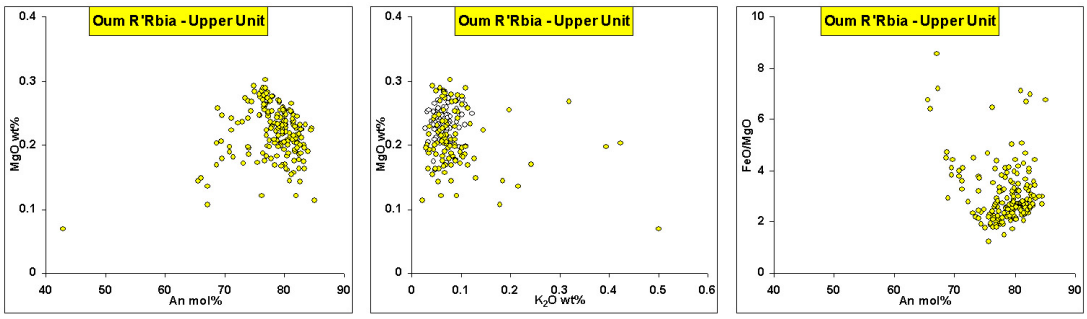

Figure 13.11: Anorthite mol% and K_2O wt% vs MgO wt% and FeO/MgO variations of all plagioclase analysed from the Upper Unit at Oum R'Rbia (EMP analyses).

the two compositional transects performed near the phenocryst rims show lower MgO and higher K_2O contents, probably due that the phenocryst crystallized from a more evolved magma (Fig. 13.9). Notably this mineral shows strong K_2O variation coupled with higher MgO content roughly coincident with anomalous extinction patches, resembling the "Tartan twinning" of potassic feldspars. This last feature, coupled with the huge presence over the almost entire phenocryst surface of little glassy brownish inclusion (which hinders any EMP analysis) and maybe resulting from a compositional ri-equilibration with the hosting magma, is unique among all plagioclases analysed, and at present it remains inexplicable. Plagioclase cores are nearly in equilibrium with the whole rock as visible in the $Ca\#_{whole-rock}$-$Ca\#_{plagio}$ diagram (Fig. 13.2). The disequilibrated high-An rim of some phenocrysts ($K_D = 1.5$) could be due decompression phenomema and/or increasing water content in the melt, as highlighted for CHA plagioclases.

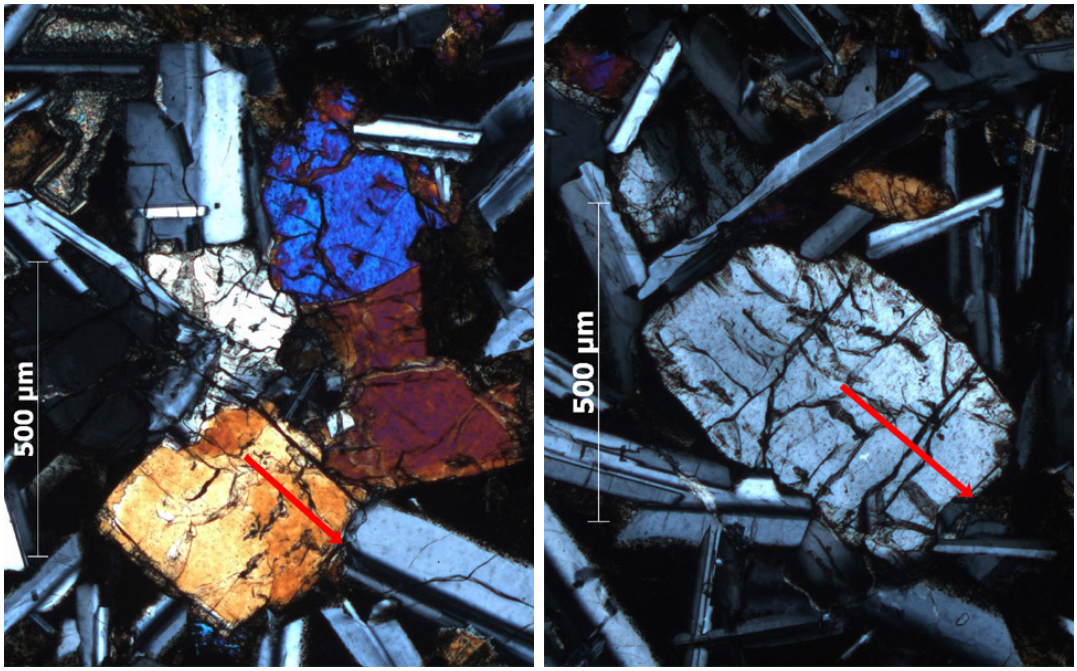

Figure 13.12: Microphotographs showing the augites AN534 cpx1 (on the left) and AN534 cpx2 (on the right) from the Lower Unit at Oum R'Rbia. ù Red arrows represent EMP transects

13.2.3 Augite (high-Ca pyroxene)

Both in the Agourai and Oum R'Rbia sections augitic clinopyroxenes have been observed, which together with plagioclase build up 90-95 vol% of the paragenesis. Like the lava piles of the CHA, but differently from those of the Maaziz

section (WM), augites are accompanied with pigeonites even if not in all units. In the Lower Unit (represented only at Oum R'Rbia with one lava flow) only augite is present, which is volumetrically subordinate to plagioclase. Only rarely phenocryst show an euhedral habitus, being more frequently poikilitic and enclosed in a plagioclase lath network. Two augites have been analysed, AN534 cpx1 and cpx2 (Fig. 13.12). Both minerals plot within the augite field in a ternary diagram Wo-En-Fs with a fairly wide compositional range (Fig. 13.13) similar to that of the augites of the Lower Unit in the CHA (see Chap. 9) and at Maaziz: $Wo_{31.9-40.0}En_{47.3-53.4}Fs_{10.5-15.4}$. Nevertheless they display a narrower Mg# range, 83.2-77.1, with normal zoning from the core to the rim (Fig. 13.14). Cr_2O_3 decreases with Mg# from 1.0-1.1 wt%, in the core, down to nearly zero at the rim. On the contrary, TiO_2 remains almost constant varying from 0.40 wt% in the core to 0.64 wt% at the rim. Only in the core of AN534 cpx1, TiO_2

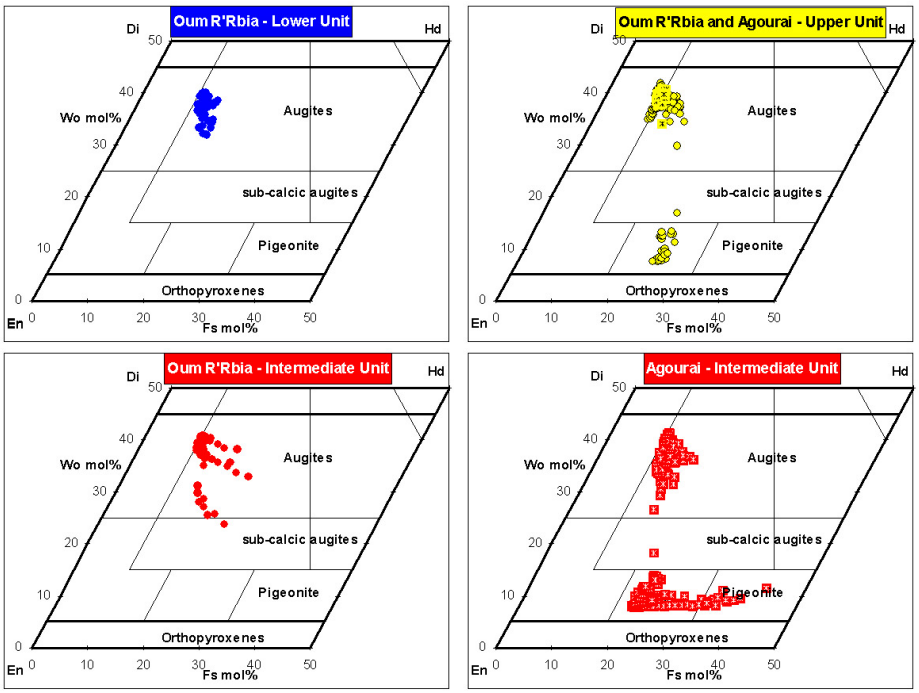

Figure 13.13: Compositions of all analysed augites and pigeonites plotted in a partial Wo-En-Fs ternary diagram for the Oum R'Rbia and Agourai sections for the Lower Unit (on the upper left side), the Intermediate Unit (on the bottom) and the Upper Unit (on the upper right side) (EMP analyses).

reaches 0.61 wt% which is correlated with high Cr_2O_3 (Fig. 13.14) and Al_2O_3 (not shown), thus probably due to the sector zoning of the crystal (Fig. 13.12). The $Mg\#_{whole-rock}$-$Mg\#_{augite}$ diagram gives a $K_{Fe-Mg}^{cpx-melt} = 0.33$ for the augite cores

(green line in Fig. 13.18), thus being in equilibrium with the parental magma and comparable both with the CHA augites and with Maaziz ones in the WM (Fig. 12.13) and confirming what found for plagioclases of the Lower Unit (Chap. 12).

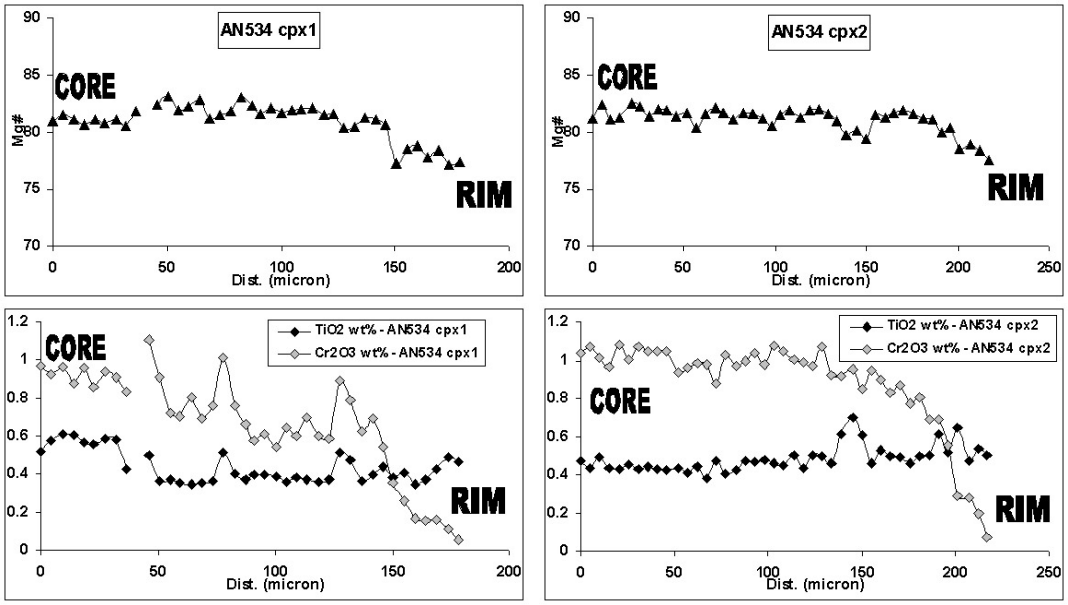

Figure 13.14: Core-rim compositional (Mg#, Cr_2O_3 and TiO_2 wt%)) traverses of augites from the Lower Unit at Oum R-Rbia (EMP analyses).

For the Intermediate Unit have 4 samples been analysed: 3 from Agourai (4 pigeonites in AN523, 2 pigeonites and 2 augites in AN525B, 1 augite in AN633, Fig. 13.17) and 1 from the Oum R'Rbia section (3 augites in AN539, Fig. 13.17). As visible from the Wo-En-Fs diagram, augites belonging the Intermediate Unit of MA span a wide compositional range similar to the homologous of the CHA, plotting in the augite field and entering in that of sub-calcic augite, this corresponding to a phenocryst augite rimmed by pigeonite, as seen for the sample AN49 pigeo2 (Chap 9 Fig. 9.33), which presents transitional composition (Fig. 13.13). The overall compositional variation is in the range $Wo_{18.3-41.0}En_{46.4-62.5}Fs_{8.9-19.1}$ with Mg# between 84.0 and 67.2 with a clear difference between the augite of sample AN525B and AN539 and the augite of sample AN633. While the first two samples show pyroxenes with Mg# values decreasing from nearly 84 in the core to 67.2 toward the rim, AN633 cpx2 show the highest En contents of the Intermediate Unit with the highest Mg# values up to 89.9 near the core decreasing to 81.1 at the rim with a saw-tooth pattern and Mg#-jump of up 4.5 units (Fig. 13.16). The difference among sample AN525B/AN539 and AN633 arise again if we compare

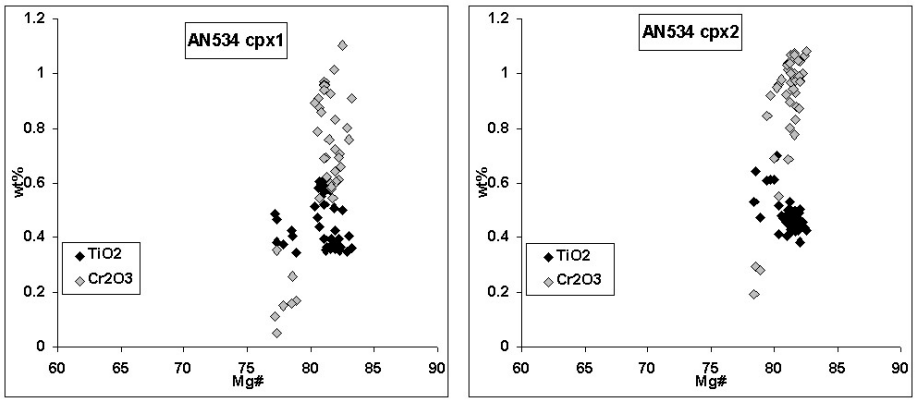

Figure 13.15: Cr_2O_3 and TiO_2 variations (EMP analyses) of augites from the Lower Unit at Oum R-Rbia showing the positive and negative correlation, respectively, with the Mg# even if values are quite scattered

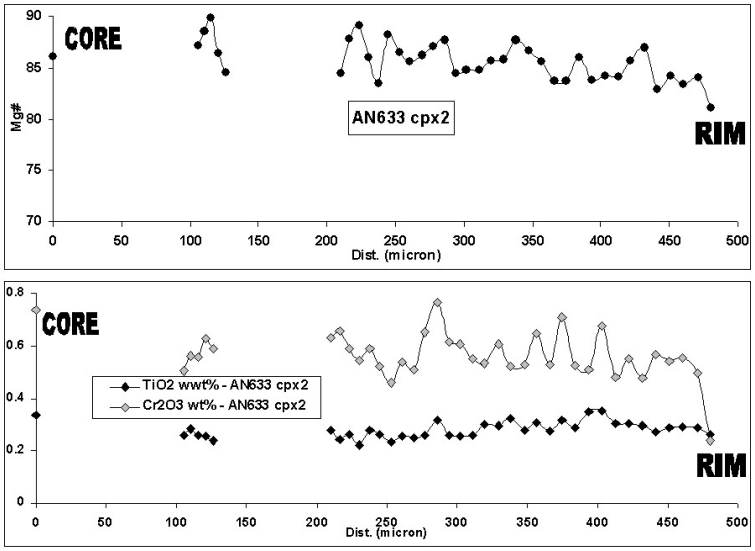

Figure 13.16: Core-rim compositional (Mg#, Cr_2O_3 and TiO_2 wt%) traverse of augite AN633 cpx2 from the Intermediate Unit (more probably with Upper Unit-like composition) at Agourai. Note the striking differences in Mg# composition between AN633 cpx2 and AN525B/AN539 augites.

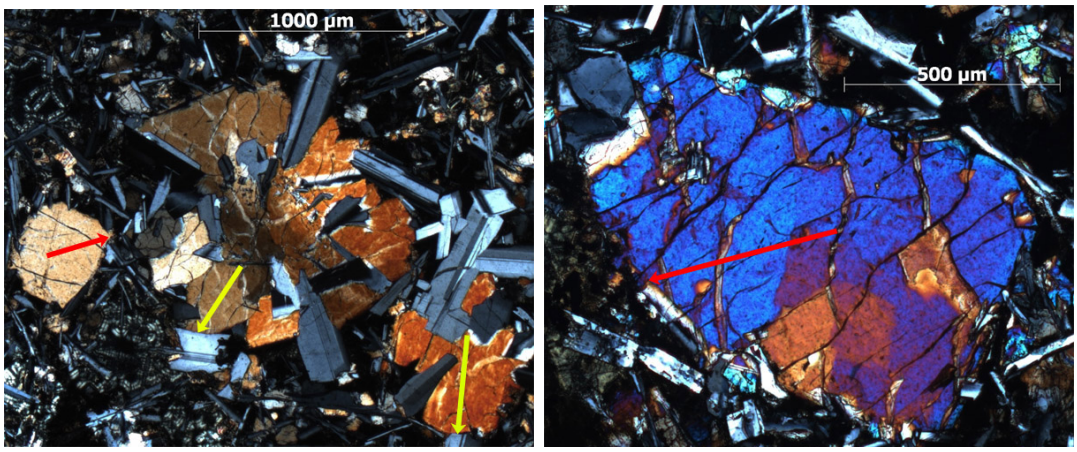

Figure 13.17: Microphotograph showing the augites AN539 cpx1,1a,1b (on the left) and AN633 cpx2 (on the right) from the Intermediate Unit at Agourai and Oum R'Rbia sections respectively. Red and yellow arrows represent EMP transect.

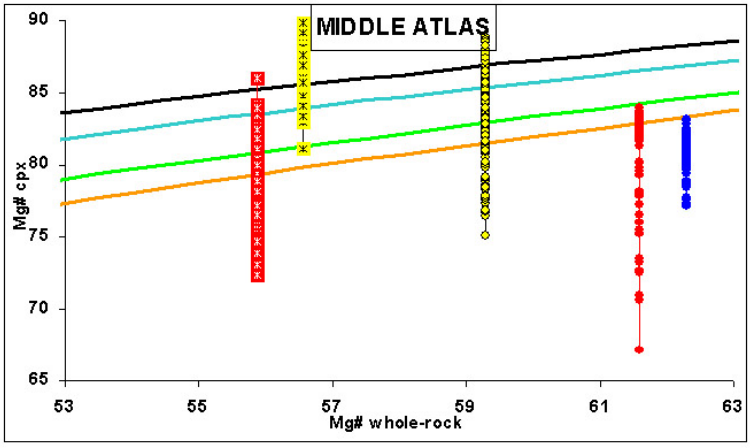

Figure 13.18: Mg# of whole-rock (XRF analyses) vs Mg# of all analysed augites (EMP analyses) in the Oum R'Rbia and Agourai section (Middle Atlas). Blue for the Lower Unit, red for the Intermediate Unit, yellow for the Upper Unit. Circles for Oum R'Rbia sequence and squares with stars for Agourai sequence. Curves represent augite compositions in equilibrium with melt for different $K_{Fe-Mg}^{cpx-melt}$: orange line $K_D = 0.33$, green line $K_D = 0.30$, blue line $K_D = 0.25$ and black line $K_D = 0.22$.

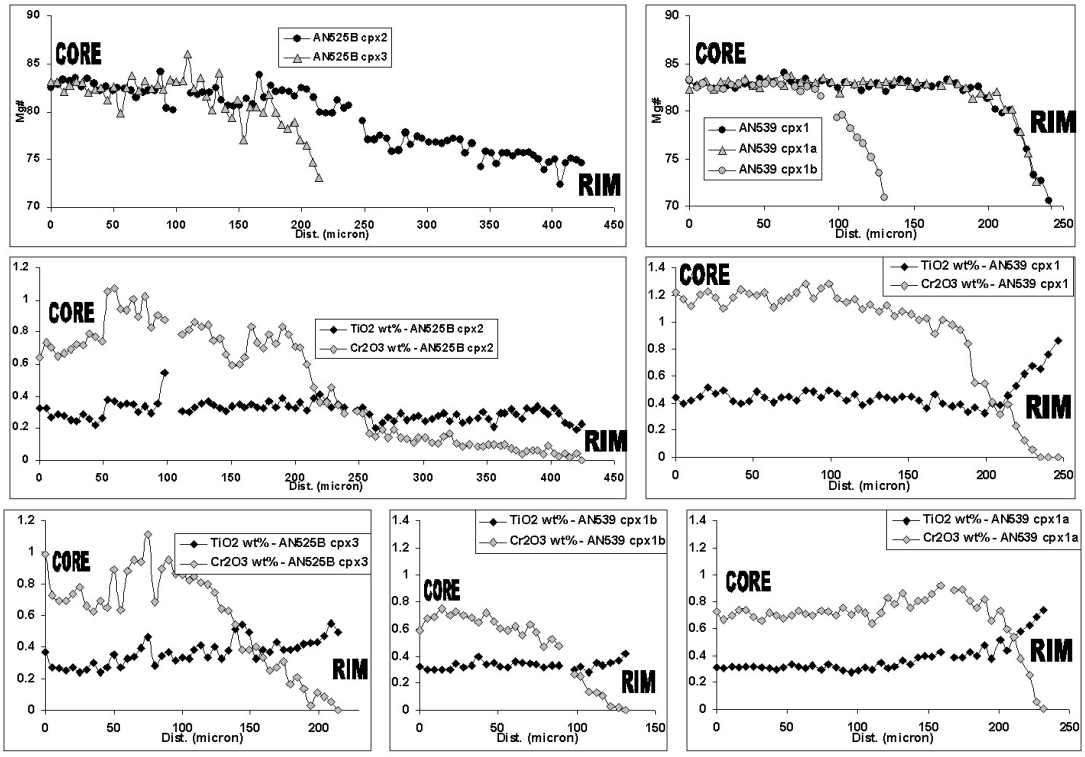

Figure 13.19: Core-rim compositional (Mg#, Cr_2O_3 and TiO_2 wt%) traverses of augite from AN525B and AN539 samples from the Intermediate Unit at Oum R-Rbia.

contents and variations of Cr_2O_3 and TiO_2: while Cr_2O_3 and TiO_2 of the former samples tend to vary positively and negatively respectively with Mg#, for the latter sample Cr_2O_3 and TiO_2 remain almost constant along the whole transect from the core to the rim (Fig. 13.19). Moreover, Cr_2O_3 and TiO_2 are somewhat comparable in AN525B/AN539 samples (0.60-0.80 wt% Cr_2O_3 in the core decreasing to zero at the rim, and TiO_2 0.30-0.40 wt% in the core increasing up to 0.60 wt% at the rim). Higher Cr_2O_3 and TiO_2 in some augites, again correlated with high Al_2O_3 contents (not shown), are probably due to sector zoning of the minerals (Fig. 13.10). On the contrary, the Cr_2O_3 and TiO_2 concentrations in AN633 cpx2 are slightly lower (0.45-076 wt% for Cr_2O_3 and 0.22-0.35 wt% for TiO_2) with a saw-tooth variation pattern along the transect which someway resembles that of Mg# one (Fig. 13.19). As a whole Mg#, Cr_2O_3 and TiO_2 of AN633 cpx2 are very similar to those displayed by augite AN540 cpx2 belonging the Upper Unit at the Oum R'Rbia section. Moreover whole-rock geochemical analyses of sample AN633 lead to think that this sample has actually an Upper Unit affinity, despite of its higher TiO_2 content with respect to Upper Unit whole-rock samples from the CHA, and despite its stratigraphic position. The $Mg\#_{whole-rock}$-$Mg\#_{augite}$ diagram gives for the Intermediate Unit augites $K_{Fe-Mg}^{cpx-melt}$ values very different for all samples. Augite cores from sample AN539 seem to be close to equilibrium with the parental magma for $K_{Fe-Mg}^{cpx-melt} = 0.30$, similar to those of the Lower Unit of the same section and again confirming what found for plagioclases of the same sample. Augite from the Agourai Intermediate Unit have much lower $K_{Fe-Mg}^{cpx-melt}$ (down to 0.22), for AN525B, or even lower for AN633, thus probably indicating high H_2O-fO_2 conditions which affected the Fe^{2+}/Mg ratio (and so Mg#) of the parental magma.

Finally, for sample AN540 from the Oum R'Rbia lava pile, the only one belonging to the Upper Unit in the MA, two augites have been analysed by EMP analyses: AN540 cpx2 and cpx3 (Fig. 13.20). The first phenocryst is a big euhedral augite with marked sector zoning (hour-glass zoning), both optical and chemical concentric zoning and tiny plagioclase micro-phenocryst enclosed even near the core (Fig. 13.20, 13.21 and **??**). AN540 cpx3 has big size and euhedral habitus, with no optical zoning but marked chemical zoning (Fig. 13.21) with enclosed plagioclase micro-phenocrysts. Two other important features of AN540 cpx3 are the presence of micrometric size phenocrysts (both plagioclase and pyroxenes) near the augite edge, which mimic a possibly previous rounded rim and the presence of pigeonite which rims the augite (Fig. 13.20). Like other augites analysed in the CHA, augites from AN540 sample plot from the Di-En enriched

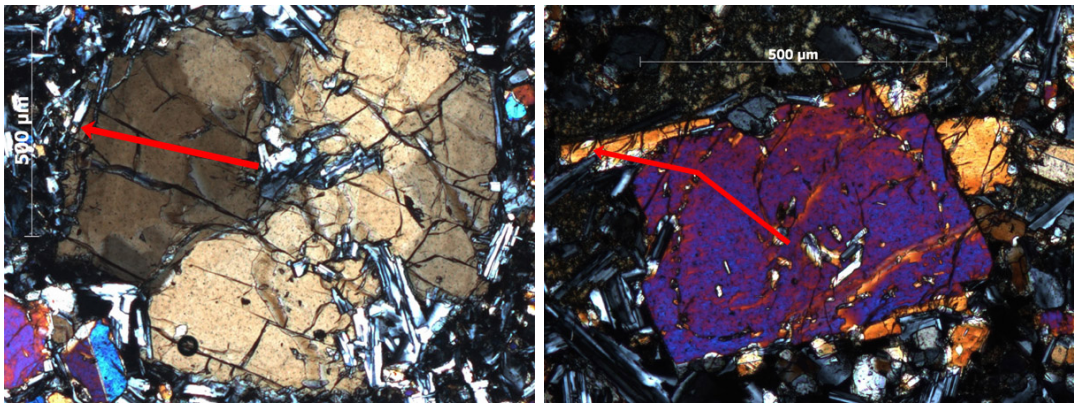

Figure 13.20: Microphotograph showing the augites AN540 cpx2 (on the left) and cpx3 (on the right) from the Upper Unit at Oum R'Rbia section. Augite AN540 cpx3 (blue-purple) is rimmed by pigeonite (orange). Red arrows represent EMP transect

side of the augite field to the sub-calcic augite field in the Wo-En-Fs diagram (Fig. 13.13) with compositions in the range $Wo_{16.9-41.8}En_{47.8-59.0}Fs_{8.6-24.0}$. The Mg# are very high for AN540 cpx2 (Fig. 13.20) varying from 88.9 and 80.9 with a saw-tooth pattern from the core toward the rim with jumps in Mg# up to 4 points (Fig. 13.21). Mg# of AN540 cpx3 varies from 76.7 to 83.3 in the core up to 85.6 in the middle of the crystal and decrease then more or less monotonously to 76.8 towards the rim down and increases again up to 81.6 before dropping down to 71.3 at the augite-pigeonite transition (Fig. 13.21). Cr_2O_3 and TiO_2 are similar to those found in the other Upper Unit augites. Cr_2O_3 in the AN540 cpx2 decreases from 0.50-0.68 wt% in the core to 0.24 wt% towards the rim with quite complex pattern which partially resembles the Mg# one except for an inverse zoning near the rim. The Cr_2O_3 concentration of AN540 cpx3 are lower than those of cpx2 and it varies with a more complex pattern (0.44-0.63 wt% in the core to 0.07 wt% before the augite-pigeonite transition, then dropping to zero). TiO_2 for AN540 cpx2 varies in the range 0.20-0.32 wt% from the core toward the rim, while AN540 cpx3 have a little higher TiO_2 content with respect to cpx2 (0.28-0.56 from the core toward the rim, decreasing again at the augite-pigeonite) and reflecting more closely the Mg# variation. Like for some augites of the Intermediate Unit, $K_{Fe-Mg}^{cpx-melt}$ of AN540 cpx2 and cpx3 are very low (less than 0.22-0.23, Fig. 13.18), similar to that found for AN633 cpx2 and for Tiourjdal and Telouet Upper unit augites (southern flank of CHA) and confirming the high $K_{Ca-Na}^{plagio-melt}$ (1.5-2) found for plagioclases of the same samples, index of high H_2O-fO_2 conditions of the parental magma from which the minerals were

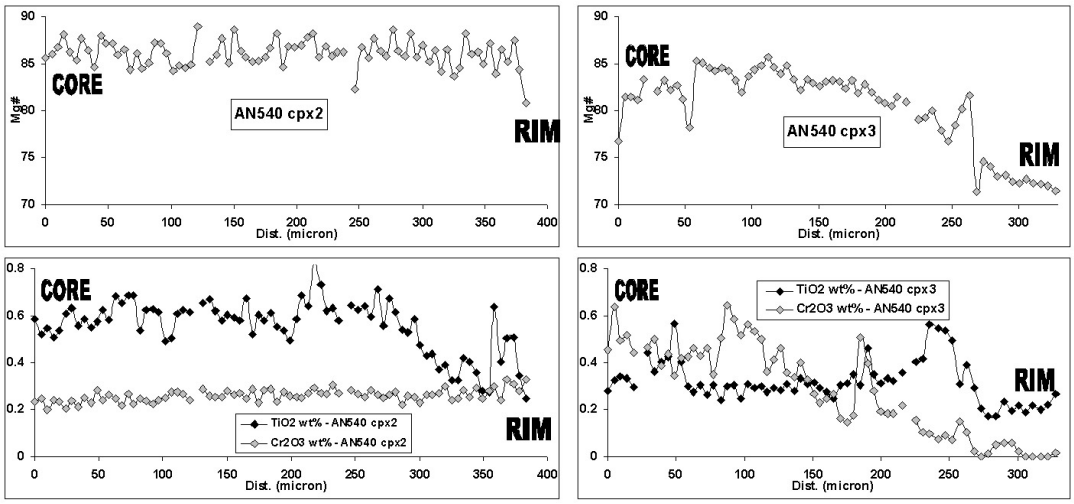

Figure 13.21: Core-rim compositional (Mg#, Cr_2O_3 and TiO_2 wt%) traverses of augites AN540 cpx2 (on the left) and AN540 cpx3 (on the right) from the Upper Unit at Oum R'Rbia (EMP analyses).

crystallizing.

13.2.4 Pigeonite (low-Ca pyroxene)

As said briefly before, pigeonites are well represented in the Agourai lava pile, where in some flows (AN523 and AN524), together with subordinate augites build up to 55-60 vol% of the paragenesis. In these samples pigeonites have large size (up to more than 1.2 mm) with euhedral habitus. In fact in the sample AN523 EMP analyses are available for pigeonites only. In other samples, like AN525B, even if pigeonite is very common it has smaller size and is present both as isolated phenocryst and as rims of augite (Fig. 13.20 and 13.22). In the Lower Unit at Oum R'Rbia pigeonite has not been detected, like in the Intermediate Unit. But in the Upper Unit it does as in the Upper Unit basalts of Oued Lahr (CHA, not analysed), both as tiny phenocryst in the microlithic ground-mass and as rims of big augite phenocryst (Fig. 13.23 on the right and Fig. 13.20 on the right). In the Intermediate Unit of the Agourai section 4 pigeonites have been analysed in the samples AN523 (cpx1, cpx2, cpx3, cpx3a) and 2 pigeonites in sample AN525B (cpx1 and cpx2). No pigeonites have been detected in the Intermediate Unit at Oum R'Rbia. Pigeonites belonging the Intermediate Unit have the widest compositional range: $Wo_{7.8-14.0}En_{45.7-71.6}Fs_{19.9-42.8}$ and most of them display a strong rimward enrichment of the Fs component (Fig. 13.13). Mg# is higher with respect to pigeonites of the CHA: from 79.0 to 72.3 in the pigeonite rimming the

Figure 13.22: Microphotograph showing the pigeonite AN523 cpx5 (on the left, not analysed) and augite rimmed by pigeonite AN525B cpx2 (on the right) from the Intermediate Unit at Agourai (Middle Atlas). AN523 cpx5 has not been analysed. Red broken arrow represents EMP transect

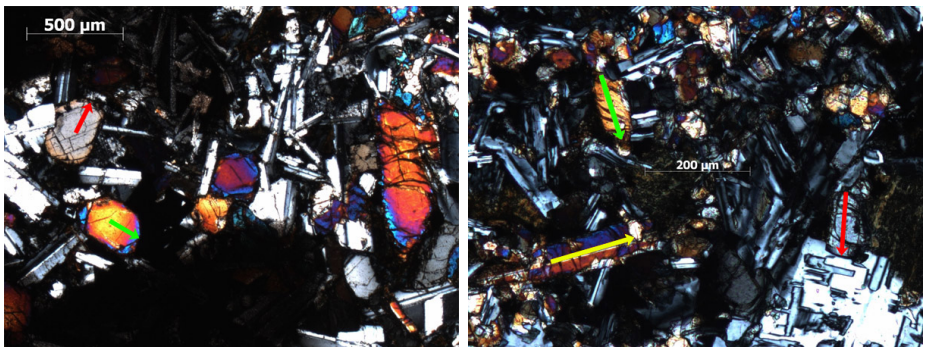

Figure 13.23: Microphotograph showing pigeonites of the sample AN523 (cpx3 and cpx3a, on the left) from the Intermediate Unit at Agourai and little pigeonite phenocrystals in the microlithic ground-mass of sample AN540 (on the right) from the Upper Unit at Oum R'Rbia. Coloured arrows represent EMP transects

augite AN525B cpx2 and from 78.3 to 52.1 for the isolated AN523 cpx2, with Mg# of the other pigeonites comprised in the latter range (Fig. 13.24). Cr_2O_3 and TiO_2

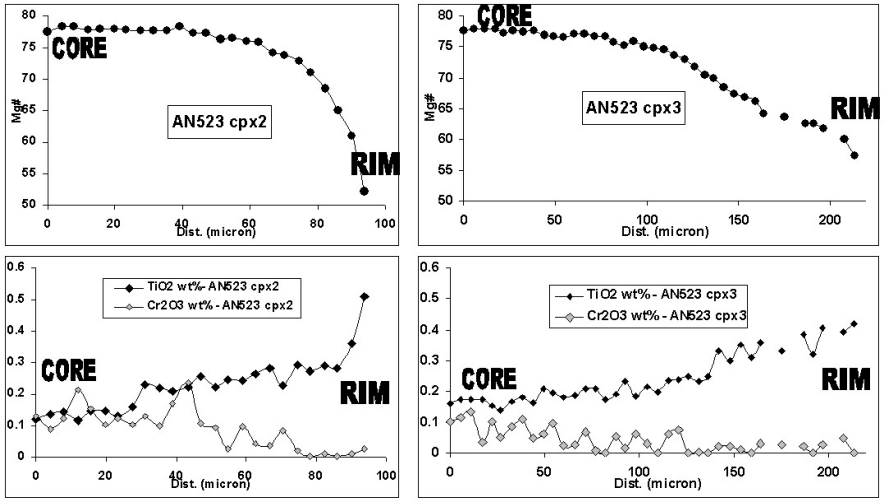

Figure 13.24: Core-rim compositional (Mg#, Cr_2O_3 and TiO_2 wt%) traverses of pigeonites AN523 cpx2 (on the left) and AN230 cpx3 (on the right) from the Intermediate Unit at Agourai (EMP analyses).

span a slightly wider rang with respect to that found in the pigeonites of the CHA Intermediate Unit. Both vary positively and negatively with Mg# respectively from the core to the rim: 0.21 to 0 wt% for Cr_2O_3 and 0.11 to 0.51 wt% for TiO_2. The other pigeonites analysed have slightly lower and higher Cr_2O_3 and TiO_2 concentrations respectively (Fig. 13.24). Nevertheless, pigeonite AN525B cpx2 gives us an other information: in the CaO core-rim compositional traverse it is possible to see a clear decrease in CaO content related to the transition from the augite core to the pigeonite rim. Within this pigeonite rim CaO (and Wo) clearly increase rimward (from near 260 to 400 μm; Fig. 13.25). Since, as pigeonites evolve their CaO content increases (**Lindsley, 1983**), the CaO drop occurring at about 50 microns from the rim could be due to the beginning of plagioclase crystallization. In the sample AN540 belonging the Upper Unit at Oum R'Rbia 4 pigeonites have been analysed including 3 micro-phenocrysts from the groundmass (Fig. 13.23) and one which rims an augite (Fig. 13.20, 13.21 and **??**). As a whole pigeonites of the Upper Unit span a more restricted compositional range with respect to those of the Intermediate Unit: $Wo_{7.5-13.4}En_{61.7-68.0}Fs_{23.2-26.5}$ (Fig. 13.13). At the same time Mg# has a more restricted range (79.8-70.6; Fig. 13.26). Cr_2O_3 and TiO_2 are very low and not correlated each other and neither with Mg#. Cr_2O_3 does not exceed 0.24 wt% and for the analysis points it is less

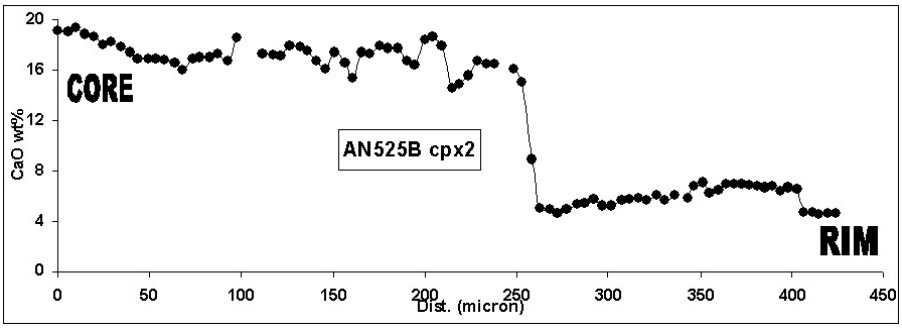

Figure 13.25: Core-rim compositional (CaO wt%) traverses of augite-pigeonite AN525B cpx2 from the Intermediate Unit at Agourai (EMP analyses). Note the little jump in CaO content at the end of the transect: probably the sigh of plagioclase crystallization

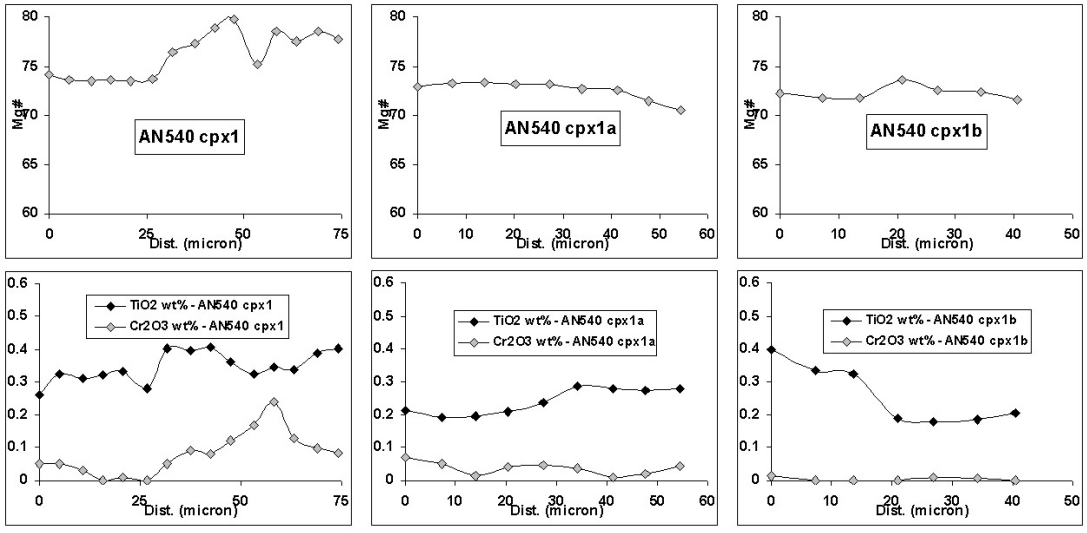

Figure 13.26: Rim-rim compositional (Mg#, Cr_2O_3 and TiO_2 wt%) traverses of pigeonites of the sample AN540 from the Upper Unit at Oum R'Rbia (EMP analyses).

than 0.10 wt%. TiO_2 varies from 0.17 to 0.40 wt% (Fig. 13.26).

14 WHOLE-ROCK GEOCHEMISTRY OF MA-WM PILES

In total 16 samples from Maaziz (WM), 13 samples from Oum R'Rbia (MA) and 16 samples from Agourai section (MA) have been analysed for major and minor elements by XRF, while 8 samples from Maaziz, 6 samples from Barrage and 8 from Agourai have been analysed for trace elements by ICP-MS. Also in the WM and in the MA, XRF and ICP-MS analyses allow to group the basaltic flows into units, as for CHA, with the notable difference that in the WM and MA the uppermost Recurrent Unit does not outcrop. Moreover, as described in the previous chapters, the Lower Unit is present with only three lava flows at Maaziz, with no more than 2 or 3 lava flows at Oum R'Rbia, while it does not outcrop at Agourai. The Intermediate Unit is the best represented in all three sections with numerous lava flows. Finally the Upper Unit is not represented at Maaziz, it is present with only one thick lava flow at Oum R'Rbia, while at Agourai it is probably represented by (at least) one lava flow interbedded with the uppermost Intermediate lava flows. In a TAS diagram (Total Alkali Silica, SiO_2 wt% vs Na_2O + K_2O wt%) samples from WM and MA plot mainly in the basaltic andesite field (Fig. 14.1, triangles for Maaziz section, circles for Barrage section and squares with star for Agourai section. Blue for the Lower Unit, red for the Intermediate Unit, yellow for the Upper Unit) with SiO_2 between 52 and 54 wt% and only 2 samples are more acid (SiO_2 ca. 56 wt%). In an AFM diagram (A = Alkali, Na_2O + K_2O wt%, F = FeO_{tot} wt% and M = MgO wt% all recalculated to 100, Fig. 14.1, curved line separating tholeiitic and calc-alkaline rocks after **Irvine & Baragar, 1971**) Ma and WM basalts define a tholeiitic evolution trend, as for CHA basalts with the increase in the Fe content and an alkali enrichment fairly visible in the 2 most evolved samples. In general, L.O.I. of the MA and WM basalts are lower than those of the CHA samples, with major elements remaining nearly constant and increasing their scattering only for very high L.O.I. (Fig. 14.2). However CaO and FeO_{tot} seem to show a negative correlation with L.O.I.$_{tot}$, while MgO is positively correlated. As for CHA basalts, TiO_2 and P_2O_5 are unaffected from secondary alteration, thus being constant and moreover allowing

to recognize the three units preserved in MA and WA (Fig. 14.2 and 14.3). MA and WM basalts are slightly to moderately evolved. All the samples have Mg# varying from 54.6 and 68.0, except one sample (AN525[AN630]) belonging to the Intermediate Unit at Agourai which has a quite evolved composition with Mg# = 43.7 and high TiO_2 (up to 2.1 wt%). In general SiO_2, TiO_2, FeO_{tot}, Na_2O, K_2O and CaO tend to increase at decreasing Mg#, while MgO, Al_2O_3 decrease with Mg#. P_2O_5 tend to remain constant. The decrease of MgO and Al_2O_3 could be driven by olivine and plagioclase fractionation, even if this should be seen also in the CaO variation. However the low CaO content at high L.O.I. could explain the lack of correlation among CaO and MgO-Al_2O_3 pair. The possible sign of olivine and plagioclase fractionation is visible in the Mg# vs CaO/MgO and CaO/Al_2O_3 diagrams, where compositions suggest a liquid line of descent controlled by olivine and clinopyroxene with only minor plagioclase fractionation (Fig. 14.4), as highlighted by the slight Sr increasing for CaO decreasing.. Cr and Ni have higher concentrations with respect to the CHA basalts. In general there is a good correlation with Mg# and between Cr and Ni (Fig. 14.5). Differently from the CHA, the Intermediate Unit is the richest in Cr and Ni, both at Maaziz, Oum R'Rbia and Agourai with Cr up to 500 ppm. The Lower Unit has a more restricted Cr range (330-360 ppm), while the Upper Unit has lower Cr (270 ppm), as described for the CHA basalts. Ni, like for Cr, reaches the highest content in the Intermediate Unit (ca. 140 ppm at Agourai), while in the Lower and Upper Unit has slightly lower contents (93-115 ppm) with one sample (AN633), with an Upper-like composition on the base of trace element contents, has only 63 ppm Ni. As said before, Cr and Ni are quite well correlated, thus again indicating olivine and minor amount of clinopyroxene fractionation. V and Sc, like in the CHA basalts, span a restricted range. In general both of them are nearly constant or slightly increasing for decreasing Mg#. Only at Agourai, V shows a steep slope (266-363 ppm) maybe due to oxide fractionation in the less evolved samples. In the other units V varies in the range 281-318 ppm. The same happens for Sc, which shows an increase at lower Mg#, with variation in the 32-39 ppm range indicating very little amount of clinopyroxene fractionation. LILE, except for Sr, are not obviously correlated with Mg#. Ba, Rb and Cs show a wide scattering if plotted with L.O.I.$_{tot}$ (Fig. 14.8, Rb and Cs not shown), even if a broad negative correlation with Mg# is visible (Mg# vs Cs not shown), as expected for a Rb and Ba enrichment towards more evolved rocks. Sr is more difficult to evaluate. The Lower and Intermediate together with the Upper Unit are well distinct but, while the Intermediate and the Upper Unit seem to have an almost constant Sr content,

the Lower Unit seems to have decreasing Sr at decreasing Mg#. However, the highest Sr contents could be due to the remobilization by aqueous fluids, since the samples which show the highest Sr have the highest L.O.I.$_{tot}$. HFSE show a good correlation with Mg#, increasing towards more evolved samples (Fig. 14.9). The three units are well distinct with decreasing concentration from the Lower to the Upper Unit, like for CHA basalts. Also in the Zr vs Zr/Nb and Th vs Th/Nb diagrams the three units are distinct. In the first, the compositional fields of the three units are similar to those of the CHA basalts (Fig. 10.11), while in Th vs Th/Nb the Lower and Intermediate Unit display slightly different compositions. In fact the Lower Unit in the MA and WM has the same Th/Nb but slightly higher Th. The Intermediate Unit displays for the same Th content much higher Th/Nb. Like for CHA, the MA and WM basalts have REE well correlated with Mg#, with the three units well differentiated on the base of the LREE concentrations. From the Lower to the Upper Unit, LREEs decrease their contents, with a progressive overlapping of the compositional fields towards the HREEs (Fig. 14.10). While the Lower and Intermediate Unit have similar REE composition to those of the CHA (i.e., 33-36 ppm Ce for the Lower Unit and 22-27 ppm for the Intermediate Unit), the Upper Unit has slight higher REE, and for MREE and HREE the Upper Unit composition overlaps completely with that of the Intermediate Unit. Also La vs La/Yb, Sm vs Sm/Nd and Lu vs Lu/Hf diagrams are very similar to those of the CHA basalts (Fig. 14.11), displaying the same trends from the Lower to the Upper Unit, but with Sm/Nd and Lu/Hf quite higher compared to the same ratios of the CHA basalts. In the next chapter we will talk about this difference. In chondrite normalized diagrams (**Andres & Grevesse, 1989**), the MA and WM basalts analysed display sub-parallel REE patterns similar to those of the CHA, with monotonous decrease from La to Lu (Fig. 14.12). It is always present the LREE enrichment compared to HREE (La/Yb_{Ch} = 4.85-5.5) to Upper Unit (La/Yb_{Ch} = 2.7-2.9) comparable with that of the CHA, but the absolute concentration are lower for the Lower Unit and higher for the Upper Unit, making more tight the three REE patterns. Another important feature is the almost absent Eu_{Ch} negative anomaly, fairly visible only in the Intermediate Unit at Agourai. Finally, in a Primitive Mantle (PM) normalized multi-element diagram (**McDonough & s. Sun, 1995**), most of the features seen in the CHA basalts, occur also in the MA and WM samples (Fig. 14.13). There is scattering in the Rb and Cs data, even if in lesser amount. HFSE concentrations well distinguish the three units, with the typical negative Nb_{PM} and Ta_{PM} anomaly and progressively decreasing HFSE contents from the Lower to the Upper Unit.

All samples of the Lower and Intermediate units display strong positive Pb_{PM} and negative Sr_{PM} anomaly except for two sample of the Lower Unit (AN534 at Oum R'Rbia and AN503 at Maaziz) and two sample of the Intermediate Unit at Oum R'Rbia (AN611 and AN539[613]). These samples show any positive Pb_{PM} and vary fair negative Sr_{PM} anomaly, this probably related to their remobilization by aqueous fluids as previously highlighted for Sr and Ba and as visible in the Ce vs Ce/Pb diagram (Fig. 14.11).

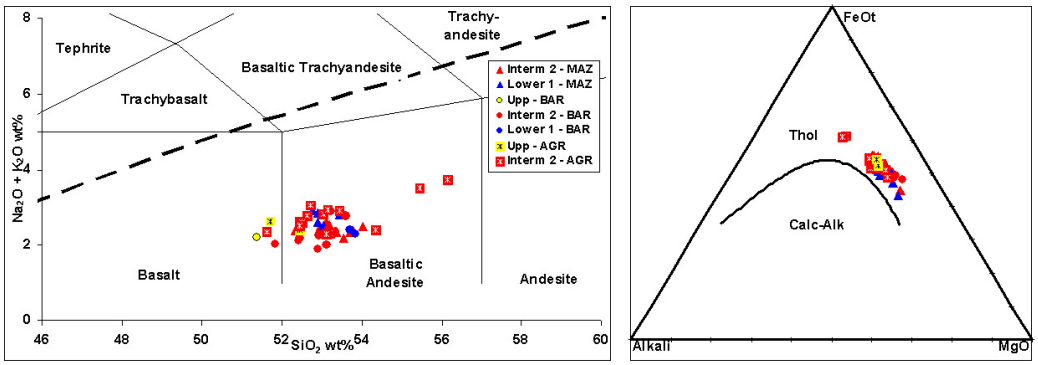

Figure 14.1: TAS and AFM classification diagram of MA and WM samples analysed by XRF.

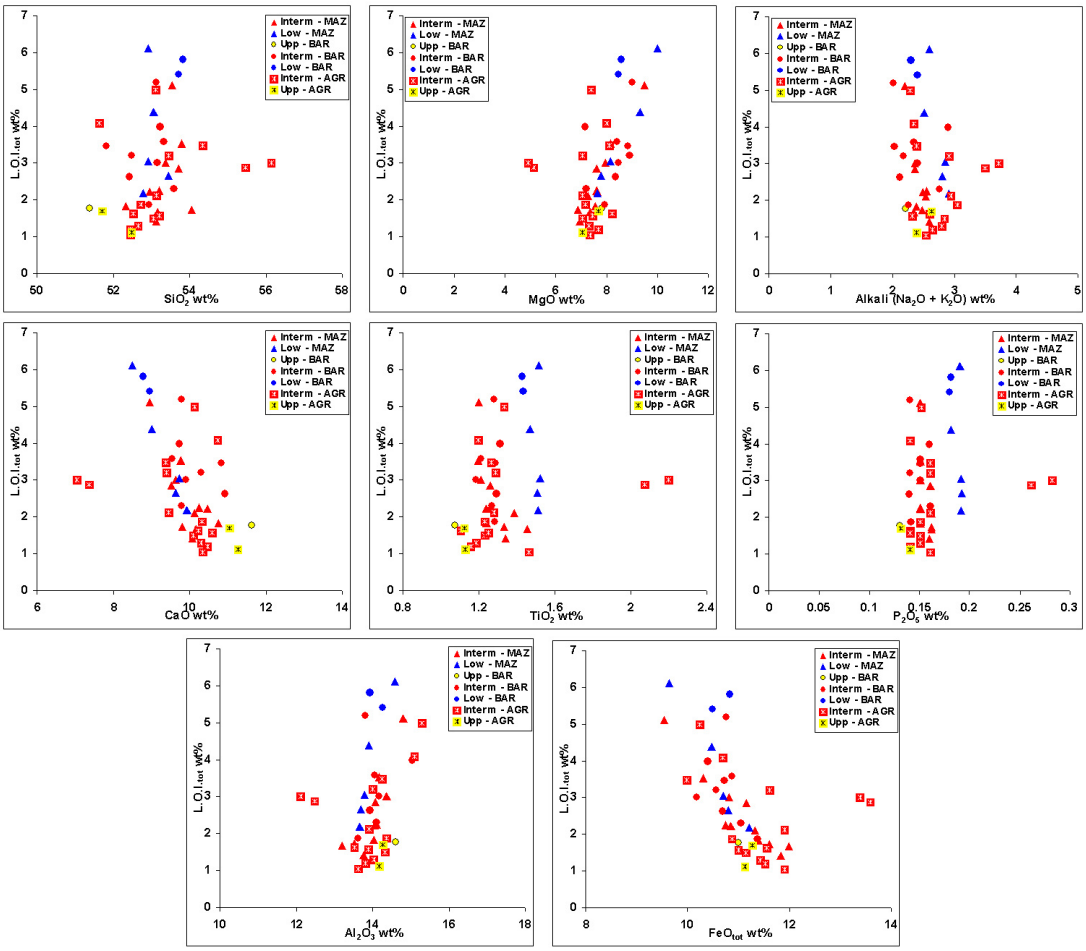

Figure 14.2: Major elements vs L.O.I.$_{tot}$ diagrams of all basalts from MA and WM analysed by XRF.

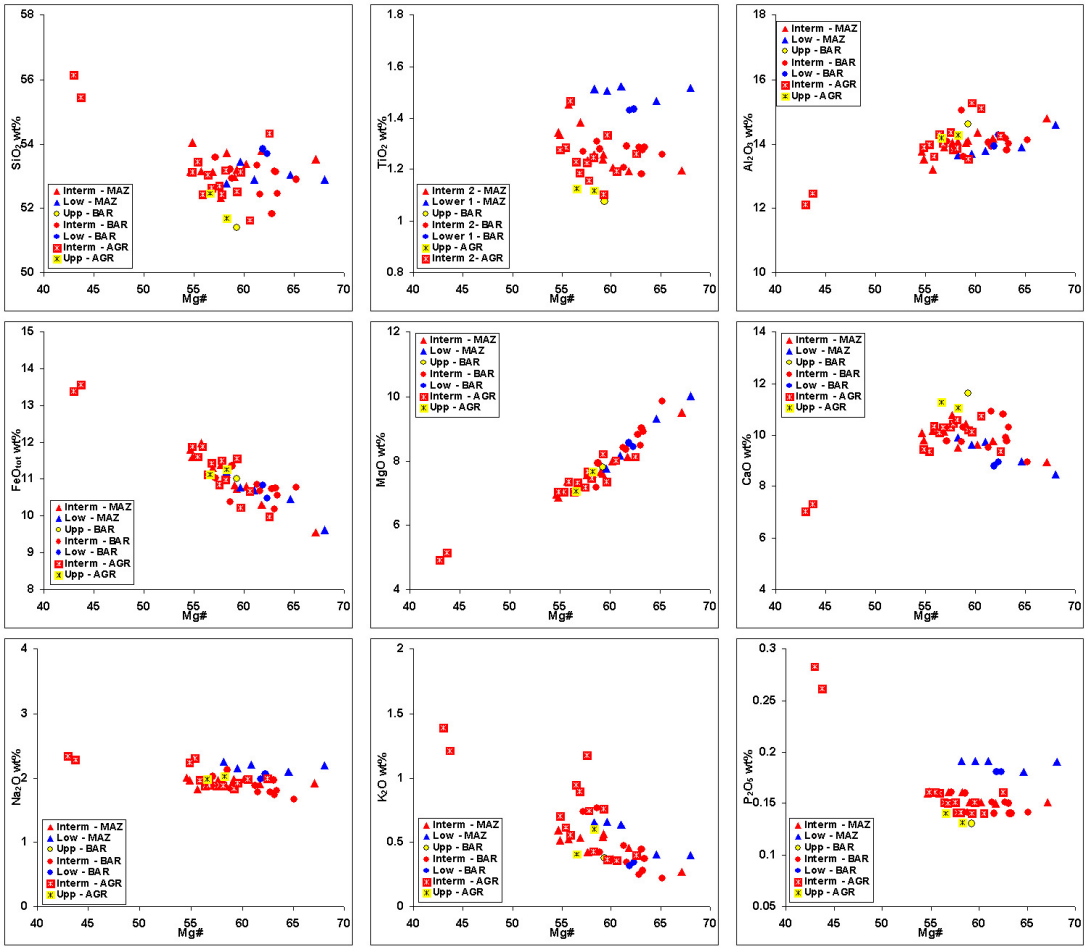

Figure 14.3: Mg# vs major elements diagrams for all MA and WM basalts analysed by XRF.

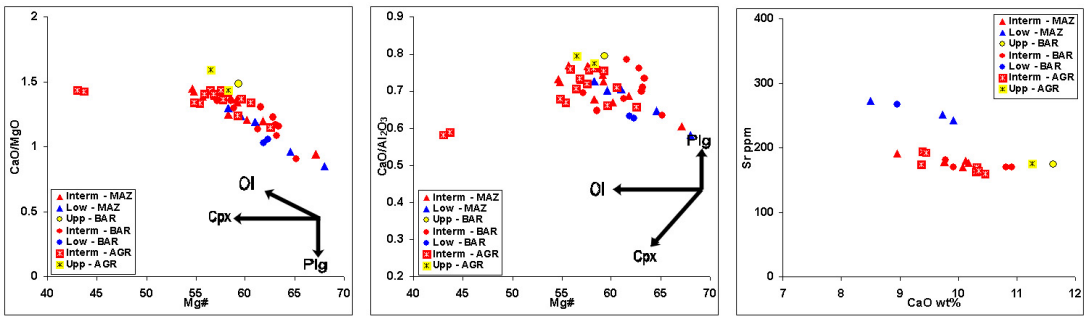

Figure 14.4: Mg# vs CaO/MgO and CaO/Al_2O_3 and CaO vs Sr diagrams for all MA and WM basalts analysed by XRF.

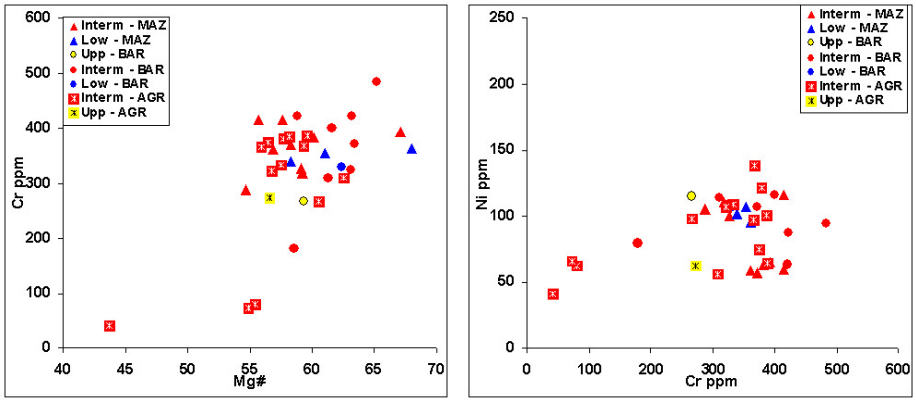

Figure 14.5: Mg# vs Cr and Cr vs Ni diagrams for all MA and WM basalts analysed by XRF.

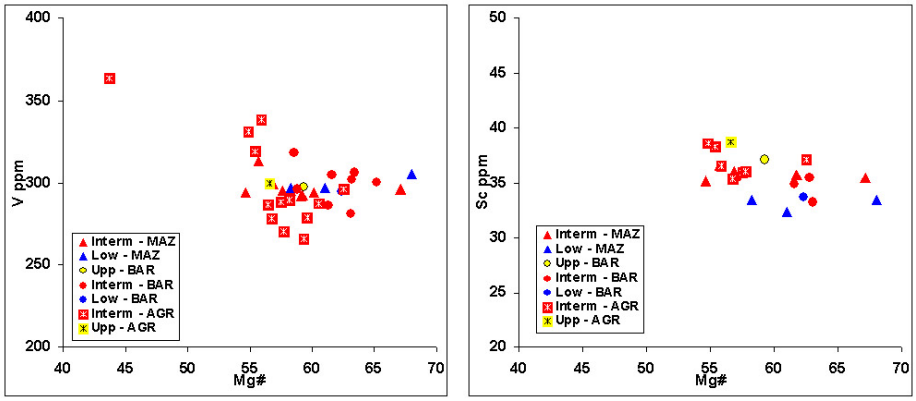

Figure 14.6: Mg# vs V and Sc diagrams for all MA and WM basalts analysed by XRF.

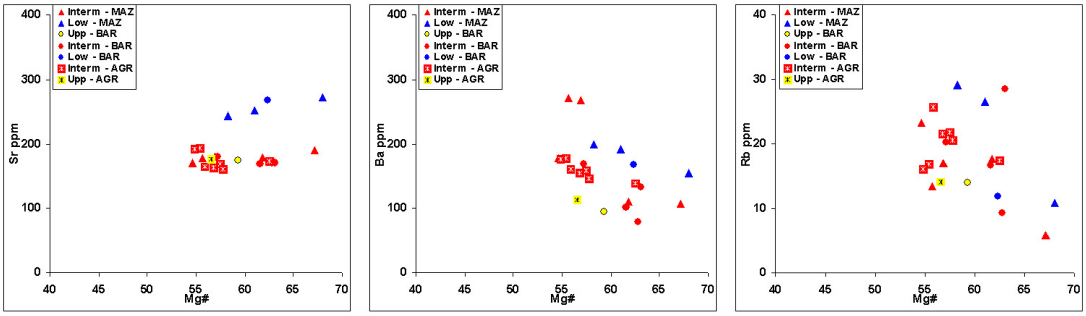

Figure 14.7: Mg# vs LILE diagrams for all MA and WM basalts analysed by ICP-MS.

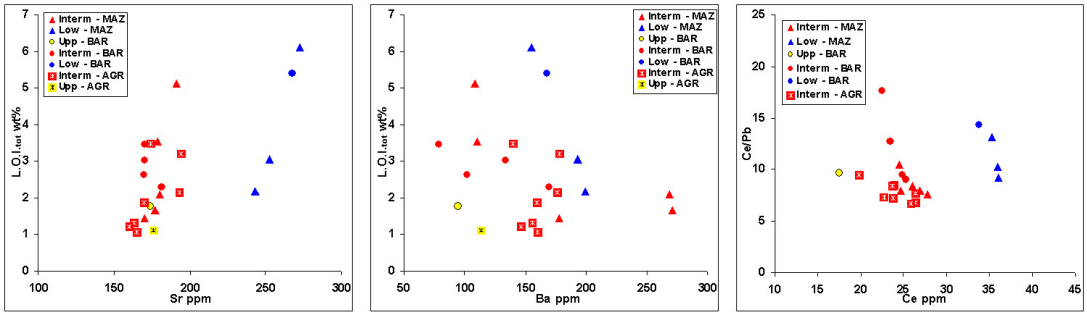

Figure 14.8: Sr and Ba vs L.O.I.$_{tot}$ and Ce vs Ce/Pb diagrams for all MA and WM basalts analysed.

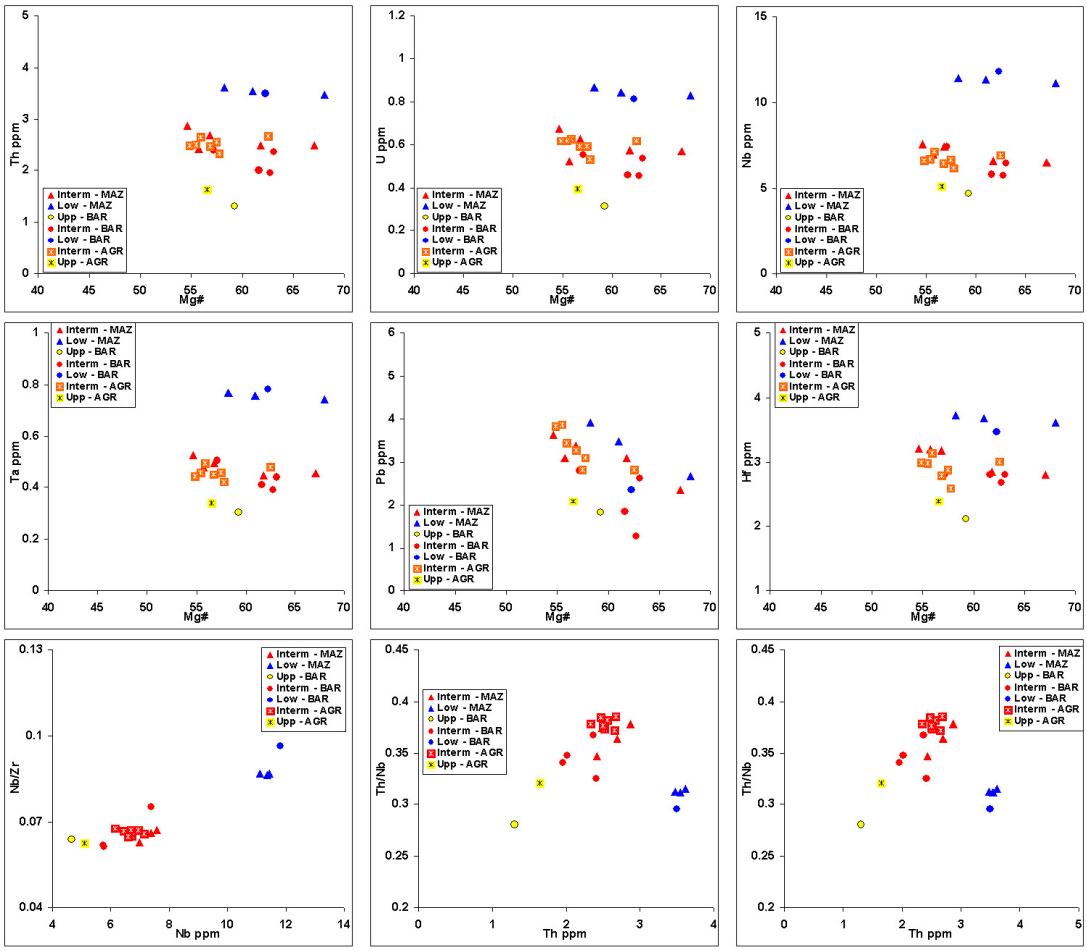

Figure 14.9: Mg# vs HFSE, Nb vs Nb/Zr and Th vs Th/Nb diagrams for all MA and WM basalts analysed by ICP-MS.

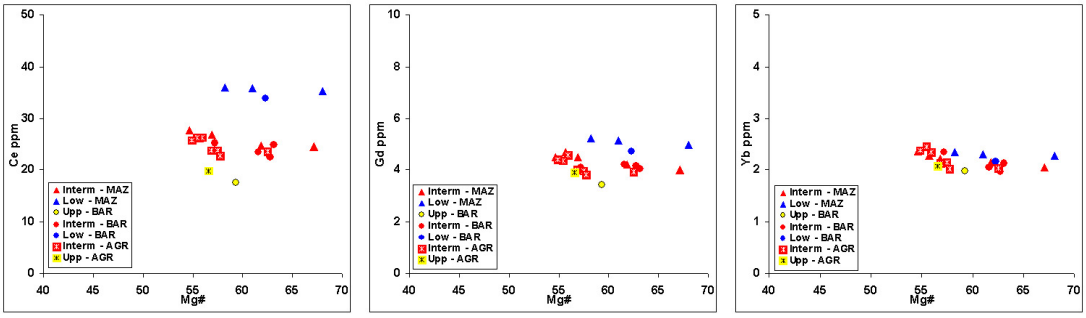

Figure 14.10: Mg# vs Ce (LREE), Gd (MREE) and Yb (HREE) diagrams for all MA and WM basalts analysed by ICP-MS.

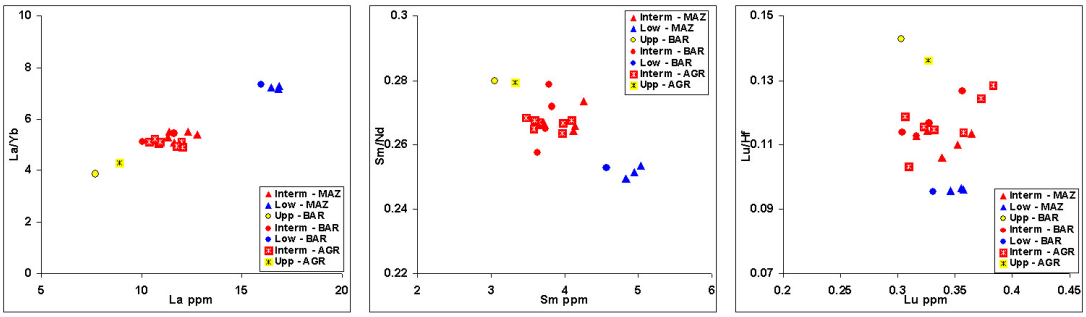

Figure 14.11: La vs La/Yb, Sm vs Sm/Nd and Lu vs Lu/Hf diagrams for all MA and WM basalts analysed by ICP-MS.

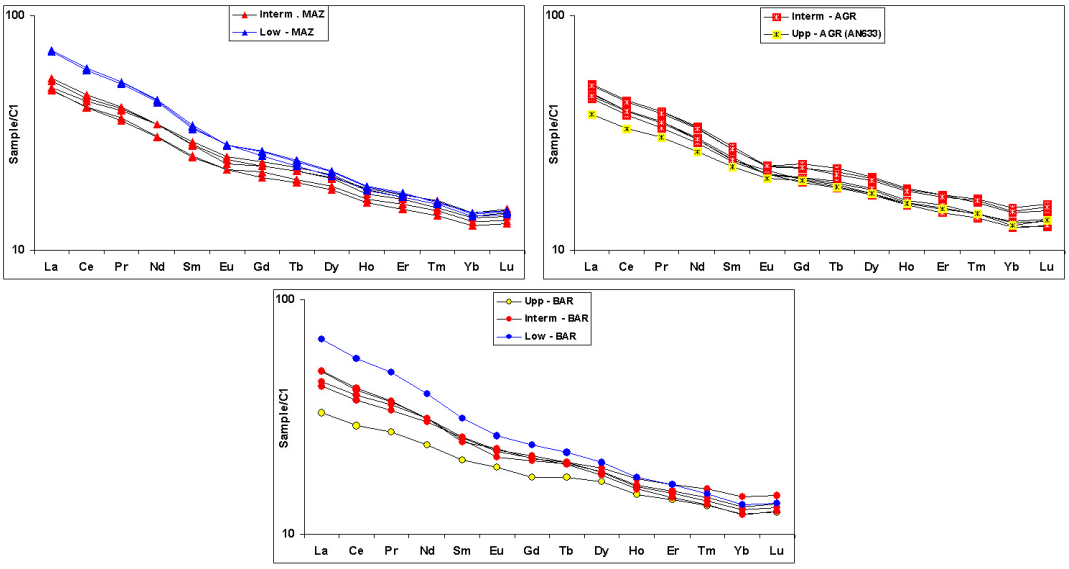

Figure 14.12: REE spider-diagrams C1 chondrite normalized (**Andres & Grevesse, 1989**) for all MA and WM basalts analysed by ICP-MS.

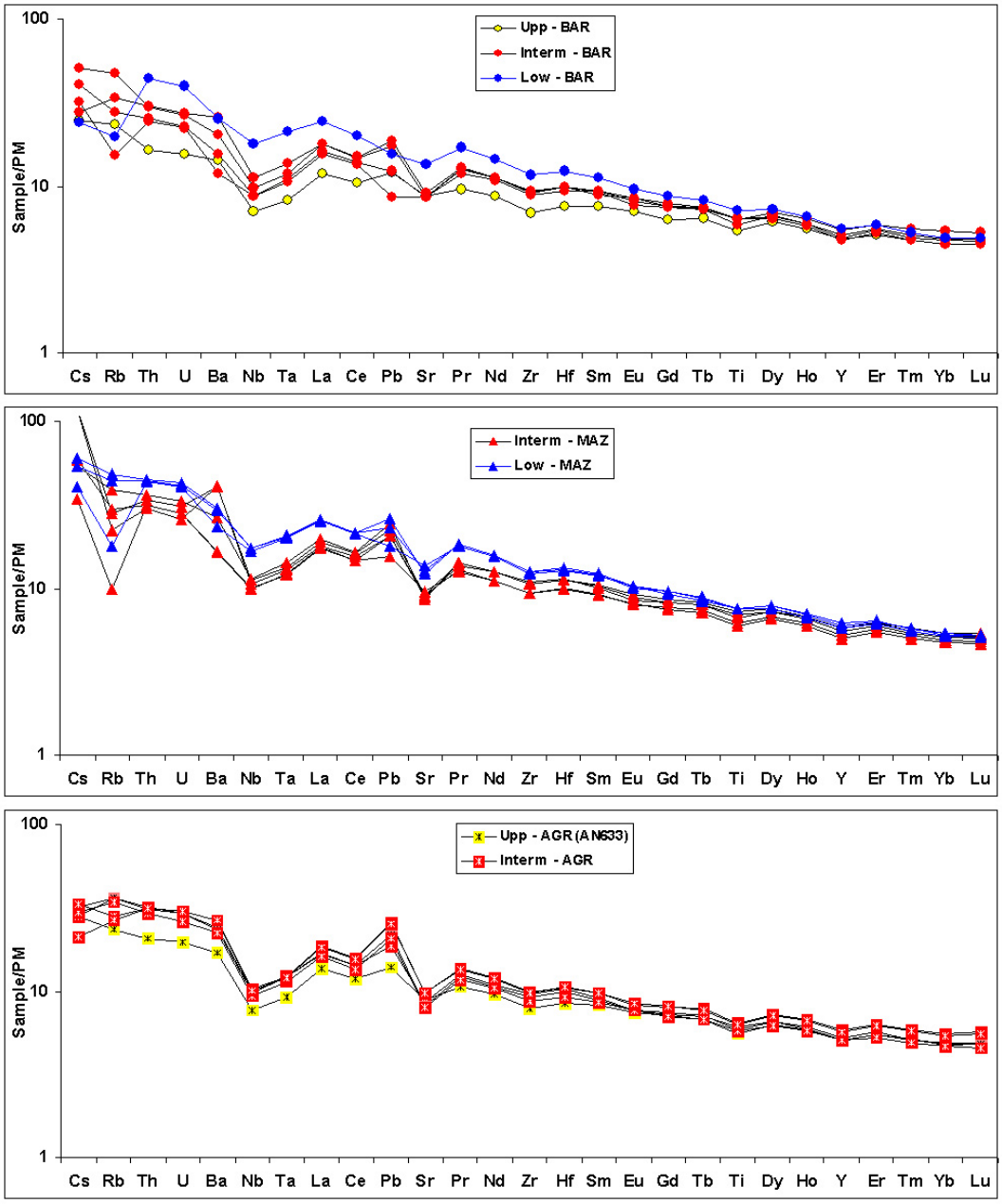

Figure 14.13: Primitive mantle normalized spider-diagram (**McDonough & s. Sun, 1995**) for all MA and WM basalts analysed by ICP-MS.

15 MOROCCAN LAVA PILES CORRELATION

In this chapter XRF and ICP-MS data, isotopic systematics and paleomagnetic data available for the samples analysed from the CHA will be used to infer about a possible magneto-chemo-stratigraphic correlation among the three lava piles of Tiourjdal, Telouet and Oued Lahr. After a similar correlation among the volcanic sections of the WM (Maaziz) and MA (Oum R'Rbia and Agourai), all data will be summarized possibly to extend this correlation at regional scale over an area ca. 10^5 Km^2 large, between Central High Atlas and Middle Atlas/Western Meseta. As shown previously major and trace elements allow to recognize a systematic time-related compositional variation among the four units which build-up the Moroccan lava piles. However many problems arise for a straightforward correlation among the sections sampled in different parts of Morocco: trace element analyses performed in different laboratories, isotopic analyses not available for all sections, different lava pile structures, magneto-stratigraphy not available for the Telouet section.

15.1 GEOCHEMICAL DATA SETS

Trace element analyses have been done in different laboratories. For the Tiourjdal section, series AN100 and TJ have been analysed at Grenoble. Samples from Telouet (series TEL) and Oued Lahr (series OL) have been analysed at Acme Analytical Laboratories in Vancouver (Canada), while samples from WM/MA (Maaziz, Agourai and Oum R'Rbia, all series AN500 and AN600) have been analysed at WSU GeoAnalytical Laboratory, Washington State University (United States). In Fig. 15.1 the differences (%) are visible between the analyses done in Vancouver (series TEL and OL) and in Washington (series AN500 and AN600) with respect to those of a reference samples (AN136 for the Lower Unit, AN141 for the Upper and AN156A for the Recurrent Unit) previously analysed at Grenoble. However, for the Vancouver data-set only one reference sample is available (AN136), so correction for systematic instrumental shift is possible only for the Lower Unit of Telouet and Oued Lahr. For the WM/MA sections

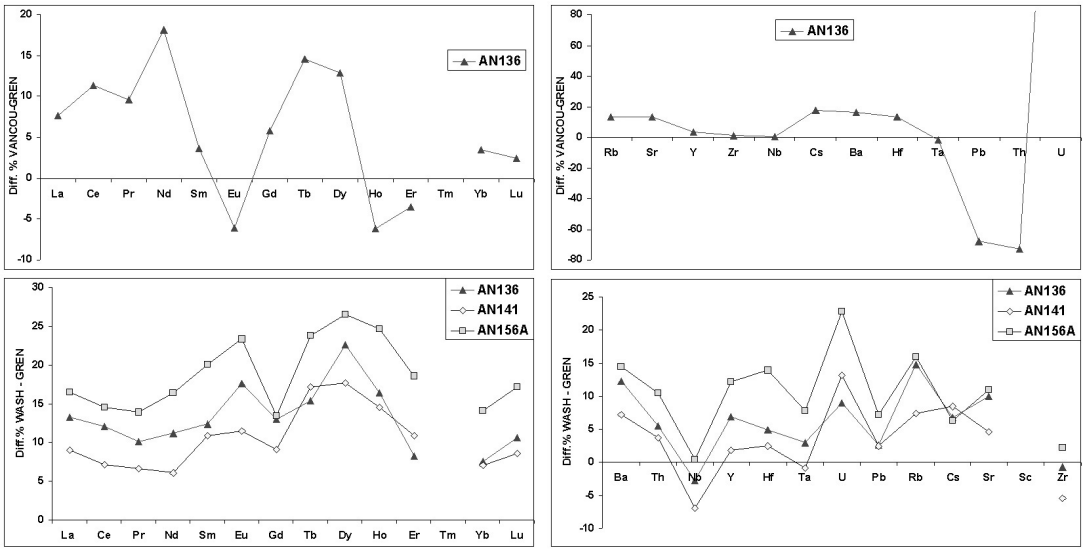

Figure 15.1: Differences % between analyses performed at Vancouver (upper two diagrams) and Washington (lower two diagrams) compared with samples already analysed at Grenoble

corrections are available for the Lower and the Upper Unit (Fig. 15.1). In the case of Telouet and Oued Lahr trace elements, corrections for most of REE are less than 10%. Only Ce, Nd, Tb and Dy are overestimated more than 10% with respect to the same element concentration measured at Grenoble, while Eu, Ho and Er are slightly underestimated (ca. 5%). Also LILE and HFSE are overestimated, up to 20% with exception of Y, Zr and Nb which are overestimated less than 5% and Ta only slightly underestimated. In practice the Y, Zr, Nb and Ta concentrations, like their relative ratios, are almost identical to those obtained from the Grenoble analyses. On the contrary, Pb and Th are underestimated (ca. 70%) while U is up to 3 times overestimated compared to Grenoble analyses. REE analysed in Washington are always overestimated with respect to analyses performed in Grenoble. In Fig. 15.1 it is visible that MREE are overestimated (except for Gd) with respect to LREE and HREE. The cause of this behaviour is not known. Differences % for La and Ce (LREE) and Yb and Lu (HREE) are very similar so LREE/HREE ratios need no or slight correction to be comparable with those calculated in the Grenoble data-set. Also LILE and HFSE are always overestimated except for Nb and Zr which are slightly underestimated in AN136 and AN141 samples (up to 5-6%). Ta is always overestimated except for sample AN141 where is only slightly underestimated (few %). More in general the highest analytic differences between new and old analyses for LILE and HFSE are reached in AN156A (Recurrent Unit) with no more than 15%. Only U is up to

22%. The most important thing is that Th, Nb, Y, Hf, Ta and Zr (the most immobile elements during secondary alteration) have analytic differences not higher than 5-6%, being so almost identical to concentrations measured in Grenoble. An other feature is visible in both the diagrams. Differences between the new and the old measures decrease from the Lower sample towards the Upper sample, while the Recurrent sample has the highest differences % among the analysed samples.

15.2 LAVA PILE STRUCTURES

The studied lava piles are structured differently in terms of the presence of the units within the volcanic sections and the number of lava flows belonging to each unit (Fig. 15.2). The four units detectable on the geochemical base are

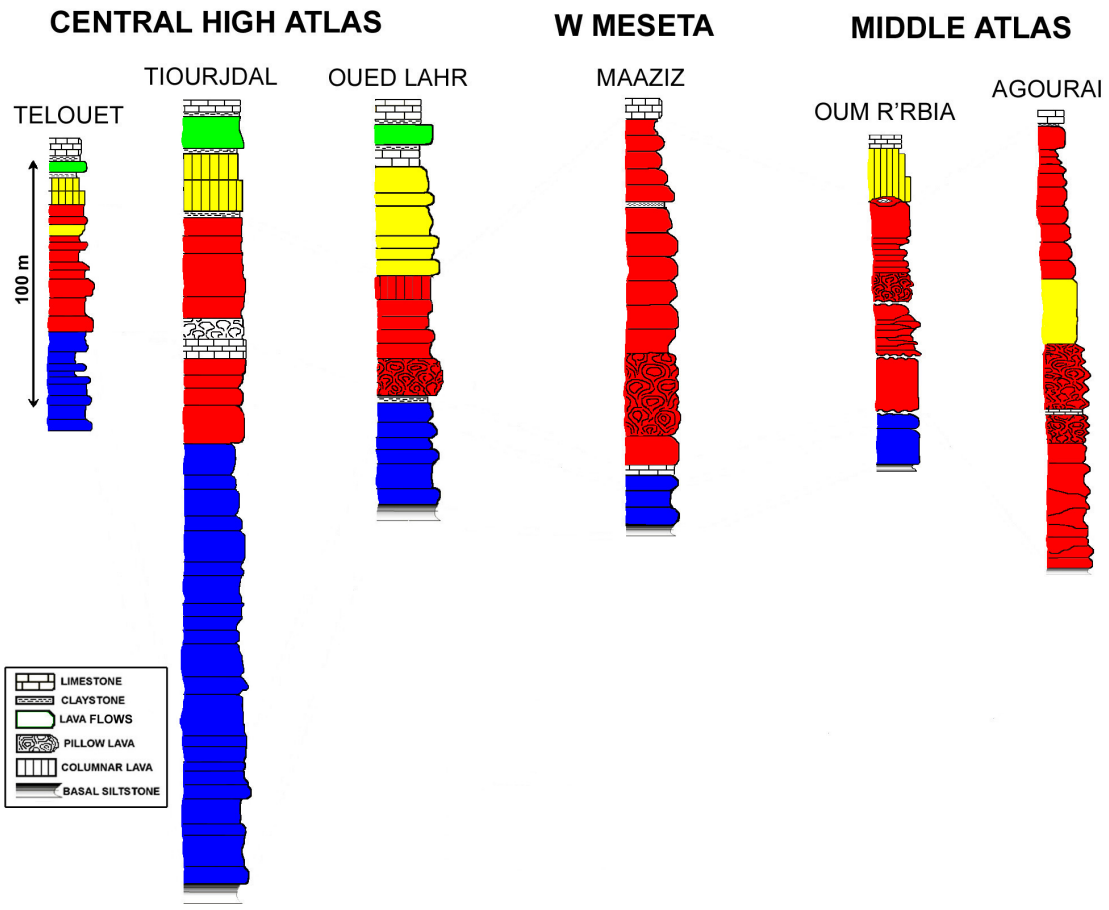

Figure 15.2: Stratigraphy of the CHA and MA/WM lava piles based on chemographic criteria. Blue for the Lower Unit, red for the Intermediate Unit, yellow for the Upper Unit and green for the Recurrent Unit.

not present in all studied sites and have global different thickness in the various

sites. For example, while the Lower Unit is present in all sites (WM, MA, Eastern Meseta and CHA), the Intermediate unit is thick in the WM, MA and CHA, but only one Intermediate Unit sample is available from the Eastern Meseta. The Upper Unit is represented occasionally in the MA and in the Eastern Meseta and in all CHA sites and finally the Recurrent Unit is present only in the CHA. More in detail, as previously described (Chap. 9), the Tiourjdal sequence seems to be the most complete, with a Lower Unit build up by 22 flows, while only 12 and 6 Lower flows are present at Telouet and Oued Lahr, respectively. On the other side the Lower Unit in MA and WM is poorly represented (3 flows at Maaziz and 1, maybe 2 flows, at Oum R'Rbia) or completely absent like at Agourai. Differently the Intermediate Unit is best preserved in the MA/WM with 9 to 13 flows sampled and numerous not sampled thin and altered flows, while in the CHA 10 lava flows are recorded at Tiourjdal and Telouet and only 6 at Oued Lahr. Also the Upper Unit is not equally recorded everywhere: at Tiourjdal only 2 flows are present, 3 at Telouet and 6 at Oued Lahr. In the MA/WM only one flow belonging to the Upper Unit at Oum R'Rbia is recorded, while one flow geochemically equivalent to Upper basalts is interbedded with the uppermost Intermediate flows at Agourai. Finally the Recurrent Unit, represented in the central High Atlas by one single flow, is completely absent in the MA/WM realm. Another problem is that not all units in each section are represented by a large number of analysed flows for trace elements and isotopic measures, first due to the low flow numbers belonging to some units and also for bad preservation of most basalts. If we add that the same chemostratigraphic units in different volcanic sections are spatially and probably temporally separated, it results that a correlation only on geochemical base results somewhat arbitrary. For these reasons, I tried to use both geochemical and paleomagnetic data to infer a possible tight correlation over all volcanic sections studied in this work.

15.3 MAGNETO-CHEMOSTRATIGRAPHIC CORRELATION

As described in the previous chapters, the 2007 sampling campaigns (Maaziz, Agourai and Oum R'Rbia sections) gave back samples for geochemistry and paleomagnetic studies. For the CHA, samples for geochemistry (Tiourjdal, Telouet and Oued Lahr) and core rocks for paleomagnetic studies (only Tiourjdal and Oued Lahr) are available from previous sampling campaigns (**Knight *et al.*, 2004**). The starting point for a stratigraphic correlation between the CHA lava

piles with those of the WM/MA operated in this work are the paleomagnetic data (i.e. paleo-inclination and paleo-declination) of sampled lava flows. In fact, paleomagnetic data allow to group lava flows in directional groups (DG), defined as "a set of consecutive lava flows with statistically indistinguishable paleomagnetic directions where the variation of the DG is less than the A95 of the mean group direction, and the jump in the direction is greater than the mean A95 of the previous group" (**Knight *et al.*, 2004**). Since the paleo-direction variations recorded within each directional group are smaller than those observed in a secular variation cycle, it follows that lava flows of each DG have been emplaced in e period shorter than about 450-years (in the hypothesis that paleosecular variations at T-J boundary were similar to those recorded in the Holocene; **Schnepp *et al.*, 2003**). At Tiourjdal, magnetostratigraphy allows to individuate 5 DG (Fig. 15.3), four with normal polarity (NP) and one with reversed polarity (RP). The first two groups (DG1 and DG2, following the nomenclature of **Knight *et al.* (2004)**) cover the entire Lower Unit. DG3 is formed by the Intermediate Unit basalts below a sedimentary layer (TJ27) which yielded a RP and defines DG4. The last group, DG5 is build up by the rest of the Intermediate Unit (above the RP) and the two lava flows belonging to the Upper Unit. Paleomagnetic data for the Recurrent Unit did not yield any confident DG (see details in **Knight *et al.*, 2004**). At Oued Lahr, four DGs have been identified, all at NP except one RP at the base of the Intermediate Unit. The first group (DG2) covers the entire Lower Unit (Fig. 15.3). Its denomination is determined by comparison with the Tiourjdal section on the base of the paleomagnetic directions (inclination and declination). The RP which marks the onset of the Intermediate Unit at Oued Lahr (sample OL7) defines the DG4, following **Knight *et al.* (2004)**. The remaining Intermediate Unit is assigned to the DG5, while the last group (DG6) is formed by the 6 lava flows that build up the Upper Unit (Fig. 15.3). The finding of the brief RP event both at Tiourjdal and Oued Lahr, in overall normal polarity sequences, allow to compare and possibly correlate (in the hypothesis that the two reversal record the same polarity inversion event) flows belonging to homologues units (Fig. 15.3). I tried to combine paleomagnetic and geochemical data to improve the correlation among lava piles, since it is possible to relate to each lava flow group (which correspond to a temporally defined DG) a well defined trace element (and isotopic) composition, with the main goal to constrain if units (or sub-units) belonging to different lava piles, sharing similar trace elements compositions are temporally related, indicating a probably common magmatic feeding system, or if homologues DGs have different compositions

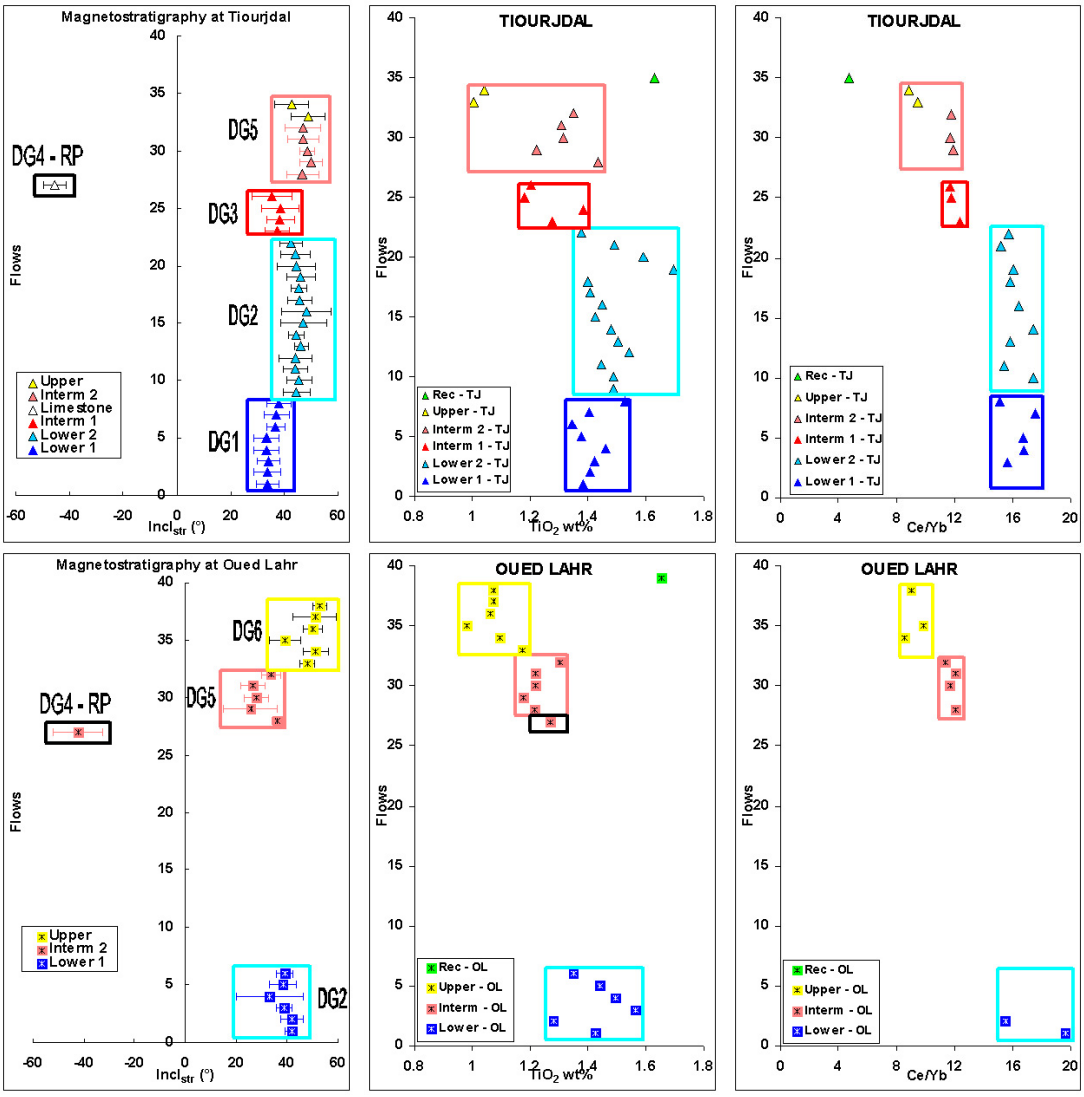

Figure 15.3: Magnetostratigraphy (mean flow inclination corrected for bedding-tilt) and chemostratigraphy (TiO_2 wt% and Ce/Yb) of the Tiourjdal and Oued Lahr sequences. The correlation between the two sections is based on paleomagnetic and geochemical data. Triangles for Tiourjdal samples and squares with black star for Oued Lahr samples. Blue and cyan for the Lower Unit (Lower 1 and Lower 2 sub-groups respectively), red and pink for the Intermediate Unit (Interm 1 and Interm 2 sub-groups respectively), yellow for the Upper Unit, green for the Recurrent Unit.

thus indicating that different magmatic systems have been active nearly at the same time. This method applied to the most complete Tiourjdal sequence allows recognizing two sub-units within the Lower (Lower 1 and Lower 2) and tow sub-units within the Intermediate Unit (Interm 1 and Interm 2) each of them corresponding to a specific DG (Fig. 15.3). In fact all four sub-units display a slightly different mean trace element composition (partially supported by isotopic data, Chap. 10). The other two sections of the CHA, Telouet and Oued Lahr, have less lava flows compared to Tiourjdal so this subdivision of the two oldest units is not visible. Using geochemical criteria it is possible to correlate the Lower Unit both at Telouet and Oued Lahr with the Lower 1 sub-group of Tiourjdal, while the Intermediate Unit at Telouet and Oued Lahr corresponds with the Interm 2 sub-group of Tiourjdal (Fig. 15.5). In fact, geochemical data show that the REE and HFSE compositions of the lava flows belonging to the Lower and the Intermediate Unit at Oued Lahr match closely in composition the Lower 1 and the Interm 2 sub-groups respectively. Ce vs Ce/Y, Sm vs Sm/Nd and Nb vs Nb/Zr diagrams (Fig. 15.5) support this correlation. The Lower 2 sub-group at Tiourjdal, even if partially overlapping with the Lower 1 sub-group is quite distinguishable having higher mean REE and HFSE concentrations and ratios. The Intermediate Unit at Oued Lahr is distinct from the Interm 1 sub-group at Tiourjdal, matching more closely the Interm 2 sub-group compositions even if with lower REE and HFSE concentrations and ratios than the Interm 2 sub-group. The Lower Unit at Telouet has composition similar to that of the Lower 1 sub-group, while the Intermediate Unit overlaps perfectly the Intermediate Unit at Oued Lahr, thus being more similar to the Interm 2 rather than to the Interm 1 sub-group (Fig. 15.5). Notably, in the Intermediate Unit at Telouet a flow with a clear Upper Unit composition (TEL21) occurs stratigraphically within the uppermost part of the Intermediate Unit (cf. below for a similar feature within the Agourai section, MA). In all three diagrams, the Upper Unit of CHA lava piles displays a narrow compositional range, except for Sm/Nd which is slightly scattered, similar to those of the Lower and Intermediate Unit. Assuming that the Nd concentration of the Intermediate and Upper Unit samples should be slightly corrected for analytical bias, similar to the Lower Unit samples, then Sm/Nd would have more narrow compositional range. If paleomagnetic data seem to support the basaltic units subdivision based on geochemical criteria, they tell us a more complex situation. For the successive correlations I used the RP at Tiourjdal (DG4, sample TJ27, white triangle in Fig. 15.3, a sedimentary layer sampled in the middle of the Intermediate Unit) and at Oued Lahr (DG4, OL7,

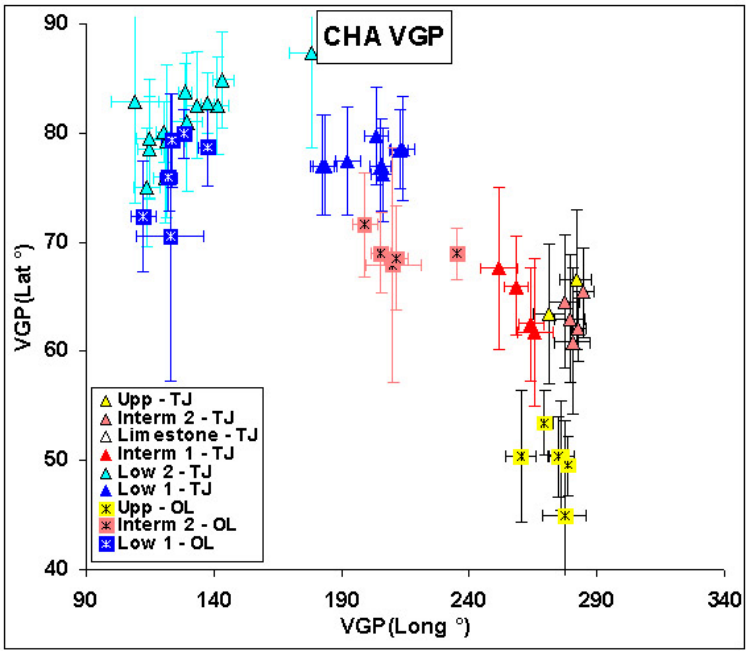

Figure 15.4: VGP (Virtual Geomagnetic Pole) longitude and latitude of the Tiourjdal and Oued Lahr basalt.

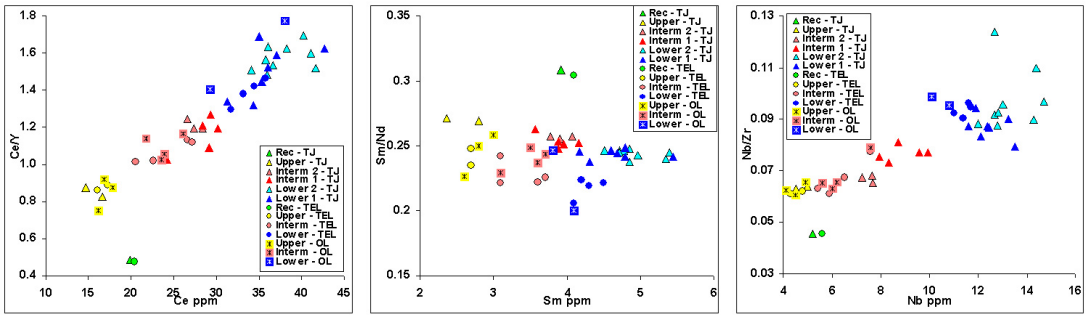

Figure 15.5: Ce vs Ce/Y, Sm vs Sm/Nd and Nb vs Nb/Zr diagrams showing as magneto-chemostratigraphy allows the correlation of the four units belonging to the three CHA lava piles. Triangles for Tiourjdal section, circles for Telouet section and squares with star for Oued Lahr section. Blue for the Lower Unit, red and pink for the Intermediate Unit, yellow for the Upper Unit and green for the Recurrent Unit.

a pillow lava just above the transition between the Lower and the Intermediate Unit) as anchor point, considering that these represent the same magnetic inversion event. While the Lower Unit at Oued Lahr seems to be geochemically similar to the Lower 1 sub-unit at Tiourjdal, its paleomagnetic directions indicate that it is nearly contemporaneous with the Lower 2 sub-unit (same DG), since the mean longitudes and latitudes of the virtual geomagnetic pole (VGP) are similar (Fig. 15.4). This eliminates almost completely the large volcano-stratigraphic gap visible in the Fig. 15.3 between the top of the Lower Unit and the RP (i.e. base of the Intermediate Unit) at the Oued Lahr sequence and it could highlight the contemporaneous presence of two geochemically slightly distinct magmatic feeding system at Tiourjdal and Oued Lahr, respectively, excluding the possibility of relative rotations between the two sequences. For the Lower Unit at Telouet (few tens of kilometres apart from Tiourjdal), the correlation is possible only on the base of trace elements content (Fig. 15.5), since no paleomagnetic date are available at present. The Intermediate 1 sub-unit of Tiourjdal has neither a geochemically nor magnetostratigraphically counterpart in the other CHA sections (Fig. 15.3,15.4,15.5) while the Intermediate 2 sub-unit, as inferred from trace element compositions, has a counterpart both at Oued Lahr and Telouet. However, VGP directions at Tiourjdal and Oued Lahr are again different (Fig. 15.4), thus indicating that the two magmatic systems are temporally unrelated. The Upper Unit, as visible in Fig. 15.3, belongs to two different DGs. At Tiourjdal, the two Upper Unit flows occur very little time after the emplacement of the underlying Intermediate 2 sub-unit. In fact both the Upper Unit and Intermediate 2 sub-unit belong the same DG (DG5). In the near Telouet sequence (few kilometers apart) interbedded within the Intermediate Unit basalts (geochemically equivalent to the Intermediate 2 sub-unit of Tiourjdal, Fig. 15.3) there is an Upper Unit flow. This could be a very compelling evidence for the hypothesis of two magmatic systems of different composition active nearly at the same time, if confirmed by paleomagnetic data. At Oued Lahr the Upper Unit, although geochemically similar to the Tiourjdal Upper unit, is temporally unrelated to it, since the VGP directions of the two units are different (Fig. 15.4). No paleomagnetic data are available for the Recurrent Unit in the CHA lava piles investigated here (see details in **Knight *et al.*, 2004**).

As seen previously (Chap. 13), the three basaltic units detected in the WM/MA volcanic sections have a narrower compositional range compared to those of the CHA. The Lower Unit flows from Maaziz and Oum R'Rbia are similar in the Ce vs Ce/Y, Sm vs Sm/Nd and Nb vs Nb/Zr diagrams (Fig. 15.6). As

seen before, analytical corrections for the Lower Unit in the Washington data-set vs Grenoble data are minimal. While Ce needs to be correct by 10-12% (towards lower values), Ce/Y is almost the same (i.e., 4% overestimated). Altogether in a Ce vs Ce/Y, the Lower Unit samples diagram need to be shifted slightly towards lower Ce concentrations, overlapping perfectly with the Lower 1 sub-group of the CHA (Fig. 15.7). In the Sm vs Sm/Nd diagram, the Lower Unit samples need to

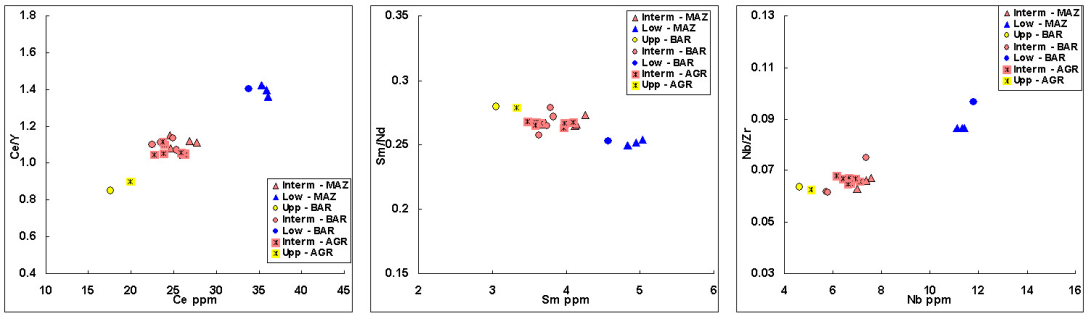

Figure 15.6: Ce vs Ce/Y, Sm vs Sm/Nd and Nb vs Nb/Zr diagrams relative to the Maaziz (WM), Agourai and Oum R'Rbia (MA). Triangles for Maaziz section, circles for Oum R'Rbia section and crossed squares for Agourai section. Blue for the Lower Unit, pink for the Intermediate Unit, yellow for the Upper Unit.

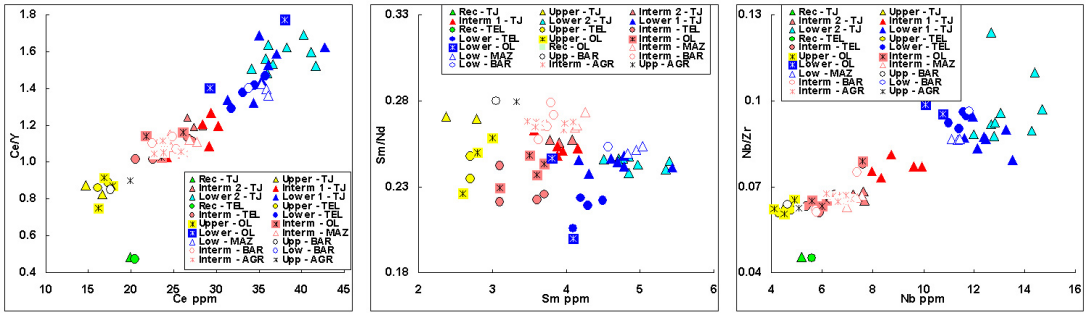

Figure 15.7: Ce vs Ce/Y, Sm vs Sm/Nd and Nb vs Nb/Zr diagrams relative to the chemographic correlation among CHA and WM/MA sequences. Colours as above. Filled and hollow symbols for the CHA and WM/MA sequences respectively.

be shifted only by 10% towards lower Sm contents, also in this case overlapping with the Lower 1 sub-group in the CHA. No corrections are needed for Nb and Nb/Zr. The Intermediate Unit of WM/MA covers a much wider range compared to that of the Lower Unit, but narrower than the Intermediate unit from the CHA (Fig. 15.6). Considering similar analytical corrections to those of the Lower and the Upper Unit, in the Ce vs Ce/Y and Sm vs Sm/Nd diagrams the Intermediate

compositions should be shifted towards lower REE contents for almost constant Ce/Y and Sm/Nd.

The WM/MA Intermediate Unit in this case should be the similar to the Interm 2 sub-group of CHA. Finally, the Upper Unit is represented by one sample at Oum R'Rbia (AN540) and probably one sample (AN540[633]) at Agourai which displays a composition with Upper-unit affinity. In fact, despite its stratigraphic position (between the uppermost Intermediate lava flows) it displays REE and HFSE compositions resembling more closely that of the Upper Unit. AN540[633] could record the same phenomenon seen in the Telouet section, where an Upper Unit flow (TEL21) occurs stratigraphically within the uppermost part of the Intermediate Unit. In the Ce vs Ce/Y, Sm vs Sm/Nd and Nb vs Nb/Zr diagrams, AN633 plots near the clearly Upper Unit sample AN540. Analytical corrections for these two samples are necessary only for REE and Y, since Nb and Nb/Zr need corrections lower than 5%, being so nearly identical to Nb and Nb/Zr compositions of the CHA Upper Unit. With regard to Ce vs Ce/Y, the Upper Unit samples are overestimated by ca. 7% in Ce content, while Ce/Y is underestimated by about 15%. With these corrections the WM/MA compositional Upper Unit field overlaps closer with the CHA homologues. In the Sm vs Sm/Nd diagram, the sample compositions are overestimated both in Sm (ca. 11%) and Sm/Nd (ca. 3%). Also here, the analytical correction induces overlap of the WM/MA Upper samples with the CHA ones (Fig. 15.7).

Paleomagnetic data (data obtained by S. Brownlee, Berkeley Geochronology Centre, U.S.A.) allow to recognize at least three DGs: two at Maaziz, three at Oum R'Rbia and at Agourai (Fig. 15.8). However, as visible in the chemostratigraphy (TiO_2 wt% and Ce/Yb in Fig. 15.8) of the three sections, some flows are not included in the DG computation, since the relative samples did not give stable mean paleomagnetic directions or were not sampled. At Maaziz the first two flows are not included in the first directional group detected (DG1) due to poor statistics of the paleomagnetic results. However, the first DG at Maaziz comprises the last Lower Unit flow and (at least) the first flow belonging the Intermediate Unit. The flows are interlayered by an about 1 m thick carbonate level. As seen for the CHA sequences, also here some paleomagnetic directional groups are defined by lava flows which belong to two compositionally different magmatic systems. The second directional group (DG2) of the MA/WM is formed by at least 5 flows which have Intermediate-like chemical compositions. The magnetostratigraphy of the Oum R'Rbia section is the most complete (Fig. 15.8). The first (DG1), like for Maaziz, is constituted by the only sampled Lower Unit flow and by the first

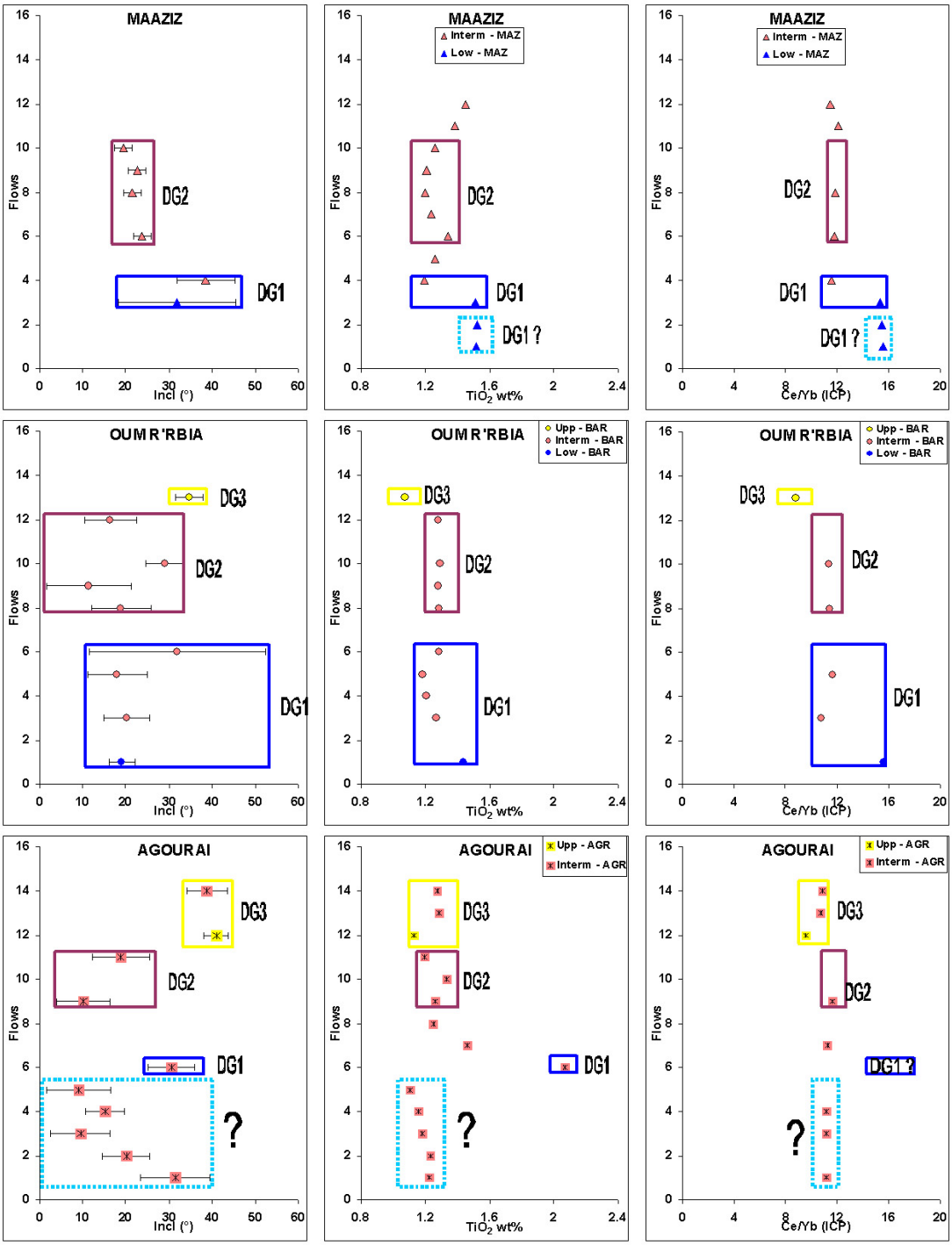

Figure 15.8: Magnetostratigraphy (DGs in coloured boxes) shown the mean flow inclination and chemostratigraphy (TiO2 wt% and Ce/Yb) of the MA/WM lava piles with of the Maaziz, Oum R'Rbia and Agourai sequences.

half (at least four lava flows) of the Intermediate Unit. The second DG is formed by the remaining part of the Intermediate Unit and it is followed by the DG3 that corresponds with the only Upper Unit flow. Magnetostratigraphy of the

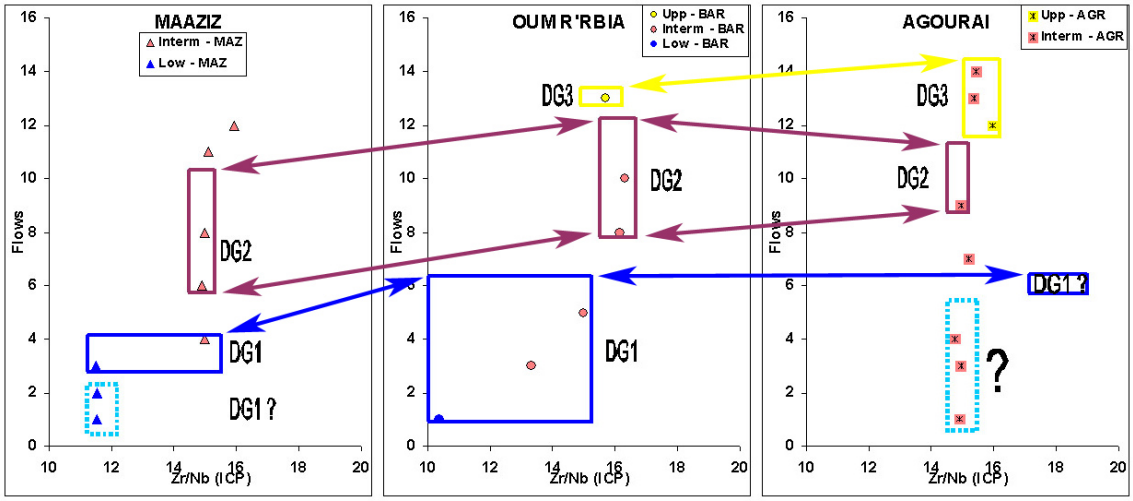

Figure 15.9: A possible magnetostratigraphic correlation among MA/WM lava piles superimposed on chemostratigraphy (Zr/Nb by ICP-MS). Coloured boxes represent only homologues DGs in different sequences, thus not implying similar basaltic composition.

Agourai section suffers more or less of the same problems encountered at Maaziz, since many lava flows at the base of the section yielded scattered paleomagnetic data (cyan dashed box in Fig. 15.6) and other flows in the middle of the section are not sampled for magnetostratigraphy because of their bad preservation. The collected samples allow to define three DGs: the first (DG1) is formed by 1 lava flow, the second (DG2) is formed by at least three flows in the middle part of the section (with a limestone layer which was not analyzed yet) and the third (DG3) comprises the uppermost flows, from the Upper Unit-like AN530[633] sample to the top of the section (Fig. 15.8). With regard to the lava flows at the base of the Agourai sequence that are not included in the defined DGs, it is possible that their emplacement took a longer time with respect to that inferred for other DGs, i.e. between each flow the magnetic directions changed enough to be different compared to those recorded in the overlying flow. This would be very interesting if compared with the "usual" magmatic activity found in CHA and MA/WM, that manifests itself as brief (few hundred years) magmatic pulses (**Knight *et al.*, 2004**). However, we note that there is no field evidence for long hiatuses between eruption of the lowermost Agourai samples (i.e. no presence of significant paleo-sole or sedimentary interlayers).

Mean VGP directions of the basaltic flows of the MA/WM sequences are visible in Fig. 15.10. At first glance it is possible to note that, differently from CHA lava flows/units, those of the MA and WM cluster more tightly, except for a couple of lava flows (Fig. 15.10). This could mean that lava flows were emplaced in a period of time shorter than that spanned in the CHA. Another striking feature is that, despite the individuation within each volcanic sequence of 2 or 3 DGs (on the base of paleomagnetic directions, inclination and declination), some of these have nearly coincident mean VGP directions. In fact, DG1 and DG2 at Oum R'Rbia (blue and purple circles in Fig. 15.11), DG2 at Maaziz (purple triangles) and Agourai (purple squares with white star) have overlapping VGP directions. This could suggest:

- extremely short magmatic event for the DGs mentioned above;
- the recognition of DG1 and DG2 at Oum R'Rbia, DG2 at Maaziz and Agourai is wrong (especially taking into account the large error bars associated with paleodirections of Oum R'Rbia lava flows, Fig. 15.8) thus implying a single magmatic pulse recorded above an area spanning ca. 5×10^4 km^2 for these DGs in the MA/WM.

On the other side, DG1 at Agourai (blue squares with white star) and Maaziz (blue triangle) and DG3 at Oum R'Rbia and Agourai (yellow circle and squares with black star) are quite clearly distinct, thus possibly representing, in the case of realistic mean VGPs, two other magmatic pulses. In DG3 (recorded only in the MA), AN633 and AN540 samples (chemical Upper Unit at Agourai and Oum R'Rbia, respectively) cluster quite near (Fig. 15.10), while the third sample belonging to DG3, AN532 (the topmost flow, yet chemically belonging to Intermediate 2 sub-unit at Agourai), plots far away from the others (VGP(long) at ca. 330°). Since, between sample AN633 and AN532 are present numerous not sampled thin lava flows (maybe more than six for a lacking stratigraphy thick at least 20-30 meters), it is possible that AN532 plots far away from AN633 and AN540 because it records a later magmatic event. However, its paleomagnetic inclination and declination (Fig. 15.8) are nearly the same of the underlying flow AN633, thus arising a difficult interpretation problem. A similar behaviour is visible at the base of the same sequence, as explained before.

Taking into account the hypothesis that the mean MA/WM VGPs are real, correlation between CHA and MA/WM lava piles (based on DGs temporally *but not* chemically equivalent) could be this:

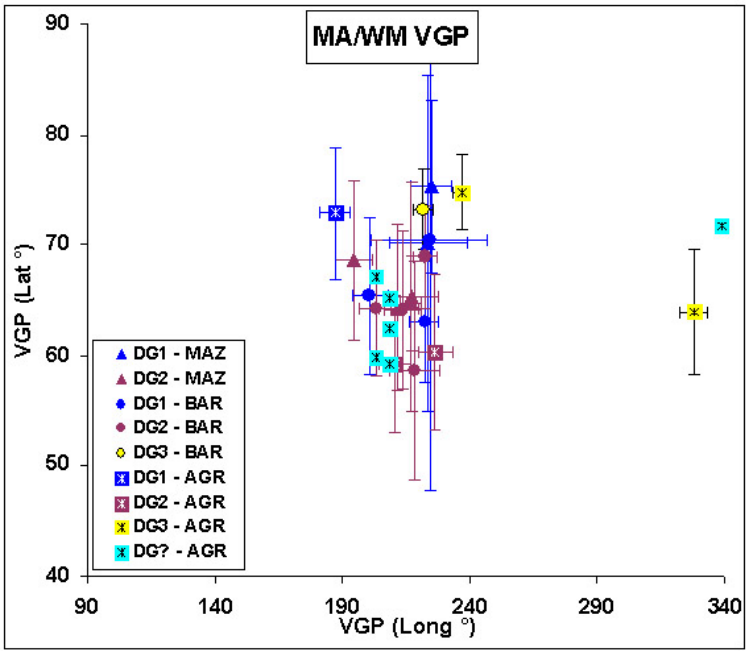

Figure 15.10: VGP (Virtual Geomagnetic Pole) longitude and latitude of the Maaziz, Oum R'Rbia and Agourai sequences. Colours codify DGs belonging each volcanic sequence. For the related geochemical affinity see Fig. 15.8.

- DG1 and DG2 at Oum R'Rbia, DG2 at Maaziz and Agourai could record the same magmatic event and these parts of the lava sequences could correlate with DG5 at Oued Lahr (i.e., the Intermediate 2 sub-unit in Fig. 15.3) (Fig. 15.11);
- DG1 at Agourai (geochemically the Lower 1 sub-unit) could correlate with the Lower 1 sub-unit of Tiourjdal, since plot close to DG1 of this sequence (Fig. 15.11);
- DG1 at Maaziz and DG3 at Agourai and Oum R'Rbia could not correlate with any CHA DGs.

On the other side, taking as real the paleodirections of single flows (to group lava flows temporally related) and using the geochemistry of associated sub-units (to relate homologues sub-units in different sequences) a possible interpretation of paleomagnetic data could be that shown in Fig. 15.9, which in part fits with what found in CHA at Tiourjdal and Oued Lahr. The situation recorded in the DG3 at Agourai and Oum R'Rbia is very similar to what found in the DG5 at Tiourjdal (and Telouet, although no paleomagnetic data are available to support this hypothesis), where the Intermediate 2 sub-unit and the Upper Unit occur

together (Fig. 15.3). The underlying DG2, at Oum R'Rbia, Agourai and at Maaziz could correlate with the Intermediate 2 sub-unit at Oued Lahr (DG5). Finally DG1 of the MA/WM, which is composed by both the Lower Unit and Intermediate Unit basalts (Fig. 15.9), poses the major problem for a regional scale correlation.

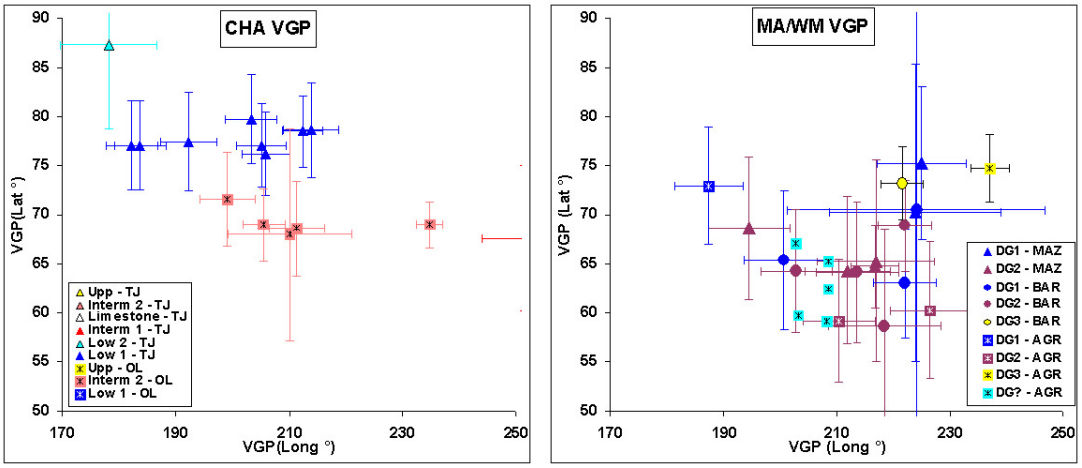

Figure 15.11: VGP (Close view of VGP (Virtual Geomagnetic Pole) longitude and latitude of the CHA (on the left) and MA/WM (on the right) sequences.

DG1 should record in a brief time the occurrence of two compositionally different magmatic systems, which based on geochemical data correspond to the Lower 1 and the Intermediate 2 sub-unit of the CHA (Fig. 15.3). However, as visible in Fig. 15.3, in the CHA both these formations are separated by the outcropping of the Lower 2 and Intermediate 1 sub-units at Tiourjdal and at Oued Lahr which are separated by a RP event. This RP event, at present has not been sampled in the MA/WM at Maaziz nor at Oum R'Rbia (Agourai is excluded since the Lower Unit does not outcrop in the DG1). This could be due to the incomplete sampling of that part of Oum R'Rbia sequences, as described in the Chap. 8. On the other side, at Maaziz the RP may be found within a 1 meter thick sedimentary layer which has not been analyzed so far. Alternatively the magnetic inversion could be recorded in the lava flows below (AN503 and AN504[602]) or above (AN509) for which paleomagnetic data are not available.

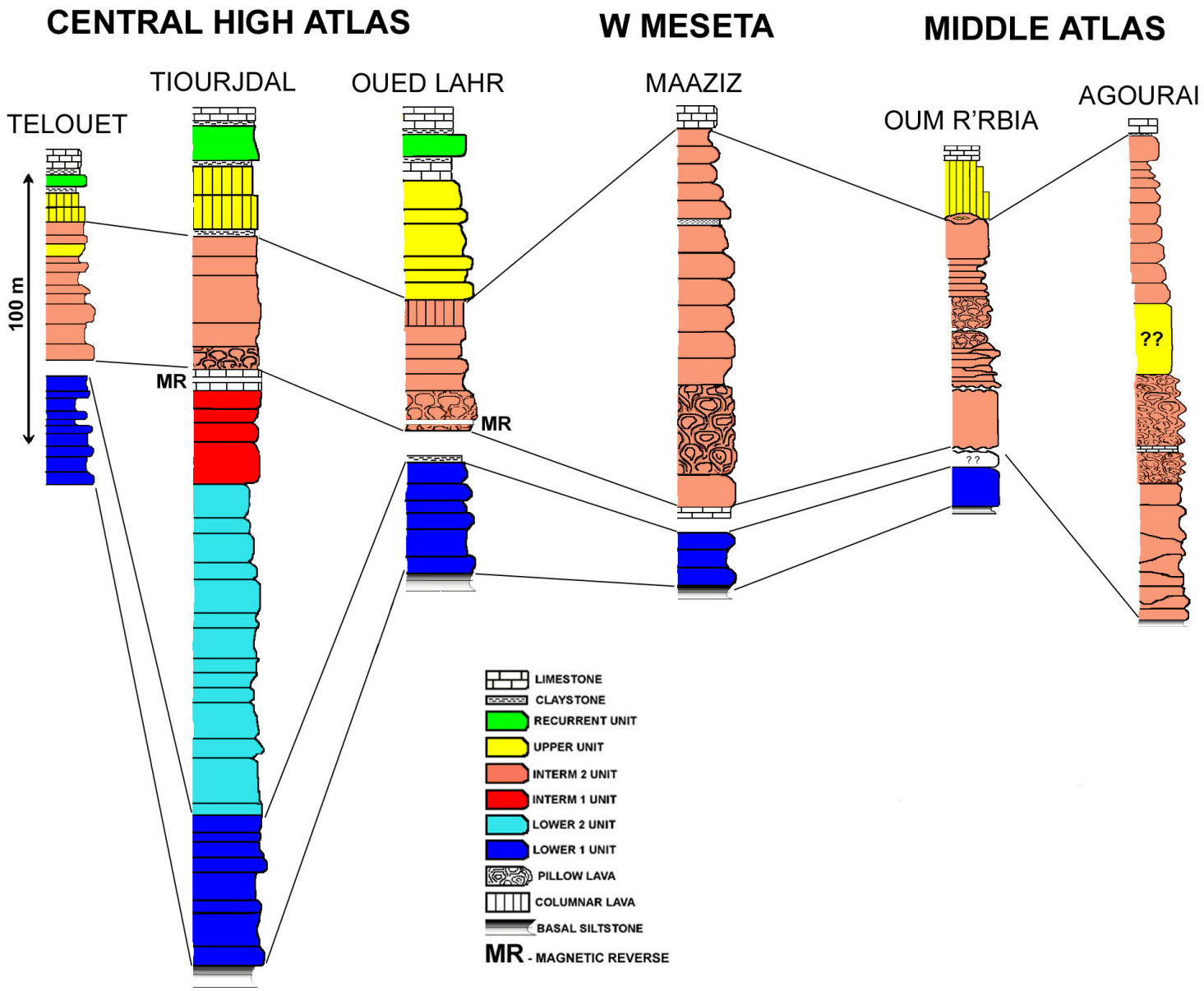

Figure 15.12: VGP (Chemostratigraphic correlation among CHA and MA/WM lava piles.

16 EVOLUTION OF THE MOROCCAN MAGMAS

As previously described, the paragenesis of the investigated Moroccan CAMP basalts is dominated by augitic pyroxenes, plagioclases, sub-ordinate pigeonites and oxides (magnetite and ilmenite). Olivines occur frequently but are mostly completely altered. Except for the latter, both pyroxenes (high-Ca and low-Ca), plagioclase and oxides allow to infer about crystallization conditions of the parental magmas en route to the surface. The results and considerations obtained from our petrographic and mineralogical study (paragenesis, major and minor elements compositions by XFR and EMP analyses, trace element compositions by LA-ICP-MS) of the basaltic rocks from each unit of each lava pile studied can be used to infer about conditions (T, P, H_2O content and fO_2), crystallization order and processes (i.e., fractional crystallization) which affected the parental magmas from which the studied Moroccan basalts were derived.

16.1 THERMO-BAROMETRY

The occurrence of pigeonite together with augite in some basalts of the Lower, Intermediate and Upper Unit, allow to determine the equilibrium temperature between these two minerals. The equilibrium crystallization temperatures (more correctly the intergranular diffusion closure temperature) of the augite-pigeonite pair has been calculated using the QUILF program (**Andersen *et al.*, 1993**). This geothermometer has been applied only on few mineral pairs (8 augite-pigeonite pairs), because of the scarce occurrence of pigeonite together with augite in the samples analyzed. Globally, the temperatures vary from 1040 to 1174°C (Tab. 16.1), values well comparable with those found in literature for other Moroccan CAMP basalts (1020-1170°C, **Bertrand, 1991**) and in Brazilian CAMP basalts (1130-1190°C, De Min et al., 2003). Only one augite-pigeonite pair yielded a much higher temperature, ca 1250°C. As showed hereafter, since crystallization pressures of the augites correlated with the pigeonites is always lower than 10 KBar and that the used geothermometer is fairly sensible to the pressure (the differences between high-P and low-P of the calculated equilibrium temperature

are in the 20-25°C range), all temperatures are calculated for a reference crystallization pressure of 5 KBar. As seen previously, in the Lower Unit crystallization

Sample	Fm	Loc	Aug comp.	Pig comp.	T (°C)	dT (°C)
AN49 pig2	Low 1	TJ - CHA	Wo36.9-En47.9-Fs14.7	Wo9.5-En60.8-Fs29.4	1056	9
OL10 cpx2	Interm 2	OL - CHA	Wo25.8-En55.4-Fs18.5	Wo10.2-En67.6-Fs22.1	1174	17
OL11 cpx2	Interm 2	OL - CHA	Wo31.1-En53.7-Fs15.1	Wo7.4-En70.3-Fs22.3	1102	31
OL11 cpx3	Interm 2	OL - CHA	Wo36.8-En51.4-Fs11.5	Wo8.2-En71.4-Fs19.8	1168	10
OL11 pig1	Interm 2	OL - CHA	Wo23.1-En54.4-Fs21.1	Wo9.4-En67.0-Fs23.2	1138	11
OL11 pig3	Interm 2	OL - CHA	Wo34.4-En48.4-Fs16.2	Wo9.2-En66.5-Fs23.8	1118	8
AN525B cpx2	Interm 2	AGR - MA	Wo31.6-En52.4-Fs16.0	Wo10.0-En69.3-Fs20.3	1246	10
AN540 cpx3	Upp	BAR - MA	Wo39.4-En48.3-Fs12.3	Wo7.98-En67.1-Fs24.9	1040	50

Figure 16.1: Equilibrium temperatures calculated for augite-pigeonite pairs with QUILF program (**Andersen *et al.*, 1993**). Fm and Loc are respectively Formation and sampling Locality.

of pigeonites occurs together with augites in the first flows (sub-unit Lower 1) of the CHA piles (Tiourjdal, Telouet and Oued Lahr) and in the last flow of the second sub-unit at Tiourjdal (sample TJ22, not analysed by EMP). For this unit, the temperature has been determined on sample AN49 pig2 which yielded 1056±9 °C (Tab. 16.1). Higher temperatures are found for the augite-pigeonite pairs of the Intermediate Unit (sub-unit 2) which is well represented, as described in the previous chapters, since pigeonite seems to be almost ubiquitous in the paragenesis of the basalts belonging to this sub-unit. Six temperature determinations have been possible, 5 in the range 1102-1174°C (for Oued Lahr, CHA) and one of 1246±10° C (Agourai, MA). The Upper Unit has only one determination on sample AN540 from the Oum R'Rbia section. The calculated temperature is relatively low, 1040±50 °C, even if the large error renders this temperature indistinguishable from those of the Intermediate Unit. A much more complete dataset has been obtained for augite crystallization pressure, by using the geobarometer of **Putirka *et al.* (1996, 2003)**, and clinopyroxene saturation temperature following **Putirka (1999)**. The main assumptions done by using this program are that the augites analysed were in equilibrium with the parental melt and that the corresponding whole-rock composition represents this melt. The crystallization pressures have been calculated only for the augite cores (some examples in Figs. 14.18 to 14.22), in particular for the cores with highest Mg# and Cr_2O_3 and lowest TiO_2 which should represent the most mafic and earliest crystallized portions of the minerals. However many problems have been encountered in applying the geobarometer, since the frequent and often very subtle sector zoning of the

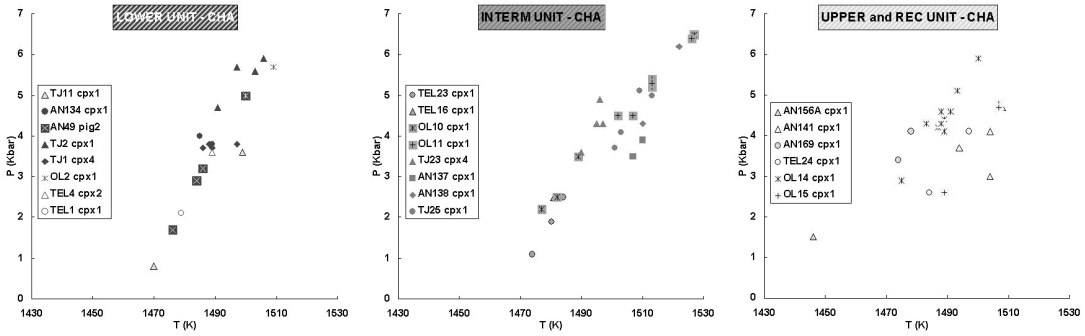

Figure 16.2: Crystallization pressure calculated with CPX-PLAG-OL THERMOBAR program (**Putirka, 1999; Putirka *et al.*, 2003**) for augite core of the CHA in equilibrium with the whole rock. Colours are blue for the sub-unit Lower 1, cyan for Lower 2, red for Interm 1, pink for Interm 2, yellow for the Upper Unit and green for the Recurrent Unit.

augites may induce disequilibrium compositions (**Shimizu, 1981**) in particular for Al_2O_3, Cr_2O_3 and TiO_2, so yielding a misleading pressure value. Globally,

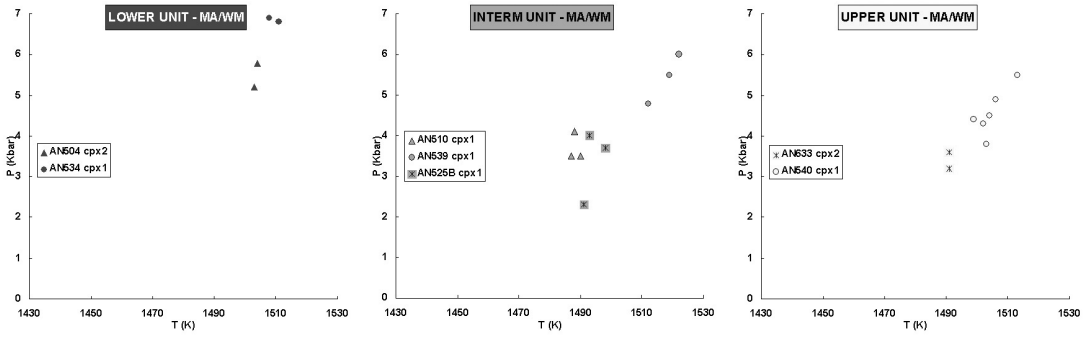

Figure 16.3: Crystallization pressure calculated with CPX-PLAG-OL THERMOBAR program (**Putirka, 1999; Putirka *et al.*, 2003**) for augite core of the NA/WM in equilibrium with the whole rock. Colours as above.

the geobarometer gives pressures varying from ca. 1 up to 7 KBar corresponding to upper to lower crustal depths for augite core composition (Fig. 16.1 and 16.2). The CHA basalts of the Lower and Intermediate Unit record an apparently wide polybaric crystallization history, with pressure values spanning between less than 1 KBar up to 6-6.5 KBar. Augites of the sub-unit Lower 1 and Interm 2 show a wider pressure range with respect to that of the sub-unit Lower 2 and Interm 1, which yielded 0.5-3.5 KBar and 3.5-6 KBar, respectively. It should be considered that the sub-unit Lower 2 is represented by only one sample (TJ11 with 2 analysed augite) and its pressure is thus poorly constrained. On the contrary, the sub-unit Interm 1 is well represented with 4 samples and 8 augites analysed,

thus suggesting a systematically higher crystallization pressure for the augites (and then of the hosting basalts) of this sub-unit compared to sub-unit Interm 2. The CHA Upper Unit yielded a similar pressure range, 2.5-6 KBar, as the Lower and Intermediate Unit, but lacks fairly low apparent pressure (<2.5 KBar), while the Recurrent Unit has the most shallow crystallization pressure (1 to 4 KBar). In the MA/WM, probably due to the low number of analysed augites, the three units show a narrower pressure range compared to that of the homologues of the CHA (Fig. 16.2). The Lower Unit (sub-group 1) has the highest pressure crystallization range (5-7 KBar). The Intermediate Unit (sub-group 2) has slightly lower pressures, between 2 and 6 KBar, while the Upper Unit basalt yielded between 3 and 5.5 KBar. In any case, it should be kept in mind that these crystallization pressures are associated with large errors (1.5-1.7 KBar, **Putirka *et al.*, 2003**) which could in part explain the wide pressure range shown above.

16.2 OXY-THERMOMETRY

Only sparse magnetite-ilmenite series oxides of the CHA Lower and Recurrent Unit basalts have been analysed to calculate fO_2 conditions. No data from MA/WM basalts are available. The use of ILMAT (**Lepage, 2003**) based on the empirical approaches given by **Andersen & Lindsley (1985)**, allows to calculate equilibrium crystallization temperature and the oxygen fugacity. For the

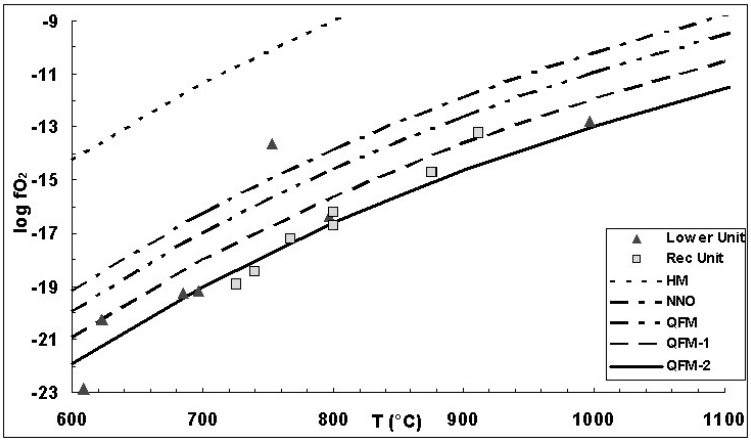

Figure 16.4: Crystallization temperature and oxygen fugacity calculated with ILMAT (**Lepage, 2003**) for magnetite-ilmenite pairs from the Lower Unit in different parts of Morocco and the Recurrent Unit from CHA.

Lower Unit we analysed different oxide pairs belonging to CHA, Eastern Meseta and Argana basalts (Tab. 16.1, courtesy of A. Marzoli), while for the Recurrent

	AN16	AN134	AN174 B	AN102	AN130	AN132	AN121	AN138 1	AN138 2	AN141_1	AN141_2	AN164_2	AN164_3	AN164_4	AN164_5a	AN164_5b	AN164_6	AN164_7	AN169 1	AN169 2	AN169 3	AN169 4	AN169 5	AN169 mi1	AN169 mi2	AN169 mi3	AN169 mi4	AN169 mi5
Ti-Mt	Marrakech	Agouim	Oujda	Alemzi	Taoguint	Nasserite	Alemzi	Agouim	Agouim	Agouim	Agouim	Telouet	Telouet	Telouet	Telouet	Telouet	Telouet	Telouet	Telouet	Telouet	Telouet	Telouet	Telouet	Telouet	Telouet	Telouet	Telouet	Telouet
SiO_2	0.23	0.14	0.11	0.26	0.12	0.06	0.27	0.17	0.13	0.16	0.26	1.72	0.15	0.74	2.71	1.50	0.30	1.56	0.05	0.15	0.26	0.15	0.22	0.05	0.14	0.26	0.14	0.21
TiO_2	24.80	28.55	22.69	20.02	23.86	2.78	6.16	28.64	28.37	20.28	15.80	24.69	23.18	22.82	23.15	23.18	23.47	24.17	23.72	26.02	25.98	22.97	26.12	23.05	25.04	25.08	22.07	25.29
Al_2O_3	1.85	1.74	1.08	2.32	1.53	7.19	0.62	1.57	1.60	1.67	1.83	1.81	1.93	1.83	1.91	1.98	1.91	2.99	1.64	1.03	1.40	1.33	1.34	1.59	0.99	1.35	1.28	1.30
FeOt	71.02	65.36	72.70	73.52	69.12	59.96	86.97	64.67	64.63	74.00	78.29	62.76	65.24	65.11	63.61	63.62	65.20	61.35	69.85	68.26	67.77	70.96	67.39	67.88	65.69	65.41	68.18	65.26
MnO	0.13	1.56	0.38	1.18	2.60	0.31	0.17	2.45	2.75	0.84	1.08	0.93	0.63	0.91	0.99	0.81	0.62	0.86	2.01	2.36	2.10	1.97	2.27	1.95	2.27	2.03	1.89	2.20
MgO	0.20	0.00	0.49	0.12	0.01	2.12	0.00	0.00	0.05	0.43	0.09	0.28	0.02	0.12	0.62	0.21	0.06	0.04	0.00	0.00	0.09	0.04	0.07	0.00	0.00	0.09	0.04	0.07
CaO	0.21	0.05	0.03	0.03	0.20	0.03	3.37	0.04	0.03	0.13	0.16	0.25	0.14	0.15	0.29	0.23	0.18	0.21	0.08	0.06	0.03	0.04	0.10	0.08	0.06	0.03	0.04	0.10
Na_2O	0.00	0.00	0.00	0.00	0.00	0.00	0.00	0.00	0.00	0.00	0.00	0.01	0.00	0.04	0.09	0.00	0.00	0.00	0.00	0.00	0.00	0.00	0.00	0.00	0.02	0.04	0.03	0.06
Cr_2O_3	0.00	0.00	0.03	0.07	0.07	25.08	0.02	0.00	0.00	0.02	0.03	0.10	0.05	0.04	0.06	0.05	0.11	0.01	0.15	0.03	0.02	0.08	0.07	0.15	0.03	0.02	0.08	0.07
Sum	98.44	97.48	97.51	97.52	97.51	97.55	97.58	97.54	97.56	97.53	97.54	92.56	91.54	92.75	93.44	91.77	91.85	91.18	97.50	97.91	97.64	97.54	97.58	94.74	94.24	94.30	93.75	94.56
Ulvospinel bases																												
Fe_2O_3	18.75	10.54	23.80	27.18	20.53	31.13	58.73	10.51	11.16	27.96	36.60	10.87	16.54	17.26	12.29	13.80	16.15	9.81	20.73	16.93	16.12	22.55	15.92	20.13	16.27	15.53	21.66	15.42
FeO	54.14	55.87	51.27	49.06	50.64	31.96	34.11	55.21	54.58	48.84	45.35	52.98	50.00	50.58	52.56	51.40	50.67	52.52	51.19	53.03	53.25	50.66	53.07	49.76	51.05	51.44	48.69	51.39
Sum	100.31	98.53	99.88	100.24	99.56	100.66	103.45	98.59	98.68	100.32	101.21	93.65	93.24	94.48	94.67	93.15	93.47	92.16	99.57	99.61	99.24	99.79	99.18	96.76	95.87	95.85	95.92	96.10
Ilm																												
SiO_2	0.22	0.09	0.03	0.11	0.14	0.02	0.25												0.25	0.08	0.02	0.06	0.05	0.58	0.08	0.02	0.06	0.05
TiO_2	50.19	50.22	50.48	50.26	50.03	46.50	48.34												49.48	50.09	51.11	49.36	51.62	50.21	50.22	51.11	49.59	51.94
Al_2O_3	0.11	0.04	0.01	0.02	0.03	0.11	0.37												0.07	0.00	0.06	0.14	0.04	0.07	0.00	0.06	0.14	0.04
FeOt	45.14	46.94	47.30	45.53	46.90	45.46	43.88												45.23	46.99	46.61	47.29	45.89	45.57	47.11	46.61	47.51	46.18
MnO	0.87	0.48	0.27	2.60	1.17	0.43	2.67												2.08	0.69	0.38	1.76	0.00	2.11	0.69	0.38	1.76	0.61
MgO	0.48	0.52	0.36	0.00	0.13	5.78	0.06												0.28	0.48	0.79	0.30	1.61	0.28	0.48	0.79	0.30	1.62
CaO	0.04	0.17	0.02	0.06	0.04	0.00	2.81												0.11	0.13	0.06	0.04	0.00	0.11	0.13	0.06	0.04	0.00
Na_2O	0.00	0.00	0.00	0.00	0.00	0.00	0.00												0.00	0.00	0.00	0.00	0.00	0.12	0.04	0.05	0.03	0.04
Cr_2O_3	0.08	0.00	0.00	0.00	0.02	0.15	0.10												0.01	0.03	0.07	0.05	0.00	0.01	0.03	0.07	0.05	0.00
Sum	97.13	98.46	98.47	98.48	98.46	98.45	98.48												97.50	98.48	99.11	99.00	99.21	99.06	98.77	99.16	99.48	100.38
Fe_2O_3	1.68	3.67	3.14	3.14	3.58	15.96	7.26												3.54	3.97	2.78	5.77	2.55	2.75	3.94	2.76	5.77	3.12
FeO	43.62	43.64	44.48	42.71	43.68	31.09	37.36												42.05	43.42	44.11	42.10	43.60	43.09	43.56	44.13	42.31	43.37
Sum	97.29	98.83	98.79	98.80	98.82	100.04	99.21												97.86	98.88	99.39	99.58	99.47	99.33	99.17	99.44	100.06	100.69
% Ulv.	70.81	82.29	64.65	57.85	68.40	9.25	17.98	82.59	81.64	57.94	45.57	77.96	72.63	70.91	73.04	73.55	73.30	78.44	67.82	74.40	74.93	65.85	75.23	70.19	76.61	76.81	67.60	77.43
% R203	1.88	3.58	3.03	3.05	3.51	14.94	7.57												3.55	3.84	2.81	5.77	2.46					
T (°C)	608.67	996.33	697.30	685.43	797.35	753.45	623.20												800.29	876.72	740.22	911.31	726.40	767.41	876.04	740.39	911.28	800.57
log f(O_2)	-22.86	-12.78	-19.16	-19.28	-16.37	-13.62	-20.27												-16.23	-14.69	-18.43	-13.24	-18.91	-17.18	-14.71	-18.43	-13.24	-16.71

Table 16.1: Crystallization temperature and oxygen fugacity calculated with ILMAT (**Lepage, 2003**) for magnetite-ilmenite pairs from the Lower Unit in different parts of Morocco and the Recurrent Unit from CHA.

Unit all points represented in Fig. 16.4 are from sample AN169 of the Telouet section, CHA. No data points are available for the Intermediate and Upper Unit, where only magnetites are detected (Tab. 16.1). As visible, magnetite-ilmenite pairs from the Lower Unit gives temperatures spanning a wide range, from 1000 to 600°C with most of them at oxygen fugacity corresponding to QFM-1 log unit and QFM-2 log unit buffer. Recurrent Unit oxides show a more narrow temperature range, from 920 and 720°C, but with similar oxygen buffer with respect to the Lower Unit. Except for a sample of the Lower Unit (AN132) which gave quite high fO_2, all the oxide pairs analysed have very low fO_2.

16.3 WATER CONTENT

As described in the previous chapter, no hydrated minerals as biotite or amphibole do occur in the paragenesis of basalts from CHA and MA/WM. This could be due to different causes: too high magma temperatures, a low water activity in the parental magma not high enough to crystallize these minerals or alternatively decompression phenomena which allow decreasing of water pressure in the magma during its differentiation, so preventing crystallization of hydrous minerals. One way to constrain the water content is by evaluating the Ca-Na exchange between plagioclase and basaltic liquid in terms of $K_D{}^{Ca-Na}$ defined as $(Ca/Na)_{plg}/(Ca/Na)_{liq}$ (**Sisson & Grove, 1993**). In the chapter relative to the mineralogical composition of plagioclases (Chap. 9), it was described that plagioclase of the Lower Unit, both in the CHA and MA/WM, are nearly in equilibrium with the whole rock, supposedly representing the parental magma. $K_D{}^{Ca-Na}$ plagioclase cores have values between 1.1 and 1.2 (or slightly higher Fig. 9.4), this meaning that the cores are nearly in equilibrium with the whole-rock for almost dry conditions (H_2O ¡ 0.50 wt%) at low crustal pressure (1-2 KBar or less). The modeling of the crystallization process with the PETROLOG program (**Danyushevsky, 2001**, see below) confirms the low water content and the relatively low crystallization pressure of the low-An plagioclase of the Lower unit (Fig. 15.7). Also equations:

$$\ln An = \frac{927.91}{T(K)} - 0.86298 - 0.02693 \times \frac{P(bar)}{T(K)} + 0.01674 \times H_2O(wt\%) \quad (16.1)$$

$$\ln K_D^{Ca-Na} = \frac{10695}{T(K)} - 6.7781 - 0.1009 \times \frac{P(bar)}{T(K)} - 0.00860 \times H_2O(wt\%) \quad (16.2)$$

from **Takagi *et al.* (2005)**, confirm this hypothesis requiring for a $K_D{}^{Ca-Na}$ =1.2-1.3 and Ca# content up to 74 for the plagioclase core, crystallization pres-

sure of ca. 1-2 KBar or even lower. Moreover the low oxygen fugacities calcu-

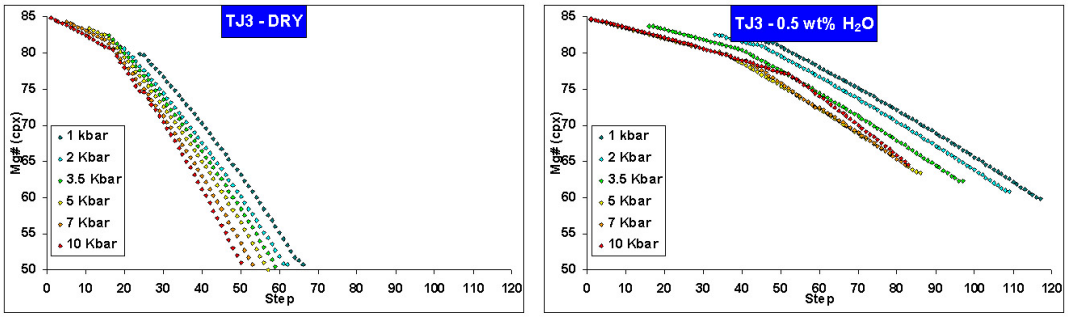

Figure 16.5: Augite composition variations (Mg#) for calculated fractionation trends at dry (left) and wet conditions (H_2O 0.5 wt%, right) at different pressures of sample TJ3, taken as representative of the Lower Unit basalts. Calculation performed with PETROLOG program (**Danyushevsky, 2001**).

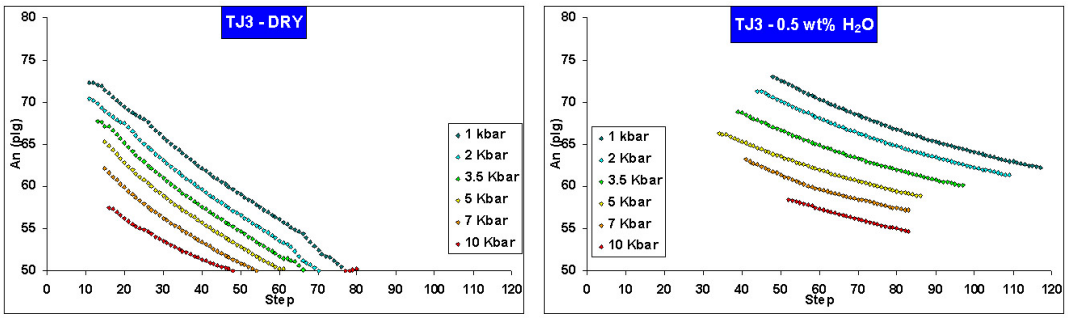

Figure 16.6: Plagioclase composition variations (An mol%) for calculated fractionation trends at dry (left) and wet conditions (H_2O 0.5 wt%, right) at different pressures of sample TJ3, taken as representative of the Lower Unit basalts. Calculation performed with PETROLOG program (**Danyushevsky, 2001**).

lated for the oxides of the Lower Unit (Fig. 16.4) confirm the low water content, since a higher H_2O activity should have increased the oxidizing conditions of the magma. On the other side, it is possible to infer higher crystallization pressures for plagioclase of the Lower Unit at Oued Lahr, where the very low An content (62-64, Fig. 9.7) and the low estimated water content (ca. 0.5 wt%) would suggest pressure in the 5-7 KBar range. The situation for the Intermediate Unit basalts is more complicated. First of all due to the observed textural features, that, although similar in paragenesis to the Lower Unit rocks, display an inequigranular texture, with euhedral to sub-euhedral big augites, elongated idiomorphic laths of plagioclase showing multiple inverse rhythmic zoning, with

rounded core and frequent brownish glassy patches included within the plagioclase crystals, altogether surrounded by a network of little euhedral plagioclase showing an acicular shape with normal zoning and poikilitic augites. Olivines

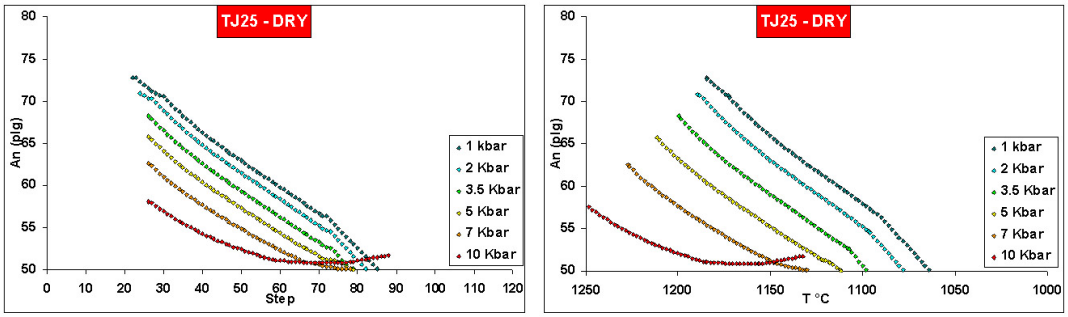

Figure 16.7: Plagioclase composition variations (An mol%) for calculated fractionation trends at dry conditions at different pressures of sample TJ25, taken as representative of the Intermediate Unit basalts. Calculation performed with PETROLOG program (**Danyushevsky, 2001**).

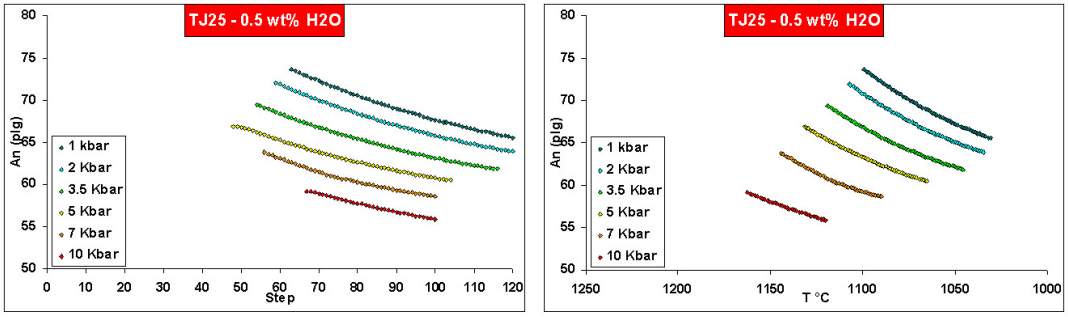

Figure 16.8: Plagioclase composition variations (An mol%) for calculated fractionation trends at wet conditions (H_2O 0.5 wt%) at different pressures of sample TJ25, taken as representative of the Intermediate Unit basalts. Calculation performed with PETROLOG program (**Danyushevsky, 2001**).

are absent (except for few samples) while remarkable is the presence of pigeonite. All these informations tell us a complex history of the Intermediate Unit parental magmas, where in the EMPA plagioclase compositions (Figs. 9.9 and 9.10) it is possible to read magma mixing events and multiply decompression phenomena. For the Intermediate Unit plagioclases $K_D{}^{Ca-Na}$ varies from 1.1 up to 2 and more (Fig. 9.4), and most of them seem to be in disequilibrium with the whole rock. In the chapter relative to the EMPA compositions, it has been noted that some plagioclase crystals display reverse multi-zoning with abrupt An jump up to 10

mol% or more. However most of these An-compositional variations apparently do not reflect magma mixing, since no variations in MgO and K_2O content are detected in the plagioclase (cf. EMP transect in Chap. 9). Neither increasing water content in the melt is sufficient to explain these An variations, as visible in Figs. 16.7, 16.8 and 16.9. I modeled with PETROLOG the fractionation trend of a basaltic melt with starting composition corresponding to sample TJ25, with different water content (dry, 0.5 and 1 wt%) and at different pressures. It results clearly that, as for Lower Unit basalts, the increase of water content shifts the beginning of plagioclase crystallization at lower temperatures at decreasing pressures and forces the plagioclase to appear earlier at middle pressures with respect to high or low pressures (Fig. 16.8 and 16.9). Differently from water, it is the pressure to exert a stronger control on An plagioclase content as visible in Figs. 16.7, 16.8 and 16.9, increasing up to 8-9 mol% passing from middle-high to sub-superficial pressures. So it is possible to think that a magma pooling at middle-high crustal depth with low water content (and so in under-saturated condition), after a certain amount of fractional crystallization of anhydrous minerals can ascend towards shallower depth and the combined effect of the increasing water and quick decompression enhances crystallization of high-An plagioclase portions (**Panjasawatwong *et al.*, 1995**; **Berndt *et al.*, 2005**; **Feig *et al.*, 2006**). The wide occurrence of pigeonite in most of the Intermediate Unit basalts is more difficult to explain. PETROLOG fails to crystallize pigeonite in every simulation done, both at high and low pressure with dry conditions. Unfortunately PETROLOG allows to simulate fractionation trends in wet conditions only with olivine, augite and plagioclase. At dry condition, the main low-Ca pyroxene is orthopyroxene, that does not appear in the studied samples. The lack of orthopyroxenes in the Moroccan basalt paragenesis could be related to the suppression at high pressure of the reaction point between olivine and silicatic melt yielding orthopyroxene. Crystallization of pigeonite could be enhanced by rapid decompression phenomena in the ascending melt, since the widening of stability plagioclase field at shallow depth and consequent lowering of CaO activity in the melt could stabilize pigeonite. On the other side it is more probable that PETROLOG simulation require different starting compositions from those used here, consequently modifying the simulated liquid line of descent. Concluding, even for most of Intermediate Unit basalts it is possible to envisage a polybaric differentiation history, as highlighted from the wide range of crystallization pressures obtained on augites, with variation in water content exerting a strong effect on the sequence of the crystallizing phases and on their compositions (especially

for plagioclases).

The Upper Unit plagioclases have the highest K_D^{Ca-Na} (about 1.5 to 2, mostly) with the highest value observed in a sample (OL14) which displays Ca# up to 88.8 with at whole-rock Ca# of 64.7 (Fig. 9.4). As described in the

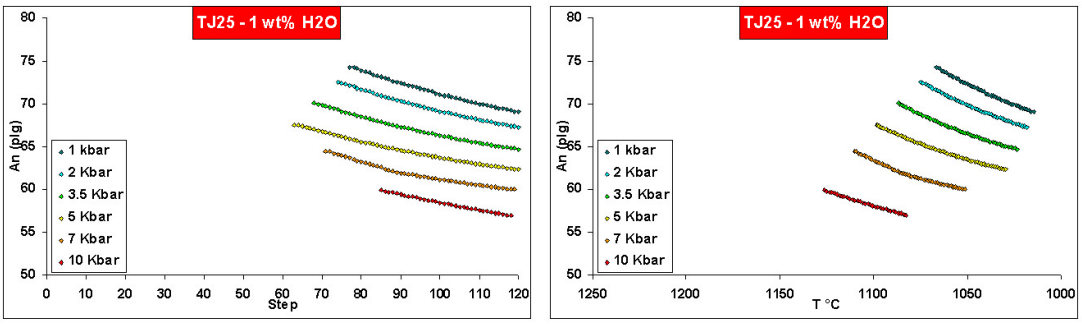

Figure 16.9: Plagioclase composition variations (An mol%) for calculated fractionation trends at wet conditions (H_2O 1 wt%) at different pressures of sample TJ25, taken as representative of the Intermediate Unit basalts. Calculation performed with PETROLOG program (**Danyushevsky, 2001**).

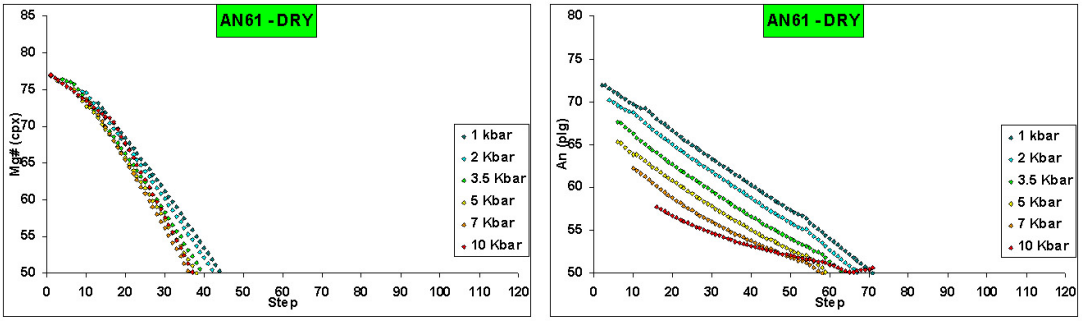

Figure 16.10: Augites (Mg#) and plagioclases (An mol%) composition variations for calculated fractionation trends at different pressures of sample AN61, taken as representative of the Recurrent Unit basalts. Calculation performed with PETROLOG program (**Danyushevsky, 2001**).

chapter relative to the mineralogical composition of mineral phases, it results that both Upper Unit plagioclases and augites crystallized from a little evolved magma (cf. the high MgO and low FeO/MgO and TiO_2 in plagioclase and high Mg# and Cr_2O_3 in the augites). Since none of the analyzed minerals seems to be in equilibrium with the whole-rock, I did not perform any simulation with PETROLOG and no water content has been estimated using equations of **Takagi *et al.* (2005)** presented above.

The K_D^{Ca-Na} plagioclase of the Recurrent Unit basalts have values near 1 and the low An plagioclase compositions revealed by EMPA analyses, suggest very low water contents or dry conditions, also supported by the low fO_2 calculated for magnetite-ilmenite pairs (Fig. 16.4). PETROLOG calculations for dry conditions support this hypothesis as visible in Fig. 16.10, where the calculated augite and plagioclase compositions (Mg# and An mol% respectively) match very well those measured by EMPA on the same phases belonging samples AN156A and AN169 (Figs. plgs and cpxs AN156A and AN169) for crystallization pressure not higher than 3.5-4 KBar. Fig. 16.10 also shows that the plagioclase stability field is expanded with respect to those of augite and olivine that fit well with the observed paragenesis dominated by plagioclases and scarce pyroxenes and olivines.

16.4 MINERAL PHASE TRACE ELEMENT COMPOSITIONS

In the previous paragraph on the base of petro-mineralogical evidences and some calculations with PETROLOG, I showed that augites and plagioclases of the Lower and Recurrent Unit are probably in equilibrium with the host rock (supposedly representing the parental melt of these minerals), while those of the Intermediate and Upper Unit seem to be in disequilibrium with the whole-rock. One way to further constrain these hypotheses is to investigate the trace element compositions of the melt in equilibrium with both augites and plagioclases. By knowing concentrations C_{ph}^i and the distribution coefficient (K_D^i) of trace element for both minerals, it could be possible to calculate the concentrations ${C_{melt}}^i$ of the same element for the melt in equilibrium with minerals by:

$$C_{melt}^i = \frac{C_{ph}^i}{K_D^i} \tag{16.3}$$

and then to compare them with the whole rock trace element compositions. In the Chap. 11, I described augites and plagioclases trace element compositions obtained by LA-ICP-MS technique. As said previously, trace element measurements have been performed on few minerals of each unit and only for the Tiourjdal sequence, and because of the highlighted problems of the LA-ICP-MS technique (i.e., few analysis spots on each mineral, concentrations averaged on a 40 μm spot size, often zoned minerals, no analyses on the vitreous groundmass) the following considerations are qualitative. Another tricky problem is the choice of the K_D^i. Determination of trace elements partition coefficients between crystal and silicate melts is a critical problem in igneous petrology since, in principle, it

allows to constrain the origin of the magma from which rocks are derived. However, after years of experimental measurements it has become clear that partition coefficients are strongly influenced by pressure, temperature, fO_2, water content, mineral and melt compositions and at present there is no satisfactory theory that takes into account all these variables, thus resulting in limited K_D^i dataset, for specific mineral-melt pairs, compositions and environmental conditions of the melt. In the past, the simplest way to obviate this problem was to admit a constant K_D^i, even if this could mean to ignore compositional effects during differentiation processes, i.e. during fractional crystallization. In the following, I will show some trace element diagrams for an hypothetical melt in equilibrium both with augites and plagioclases. For the former, I used the constant K_D^i dataset of **Hill *et al.* (2000)**. For the latter, I used two different approaches: in the first I used constant partitioning coefficient after **Aigner-Torres *et al.* (2007)**, while in the second, I used the partitioning compilation obtained with a K_D^i semi-empirical parameterization from **Bedard (2006)**. The equations used for the parameterizations are calibrated for SiO_2 in plagioclase content. Unfortunately, since analysed plagioclases display very low concentration for most trace elements (details in Chap. 11), it is possible to compare them with augites only for few elements. In the following I will use Ce, Eu, Y (as proxy for HREE) and Sr to infer if both augites and plagioclases are in equilibrium with whole rock and to obtain some info about melt composition equilibrated with these minerals.

Ce vs Ce/Y diagrams for the whole rocks and melt in equilibrium with augites ($melt_{aug}$)(Fig. 16.11) are nearly identical. The four units are different from each other having Ce and Ce/Y of the equilibrated melt systematically lower with respect to those of the whole-rocks (Fig. 16.11). This could mean that 1) augites crystallized from a less evolved melt with lower Ce (and higher Y), thus being not in equilibrium with the whole rock or 2) the K_D set used here ($K_D^{Ce} = 0.148$ and $K_D^Y = 0.64$, **Hill *et al.* (2000)**) are not appropriate. In Fig. 16.12, Ce and Ce/Y are shown for melt in equilibrium with plagioclases ($melt_{plg}$), calculated using constant K_D ($K_D^{Ce} = 0.046$ and $K_D^Y = 0.008$) after **Aigner-Torres *et al.* (2007)** and K_d parameterized against SiO_2 plagioclase content (and fixed temperature at 1250 °C) after **Bedard (2006)** (eqs. 42b and 50b for Ce and Y respectively). The four units are roughly distinguished among them even if data points are scattered due the low Ce and Y concentration in plagioclase. The two K_D datasets result in slightly different calculated melt compositions, in particular Bedard's partition coefficients result in slightly lower Ce and Y melt values. By contrast, the partition coefficients of Aigner-Torres et al. allow a better distinction among the four

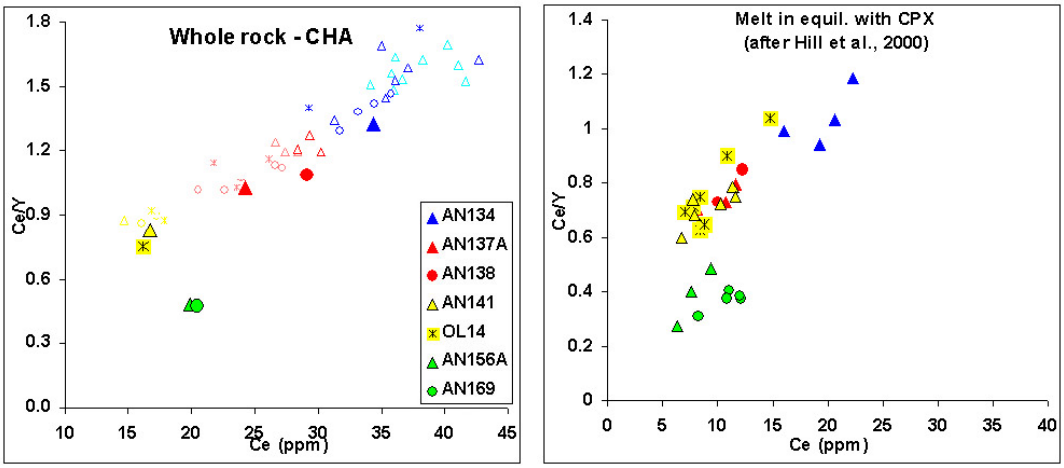

Figure 16.11: Ce vs Ce/Y diagrams for whole rocks (on the left) and for the calculated melt in equilibrium with augites after Hill et al., 2000 (on the right). In the CHA whole rocks diagram are highlighted the samples analysed by LA-ICP-MS. Blue for the Lower Unit, red for the Intermediate Unit, yellow for the Upper Unit and green for the Recurrent Unit.

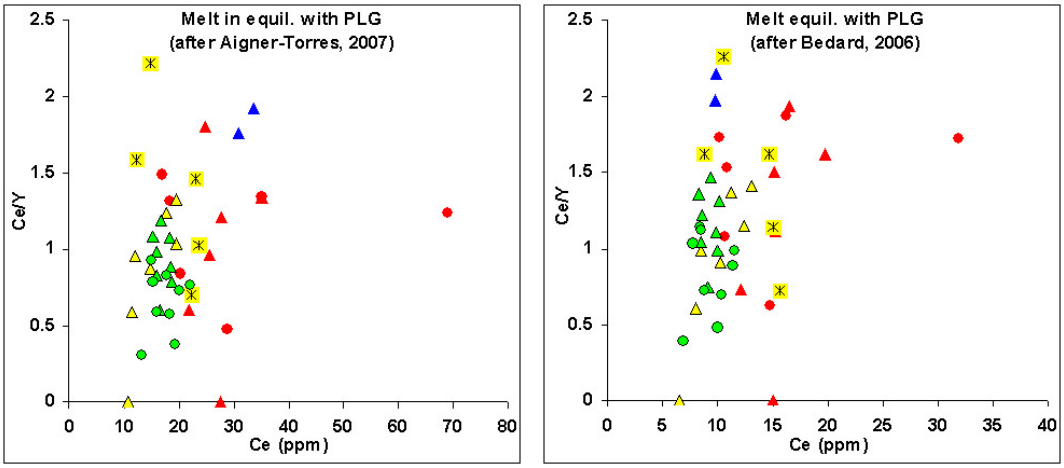

Figure 16.12: Ce vs Ce/Y diagrams for the calculated melt in equilibrium with plagioclases after **Aigner-Torres *et al.* (2007)** (on the left) and after **Bedard (2006)** (on the right). Colours as above.

units. Using the constant K_Ds (**Aigner-Torres *et al.*, 2007**), the calculated Ce of melt$_{plg}$ is comparable with Ce of the whole rock, but higher than that in melt$_{aug}$ while Ce/Y is roughly comparable or higher with respect to whole-rock and much higher compared with augite, although values are heavily scattered. This could suggest an earlier crystallization of augite compared to plagioclase (Fig. 16.11). If we consider instead the K_D of Bédard, Ce of melt$_{plg}$ is comparable with that of melt equilibrated with augite, whereas it is lower compared with the whole rock. Moreover Ce/Y is higher than both whole rock and melt$_{aug}$, thus implying low Y contents. However, it should be highlighted that the low Ce and Y content in the plagioclase (less than 2 ppm) and thus relatively large analytical errors, coupled with low partition coefficients in plagioclase (ca. 0.02 and 0.008 for Ce and Y, respectively) leads to large uncertainties of the calculated equilibrium melt. An interesting feature common to both K_D plagioclase modellization is that Recurrent melt$_{plg}$ have Ce/Y values higher compared to those of augites, even if quite scattered. Since Ce content is comparable in both minerals, this suggest roughly contemporaneous crystallization of augite and plagioclase in Recurrent basalts.

Another suitable element is Sr, since its compatibility in plagioclase and consequent depletion in the residual melt during plagioclase crystallization. By calculating Sr composition of melt in equilibrium with mineral phases it is possible to recognize earlier plagioclase crystallization and fractionation. Ce vs Sr of melt$_{aug}$ (Fig. 16.13) and melt$_{plg}$ (Fig. 16.14) display clearly distinct compositions for the four units and display strong similarities with to whole rock data, although differently from whole rock the Intermediate and Upper Unit have overlapped compositional fields. Sr content in the melt$_{aug}$ displays quite scattered values ($K_D^{Sr} = 0.063$, **Hill *et al.*, 2000**), i.e. great variation between phenocryst core and rim and so it is difficult to say if augites are in equilibrium with whole rock. Despite this, Sr content in the melt$_{aug}$ displays a behaviour compatible with earlier augite crystallization with respect to plagioclase, since melt$_{aug}$ of most analysed augite cores have higher Sr contents than rims. Since Sr is incompatible in augite, it should increase its content in the melt in equilibrium, unless plagioclase crystallization fractionate it. Also for Sr, there is a clear difference between melt$_{plg}$ calculated with constant ($K_D^{Sr} = 1.6$, **Aigner-Torres *et al.*, 2007**) and parameterized K_d, using eq. 19a of **Bedard (2006)** (Fig. 16.14). Differently from augites, Sr variations within plagioclases are narrower. Using constant K_D, only Recurrent Unit plagioclases seem to be in equilibrium with the host whole rock, while the Lower, Intermediate and Upper Unit plagioclases yield slightly different calculated Sr compositions compared with whole rocks. On

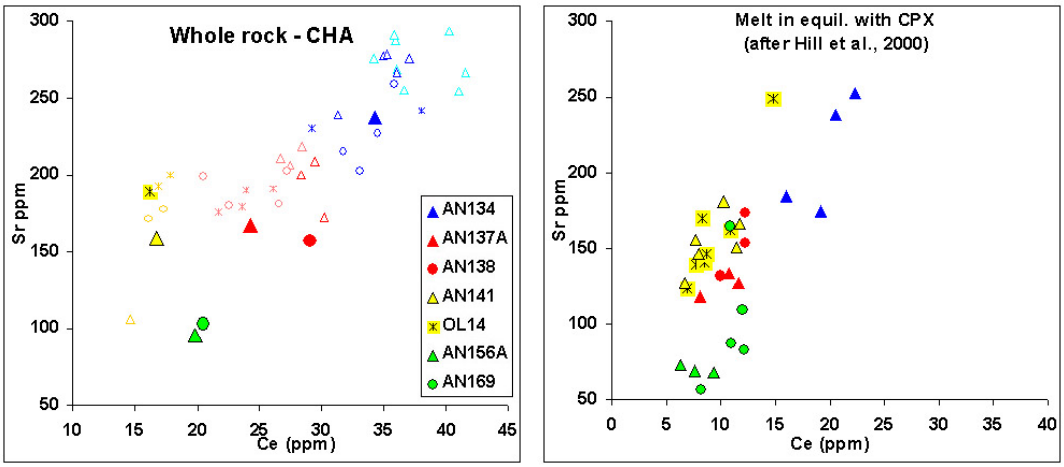

Figure 16.13: Ce vs Sr diagrams for whole rocks (on the left) and for the calculated melt in equilibrium with augites after **Hill *et al.* (2000)** (on the right). In the CHA whole rocks diagram are highlighted the samples analysed by LA-ICP-MS. Colours as above.

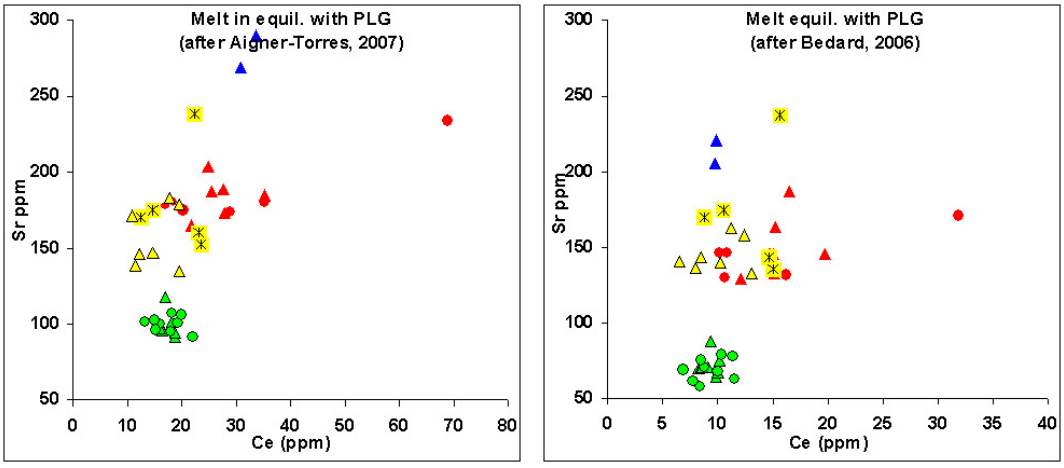

Figure 16.14: Ce vs Sr diagrams for the calculated melt in equilibrium with plagioclases after **Aigner-Torres *et al.* (2007)** (on the left) and after **Bedard (2006)** (on the right). Colours as above.

the contrary, using Bédard's parameterization, all minerals analysed have lower Sr content than whole rock. Since Sr is not compatible in augite and almost all Sr bulk rock content is yielded by plagioclase, the lower Sr concentration in the equilibrated melt using **Bedard (2006)** is probably wrong.

Sr/Eu of calculated melt in equilibrium with augites are higher than those of whole rock, due to the low Eu content in phenocrysts (Fig. 16.15). Although Eu is nearly compatible in clinopyroxene ($K_D^{Eu} = 0.75$, **Hill *et al.*, 2000**), its low concentration could be due to an earlier augite crystallization in a little evolved melt. The Eu vs Sr diagram shows that for an almost constant Eu, Sr decreases from the Lower to Recurrent Unit, maybe indicating a increasing contribution of plagioclase crystallization during melt differentiation. Eu and Sr/Eu in $melt_{plg}$

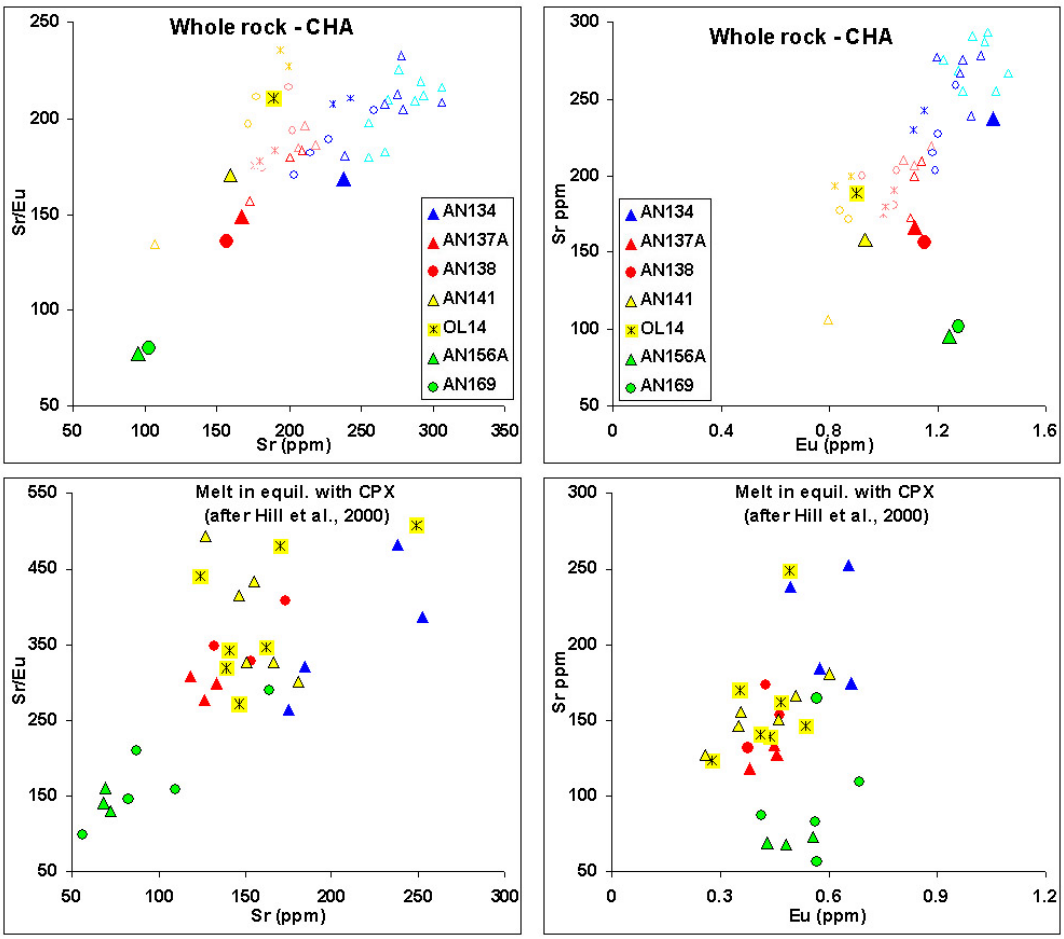

Figure 16.15: Eu vs Sr (above) and Sr vs Sr/Eu (below) diagrams for whole rocks (on the left) and for the calculated melt in equilibrium with augites after **Hill *et al.* (2000)** (on the right). In the CHA whole rocks diagram are highlighted the samples analysed by LA-ICP-MS. Colours as above.

show strong variations depending on applied K_D as visible in Fig. 16.16. Using constant K_D ($K_D^{Eu} = 0.91$, **Aigner-Torres *et al.*, 2007**), for Sr content similar to those of the whole rock, melt Eu concentrations are lower than whole rock and comparable to those calculated for $melt_{aug}$. Sr/Eu is consequently higher than both $melt_{aug}$ and whole rock. Sr/Eu of the Lower and Recurrent units in Fig. 16.16, are roughly comparable with the same ratio obtained from augites, while the Intermediate and Upper Unit display wider Sr/Eu variation ranges compared to Sr variations. Since both these elements are compatible in plagioclase this could be due to Eu compatibility variation which in turn could be related to fO_2 variations, although difficult to explain, during plagioclase crystallization. On the contrary, with the Bedard K_D (eq. 46b, **Bedard, 2006**) melt Eu is higher than whole rock, with Sr/Eu extremely low compared not only with $melt_{aug}$ but even with the bulk rock. Although the Bédard parameterization should result more realistic than using constant K_D, it yields results hardly explainable, at least for the Sr-Eu pair.

16.5 CRYSTALLIZATION ORDER

To define the order and crystallization conditions of the CAMP Moroccan basalts, besides the petrographic observations of relationships among mineral phases, EMP analyses and the previously described constraints on T, P, fO_2 and water content, I used the PETROLOG program, which performs modeling of magma fractionation at variable H_2O contents and P. This program models fractionation trends of a basaltic melt from a starting composition (in major and minor elements), water content and pressure (**Danyushevsky, 2001**). To simulate fractionation trends and to estimate what phases are involved during differentiations (i.e. what minerals fractionate) and drive the composition of basalts, I used as starting composition for each unit, the less evolved basalt, with the highest Mg#, Cr and Ni content and with the lowest TiO_2 and $L.O.I._{tot}$ possible. Then, I tried to simulate for different water contents (i.e., 0.1, 0.2, 0.5, 1 and 2 wt% and dry conditions) and with pressure values consistent with those calculated with the Putirka geobarometer on augites (1, 2, 3.5, 5, 7 and 10 KBar), in order to define what is the near-liquidus crystallization sequence. Unfortunately, as said before, PETROLOG simulates fractionation trends in wet conditions with olivine, augite and plagioclase as liquidus phases, only. At dry conditions PETROLOG can simulate the crystallization and the compositional evolution of 8 phases including residual melt: spinel, olivine, orthopyroxene, augite, plagioclase, pigeonite,

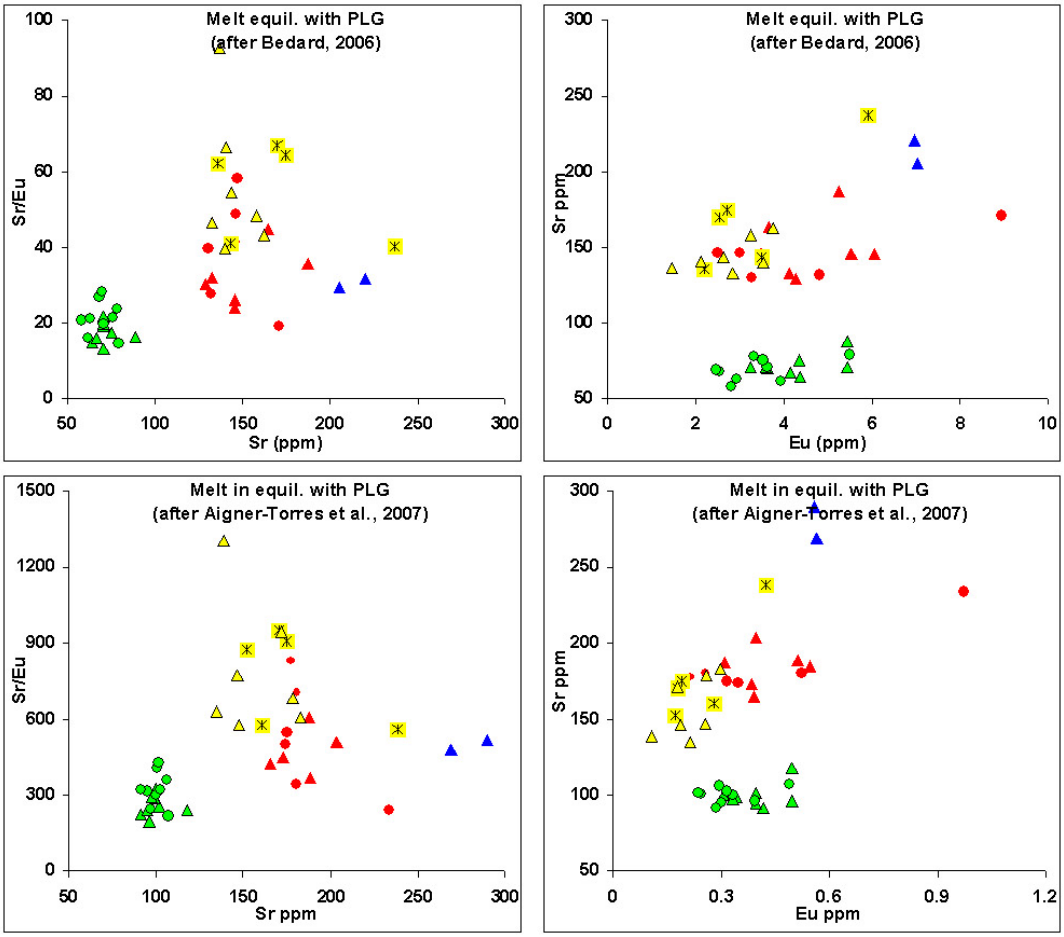

Figure 16.16: Eu vs Sr (above) and Sr vs Sr/Eu (below) diagrams for the calculated melt in equilibrium with plagioclases after **Aigner-Torres *et al.* (2007)** (on the left) and after **Bedard (2006)** (on the right). Colours as above.

ilmenite, and magnetite. In the Lower Unit, almost all olivines, even if altered, have euhedral shape like augites and are modally little important. So it is possible to think that earlier olivine fractionation was important, as highlighted in the whole rock geochemistry descriptions (Chap. **??**). Augites show well shaped and big size (>500-600 μm) phenocrysts with no olivines and (few) plagioclases enclosed within. Plagioclases have nearly constant and relatively little dimensions (<400-500 μm), thus probably indicating that they begun to crystallize more or less at the same time. Taking in account all these informations it is possible to think that olivines was the first crystallizing phase, followed by augite and finally by plagioclase. Considering An content, plagioclases could have crystallized at lower pressure compared to augites (cf. PETROLOG data, see above) in a melt with low water content (see previous section) (Fig. 16.6). All these information, together with the relatively high crystallization pressure inferred for augite cores (calculated after **Putirka *et al.*, 2003**) and the supposed low water content, match well with what found in literature about the near-liquidus crystallization sequence of a tholeiitic basalt at mid-high crustal pressure (5-7 KBar) (**Danyushevsky *et al.*, 1996**; **Danyushevsky, 2001**), where the high initial crystallization pressure enhances the stability field of pyroxene compared to olivine. A small amount of water together with relatively high pressure suppresses plagioclase crystallization, that appears at liquidus for the Lower Unit basalts only at low pressure (cf. An content from PETROLOG). As said before, in some flows belonging to the Lower Unit, pigeonite appears together with augite. Dry or poorly hydrous conditions are probably required for significant pigeonite crystallization (**Baker & Eggler, 1987**) and EMPA analyses suggest that pigeonite follows augite in the crystallization sequence but precedes the oxides. In fact the low pigeonite Cr_2O_3 concentration indicates that, before its crystallization, occurred important augite crystallization, while the TiO_2 increasing of at decreasing Mg# indicates that the melt was not yet saturated in oxides when pigeonite was crystallizing. Low equilibrium temperature on the augite-pigeonite pair of Lower basalt AN49 confirms the late appearing at liquidus of pigeonite (Fig. 9.28). Finally the oxides, present in the glassy groundmass or between other phases with allotriomorphic habitus, join the assemblage in a late stage as witnessed by low crystallization temperature found with QUILF. EMP analyses on augites confirm this, since it was showed in Chap. 9 that TiO_2 in augite increases as clinopyroxene evolves, then decreases for Mg# as low as 65, when the equilibrium melt probably saturated with respect to oxides. In the Intermediate Unit basalts the crystallization sequence is nearly the same, even if the situation

is complicated by different factors as explained before. In fact in the Intermediate Unit samples are present two kind of plagioclase phenocrysts. The first represented by big (>600 μm) roughly euhedral phenocryst with frequent rounded core with glassy patches enclosed within and showing inverse An-zoning. The An core content suggest that crystallized more or less at middle crustal depth (4-5 KBar, Fig. 16.8). The second kind of plagioclase have more little size (<200-300 μm), An normal zoned and no rounded core or glassy inclusion. These informations maybe record at least two plagioclase crystallization phases, in which the big ones begun to crystallize early in a slightly wet melt. A rapid ascent (decompression phenomena) of the melt make plagioclases in disequilibrium with the hosting magma, creating rounded cores and let melt drops enclosed in the mineral and at the same time increasing An content of the new crystallizing plagioclase around the old core. The An uncorrelated and decreasing MgO plagioclase content (Chap. 9) could confirm this hypothesis. In some samples augites precedes plagioclase crystallization, being favored by the higher pressure (6-7 KBar, sample AN137A, Fig. 16.2). Pigeonite crystallization is probably successive to that of pyroxenes (see the low equilibrium temperatures of augite-pigeonite pairs, Tab. 16.1) but preceding that of oxides, since TiO_2 increases both in evolving augites and pigeonites. Finally oxides join the assemblage in the late stage of differentiation. Textures of Upper Unit basalts are porphyric with big euhedral augites, few plagioclases and rare olivine phenocrysts. Major and minor element compositions indicate that both augites and plagioclases have crystallized from a melt with a less evolved composition with respect to that of the whole rock (Chap. 9). Augites crystallized mostly at middle crustal depth (4-5 KBar) with few sample at higher or lower pressure. Successive magma batches (unfortunately trace elements on plagioclases and augites can not constraint if with slightly different compositions) could have transported these phenocrysts towards surface. Petrographic inspection of the Recurrent Unit basalts has showed that the paragenesis in dominated by big euhedral plagioclase phenocrysts with only minor and rare augites plus altered olivines and oxides of magnetite-ilmenite series in a microlithic groundmass. It is difficult to say what was the first phases to appear at liquidus, but plagioclase crystallization is very important compared to that of augites which are modally less important. An plagioclase and Mg# augite compositions calculate with PETROLOG (Fig. 16.10) indicate that both minerals crystallize at middle-low crustal depth (2-4 KBar), as confirmed by the quite low augite crystallization pressures (Fig. 16.2). In the plagioclase EMPA analyses (e.g. AN169 plg1, Figs. 9.19) are recorded an An and MgO content increase,

just before the rim phenocrysts. This could record a possible magma mixing event with a less evolved magma prior the ascent to the surface and subsequent emplacement. Finally only at low temperatures oxides begun to crystallize (Fig. 16.4).

17 CONCLUSIONS

The Central Atlantic Magmatic Province (CAMP), one of the largest Mesozoic continental flood basalts (CFBs) recognized on the planet, covers an estimated (and conservative) surface of more than 10^7 km^2 over four continents in the circum-Atlantic domain. Mainly represented by sills and dikes with few and poorly preserved relatively thin lava flow sequences in Paleozoic-Mesozoic sedimentary basins, CAMP emplaced along old Ercynian-Alleghenian sutures, inherited from the Pangaea building and re-activated in the extensional regime of pangean rifting in Late-Triassic time, and in circum-cratonic areas around the newly forming Atlantic Ocean. The magmatic activity spanned ca. 10 Ma, with a main peak occurred at 199-200 Ma (mostly $^{40}Ar/^{39}Ar$ ages) preceding by few million years the initial opening of the Central Atlantic ocean. Two less important and voluminous peaks occurred at ca. 195 and 192 Ma. The close occurrence of the 199-200 Ma magmatic peak with one of the most important Phanerozoic biotic crises which marks the Triassic-Jurassic boundary, arises the possibility that this biological turnover is related to the CAMP event. In Morocco, north west Africa, CAMP occurs mainly in middle-late Mesozoic syn-depositional sedimentary basins, as lava flows and minor sills and dikes intruding Palaeozoic basement. The volcanic lava flow sequences reach maximum thickness (up to 300 m) in the central portion of the High Atlas chain, while progressively thinner volcanic sequences are present in the distant Moroccan provinces (i.e. Oujda Mountains) or more eastward in the Algerian Atlas. Three lava piles in the Central High Atlas chain (Tiourjdal, Telouet and Oued Lahr sections), partially studied in previous works, are here studied in detail flow by flow and compared to three new lava sequences in the Moroccan Western Meseta (Maaziz section) and the Middle Atlas (Agourai and Oum R'Rbia sections) sampled flow by flow for geochemical and magnetostratigraphic studies. Volcanic sequences are composed of variable number of flows (up to 34 in the most complete Tiourjdal section), with rarely interbedded sedimentary layers, testifying the brevity of the magmatic event. Major (TiO_2) and trace elements (LREE/HREE and LILE/HFSE) allow recognizing systematic time-related compositional variations within lava

piles and definition of four main chemostratigraphic units. From the base to the top of the lava piles following units are defined: the Lower, Intermediate, Upper Unit (present in most studied lava sequences) which are associated with the main magmatic peak, while a fourth group, the Recurrent Unit, is associated with a second younger (ca. 196 Ma) and less voluminous magmatic event preserved in the Central High Atlas basins only. The volcanic rocks mainly consist of quartz normative tholeiitic basaltic andesites and few basalts, with petrographic, mineralogical and geochemical features resemble those of other CAMP low-Ti rocks. Basaltic andesites present textures from hypocrystalline intergranular to sub-ophitc and porphyric with a paragenesis dominated invariably by plagioclase, augitic pyroxene, minor (locally important) pigeonite, Fe-Ti oxides and (always altered) olivine. No hydrated minerals (biotite and hornblende), zircons or apatites have been observed, as is compatible with the little evolved character of the basalts. Although sometimes heavily weathered, whole-rock compositions are characterized by higher SiO_2, K_2O and TiO_2 compared to N-MORB. They are enriched in LREE and LILE with respect to HREE and HFSE and have negative Nb-Ta_{PM} anomaly, typical of CAMP rocks (with few exceptions) as of other LIPs (Large Igneous Provinces), negative Sr_{PM} anomaly and variable Pb_{PM} anomaly, maybe linked to remobilization by fluids during post-magmatic processes. The few Sr-Nd isotopic data available for the studied rocks indicate variably enriched compositions for the older units, while a more depleted astenosphere-like character characterizes the younger Recurrent Unit. Simple computer modelling on whole-rock composition variations suggests a complex polybaric differentiation history in lower to relatively shallower crust magma chambers at relatively low temperature (1150-1200 °C), H_2O contents (< 2wt%) and fO_2 (QFM-1 to QFM buffers). At middle-high pressure, computer modelling suggests liquid lines of descent at nearly dry condition (0.1-0.2 wt% H_2O) driven by subsequent crystallization of olivine, olivine + augite, augite (±pigeonite) + plagioclase and only in the late stage (ca. 800-900 °C) followed by Fe(-Ti) oxide. At lower pressure (relatively higher water contents, 0.5 wt%) plagioclase joins earlier the liquidus assemblage, showing higher anorthite compositions. The wide occurrence of pigeonite in most flows, probably highlights efficient degassing processes during magma ascent and/or eruption, as its presence requires (almost) dry magmatic conditions (and possibly previous plagioclase crystallization that lower the melt CaO activity, thus making possible pigeonite crystallization). The inferred crystallization order is consistent with the mineralogical (EMP analyses) studies on phases (Anorthite content variations in plagioclase and TiO_2 and Cr_2O_3 content

in augite-pigeonite pair) and in the features observed on mineral phases as in their relationships. Unfortunately, the sparse trace element mineral phase compositions by LA-ICP-MS on augites and plagioclases of Tiourjdal sequence do not allow to gather further informations about crystallization order and/or eventual fractionation processes, whereas major and trace elements on whole-rock allow to infer a differentiation pattern driven mostly by olivine, clinopyroxene and minor plagioclase. On the other side, LA-ICP-MS on phases and relative melt compositions calculated in equilibrium with minerals, confirms the progressive depletion in LREE with respect to HREE from the Lower to Recurrent Unit, as highlighted by ICP-MS analyses on whole-rock. Petrographic (paragenesis, mineral phase relationships), mineralogic (major, minor and trace element compositions), geochemical (major, minor, trace element whole-rock composition) and magnetostratigraphic (declination and inclination paleomagnetic of lava flows) systematic studies have been operated in order to correlate the six volcanic sequences over an area spanning more than 10_5 km_2. In particular, a careful geochemical comparison between lava piles, based on immobile elements (Ce, Yb, Sm, Nd, Zr and Nb) matched with magnetostratigraphic data, allows to recognize first of all a second order geochemical subdivision within volcanic sequences, identifying two well defined sub-units both in the Lower and Intermediate Unit. This view is partially supported by Sr-Nd isotopic systematics, at least in the Tiourjdal sequence. Moreover, the newly defined sub-units, are not recorded in all lava piles and with the same volcanic volumes, thus arising a number of questions about the causes (compositional heterogeneity of the magma source, crustal control on the magma chambers setting, paleo-topography, undetected volcanostratigraphic gaps?) which make the Moroccan CAMP activity geographically discontinuous. On the other side, magnetostratigraphy highlights that these subunits are only occasionally contemporaneous, since VGP direction are partially concordant between CHA and MA/WM piles. While in the CHA, it seems that volcanic activity spanned a relatively long time manifested itself as multiple geochemically distinct magmatic pulses, in the MA/WM most of the basalts, even belonging to distinct chemographic sub-units, are emplaced in a very short time followed (and maybe preceded) by a longer duration of episodic activity. Magnetostratigraphic investigations indicate also the CHA and MA/WM volcanism may be slightly diachronous, since VGPs from the two areas do not precisely overlap, in general. This leaves some open questions on magma dynamics: do the geochemically equivalent but slightly diachronous sub-units express a migration of the magmatism recorded at regional level as proposed by several authors

for the whole CAMP magmatism? Are geochemically slightly different yet synchronous sub-units in the CHA and MA/WM produced by the same plumbing system? Or are they generated from distinct magma chambers systems, reflecting heterogeneous mantle sources? Globally, geochemical and magnetostratigraphic analyses highlight for the Moroccan CAMP a much more complex history of the volcanic record than previously recognized and show , comparing both methodologies (together with geochronological and palynological data), that it is possible to operate tight correlations among lava sequences, in order to reconstruct a precise volcanic chronostratigraphy, first step for any genetic model that tries to explain the geodynamic significance and the origin and differentiation of (CAMP) basalts.

18 $^{40}Ar/^{39}Ar$ DATING OF ENA-CAMP BASALT

18.1 INTRODUCTION

The Central Atlantic Magmatic Province (CAMP, **Marzoli *et al.*, 1999**) is one of the most widespread Large Igneous Province (LIP, **Coffin & Eldholm, 1994**) known. It is mostly represented by intrusive basaltic rocks (sills and dikes) and few lava flows sequences emplaced and preserved in late Mesozoic syn-rift basins formed few million years prior the supercontinent Pangea break-up. At present CAMP is dismembered over four continents around circum-Atlantic area, covering a surface of 10^7 km^2 and with a (conservative) estimated original volume of 2×10^6 km^3 (**Marzoli *et al.*, 1999**, **McHone, 2003**). In recent years the available of more and more precise and accurate ages (mostly 40Ar/39Ar on plagioclases) of the samples from all areas of the province, strongly support the hypothesis of a brief and episodic magmatic event. The results indicate that the whole magmatic event spanned ca. 10 Ma with a main peak at ca. 199 Ma (199.1±1.0 Ma, $^{40}Ar/^{39}Ar$ ages), in which ca. 90% of the volcanic products were emitted in 1 Ma or less (probably <600 Ka)(**Sebai *et al.*, 1991**; **Deckart, 1996**; **Baksi & Archibald, 1997**; **Hames *et al.*, 2000**; **DeMin *et al.*, 2003**; **Marzoli *et al.*, 1999, 2004**; **Knight *et al.*, 2004**; **Beutel *et al.*, 2005**; **Nomade *et al.*, 2007**; **Verati *et al.*, 2005, 2007**; **Olsen *et al.*, 1996, 2003**; **Whiteside *et al.*, 2007**; **Jourdan *et al.*, 2009**), while two volumetrically minor and distinct magmatic peaks are centred at 195 and 192 Ma (**Nomade *et al.*, 2007**) connected with the forthcoming oceanization process. Since a number of studies have highlighted that 40Ar/39Ar ages are systematically younger than U-Pb ages by ca.1% (**Renne *et al.*, 1998**; **Renne, 2000**; **Villeneuve *et al.*, 2000**; **Min *et al.*, 2000, 2001**; **Nomade *et al.*, 2004**; **Schoene *et al.*, 2006**; **Schaltegger *et al.*, 2008**), the close occurrence of the main volcanic event with one of the most important extinction event of the Phanerozoic age (**Sepkowski, 1996**) at the Triassic-Jurassic boundary (201.58±0.28 Ma proposed by **Schaltegger *et al.* (2008)** based on U-Pb method), arise the question if the biological turnover is or not genetically linked to the CAMP event and more in general if

the origin of numerous LIPs described in literature have possible implications on the mass extinctions (**Courtillot *et al.*, 1999**) periodically occurred on Earth. Beside to petrologic, paleomagnetic and palynologic studies which try to investigate the genesis of these huge volcanic provinces and their relationship with the extinction event, a promising method that provides to better constrain this hypothesis is to investigate the timing (absolute and relative ages) of volcanic events by several inter-calibrated geochronometers in order to build up a robust and statistically reliable ages database, start point of any genetic model which try to explain the geographic and temporal dynamic of such events. Unfortunately because of the scarce occurrence of evolved rocks belonging the CAMP (which do not allow to use the robust and precise U-Pb method) the wide extension of the province and the frequent alteration of magmatic products, the distribution of the CAMP ages is by far to be geographically homogeneous and complete (with regard to both effusive and intrusive rocks), being more than half of the data available regarding the African sub-provinces. The eastern North America CAMP sub-province is affected by this analytical bias since until recent (**Beutel *et al.*, 2005**, **Nomade *et al.*, 2007**, **Jourdan *et al.*, 2009**) very scarce robust ages data were not available. In this work we will present 13 new statistically robust $^{40}Ar/^{39}Ar$ plateau ages obtained on plagioclases and biotites separates from lava flows and sills from Newark (New York-New Jersey-Pennsylvania states) and Culpeper basins (Virginia-Maryland states) belonging the Newark Supergroup, a series of continental exposed Mesozoic syn-rift basins, where CAMP products occur interbedded within thick highly cyclical continental sediment sequences.

18.2 GEOLOGY AND STRATIGRAPHY OF NEWARK AND CULPEPER BASINS

The late Palaeozoic Variscan-Alleghanian orogeny culminated in the closure of the Iapetus Ocean and assembly of the North American and African continents into the Pangea supercontinent. The new thrust faults formed during the Palaeozoic orogeny were successively reactivated in the Middle Triassic time as normal faults developing rift basins all around the Central Atlantic domain both in eastern North America and western Africa. At present the Newark Supergroup (**Manspeizer & Cousminer, 1988**) is represented by several late Triassic rift basins occurring from Nova Scotia (Fundy Basin, Canada) to South Eastern U.S.A. (Jedburg Basin, South Carolina), filled by late Triassic-early Jurassic km-thick syn-rift continental sediments in which it is possible to recognize a detailed

cyclostratigraphy of sedimentary strata, interpreted as controlled by Milankovitch cycles (**Olsen *et al.*, 1996**). Within syn-rift sedimentary strata outcrop basaltic flows and intrusive rocks (dikes and sills), belonging to the Central Atlantic Magmatic Province (CAMP, **Marzoli *et al.*, 1999**). The lava flows occur just above a palynological turnover interpreted as the local expression of the Triassic-Jurassic extinction event (**Fowell, 1993**; **Fowell, 1994**). The Newark and Culpeper basins are two of the syn-rift Newark Supergroup system. Hereafter will be summarize the volcano-sedimentary stratigraphy of both basins. The Newark Basin is the largest and best known among the exposed basins of the northeast America Mesozoic rift system (**Olsen *et al.*, 1996**). It is more than 200 km long and 60 km wide with kilometric thick sedimentary sequence comprehensive of the intercalated CAMP basalts, and a half-graben structure delimitated on its north-western margin by a normal fault system (**Hozik, 1992**). The oldest sedimentary outcropping unit is the mostly fluvial Stockton Formation (Fm.) overlied by the highly cyclical lacustrine Lockatong Fm. and followed by the Passaic Fm. Overlying this basal sequence there are three basaltic units and two interbedded sedimentary units. The oldest basaltic unit is the Orange Mountain basalt (170-180 m thick) composed by three chemically homogeneous high-TiO2 (TiO_2 = 1.1-1.2 wt%) quartz normative (HTQ) tholeiite flows and equivalent (based on concentrations of immobile elements) to the Palisades Sill in the same basin, the Talcott basalt of the Hartford basin and Mount Zion Church basalt of the Culpeper basin (cf. below). Moreover is chemically correlated to the basaltic CAMP Intermediate Unit formation of the Moroccan Mesozoic syn-rift basins in northwest Africa (unpublished data, Fig. 18.2). The Orange Mountain basalt is overlied by the Feltville Fm, made by siltstone and sandstone sedimentary data. The intermediate basaltic unit is the Preakness basalt, more than 250 m thick and made up by at least three lava flows. Its composition is more variable compared to that of the older Orange Mountain basalt. The two lowermost flows have an low-TiO_2 (TiO_2 = 0.8-1.0 wt%) quartz normative composition (LTQ), whereas the uppermost flow has an high-Fe (FeO_{tot} = 12-14 wt%) quartz normative composition (HFQ) which allows to correlate it to the Holyoke basalt (Hartford basin), the Sander basalt (Culpeper basin, cf. below) and the Deerfield basalt (Deerfield basin). No Moroccan counterpart of this basaltic unit has been detected at present. The last basaltic unit is the thinner Hook Mountain basalt ($\sim$100 m thick), composed by at least two high-Fe and TiO_2 (TiO_2 ca. 1.45 wt% and FeO_{tot} ca. 17 wt%) quartz normative (HFTQ) lava flows and interbedded between the underlying Towaco Fm. and the overlying and youngest Boonton

Fm. (Olsen and Kent, 1996). The youngest basaltic unit is chemically equivalent to the Hampden basalt of the Hartford basin and similar to the Moroccan Recurrent Unit in west Africa (**Marzoli *et al.*, 2004**). The 150 Km long and 25 km wide Culpeper Basin is the southernmost exposed basin which shows intercalated basalt flows, since in the southern United States, basalt flows overlie rift basins (**Withjack *et al.*, 1998**). Like the Newark basin, it has a half-graben structure with the western border bounded by a normal fault system (**Hozik, 1992**). The seven sedimentary formations, the three lava flow units and the sill intercalated that build up the stratigraphy of the basin dip towards the western border with progressively increasing dips. The Catharpin Creek Fm. is the uppermost part of the thick sedimentary formation underlying the Mount Zion Church basalt flows ($\sim$140 m thick) made up by at least two lava flows (HTQ, $TiO_2 = 1.2$ wt%) separated by sedimentary layers. The Midland Fm. separates this basaltic unit from the upper Hickory Grove basalt (HFTQ, TiO_2=0.75-1.30 wt% and FeO_{tot} = 12-15 wt%) composed by at least three lava flows, not ubiquitous in the entire basin and each separated by sedimentary lenses, for a thickness up to 380 m toward north near the border fault (**Hozik, 1992**). Apparently this unit has chemically equivalent neither in the Newark Supergroup nor in the Moroccan CAMP subprovince. Upward, the Turkey Run Fm. separates the Hickory Grove basalt from the uppermost and thickest Sander basalt (up to 600 m), composed by at least three lava flows (HFTQ HFQ and LTQ) separated by sedimentary lenses. The Sander basalt is chemically similar to the Preakness basalt.

18.3 PREVIOUS GEOCHRONOLOGY

Until the recent $^{40}Ar/^{39}Ar$ plateau ages compilation on plagioclases separated from lava flows from the Fundy basin (Nova Scotia, Canada) and Hartford and Deerfield basins (NE U.S.A.) of **Jourdan *et al.* (2009)**, few reliable $^{40}Ar/^{39}Ar$ ages were available for lava flows of the eastern North America (ENA) CAMP sub-province. Excluding ages obtained by $^{40}Ar/^{39}Ar$ on whole rocks and analyses for which the monitor is unknown, ages (cf. below) from **Hames *et al.* (2000)** (5 ages), **Beutel *et al.* (2005)** (5 ages) and **Nomade *et al.* (2007)** (8 ages) are useful for a statistical meaningful comparison with the new age determination described in this work. Previous $^{40}Ar/^{39}Ar$ studies on mineral separates are from **Sutter (1988)** who analysed a biotite from a recrystallized xenolith of the Stockton Fm. close to the Palisades sill and a hornblende separate from a granophyric differentiate of the Germana Bridge diabase sheet. The biotite yielded a poorly

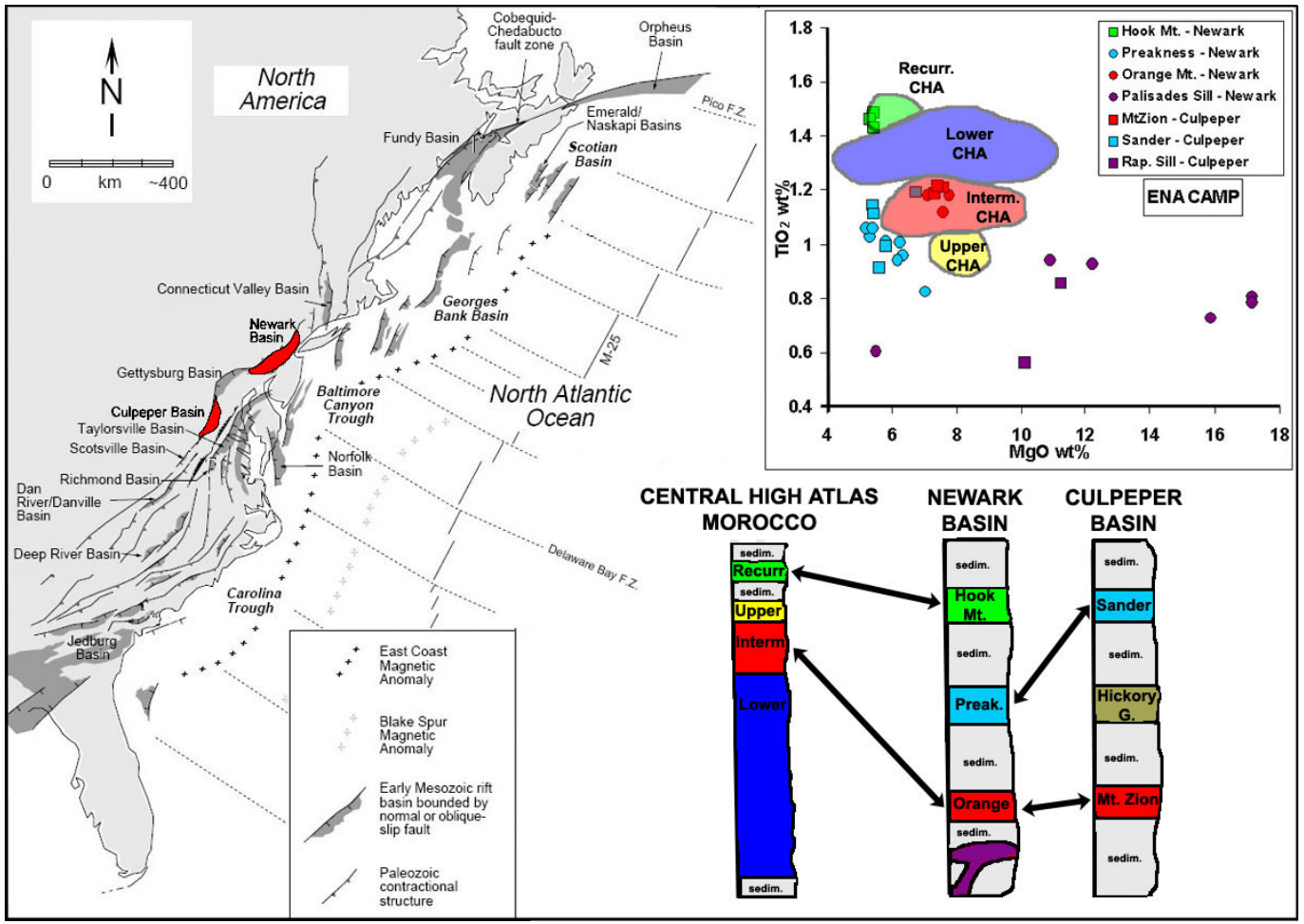

Figure 18.1: Location of Newark and Culpeper basins in the Eastern North America (modified after **Withjack *et al.*, 1998**). Also shown a schematic volcanostratigraphy and the compositional fields (MgO wt% vs TiO_2 wt%) of Newark and Culpeper basalts compared to those of the Centra High Atlas lava sequences.

constrained age recalculated by **Baksi (2003)** at 203.0±1.2 Ma (plateau age) while the hornblende gave an age of 200.9±1.0 Ma recalculated by **Hames *et al.* (2000)** at 203 Ma. In the same paper, Hames described $^{40}Ar/^{39}Ar$ incremental heating ages on plagioclase separates from sample collected from lava flow of the Orange Mountain basalt, which yielded a miniplateau age of 201.0±2.1 Ma (2σ level), and one sample collected from the Hook Mountain basalt, with a plateau age of 198.9±2.0 Ma (2σ level). Two samples collected in different positions of the same diabase dike in South Carolina produced similar plateau ages of 198.8±2.2 and 199.5±1.8 Ma (2σ level), respectively. Plagioclases collected from another dike in the same basin yielded a plateau age of 199.7±1.5 (2σ level) (**Hames *et al.*, 2000**). **Beutel *et al.* (2005)** analysed five sample from diabase dikes of the North and South Carolina (SE U.S.A.) obtaining 3 good plateau ages ranging from 197.6±1.5 to 198.8±1.8 Ma (2σ level) and two other plateau with discordant ages. **Nomade *et al.* (2007)** analysed eight plagioclase separates from seven basaltic samples from the same North and South Carolina (SE U.S.A.) CAMP dolerite dike swarms of **Beutel *et al.* (2005)** and one lava flow from the Orange Mountain basalt (Newark basin, NE U.S.A.) from the same locality of **Hames *et al.*, 2000**. The dike ages yielded plateau ranging from 195.8±1.6 to 200.9±1.5 Ma (2σ level) while the Orange Mountain sample gave a slightly younger age compared to that of Hames (199.0±1.6 Ma at 2σ level). Finally **Jourdan *et al.* (2009)** analysed eleven samples which yielded 10 plateau, 2 mini-plateau and 1 isochron $^{40}Ar/^{39}Ar$ ages on lava flows from eastern U.S.A. (3 analyses on three samples in the Hartford and Deerfield basins, eastern U.S.A.) and Nova Scotia, Canada (10 analyses on 8 rocks from the Fundy basin). In the Hartford and Deerfield basins plateau ages obtained on three ultra-sericitizied plagioclase selections from basalts range from 198.6±2.0 to 199.8±1.1 Ma (2σ level), that the authors interpretate as syn-emplacement hydrothermal activity. In the Fundy basin plateau ages range from 198.9±0.7 to 201.0±1.4 Ma (2σ level) with an isochron age of 199.8±1.4 Ma (2? level) and two younger mini-plateau ages of 190.6±1.0 and 197.8±1.0 Ma (2σ level). Also with regard to the U/Pb method few age determinations are available because of the scarce occurrence of evolved rocks in the ENA CAMP magmatic products. **Dunning & Hodych (1990)** analysed two fractions of zircon extracted from granophyric lenses of the Palisades and nine from the Gettysburg sills, obtaining mean $^{206}Pb/^{238}U$ ages of 200.9±1.0 Ma for the first and 201.3±1.0 Ma for the second. Four fractions of baddeleyite from the Palisades sill yielded concordant $^{206}Pb/^{238}U$ ages from 199.8 and 201.8 Ma (errors not mentioned in **Dunning & Hodych, 1990**). The

same authors analysed three zircon fractions collected from pegmatitic lenses within the North Mountain basalt (Fundy basin, Canada). Two of these yielded $^{206}Pb/^{238}U$ concordant ages of 202.0±1.06 and 201.4±0.81 Ma, respectively. The third zircon aliquot yielded a slightly discordant age (**Hodych & Dunning, 1992**). And from the same locality **Schoene *et al.* (2006)** analysed a collection of ten air-abraded zircon grains, which yielded a weighted mean $^{206}Pb/^{238}U$ age of 201.27±0.03/0.06/0.27 Ma (internal error only/including tracer calibration error/including tracer calibration and decay constant errors), all concordant with the previous.

18.4 SAMPLE DESCRIPTION AND ANALYTICAL PROCEDURE

We selected 10 fresh samples, 8 from the Newark Basin (NEW69 and NEW133, from two different lava flows of the Orange Mountain basalt, NEW52 from one lava flow of the Preakness basalt, NEW73 and NEW74 from two different basalts of the Hook Mountain basalt, NEW135, NEW16 and NEW18, respectively from the base, middle and top of the Palisades sill) and 2 from the Culpeper Basin (CUL8 from the Rapidan sill, CUL17 from one lava flow of the Sander basalt and CUL13 from one lava flow of the Hickory Groove basalt). These samples were analyzed for $^{40}Ar/^{39}Ar$ on unaltered, optically transparent, plagioclase and biotite separates (see data Table 2). Six samples are tholeiitic basalts with TiO_2 content ranging from 1.02 and 1.47 wt% with a paragenesis dominated by plagioclase, augite/pigeonite, minor oxides and rare biotite and apatite. The remaining four samples belong to two sills, three to the Palisades sill in the Newark Basin and one to the Rapidan sill in the Culpeper basin (see data Table 2). The primary paragenesis of the sills consists of olivines, augites, orthopyroxenes, plagioclases, hydrous minerals (biotite and amphibole), oxides, graphic quartz and apatite needles. After crushing, samples were sieved, washed in distilled water and dried. Finally minerals were separated using a Frantz Isodynamic Separator, and then carefully hand-picked under a binocular microscope. 10-12 mg of plagioclase have been hand-picked from each sample from two different size fractions, 200-315 and 160-200 μm, while for biotites we have collected few tens of grains from 2 samples (NEW135 and CUL8). The selected plagioclase and biotite samples were further leached in diluted HF for one minute and then thoroughly rinsed with distilled water in an ultrasonic cleaner. Samples were loaded into 5 large wells in an aluminium disc with 1.9 cm diameter and 0.3 cm depth aluminum disc.

These wells were bracketed by three small wells that included Hb3gr hornblende used as a neutron fluence monitor for which an age of 1072±11 Ma was adopted (Turner et al., 1971; Jourdan et al., 2006) and a good in-between-grains reproducibility has been demonstrated (**Jourdan *et al.*, 2006**; **Jourdan & Renne, 2007**). The discs were Cd-shielded (to minimize undesirable nuclear interference reactions) and irradiated for 25 hours in the Hamilton McMaster University nuclear reactor (Canada) in position 5C. The mean J-values (1σ) computed from standard grains within the small pits range from 0.008680±0.000023 (0.26%) to 0.008835±0.000014 (0.16%) (see data Table 3) determined as the average and standard deviation of J-values of the small wells for each irradiation disc. Mass discrimination (1σ) was monitored using an automatic air pipette and provided a variable value from 1.005296±0.002814 (0.28%) to 1.00649±0.00352 (0.351%) per dalton (atomic mass unit) (see data Table 3). The correction factors for interfering isotopes were $(^{39}Ar/^{37}Ar)_{Ca} = 7.30\times10^{-4}$ (±11%), $(^{36}Ar/^{37}Ar)_{Ca} = 2.82\times10^{-4}$ (±1%) and $(^{40}Ar/^{39}Ar)_{K} = 6.76\times10^{-4}$ (±32%). The $^{40}Ar/^{39}Ar$ analyses were performed at the Western Australian Argon Isotope Facility at Curtin University, operated by a consortium consisting of Curtin University and the University of Western Australia. The samples were step-heated using a 110 W Spectron Laser Systems, with a continuous Nd-YAG (IR; 1064 nm) laser rastered over the sample during 1mn to ensure homogenously distributed temperature. The gas was purified in a stainless steel extraction line using three SAES AP10 getters and a liquid nitrogen condensation trap. Ar isotopes were measured in static mode using a MAP 215-50 mass spectrometer (resolution of ∼600; sensitivity of 2×10^{-14} mol/V) with a Balzers SEV 217 electron multiplier mostly using 9 to 10 cycles of peak-hopping. The data acquisition was performed with the Argus program written by M.O. McWilliams and ran under a LabView environment. The raw data were processed using the ArArCALC software (**Koppers, 2002**) and the ages have been calculated using the decay constants recommended by **Steiger & Jäger (1977)**). Blanks were monitored every 3 to 4 steps and typical ^{40}Ar blanks range from 1×10^{-16} to 2×10^{-16} mol. Ar isotopic data corrected for blank, mass discrimination and radioactive decay are given in Annex xx. Individual errors in Annex xx are given at the 1σ level. Our criteria for the determination of a plateau are as follows: plateaus must include at least 70% of ^{39}Ar; the plateau should be distributed over a minimum of 3 consecutive steps agreeing at 95% confidence level and satisfying a probability of fit (P) of at least 0.05. Plateau ages (Table 2 and Fig. XXX) are given at the 2σ level and are calculated using the mean of all the plateau steps, each weighted by

the inverse variance of their individual analytical error. Integrated ages (2σ) are calculated using the total gas released for each Ar isotope (Table 2). Inverse isochrons include the maximum number of steps with a probability of fit ≥ 0.05. The uncertainties on the $^{40}Ar^*/^{39}Ar$ ratios of the monitors are included in the calculation of the integrated and plateau age uncertainties, but not the errors on the age of the monitor and on the decay constant (internal errors only, see discussion in **Min *et al.* (2000)**.

18.5 $^{40}Ar/^{39}Ar$ RESULTS AND DISCUSSION

18.5.1 Newark basin samples

For the Newark basin we have obtained 10 plateau ages from 8 samples: 5 lava flows from the three basaltic unit (two from the youngest the Orange Mountain, one for the Preakness and two for the Hook Mountain basalt), and 3 samples from the base, the middle and the top of the Palisades sill (TABLE 1). Samples from the Orange Mountain basalt (NEW69 and NEW133, plagioclase separates) from two different lava flows in different localities, yielded indistinguishable coincident plateau ages of 199.04±2.25 and 200.98±2.58 Ma (all errors are reported at the 2σ level). Plateau ages comprise >90% of the $^{39}Ar_{tot}$ released, with nearly undisturbed Ca/K spectra at values consistent with microprobe analyses (∼100). Only the lowest temperature steps display lower Ca/K, associated with higher apparent ages, this being probably related to minor amount of argon excess, a quite feature common in all samples analyzed in this work (Fig. PLATEAU) and in other present in literature (**Deckart *et al.*, 1997**; **Beutel *et al.*, 2005**; **Nomade *et al.*, 2007**; **Jourdan *et al.*, 2009**). However, inverse isochron diagram (**Heizler & Harrison, 1988**) indicates an initial $^{40}Ar/^{36}Ar$ generally indistinguishable from atmospheric value of 295.5 (**Steiger & Jäger, 1977**) with ages of 195.87±4.90 and 203.35±5.20 Ma for NEW69 and NEW133, respectively. The plateau ages of samples NEW69 and NEW133 are coincident (within errors) with that of 201.0±2.1 Ma obtained by **Hames *et al.* (2000)** on sample 6J of the same basaltic unit (but different location, see **Hames *et al.* (2000)** for references) and that of 199.0±2.0 Ma obtained by **Nomade *et al.*, 2007** on a plagioclase separate from the same split of Hames. However, it is noteworthy the fact that both Hames and Nomade ages do not fully satisfied our plateau age criteria, comprising ca. 41% (plateau age by Hames) and 54% (plateau age by Nomade) of the $^{39}Ar_{tot}$ released, and the samples suffering the presence of alteration phases (low apparent ages correlated with low Ca/K) and excess argon (age

spectrum with pronounced saddle-shaped form), for Hames and Nomade sample, respectively. Sample from the Preakness basalt (NEW52, plagioclase separates) yielded a plateau age of 200.43±1.62 Ma (97% of $^{39}Ar_{tot}$) and flat Ca/K spectrum (∼67). The inverse isochron age (200.07±3.53 Ma) is undistinguishable from the plateau age, and yield an initial $^{40}Ar/^{36}Ar$ of 303±68, overlapped with atmospheric composition. Two samples (plagioclase separates) were analyzed for the Hook Mountain basalt, NEW73 and NEW74. Sample NEW73 (the lowermost basalt) yielded a plateau age of 190.31±2.51 Ma, much younger than the overlying NEW74 lava flow (plateau age of 198.98±1.98 Ma). The age spectrum of NEW73 is slightly disturbed and the Ca/K spectrum is broadly tilde-shape, having the lowest and middle T steps lower Ca/K compared with those of high T steps. The inverse isochron yield $^{40}Ar/^{36}Ar$ intercept of 323±53, and an age of 188.50±4.23 Ma consistent with the plateau age. Taking into account the low Ca/K of the lowest T steps it is possible to think that the plateau age does not represent the magmatic crystallization age but maybe records a hydrothermal event and crystallization of alteration phases. It seems unlikely that the hypothetical hydrothermal event affected only the lowermost flow, leaving the overlying unaffected (cf. sample NEW74 description below). Alternatively, sample NEW73 may have suffered Ar loss by a re-heating event, in the hypothesis that the second lava flow (sample NEW74) did emplace soon after the emplacement of the first one, acting as a thermic blanket for the underlying, recently and hot lava flow, thus allowing a longer cooling time. However, considering the limited thickness (few meters) of the upper flow NEW74, is not likely such long thermal incubation. Another interpretation of the young age for NEW73 comes from the possibility that this sample belongs to a sill. Compelling field evidences for this hypothesis are lacking, since on the base of field-work investigation it has not been possible to detect the base of this supposed "sill", being visible only the contact with the overlying flow. On the other side in the Hartford/Deerfield basin there is a sill geochemically equivalent to Hook Mt. and Hampden basalts, the French King sill (Andrea Marzoli pers. comm.), thus indicative that these magma may have been intrusives. The overlying NEW74 displays a nearly undisturbed plateau age and Ca/K spectrum (except for one step with lower Ca/K). The inverse isochron age is identical to the plateau age, 197.69±3.11 Ma, with atmospheric $^{40}Ar/^{36}Ar$ intercept of 314±40. Even in this case, although NEW74 plateau age is coincident with that of 198.8±2.0 Ma obtained by **Hames *et al.* (2000)** on sample 7B from the same basaltic unit (and same locality of NEW74), the Hames result does not satisfied our plateau age criteria, comprising ca. 68% of $^{39}Ar_{tot}$ released, more-

over suffering of Ar excess (age spectrum with saddle-shaped form). The three samples from the Palisades sill yielded five plateau ages (on three plagioclase and two on biotite separates). Plagioclases of NEW135 yielded a plateau age of 201.24±1.81 Ma, defined by 87% of the of $^{39}Ar_{tot}$ released, and a nearly flat Ca/K spectrum (52±2) with an indistinguishable inverse isochron age of 200.85±2.23 Ma, and an atmospheric initial $^{40}Ar/^{36}Ar$ (302±19). The two repeated analyses on biotite separate yielded two indistinguishable plateau ages of 200.60±3.12 (for NEW135-bio) and 200.14±1.22 Ma (for NEW135-bio2), and coincident with that of plagioclase. The lower uncertainty of NEW135-bio2 is due to the larger amount of biotite grains analyzed compared to the first run (5-6 biotite grains), as also highlighted from inverse isochron age of 199.17±8.24 Ma for the first run and 199.75±1.66 Ma for the second (and precise) one ($^{40}Ar/^{36}Ar$ intercept at 319±68). Sample NEW16, collected from the middle of the sill (ca. 50-60 m above the base) yielded a younger plateau age of 196.01±1.88 Ma compared to NEW135, collected ca. 10 m above the base of the sill. NEW16 displays a more disturbed age spectrum in the lower temperature steps, with younger apparent ages (except for the lowest temperature step) and lower Ca/K values in the relative spectrum, maybe imputable to the presence of little amounts of K-rich alteration phases (isochron age of 193.07±3.40 Ma, $^{40}Ar/^{36}Ar$ intercept at 337±42). Finally the uppermost sample NEW18 yielded an even younger plateau age, 193.62±2.07 Ma even if overlapping within error with the age of NEW16. The Ca/K spectrum is more flat compared to NEW16 (Ca/K = 36±2), except in the lowest T steps where it also displays lower apparent ages. The interpretation of these last two plateau ages, younger compared to that of the basal NEW135, needs to be discussed further. Generally, $^{40}Ar/^{39}Ar$ plateau ages obtained on sill samples tend to spread towards younger ages especially when sampled in the middle of the magmatic body. For NEW135, the plateau age probably represents the intrusion age because of its proximity to the basal contact with the intruded sediments, thus leading to a faster cooling and so early crystallization. The younger age of NEW16 may be interpretated as a slow cooling age for this sample collected in the middle portion of the sill (50-60 above the base and 90-100 below the top of the sill), which may have taken a longer time to cool down below the Ar closure temperature, allowing a major Ar radiogenic diffusion with respect to the cooler sill margins. The young age of NEW18 (comparable with the underlying NEW16) is more tricky to interpret. One possibility is that the position where NEW18 has been sampled in the sill (20-30 below the sill top) could not respect its paleo-position. In fact, if a big sill portion (above the actual NEW18 position)

has been eroded (together with the sedimentary cover), NEW18 position would be nearer to middle portion of the sill. In this view the plateau age of NEW18 would record a long cooling history, like for NEW16.

18.5.2 Culpeper basin samples

Three plateau ages for two samples from the Culpeper basin have been obtained, one for lava flow belonging to the Sander basalt and one for the Rapidan sill (TABLE 1). Sample CUL17 from the Sander basalt yielded a plateau age of 199.96±1.25 Ma (95% of the $^{39}Ar_{tot}$ released), coupled with a quite flat Ca/K spectrum. Inverse isochron age is coincident with the plateau age (198.80±1.92 Ma) and atmospheric $^{40}Ar/^{36}Ar$ intercept (310±19). CUL8 from the Rapidan sill yielded two indistinguishable $^{40}Ar/^{39}Ar$ plateau ages from plagioclase and biotite separates. Plagioclase yielded a plateau age of 199.25±1.31 Ma, and quite flat low-Ca/K spectrum (0.1-15). The inverse isochron (age of 198.98±1.42 Ma) overlaps the plateau age yielding atmospheric initial $^{40}Ar/^{36}Ar$ (304±17). The biotite separate yielded a plateau age of 200.09±1.46 Ma, inverse isochron age of 198.47±2.36 Ma and atmospheric initial $^{40}Ar/^{36}Ar$ (334±44).

18.6 DURATION OF ENA-CAMP

In the Culpeper basin, the sample from the Rapidan sill (CUL8) yields a mean weighted age (plagioclase and biotite separates) of 199.62±0.98 Ma, while CUL17 from the Sander basalt yields a plateau age at 199.96±1.25 Ma, statistically equivalent and giving a mean weighted age for the Culpeper samples of 199.75±0.77 Ma (2σ level). Newark CAMP basalts yielded plateau ages ranging from 201.24±1.81 to 190.31±2.51 Ma. As explained before, three of these ages are significantly younger (NEW73 at 190.31±2.51 Ma, NEW18 at 193.62±2.07 Ma and NEW16 at 196.10±1.88 Ma), with respect to the others. While NEW 16 and NEW18 may represent cooling ages of the Palisades sill, the $^{40}Ar/^{39}Ar$ age of NEW73 may be interpreted either as an alteration age (even if the age spectrum is undisturbed and the Ca/K consistent with microprobe data for the analyzed plagioclase) or as magmatic age, yet in this case, considering the clearly older age of immediately overlying NEW74 (198.98±1.98 Ma). the sample should be an intrusive basalt (even if there is no clear field evidence for this). The three plateau ages obtained on sample NEW135 from the Palisades sill (1 plagioclase and 2 biotite separates) yield a mean weighted age of 200.48±0.94 Ma. The two analysed samples from the Orange Mountain basalts (NEW133 and NEW69) yield a mean

Table 18.1: Table 1

General characteristics								Plateau characteristics					Inverse isochron characteristics				
Sample	Lab N°	Coordinates	Unit	Notes	Mineral	Integrated age (Ma, ±2σ)	n	Plateau age (Ma, ±2σ)	Total ^{39}Ar released (%)	Attribute	MSWD	P	Isochron age (Ma, ±2σ)	n	$^{40}Ar/^{36}Ar$ intercept (±2σ)	MSWD	Observation
Newark Basin																	
NEW73	NEW-73-plagio	40°49'03.6''N 74°19'45.4''E	Hook Mountain	first flow	Plagioclase	194.36 ± 2.49	16	**190.31 ± 2.51**	90%	plateau	1.4	0.17	188.50 ± 4.23	12	323 ± 53	1.36	Clustering near $^{39}Ar/^{40}Ar$ axis
NEW74	NEW-74-plagio	40°49'03.6''N 74°19'45.4''E	Hook Mountain	second flow	Plagioclase	200.54 ± 1.96	15	**198.80 ± 1.89**	99%	plateau	0.84	0.61	197.69 ± 3.11	13	314 ± 40	0.83	Clustering near $^{39}Ar/^{40}Ar$ axis
NEW52	NEW-52-plg2	40°40'33.5''N 74°24'32''E	Preakness	flow	Plagioclase	201.23 ± 1.63	14	**200.43 ± 1.62**	97%	plateau	0.39	0.95	200.07 ± 3.53	11	303 ± 68	0.43	Clustering near $^{39}Ar/^{40}Ar$ axis
NEW69	NEW-69-plagio	40°47'35''N 74°14'53.2''E	Orange Mountain	Lower Orange Mt. flow	Plagioclase	204.98 ± 2.49	16	**199.04 ± 2.25**	94%	plateau	0.78	0.68	195.87 ± 4.90	13	335 ± 54	0.62	Clustering near $^{39}Ar/^{40}Ar$ axis
NEW133	NEW-133-plagio	40°18'53.2''N 75°50'53.4''E	Orange Mountain	basalt above fern spike	Plagioclase	202.45 ± 2.62	14	**200.98 ± 2.58**	95%	plateau	0.62	0.83	203.35 ± 5.20	13	279 ± 33	0.59	Clustering near $^{39}Ar/^{40}Ar$ axis
NEW135	NEW-135-bio	40°50'47.4''N 73°57'53.5''E	Palisades	base of sill	Biotite	204.54 ± 2.76	9	**200.60 ± 3.12**	72%	plateau	1.06	0.38	199.17 ± 8.24	5	304 ± 44	1.34	Clustering near $^{39}Ar/^{40}Ar$ axis
NEW135	NEW-135-bio2	40°50'47.4''N 73°57'53.5''E	Palisades	base of sill	Biotite (2nd aliquot)	200.94 ± 1.22	14	**200.14 ± 1.22**	86%	plateau	0.85	0.55	199.75 ± 1.66	8	319 ± 68	0.91	Clustering near $^{39}Ar/^{40}Ar$ axis
NEW135	NEW-135-plagio	40°50'47.4''N 73°57'53.5''E	Palisades	base of sill	Plagioclase	220.32 ± 3.00	18	**201.24 ± 1.81**	87%	plateau	1.14	0.31	200.85 ± 2.23	17	302 ± 19	1.18	Clustering near $^{39}Ar/^{40}Ar$ axis
NEW16	NEW-16-plagio	40°51'32.2''N 73°57'32.6''E	Palisades	middle of sill	Plagioclase	195.55 ± 1.74	18	**196.01 ± 1.88**	87%	plateau	1.50	0.12	193.07 ± 3.40	12	337 ± 42	1.12	Clustering near $^{39}Ar/^{40}Ar$ axis
NEW18	NEW-18-plg2	40°53'33.5''N 73°56'28.2''E	Palisades	top of sill	Plagioclase	193.27 ± 2.21	12	**193.62 ± 2.07**	88%	plateau	1.03	0.41	194.57 ± 3.67	8	285 ± 33	1.14	Clustering near $^{39}Ar/^{40}Ar$ axis
Culpeper Basin																	
CUL17	CUL-17-plagio	38°50'32.2''N 77°39'50.8''E	Sander	flow	Plagioclase	200.34 ± 1.26	19	**199.96 ± 1.25**	95%	plateau	0.88	0.59	198.80 ± 1.92	17	310 ± 19	0.75	Clustering near $^{39}Ar/^{40}Ar$ axis
CUL8	CUL-8-plagio	38°21'27.2''N 77°59'12.6''E	Rapidan	sill	Plagioclase	200.30 ± 1.33	23	**199.25 ± 1.31**	98%	plateau	0.63	0.89	199.98 ± 1.42	20	304 ± 17	0.61	Clustering near $^{39}Ar/^{40}Ar$ axis
CUL8	CUL-8-bio	38°21'27.2''N 77°59'12.6''E	Rapidan	sill	Biotite	200.89 ± 1.46	18	**200.09 ± 1.46**	99%	plateau	0.87	0.6	199.47 ± 2.36	16	334 ± 44	0.67	Clustering near $^{39}Ar/^{40}Ar$ axis

weighted age of 199.90±1.70 Ma. The overlying Preakness (NEW52) and Hook Mountain (NEW74) basalt flows yielded plateau ages of 200.43±1.62 Ma and 198.80±1.89 Ma. Excluding the three youngest ages, plateau ages in the Newark basin span the range from 200.48±0.94 (sample NEW135 plagioclase+biotites) to 198.80±1.89 Ma (sample NEW74), all these ages being indistinguishable. Considering the 4 mean weighted ages of each unit (3 lava flows and 1 sill), we obtain a mean age of 200.16±0.64 Ma for the CAMP magmatism in the Newark basin, indistinguishable from the Culpeper mean age. Although the mean age of our compilation is in perfect agreement with weighted mean age obtained by **Jourdan *et al.* (2009)** for CAMP basalts from Nova Scotia (199.6±0.6 Ma), it is slightly older with respect both to the mean age of eastern U.S.A. dykes and sills (198.9±0.3 Ma) and to the mean age of Moroccan CAMP lava flows (198.9±0.5 Ma) compiled by those authors. In a probably density plot (Fig. 18.3), the new $^{40}Ar/^{39}Ar$ plateau ages obtained in this work (excluding the three youngest ages) have a nearly Gaussian distribution with peak at ca. 200.1 Ma. This distribution shows a slightly older peak age compared to other previously analyzed ENA-CAMP samples and compared to the entire CAMP (only plateau ages are used)(Fig. 18.4). The diagram shows also the CA-TIMS U/Pb age of the Triassic-Jurassic (201.58±0.28 Ma, **Schaltegger *et al.*, 2008**). Since a number of studies have highlighted that $^{40}Ar/^{39}Ar$ ages are systematically younger than U-Pb ages by ca. 1% (**Renne *et al.*, 1998**; **Renne, 2000**; **Villeneuve *et al.*, 2000**; **Min *et al.*, 2000, 2001**; **Nomade *et al.*, 2004**; **Schoene *et al.*, 2006**; **Schaltegger *et al.*, 2008**), the CAMP basalts may well be synchronous with the T-J boundary. As highlighted previously, more problematic is the interpretation of the three younger ages obtained on NEW73, NEW18 and NEW16 (190.31±2.51, 196.10±1.88 and 193.62±2.07 Ma, respectively) and their geodynamic implication in the ca. 200 Ma ENA-CAMP magmatic peak frame-work. We have discussed that the young age for NEW73 (at 190.31±2.51 Ma) is defined by a statistically solid age spectrum, yet a slight, almost cryptic alteration could envisaged considering the slightly disturbed age and Ca/K spectra are slightly disturbed both having tilde-shape form. However, the relatively wide range of measured Ca/K variation (from 50 to 100) is consistent with the composition of plagioclase phenocrysts from this sample, analyzed by EMP, which are characterized by abrupt An variations between about An_{50-55} and An_{67} with associated Ca/K variations in the range 20-70 (Fig. 18.2). Excluding the possibility that the NEW73 age spectrum represents an alteration plateau, a second hypothesis could be that NEW73 represents a late magmatic intrusion as that hypothesized

in Nova Scotia by **Jourdan *et al.* (2009)**. In the nearby Hartford/Deerfield basin, a magma with Hook Mt.-like composition intruded in the shallow sediments and formed the so called French King sill. However, field observations indicate that at the outcrop where NEW73 was sampled there is no evidence for a metamorphic basal contact as would be typical for a shallow level intrusion in sedimentary layers. This poses serious problems for the interpretation of the young age of NEW73 as a magmatic crystallization/cooling age. The young ages

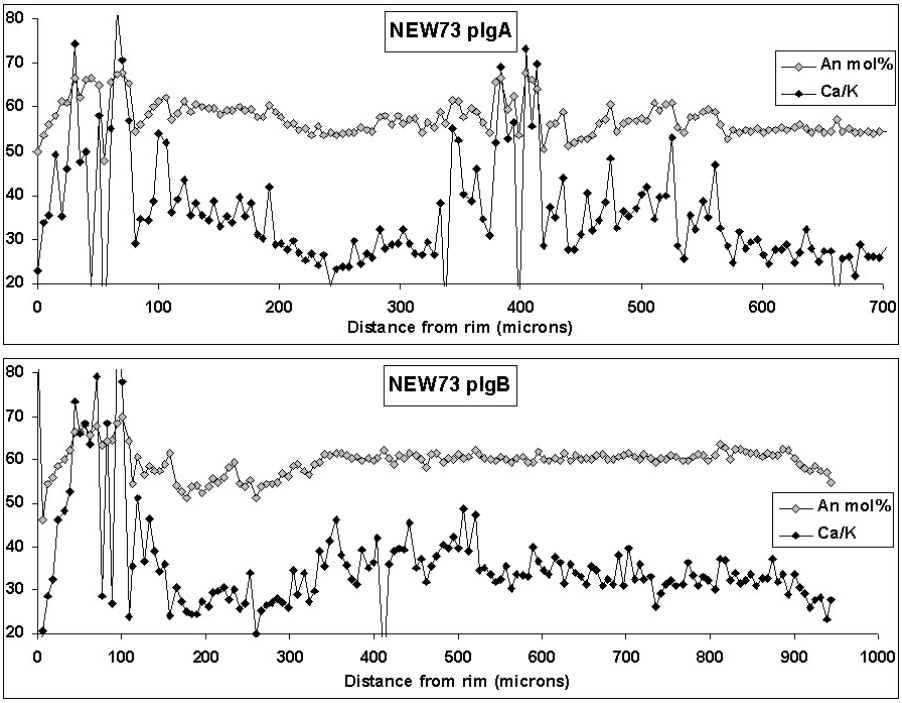

Figure 18.2: An mol% and Ca/K compositional variation in two plagioclases of NEW73 sample analyzed by EMP.

NEW16 and NEW18 from the Palisades sill (196.10±1.88 and 193.62±2.07 Ma, respectively) are at the same time not simple to interpret and intriguing. In the previous section, we have suggested that the young plateau age for NEW16 could be explained if we take into account its relative position at about half of the Palisades sill. Plagioclases in the inner part of the sill cool down slowly compared to those of the sill margins, near the contact with intruded sediments. This could explain the younger age of NEW16 compared to that of NEW135 which instead was sampled near the base of the sill. The young NEW18 age could be subject to more than one interpretation. This sample was collected on top of the southern part of the present outcrop of the sill. It was corresponds to the upper sill, yet, considering the dip of the intrusion, it does most probably not belong to the very

top of it. In this view, the young age of NEW18 could represent, as for NEW16, a cooling age. A second possibility could be that NEW18 represents a late magmatic injection. A very recent work (**Puffer et al., in press**) support the

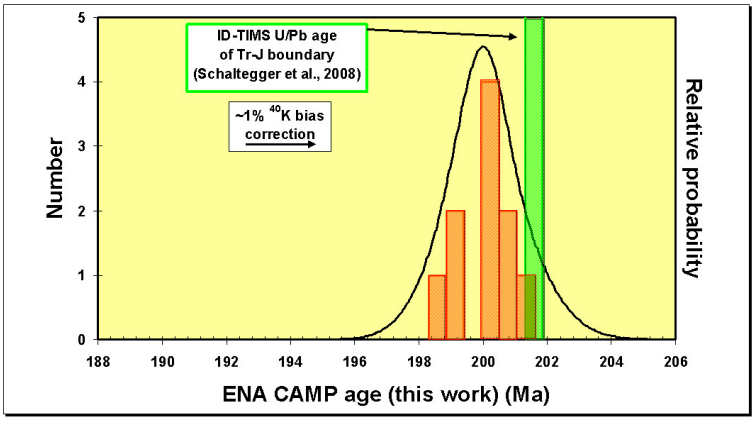

Figure 18.3: Age-probability density distribution of the $^{40}Ar/^{39}Ar$ plateau ages obtained in this work, calculated with Isoplot/Ex (**Ludwig, 2003**) (NEW73, NEW16 and NEW18 plateau ages are excluded)

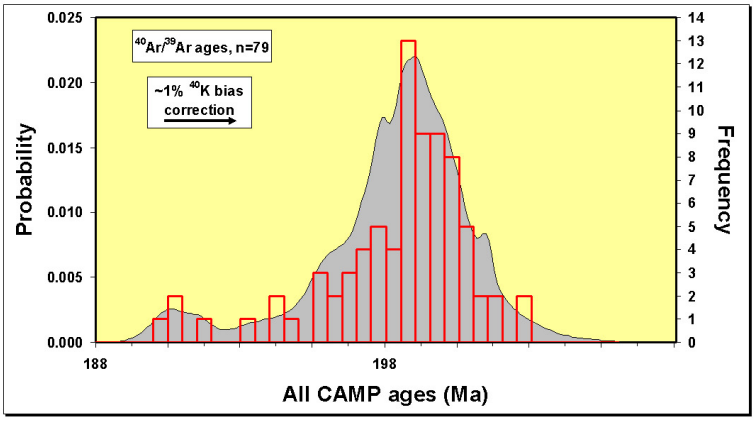

Figure 18.4: Age-probability density distribution (**Sircombe, 2004**) of $^{40}Ar/^{39}Ar$ plateau ages of all CAMP (comprising our new $^{40}Ar/^{39}Ar$ ages). Compilation from **Jourdan *et al.* (2009)**.

hypothesis of multiple intrusion history for the Palisades sill (as also stressed by vertical chemical variation due to less differentiated magma injection in **Shirley (1987)**), with an earlier stage for the lower sill portion and a later stage for the upper section. If by one side, the two young age of NEW16 and NEW18 confirm, within the error, the first hypothesis, i.e., both samples belong to the inner part

of the cooling sill, thus representing a cooling plateau age, on the other side, the poor constrained paleo-position of NEW18 in the body sill and the proved occurrence of late magmatic intrusion within the main body sill, could lean toward the second hypothesis, i.e., that NEW18 represents a late intrusive event, occurred within the main Palisades sill along weakness directions consequent to its long time (thousand years) cooling history.

18.7 CONCLUSION

Thirteen new statistically robust $^{40}Ar/^{39}Ar$ plateau ages have been obtained on plagioclase and biotite separates from lava flows and sills from the Newark and Culpeper basins, Eastern North America. Ten plateau ages ranging from 201.24±1.81 to 198.80±1.89 Ma, confirm previous $^{40}Ar/^{39}Ar$ ages obtained on both lava flow and sill samples from the North American CAMP. The Gaussian distribution of our new plateau ages highlights a main magmatic peak at 200.1 Ma, slightly older than the main CAMP magmatic peak (ca. 199 Ma), obtained from a global $^{40}Ar/^{39}Ar$ age compilation, thus supporting the hypothesis of a possible southward migration of the magmatic centers during the CAMP event, as previously suggested by **Baksi, 2003**, **Nomade *et al.*, 2007** and **Jourdan *et al.*, 2009**.

Three substantially younger ages, varying from 196.01±1.88 to 190.31±2.51 Ma obtained on one lava flow and two sill samples, are more difficult to explain. If by one side, it is not possible to exclude a long (thousand years) cooling history for sill samples (thus yielding younger $^{40}Ar/^{39}Ar$ plateau age), on the other side the hypothesis of a late intrusive magmatic stage in the ENA-CAMP is supported by a recent work ((**Puffer et al., in press**)) about the multiple intrusion history of the Palisades sill.

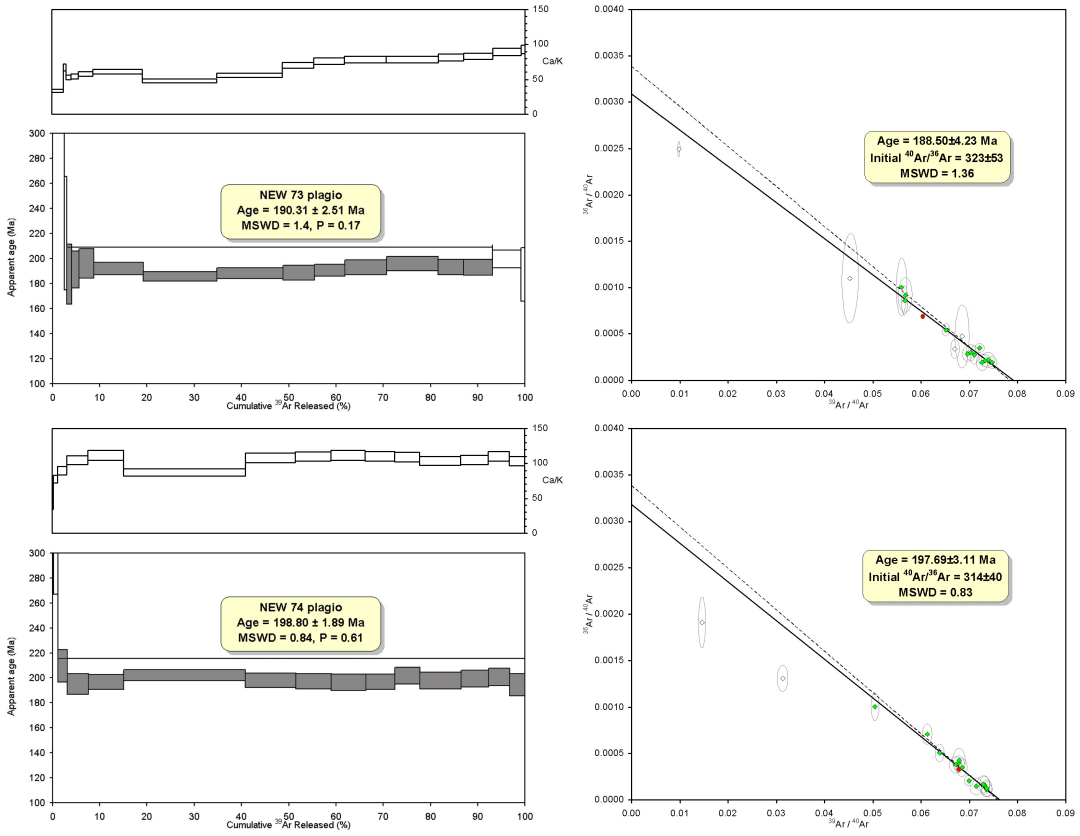

Figure 18.5: Age spectra with associated Ca/K ratios and inverse isochron of the plagioclases from NEW73 and NEW74 samples (Hook Mountain basalt, Newark basin). Errors are reported at 2σ level.

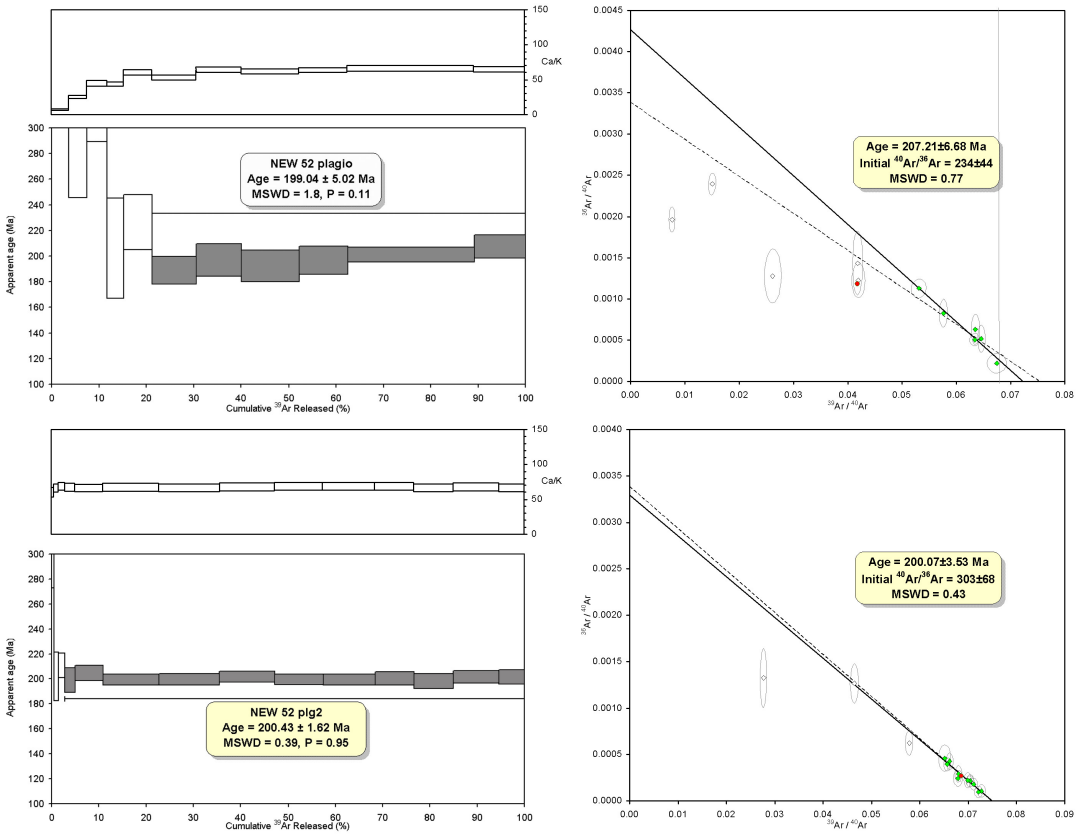

Figure 18.6: Plateau age and inverse isochron of the two plagioclase runs from NEW52 sample (Preakness basalt, Newark basin). Errors are reported at 2σ level.

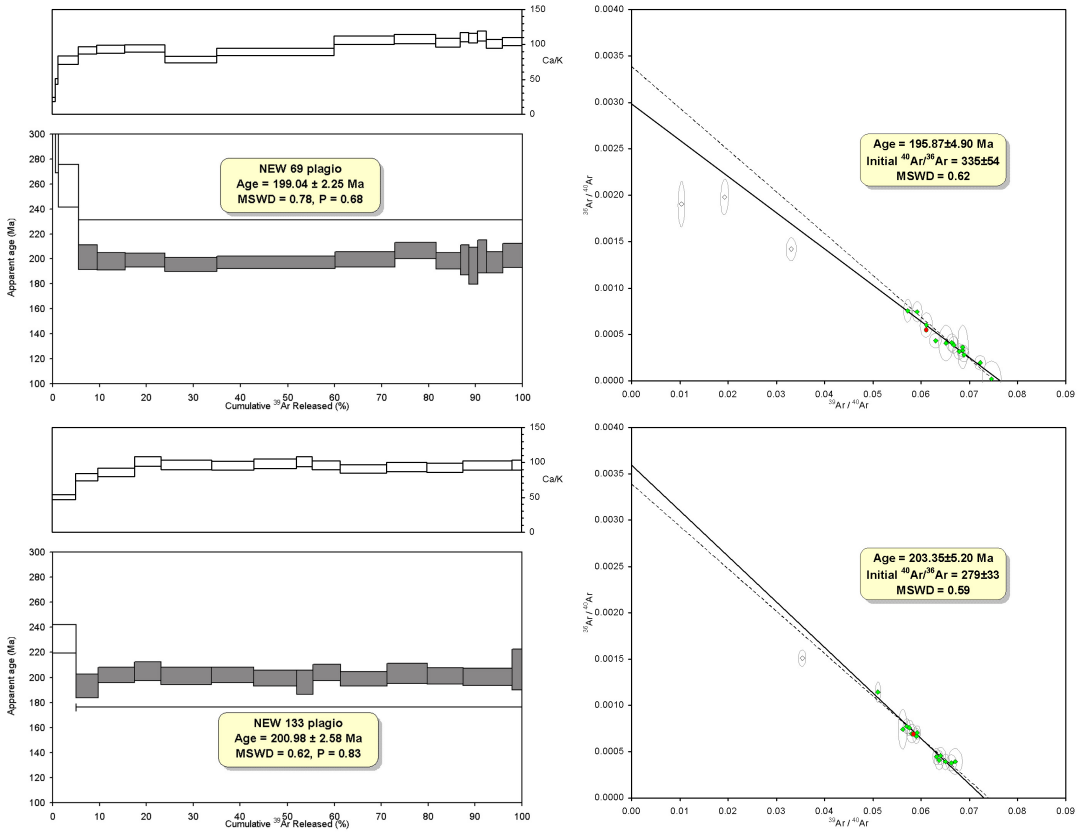

Figure 18.7: Age spectra with associated Ca/K ratios and inverse isochron of the plagioclase from NEW69 and NEW133 samples (Orange Mountain basalt, Newark basin). Errors are reported at 2σ level.

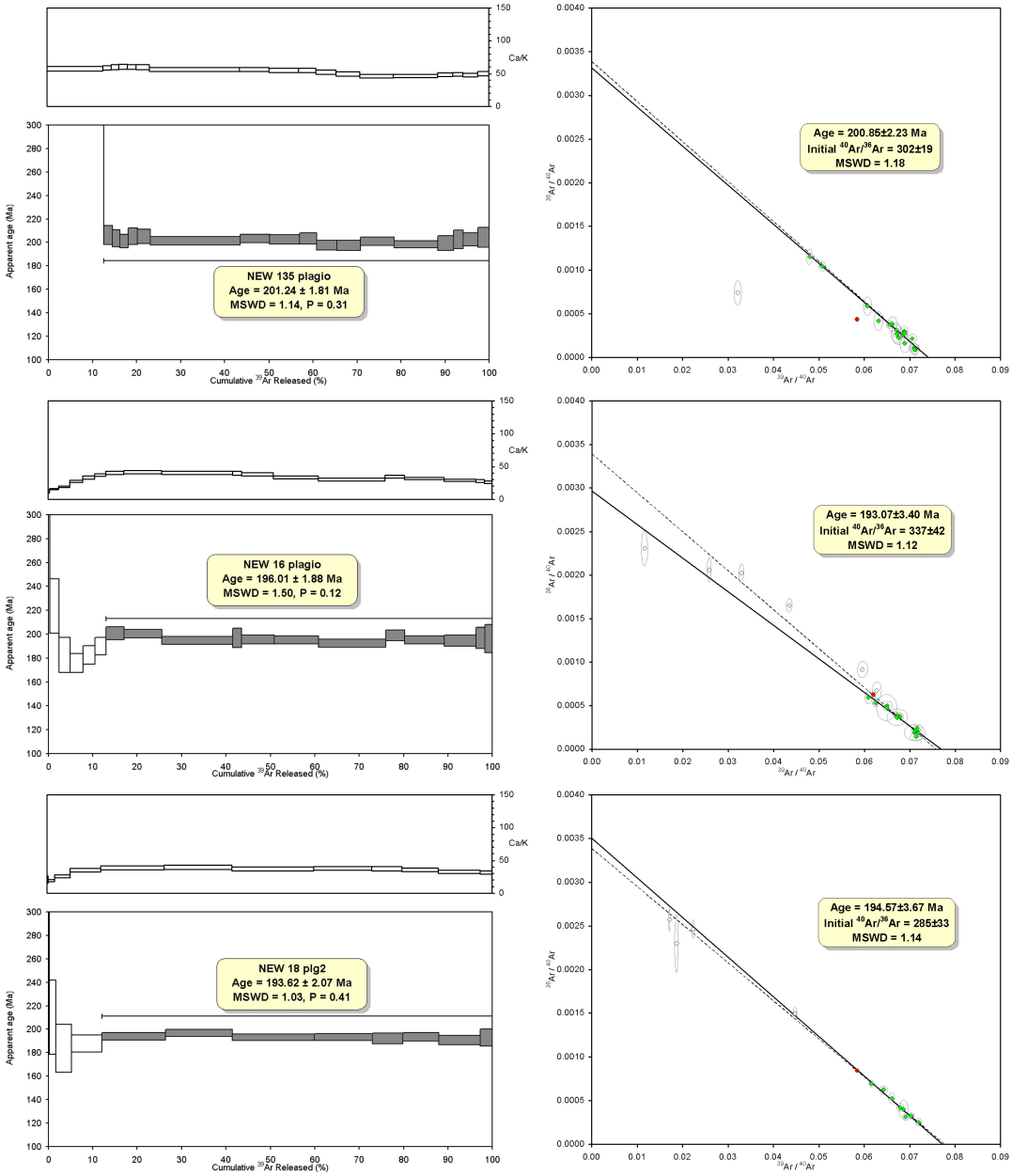

Figure 18.8: Age spectra with associated Ca/K ratios and inverse isochron of the plagioclases from NEW135, NEW16 and NEW18 samples (base, middle and top of the Palisades sill, respectively, Newark basin). Errors are reported at 2σ level.

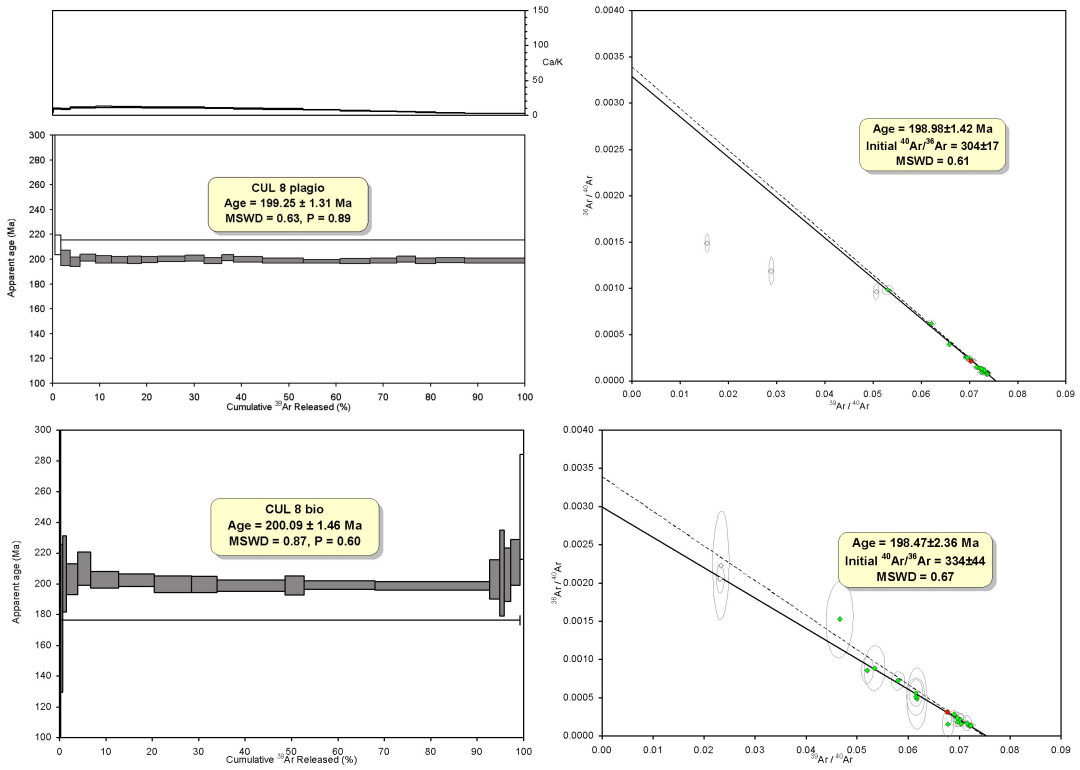

Figure 18.9: Age spectra with associated Ca/K ratios and inverse isochron of the plagioclase and biotite from CUL8 sample (Rapidan sill, Culpeper basin). Errors are reported at 2σ level.

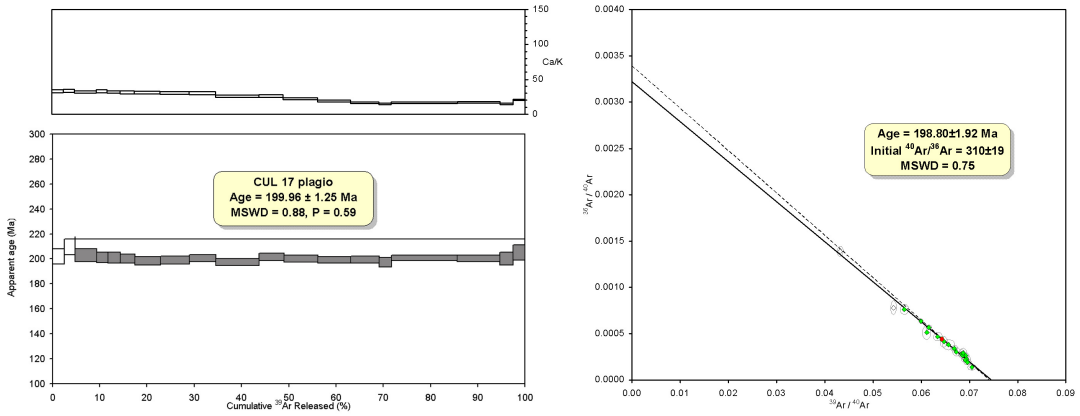

Figure 18.10: Age spectra with associated Ca/K ratios and inverse isochron of the plagioclase from CUL17 sample (Sander basalt, Culpeper basin). Errors are reported at 2σ level.

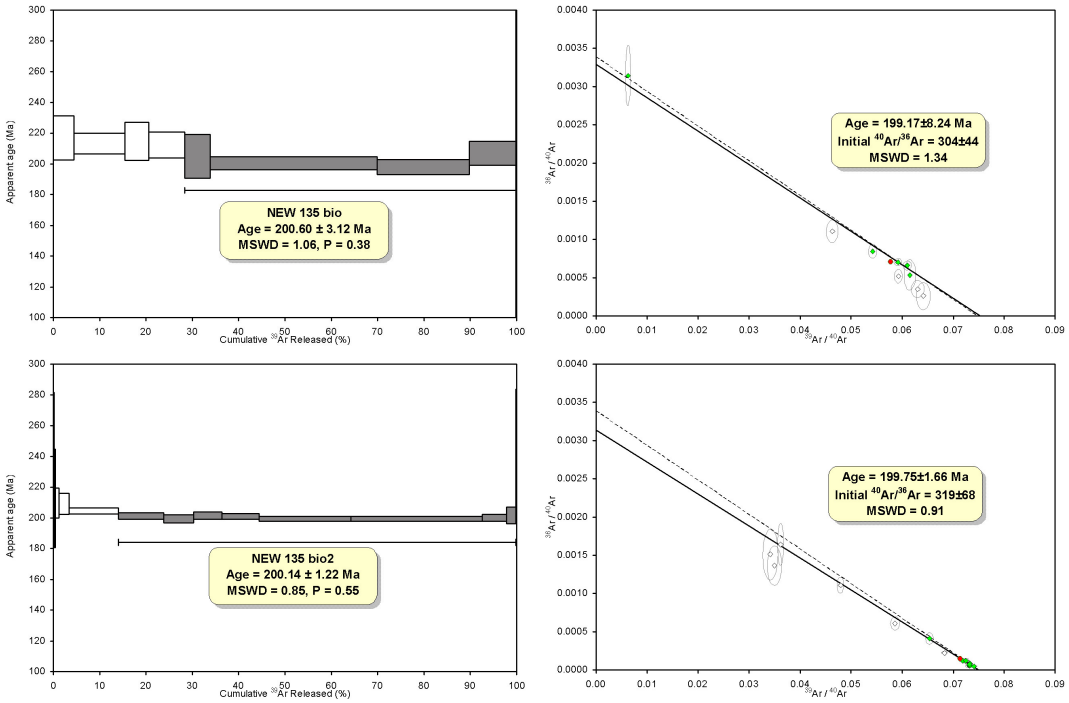

Figure 18.11: Plateau age and inverse isochron of the biotite separates from NEW135 sample (Palisades sill, Newark basin). Errors are reported at 2σ level.

A APPENDIX

A.1 WHOLE-ROCK COMPOSITIONS

	Lower											
wt%	**TJ1**	**TJ2**	**AN49**	**TJ3**	**TJ4**	**AN134**	**TJ5**	**TJ6**	**TJ7**	**TJ8**	**TJ9**	**TJ10**
SiO_2	52.83	53.13	54.08	53.47	53.99	53.67	53.55	52.57	54.46	53.87	52.36	52.93
TiO_2	1.38	1.41	1.36	1.42	1.46	1.43	1.38	1.35	1.40	1.53	1.49	1.49
Al_2O_3	14.36	14.59	15.28	14.24	14.85	14.28	14.68	15.15	14.75	14.88	14.86	15.03
Fe_2O_3	9.79	9.75	8.26	9.46	9.67	9.92	9.56	9.17	9.97	9.58	10.03	10.58
MnO	0.11	0.12	0.12	0.15	0.15	0.18	0.15	0.13	0.10	0.07	0.09	0.07
MgO	8.53	7.83	6.98	7.88	6.85	7.25	7.75	9.17	7.47	8.73	10.60	9.33
CaO	9.78	9.79	10.63	9.92	9.63	9.97	9.90	9.52	8.48	8.14	6.72	7.44
Na_2O	2.31	2.28	2.16	2.32	2.41	2.15	2.31	2.40	2.41	2.36	2.36	2.33
K_2O	0.74	0.94	0.97	0.96	0.79	0.98	0.55	0.37	0.80	0.65	1.31	0.62
P_2O_5	0.15	0.16	0.15	0.16	0.18	0.17	0.17	0.15	0.15	0.18	0.17	0.17
SUM	99.99	99.99	100.00	99.99	99.99	100.00	99.99	99.99	99.99	99.99	99.99	99.99
Loss 110°	1.45	0.91		0.82	1.12		1.49	1.71	1.37	2.25	3.16	2.82
L.O.I.	1.86	1.15		1.08	1.23		1.67	2.14	2.03	3.10	4.50	4.14
$L.O.I._{tot}$	3.31	2.06		1.9	2.35		3.16	3.85	3.4	5.35	7.66	6.96
Mg#	**64.09**	**62.20**	**63.39**	**63.06**	**59.22**	**59.96**	**62.42**	**67.20**	**60.56**	**65.11**	**68.41**	**64.37**
XRF (ppm)												
Sc	17	19	34	18	17	34	16	17	20	18	20	19
V	270	275	256	288	261	263	260	272	292	281	274	268
Cr	383	331	331	387	280	288	316	314	290	299	324	347
Co	45	43	39	43	39	37	39	43	37	39	43	44
Ni	107	105	60	108	83	92	91	91	83	87	84	80
Cu	59	69		99	109		123	107	76	48	158	67
Zn	62	56		62	69		67	64	48	34	43	41
Ga	16	17		18	17		18	18	17	17	16	17
Rb	12	22	31	29	20	30	13	6	17	10	18	8
Sr	236	238	237	235	253	227	248	263	250	256	253	264
Y	27	28	25	25	28	26	28	26	24	27	26	26
Zr	125	132	115	132	145	131	133	119	123	136	128	128
Nb	12	13	11	13	15	13	14	12	12	13	12	13
Ba	225	237	224	243	267	255	216	176	227	198	158	142
La	<10	12	17	<10	25	24	<10	<10	25	<10	21	12
Ce	21	41	33	35	32	37	38	20	27	33	37	29
Nd	16	20	18	14	14	20	22	21	12	16	24	26
Pb	<3	<3		<3	<3	11	<3	<3	<3	<3	<3	<3
Th	<3	<3	5	<3	<3	6	<3	<3	<3	<3	<3	<3
U	<3	3	2	3	<3	3	<3	<3	<3	<3	3	<3
Norma												
Qz	2.17	2.93	5.29	3.19	5.21	4.69	4.49	1.9	5.77	4.74		3.09
Co												
Or	4.37	5.55	5.73	5.67	4.66	5.78	3.25	2.18	4.72	3.84	7.73	3.66
Ab	19.53	19.27	18.26	19.61	20.37	18.17	19.53	20.29	20.37	19.95	19.95	19.7
An	26.62	26.79	29.12	25.6	27.36	26.41	28.05	29.46	27.06	28.08	26.07	28.71
Le												
Ne												
Di	17.03	16.92	18.43	18.4	15.76	17.96	16.28	13.61	11.47	9.04	4.97	5.76
Hy	25.39	23.6	18.65	22.62	21.56	21.96	23.54	27.83	25.65	29.14	34.74	33.76
Ol											1.3	
Mt	1.86	1.86	1.57	1.8	1.84	1.89	1.82	1.74	1.9	1.82	1.91	2.01
Ilm	2.63	2.68	2.59	2.7	2.78	2.72	2.63	2.57	2.66	2.91	2.83	2.83
Ap	0.33	0.35	0.33	0.35	0.39	0.37	0.37	0.33	0.33	0.39	0.37	0.37
Sum	**99.93**	**99.95**	**99.97**	**99.94**	**99.93**	**99.95**	**99.96**	**99.91**	**99.93**	**99.91**	**99.87**	**99.89**

Figure A.1: XRF and normative compositions of Tiourjdal samples.

	Lower												
	TJ11	**TJ12**	**TJ13**	**TJ14**	**TJ15**	**TJ16**	**TJ17**	**TJ18**	**TJ19**	**TJ20**	**TJ21**	**TJ22**	**TJ23**
SiO_2	52.73	51.35	51.67	51.65	52.03	52.97	52.28	52.58	53.41	52.83	53.70	52.97	53.31
TiO_2	1.45	1.54	1.50	1.48	1.43	1.45	1.41	1.40	1.70	1.59	1.49	1.38	1.28
Al_2O_3	14.45	15.43	14.79	14.67	15.03	14.50	14.65	14.06	14.06	15.29	14.26	13.61	14.33
Fe_2O_3	9.85	9.79	10.61	10.32	9.89	9.95	10.26	10.41	10.98	10.44	10.12	10.40	10.26
MnO	0.16	0.11	0.09	0.14	0.16	0.13	0.10	0.12	0.14	0.06	0.14	0.15	0.17
MgO	8.92	9.77	9.36	9.40	9.79	8.77	9.21	9.02	6.82	9.54	7.33	8.90	7.78
CaO	9.59	8.91	9.03	9.54	8.70	9.36	9.22	9.82	9.49	6.18	9.33	9.42	10.06
Na_2O	2.20	2.34	2.35	2.29	2.43	2.26	2.22	2.06	2.46	2.11	2.34	2.14	2.23
K_2O	0.48	0.57	0.41	0.33	0.37	0.44	0.49	0.35	0.74	1.77	1.12	0.87	0.44
P_2O_5	0.16	0.17	0.17	0.16	0.16	0.16	0.16	0.15	0.19	0.17	0.17	0.14	0.14
SUM	99.99	99.99	99.99	99.99	99.99	99.99	99.99	99.99	99.99	99.99	99.99	99.99	99.99
Loss 110°	1.72	2.27	1.99	1.86	2.36	1.84	1.79	1.81	1.06	3.12	0.58	1.06	1.14
L.O.I.	2.38	3.64	3.07	2.70	3.39	2.61	3.01	2.96	1.34	4.24	1.26	1.49	1.23
$L.O.I._{tot}$	4.1	5.91	5.06	4.56	5.75	4.45	4.8	4.77	2.4	7.36	1.84	2.55	2.37
Mg#	**64.99**	**67.17**	**64.37**	**65.12**	**66.97**	**64.37**	**64.77**	**63.98**	**56.00**	**65.73**	**59.76**	**63.68**	**60.83**
XRF													
Sc	16	19	17	19	18	18	18	17	17	22	17	16	18
V	276	289	279	281	281	274	274	279	308	263	283	267	290
Cr	351	351	327	348	385	327	347	344	249	278	283	351	245
Co	47	44	45	46	47	46	43	47	46	43	44	51	46
Ni	85	89	87	86	106	86	87	96	73	68	88	120	88
Cu	62	91	59	81	157	100	50	43	43	75	23	35	158
Zn	71	69	38	60	101	71	45	57	69	43	74	70	72
Ga	17	17	17	18	16	17	17	16	18	17	19	17	16
Rb	4	11	5	3	7	11	11	5	21	43	28	20	16
Sr	258	262	264	261	257	247	251	245	249	238	229	219	179
Y	26	26	29	24	23	25	25	25	32	24	27	27	24
Zr	129	130	128	129	122	130	127	120	157	136	141	124	106
Nb	14	13	14	13	13	13	14	13	15	14	15	13	11
Ba	237	186	152	168	170	183	176	164	228	189	238	205	166
La	10	14	24	<10	25	18	<10	23	<10	13	25	<10	10
Ce	34	25	31	28	18	19	28	36	43	27	29	40	16
Nd	20	15	13	29		27	20	25	23	28	28	27	12
Pb	<3	<3	<3	<3	<3	<3	<3	<3	<3	<3	<3	<3	<3
Th	<3	<3	<3	<3	<3	<3	<3	<3	<3	<3	<3	<3	<3
U	<3	<3	<3	<3	<3	<3	<3	4	<3	<3	4	<3	<3
Norma	2.99		0.76	0.88	0.8	3.46	2	3.37	4.53	1.45	3.88	2.54	4.38
Qz													
Co	2.83	3.36	2.42	1.95	2.18	2.6	2.89	2.07	4.37	10.45	6.61	5.14	2.6
Or	18.6	19.78	19.86	19.36	20.54	19.1	18.77	17.41	20.79	17.84	19.78	18.09	18.85
Ab	28.12	29.9	28.58	28.76	29	28.11	28.55	28.07	25.13	27.01	25.09	24.95	27.78
An													
Le													
Ne	14.97	10.68	12.28	14.24	10.64	14.06	13.13	16.01	17.03	2.05	16.44	17	17.35
Di	27.44	30.19	30.74	29.59	31.8	27.59	29.61	28.01	22.36	35.69	23.02	27.3	24.31
Hy		0.82											
Ol	1.87	1.86	2.02	1.96	1.88	1.89	1.95	1.98	2.09	1.99	1.93	1.98	1.95
Mt	2.76	2.93	2.85	2.82	2.72	2.76	2.68	2.66	3.23	3.02	2.83	2.63	2.44
Ilm	0.35	0.37	0.37	0.35	0.35	0.35	0.35	0.33	0.41	0.37	0.37	0.31	0.31
Ap	**99.93**	**99.89**	**99.88**	**99.91**	**99.91**	**99.92**	**99.93**	**99.91**	**99.94**	**99.87**	**99.95**	**99.94**	**99.97**

Figure A.2: XRF and normative compositions of Tiourjdal samples.

	Intermediate										Upper		Recurrent
	AN137A	TJ24	TJ25	TJ26	AN138	TJ28	TJ29	TJ30	TJ31	TJ32	AN140	AN 141	AN156A
SiO_2	53.23	53.15	53.39	53.83	53.64	50.80	52.95	53.27	53.22	53.03	51.43	52.14	50.58
TiO_2	1.16	1.38	1.18	1.21	1.16	1.43	1.22	1.31	1.31	1.35	1.00	1.04	1.63
Al_2O_3	13.94	14.83	13.43	14.60	13.42	17.52	14.75	14.51	14.64	14.71	15.03	14.87	13.55
Fe_2O_3	10.47	13.60	10.44	10.01	10.20	9.50	10.26	10.57	10.27	10.55	9.95	9.97	15.01
MnO	0.18	0.09	0.16	0.13	0.17	0.14	0.18	0.17	0.15	0.16	0.18	0.18	0.28
MgO	7.79	5.71	8.40	7.02	8.52	9.39	7.42	7.08	7.48	7.22	8.27	7.74	5.76
CaO	10.70	7.09	9.92	10.07	9.97	7.07	10.49	10.31	10.06	10.27	12.03	11.45	10.43
Na_2O	2.00	2.19	2.07	2.16	1.90	2.48	2.13	2.18	2.17	2.16	1.78	1.90	2.18
K_2O	0.38	1.79	0.83	0.83	0.84	1.48	0.44	0.43	0.56	0.40	0.21	0.59	0.39
P_2O_5	0.14	0.16	0.16	0.14	0.17	0.16	0.14	0.14	0.14	0.14	0.11	0.11	0.17
SUM	100.00	99.98	99.99	99.99	100.00	99.99	99.99	99.99	99.99	99.99	100.00	100.00	99.97
Loss 110°		3.07	0.35	0.68		3.08	1.06	0.74	0.98	0.97			
L.O.I.		2.90	0.67	1.09		3.51	1.36	1.49	1.75	2.14	1.32	0.58	1.51
$L.O.I._{tot}$	2.24	5.97	1.02	1.77	1.13	6.59	2.42	2.23	2.73	3.11	1.32	0.58	1.51
Mg#	**60.38**	**46.23**	**62.24**	**58.97**	**63.11**	**66.96**	**59.71**	**57.84**	**59.89**	**58.38**	**63.02**	**61.41**	**44.02**
XRF													
Sc	51	21	18	18	45	25	16	17	17	17	42	39	39
V	423	260	246	269	278	315	291	303	299	300	216	272	281
Cr	110	159	355	224	326	285	250	187	186	184	328	229	235
Co	51	32	49	45	43	41	42	42	43	42	42	42	44
Ni	69	42	121	77	104	68	75	63	60	59	108	91	90
Cu		108	58	53		130	151	63	66	134			
Zn		47	73	53		77	84	80	75	68			
Ga		15	16	17		18	16	17	17	17			
Rb	9	33	29	26	19	17	15	10	10	11	31	7	8
Sr	106	174	161	178	166	209	196	192	196	198	156	168	178
Y	38	28	28	25	23	24	24	26	26	26	27	20	21
Zr	117	116	121	108	99	118	106	111	110	113	117	73	76
Nb	8	9	11	10	9	10	8	10	10	9	10	6	6
Ba	190	184	205	183	184	122	170	192	199	183	218	99	68
La	11	12	10	17	20	<10	15	<10	<10	<10	20	10	13
Ce	20	27	26	34	31	28	22	22	22	17	31	24	22
Nd	11	19	18		16	21	13	23		17	18	16	12
Pb	12	<3	<3	<3	12	<3	<3	<3	<3	<3	14	12	10
Th	5	<3	<3	<3	6	<3	<3	<3	<3	<3	6	4	4
U	<2	4	<3	<3	2	3	<3	3	<3	<3	2	2	2
Norma													
Qz	4.89	3.98	3.58	5.1	4.55		4.27	5.09	4.49	4.81	2.1	2.54	2.11
Co													
Or	2.24	10.57	4.9	4.9	4.96	8.74	2.6	2.54	3.31	2.36	1.24	3.48	2.3
Ab	16.91	18.51	17.5	18.29	16.06	20.96	18	18.43	18.34	18.26	15.05	16.06	18.43
An	27.92	25.34	24.89	27.68	25.6	32.29	29.37	28.52	28.54	29.25	32.39	30.29	26.02
Le													
Ne													
Di	19.86	7.33	19.02	17.52	18.57	1.4	17.83	17.83	16.75	17.05	21.7	21.1	20.6
Hy	23.63	28.64	25.46	21.99	25.68	23.54	23.28	22.71	23.78	23.33	23.44	22.36	24.15
Ol						8.09							
Mt	1.99	2.59	1.99	1.9	1.94	1.81	1.95	2.01	1.95	2.01	1.89	1.9	2.86
Ilm	2.21	2.63	2.24	2.3	2.21	2.72	2.32	2.49	2.49	2.57	1.9	1.98	3.1
Ap	0.31	0.35	0.35	0.31	0.37	0.35	0.31	0.31	0.31	0.31	0.24	0.24	0.37
Sum	**99.96**	**99.94**	**99.93**	**99.99**	**99.94**	**99.9**	**99.93**	**99.93**	**99.96**	**99.95**	**99.95**	**99.95**	**99.94**

Figure A.3: XRF and normative compositions of Tiourjdal samples.

	Lower										Intermediate	
wt%	**TEL1**	**TEL2**	**TEL3**	**TEL4**	**TEL6**	**TEL7**	**TEL9**	**TEL10**	**TEL11**	**TEL12**	**TEL13**	**TEL15**
SiO_2	52.41	51.01	54.27	56.43	49.63	49.32	54.75	54.42	53.46	54.59	54.20	59.30
TiO_2	1.46	1.50	1.44	1.41	1.33	1.61	1.42	1.55	1.46	1.41	1.25	1.12
Al_2O_3	13.97	13.85	13.94	12.79	16.11	15.10	13.19	13.85	14.07	13.20	14.79	12.22
Fe_2O_3	10.81	12.25	10.69	10.91	9.92	11.25	11.30	11.57	10.52	11.49	10.37	9.57
MnO	0.10	0.12	0.13	0.12	0.09	0.13	0.09	0.08	0.16	0.11	0.09	0.09
MgO	7.34	8.69	8.55	6.69	5.49	7.83	6.03	6.95	7.92	7.49	8.78	6.93
CaO	10.54	8.84	7.80	8.76	15.31	11.64	9.92	7.62	9.62	8.62	6.95	7.38
Na_2O	2.61	2.80	2.79	2.24	1.58	2.61	2.36	2.41	2.22	2.48	3.01	2.25
K_2O	0.59	0.77	0.23	0.50	0.38	0.33	0.79	1.38	0.41	0.45	0.42	1.02
P_2O_5	0.16	0.16	0.15	0.15	0.15	0.18	0.16	0.17	0.16	0.16	0.14	0.13
SUM	100.00	100.00	100.00	100.00	100.00	100.00	100.00	100.00	100.00	100.00	100.00	100.00
Loss 110°	*1.67*	*1.50*	*1.47*	*1.07*	*1.61*	*1.75*	*1.26*	*1.36*	*2.44*	*1.17*	*1.23*	*1.29*
L.O.I.	*4.70*	*4.35*	*2.94*	*2.17*	*4.22*	*4.74*	*2.72*	*2.65*	*1.52*	*3.37*	*3.90*	*4.76*
$L.O.I._{tot}$	6.37	5.85	4.41	3.24	5.83	6.49	3.98	4.01	3.96	4.54	5.13	6.05
Mg#	**58.20**	**59.25**	**62.11**	**55.67**	**53.13**	**58.79**	**52.22**	**55.17**	**60.65**	**57.18**	**63.44**	**59.74**
XRF (ppm)												
Sc	14.79	17.79	17.49	17.03	3.86	13.65	14.50	19.01	15.75	17.37	22.20	17.29
V	277.89	280.85	277.59	266.96	258.87	301.85	263.00	278.56	278.71	260.41	293.72	242.20
Cr	313.66	302.50	304.74	245.87	312.64	327.38	236.98	193.13	278.23	256.88	227.50	171.65
Co	41.48	49.52	46.65	41.61	32.11	42.92	38.79	38.97	46.10	43.63	48.29	39.08
Ni	81.93	78.14	87.85	81.57	76.18	94.45	87.57	57.88	71.36	71.69	75.52	60.79
Cu	42.51	57.90	106.58	57.19	33.15	205.72	38.60	43.00	173.93	87.73	169.15	60.03
Zn	28.65	30.22	145.49	99.66	12.90	52.46	18.92	19.01	66.65	44.48	64.04	46.60
Ga	16.85	15.72	16.92	16.55	22.88	17.11	17.48	16.32	15.75	15.08	14.52	12.50
Rb	26.97	28.06	3.25	10.06	9.13	7.67	22.37	47.42	25.55	10.50	6.93	21.89
Sr	176.77	175.59	189.36	186.75	101.52	213.02	197.80	207.05	223.97	176.03	191.83	147.03
Y	27.15	25.14	25.81	27.09	23.07	24.59	25.64	28.03	24.49	25.30	24.76	24.80
Zr	119.00	123.71	117.19	119.31	111.87	133.06	121.66	131.12	121.49	114.93	102.36	92.54
Nb	13.48	13.28	13.48	12.58	12.81	13.75	14.21	14.59	12.20	11.84	9.01	7.70
Ba	146.81	179.36	132.87	160.82	137.77	142.42	214.03	297.86	185.26	165.72	153.12	249.53
La	15.54	21.65	25.14	16.93	3.77	11.31	13.44	6.62	<10	5.92	10.44	10.24
Ce	43.44	38.32	29.73	22.55	23.17	31.42	26.98	32.25	40.05	36.27	11.48	33.63
Nd	29.31	14.40	17.49	21.58	29.00	27.96	17.76	12.77	27.95	15.08	15.08	18.79
Pb	7.02	6.50	7.55	8.13	5.93	6.73	7.39	8.35	8.07	6.87	5.69	6.86
Th	0.00	0.00	0.00	0.00	0.00	0.00	0.00	0.00	<3	0.00	0.00	<3
U	3.46	3.95	2.39	1.94	2.73	1.96	2.11	1.73	<3	4.49	2.56	3.01
Norma												
Qz	1.36		4.67	10.9	1.12		7	5.18	5.08	6.4	3.09	14.21
Co												
Or	3.48	4.55	1.36	2.95	2.24	1.95	4.66	8.15	2.42	2.66	2.48	6.02
Ab	22.06	23.67	23.58	18.93	13.36	22.06	19.95	20.37	18.77	20.96	25.44	19.02
An	24.65	22.94	24.82	23.36	35.73	28.5	23.04	22.89	27.2	23.55	25.6	20.22
Le												
Ne												
Di	21.82	16.29	10.52	15.74	32.41	23.01	20.78	11.37	15.93	14.93	6.49	12.73
Hy	21.4	19.84	29.86	22.99	10.38	8.91	19.33	26.46	25.42	26.23	32.16	23.52
Ol		7.14				9.97						
Mt	2.06	2.33	2.03	2.07	1.89	2.14	2.15	2.2	2	2.19	1.97	1.82
Ilm	2.78	2.85	2.74	2.68	2.53	3.06	2.7	2.95	2.78	2.68	2.38	2.12
Ap	0.35	0.35	0.33	0.33	0.33	0.39	0.35	0.37	0.35	0.35	0.31	0.28
Sum	**99.96**	**99.96**	**99.91**	**99.95**	**99.99**	**99.99**	**99.96**	**99.94**	**99.95**	**99.95**	**99.92**	**99.94**

Figure A.4: XRF and normative compositions of Telouet samples.

	Intermediate						Upper	Intermediate		Upper		Recurrent
wt%	**TEL16**	**TEL17**	**TEL18**	**TEL19a**	**TEL19b**	**TEL20**	**TEL21**	**TEL22**	**TEL23**	**TEL24**	**TEL25**	**AN 169**
SiO_2	52.94	52.41	49.37	50.59	50.95	51.64	53.89	54.14	52.73	51.26	50.13	51.43
TiO_2	1.26	1.28	1.35	1.29	1.25	1.31	1.08	1.23	1.21	1.06	1.10	1.56
Al_2O_3	14.12	14.68	15.63	14.15	14.33	14.65	13.89	15.06	14.63	14.72	15.10	13.62
Fe_2O_3	11.40	11.13	10.20	12.56	10.51	11.21	10.41	9.86	10.89	11.01	11.40	14.22
MnO	0.17	0.18	0.12	0.19	0.17	0.12	0.16	0.20	0.16	0.17	0.21	0.31
MgO	7.14	8.52	8.08	8.19	9.81	8.46	8.23	7.04	7.22	7.78	8.25	6.04
CaO	10.28	8.55	12.85	10.58	10.08	10.51	10.08	9.54	10.60	11.70	11.54	10.31
Na_2O	2.17	2.53	1.94	2.17	2.56	1.80	1.87	2.26	2.06	1.94	1.96	2.01
K_2O	0.37	0.55	0.33	0.15	0.21	0.17	0.29	0.52	0.37	0.26	0.20	0.36
P_2O_5	0.15	0.15	0.13	0.12	0.12	0.13	0.10	0.14	0.13	0.10	0.11	0.16
SUM	100.00	100.00	100.00	100.00	100.00	100.00	100.00	100.00	100.00	100.00	100.00	100.00
Loss 110°	*1.25*	*2.10*	*1.48*	*0.85*	*1.06*	*3.22*	*1.45*	*1.61*	*1.54*	*0.76*	*1.26*	
L.O.I.	*0.60*	*3.10*	*3.55*	*1.07*	*2.06*	*1.92*	*3.17*	*1.96*	*0.97*	*0.44*	*1.53*	
$L.O.I._{tot}$	1.85	5.20	5.03	1.92	3.12	5.14	4.62	3.57	2.51	1.20	2.79	0.51
Mg#	**56.20**	**61.07**	**61.86**	**57.20**	**65.65**	**60.74**	**61.81**	**59.41**	**57.60**	**59.16**	**59.71**	**46.53**
XRF (ppm)												
Sc	16.59	20.57	12.82	18.64	19.67	17.26	17.36	18.71	17.94	15.41	15.65	50
V	287.09	287.05	310.36	300.32	305.95	286.67	260.29	289.19	286.23	291.36	302.13	422
Cr	260.98	212.73	354.14	387.81	445.16	324.90	354.91	275.60	220.62	267.95	308.54	118
Co	46.62	46.45	44.92	49.24	47.47	47.90	40.92	43.01	44.94	45.05	47.24	47
Ni	89.61	71.76	93.93	87.39	99.59	84.52	84.13	73.09	67.95	98.40	228.54	67
Cu	188.74	181.73	157.18	291.40	384.81	383.14	115.60	160.07	104.80	16.70	20.32	
Zn	56.24	85.23	23.74	81.60	68.88	46.29	55.32	167.21	55.28	57.11	73.30	
Ga	14.43	15.64	15.48	14.03	15.02	15.18	14.88	15.04	15.79	14.33	14.97	
Rb	35.53	12.13	6.93		3.68	9.58	6.77	8.87	12.67	17.49		9
Sr	179.42	173.86	162.87	170.95	183.59	160.50	153.94	189.87	185.13	171.52	166.91	103
Y	27.87	26.26	26.31	23.93	24.22	25.61	20.98	25.07	25.64	23.22	25.47	35
Zr	108.85	104.47	102.00	101.81	92.62	97.42	80.50	100.87	98.76	78.45	82.24	111
Nb	9.42	9.67	8.17	8.93	7.94	8.73	7.34	7.52	7.51	8.30	6.61	8
Ba	175.59	122.01	140.84	82.39	99.69	87.65	94.43	186.50	184.35	127.85	83.89	104
La	12.76	11.09	20.99	13.93	<10	<10	<10	<10	18.82	16.70	<10	11
Ce	31.70	31.09	22.79	19.03	32.16	13.94	19.46	21.79	28.76	<10	<10	19
Nd	<10	22.66	22.03	22.66	24.61	27.41	27.66	12.15	17.45	26.68	18.37	11
Pb	6.48	6.54	6.65	<5	7.07	5.88	6.58	6.65	6.43	5.93	5.64	14
Th	<3	<3	<3	<3	<3	<3	<3	<3	<3	<3	<3	6
U	3.34	<3	<3	<3	<3	4.65	3.43	<3	<3	<3	<3	2
Norma												
Qz	4.59	1.39		0.21		3.37	6.45	6.24	4.44	1.59		4.01
Co												
Or	2.18	3.25	1.95	0.89	1.24	1	1.71	3.07	2.18	1.53	1.18	2.13
Ab	18.34	21.39	16.4	18.34	21.64	15.22	15.81	19.1	17.41	16.4	16.57	16.99
An	27.68	27.06	32.95	28.41	26.98	31.38	28.64	29.4	29.57	30.68	31.8	27.06
Le												
Ne												
Di	18.39	11.76	24.46	19.16	18.09	16.29	16.94	13.94	18.22	21.92	20.28	19.23
Hy	23.87	30.18	14.34	27.83	21.73	27.78	26.16	23.66	23.48	23.52	24.38	24.54
Ol			5.1		5.64						1.25	
Mt	2.17	2.12	1.94	2.39	2	2.13	1.98	1.88	2.07	2.09	2.17	2.7
Ilm	2.4	2.44	2.57	2.45	2.38	2.49	2.05	2.34	2.3	2.02	2.09	2.96
Ap	0.33	0.33	0.28	0.26	0.26	0.28	0.22	0.31	0.28	0.22	0.24	0.35
Sum	**99.95**	**99.92**	**99.99**	**99.94**	**99.96**	**99.94**	**99.96**	**99.94**	**99.95**	**99.97**	**99.96**	**99.97**

Figure A.5: XRF and normative compositions of Telouet samples.

	Lower						Intermediate			
wt%	**OL1**	**OL2**	**OL3**	**OL4**	**OL5**	**OL6**	**OL7**	**OL8**	**OL9**	**OL10**
SiO_2	53.18	52.22	48.01	55.01	51.92	51.60	49.89	54.53	52.45	52.84
TiO_2	1.43	1.28	1.57	1.50	1.44	1.35	1.27	1.21	1.18	1.22
Al_2O_3	13.32	13.24	15.50	13.60	14.33	13.98	14.61	13.94	13.49	14.35
Fe_2O_3	11.99	11.46	13.76	14.49	11.57	12.18	11.52	10.88	11.73	10.63
MnO	0.11	0.16	0.13	0.08	0.13	0.15	0.19	0.14	0.13	0.16
MgO	8.25	8.73	8.80	6.90	7.56	8.75	8.29	7.71	9.87	8.15
CaO	8.50	9.87	8.73	3.95	8.74	8.78	9.79	8.61	7.40	10.19
Na_2O	1.95	2.06	2.70	3.01	2.25	2.59	1.68	2.23	2.12	2.09
K_2O	1.13	0.84	0.62	1.28	1.89	0.46	2.61	0.62	1.51	0.25
P_2O_5	0.15	0.13	0.17	0.18	0.16	0.14	0.15	0.14	0.12	0.13
SUM	100.00	100.00	100.00	100.00	100.00	100.00	100.00	100.00	100.00	100.00
Loss 110°	*2.28*	*1.64*	*2.24*	*3.15*	*1.41*	*1.57*	*1.97*	*1.51*	*1.99*	*2.40*
L.O.I.	*1.36*	*0.18*	*3.12*	*3.81*	*3.47*	*2.80*	*3.22*	*2.25*	*4.16*	*1.20*
$L.O.I._{tot}$	3.64	1.82	5.36	6.96	4.88	4.37	5.19	3.76	6.15	3.6
Mg#	**58.50**	**60.95**	**56.72**	**49.40**	**57.26**	**59.55**	**59.61**	**59.21**	**63.29**	**61.10**
XRF (ppm)										
Sc	17	14	20	24	16	17	17	21	19	16
V	279	269	302	280	275	269	283	280	266	285
Cr	408	508	411	327	370	323	222	223	297	317
Co	45	137	47	50	43	48	78	44	47	45
Ni	116	142	108	78	114	93	76	72	81	78
Cu	99	11	70	64	109	78	148	78	104	182
Zn	44	51	44	38	34	42	35	57	36	69
Ga	16	6	18	12	17	16	12	15	15	15
Rb	26	27	10	21	30	10	45	13	30	20
Sr	219	205	229	166	181	193	198	173	153	169
Y	25	23	28	25	27	21	25	27	21	25
Zr	114	105	132	121	125	113	106	101	92	96
Nb	12	12	13	13	13	13	10	10	7	8
Ba	211	215	211	207	364	166	517	167	221	126
La	12	18	26	18	12	<10	18	16	12	16
Ce	37	33	43	24	33	33	38	26	14	14
Nd	23	17	19	32	12	22	<10	19	15	24
Pb	8	7	<5	5	7	6	6	7	6	7
Th	<3	<3	<3	<3	<3	<3	<3	<3	<3	<3
U	<3	3	<3	<3	<3	<3	<3	<3	3	<3
Norma										
Qz	4	1.44		5.64				6.47		8.19
Co				0.51						
Or	6.65	4.96	3.66	7.56	11.16	2.72	15.41	3.66	8.91	1.48
Ab	16.48	17.41	22.82	25.44	19.02	21.89	14.2	18.82	17.92	17.67
An	24.26	24.39	28.33	18.42	23.41	25.15	24.61	26.19	22.82	29.02
Le										
Ne										
Di	13.88	19.42	11.4		15.54	14.34	18.85	12.8	10.69	16.49
Hy	29.35	27.42	9.52	36.35	23.6	29.96	8.91	27.32	34.29	17.71
Ol			18.28		1.92	0.67	13.09		0.54	
Mt	2.28	2.18	2.62	2.76	2.2	2.32	2.19	2.07	2.23	6.81
Ilm	2.72	2.44	2.99	2.85	2.74	2.57	2.42	2.3	2.24	2.32
Ap	0.33	0.28	0.37	0.39	0.35	0.31	0.33	0.31	0.26	0.28
Sum	**99.95**	**99.94**	**99.99**	**99.92**	**99.94**	**99.93**	**100.01**	**99.94**	**99.9**	**99.97**

Figure A.6: XRF and normative compositions of Oued Lahr samples.

	Intermediate		Upper						Recurrent
wt%	OL11	OL12	OL13	OL14	OL15	OL16	OL17	OL18	AN 61
SiO_2	52.14	52.18	51.35	52.22	51.43	51.56	51.42	51.44	51.41
TiO_2	1.22	1.30	1.17	1.10	0.98	1.06	1.07	1.07	1.65
Al_2O_3	13.81	14.18	15.31	14.91	14.70	14.69	14.90	14.68	13.74
Fe_2O_3	11.21	11.25	10.38	10.34	10.43	10.78	10.41	10.73	12.90
MnO	0.15	0.13	0.22	0.22	0.14	0.19	0.19	0.18	0.36
MgO	8.93	8.82	9.10	8.57	8.72	7.96	8.31	8.22	6.73
CaO	10.38	10.03	7.71	9.90	11.47	11.51	10.95	11.39	10.52
Na_2O	1.82	1.78	1.77	2.31	1.83	1.90	2.39	1.91	2.17
K_2O	0.21	0.19	2.87	0.31	0.19	0.24	0.25	0.25	0.34
P_2O_5	0.12	0.13	0.12	0.11	0.10	0.11	0.11	0.11	0.17
SUM	100.00	100.00	100.00	100.00	100.00	100.00	100.00	100.00	100.00
Loss 110°	*2.13*	*3.13*	*1.84*	*1.45*	*2.12*	*1.69*	*1.18*	*1.54*	
L.O.I.	*1.01*	*1.63*	*3.26*	*2.18*	*1.10*	*0.90*	*1.72*	*0.66*	
$L.O.I._{tot}$	3.14	4.76	5.1	3.63	3.22	2.59	2.9	2.2	0.24
Mg#	**62.02**	**61.62**	**64.25**	**62.94**	**63.13**	**60.21**	**62.08**	**61.10**	**51.69**
XRF (ppm)									
Sc	17	17	22	19	16	17	19	17	50
V	278	287	296	289	266	294	287	290	412
Cr	410	339	201	242	278	243	250	247	101
Co	52	45	42	40	40	44	42	83	48
Ni	98	83	86	84	139	85	89	90	69
Cu	113	122	27	35	105	53	52	34	
Zn	57	48	104	142	48	68	82	81	
Ga	16	15	16	14	14	15	17	12	
Rb	15	13	43	6	9	4	4	<3	8
Sr	160	165	184	164	176	168	190	178	106
Y	23	26	19	24	20	23	23	23	37
Zr	91	97	80	78	71	78	77	79	113
Nb	9	9	7	6	8	7	7	6	8
Ba	112	83	331	82	79	124	90	127	255
La	<10	<10	<10	<10	<10	<10	<10	<10	9
Ce	24	28	23	18		18	12	15	17
Nd	21	18	16	30	14	16	22	13	9
Pb	6	6	7	7	6	6	7	6	
Th	<3	<3	<3	<3	<3	<3	<3	<3	4
U	<3	3	4	3	3	3	<3	5	2
Norma									
Qz	3.48	4.16		1.69	1.73	2.25		1.85	2.87
Co									
Or	1.24	1.12	16.94	1.83	1.12	1.42	1.48	1.48	2.01
Ab	15.38	15.05	14.96	19.53	15.47	16.06	20.2	16.15	18.34
An	28.88	30.13	25.34	29.39	31.32	30.83	29.18	30.73	26.74
Le									
Ne									
Di	17.84	15.35	9.88	15.52	20.35	20.94	19.97	20.51	20.17
Hy	28.41	29.24	19.34	27.68	25.89	24.16	24.65	24.91	23.87
Ol			9.03				0.23		
Mt	2.13	2.14	1.97	1.97	1.98	2.05	1.98	2.04	2.45
Ilm	2.32	2.47	2.23	2.09	1.86	2.02	2.04	2.04	3.14
Ap	0.26	0.28	0.26	0.24	0.22	0.24	0.24	0.24	0.37
Sum	**99.94**	**99.94**	**99.95**	**99.94**	**99.94**	**99.97**	**99.97**	**99.95**	**97.62**

Figure A.7: XRF and normative compositions of Oued Lahr samples

	Lower						Intermediate									
wt%	**AN503**	**AN504**	**AN602**	**AN506**	**AN603**	**Carbonate**	**AN508**	**AN604**	**AN509**	**AN510**	**AN605**	**AN511**	**AN606**	**AN607**	**AN608**	**AN627**	**AN628**
SiO_2	52.91	52.91	53.45	52.78	53.05		52.97	53.78	53.21	53.12	54.04	52.33	53.54	53.37	53.72	53.12	53.15
TiO_2	1.52	1.52	1.51	1.51	1.47		1.24	1.20	1.26	1.34	1.33	1.24	1.20	1.21	1.26	1.38	1.45
Al_2O_3	14.57	13.78	13.69	13.65	13.91		14.05	14.17	14.09	13.76	13.52	14.03	14.80	14.37	14.07	13.89	13.20
Fe_2O_3	9.64	10.70	10.79	11.21	10.46		10.84	10.30	10.73	11.82	11.60	11.38	9.54	10.80	11.15	11.32	11.99
MnO	0.07	0.16	0.17	0.19	0.12		0.16	0.14	0.16	0.17	0.16	0.16	0.12	0.13	0.15	0.18	0.16
MgO	10.02	8.16	7.77	7.63	9.32		7.65	8.13	7.61	6.95	6.88	7.56	9.50	7.97	7.60	7.28	7.36
CaO	8.49	9.72	9.63	9.92	8.99		10.45	9.76	10.24	10.08	9.82	10.76	8.96	9.64	9.53	10.13	10.18
Na_2O	2.20	2.21	2.15	2.25	2.09		1.94	1.91	1.99	2.01	1.97	1.96	1.91	1.98	1.93	2.00	1.82
K_2O	0.40	0.64	0.66	0.66	0.41		0.54	0.46	0.56	0.59	0.52	0.42	0.27	0.37	0.43	0.54	0.52
P_2O_5	0.19	0.19	0.19	0.19	0.18		0.15	0.15	0.15	0.16	0.16	0.15	0.15	0.15	0.16	0.16	0.16
SUM	100	100	100	100	100		100	100	100	100	100	100	100	100	100	100	100
Loss 110°	3.71	1.45	1.52	1.06	2.75		1.27	2.28	1.21	0.94	1.12	0.97	3.21	1.97	1.94	1.41	1.20
L.O.I.	2.40	1.60	1.15	1.12	1.65		0.97	1.25	1.05	0.49	0.60	0.87	1.92	1.03	0.92	0.70	0.47
$L.O.I._{tot}$	6.11	3.05	2.67	2.18	4.40		2.24	3.53	2.26	1.43	1.72	1.84	5.13	3.00	2.86	2.11	1.67
Mg#	**68.05**	**60.97**	**59.60**	**58.25**	**64.60**		**59.11**	**61.79**	**59.23**	**54.64**	**54.84**	**57.64**	**67.11**	**60.20**	**58.28**	**56.86**	**55.70**
XRF (ppm)																	
Sc																	
V	305	297		297			292		292	294		295	296	294	295	299	313
Cr	362	354		339			327		318	289		416	393	384	371	362	416
Co	44	45		46			43		45	44		44	39	41	39	38	40
Ni	95	108		102			100		111	106		116	65	63	57	59	60
Cu	140	179		166			199		186	188		262	185	193	179	148	65
Zn	59	71		76			68		65	76		72	58	67	78	79	72
Ga	19	20		20			19		18	17		17	28	27	29	25	18
Rb	17	33		35			28		31	29		28	25	32	37	36	27
Sr	281	258		248			180		184	179		190	215	203	201	200	194
Y	28	28		28			25		27	29		25	13	11	12	12	13
Zr	121	124		127			105		106	118		99	110	108	112	122	122
Nb	12	14		13			9		9	9		8	19	19	20	21	20
Ba	182	226		233			161		178	209		430	71	91	108	225	241
La	<10	<10		10			<10		<10	<10		<10	<10	<10	<10	<10	<10
Ce	<10	<10		11			<10		<10	19		<10	32	26	16	<10	<10
Nd	17	24		24			21		21	<10		<10	<10	<10	<10	<10	10
Pb	11	9		9			9		11	8		8	38	30	29	28	22
Th	<3	<3		7			5		<3	<3		4	5	16	21	29	35
U	<3	<3		<3			<3		<3	<3		<3	<3	<3	<3	<3	<3
Norma																	
Qz	3.2	3.52	4.94	3.4	4.09		4.66	6.18	4.95	5.34	7.35	3.76	5.52	5.64	6.69	5.29	6.1
Co																	
Or	2.36	3.78	3.9	3.9	2.42		3.19	2.72	3.31	3.48	3.07	2.48	1.59	2.18	2.54	3.19	3.07
Ab	18.6	18.68	18.17	19.02	17.67		16.4	16.15	16.82	16.99	16.65	16.57	16.15	16.74	16.31	16.91	15.38
An	28.69	25.78	25.74	25.19	27.35		28.02	28.72	27.85	26.77	26.5	28.23	31	29.22	28.45	27.32	26.3
Le																	
Ne																	
Di	9.86	17.33	17.03	18.7	13.07		18.73	15.3	18.02	18.31	17.46	19.87	10.11	14.43	14.6	18.01	19.07
Hy	32.07	25.51	24.84	24.32	30.14		24.19	26.32	24.25	23.92	23.84	24.2	31.12	27.04	26.49	24.13	24.63
Ol																	
Mt	1.83	2.04	2.05	2.13	1.9		2.06	1.96	2.04	2.25	2.21	2.16	1.81	2.05	2.12	2.15	2.28
Ilm	2.88	2.89	2.86	2.87	2.8		2.36	2.28	2.4	2.55	2.53	2.36	2.28	2.3	2.4	2.63	2.76
Ap	0.41	0.41	0.41	0.41	0.39		0.33	0.33	0.33	0.35	0.35	0.33	0.33	0.33	0.35	0.35	0.35
Sum	**99.9**	**99.94**	**99.94**	**99.94**	**99.83**		**99.94**	**99.96**	**99.97**	**99.96**	**99.96**	**99.96**	**99.91**	**99.93**	**99.95**	**99.98**	**99.94**

Figure A.8: XRF and normative compositions of Maaziz samples.

	Intermediate									
wt%	**AN521**	**AN629**	**AN522**	**AN523**	**AN524**	**AN525**	**AN630**	**AN525B**	**AN526**	**AN631**
SiO_2	52.71	53.05	52.65	52.45	52.51	55.46	56.15	52.44	53.19	54.34
TiO_2	1.23	1.23	1.19	1.16	1.10	2.07	2.20	1.47	1.25	1.26
Al_2O_3	14.35	14.30	14.02	13.81	13.51	12.46	12.12	13.62	13.88	14.24
Fe_2O_3	10.87	11.14	11.43	11.51	11.56	13.58	13.39	11.90	11.00	9.98
MnO	0.14	0.15	0.16	0.16	0.16	0.17	0.16	0.19	0.19	0.14
MgO	7.18	7.04	7.33	7.68	8.20	5.14	4.92	7.35	7.46	8.12
CaO	10.32	10.10	10.30	10.46	10.21	7.35	7.05	10.34	10.58	9.36
Na_2O	1.87	1.88	1.89	1.89	1.84	2.29	2.33	1.97	1.87	1.99
K_2O	1.18	0.95	0.89	0.75	0.76	1.21	1.39	0.56	0.43	0.40
P_2O_5	0.15	0.15	0.15	0.14	0.14	0.26	0.28	0.16	0.14	0.16
SUM	100	100	100	100	100	100	100	100	100	100
Loss 110°	1.43	1.29	0.94	0.90	1.14	1.98	2.07	0.68	1.04	2.31
L.O.I.	0.45	0.22	0.37	0.31	0.50	0.91	0.94	0.37	0.55	1.17
$L.O.I._{tot}$	1.88	1.51	1.31	1.21	1.64	2.89	3.01	1.05	1.59	3.48
Mg#	**57.50**	**56.43**	**56.78**	**57.74**	**59.26**	**43.70**	**42.97**	**55.87**	**58.16**	**62.52**
XRF (ppm)										
Sc										
V	288	286	278	270	266	363		338	290	296
Cr	332	375	323	380	367	41		365	386	309
Co	51	45	54	53	53	51		49	48	39
Ni	109	75	107	122	138	41		98	101	56
Cu	103	136	97	137	99	256		218	118	142
Zn	65	70	292	69	70	81		77	100	61
Ga	17	19	16	15	16	18		17	18	28
Rb	25	44	26	25	25	31		31	23	38
Sr	178	195	174	169	163	176		173	178	200
Y	21	11	23	22	22	36		24	20	12
Zr	118	115	111	108	109	213		127	108	114
Nb	3	18	4	3	4	10		3	5	21
Ba	198	111	193	182	182	316		192	176	106
La	13	<10	14	<10	19	13		<10	<10	<10
Ce	11	28	12	<10	11	30		<10	<10	29
Nd	34	<10	27	26	21	33		28	20	<10
Pb	8	33	22	7	7	<5		6	9	34
Th	<3	7	<3	4	<3	9		4	10	6
U	<3	<3	<3	<3	<3	<3		<3	<3	<3
Norma										
Qz	3.35	4.66	3.69	3.27	3.13	10.23	11.27	4.39	5.68	7.22
Co										
Or	6.97	5.61	5.25	4.43	4.49	7.14	8.21	3.31	2.54	2.36
Ab	15.81	15.89	15.98	15.98	15.55	19.36	19.7	16.65	15.81	16.82
An	27.26	27.76	27.13	26.97	26.35	20.14	18.5	26.66	28.2	28.73
Le										
Ne										
Di	18.87	17.59	18.92	19.72	19.19	12.23	12.25	19.41	19.2	13.6
Hy	22.97	23.65	24.23	24.9	26.63	23.75	22.68	23.89	23.76	26.56
Ol										
Mt	2.07	2.12	2.17	2.19	2.2	2.58	2.55	2.21	2.09	1.9
Ilm	2.34	2.34	2.25	2.2	2.09	3.94	4.19	2.8	2.38	2.4
Ap	0.33	0.33	0.33	0.31	0.31	0.57	0.61	0.35	0.31	0.35
Sum	**99.97**	**99.95**	**99.95**	**99.97**	**99.94**	**99.94**	**99.96**	**99.67**	**99.97**	**99.94**

Figure A.9: XRF and normative compositions of Agourai samples.

	Intermediate			Upper		Intermediate		
wt%	AN632	carbonate	AN528	AN529	AN530	AN633	??	AN531	AN532
SiO_2	53.11			51.63	51.70	52.46		53.44	53.14
TiO_2	1.33			1.19	1.12	1.13		1.29	1.28
Al_2O_3	15.28			15.10	14.26	14.18		14.00	13.91
Fe_2O_3	10.24			10.69	11.26	11.13		11.61	11.89
MnO	0.12			0.17	0.17	0.24		0.16	0.18
MgO	7.37			8.01	7.68	7.07		7.04	7.05
CaO	10.11			10.73	11.05	11.27		9.38	9.45
Na_2O	1.92			1.98	2.02	1.98		2.30	2.23
K_2O	0.36			0.36	0.61	0.41		0.61	0.70
P_2O_5	0.15			0.14	0.13	0.14		0.16	0.16
SUM	100.00			100	100	100		100	100
Loss 110°	3.42			2.51	1.23	0.80		2.40	1.56
L.O.I.	1.57			1.58	0.48	0.32		0.82	0.58
$L.O.I._{tot}$	4.99			4.09	1.71	1.12		3.22	2.14
Mg#	**59.60**			**60.56**	**58.29**	**56.55**		**55.42**	**54.85**
XRF (ppm)									
Sc									
V	279			287		300		319	331
Cr	388			267		273		80	73
Co	44			46		39		45	45
Ni	65			98		63		63	66
Cu	135			129		111		63	98
Zn	68			82		111		74	76
Ga	23			14		24		17	21
Rb	30			15		33		21	22
Sr	207			196		201		205	202
Y	14			20		10		24	22
Zr	115			95		92		115	113
Nb	22			<3		19		5	<3
Ba	103			129		56		216	218
La	<10			<10		<10		<10	<10
Ce	49			17		23		16	19
Nd	<10			16		<10		24	24
Pb	37			9		35		7	7
Th	14			<3		28		<3	<3
U	<3			<3		<3		<3	<3
Norma									
Qz	6.04			2.29	1.56	3.93		4.78	4.28
Co									
Or	2.13			2.13	3.6	2.42		3.6	4.13
Ab	16.23			16.74	17.08	16.74		19.44	18.85
An	32			31.24	28.03	28.58		26.06	25.87
Le									
Ne									
Di	14.07			17.26	21.31	21.74		16.01	16.48
Hy	24.68			25.7	23.83	21.99		25.03	25.29
Ol									
Mt	1.95			2.03	2.14	2.12		2.21	2.26
Ilm	2.53			2.26	2.13	2.14		2.45	2.44
Ap	0.33			0.31	0.28	0.31		0.35	0.35
Sum	**99.96**			**99.96**	**99.96**	**99.97**		**99.93**	**99.95**

Figure A.10: XRF and normative compositions of Agourai samples.

	Lower		Intermediate										Upper
wt%	AN534	AN609	AN535	AN610	AN536	AN537	AN538	AN611	AN612	AN539	AN613	AN614	AN540
SiO_2	53.71	53.84	53.22	53.59	53.33	53.16	52.46	51.82	53.12	52.43	52.91	52.92	51.39
TiO_2	1.44	1.43	1.31	1.27	1.21	1.19	1.29	1.29	1.28	1.29	1.26	1.28	1.07
Al_2O_3	14.26	13.93	15.04	14.09	14.04	14.17	14.00	14.21	13.80	13.92	14.12	13.62	14.61
Fe_2O_3	10.48	10.83	10.39	11.04	10.86	10.17	10.56	10.72	10.76	10.69	10.80	11.37	11.00
MnO	0.11	0.12	0.09	0.13	0.12	0.14	0.15	0.13	0.10	0.14	0.08	0.15	0.15
MgO	8.45	8.57	7.17	7.18	8.41	8.49	8.92	8.82	9.01	8.37	9.85	7.93	7.82
CaO	8.96	8.80	9.73	9.77	9.53	9.91	10.29	10.82	9.78	10.91	8.96	10.31	11.62
Na_2O	2.07	1.98	2.12	2.03	1.87	1.96	1.81	1.78	1.73	1.77	1.66	1.84	1.83
K_2O	0.34	0.31	0.77	0.74	0.47	0.44	0.37	0.25	0.28	0.34	0.22	0.42	0.38
P_2O_5	0.18	0.18	0.16	0.16	0.15	0.15	0.14	0.15	0.14	0.14	0.14	0.14	0.13
SUM	100.00	100.00	100.00	100.00	100.00	99.78	100.00	100.00	100.00	100.00	100.00	100.00	100.00
Loss 110°	2.99	3.24	2.40	1.66	2.06	1.71	1.90	2.29	3.18	1.51	4.83	1.32	0.92
L.O.I.	2.43	2.57	1.60	0.65	1.53	1.31	1.30	1.18	2.01	1.13	3.34	0.56	0.85
$L.O.I_{tot}$	5.42	5.81	4.00	2.31	3.59	3.02	3.20	3.47	5.19	2.64	8.17	1.88	1.77
Mg#	**62.30**	**61.84**	**58.58**	**57.14**	**61.33**	**63.09**	**63.36**	**62.76**	**63.18**	**61.59**	**65.15**	**58.83**	**59.28**
XRF (ppm)													
Sc													
V	295		318		286	281	306		302	305	300	296	298
Cr	329		180		310	325	372		422	399	484	422	267
Co	47		43		47	47	43		47	54	48	40	45
Ni	106		79		114	109	107		64	116	95	88	115
Cu	118		100		182	190	328		189	274	155	116	132
Zn	93		47		70	79	79		70	91	65	97	68
Ga	22		24		20	19	22		25	23	28	30	21
Rb	18		27		33	34	26		24	23	23	40	18
Sr	288		198		181	179	175		200	180	194	196	184
Y	23		21		19	20	17		10	19	9	13	17
Zr	126		110		109	109	104		105	106	107	107	82
Nb	8		4		<3	<3	<3		21	4	19	20	<3
Ba	215		221		186	181	145		53	134	33	80	133
La	16		<10		11	<10	13		<10	21	<10	<10	11
Ce	22		16		21	16	34		27	27	15	<10	<10
Nd	36		22		19	19	13		<10	29	<10	<10	18
Pb	12		9		9	11	9		16	10	15	17	8
Th	<3		<3		5	<3	<3		13	5	10	9	<3
U	<3		<3		<3	<3	<3		<3	<3	<3	<3	<3
Norma													
Qz	6.17	6.77	4.64	5.54	5.44	4.76	3.85	3.12	5.62	4.24	5.35	5.13	2.03
Co													
Or	2.01	1.83	4.55	4.37	2.77	2.6	2.18	1.48	1.65	2.01	1.3	2.48	2.24
Ab	17.5	16.74	17.92	17.16	15.81	16.57	15.3	15.05	14.62	14.96	14.03	15.55	15.47
An	28.6	28.19	29.24	27.14	28.52	28.55	28.97	30.03	29.05	29.02	30.41	27.65	30.51
Le													
Ne													
Di	11.97	11.66	14.75	16.68	14.54	16.01	17.26	18.5	15.13	19.77	10.67	18.53	21.56
Hy	28.56	29.56	24.04	24.2	28.16	26.7	27.6	26.95	29.08	25.17	33.4	25.69	23.73
Ol													
Mt	1.99	2.06	1.98	2.1	2.07	1.94	2.01	2.04	2.05	2.03	2.05	2.16	2.09
Ilm	2.74	2.72	2.49	2.42	2.3	2.26	2.45	2.45	2.44	2.45	2.4	2.44	2.04
Ap	0.39	0.39	0.35	0.35	0.33	0.33	0.31	0.33	0.31	0.31	0.31	0.31	0.28
Sum	**99.93**	**99.92**	**99.96**	**99.96**	**99.94**	**99.72**	**99.93**	**99.95**	**99.95**	**99.96**	**99.92**	**99.94**	**99.95**

Figure A.11: XRF and normative compositions of Oum R'Rbia samples.

A.2 ICP-MS AND ISOTOPIC COMPOSITIONS

	Lower											
wt%	**TJ1**	**TJ2**	**AN49**	**TJ3**	**TJ4**	**AN134**	**TJ5**	**TJ6**	**TJ7**	**TJ8**	**TJ9**	**TJ10**
SiO_2	52.83	53.13	54.08	53.47	53.99	53.67	53.55	52.57	54.46	53.87	52.36	52.93
TiO_2	1.38	1.41	1.36	1.42	1.46	1.43	1.38	1.35	1.40	1.53	1.49	1.49
Al_2O_3	14.36	14.59	15.28	14.24	14.85	14.28	14.68	15.15	14.75	14.88	14.86	15.03
Fe_2O_3	9.79	9.75	8.26	9.46	9.67	9.92	9.56	9.17	9.97	9.58	10.03	10.58
MnO	0.11	0.12	0.12	0.15	0.15	0.18	0.15	0.13	0.10	0.07	0.09	0.07
MgO	8.53	7.83	6.98	7.88	6.85	7.25	7.75	9.17	7.47	8.73	10.60	9.33
CaO	9.78	9.79	10.63	9.92	9.63	9.97	9.90	9.52	8.48	8.14	6.72	7.44
Na_2O	2.31	2.28	2.16	2.32	2.41	2.15	2.31	2.40	2.41	2.36	2.36	2.33
K_2O	0.74	0.94	0.97	0.96	0.79	0.98	0.55	0.37	0.80	0.65	1.31	0.62
P_2O_5	0.15	0.16	0.15	0.16	0.18	0.17	0.17	0.15	0.15	0.18	0.17	0.17
SUM	99.99	99.99	100.00	99.99	99.99	100.00	99.99	99.99	99.99	99.99	99.99	99.99
ICP-MS (ppm)												
Rb			28.260	31.06	22.04	28.401	14.60		18.38	11.31		7.26
Sr			239.122	266.66	306.27	237.454	275.56		277.97	278.82		293.38
Y			23.389	23.63	26.30	25.963	23.30		20.70	24.43		23.73
Zr			126.450	145.38	170.72	147.204	141.80		133.28	143.62		138.04
Nb			11.939	12.12	13.52	13.254	12.38		11.62	12.46		12.69
Cs			1.000	1.11	1.60	0.911	1.73		0.88	0.54		0.36
Ba			202.640	257.40	290.29	239.664	217.79		238.52	196.29		135.99
La			14.858	16.30	19.38	15.452	16.85		16.18	15.89		19.14
Ce			31.351	36.09	42.70	34.316	37.05		34.95	35.30		40.24
Pr			4.010	4.38	5.18	4.553	4.52		4.20	4.40		4.75
Nd			16.960	19.21	22.56	18.680	19.80		18.10	19.25		20.39
Sm			4.167	4.69	5.44	4.606	4.78		4.30	4.78		4.85
Eu			1.324	1.28	1.47	1.409	1.30		1.20	1.36		1.38
Gd			4.378	4.37	5.05	4.892	4.53		3.87	4.72		4.42
Tb			0.689	0.74	0.84	0.778	0.73		0.65	0.77		0.75
Dy			4.065	4.64	5.22	4.636	4.63		4.09	4.81		4.73
Ho			0.840	0.88	0.97	0.921	0.86		0.76	0.90		0.89
Er			2.388	2.55	2.82	2.545	2.49		2.22	2.65		2.59
Tm				0.34	0.37		0.33		0.29	0.35		0.34
Yb			1.928	2.31	2.55	2.298	2.22		1.99	2.34		2.31
Lu			0.282	0.32	0.35	0.313	0.30		0.27	0.32		0.32
Hf			3.200	3.59	4.13	3.655	3.51		3.25	3.65		3.47
Ta			0.704			0.778						
Pb			4.237	3.99	5.21	4.555	3.71		4.61	2.63		3.23
Th			2.987	2.71	3.15	3.404	2.63		2.43	2.81		2.90
U			0.718	0.65	0.77	0.730	0.62		0.61	0.65		0.71
Sc												
V												
Isotopes												
$^{87}Sr/^{86}Sr$			0.707324	0.706911	0.706569	0.706812	0.706561		0.706564			
$^{87}Sr/^{86}Sr_{(200Ma)}$			0.706351	0.705953	0.705977	0.705828	0.706125		0.70602			
$^{143}Nd/^{144}Nd$			0.512565	0.512557	0.512546	0.512578	0.512569		0.512561			
$^{143}Nd/^{144}Nd_{(200Ma)}$			0.512371	0.512364	0.512355	0.512383	0.512378		0.512373			
Paleomagnetism	**TJ1**	**TJ2**	**AN49**	**TJ3**	**TJ4**	**AN134**	**TJ5**	**TJ6**	**TJ7**	**TJ8**	**TJ9**	**TJ10**
Decl(geo)	358.6	1.5		358.9	3.1		3.5	358.3	358.1	0.3	9.4	13.7
Incl(geo)	20.0	19.8		20.3	19.0		19.1	23.2	23.4	23.9	30.0	30.7
A95	4.3	5.0		4.3	4.5		4.5	3.6	4.8	4.5	5.0	4.7
DG	1	1	1	1	1	1	1	1	1	1	2	2

Figure A.12: ICP-MS and isotopic compositions of Tiourjdal samples.

	Lower												
	TJ11	**TJ12**	**TJ13**	**TJ14**	**TJ15**	**TJ16**	**TJ17**	**TJ18**	**TJ19**	**TJ20**	**TJ21**	**TJ22**	**TJ23**
SiO_2	52.73	51.35	51.67	51.65	52.03	52.97	52.28	52.58	53.41	52.83	53.70	52.97	53.31
TiO_2	1.45	1.54	1.50	1.48	1.43	1.45	1.41	1.40	1.70	1.59	1.49	1.38	1.28
Al_2O_3	14.45	15.43	14.79	14.67	15.03	14.50	14.65	14.06	14.06	15.29	14.26	13.61	14.33
Fe_2O_3	9.85	9.79	10.61	10.32	9.89	9.95	10.26	10.41	10.98	10.44	10.12	10.40	10.26
MnO	0.16	0.11	0.09	0.14	0.16	0.13	0.10	0.12	0.14	0.06	0.14	0.15	0.17
MgO	8.92	9.77	9.36	9.40	9.79	8.77	9.21	9.02	6.82	9.54	7.33	8.90	7.78
CaO	9.59	8.91	9.03	9.54	8.70	9.36	9.22	9.82	9.49	6.18	9.33	9.42	10.06
Na_2O	2.20	2.34	2.35	2.29	2.43	2.26	2.22	2.06	2.46	2.11	2.34	2.14	2.23
K_2O	0.48	0.57	0.41	0.33	0.37	0.44	0.49	0.35	0.74	1.77	1.12	0.87	0.44
P_2O_5	0.16	0.17	0.17	0.16	0.16	0.16	0.16	0.15	0.19	0.17	0.17	0.14	0.14
SUM	99.99	99.99	99.99	99.99	99.99	99.99	99.99	99.99	99.99	99.99	99.99	99.99	99.99
ICP-MS													
Rb	4.56		5.85	3.48		9.83		4.25	20.77		31.85	23.21	18.20
Sr	276.02		287.31	305.53		268.52		291.26	254.83		267.01	255.06	209.15
Y	22.65		24.21	23.56		22.04		22.90	25.71		27.33	23.86	23.14
Zr	131.00		138.29	145.95		136.21		135.64	151.42		159.12	102.36	107.61
Nb	14.40		12.82	12.79		13.03		12.00	14.69		14.28	12.68	8.74
Cs	0.90		0.39	0.52		1.67		0.76	2.58		0.95	0.90	1.60
Ba	216.33		156.62	169.29		184.75		185.13	226.55		262.27	232.65	171.40
La	15.54		15.97	17.39		16.60		16.32	18.95		18.84	16.27	13.10
Ce	34.18		35.94	38.26		36.09		35.81	41.08		41.60	36.63	29.39
Pr	4.20		4.44	4.67		4.44		4.43	5.10		5.08	4.40	3.57
Nd	18.32		19.58	20.44		19.10		19.36	22.23		22.06	19.22	15.74
Sm	4.51		4.85	4.97		4.71		4.78	5.34		5.40	4.71	3.95
Eu	1.22		1.37	1.41		1.28		1.33	1.42		1.46	1.29	1.14
Gd	4.23		4.67	4.71		4.32		4.42	4.83		5.11	4.37	3.91
Tb	0.71		0.75	0.76		0.73		0.75	0.83		0.86	0.74	0.68
Dy	4.47		4.68	4.67		4.51		4.68	5.19		5.38	4.69	4.45
Ho	0.84		0.88	0.86		0.85		0.88	0.98		1.03	0.89	0.86
Er	2.45		2.54	2.47		2.47		2.55	2.85		3.02	2.59	2.56
Tm	0.33		0.34	0.33		0.34		0.35	0.39		0.41	0.35	0.35
Yb	2.22		2.28	2.20		2.20		2.27	2.57		2.74	2.33	2.37
Lu	0.31		0.31	0.30		0.32		0.32	0.36		0.39	0.32	0.33
Hf	3.37		3.48	3.64		3.61		3.59	3.84		4.07	3.46	2.99
Ta													
Pb	2.60		1.94	2.18		3.56		2.57	4.72		5.19	4.01	3.30
Th	2.75		2.86	2.94		3.38		3.20	3.67		3.87	3.28	2.33
U	0.66		0.69	0.70		0.83		0.76	0.85		0.95	0.82	0.57
Sc													
V													
Isotopes													
$^{87}Sr/^{86}Sr$			0.706811			0.707067			0.707064			0.706978	0.70693
$^{87}Sr/^{86}Sr_{(200Ma)}$			0.706643			0.706766			0.706393			0.706229	0.706214
$^{143}Nd/^{144}Nd$			0.512546			0.512516			0.51256			0.512557	0.51248
$^{143}Nd/^{144}Nd_{(200Ma)}$			0.51235			0.512321			0.51237			0.512363	0.512281
Paleomagnetism	**TJ11**	**TJ12**	**TJ13**	**TJ14**	**TJ15**	**TJ16**	**TJ17**	**TJ18**	**TJ19**	**TJ20**	**TJ21**	**TJ22**	**TJ23**
Decl(geo)	8.0	10.6	8.6	8.7	4.3	10.5	7.0	12.0	13.0	12.5	17.3	15.8	341.1
Incl(geo)	29.6	29.5	31.8	29.9	33.0	33.7	31.4	30.5	31.2	29.7	32.3	30.9	29.8
A95	4.5	6.3	2.6	2.8	8.5	9.2	4.5	2.8	5.4	7.0	5.4	4.2	4.6
DG	2	2	2	2	2	2	2	2	2	2	2	2	3

Figure A.13: ICP-MS and isotopic compositions of Tiourjdal samples.

	Intermediate										Upper		Recurrent
	AN137A	TJ24	TJ25	TJ26	AN138	TJ28	TJ29	TJ30	TJ31	TJ32	AN140	AN 141	AN156A
SiO_2	53.23	53.15	53.39	53.83	53.64	50.80	52.95	53.27	53.22	53.03	51.43	52.14	50.58
TiO_2	1.16	1.38	1.18	1.21	1.16	1.43	1.22	1.31	1.31	1.35	1.00	1.04	1.63
Al_2O_3	13.94	14.83	13.43	14.60	13.42	17.52	14.75	14.51	14.64	14.71	15.03	14.87	13.55
Fe_2O_3	10.47	13.60	10.44	10.01	10.20	9.50	10.26	10.57	10.27	10.55	9.95	9.97	15.01
MnO	0.18	0.09	0.16	0.13	0.17	0.14	0.18	0.17	0.15	0.16	0.18	0.18	0.28
MgO	7.79	5.71	8.40	7.02	8.52	9.39	7.42	7.08	7.48	7.22	8.27	7.74	5.76
CaO	10.70	7.09	9.92	10.07	9.97	7.07	10.49	10.31	10.06	10.27	12.03	11.45	10.43
Na_2O	2.00	2.19	2.07	2.16	1.90	2.48	2.13	2.18	2.17	2.16	1.78	1.90	2.18
K_2O	0.38	1.79	0.83	0.83	0.84	1.48	0.44	0.43	0.56	0.40	0.21	0.59	0.39
P_2O_5	0.14	0.16	0.16	0.14	0.17	0.16	0.14	0.14	0.14	0.14	0.11	0.11	0.17
SUM	100.00	99.98	99.99	99.99	100.00	99.99	99.99	99.99	99.99	99.99	100.00	100.00	99.97
ICP-MS													
Rb	16.645		28.49	30.01	26.829		14.92	9.62		10.12	1.55	12.747	6.134
Sr	166.582		172.41	200.08	156.755		210.76	206.46		219.10	106.68	158.810	95.519
Y	23.618		25.24	23.42	26.724		21.40	22.94		23.73	16.77	20.119	41.037
Zr	105.551		124.60	114.15	129.219		107.66	112.04		117.76	71.87	78.054	114.854
Nb	7.964		9.61	8.35	9.951		7.25	7.65		7.69	4.52	4.989	5.209
Cs	1.363		0.75	1.28	0.751		1.00	0.59		0.65	0.21	0.402	0.779
Ba	143.002		202.83	195.37	188.167		162.55	189.93		178.10	83.57	111.889	164.332
La	11.069		13.72	12.80	13.076		11.84	12.17		12.78	6.32	7.169	8.572
Ce	24.248		30.20	28.34	29.092		26.62	27.40		28.40	14.68	16.593	19.850
Pr	3.193		3.74	3.48	3.748		3.34	3.44		3.58	1.98	2.298	2.769
Nd	13.563		16.45	15.29	15.627		14.69	15.27		15.85	8.74	10.346	12.696
Sm	3.561		4.15	3.88	3.876		3.78	3.90		4.08	2.37	2.789	3.918
Eu	1.118		1.10	1.11	1.150		1.07	1.12		1.18	0.79	0.931	1.242
Gd	3.993		4.31	3.89	4.234		3.86	3.98		4.17	2.83	3.138	5.486
Tb	0.647		0.73	0.68	0.713		0.64	0.68		0.71	0.48	0.537	0.997
Dy	4.012		4.78	4.47	4.342		4.17	4.36		4.58	2.87	3.403	6.679
Ho	0.847		0.93	0.87	0.946		0.81	0.85		0.89	0.63	0.718	1.487
Er	2.418		2.78	2.61	2.742		2.41	2.53		2.64	1.74	2.027	4.441
Tm			0.38	0.35			0.32	0.35		0.36	0.23		
Yb	2.123		2.57	2.42	2.379		2.24	2.34		2.42	1.55	1.872	4.217
Lu	0.321		0.35	0.34	0.347		0.31	0.33		0.34	0.23	0.282	0.642
Hf	2.654		3.23	2.94	3.244		2.82	2.91		3.06	1.79	2.078	3.072
Ta	0.485				0.611						0.27	0.308	0.336
Pb	3.071		3.68	3.89	3.657		3.35	3.32		3.54	1.72	2.415	3.317
Th	2.204		2.55	2.32	2.868		2.04	2.04		2.15	0.86	1.266	2.142
U	0.482		0.59	0.56	0.652		0.46	0.48		0.48	0.23	0.296	0.550
Sc													
V													
Isotopes													
$^{87}Sr/^{86}Sr$	0.706964		0.707499		0.7076			0.707988		0.707283		0.706248	0.705569
$^{87}Sr/^{86}Sr_{(200Ma)}$	0.706142		0.706139		0.706191			0.707605		0.706903		0.705587	0.705040482
$^{143}Nd/^{144}Nd$	0.512485		0.512458		0.512465			0.512453		0.512444	0.512561	0.512547	0.512724
$^{143}Nd/^{144}Nd_{(200Ma)}$	0.512277		0.512258		0.512269			0.512251		0.512241	0.512347	0.512334	0.512479954
Paleomagnetism	AN137A	TJ24	TJ25	TJ26	AN138	TJ28	TJ29	TJ30	TJ31	TJ32	AN140	AN 141	AN156A
Decl(geo)		336.4	335.6	343.7		337.9	340.7	337.1	337.9	335.8	341.7	338.2	
Incl(geo)		32.5	32.6	26.8		39.4	42.2	48.6	39.5	39.9	41.0	35.2	
A95		5.2	6.8	7.4		6.1	4.1	2.8	5.8	6.7	6.4	6.4	
DG	3	3	3	3	3	5	5	5	5	5	5	5	5

Figure A.14: ICP-MS and isotopic compositions of Tiourjdal samples.

	Lower										Intermediate	
wt%	**TEL1**	**TEL2**	**TEL3**	**TEL4**	**TEL6**	**TEL7**	**TEL9**	**TEL10**	**TEL11**	**TEL12**	**TEL13**	**TEL15**
SiO_2	52.41	51.01	54.27	56.43	49.63	49.32	54.75	54.42	53.46	54.59	54.20	59.30
TiO_2	1.46	1.50	1.44	1.41	1.33	1.61	1.42	1.55	1.46	1.41	1.25	1.12
Al_2O_3	13.97	13.85	13.94	12.79	16.11	15.10	13.19	13.85	14.07	13.20	14.79	12.22
Fe_2O_3	10.81	12.25	10.69	10.91	9.92	11.25	11.30	11.57	10.52	11.49	10.37	9.57
MnO	0.10	0.12	0.13	0.12	0.09	0.13	0.09	0.08	0.16	0.11	0.09	0.09
MgO	7.34	8.69	8.55	6.69	5.49	7.83	6.03	6.95	7.92	7.49	8.78	6.93
CaO	10.54	8.84	7.80	8.76	15.31	11.64	9.92	7.62	9.62	8.62	6.95	7.38
Na_2O	2.61	2.80	2.79	2.24	1.58	2.61	2.36	2.41	2.22	2.48	3.01	2.25
K_2O	0.59	0.77	0.23	0.50	0.38	0.33	0.79	1.38	0.41	0.45	0.42	1.02
P_2O_5	0.16	0.16	0.15	0.15	0.15	0.18	0.16	0.17	0.16	0.16	0.14	0.13
SUM	100.00	100.00	100.00	100.00	100.00	100.00	100.00	100.00	100.00	100.00	100.00	100.00
ICP-MS (ppm)												
Rb				10.9			22.9		26.3	9.3		
Sr				214.8			227.2		259	203.1		
Y				24.5			24.3		24.4	24		
Zr				120.7			123.4		126.1	119.2		
Nb				11.6			11.7		11.4	11		
Cs				0.4			0.5		1.6	0.2		
Ba				141.6			198.1		178.8	154.9		
La				13.4			15.8		14.8	14.3		
Ce				31.7			34.5		35.8	33.1		
Pr				4.17			4.54		4.67	4.14		
Nd				19.9			19.6		20.3	18.8		
Sm				4.1			4.3		4.5	4.2		
Eu				1.18			1.2		1.27	1.19		
Gd				4.59			4.55		4.72	4.32		
Tb				0.83			0.82		0.83	0.76		
Dy				4.76			4.71		4.61	4.49		
Ho				0.87			0.8		0.81	0.77		
Er				2.62			2.33		2.38	2.38		
Tm				0.38			0.36		0.36	0.36		
Yb				2.25			2.2		2.25	2.1		
Lu				0.31			0.31		0.3	0.3		
Hf				3.4			3.7		3.4	3		
Ta				0.7			0.7		0.8	0.8		
Pb				1.7			2		0.9	2.1		
Th				3.7			4.1		3.4	3.2		
U				0.7			0.9		0.8	1		
Sc												
V				275			294		288	274		
Isotopes												
$^{87}Sr/^{86}Sr$												
$^{87}Sr/^{86}Sr_{(200Ma)}$												
$^{143}Nd/^{144}Nd$												
$^{143}Nd/^{144}Nd_{(200Ma)}$												
Paleomagnetism	**TEL1**	**TEL2**	**TEL3**	**TEL4**	**TEL6**	**TEL7**	**TEL9**	**TEL10**	**TEL11**	**TEL12**	**TEL13**	**TEL15**
Decl(geo)												
Incl(geo)												
A95												
DG												

Figure A.15: ICP-MS and isotopic compositions of Telouet samples.

	Intermediate						Upper	Intermediate		Upper		Recurrent
wt%	**TEL16**	**TEL17**	**TEL18**	**TEL19a**	**TEL19b**	**TEL20**	**TEL21**	**TEL22**	**TEL23**	**TEL24**	**TEL25**	**AN 169**
SiO_2	52.94	52.41	49.37	50.59	50.95	51.64	53.89	54.14	52.73	51.26	50.13	51.43
TiO_2	1.26	1.28	1.35	1.29	1.25	1.31	1.08	1.23	1.21	1.06	1.10	1.56
Al_2O_3	14.12	14.68	15.63	14.15	14.33	14.65	13.89	15.06	14.63	14.72	15.10	13.62
Fe_2O_3	11.40	11.13	10.20	12.56	10.51	11.21	10.41	9.86	10.89	11.01	11.40	14.22
MnO	0.17	0.18	0.12	0.19	0.17	0.12	0.16	0.20	0.16	0.17	0.21	0.31
MgO	7.14	8.52	8.08	8.19	9.81	8.46	8.23	7.04	7.22	7.78	8.25	6.04
CaO	10.28	8.55	12.85	10.58	10.08	10.51	10.08	9.54	10.60	11.70	11.54	10.31
Na_2O	2.17	2.53	1.94	2.17	2.56	1.80	1.87	2.26	2.06	1.94	1.96	2.01
K_2O	0.37	0.55	0.33	0.15	0.21	0.17	0.29	0.52	0.37	0.26	0.20	0.36
P_2O_5	0.15	0.15	0.13	0.12	0.12	0.13	0.10	0.14	0.13	0.10	0.11	0.16
SUM	100.00	100.00	100.00	100.00	100.00	100.00	100.00	100.00	100.00	100.00	100.00	100.00
ICP-MS (ppm)												
Rb	34.5				2.6	8.2	5.6		12.3	16.3		6.304
Sr	181				199.3	180.4	171.5		202.8	177.5		102.253
Y	23.5				20.2	22.2	18.7		24.3	19.4		42.986
Zr	97.9				85.6	96.7	77.4		96.3	70.6		123.355
Nb	7.6				5.4	5.9	4.8		6.5	4.3		5.588
Cs	1.4				0.1	1.1	0.2		1.1	0.6		0.590
Ba	142.6				87.6	62.7	76.2		164.9	89.4		120.813
La	14.3				8	9.8	6.2		12.5	7.2		8.763
Ce	26.6				20.5	22.6	16.1		27.2	17.3		20.475
Pr	3.47				2.81	3.04	2.3		3.6	2.36		2.780
Nd	16.2				12.8	14	10.9		16.4	11.5		13.444
Sm	3.6				3.1	3.1	2.7		3.7	2.7		4.091
Eu	1.04				0.92	1.01	0.87		1.05	0.84		1.280
Gd	3.98				3.6	3.89	3.27		4.16	3.24		5.449
Tb	0.76				0.67	0.71	0.61		0.73	0.61		1.049
Dy	4.48				3.81	3.94	3.49		4.38	3.58		6.865
Ho	0.79				0.67	0.71	0.62		0.78	0.65		1.527
Er	2.46				2.04	2.17	1.82		2.38	1.89		4.632
Tm	0.36				0.31	0.32	0.24		0.36	0.29		
Yb	2.17				1.8	1.98	1.61		1.97	1.75		4.180
Lu	0.32				0.26	0.28	0.23		0.3	0.25		0.683
Hf	2.9				2.6	2.6	2.6		2.7	2.1		3.258
Ta	0.5				0.4	0.4	0.3		0.4	0.3		0.352
Pb	0.9				2.8	1.3	1.1		0.8	0.7		2.693
Th	2.5				1.7	1.6	1.8		2	1.3		2.155
U	0.6				0.5	0.4	0.4		0.5	0.3		0.575
Sc												
V	301				322	299	286		292	283		
Isotopes												
$^{87}Sr/^{86}Sr$												0.705569
$^{87}Sr/^{86}Sr_{(200Ma)}$												0.705062
$^{143}Nd/^{144}Nd$												0.512689
$^{143}Nd/^{144}Nd_{(200Ma)}$												0.512448
Paleomagnetism	**TEL16**	**TEL17**	**TEL18**	**TEL19a**	**TEL19b**	**TEL20**	**TEL21**	**TEL22**	**TEL23**	**TEL24**	**TEL25**	**AN 169**
Decl(geo)												
Incl(geo)												
A95												
DG												

Figure A.16: ICP-MS and isotopic compositions of Telouet samples.

	Lower						Intermediate			
wt%	**OL1**	**OL2**	**OL3**	**OL4**	**OL5**	**OL6**	**OL7**	**OL8**	**OL9**	**OL10**
SiO_2	53.18	52.22	48.01	55.01	51.92	51.60	49.89	54.53	52.45	52.84
TiO_2	1.43	1.28	1.57	1.50	1.44	1.35	1.27	1.21	1.18	1.22
Al_2O_3	13.32	13.24	15.50	13.60	14.33	13.98	14.61	13.94	13.49	14.35
Fe_2O_3	11.99	11.46	13.76	14.49	11.57	12.18	11.52	10.88	11.73	10.63
MnO	0.11	0.16	0.13	0.08	0.13	0.15	0.19	0.14	0.13	0.16
MgO	8.25	8.73	8.80	6.90	7.56	8.75	8.29	7.71	9.87	8.15
CaO	8.50	9.87	8.73	3.95	8.74	8.78	9.79	8.61	7.40	10.19
Na_2O	1.95	2.06	2.70	3.01	2.25	2.59	1.68	2.23	2.12	2.09
K_2O	1.13	0.84	0.62	1.28	1.89	0.46	2.61	0.62	1.51	0.25
P_2O_5	0.15	0.13	0.17	0.18	0.16	0.14	0.15	0.14	0.12	0.13
SUM	100.00	100.00	100.00	100.00	100.00	100.00	100.00	100.00	100.00	100.00
ICP-MS (ppm)										
Rb	26.7	25.6						13.6		19.5
Sr	242.4	230.4						190.8		190.3
Y	21.4	20.8						22.4		22.7
Zr	113.1	102.3						96.3		94.6
Nb	10.8	10.1						7.6		6.2
Cs	0.3	1						0.2		1.5
Ba	195.5	191.9						129.7		103.6
La	19.2	13						11.8		10.6
Ce	38	29.2						26.1		23.9
Pr	4.71	3.77						3.32		3.17
Nd	20.5	15.4						15.2		14.1
Sm	4.1	3.8						3.7		3.5
Eu	1.15	1.11						1.05		1.04
Gd	4.15	3.92						3.77		3.8
Tb	0.75	0.7						0.75		0.73
Dy	4.13	4.12						4.34		4.19
Ho	0.74	0.73						0.75		0.76
Er	2.09	2.07						2.19		2.28
Tm	0.31	0.3						0.36		0.36
Yb	1.94	1.88						2.16		2.04
Lu	0.27	0.26						0.33		0.3
Hf	3.4	3.3						2.6		3
Ta	0.7	0.8						0.5		0.4
Pb	2.5	11.1						3.4		1.5
Th	2.9	3.5						2.4		2.2
U	0.7	0.7						0.6		0.4
Sc										
V	291	272						286		290
Isotopes										
$^{87}Sr/^{86}Sr$										
$^{87}Sr/^{86}Sr_{(200Ma)}$										
$^{143}Nd/^{144}Nd$										
$^{143}Nd/^{144}Nd_{(200Ma)}$										
Paleomagnetism	**OL1**	**OL2**	**OL3**	**OL4**	**OL5**	**OL6**	**OL7**	**OL8**	**OL9**	**OL10**
Decl(geo)	8.8	16.5	14.9	11.7	7.2	8.2	143.9	349.2	343.9	351.6
Incl(geo)	38.1	39.2	34.2	39.1	43	42.2	-55.9	24.4	26.5	27.9
A95	2.3	4.3	3.1	13.2	5.1	3.5	9.8	2.4	10.8	4.8
DG	2	2	2	2	2	2	4	5	5	5

Figure A.17: ICP-MS and isotopic compositions of Oued Lahr samples.

	Intermediate		Upper						Recurrent
wt%	**OL11**	**OL12**	**OL13**	**OL14**	**OL15**	**OL16**	**OL17**	**OL18**	**AN 61**
SiO_2	52.14	52.18	51.35	52.22	51.43	51.56	51.42	51.44	51.41
TiO_2	1.22	1.30	1.17	1.10	0.98	1.06	1.07	1.07	1.65
Al_2O_3	13.81	14.18	15.31	14.91	14.70	14.69	14.90	14.68	13.74
Fe_2O_3	11.21	11.25	10.38	10.34	10.43	10.78	10.41	10.73	12.90
MnO	0.15	0.13	0.22	0.22	0.14	0.19	0.19	0.18	0.36
MgO	8.93	8.82	9.10	8.57	8.72	7.96	8.31	8.22	6.73
CaO	10.38	10.03	7.71	9.90	11.47	11.51	10.95	11.39	10.52
Na_2O	1.82	1.78	1.77	2.31	1.83	1.90	2.39	1.91	2.17
K_2O	0.21	0.19	2.87	0.31	0.19	0.24	0.25	0.25	0.34
P_2O_5	0.12	0.13	0.12	0.11	0.10	0.11	0.11	0.11	0.17
SUM	100.00	100.00	100.00	100.00	100.00	100.00	100.00	100.00	100.00
ICP-MS (ppm)									
Rb	14.3	11.7		4.3	7.2			2.5	
Sr	175.5	179.7		189.2	193.3			199.8	
Y	19	23		21.6	18.3			20.4	
Zr	85.9	94.9		74.2	65.7			74.8	
Nb	5.6	6		4.5	4.1			4.9	
Cs	1.4	1.4		0.2	0.9			0.3	
Ba	83.6	63.1		70	64.1			105	
La	9.8	9.2		6	6.9			7.1	
Ce	21.7	23.6		16.2	16.8			17.8	
Pr	2.83	3.16		2.27	2.28			2.45	
Nd	13.5	15.2		11.2	11.5			11.6	
Sm	3.1	3.6		2.8	2.6			3	
Eu	1	1.01		0.9	0.82			0.88	
Gd	3.51	3.97		3.29	2.99			3.35	
Tb	0.66	0.72		0.63	0.57			0.65	
Dy	3.86	4.35		4.01	3.38			3.85	
Ho	0.7	0.77		0.72	0.63			0.69	
Er	2	2.23		2.16	1.83			2.1	
Tm	0.28	0.33		0.3	0.3			0.31	
Yb	1.8	2.08		1.9	1.71			1.98	
Lu	0.26	0.29		0.28	0.26			0.27	
Hf	2.7	2.6		2.1	1.9			2.1	
Ta	0.4	0.4		0.3	0.3			0.3	
Pb	0.9	0.7		1.5	0.8			1.7	
Th	1.8	2.4		1.5	1.5			1	
U	0.5	0.5		0.3	0.3			0.3	
Sc									
V	300	300		300	283			297	
Isotopes									
$^{87}Sr/^{86}Sr$									
$^{87}Sr/^{86}Sr_{(200Ma)}$									
$^{143}Nd/^{144}Nd$									
$^{143}Nd/^{144}Nd_{(200Ma)}$									
Paleomagnetism	**OL11**	**OL12**	**OL13**	**OL14**	**OL15**	**OL16**	**OL17**	**OL18**	**AN 61**
Decl(geo)	344.8	343.6	311.7	311.3	320.8	314.5	312.8	316	
Incl(geo)	34.2	35.7	53.5	53.7	50.2	41.5	50	48.6	
A95	4.8	3.7	2.9	5	6	3.7	8.6	2.7	
DG	5	5	6	6	6	6	6	6	

Figure A.18: ICP-MS and isotopic compositions of Oued Lahr samples.

	Lower					Intermediate										
wt%	**AN503**	**AN504**	**AN602**	**AN506**	**AN603**	**Carbonate**	**AN508**	**AN604**	**AN509**	**AN510**	**AN605**	**AN511**	**AN606**	**AN607**	**AN608**	**AN627**	**AN628**
SiO_2	52.91	52.91	53.45	52.78	53.05		52.97	53.78	53.21	53.12	54.04	52.33	53.54	53.37	53.72	53.12	53.15
TiO_2	1.52	1.52	1.51	1.51	1.47		1.24	1.20	1.26	1.34	1.33	1.24	1.20	1.21	1.26	1.38	1.45
Al_2O_3	14.57	13.78	13.69	13.65	13.91		14.05	14.17	14.09	13.76	13.52	14.03	14.80	14.37	14.07	13.89	13.20
Fe_2O_3	9.64	10.70	10.79	11.21	10.46		10.84	10.30	10.73	11.82	11.60	11.38	9.54	10.80	11.15	11.32	11.99
MnO	0.07	0.16	0.17	0.19	0.12		0.16	0.14	0.16	0.17	0.16	0.16	0.12	0.13	0.15	0.18	0.16
MgO	10.02	8.16	7.77	7.63	9.32		7.65	8.13	7.61	6.95	6.88	7.56	9.50	7.97	7.60	7.28	7.36
CaO	8.49	9.72	9.63	9.92	8.99		10.45	9.76	10.24	10.08	9.82	10.76	8.96	9.64	9.53	10.13	10.18
Na_2O	2.20	2.21	2.15	2.25	2.09		1.94	1.91	1.99	2.01	1.97	1.96	1.91	1.98	1.93	2.00	1.82
K_2O	0.40	0.64	0.66	0.66	0.41		0.54	0.46	0.56	0.59	0.52	0.42	0.27	0.37	0.43	0.54	0.52
P_2O_5	0.19	0.19	0.19	0.19	0.18		0.15	0.15	0.15	0.16	0.16	0.15	0.15	0.15	0.16	0.16	0.16
SUM	100	100	100	100	100		100	100	100	100	100	100	100	100	100	100	100
ICP-MS (ppm)																	
Rb	10.8	26.5		29.2				17.8		23.3			5.9			17.0	13.4
Sr	272	252		243				179		170			191			180	177
Y	24.81	25.71		26.45				22.81		24.97			21.33			23.90	24.96
Zr	128	131		132				99		113			98			112	111
Nb	11.11	11.36		11.44				6.63		7.58			6.52			7.40	6.99
Cs	0.86	1.14		1.27				1.25		1.13			0.72			2.51	2.52
Ba	155	193		199				110		178			108			269	271
La	16.44	16.86		16.83				11.32		12.75			11.42			12.31	11.61
Ce	35.33	35.90		36.04				24.67		27.72			24.53			26.86	26.09
Pr	4.56	4.65		4.67				3.28		3.63			3.20			3.58	3.50
Nd	19.38	19.68		19.85				13.91		15.55			13.74			15.59	15.58
Sm	4.84	4.95		5.03				3.71		4.11			3.66			4.14	4.26
Eu	1.58	1.57		1.57				1.24		1.31			1.24			1.37	1.41
Gd	4.97	5.17		5.23				4.22		4.52			4.01			4.51	4.70
Tb	0.83	0.87		0.88				0.73		0.79			0.71			0.79	0.82
Dy	5.06	5.24		5.29				4.55		4.95			4.40			4.89	5.10
Ho	1.00	1.03		1.05				0.92		1.02			0.89			0.97	1.01
Er	2.68	2.75		2.80				2.50		2.74			2.39			2.64	2.69
Tm	0.38	0.39		0.39				0.36		0.39			0.34			0.37	0.38
Yb	2.28	2.32		2.35				2.14		2.36			2.07			2.23	2.28
Lu	0.35	0.36		0.36				0.33		0.36			0.32			0.34	0.35
Hf	3.61	3.68		3.72				2.85		3.21			2.80			3.18	3.20
Ta	0.74	0.76		0.77				0.45		0.53			0.46			0.49	0.48
Pb	2.67	3.49		3.92				3.09		3.64			2.34			3.37	3.10
Th	3.48	3.54		3.61				2.49		2.87			2.49			2.69	2.43
U	0.83	0.84		0.87				0.58		0.67			0.57			0.63	0.52
Sc	33.4	32.3		33.4				35.7		35.2			35.5			36.0	36.5
V																	
Isotopes																	
$^{87}Sr/^{86}Sr$		0.707211								0.707393						0.706937	
$^{87}Sr/^{86}Sr_{(200Ma)}$		0.706345								0.706269						0.706162	
$^{143}Nd/^{144}Nd$																	
$^{143}Nd/^{144}Nd_{(200Ma)}$																	
Paleomagnetism	**MA01**	**MA02**		**MA03**		**MAL01**		**MA04**		**MA05**			**MA07**	**MA08**	**MA09**		
Decl(geo)				347.5				350.2		357			347.2	347.5	349		
Incl(geo)				31.9				38.6		23.8			21.5	22.7	19.4		
A95				13.5				6.6		6.8			3.9	9.7	7.2		
DG				1				1		2			2	2	2		

Figure A.19: ICP-MS and isotopic compositions of Maaziz samples.

	Intermediate									
wt%	AN521	AN629	AN522	AN523	AN524	AN525	AN630	AN525B	AN526	AN631
SiO_2	52.71	53.05	52.65	52.45	52.51	55.46	56.15	52.44	53.19	54.34
TiO_2	1.23	1.23	1.19	1.16	1.10	2.07	2.20	1.47	1.25	1.26
Al_2O_3	14.35	14.30	14.02	13.81	13.51	12.46	12.12	13.62	13.88	14.24
Fe_2O_3	10.87	11.14	11.43	11.51	11.56	13.58	13.39	11.90	11.00	9.98
MnO	0.14	0.15	0.16	0.16	0.16	0.17	0.16	0.19	0.19	0.14
MgO	7.18	7.04	7.33	7.68	8.20	5.14	4.92	7.35	7.46	8.12
CaO	10.32	10.10	10.30	10.46	10.21	7.35	7.05	10.34	10.58	9.36
Na_2O	1.87	1.88	1.89	1.89	1.84	2.29	2.33	1.97	1.87	1.99
K_2O	1.18	0.95	0.89	0.75	0.76	1.21	1.39	0.56	0.43	0.40
P_2O_5	0.15	0.15	0.15	0.14	0.14	0.26	0.28	0.16	0.14	0.16
SUM	100	100	100	100	100	100	100	100	100	100
ICP-MS (ppm)										
Rb	21.8		21.6	20.6				25.7		17.4
Sr	170		163	160				165		174
Y	21.69		22.55	21.65				25.06		21.14
Zr	100		96	91				108		104
Nb	6.69		6.44	6.17				7.13		6.94
Cs	0.59		0.68	0.63				1.04		0.87
Ba	160		155	147				160		140
La	10.86		10.95	10.38				12.00		10.67
Ce	23.86		23.76	22.69				26.35		23.65
Pr	3.16		3.14	2.97				3.48		3.12
Nd	13.67		13.43	12.98				15.28		13.50
Sm	3.65		3.60	3.49				4.09		3.58
Eu	1.18		1.19	1.18				1.29		1.23
Gd	3.97		4.02	3.85				4.60		3.95
Tb	0.70		0.71	0.67				0.81		0.69
Dy	4.40		4.43	4.18				5.01		4.26
Ho	0.89		0.90	0.87				1.02		0.86
Er	2.40		2.47	2.30				2.72		2.30
Tm	0.34		0.35	0.33				0.39		0.33
Yb	2.14		2.13	2.03				2.35		2.04
Lu	0.33		0.32	0.31				0.36		0.31
Hf	2.88		2.79	2.59				3.13		3.01
Ta	0.46		0.45	0.42				0.50		0.48
Pb	2.81		3.26	3.10				3.44		2.82
Th	2.56		2.48	2.34				2.65		2.67
U	0.59		0.59	0.54				0.63		0.62
Sc	35.9		35.4	36.0				36.5		37.1
V										
Isotopes										
$^{87}Sr/^{86}Sr$								0.707061		0.707191
$^{87}Sr/^{86}Sr_{(200Ma)}$								0.705776		0.706367
$^{143}Nd/^{144}Nd$										
$^{143}Nd/^{144}Nd_{(200Ma)}$										
Paleomagnetism	AG01	AG02	AG03	AG05	AG06	AG07				AG08
Decl(geo)	353.2	350.4	348.6	349.5	351.2	359.5				347.6
Incl(geo)	31.4	20.1	9.4	15.2	9.1	30.6				10.1
A95	8	5.5	6.9	4.5	7.5	5.4				6.3
DG						1				2

Figure A.20: ICP-MS and isotopic compositions of Agourai samples.

	Intermediate			Upper		Intermediate		
wt%	AN632	carbonate	AN528	AN529	AN530	AN633	??	AN531	AN532
SiO_2	53.11			51.63	51.70	52.46		53.44	53.14
TiO_2	1.33			1.19	1.12	1.13		1.29	1.28
Al_2O_3	15.28			15.10	14.26	14.18		14.00	13.91
Fe_2O_3	10.24			10.69	11.26	11.13		11.61	11.89
MnO	0.12			0.17	0.17	0.24		0.16	0.18
MgO	7.37			8.01	7.68	7.07		7.04	7.05
CaO	10.11			10.73	11.05	11.27		9.38	9.45
Na_2O	1.92			1.98	2.02	1.98		2.30	2.23
K_2O	0.36			0.36	0.61	0.41		0.61	0.70
P_2O_5	0.15			0.14	0.13	0.14		0.16	0.16
SUM	100.00			100	100	100		100	100
ICP-MS (ppm)									
Rb						14.1		16.9	16.1
Sr						176		194	193
Y						21.99		25.17	24.48
Zr						82		103	102
Nb						5.11		6.73	6.62
Cs						0.59		0.69	0.44
Ba						113		177	176
La						8.91		12.03	11.77
Ce						19.84		26.35	25.88
Pr						2.70		3.48	3.42
Nd						11.93		15.06	14.90
Sm						3.33		3.97	3.98
Eu						1.13		1.28	1.29
Gd						3.90		4.38	4.42
Tb						0.67		0.78	0.76
Dy						4.26		4.93	4.83
Ho						0.88		1.01	0.99
Er						2.39		2.74	2.69
Tm						0.35		0.40	0.39
Yb						2.07		2.45	2.38
Lu						0.33		0.38	0.37
Hf						2.40		2.98	2.99
Ta						0.34		0.46	0.45
Pb						2.09		3.87	3.83
Th						1.64		2.52	2.49
U						0.40		0.62	0.62
Sc						38.7		38.3	38.6
V									
Isotopes									
$^{87}Sr/^{86}Sr$						0.706368			
$^{87}Sr/^{86}Sr_{(200Ma)}$						0.705709			
$^{143}Nd/^{144}Nd$									
$^{143}Nd/^{144}Nd_{(200Ma)}$									
Paleomagnetism	AGL1			AG09		AG10	AG11		AG12
Decl(geo)				340.8		347.1			345.5
Incl(geo)				18.9		40.9			38.8
A95				6.7		2.8			4.7
DG				2		3			3

Figure A.21: ICP-MS and isotopic compositions of Agourai samples.

	Lower		Intermediate										Upper
wt%	AN534	AN609	AN535	AN610	AN536	AN537	AN538	AN611	AN612	AN539	AN613	AN614	AN540
SiO_2	53.71	53.84	53.22	53.59	53.33	53.16	52.46	51.82	53.12	52.43	52.91	52.92	51.39
TiO_2	1.44	1.43	1.31	1.27	1.21	1.19	1.29	1.29	1.28	1.29	1.26	1.28	1.07
Al_2O_3	14.26	13.93	15.04	14.09	14.04	14.17	14.00	14.21	13.80	13.92	14.12	13.62	14.61
Fe_2O_3	10.48	10.83	10.39	11.04	10.86	10.17	10.56	10.72	10.76	10.69	10.80	11.37	11.00
MnO	0.11	0.12	0.09	0.13	0.12	0.14	0.15	0.13	0.10	0.14	0.08	0.15	0.15
MgO	8.45	8.57	7.17	7.18	8.41	8.49	8.92	8.82	9.01	8.37	9.85	7.93	7.82
CaO	8.96	8.80	9.73	9.77	9.53	9.91	10.29	10.82	9.78	10.91	8.96	10.31	11.62
Na_2O	2.07	1.98	2.12	2.03	1.87	1.96	1.81	1.78	1.73	1.77	1.66	1.84	1.83
K_2O	0.34	0.31	0.77	0.74	0.47	0.44	0.37	0.25	0.28	0.34	0.22	0.42	0.38
P_2O_5	0.18	0.18	0.16	0.16	0.15	0.15	0.14	0.15	0.14	0.14	0.14	0.14	0.13
SUM	100.00	100.00	100.00	100.00	100.00	99.78	100.00	100.00	100.00	100.00	100.00	100.00	100.00
ICP-MS (ppm)													
Rb	11.8			20.3		28.6		9.3		16.7			14.0
Sr	268			181		170		171		170			174
Y	24.10			23.59		21.93		20.44		21.12			20.61
Zr	122			99		97		93		94			73
Nb	11.82			7.40		6.45		5.75		5.79			4.66
Cs	0.51			0.58		1.08		0.67		0.85			0.52
Ba	168			169		133		78		102			94
La	15.97			11.70		11.63		10.07		10.50			7.71
Ce	33.80			25.28		24.90		22.52		23.49			17.58
Pr	4.35			3.29		3.26		3.02		3.18			2.42
Nd	18.08			14.08		14.11		13.62		14.10			10.89
Sm	4.57			3.63		3.74		3.80		3.83			3.05
Eu	1.47			1.29		1.19		1.26		1.29			1.08
Gd	4.74			4.11		4.06		4.15		4.25			3.45
Tb	0.81			0.73		0.73		0.72		0.73			0.63
Dy	4.90			4.64		4.48		4.31		4.44			4.07
Ho	0.97			0.96		0.89		0.87		0.89			0.82
Er	2.58			2.59		2.44		2.29		2.38			2.24
Tm	0.36			0.38		0.35		0.32		0.33			0.32
Yb	2.17			2.35		2.13		1.97		2.07			1.99
Lu	0.33			0.36		0.33		0.30		0.32			0.30
Hf	3.46			2.81		2.81		2.68		2.80			2.12
Ta	0.78			0.50		0.44		0.39		0.41			0.30
Pb	2.35			2.80		2.62		1.28		1.84			1.82
Th	3.50			2.41		2.37		1.96		2.01			1.31
U	0.81			0.55		0.54		0.46		0.46			0.32
Sc	33.7			35.5		33.2		35.5		34.9			37.1
V													
Isotopes													
$^{87}Sr/^{86}Sr$						0.70765		0.70696					0.70612
$^{87}Sr/^{86}Sr_{(200Ma)}$						0.706264		0.706516					0.705454
$^{143}Nd/^{144}Nd$													
$^{143}Nd/^{144}Nd_{(200Ma)}$													
Paleomagnetism	BA01			BA02		BA03	BA04	BA06	BA07	BA08		BA10	BA11
Decl(geo)	360.5			344.1		353.6	347.4	347.9	343.4	347.1		352.5	349.6
Incl(geo)	19.1			20.2		17.9	31.9	18.9	11.4	28.9		16.4	34.7
A95	3			5.3		6.9	20.3	6.9	9.8	4.2		6	3.2
DG	1			1		1	1	2	2	2		2	3

Figure A.22: ICP-MS and isotopic compositions of Oum R'Rbia samples.

A.3 LA-ICP-MS COMPOSITIONS

	AN134		AN137A			AN137A			AN138	AN138				OL14
	PLG1	PLG1	PLG2	PLG2	PLG2	PLG3	PLG3	PLG3	PLG1	PLG3	PLG3	PLG3	PLG3	PLG1
EMP	*CORE*	*CORE1*	*CORE*	*CORE1*	*RIM*	*CORE*	*CORE1*	*RIM*	*CORE*	*CORE*	*CORE1*	*RIM*	*RIM1*	*CORE*
Na_2O	3.04	3.00	1.88	2.46	2.86	3.04	3.04	3.04	2.78	3.31	3.48	4.18	4.18	1.54
MgO	0.19	0.19	0.32	0.26	0.30	0.25	0.25	0.59	0.24	0.26	0.26	0.15	0.15	0.28
Al_2O_3	30.50	30.55	32.07	31.09	30.27	30.02	30.02	29.12	30.94	30.04	29.99	28.71	28.71	33.23
SiO_2	49.78	49.72	48.86	50.49	51.58	52.05	52.05	51.70	50.70	52.74	53.10	54.60	54.60	47.99
K_2O	0.14	0.14	0.09	0.10	0.13	0.13	0.13	0.18	0.11	0.16	0.15	0.24	0.24	0.05
CaO	14.62	14.54	16.53	15.59	14.69	14.53	14.53	13.81	15.37	14.23	13.93	12.59	12.59	17.60
TiO_2	0.06	0.05	0.03	0.03	0.04	0.04	0.04	0.05	0.03	0.05	0.04	0.07	0.07	0.02
MnO	0.03	0.03	0.03	0.02	0.02	0.02	0.02	0.02	0.02	0.00	0.03	0.01	0.01	0.03
FeO_{tot}	0.53	0.52	0.62	0.63	0.80	0.60	0.60	1.55	0.51	0.52	0.53	0.71	0.71	0.59
An mol%	72.05	71.87	82.45	79.34	73.10	71.97		72.68	74.83	69.89	76.65	68.97		86.07
Ti ppm	359.04	295.98	161.84	193.19	217.88	239.16	239.16	301.14	193.37	282.32	219.38	393.63	393.63	118.44
LA-ICP-MS														
CaO wt%	14.44	14.44	16.53	15.59	14.69	14.53	14.53	13.81	15.37	14.23	13.93	12.59	12.59	17.60
SiO_2 wt%	69.60	72.07	66.55	57.34	51.83	58.44	52.47	49.03	54.70	53.31	54.78	54.49	64.77	62.53
TiO_2 wt%	0.05	0.06	0.03	0.03	0.04	0.06	0.04	0.03	0.03	0.04	0.04	0.04	0.07	0.02
Ti ppm	321.51	389.57	167.96	187.56	247.18	352.78	210.53	198.37	207.63	224.76	253.88	251.75	431.01	119.71
B^{11}	1.35	0.97	2.55	4.00	1.72	1.39	3.18	3.36	<1.33	<0.81	5.17	1.80	2.56	5.17
Li^7	18.19	18.21	15.37	11.79	24.75	22.66	20.40	21.44	13.33	14.94	16.72	13.51	16.02	3.60
Rb	0.60	0.85	0.31	0.61	0.86	0.57	0.72	0.48	0.39	0.63	0.62	0.83	3.85	1.27
Sr	430.77	463.71	326.19	300.67	295.75	302.04	276.39	264.71	288.92	279.97	279.07	288.26	373.72	381.41
Ba	56.71	70.55	34.13	33.44	42.11	36.22	34.71	33.41	28.53	36.39	41.46	47.30	98.60	45.42
Pb	0.53	0.82	0.49	0.68	1.30	0.62	0.68	0.50	0.52	0.76	0.78	1.59	3.07	1.00
Cs	<0.0118	0.02	0.03	0.02	0.03	0.02	0.01	0.03	<0.020	<0.0115	<0.0191	<0.0099	0.18	0.07
Sc	1.90	2.19	2.56	2.45	2.32	3.09	2.38	2.05	2.00	1.03	1.95	1.21	1.58	1.81
V	6.90	7.62	5.68	4.89	5.53	9.15	5.54	5.79	4.31	5.94	9.78	6.53	9.09	5.55
Cr	<1.80	<1.76	<1.39	1.87	<1.09	3.47	<1.36	<1.07	3.24	<1.27	4.01	<1.13	<2.19	6.95
Co	1.67	1.79	2.16	1.28	1.95	2.67	1.69	1.68	2.24	1.81	2.78	1.40	2.53	2.52
Ni	0.76	1.71	1.40	1.26	1.38	2.29	2.30	1.66	0.95	<0.26	3.74	0.50	1.63	4.98
Zn	6.71	10.58	8.34	7.54	11.32	7.51	6.70	7.75	6.58	6.50	7.28	9.69	15.56	6.71
Zr	<0.023	0.03		0.87	0.49	1.43	0.78	0.41	0.60	0.71	1.75	0.81	7.18	0.27
Nb	0.03	<0.0176		<0.0150	0.06	0.09	0.09	0.04	0.02	0.01	0.04	0.03	0.20	<0.00
Hf	<0.00	<0.037	<0.0313	<0.0231	<0.035	<0.00	<0.00	<0.00	<0.058	<0.034	0.18	0.03	0.20	0.05
Ta	<0.0071	<0.0102	<0.00	<0.0046		0.00	<0.0073	0.01	<0.0118	0.01	0.02	0.01	0.02	0.01
Th	<0.00	<0.00	0.01		0.01	0.02	0.01	0.00	0.03	<0.0129	0.05	0.02	0.27	0.01
U	0.01	<0.0114	<0.00			0.01	0.01	0.01	<0.00	0.01	0.01	0.06	0.04	<0.00
Y	0.14	0.14	0.11	0.21	0.21		0.18	0.29	0.11	0.19	0.48	0.21	0.45	0.26
La	0.82	1.05	0.57	0.58	0.74	0.84	0.53	0.53	0.49	0.63	0.80	0.81	1.45	0.49
Ce	1.42	1.55	1.14	1.17	1.62	1.27	1.28	1.00	0.85	0.94	1.33	1.62	3.17	1.03
Pr														
Nd	0.44	0.58	0.60	0.28	0.68	0.57	0.48	0.30	0.34	0.27	0.48	0.51	1.28	0.46
Sm	0.11	0.05	0.14	0.04	0.04				0.12	0.07	0.15	<0.050	0.36	0.11
Eu	0.52	0.51	0.36	0.28	0.50	0.47	0.35	0.35	0.23	0.29	0.32	0.48	0.89	0.39
Gd	0.06	<0.044	0.03	0.03	<0.034		0.07	0.07	<0.102	<0.042	<0.00	<0.036	0.06	<0.058
Tb	<0.0067	0.01	0.01	0.02	0.01		<0.0069	0.01	<0.00	<0.0062	<0.00	0.01	<0.0216	<0.00
Dy	0.04	0.03	0.02	0.04	0.05		0.02	0.08	0.04	0.03	0.14	0.07	0.11	0.07
Ho	<0.00	<0.00	0.01	0.01	0.00		0.01	0.01	<0.0113	0.02	0.03	0.01	<0.0162	<0.00
Er	0.04	<0.00						0.02	<0.047	<0.00	0.05	0.03	0.08	
Tm	<0.00	<0.00					<0.0071	<0.00	<0.00	<0.00	<0.00	<0.00	<0.00	
Yb	<0.00	0.08						<0.0263	<0.074	<0.042	<0.00	<0.00	0.06	
Lu	<0.00	0.01						<0.0043	<0.0119	<0.0069	<0.0161	<0.0083	0.04	

Figure A.23: LA-ICP-MS compositions of CHA plagioclases.

	OL14			AN141					AN141		AN141	AN156A		
	PLG1	PLG1	PLG1	PLG1	PLG1	PLG1	PLG1	PLG1	PLG2	PLG2	PLG3	PLG1	PLG1	PLG1
EMP	*RIM*	*RIM1*	*RIM2*	*RIM3*	*CORE*	*CORE1*	*RIM*	*RIM1*	*CORE*	*CORE1*	*CORE*	*CORE*	*CORE1*	*RIM*
Na_2O	1.53	1.53	2.19	2.19	1.59	1.61	1.60	1.92	2.30	2.30	2.84	3.43	3.43	3.17
MgO	0.22	0.22	0.26	0.26	0.16	0.19	0.20	0.17	0.22	0.22	0.23	0.18	0.18	0.23
Al_2O_3	33.21	33.21	31.92	31.92	33.10	33.22	33.10	32.57	31.72	31.72	30.93	29.37	29.37	29.69
SiO_2	47.71	47.71	49.57	49.57	47.94	48.08	48.08	48.63	49.62	49.62	50.71	52.39	52.39	51.75
K_2O	0.03	0.03	0.06	0.06	0.05	0.04	0.05	0.06	0.07	0.07	0.09	0.17	0.17	0.12
CaO	17.74	17.74	16.48	16.48	17.29	17.38	17.37	16.89	16.14	16.14	15.25	13.80	13.80	14.27
TiO_2	0.02	0.02	0.02	0.02	0.02	0.03	0.02	0.02	0.02	0.02	0.03	0.04	0.04	0.05
MnO	0.01	0.01	0.01	0.01	0.02	0.02	0.02	0.01	0.02	0.02	0.02	0.01	0.01	0.02
FeO_{tot}	0.59	0.59	0.70	0.70	0.63	0.55	0.57	0.65	0.60	0.60	0.65	0.71	0.71	0.92
An mol%	86.34		79.56		85.46	85.43	83.31	85.48	79.20	79.20	74.43	68.39		71.67
Ti ppm	124.32	124.32	139.42	139.42	109.81	186.53	97.34	138.58	139.54	139.54	181.74	250.37	250.37	298.98
LA-ICP-MS														
CaO wt%	17.74	17.74	16.48	16.48	17.29	17.38	17.37	16.89	16.14	16.14	15.25	13.80	13.80	14.27
SiO_2 wt%	53.69	57.52	73.33	63.69	50.23	41.21	48.30	48.37	47.69	56.65	54.74	55.28	50.36	54.43
TiO_2 wt%	0.02	0.02	0.03	0.03	0.02	0.02	0.02	0.02	0.03	0.02	0.03	0.04	0.04	0.04
Ti ppm	105.51	124.36	169.49	188.00	110.43	94.27	118.45	111.48	152.49	136.40	167.21	252.50	247.95	240.95
B^{11}	1.48	3.43	4.07	1.79	<1.40	1.66	2.26	0.95	2.70	2.63	4.28	<1.21	<0.75	0.83
Li^7	4.09	4.83	14.14	10.27	5.61	6.25	8.17	8.44	12.27	18.80	12.90	14.13	16.40	23.27
Rb	0.28	0.62	1.63	0.82	0.18	0.16	0.30	0.26	0.40	0.55	0.34	0.62	0.82	0.45
Sr	272.17	280.06	256.84	243.11	233.89	222.25	235.58	215.59	292.33	285.27	274.63	146.44	151.58	161.97
Ba	19.30	19.95	34.06	24.61	19.71	15.50	18.41	16.92	31.23	32.83	22.86	30.73	31.22	26.59
Pb	0.24	0.39	0.66	0.64	0.31	0.35	0.52	0.70	0.42	0.48	0.30	0.52	0.51	0.53
Cs	<0.0104	0.02	0.10	<0.0110	<0.0110	<0.0102	0.01	0.02	0.03	0.03	0.01	0.01	<0.0144	<0.0061
Sc	1.75	1.71	1.84	1.13	2.50	1.47	1.84	1.47	2.19	1.76	1.41	1.26	1.47	1.29
V	3.57	3.06	4.24	4.01	2.69	2.04	2.60	3.45	4.37	3.86	3.79	6.21	5.54	5.04
Cr	3.14	<1.28	3.42	1.30	<1.63	<1.36	2.57	<1.88	<1.37	<0.97	<1.86	<1.99	<1.33	<1.38
Co	1.33	1.28	1.78	1.55	0.95	0.93	0.95	0.82	2.09	1.34	1.95	1.46	1.29	1.65
Ni	1.20	1.38	1.39	1.92	<0.32	<0.21	<0.34	<0.31	1.99	0.23	1.46	0.68	0.77	1.26
Zn	4.19	7.01	7.45	9.79	3.42	3.10	3.34	4.23	4.67	6.18	5.26	6.47	7.34	9.14
Zr	<0.00	0.18	0.73	1.10	0.12	0.10	0.46	0.64	<0.0291	0.14	<0.0279	<0.030	0.04	0.05
Nb	<0.0124	0.04	0.07	0.04	<0.0119	0.01	0.04	<0.028	<0.0223	<0.0118	<0.0261	<0.00	0.01	0.01
Hf	<0.00	<0.050	<0.00	<0.033	<0.00	<0.025	<0.0296	0.05	<0.0305	<0.0186		<0.00	<0.00	<0.00
Ta	<0.00	<0.0071	0.01	0.02	<0.00	<0.00	0.01	0.00	<0.0059	<0.0036	<0.00	<0.00	<0.0121	<0.00
Th	<0.00	0.02	0.03	0.05	<0.00	0.01	0.02	0.03	<0.0071	<0.0043	<0.0096	<0.0184	<0.0094	<0.00
U	<0.00	0.01	0.10	0.11	<0.0069	0.01	<0.0108	0.02	<0.0110	0.01	<0.00	<0.00	<0.00	<0.0117
Y	0.06	0.05	0.13	0.18	0.10	0.16	0.14	0.12	0.12	0.15		0.17	0.19	0.14
La	0.34	0.35	0.52	0.59	0.32	0.28	0.49	0.42	0.51	0.43	0.30	0.52	0.49	0.42
Ce	0.57	0.68	1.06	1.09	0.55	0.53	0.68	0.90	0.82	0.90	0.50	0.86	0.87	0.84
Pr														
Nd	0.22	0.16	0.42	0.39	0.24	0.16	0.13	0.30	0.25	0.38		0.32	0.15	0.39
Sm	0.05	0.07	0.09	0.04	<0.039	<0.030			<0.036	<0.0312		0.03	0.06	0.10
Eu	0.16	0.18	0.25	0.16	0.17	0.10	0.23	0.20	0.27	0.24	0.17	0.38	0.36	0.36
Gd	0.10	0.04	<0.060	0.06	<0.038	<0.041			<0.036			<0.060	0.07	0.06
Tb	0.01	<0.00	0.01	0.01	<0.0060	0.00	<0.0055	0.01	<0.00	0.00	<0.00	0.01	0.02	0.01
Dy	0.03	<0.027	0.05	0.03	0.02	<0.026	0.02	0.04	0.03	0.05	0.02	0.03	0.10	<0.027
Ho	<0.0072	<0.00	0.01	<0.00	<0.00	<0.0049	<0.0102	0.00	<0.0061	0.00	<0.0083	<0.0094	<0.0068	<0.0121
Er														
Tm														
Yb														
Lu														

Figure A.24: LA-ICP-MS compositions of CHA plagioclases.

	AN156A	AN156A				AN169			AN169			AN169		
	PLG1	PLG2	PLG2	PLG2	PLG2	PLG1	PLG1	PLG1	PLG2	PLG2	PLG2	PLG4	PLG4	PLG4
EMP	*RIM1*	*CORE*	*CORE1*	*RIM*	*RIM1*	*CORE*	*INTERM*	*RIM*	*CORE*	*RIM*	*RIM2*	*CORE*	*RIM*	*RIM1*
Na_2O	3.17	3.39	3.39	3.18	3.30	3.72	4.34	3.36	3.67	3.20	3.69	3.99	3.16	3.16
MgO	0.23	0.17	0.17	0.19	0.17	0.13	0.15	0.17	0.17	0.13	0.14	0.13	0.13	0.13
Al_2O_3	29.69	29.69	29.69	30.09	29.79	29.27	28.13	29.87	29.47	30.35	29.52	28.94	29.90	29.90
SiO_2	51.75	52.36	52.36	51.76	52.10	52.82	54.34	51.96	52.62	51.46	52.76	53.26	51.41	51.41
K_2O	0.12	0.15	0.15	0.12	0.13	0.16	0.20	0.15	0.14	0.13	0.16	0.20	0.14	0.14
CaO	14.27	13.79	13.79	14.27	13.97	13.37	12.14	14.00	13.56	14.45	13.51	12.82	14.42	14.42
TiO_2	0.05	0.03	0.03	0.03	0.04	0.04	0.03	0.04	0.04	0.04	0.03	0.05	0.05	0.05
MnO	0.02	0.02	0.02	0.01	0.01	0.01	0.01	0.01	0.01	0.02	0.01	0.01	0.02	0.02
FeO_{tot}	0.92	0.61	0.61	0.73	0.73	0.70	0.63	0.67	0.66	0.80	0.64	0.66	0.78	0.78
An mol%		68.61		70.94	69.91	65.89	60.03	68.88	66.53	71.32	66.61	63.10	70.99	70.99
Ti ppm	298.98	177.00	177.00	198.80	224.18	262.18	170.23	210.93	253.31	224.59	186.05	270.69	312.89	312.89
LA-ICP-MS														
CaO wt%	14.27	13.79	13.79	14.27	13.97	13.37	12.14	14.00	13.56	14.45	13.51	12.82	14.42	14.42
SiO_2 wt%	66.37	58.05	58.63	55.20	54.34	66.22	60.48	63.42	60.23	66.29	58.05	58.26	72.08	72.81
TiO_2 wt%	0.04	0.04	0.04	0.04	0.04	0.04	0.04	0.04	0.04	0.04	0.04	0.04	0.04	0.04
Ti ppm	228.75	233.76	220.70	249.51	225.04	243.01	229.51	237.52	233.99	227.40	224.42	265.05	251.99	226.03
B^{11}	2.23	1.26	1.29	<0.88	<0.74	1.62	5.53	2.10	1.79	<1.19	<1.26	<1.19	1.52	2.31
Li^7	30.29	12.34	9.07	26.56	13.89	19.62	21.97	19.32	15.90	24.17	15.59	26.33	16.17	23.51
Rb	0.51	0.52	0.53	0.51	0.56	0.88	0.72	0.62	0.58	0.60	0.52	0.58	0.51	0.87
Sr	189.38	158.50	160.08	153.44	155.87	161.42	152.62	159.34	162.90	163.58	146.26	154.61	171.33	169.52
Ba	32.46	25.96	30.30	25.26	25.05	30.85	31.61	30.58	28.27	28.09	30.31	30.79	29.72	32.28
Pb	0.61	0.51	0.67	0.56	0.57	0.63	0.53	0.61	0.39	0.54	0.85	1.26	1.14	1.65
Cs	0.01	<0.0082	<0.0085	<0.0102	0.01	<0.0153	<0.0102	<0.0083	0.01	<0.0129	<0.0102	<0.0106	0.02	<0.0142
Sc	1.68	1.76	1.41	1.39	1.50	1.63	1.14	1.37	1.96	1.66	1.18	1.18	1.61	0.98
V	5.82	5.24	5.81	5.31	5.58	6.28	4.72	5.17	5.92	5.48	5.40	5.08	6.08	5.01
Cr	1.81	4.34	1.53	<1.25	2.20	<1.29	<1.18	<1.15	<0.94	1.21	1.46	<1.22	<1.29	<1.10
Co	1.74	1.26	1.73	1.68	1.54	3.11	1.22	1.66	2.80	1.30	1.19	1.03	1.51	1.14
Ni	0.80	0.66	0.51	0.64	0.62	0.82	0.42	<0.22	1.82	0.53	<0.19	<0.22	<0.34	0.59
Zn	9.91	7.18	6.25	8.51	6.98	10.68	5.87	8.08	7.36	6.59	9.60	5.36	8.52	9.27
Zr	0.10	0.03	0.11	0.14	0.12	0.65	0.23	0.06	0.34	<0.031	0.62	0.09	0.18	0.45
Nb	<0.0114	<0.0112	0.02	0.01	<0.0183	<0.00	0.02	<0.0091	<0.0105	<0.0115	<0.020	0.02	0.02	0.05
Hf	<0.00	<0.00	<0.00	<0.030	<0.055	<0.0320	<0.00	<0.00	<0.021	<0.033	<0.029	<0.048	<0.040	<0.032
Ta	<0.0098	<0.0068	<0.00	0.02	<0.00	0.01	0.01	<0.00	<0.00	<0.00	<0.0056	<0.0065	<0.0076	0.00
Th	0.02	<0.00	0.02	<0.0081	<0.0106	0.03	0.01	0.01	0.01	<0.0078	0.02	0.02	<0.0092	0.03
U	0.03	<0.0136	<0.0066	<0.00	<0.0128	0.02	0.01	<0.0054	<0.0044	<0.00	0.03	0.01	0.01	0.01
Y	0.11	0.11	0.15	0.22	0.13	0.41	0.17	0.22	0.34	0.13	0.23	0.16	0.25	0.22
La	0.44	0.36	0.40	0.38	0.46	0.43	0.50	0.33	0.37	0.46	0.62	0.42	0.42	0.55
Ce	0.78	0.71	0.74	0.76	0.73	0.88	0.82	0.74	0.61	0.69	1.01	0.70	0.84	0.92
Pr														
Nd	0.24	0.20	0.33	0.35	0.33	0.42	0.25	0.34	0.25	0.28	0.33	0.27	0.20	
Sm	0.06	0.07	0.08	<0.052	0.05	0.11	0.05	0.08		<0.052	<0.032	0.07	0.03	0.09
Eu	0.45	0.31	0.28	0.45	0.30	0.22	0.28	0.30	0.22	0.29	0.26	0.36	0.45	0.27
Gd	0.06	<0.042	0.07	<0.00	<0.084	0.13	0.03	0.08	<0.025	<0.038	<0.00	0.09	0.11	0.04
Tb	0.01	0.00	<0.00	0.00	0.00	0.01	<0.0090	0.01	0.01	0.01	0.01	<0.0085	0.02	0.02
Dy	0.02	0.06	0.02	0.06	<0.00	0.03	0.03	0.03	0.12	<0.025	0.09	0.06	0.05	0.13
Ho	0.01	<0.00	0.01	0.01	0.00	0.01	<0.0055	0.01	<0.0041	0.00	0.03	0.01	0.01	<0.0106
Er		<0.039	<0.00	<0.00	0.07	0.02	0.08	0.02	<0.0168	<0.026	<0.0226	0.04	<0.00	0.02
Tm		0.00	<0.00	0.00	<0.00	<0.0085	0.01	0.00	<0.0040	0.01	0.01	<0.00	<0.0073	<0.0084
Yb		<0.043	<0.036	<0.00	<0.00	<0.057	<0.036	0.06	<0.00	<0.00	0.03	<0.00	<0.050	<0.041
Lu		0.01	<0.0058	<0.0061	<0.00	0.01	0.01	0.01	<0.00	<0.00	<0.0084	<0.0069	<0.0115	<0.0067

Figure A.25: LA-ICP-MS compositions of CHA plagioclases.

	AN134		AN134			AN137A			AN138	
	CPX1	CPX1	CPX2	CPX2	CPX1	CPX1	CPX1	CPX1	CPX1	CPX1
EMP	*CORE*	*RIM*	*CORE*	*RIM*	*CORE*	*INTERM*	*RIM*	*3*	*2*	*1*
Na_2O	0.15	0.16	0.20	0.13	0.18	0.14	0.13	0.14	0.20	0.16
MgO	17.46	18.07	17.26	18.13	17.68	19.01	17.98	18.19	17.97	18.63
Al_2O_3	2.16	1.69	2.55	1.38	2.67	1.80	1.43	2.19	2.76	2.12
SiO_2	52.64	53.46	52.59	53.68	52.64	53.87	53.37	53.15	52.59	53.41
CaO	18.21	18.76	19.39	18.01	18.92	17.87	18.03	18.35	19.34	18.47
TiO_2	0.62	0.40	0.48	0.45	0.41	0.28	0.36	0.37	0.38	0.30
Cr_2O_3	0.21	0.44	1.06	0.23	1.10	0.62	0.15	0.69	1.03	0.77
MnO	0.20	0.20	0.19	0.23	0.20	0.19	0.22	0.21	0.17	0.19
FeO_{tot}	8.63	7.49	6.68	8.69	6.85	7.12	8.53	7.41	6.50	6.72
Mg#	80.56	83.18	84.11	81.03	84.11	84.54	81.20	83.41	85.01	85.03
Ti ppm	3688.40	2417.92	2873.16	2711.75	2459.03	1683.41	2145.85	2194.40	2255.66	1808.57
Cr ppm	1470.76	3022.40	7284.85	1584.31	7545.80	4256.22	1014.06	4708.41	7018.62	5259.40
LA-ICP-MS										
CaO wt%	18.21	18.76	19.39	18.01	18.92	17.87	18.03	18.35	19.34	18.47
SiO_2 wt%	53.38	50.91	62.27	52.34	44.33	55.61	54.38	53.31	51.91	52.67
TiO_2 wt%	0.47	0.46	0.47	0.39	0.32	0.24	0.33	0.30	0.31	0.27
Ti ppm	2809.40	2759.51	2846.15	2341.08	1897.24	1468.17	1965.27	1800.51	1841.66	1632.25
B^{11}	2.05	1.96	4.47	<0.97	5.04	2.62	3.62	3.58	1.66	2.20
Li^7	9.87	10.60	11.96	11.04	1.73	2.52	3.16	13.15	10.40	13.08
Rb	<0.056	0.07	0.19	<0.034	<0.044	<0.045	0.14	0.95	0.36	1.03
Sr	11.02	14.99	15.91	11.64	8.44	7.45	7.99	9.67	10.92	8.30
Ba	0.37	1.53	<0.22	<0.052	<0.082	<0.064	0.25	0.18	0.05	0.52
Pb	0.06	0.15	0.27	0.09	0.08	0.07	0.30	0.44	0.46	0.14
Cs	<0.0210	<0.0108	0.02	0.01	0.02	<0.0077	0.02	0.04	0.03	0.05
Sc	99.13	101.28	104.73	88.90	89.30	68.27	81.50	81.59	81.16	77.29
V	457.19	474.27	473.41	379.14	360.22	287.05	375.34	300.93	275.46	280.09
Cr	2450.64	4245.44	5585.72	2850.22	5548.11	4206.10	1331.86	5146.84	5578.49	4176.59
Co	60.21	51.24	51.19	47.88	49.18	55.73	66.35	52.77	48.27	52.76
Ni	222.74	218.51	223.84	214.59	228.16	271.76	235.42	250.31	245.33	243.95
Zn	50.63	39.30	31.32	37.96	40.38	47.81	57.13	37.42	30.83	36.27
Zr	11.62	13.85	12.00	8.11	6.63	3.45	5.41	7.96	7.55	6.47
Nb	<0.016	<0.0224	0.05	<0.0127	0.02	<0.0134	0.07	0.10	0.09	0.04
Hf	0.53	0.61	0.60	0.35	0.32	0.15	0.16	0.41	0.30	0.26
Ta	0.01	<0.0075	<0.0079	0.01	0.00	0.01	<0.00	0.00	<0.0144	<0.00
Th	0.03	<0.020	0.03	0.01	0.01	0.01	<0.0078	0.01		<0.028
U	<0.0106	0.02	0.03	<0.00	0.00	<0.0057	<0.0070	0.01	<0.0288	<0.00
Y	12.99	12.77	12.03	10.32	9.42	7.36	9.34	9.17	9.26	8.77
La	0.77	0.79	0.88	0.64	0.42	0.30	0.40	0.46	0.48	0.37
Ce	2.84	3.05	3.30	2.37	1.59	1.20	1.72	1.81	1.81	1.48
Pr	0.66	0.63	0.68	0.50	0.32	0.26	0.34	0.34	0.38	0.34
Nd	3.90	4.63	4.10	3.23	2.32	1.72	1.93	2.24	2.70	1.98
Sm	1.75	1.71	1.80	1.08	0.94	0.60	1.02	1.08	0.90	0.95
Eu	0.50	0.37	0.49	0.43	0.34	0.29	0.34	0.35	0.32	0.28
Gd	2.10	2.08	1.95	2.16	1.18	1.06	1.23	1.61	1.75	1.69
Tb	0.42	0.35	0.39	0.38	0.24	0.25	0.27	0.34	0.31	0.25
Dy	2.98	2.22	2.31	2.15	1.80	1.49	1.62	1.73	2.11	1.85
Ho	0.59	0.52	0.44	0.39	0.35	0.30	0.41	0.38	0.39	0.34
Er	1.37	1.27	1.24	1.25	0.96	0.69	1.14	1.14	0.83	1.06
Tm	0.27	0.21	0.17	0.16	0.16	0.11	0.14	0.17	0.12	0.15
Yb	1.32	1.34	1.15	1.38	0.80	0.73	0.90	0.88	0.99	1.03
Lu	0.24	0.20	0.15	0.18	0.12	0.12	0.15	0.11	0.15	0.13

Figure A.26: LA-ICP-MS compositions of CHA augites.

	OL14				OL14			AN141			
	CPX1	CPX1	CPX2	CPX2	CPX2	CPX2	CPX2	CPX1	CPX1	CPX1	CPX1
EMP	*CORE*	*RIM*	*CORE*	*CORE1*	*INTERM*	*INTERM1*	*RIM*	*CORE*	*CORE1*	*RIM*	*RIM1*
Na_2O	0.18	0.18	0.21	0.21	0.16	0.16	0.18	0.18	0.19	0.18	0.19
MgO	17.82	18.26	17.89	17.36	18.49	18.57	17.75	17.45	17.88	18.57	18.46
Al_2O_3	2.93	1.94	2.63	3.94	2.24	2.18	2.60	3.25	3.27	2.31	2.15
SiO_2	52.86	53.82	53.08	52.09	53.28	53.48	52.87	52.61	52.83	53.65	53.86
CaO	19.16	19.24	19.72	19.54	19.11	19.05	20.07	20.40	19.27	19.67	19.83
TiO_2	0.32	0.25	0.30	0.39	0.28	0.28	0.34	0.37	0.35	0.24	0.28
Cr_2O_3	0.70	0.37	0.76	0.85	0.62	0.56	0.41	1.02	0.96	0.70	0.57
MnO	0.18	0.18	0.15	0.17	0.18	0.19	0.16	0.14	0.14	0.16	0.15
FeO_{tot}	6.01	6.23	5.90	6.23	6.23	6.26	6.11	5.62	6.03	5.64	5.86
Mg#	85.87	85.74	86.14	85.11	85.88	85.87	85.61	86.43	85.88	87.09	86.58
Ti ppm	1921.13	1527.81	1771.64	2347.55	1686.23	1676.10	2014.70	2215.20	2094.36	1463.93	1678.50
Cr ppm	4793.73	2501.58	5179.83	5832.49	4231.59	3799.31	2826.10	6979.01	6565.68	4822.87	3879.36
LA-ICP-MS											
CaO wt%	19.16	19.24	19.72	19.54	19.11	19.11	20.07	20.40	19.27	19.67	19.83
SiO_2 wt%	53.28	51.16	63.06	63.78	59.37	50.29	53.12	49.83	50.25	55.39	52.70
TiO_2 wt%	0.24	0.23	0.27	0.31	0.25	0.31	0.29	0.33	0.35	0.23	0.24
Ti ppm	1451.41	1358.05	1621.91	1887.04	1520.12	1876.77	1722.12	1974.80	2077.35	1404.99	1463.17
B^{11}	<1.26	<0.94	2.58	2.93	0.99	<0.82	1.27	2.87	4.31	<1.77	1.55
Li^7	2.82	2.13	2.60	3.37	2.26	1.71	1.11	2.78	3.92	4.37	6.97
Rb	<0.046	<0.041	0.27	1.44	0.04	0.11	0.11	0.05	0.10	<0.045	0.17
Sr	8.77	7.79	10.70	15.70	8.88	10.22	9.22	11.37	9.51	8.00	9.77
Ba	0.04	<0.00	0.24	1.99	0.23	0.91	0.38	0.07	0.39	<0.096	0.48
Pb	0.14	0.09	0.10	0.05	0.10	0.22	0.09	0.24	0.30	0.20	0.24
Cs	0.02	<0.0107	0.09	0.37	<0.0142	0.01	<0.0161	<0.0112	0.02	<0.0115	<0.0149
Sc	74.92	74.37	85.59	102.11	81.40	82.73	83.09	97.29	101.09	75.74	78.15
V	223.69	205.07	258.25	337.11	225.85	267.74	266.89	230.88	247.95	178.85	183.34
Cr	3650.36	2205.94	4652.66	5119.20	4020.79	4442.17	2567.97	6363.82	4346.88	4787.77	3183.78
Co	48.23	44.86	47.22	56.83	54.76	45.76	52.50	42.45	47.49	51.31	43.64
Ni	251.00	225.80	271.03	345.57	259.24	219.95	228.06	227.47	227.58	288.35	242.06
Zn	29.34	29.27	29.87	28.64	30.84	31.95	30.50	25.29	30.56	31.08	29.33
Zr	4.75	3.80	6.10	10.38	5.64	7.15	5.08	6.99	8.58	3.89	4.82
Nb	0.02	0.02	0.07	0.10	0.02	0.01	0.02	0.02	0.07	0.02	<0.0231
Hf	0.13	0.17	0.36	0.28	0.35	0.32	0.29	0.40	0.36	0.25	0.21
Ta	<0.0090	<0.00	0.01	0.01	0.00	<0.0071	0.01	0.00	0.00	<0.00	<0.0087
Th	0.01	<0.00	<0.0097	0.05	<0.0127	0.02	0.02	0.01		<0.00	0.01
U	0.01	0.01	0.01	0.04	<0.00	0.02	<0.0121	0.01		<0.0081	<0.0091
Y	6.92	6.43	7.13	9.04	8.55	7.68	8.57	9.09	9.30	7.18	6.68
La	0.26	0.26	0.39	0.50	0.37	0.48	0.47	0.28	0.43	0.34	0.34
Ce	1.15	1.03	1.24	2.18	1.25	1.60	1.29	1.52	1.69	0.99	1.15
Pr	0.24	0.17	0.29	0.37	0.24	0.32	0.22	0.30	0.37	0.18	0.29
Nd	1.32	1.23	1.69	2.24	1.83	2.26	2.08	1.86	2.31	0.88	1.47
Sm	0.72	0.70	0.84	1.05	0.86	0.90	0.87	1.08	0.92	0.61	0.57
Eu	0.33	0.21	0.27	0.37	0.31	0.35	0.40	0.45	0.35	0.19	0.27
Gd	1.03	0.83	1.78	1.43	1.37	1.04	1.35	1.34	1.65	1.00	1.08
Tb		0.21	0.21	0.38	0.22	0.23	0.23	0.27	0.25	0.20	0.23
Dy	1.32	1.33	1.31	1.64	1.88	1.61	1.54	1.90	1.71	1.66	1.34
Ho	0.26	0.24	0.36	0.45	0.29	0.27	0.42	0.34	0.43	0.31	0.30
Er			0.95	1.19	0.81	0.98	1.06	1.04	1.39	0.86	0.99
Tm	0.08	0.08	0.11	0.12	0.12	0.09	0.15	0.16	0.18	0.14	0.11
Yb	0.61	0.65	1.21	1.25	0.61	0.68	1.01	0.46	1.57	0.61	0.63
Lu	0.09	0.10	0.09	0.14	0.10	0.13	0.13	0.10	0.18	0.12	0.09

Figure A.27: LA-ICP-MS compositions of CHA augites.

	AN141		AN156A			AN169A			AN169A	
	CPX2	CPX2	CPX1	CPX1	CPX1	CPX1	CPX1	CPX1	CPX2	CPX2
EMP	*CORE*	*RIM*	*CORE*	*INTERM*	*RIM*	*CORE*	*RIM*	*RIM1*	*CORE*	*RIM*
Na_2O	0.16	0.19	0.17	0.18	0.20	0.17	0.19	0.21	0.22	0.17
MgO	18.15	17.57	16.45	16.28	16.20	17.06	15.77	16.16	16.06	13.73
Al_2O_3	2.78	2.85	1.63	1.86	1.93	1.72	2.51	2.45	2.63	1.95
SiO_2	53.13	53.00	52.49	52.37	52.26	52.52	51.38	51.78	51.61	50.57
CaO	19.46	20.29	17.85	18.01	17.87	16.30	18.18	17.19	17.56	16.92
TiO_2	0.33	0.34	0.37	0.39	0.40	0.32	0.52	0.46	0.50	0.69
Cr_2O_3	0.81	0.78	0.26	0.24	0.19	0.30	0.35	0.36	0.45	0.04
MnO	0.16	0.15	0.25	0.27	0.26	0.28	0.25	0.27	0.25	0.30
FeO_{tot}	5.95	5.82	10.39	10.30	10.82	11.10	10.29	10.71	10.17	14.29
Mg#	86.21	86.08	76.44	76.40	75.43	75.91	75.85	75.56	76.39	66.33
Ti ppm	1961.53	2013.18	2218.50	2319.08	2376.44	1910.17	3099.79	2746.93	2985.61	4111.73
Cr ppm	5564.76	5356.24	1761.14	1650.23	1330.64	2042.55	2388.14	2494.81	3095.40	285.40
LA-ICP-MS										
CaO wt%	19.46	20.29	17.85	18.01	17.87	16.30	18.18	17.19	17.56	16.92
SiO_2 wt%	50.35	51.49	47.04	38.40	50.59	59.30	49.95	50.44	53.68	54.89
TiO_2 wt%	0.25	0.32	0.32	0.34	0.36	0.38	0.47	0.42	0.41	0.46
Ti ppm	1519.93	1903.21	1924.92	2047.40	2177.34	2270.35	2818.64	2539.53	2431.81	2750.53
B^{11}	<1.32	1.71	<0.79	<0.41	0.79	2.18	<0.91	1.81	3.09	1.66
Li^7	5.37	4.79	3.27	2.10	3.24	12.96	13.81	9.09	13.85	12.10
Rb	<0.045	<0.043	<0.039	0.04	<0.034	0.07	<0.042	<0.035	0.26	0.09
Sr	9.22	10.47	4.36	4.29	4.57	3.57	5.21	5.49	10.34	6.89
Ba	<0.109	0.27	<0.043	0.13	0.09	<0.057	0.31	0.31	1.27	0.87
Pb	0.00	0.10	0.07	0.20	0.05	<0.033	0.40	0.42	0.54	0.67
Cs	<0.0107	<0.0073	<0.0090	<0.0108	<0.0096	<0.0078	<0.0081	<0.0103	0.02	0.01
Sc	85.18	102.97	108.91	111.27	110.53	124.93	141.26	131.99	131.69	128.58
V	185.84	238.34	370.93	357.94	391.85	386.09	465.21	457.43	412.79	538.80
Cr	5127.53	4869.54	1544.48	1429.73	1094.03	2105.27	2179.45	2130.44	2405.67	1687.71
Co	41.54	42.17	59.47	60.74	70.49	74.24	66.02	58.64	60.68	61.62
Ni	237.14	222.57	216.62	226.14	224.20	251.41	199.69	197.27	229.32	179.87
Zn	25.14	26.41	66.32	49.23	73.55	85.56	57.11	57.92	61.75	67.08
Zr	5.64	7.70	5.60	5.65	6.82	6.75	10.19	9.30	9.38	11.65
Nb	<0.0166	<0.0161	0.01	<0.0085	<0.00	0.03	<0.018	0.04	0.03	0.02
Hf	0.29	0.61	0.34	0.19	0.33	0.64	0.55	0.54	0.38	0.80
Ta	<0.0062	<0.0105	<0.0062	<0.0052	<0.0066	0.01	0.02	<0.00	0.01	<0.0053
Th	<0.0104	<0.0101	0.00	0.01	<0.0088	<0.00	0.01	0.02	0.01	0.04
U	<0.0065	0.01	0.01	<0.0085	0.00	0.01	<0.00	0.01	0.01	0.01
Y	7.41	9.94	12.23	12.37	14.88	16.96	20.71	17.32	18.56	19.89
La	0.28	0.43	0.26	0.37	0.23	0.43	0.46	0.42	0.49	0.53
Ce	1.17	1.73	1.13	1.39	0.94	1.22	1.80	1.62	1.61	1.77
Pr	0.22	0.29	0.26	0.28	0.25	0.24	0.41	0.38	0.34	0.32
Nd	1.30	2.10	1.92	1.91	1.65	1.58	2.03	2.24	2.03	2.90
Sm	0.60	1.02	0.94	0.83	0.90	0.79	1.26	1.10	1.05	1.55
Eu	0.26	0.38	0.32	0.36	0.42	0.43	0.42	0.31	0.43	0.51
Gd	1.14	1.32	1.66	2.21	1.67	2.05	2.20	2.19	2.15	2.55
Tb	0.23	0.24	0.27	0.36	0.37	0.39	0.41	0.43	0.42	0.55
Dy	1.44	1.78	2.72	2.96	2.75	2.89	4.21	2.92	3.54	3.69
Ho	0.36	0.39	0.63	0.68	0.64	0.67	1.02	0.70	0.70	0.82
Er	0.72	0.99	1.58	1.85	1.93	1.79	2.45	2.00	1.84	2.19
Tm	0.12	0.14	0.17	0.26	0.23	0.32	0.31	0.30	0.27	0.31
Yb	0.80	1.10	1.82	1.82	1.85	2.27	2.50	2.66	2.06	1.98
Lu	0.10	0.14	0.24	0.21	0.29	0.36	0.29	0.26	0.36	0.40

Figure A.28: LA-ICP-MS compositions of CHA augites.

A.4 LA-ICP-MS MINERAL PHOTOS

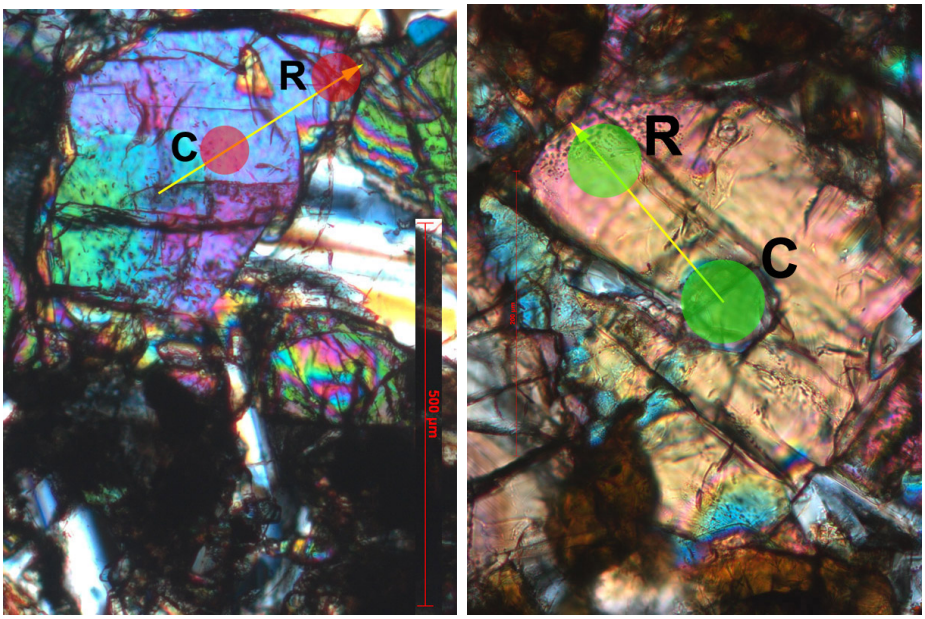

Figure A.29: Augites AN134cpx1 (on the left) and cpx2 (on the right) analysed by LA-ICP-MS. Yellow arrows represent EMP transects while red and green circles represent LA spots.

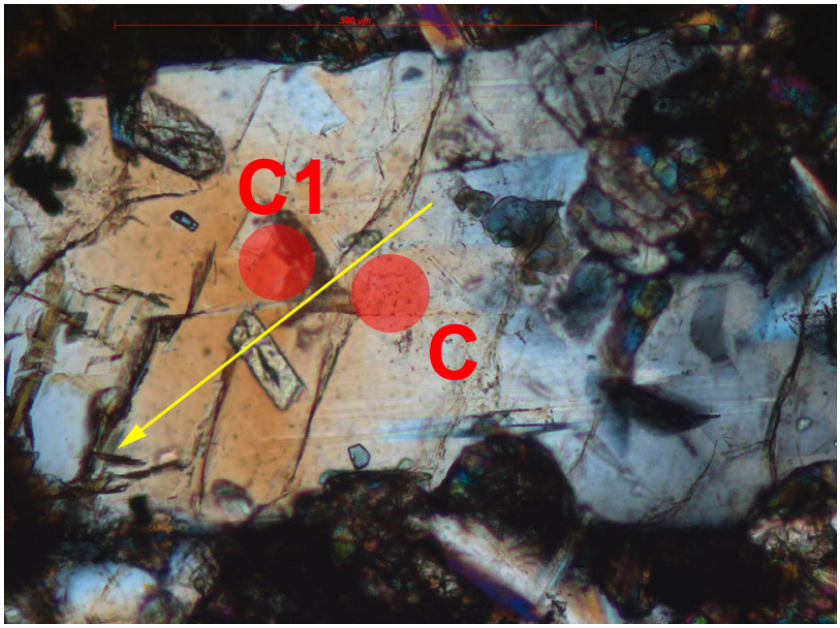

Figure A.30: Plagioclase AN134plg1 analysed by LA-ICP-MS. Yellow arrows represent EMP transects while red circles represent LA spots.

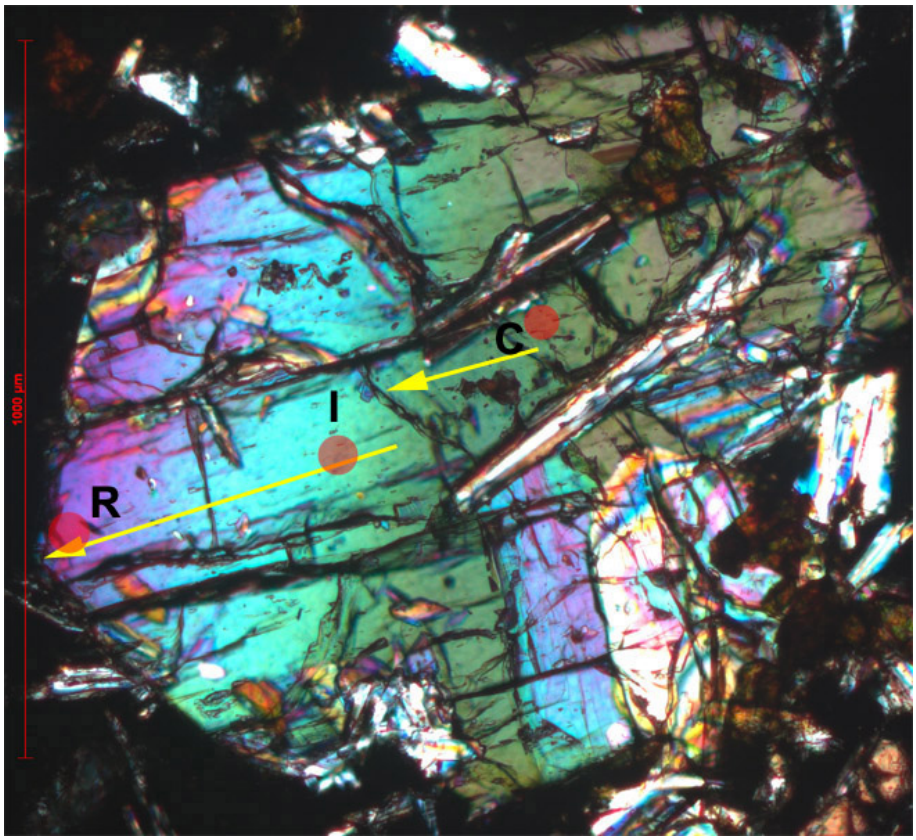

Figure A.31: Augite AN137Acpx1 analysed by LA-ICP-MS. Yellow arrows represent EMP transects while red circles represent LA spots.

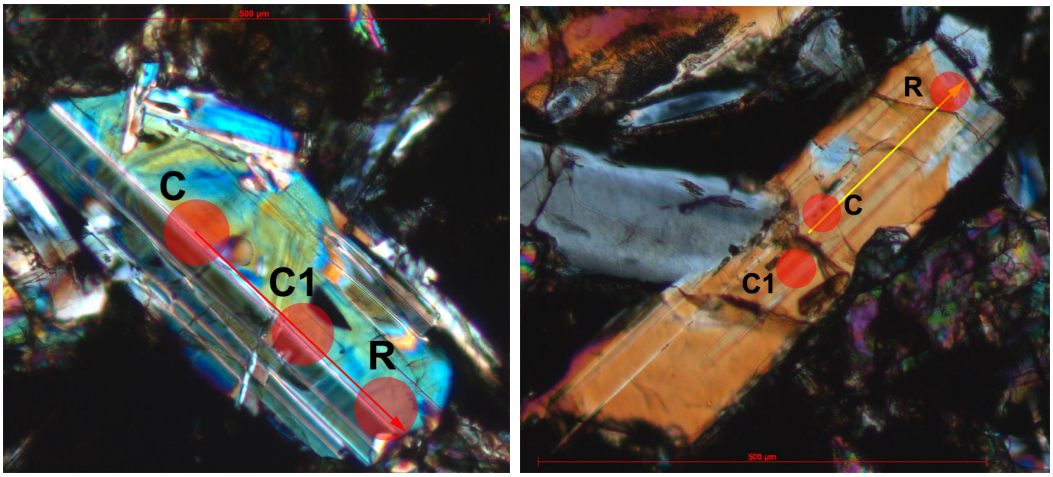

Figure A.32: Plagioclases AN137Aplg2 (on the left) and plg3 (on the right) analysed by LA-ICP-MS. Yellow arrows represent EMP transects while red circles represent LA spots.

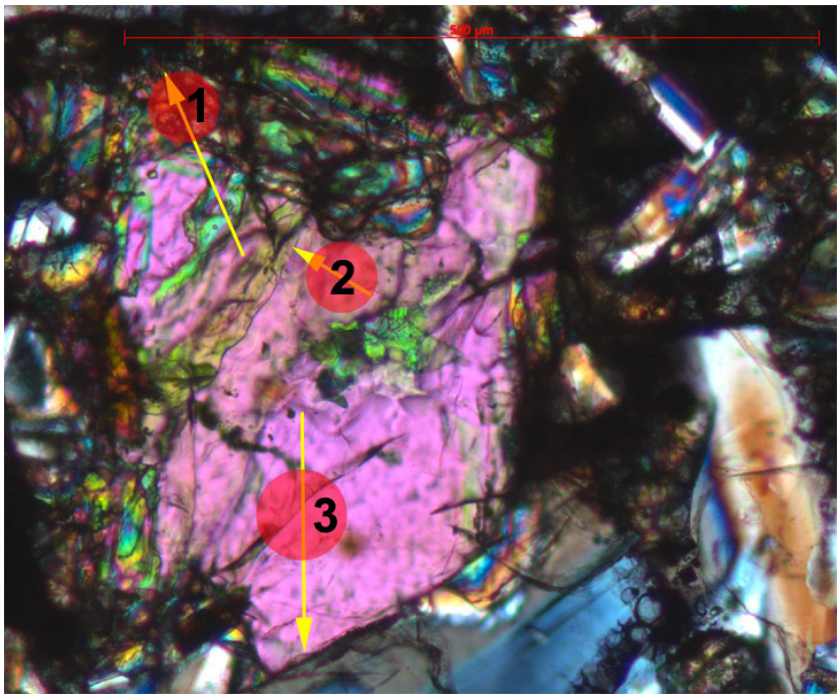

Figure A.33: Augite AN138cpx1 analysed by LA-ICP-MS. Yellow arrows represent EMP transects while red circles represent LA spots.

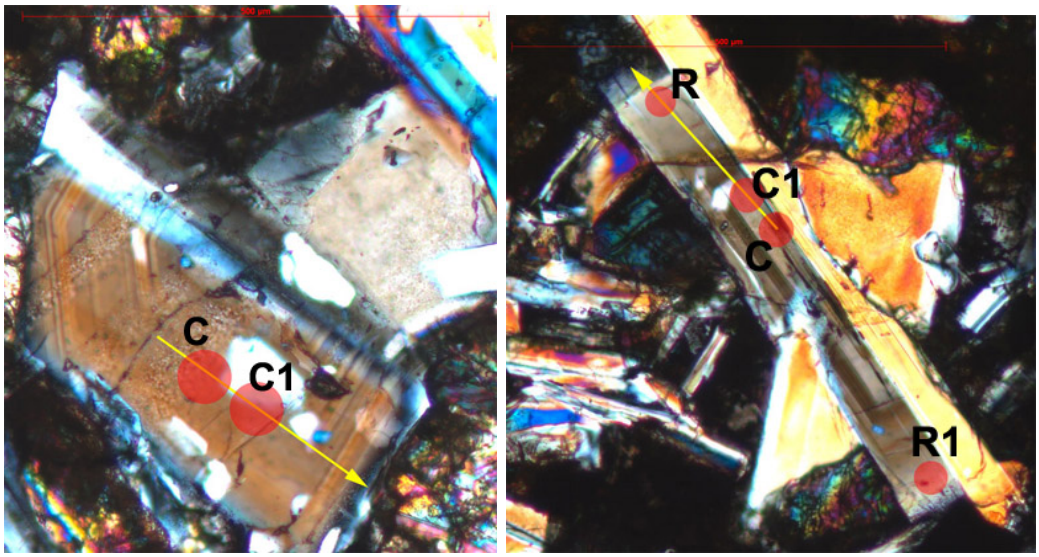

Figure A.34: Plagioclases AN138plg1 (on the left) and plg3 (on the right) analysed by LA-ICP-MS. Yellow arrows represent EMP transects while red circles represent LA spots.

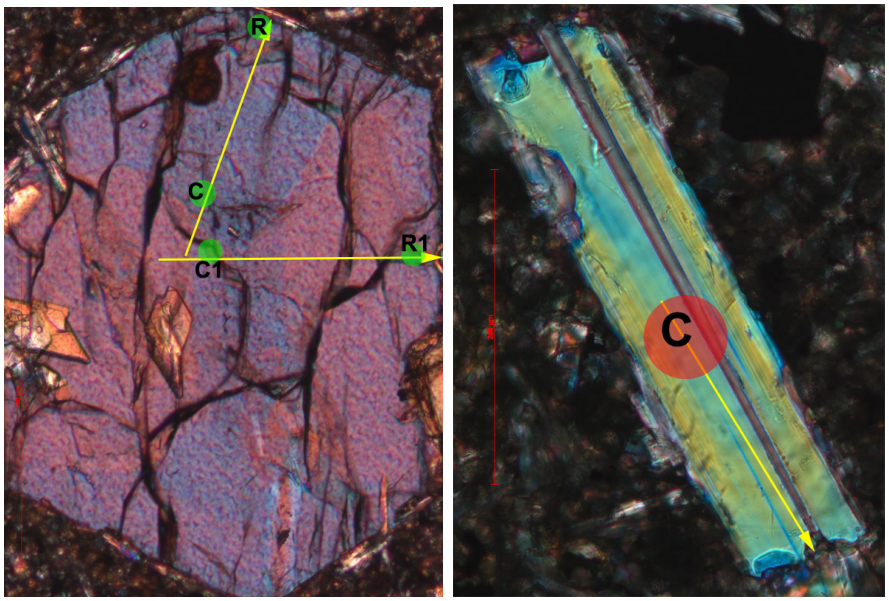

Figure A.35: Augite AN141cpx1 (on the left) and plagioclase AN141plg3 (on the right) analysed by LA-ICP-MS. Yellow arrows represent EMP transects while green and red circles represent LA spots.

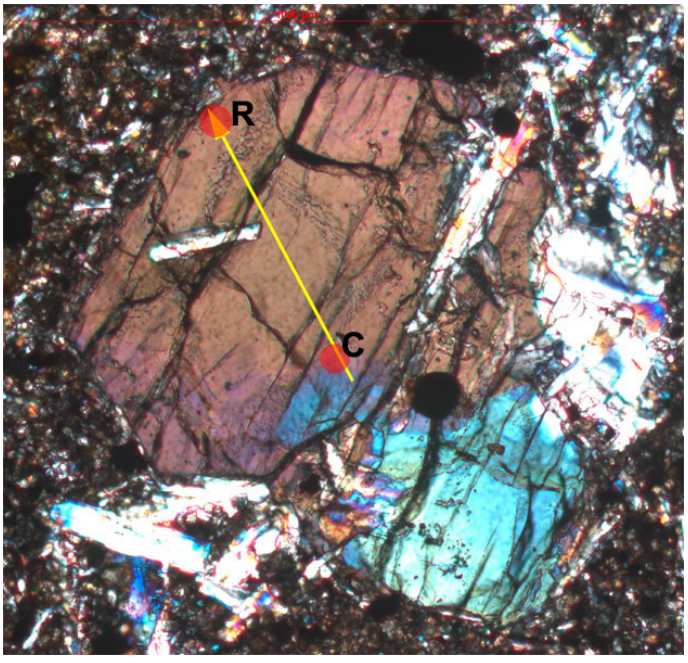

Figure A.36: Augite AN141cpx2 analysed by LA-ICP-MS. Yellow arrows represent EMP transects while red circles represent LA spots.

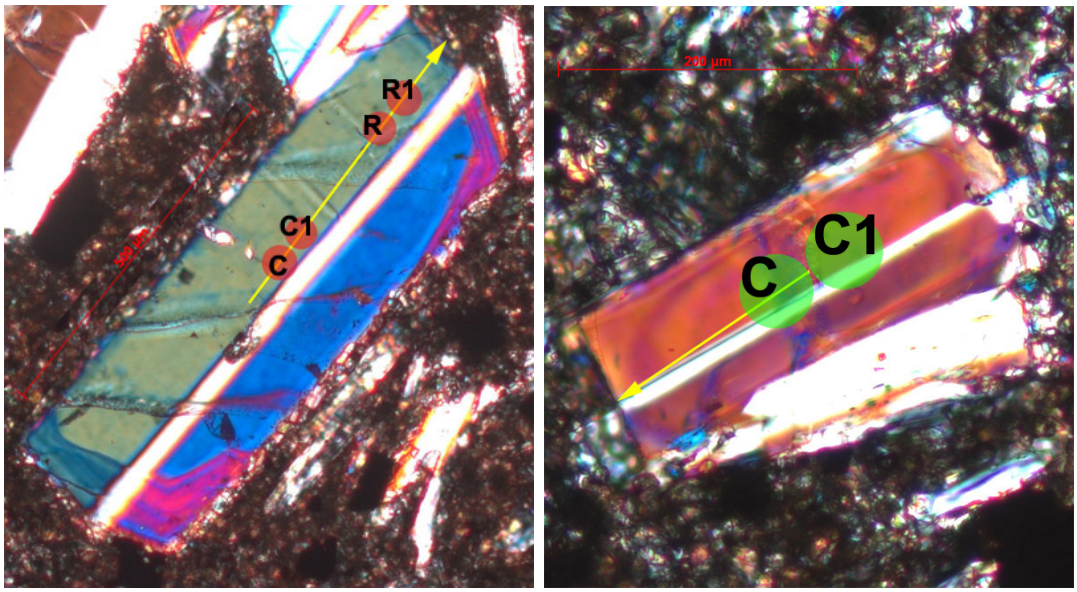

Figure A.37: Plagioclases AN141plg1 (on the left) and plg2 (on the right) analysed by LA-ICP-MS. Yellow arrows represent EMP transects while green and red circles represent LA spots.

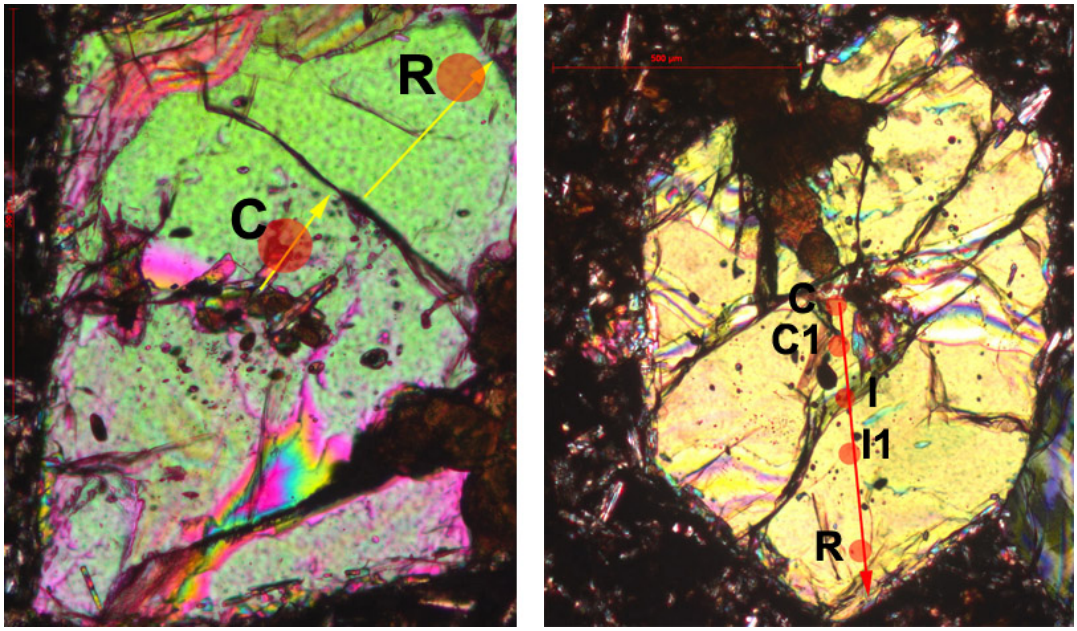

Figure A.38: Augites OL14cpx1 (on the left) and cpx2 (on the right) analysed by LA-ICP-MS. Yellow arrows represent EMP transects while red circles represent LA spots.

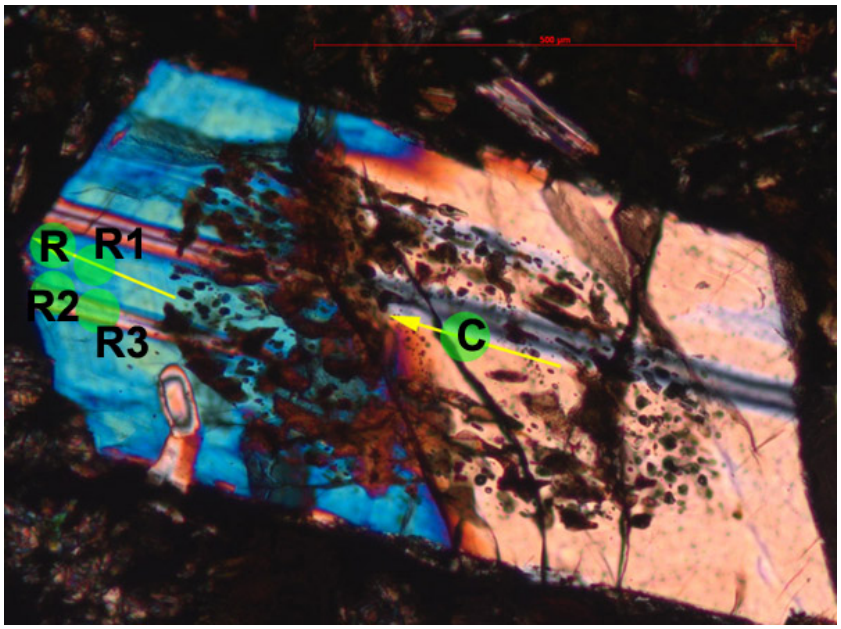

Figure A.39: Plagioclase OL14plg1 analysed by LA-ICP-MS. Yellow arrows represent EMP transects while green circles represent LA spots.

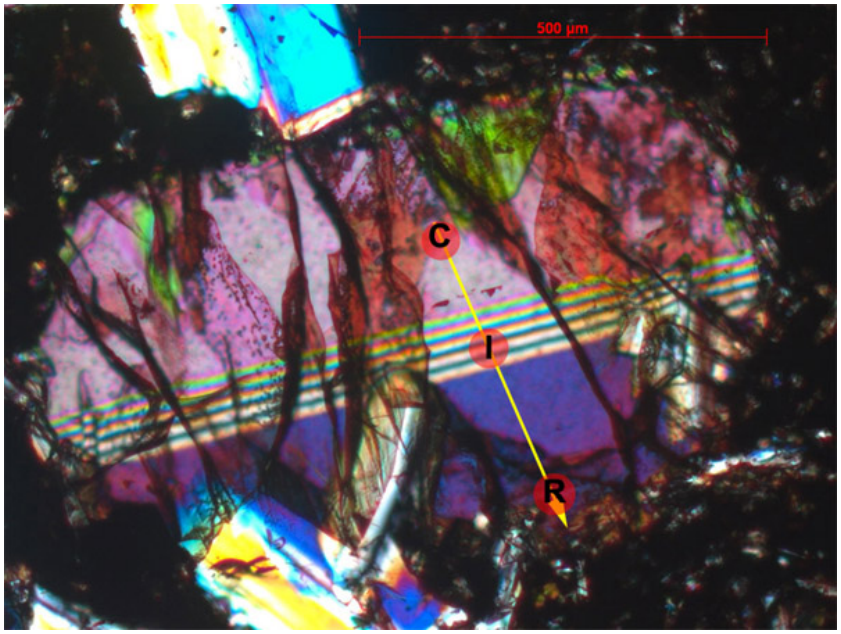

Figure A.40: Augite AN156Acpx1 analysed by LA-ICP-MS. Yellow arrows represent EMP transects while red circles represent LA spots.

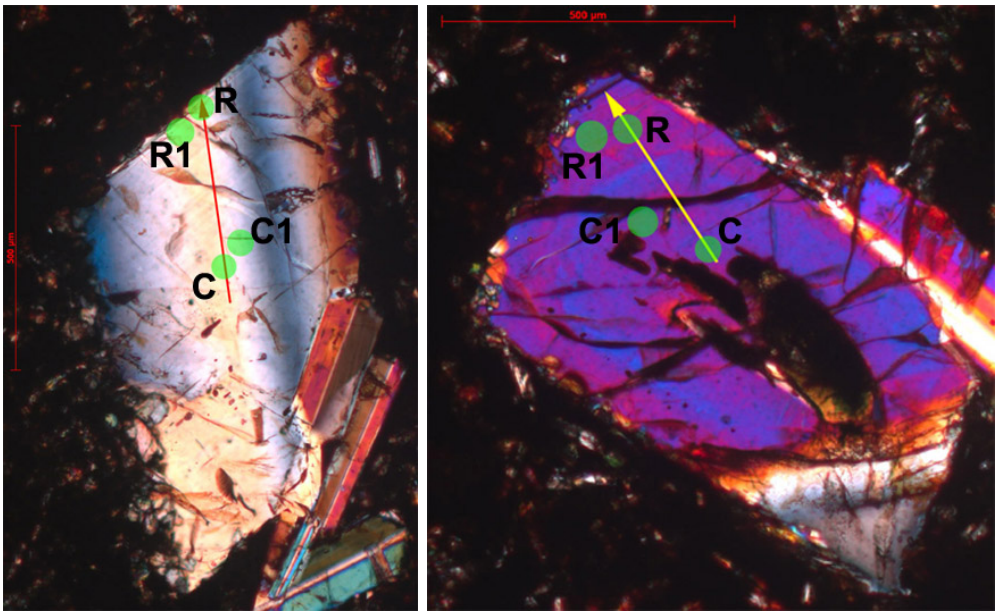

Figure A.41: Plagioclases AN156Aplg1 (on the left) and plg2 (on the right) analysed by LA-ICP-MS. Yellow and red arrows represent EMP transects while green circles represent LA spots.

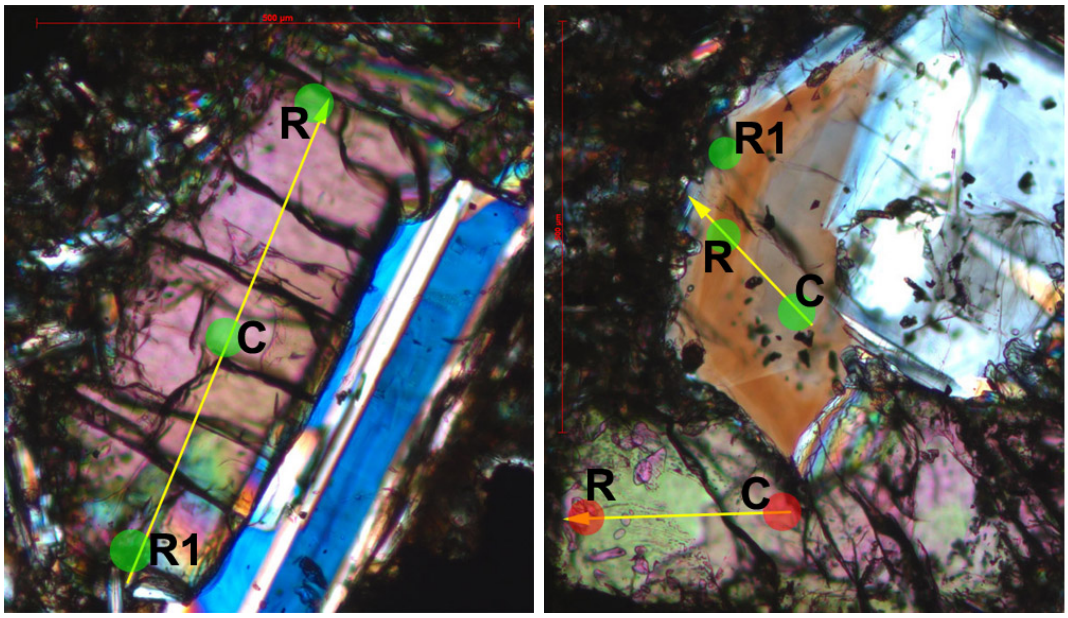

Figure A.42: Augites AN169Acpx1 (on the left), AN169cpx2 (on the right) and plagioclase AN169plg4 (on the right) analysed by LA-ICP-MS. Yellow arrows represent EMP transects while green and red circles represent LA spots.

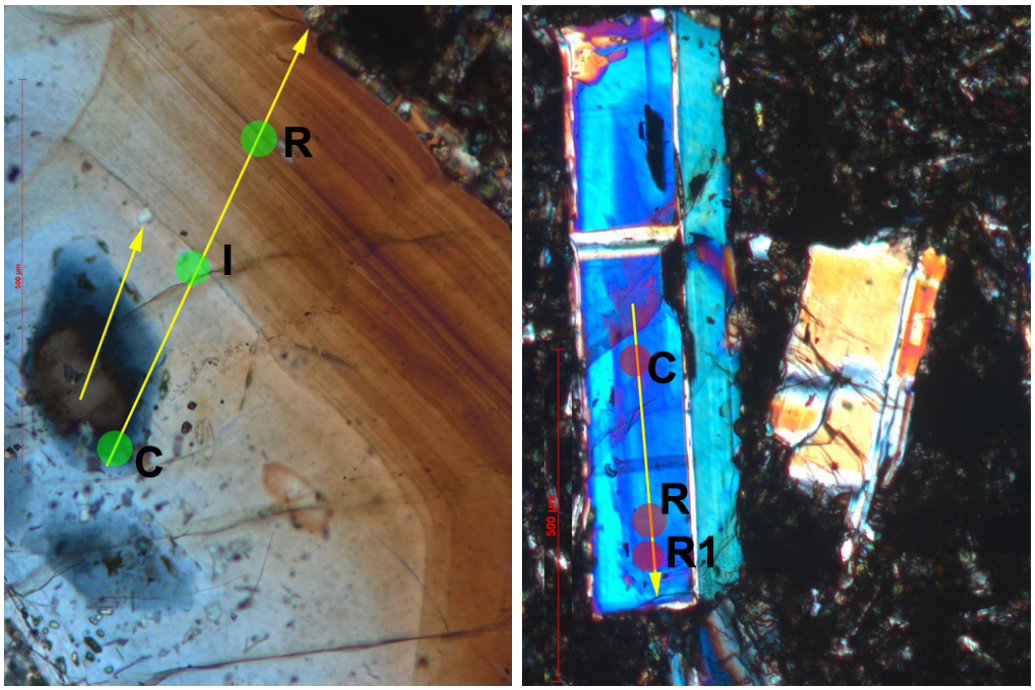

Figure A.43: Plagioclases AN169Aplg1 (on the left) and plg2 (on the right) analysed by LA-ICP-MS. Yellow arrows represent EMP transects while red and green circles represent LA spots.

Bibliography

Aigner-Torres, M., Blundy, J., Ulmer, P. & Pettke, T. (2007). Laser ablation icpms study of trace element partitioning between plagioclase and basaltic melts:an experiemntal approch. *Contrib. Mineral. Petrol.*, **153**, 647–667.

Almeida, F.F.M. (1986). Distribução regional e relações tectônicas do magmatismo pós-paleozóico no brazil. *Revista Brasileira de Geocîencias*, **16**, 325–349.

Andersen, D. & Lindsley, D. (1985). New (and final!) models for the timagnetite/ilmenite geothermometer and oxygen barometer. *Abstract AGU 1985 Spring Meeting Eos Transactions*, **66**, 416.

Andersen, D.J., Lindsley, D.H. & Davidson, P.M. (1993). Quilf: A pascal program to assess equilibria among fe-mg-mn-ti oxides, pyroxenes, olivine and quartz. *Computer & Geosciences*, **19**, 1333–1350.

Anderson, D.L. (1994). The sublithospheric mantle as the source of subcontinental flood basalts: the case against the continental lithosphere and plume head reservoir. *Earth Planet. Sci. Lett.*, **123**, 269–280.

Andres, E. & Grevesse, N. (1989). Abundances of the elements: meteoritic and solar. *Geochim. Cosmochim. Acta*, **53**, 197–214.

Arboleya, M.L., Teixell, A., Charroud, M. & Julivert, M. (2004). A structural transect through the high and middle atlas of morocco. *J. Afr. Earth Sci.*, **39**, 319–327.

Ayarza, P., Lobato, F.A., Teixell, A., Arboleya, M.L., Tesòn, E., Julivert, M. & Charroud, M. (2005). Crustal structure under the central high atlas mountains (morocco) from geological and gravity data. *Tectonophys.*, **400**, 67–84.

Baker, D.R. & Eggler, D.H. (1987). Composition of anhydrous and hydrous melts coexisting with plagioclase, augite and olivine or low-ca pyroxene from 1 atm to 8 kbar: Application to the aleutian volcanic center of atka. *Am. Min.*, **72**,

12–28.

Baksi, A.K. (2003). *Critical evaluation of $^{40}Ar/^{39}Ar$ ages for the Central Atlantic Magmatic Province: timing, duration and possible migration of magmatic centers*. In: W. E. Hames, J. G. McHone, P. R. Renne, C. Ruppel (Eds.), The Central Atlantic Magmatic Province: Insights from frangments of Pangea, AGU Geophys. Mon. 136.

Baksi, A.K. & Archibald, D.A. (1997). Mesozoic igneous activity in the maranhao province, northern brazil: ^{40}ar/^{39}ar evidence for separate episodes of basaltic magmatism. *Earth Planet. Sci. Lett.*, **151**, 139–153.

Bas, M.J.L., Maître, R.W.L. & Woolley, A.R. (1992). The construction of the total alkali-silica chemical classification of volcanic rocks. *Miner. Petr.*, **46**, 1–22.

Baudelot, S., Charrière, A., Ouarhache, D. & Sabaoui, A. (1990). Données palynologiques nouvelles concernant l'ordovicien et le trias-lias du moyen atlas (maroc). *Géologie Méditerranéenne*, **XVII**, 263–277.

Beauchamp, B. (1987). The p-t and other late paleozoic stress release events in nw pangea abstract. *Gaea Heidelbergensis*, **3**, 68.

Beauchamp, B. (1997). The p-t and other stress-release events in nw pangea. *Pangea (abs.), Gaea Heidelbergensis*, **3**, 68.

Beauchamp, J. (1988). *Triassic sedimentation and rifting in the High Atlas (Morocco)*. In: Manspeizer, W. (Ed.), Triassic-Jurassic Rifting. Developments in Geotectonics, 22. Elsevier, New York.

Beauchamp, W., Allmendinger, R., Barazangi, M., Demnati, A., Alji, M.E. & Dahmani, M. (1999). Inversion tectonics and evolution of the high atlas mountains, morocco, based on a geologicalegeophysical transect. *Tectonics*, **18**, 163–185.

Beckinsale, R.D., Bowles, J.F., Pankhurst, R.J. & Wells, M.K. (1977). Rubidium-strontium age studies and geochemistry of acid veins in the freetown complex, sierra leone. *Mineralogical Magazine*, **41**, 501–511.

Bedard, J.H. (2006). Trace element partitioning in plagioclase feldspar. *Geochim. Cosmochim. Acta*, **70**, 3717–3742.

Bellieni, G., Piccirillo, E.M., Cavazzini, G., Petrini, R., Comin-Chiaramonti, P.,

Nardy, A.J.R., Civetta, L., Melfi, A.J. & Zantedeschi, P. (1990). Low and high tio_2 mesozoic tholeiitic magmatism of the maranhao basin (ne brazil) : K/ar age, geochemistry, petrology, isotope characteristics and relationships with mesozoic low- and high-tio_2 flood basalts of the paranà basin (se brazil). *N. J. Miner. Abh.*, **162**, 1–33.

Benson, R.N. (2003). *Age estimates of the seaward-dipping volcanic wedge, earliest oceanic crust, and earliest drift-stage sediments along the North American Atlantic continental margin*. In: W. E. Hames, J. G. McHone, P. R. Renne, C. Ruppel (Eds.), The Central Atlantic Magmatic Province: Insights from frangments of Pangea, AGU Geophys. Mon. 136.

Berndt, J., Koepke, J. & Holtz, F. (2005). An experimental investigation of the influence of water and oxygen fugacity on differentiation of morb at 200 mpa. *J. Petrol.*, **46**, 135–167.

Bertrand, H. (1991). *The Mesozoic tholeiitic province of northwest Africa: A volcano-tectonic record of the early opening of the Central Atlantic*. In Kampuzu A. B., Lulaba R. T. (Eds), Magmatism in extensional settings: The Phanerozoic African Plate.

Bertrand, H. & Coffrant, D. (1986). Le sill doléritique du kaarta (mali occidental): un exemple de fractionnement par flow differentiation? *Réunion Ann. Sci. Terre*, **11**, 16.

Bertrand, H. & Villeneuve, M. (1989). Témoins de l'ouverture de l'atlantique central au début du jurassique: les dolérites tholéiitiques continentales de guinée (afrique de l'ouest). *C. R. Acad. Sci. Paris*, **308**, 93–98.

Bertrand, H., Dostal, J. & Dupuy, C. (1982). Geochemistry of early mesozoic tholeiites from morocco. *Earth Planet. Sci. Lett.*, **58**, 225–239.

Bertrand, H., Liegeois, J.P., Deckart, K. & Féraud, G. (1999). High-ti tholeiites in guyana and their connection with the central atlantic cfb province: elemental and nd-sr-pb isotopic evidence for preferential zone of mantle upwelling in course of rifting. *AGU spring meeting (Abst. p.317)..*

Bertrand, H., Fornari, M., Marzoli, A., Sempere, T. & Féraud, G. (2005). *Early Mesozoic rift-related magmatism in the Bolivian Andes and Subandes: the southernmost record of the Central Atlantic Magmatic Province*. 6^{th} International Symposium on Andean Geodynamics (Barcelona), Extended abstracts.

Besse, J. & Courtillot, V. (2002). Apparent and true polar wander and the geometry of the geomagnetic field over the last 200 ma. *J. Geophys. Res.*, **107B**, 31.

Beutel, E.K., Nomade, S., Fronabarge, A.K. & Renne, P.R. (2005). Pangea's complex breakup: A new rapidly changing stress field model. *Earth Planet. Sci. Lett.*, **236**, 471–485.

Bindeman, I.N. & Davies, A.M. (2000). Trace element partitioning between plagioclase and melt: Investigation of dopant influence on partition behaviour. *Geochim. Cosmochim. Acta*, **64**, 2863–2878.

Bindeman, I.N., Davies, A.M. & Drake, M.J. (1998). Ion microprobe study of plagioclase-basalt partition experiments at natural concentration levels of trace elements. *Geochim. Cosmochim. Acta*, **62**, 1175–1193.

Bird, D.E., Hall, S.A., Burke, K. & Casey, J.F. (2005). *Late Jurassic - Early Cretaceous tectonic reconstructions of the Central and South Atlantic Oceans (abstract)*. Eos. Trans. Am. Geophys. Union, 86, Joint Assembly Supplement.

Cebriá, J.M., López-Ruiz, J., Doblas, M., Martins, L.T. & Munhá, J. (2003). Geochemistry of the early jurassic messejana/plasencia dyke (portugal/spain): Implications on the origin of the central atlantic magmatic province. *J. Petrol.*, **44**, 547–568.

Chabou, M.C., Sebai, A., Féraud, G. & Bertrand, H. (2007). Datation ^{40}ar/^{39}ar de la province magmatique de l'atlantique central dans le sud-ouest algérien. *C. R. Geoscience*, **339**, 970–978.

Chalokwu, C.I. (2001). Petrology of the freetown layered complex, sierra leone: Part ii. magma evolution and crystallisation conditions. *J. Afr. Earth Sci.*, **32**, 519–540.

Chalokwu, C.I., Ripley, E. & Park, Y. (1999). Oxygen isotopic systematics of an open-system magma chamber: An example from the freetown complex of sierra leone. *Geochim. Cosmochim. Acta*, **63**, 675–685.

Coffin, M.F. & Eldholm, O. (1994). Large igneous provinces: crustal structure, dimensions, and external consequences. *Rev. Geophys.*, **32**, 1–36.

Cohen, A.S. & Coe, A.L. (2002). New geochemical evidence for the onset of volcanism in the central atlantic magmatic province and environmental change at the triassic-jurassic boundary. *Geology*, **30**, 267–270.

Coltice, N., Phillips, B.R., Bertrand, H., Ricard, Y. & Rey, P. (2007). Global warming of the mantle at the origin of flood basalts over supercontinents. *Geology*, **35**, 391–394.

Costa, F., Chakraborty, S. & Dohmen, R. (2003). Diffusion coupling between trace and major elements and a model for calculation of magma residence times using plagioclase. *Geochim. Cosmochim. Acta*, **67**, 2189–2200.

Courtillot, V., Jaupart, C., Manighetti, I., Tapponnier, P. & Besse, J. (1999). On causal links between flood basalts and continental breakup. *Earth Planet. Sci. Lett.*, **166**, 177–195.

Cousminer, H. & Manspeizer, W. (1976). Triassic pollen date moroccan high atlas and the incipient rifting of pangea as middle carnian. *Science*, **191**, 943–945.

Crasquin-Soleau, S., Rakus, M., Oujidi, M., Courel, L., Touhami, M.E. & Benaouiss, N. (1997). Découverte d'une faune d'ostracodes dans le trias des monts d'oujda (maroc): relations paléogéographiques entre les plates-formes nord et sud de la téthys. *C. R. Acad. Sci. Paris*, **324**, 111–118.

Dalrymple, G.B., Gromme, C.S. & White, R.W. (1975). Potassium/argon age and paleomagnetism of diabase dikes in liberia: initiation of central atlantic rifting? *Geol. Soc. Am. Bull.*, **86**, 399–411.

Dalziel, I.W.D. (1991). Pacific margins of laurentia and east antarctica-australia as a conjugate rift pair; evidence and implications for an eocambrian supercontinent. *Geology*, **19**, 598.

Danyushevsky, L.V. (2001). The effect of small amounts of h_2o on crystallization of mid-ocean ridge and backarc basin magmas. *J. of Volcanology and Geothermal Res.*, **110**, 265–280.

Danyushevsky, L.V., Sobolev, A.V. & Dmitriev, L.V. (1996). Estimation of the pressure of crystallization and h_2o content of morb and babb glasses: calibration of an empirical technique. *Miner. Petr.*, **57**, 185–204.

Davison, I. (2005). Central atlantic margin basins of north west africa: Geology and hydrocarbon potential (morocco to guinea). *J. Afr. Earth Sci.*, **43**, 254–274.

de Lamotte, D.F., Bezar, B.S. & Bracène, R. (2000). The two main steps of the atlas building and geodynamics of the western mediterranean. *Tectonics*, **19**, 740–761.

Deckart, K. (1996). *Etude du magmatisme associé au rifting de l'Atlantique Central et Sud: géochronologie $^{40}Ar/^{39}Ar$ et geóchimie sur les intrusions jurassiques de Guinée et Guyane française/Surinam, et crétacées du Brésil*. Master's thesis, Unpublished Thése d' Université, Géoscience Azur, Documents et travaux no. 2, Université de Nice-Sophia Antipolis.

Deckart, K., Féraud, G. & Bertrand, H. (1997). Age of jurassic continental tholeiites of french guyana, surinam and guinea: Implications for the initial opening of the central atlantic ocean. *Earth Planet. Sci. Lett.*, **150**, 205–220.

Deckart, K., Bertrand, H. & Liégeois, J.P. (2005). Geochemistry and sr, nd, pb isotopic composition of the central atlantic magmatic province (camp) in guyana and guinea. *Lithos*, **82**, 289–314.

DeMin, A., Piccirillo, E., Marzoli, A., Bellieni, G., Renne, P., Ernesto, M. & Marques, L. (2003). *The Central Atlantic Magmatic Province (CAMP) in Brazil: petrology, geochemistry, $^{40}Ar/^{39}Ar$ ages, paleomagnetism and geodynamic implications*. In: W. E. Hames, J. G. McHone, P. R. Renne, C. Ruppel (Eds.), The Central Atlantic Magmatic Province: Insights from frangments of Pangea, AGU Geophys. Mon. 136.

der Meijde, M.V., der Lee, S.V. & Giardini, D. (2003). Crustal structure beneath broad-band seismic stations in the mediterranean region. *Geophys. J. Intern.*, **152**, 729–739.

Diallo, D., Bertrand, H., Azambre, B., Gregoire, M. & Caseiro, J. (1992). Le complexe basique-ultrabasique du kakoulima (guinée-conakry): une intrusion tholeiitique stratifiée liée au rifting de l'atlantique central. *C. R. Acad. Sci. Paris*, **314**, 937– 943.

Doherty, W. (1989). An internal standardization procedure for the determination of yttrium and the rare earth elements in geological materials by inductively coupled plasma-mass spectrometry. *Spectrochimica Acta*, **44B**, 263–280.

Dooley, R.E. & Wampler, J.M. (1983). *Potassium-argon relations in diabase dikes of Georgia - The influence of excess ^{40}Ar on the geochronology of early Mesozoic igneous and tectonic events*. in Gohn, G., Ed., Studies related to the Charleston, South Carolina, earthquake of 1886 - tectonics and seismicity: U.S. geological Survey Professional Paper 1313.

Doré, A.G. (1991). The structural formation and evolution of mesozoic seaways between europe and the artict. *Palaeogeog. Palaeoclim. Palaeoecol.*, **87**, 441–

492.

Dostal, J. & Durning, M. (1998). Geochemical constraints on the origin and evolution of early mesozoic dikes in atlantic canada. *Eur. J. Mineral.*, **10**, 79–93.

Dostal, J. & Greenough, J.D. (1992). *Geochemistry and petrogenesis of the early Mesozoic North Mountain basalts of Nova Scotia, Canada*. In: J.H. Puffer and P.C. Ragland, Editors, Eastern North American Mesozoic Magmatism, Geological Society of America Special Paper vol. 268.

Dunn, A.M., Reynolds, P.H., Clarke, D.B. & Ugidos, J.M. (????). A comparison of the age and composition of the shelburne dyke, nova scotia, and the messejana dyke, spain.

Dunning, G.R. & Hodych, J.P. (1990). U/pb zircon and baddeleyite ages for palisades and gettysburg sills of the northeastern united states: implication for the age of the triassic/jurassic boundary. *Geology*, **18**, 795–798.

Dupuy, C., Marsh, J., Dostal, J., Michard, A. & Testa, S. (1988). Asthenospheric and lithospheric sources for mesozoic dolerites from liberia (africa): trace element and isotopic evidence. *Earth Planet. Sci. Lett.*, **87**, 100–110.

Ellouz, N., Patriat, M., Gaulier, J.M., Bouatmani, R. & Sabounji, S. (2003). From rifting to alpine inversion: Mesozoic and cenozoic subsidence history of some moroccan basins. *Sedim. Geol.*, **156**, 185–212.

Ernesto, M., Bellieni, G., Piccirillo, E.M., Marques, L.S., Min, A.D., Pacca, I.G., Martins, G. & Macedo, J.W.P. (2003). *Paleomagnetic and Geochemical constraints on the timing and duration of the CAMP activity in Northeastern Brazil*. In: W. E. Hames, J. G. McHone, P. R. Renne, C. Ruppel (Eds.), The Central Atlantic Magmatic Province: Insights from frangments of Pangea, AGU Geophys. Mon. 136.

Feig, S.T., Koepke, J. & Snow, J.E. (2006). Effect of water on tholeiitic phase equilibria: an experimental study under oxidizing conditions. *Contrib. Mineral. Petrol.*, **152**, 611–638.

Giese, P. & Jacobshagen, V. (1992). Inversion tectonics of intracontinental ranges: High and middle atlas, morocco. *Geologische Rundschau*, **8**, 249–259.

Gomez, F., Allmendinger, R., Barazangi, M., Er-Raji, A. & Dahmani, M. (1998). Crustal shortening and vertical strain partitioning in the middle atlas moun-

tains of morocco. *Tectonics*, **17**, 520–533.

Greenough, J.D. & Papezik, V.S. (1987). Note on the petrology of north mountain basalt from the wildcat oil well mobil gulf chinampas - 37, bay of fundy, canada. *Can. J. Earth Sci.*, **24**, 1255–1260.

Hames, W.E., Renne, P.R. & Ruppel, C. (2000). New evidence for geologically instantaneous emplacement of the earliest jurassic central atlantic magmatic province basalts on the north american margin. *Geology*, **28**, 859–862.

Harfi, A.E., Lang, J., Salomon, J. & Chellai (2001). Cenozoic sedimentary dynamics of the ouarzazate foreland basin (central high atlas mountains, morocco). *Intern. J. Earth Sci.*, **90**, 393–411.

Harfi, A.E., Guiraud, M. & Lang, J. (2006). Deep-rooted "thick skinned" model for the high atlas mountains (morocco). implications for the structural inheritance of the southern tethys passive margin. *J. of Structural Geol.*, **28**, 1958–1976.

Hattori, K. & Chalokwu, C.I. (1995). Source for early magmatism related to the opening of the atlantic ocean: Sr- and nd-isotopes of mineral separates from the freetown complex of sierra leone. *Am. Geophys. Union Fall meeting, E.O.S.*, **76**, 687.

Heatherington, A. & Muller, P. (1999). Lithospheric sources of north florida, usa tholeiites and implication for the origin of the suwannee terrane. *Lithos*, **49**, 215–233.

Heizler, M.T. & Harrison, T.M. (1988). Multiple trapped argon isotope components by ^{40}ar/^{39}ar isochron analysis. *Geochim. Cosmochim. Acta*, **52**, 1295–1303.

Hesselbo, S.P., Robinson, S.A., Surlyk, F. & Piasecki, S. (2002). Terrestrial and marine mass extinction at the triassic-jurassic boundary synchronized with initiation of massive volcanism. *Geology*, **30**, 251–254.

Hill, E., Wood, B. & Blundy, J. (2000). The effect of ca-tschermaks component on trace element partitioning between clinopyroxene and silicate melt. *Lithos*, **53**, 205–217.

Hill, R.I. (1991). Starting plumes and continental breakup. *Earth Planet. Sci. Lett.*, **104**, 398–416.

Hill, R.I., Campbell, I.H., Davies, G.F. & Griffiths, R.W. (1992). Mantle plume and continental tectonics. *Science*, **256**, 186–193.

Hodych, J.P. & Dunning, G.R. (1992). Did the manicougan impact trigger end-of-triassic mass extinction? *Geology*, **20**, 51–54.

Hodych, J.P. & Hayatsu, A. (1988). Paleomagnetism and k.ar isochron dates of early jurassic basaltic flows and dikes of atlantic canada. *Can. J. Earth Sci.*, **25**, 1972–1989.

Holbrook, W.S. & Keleman, P.B. (1993). Large igneous province on the us atlantic margin and implications for magmatism during continental breakup. *Nature*, **364**, 433–436.

Hollard, H. (1973). La mise en place au lias des dolerites dans le paléozöique moyen du ne des plaines du drâa et du basin de tindouf (sud de l'anti-atlas central, maroc). *C. R. Acad. Sci. Paris*, **277**, 553–556.

Hounslow M. W., G.W., P. E. Posen (2004). Magnetostratigraphy and biostratigraphy of the upper triassic and the lowermost jurassic succession, st. audrie's bay. *Palaeogeog. Palaeoclim. Palaeoecol.*, **213**, 331–358.

Hozik, M.J. (1992). Paleomagnetism of igneous rocks in the culpeper, newark, and hartford/deerfield basins. *In: Puffer, J.H., Ragland, P.C. (Eds.), Eastern North American Mesozoic Magmatism. Geological Society of America Special Paper*, **268**, 279–308.

Irvine, T.N. & Baragar, W.R.A. (1971). A guide to the chemical classification of the common volcanic rocks. *Can. J. Earth Sci.*, **8**, 523–548.

Jenner, G.A., Longerich, H.P., Jackson, S.E. & Fryer, B.J. (1990). Icp-ms - a powerful tool for high-precision trace-element analysis in earth science: Evidence from analysis of selected u.s.g.s. reference samples. *Chem. Geol.*, **83**, 133–148.

Jourdan, F. & Renne, P.R. (2007). Age calibration of the fish canyon sanidine ^{40}ar/^{39}ar dating standard using primary k-ar standards. *Geochim. Cosmochim. Acta*, **71**, 387–402.

Jourdan, F., Marzoli, A., Bertrand, H., Cosca, M. & Fontignie, D. (2003). *The northernmost CAMP: $^{40}Ar/^{39}Ar$ age, petrology and Sr-Nd-Pb isotope geochemistry of the Kerforne Dike, Brittany, France*. In: W. E. Hames, J. G. McHone, P. R. Renne, C. Ruppel (Eds.), The Central Atlantic Magmatic Province: Insights from frangments of Pangea, AGU Geophys. Mon. 136.

Jourdan, F., Verati, C. & Féraud, G. (2006). Intercalibration of the hb3gr ^{40}ar/^{39}ar dating standard. *Chem. Geol.*, **231**, 177–189.

Jourdan, F., Marzoli, A., Bertrand, H., Cirilli, S., Tanner, L., Kontak, D.J., McHone, G., Renne, P. & Bellieni, G. (2009). ^{40}ar/^{40}ar ages of camp in north america: implications for the triassic-jurassic boundary and the ^{40}k decay constant bias. *Lithos*, **98**.

Kent, D.V. & Olsen, P.E. (2006). Magnetostratigraphy of the triassic-jurassic boundary interval and the tempo of camp volcanism. *Geological Society of America Abstracts with Program*, **38-7**, 398.

King, P.B. (1961). Systematic pattern of triassic dikes in the appalachian region. *U.S. Geol. Surv., Prof. Pap.*, **424B**.

King, P.B. (1971). Systematic pattern of triassic dikes in the appalachian region second report. *U.S. Geol. Surv., Prof. Pap.*, **750D**.

King, S.D. & Anderson, D.L. (1995). An alternative mechanism of flood basalt formation. *Earth Planet. Sci. Lett.*, **136**, 269–279.

King, S.D. & Anderson, D.L. (1998). Edge-driven convection. *Earth Planet. Sci. Lett.*, **160**, 289–296.

Knight, K.B., Nomade, S., Renne, P.R., Marzoli, A., Bertrand, H. & Youbi, N. (2004). The central atlantic magmatic province at he triassic-jurassic boundary: paleomagnetic and ^{40}ar/^{39}ar evidence from morocco for brief, episodic volcanism. *Earth Planet. Sci. Lett.*, **228**, 143–160.

Kontak, D.J. (2008). On the edge of camp: Geology and volcanology of the jurassic north mountain basalt, nova scotia. *Lithos*, **101**, 74–101.

Kontak D. J., D.A.A. (2003). ^{40}ar/^{39}ar age dating of the jurassic north mountain basalt, southern nova scotia. *Atlantic Geology*, **39**, 47–54.

Koppers, A.A.P. (2002). Ararcalc-software for ^{40}ar/^{39}ar age calculations. *Computers & Geosciences*, **28**, 605–619.

Lanphere, M.A. (1983). *^{40}Ar/^{39}Ar ages of basalt from clubhouse Crossroads test hole #2, near Charleston, South Carolina*. in Studies related to the Charleston, south Carolina, Earthquake of 1886 - Tectonics and Seismicity, edited by G. S. Gohn, U.S. Geol. Surv. Prof. Paper, 1313.

Laville, A.P., E. (1991). La distension crustale atlantique et atlasique au maroc

au début du mésozoïque: Le rejeu des structures hercyniennes. *Bull. Soc. Géol. France*, **162**, 1161–1171.

Laville, E., Piqué, A., Amrhar, M. & Charroud, M. (2004). A restatement of the mesozoic atlasic rifting (morocco). *J. Afr. Earth Sci.*, **38**, 145–153.

Lécorché, J., Dallmeyer, R.D. & Villeneuve, M. (1989). *Definition of tectonostratigraphic terranes in the Mauritanide, Bassaride and Rokelide orogenes, West Africa*. In R. D. Dallmeyer (Ed.), Terranes in the Circum-Atlantic Paleozoic orogens, Vol. 230, Geological Society of America Special Paper.

Leblanc, M. (1973). Le grand dyke de dolerite de l'anti-atlas et le magmatisme jurassique du sud-marocain. *C. R. Acad. Sci. Paris*, **276**, 2943–2946.

Lepage, L.D. (2003). Ilmat: an excel worksheet for ilmenite-magnetite geothermometry and geobarometry. *Computers & Geosciences*, **29**, 673–678.

Lindsley, D.H. (1983). Pyroxene thermometry. *Am. Min.*, **68**, 477–493.

Longerich, H.P., Jenner, G.A., Fryer, B.J., & Jackson, S.E. (1990). Inductively coupled plasma-mass spectrometric analysis of geological samples: A critical evaluation based on case studies. *Chem. Geol.*, **83**, 105–118.

Ludwig, K.R. (2003). Isoplot/ex 3: A geochronological toolkit for microsoft excel. *Berkeley Geochronology Center Special Publication*, **no.4**, 70.

Mahmoudi, A. & Bertrand, H. (2007). Identification géochimique de la province magmatique de l'atlantique central an domain plissé: exemple du moyen atlas marocain. *C.R. Geoscience*, **330**, 545–552.

Maillard, A., Malod, J., Thiébot, E., Klingenhoefer, F. & Réhault, J.P. (2006). Imaging a lithospheric detachment at the continent-ocean crustal transition off morocco. *Earth Planet. Sci. Lett.*, **241**, 686–698.

Makris, J., Demnati, A. & Klubman, J. (1985). Deep seismic soundings in morocco and a crust and upper mantel model deduced from seismic and gravity data. *Ann. Geophys.*, **3**, 369–380.

Manspeizer, W. (1994). *The breakup of Pangea and its impact on climate: consequences of Variscan-Alleghenide orogenic collapse*. In: Klein, G.D. (Ed.), Pangea: Paleoclimate, Tectonics and Sedimentation during Accretion, Zenith and Breakup of a Supercontinent, Geological Society of America, Special Paper 228.

Manspeizer, W. & Cousminer, H.L. (1988). Late triassic-early jurassic synrift basins of the u.s. atlantic margin. *in Sheridan R.E., and Grow J.A. Eds., The Geology of North America. The Atlantic Continental Margin, U.S.: Geological Society of America*, **vol I-2**, 197–216.

Martins, L.T., Madeira, J., Youbi, N., Munhà, J., Mata, J. & Kerrich, R. (2008). Rift-related magmatism of the central atlantic magmatic province in algarve, southern portugal. *Lithos*, **101**, 102–124.

Marzoli, A., Renne, P., Piccirillo, E.M., Ernesto, M., Bellieni, G. & Min, A.D. (1999). Extensive 200 million year old continental flood basalt of the central atlantic magmatic province. *Science*, **23**, 616–618.

Marzoli, A., Bertrand, H., Knight, K.B., Cirilli, S., Buratti, N., Verati, C., Nomade, S., Renne, P.R., Youbi, N., Martini, R., Allenbach, K., Neuwerth, R., Rapaille, C., Zaninetti, L. & Bellieni, G. (2004). Synchrony of the central atlantic magmatic province and the triassic- jurassic boundary climatic and biotic crisis. *Geology*, **32**, 973–976.

Mauche R., L.M.J.J.H., G. Faure (1989). Anomalous isotopic compositions of sr, ar and o in the mesozoic diabase dikes of liberia, west africa. *Contrib. Mineral. Petrol.*, **101**, 12–18.

McDonough, W.F. & s. Sun, S. (1995). The composition of the earth. *Chem. Geol.*, **120**, 223–253.

McHone, J.G. (2000). Non-plume magmatism and tectonics during the opening of the central atlantic ocean. *Tectonophys.*, **316**, 287–296.

McHone, J.G. (2003). *Volatile emissions from Central Atlantic Magmatic Province basalts: mass assumptions and environmental consequences*. In: W. E. Hames, J. G. McHone, P. R. Renne, C. Ruppel (Eds.), The Central Atlantic Magmatic Province: Insights from frangments of Pangea, AGU Geophys. Mon. 136.

McHone, J.G. (2005). *Emplacement Structures in North Mountain Basalt at Grand Manan Island, New Brunswick*. Geological Association of Canada-Mineralogical Association of Canada, Program with Abstracts (CD-ROM).

Meddah, A., Bertrand, H. & Elmi, S. (2007). La province magmatique de l'atlantique central dans le bassin des ksour (atlas saharien, algérie). *C. R. Geoscience*, **339**, 24–30.

Merle, R., Marzoli, A., Bertrand, H., Verati, C., Reisberg, L., Zimmermann, C., Chiaradia, M., Bellieni, G. & Ernesto, M. (2008). Ar ages and sr-nd-pb-os geochemistry of camp tholeiites from western maranhao basin (ne brazil): implications for low and high-ti basalt sources. *Earth Planet. Sci. Lett.*.

Michard, A. (1976). Eléments de géologie marocaine. *Notes et Mémoires du Service Géologique du Maroc*, **252**, 408.

Min, K., Mundil, R., Renne, P.R. & Ludwig, K.R. (2000). A test for systematic errors in ^{40}ar/^{39}ar geochronology through comparison with u-pb analysis of a 1.1 ga rhyolite. *Geochim. Cosmochim. Acta*, **64**, 73–98.

Min, K., Renne, P.R. & Huff, W.D. (2001). ^{40}ar/^{39}ar dating of ordovician k-bentonites in laurentia and baltoscandia. *Earth Planet. Sci. Lett.*, **185**, 121–134.

Morgan, W.J. (1983). Hotspot tracks and the early rifting of the atlantic. *Tectonophys.*, **94**, 123–139.

Nomade, S., Théveniaut, H., Chen, Y., Pouclet, A. & Rigollet, C. (2000). Paleomagnetic study of french guyana early jurassic dolerites: hypothesis of a multistage magmatic event. *Earth Planet. Sci. Lett.*, **184**, 155–168.

Nomade, S., Pouclet, A. & Chen, Y. (2002). The french guyana doleritic dykes: geochemical evidence of three populations and new data for the jurassic central atlantic magmatic province. *J. Geodyn.*, **34**, 595–614.

Nomade, S., Renne, P.R. & Merkle, R.K.W. (2004). ^{40}ar/^{39}ar age constraints on ore deposition and cooling of the bushveld complex, south africa. *J. Geol. Soc. Lond.*, **161**, 411–420.

Nomade, S., Knight, K.B., Beutel, E., Renne, P.R., Vérati, C., Feraud, G., Marzoli, A., Youbi, N. & Bertrand, H. (2007). Chronology of the central atlantic magmatic province: Implications for the central atlantic rifting processes and the triassic-jurassic biotic crisis. *Palaeogeog. Palaeoclim. Palaeoecol.*, **244**, 324–342.

Oh, J., Austin, J.A., Phillips, J.D., Coffin, M.F. & Stoffa, P.L. (1995). Seaward-dipping reflectors offshore the southeastern united states: seismic evidence for extensive volcanism accompanying sequential formation of the carolina trough and blake platea basin. *Geology*, **23**, 9–12.

Olsen, P.E., Schische, R.W. & Fedosh, M.S. (1996). *580 Ky duration of the*

Early Jurassic flood basalt event in eastern North America estimated using Milankovitch cyclostratigraphy. In: Morales M. (Ed.), The continental Jurassic. Museum of Northen Arizona Bulletin, vol. 60.

Olsen, P.E., Kent, D.V., Touhami, M.E. & Puffer, J. (2003). *Cyclo-, magneto-, and bio-stratigraphic constraints on the duration of the CAMP event and its relationship to the Triassic-Jurassic boundary*. In: W. E. Hames, J. G. McHone, P. R. Renne, C. Ruppel (Eds.), The Central Atlantic Magmatic Province: Insights from frangments of Pangea, AGU Geophys. Mon. 136.

Oujidi, M. (1996). *Evolution tectono-sédimentaire des Monts d'Oujda (Maroc oriental) au cours du Trias et du Lias basal*. in Le Permien et le Trias du Maroc: Etat des connaissances, edited by F. Medina, Editions PUMAG, Marrakech.

Ouorhache, D. (1987). *Etude géologique dans le Paléozoique et le Trias de la bordure NW du Causse moyen Atlasique (S et SW de Fés, Maroc)*. Master's thesis, Thèse de Doctorat de 3ème Cycle, Univ. Paul Sabatier, Toulouse.

Panjasawatwong, Y., Danyushevsky, L., Crawford, A.J. & Harris, K.L. (1995). An experimental study of the effects of melt composition on plagioclase-melt equilibria at 5 kbar and 10 kbar; implications for the origin of magmatic high-an plagioclase. *Contrib. Mineral. Petrol.*, **118**, 420–432.

Papike, J.J., Cameron, K.L. & Baldwin, K. (1974). Amphiboles and pyroxenes: characterization of other than quadrilateral components and estimates of ferric iron from microprobe data. *Geol. Soc. America, Abstr. with Progr.*, **6**, 1053–1054.

Patchtère, P.D. (1983). *Le volcanisme Permien et fini-triasique dans le Haut Atlas de Marrakech (Maroc): Approche pétrologique et géeochimique*. Master's thesis, Thèse 3ème cycle, Univ. Scientifique et Médicale de Grenoble.

Pe-Piper, G., Jansa, L.F. & Lambert, R.S.J. (1992). *Early Mesozoic magmatism of the eastern Canadian margin*. In: Puffer. J. H., P. C. Ragland (Eds.), Eastern North American Mesozoic magmatism. Geol. Soc. Am., Spec. Paper, vol. 268.

Peate, D.W. (1997). *The Paranà-Etendeka province*. In: Mahoney J. J., M. F. Coffin (Eds), Large Igneous Provinces: Continental, oceanic and planetary flood volcanism. AGU, Geophys. Mon., vol. 100.

Piqué, A. & Laville, E. (????). Les series triasiques du maroc, marqueurs du.

Piqué, A. & Laville, E. (1996). The central atlantic rifting: reactivation of pale-

ozoic structures? *J. Geodyn.*, **21**, 235–255.

Piqué, A., Tricart, P., Guiraud, R., Laville, E., Bouaziz, S., Amrhar, M. & Ouali, R.A. (2002). The mesozoic-cenozoic atlas belt (north africa): an overview. *Geodynam. Acta*, **15**, 185–208.

Putirka, K. (1999). Clinopyroxene + liquid equilibria. *Contrib. Mineral. Petrol.*, **135**, 151–163.

Putirka, K., Jonhson, M., Kinzler, R., Longhi, J. & Walker, D. (1996). Thermobarometry of mafic igneous rocks based on clinopyroxenes-liquid equilibria, 0-30 kb. *Contrib. Mineral. Petrol.*, **123**, 92–108.

Putirka, K., Mikaelian, H., Ryerson, F. & Shaw, H. (2003). New clinopyroxene-liquid thermobarometers for mafic, evolved and volatile-bearing lava compositions, with applications to lavas from tibet and the snake-river plain, id. *Am. Min.*, **88**, 1542–1554.

Rast, N. (1990). *The evolution of the Appalachian chain*. In: A. W. Bally, A. R. Palmer (Eds.), The Geology of North America, A. Boulder: Geological Society of America.

Renne, P.R. (2000). ^{40}ar/^{39}ar age of plagioclase from acapulco meteorite and the problem of systematic errors in cosmochronology. *Earth Planet. Sci. Lett.*, **175**, 13–26.

Renne, P.R., Swisher, C.C., Deino, A.L., Karner, D.B., Owens, T.L. & DePaolo, D.J. (1998). Intercalibration of standards, absolute ages and incertainties in ^{40}ar/^{39}ar dating. *Chem. Geol.*, **145**, 117–152.

Richards, M.A., Duncan, R.A. & Courtillot, V. (1989). Flood basalts and hot spot tracks: Plume head and tails. *Science*, **246**, 103–107.

Rimi, A. (1999). Mantle heat flow and geotherms for the main geologic domains in morocco. *J. Earth Sci.*, **88**, 458–466.

Rossi, P., Cocherie, A. & amd Y. Ternet, C.M.F. (2003). Datation u/pb sur zircons des dolérites tholéiitiques pyrénéennes (ophites) à la limite trias/jurassique et relations avec les tufs volcaniques dits « infra-liasiques » nord-pyrénéens. *C.R. Geoscience*, **335**, 1071–1080.

Roy, P.L. & Piqué, A. (2001). Triassic-liassic western moroccan synrift basins in relation to the central atlantic opening. *Marine Geology*, **172**, 359–381.

Roy, P.L., Piqué, A., Gall, B.L., Brahim, L.A., Morabet, A.M. & Demnati, A. (1997). Les basins côtiers triasico-liasiques du maroc occidental et la diachronie du rifting intra-continental de l'atlantique central. *Bull. Soc. Géol. France*, **168**, 637–648.

Russo, P. & Russo, L. (1934). Le grand accident sud-atlasien. *Bulletin de la Société géologique de France*, **4**, 375–384.

Sahabi, M., Aslanian, D. & Olivet, J.L. (2005). A new starting point for the history of the central atlantic. *C.R. Geoscience*, **336**, 1041–1052.

Sandvol, E., Calvert, A. & Berazangui, M. (1998). Grid search modelling of receiver functions: implications for crustal structure in the midlle east and north africa. *J. Geophys. Res.*, **103**, 26899–26917.

Schaltegger, U., Guex, J., Bartolini, A., Schoene, B. & Ovtcharova, M. (2008). Precise u-pb age constraints for end-triassic mass extinction, its correlation to volcanism and hettangian post-extinction recovery. *Earth Planet. Sci. Lett.*, **267**, 266–275.

Schnepp, E., Pucher, R., Goedicke, C., Manzano, A., Müller, U. & Lanos, P. (2003). Paleomagnetic directions and thermoluminescence dating from a bread oven-floor sequence in lübeck (germany): a record of 450 years of geomagnetic secular variation. *J. Geophys. Res.*, **108**, 1–14.

Schoene, B., Crowel, J.L., Condon, D.J., Schmitz, M.D. & Bowring, S.A. (2006). Reassessing the uranium decay constants for geochronology using id-tims u-pb data. *Geochim. Cosmochim. Acta*, **70**, 426–445.

Sebai, A., Féraud, G., Bertrand, H. & Hanes, J. (1991). ^{40}ar/^{39}ar dating and geochemistry of tholeiitic magmatism related to the early opening of the central atlantic rift. *Earth Planet. Sci. Lett.*, **104**, 455–472.

Seber, D., Barazangui, M., Tadili, B.A., Ramdani, M., Ibenbrahim, A. & Sari, D.B. (1996). Three dimensional upper mantle structure beneath the intraplate atlas and interplate rif mountains of morocco. *J. Geophys. Res.*, **101**, 3125–3138.

Seber, D., Sandvol, E., Sandvol, C., Brindisi, C. & Barazangui, M. (2001). Crustal model for the middle east and north africa region: implications for the isostatic compensation mechanism. *Geophys. J. Int.*, **147**, 630– 638.

Sempere, T., Carlier, G., Soler, P., Fornari, M., Carlotto, V., Jacay, J., Arispe, O.,

Néraudeau, D., Càrdenas, J., Rosas, S. & Jiménez, N. (2002). Late permian-middle jurassic lithospheric thinning in peru and bolivia, and its bearing on andean-age tectonics. *Tectonophys.*, **345**, 153–181.

Sepkowski, J.J. (1996). *Patterns of Phanerozoic extinction: a perspective from global data bases*. In: Walliser, O. H. (Ed.), Global events and event stratigraphy in the Phanerozoic, Springer, Berlin.

Shimizu, N. (1981). Trace element incorporation into growing augite phenocryst. *Nature*, **289**, 575–577.

Shirley, D.N. (1987). Differentiation and compaction in the palisades sill, new jersey. *J. Petrol.*, **28**, 835–865.

Sircombe, K. (2004). Agedisplay: an excel workbook to evaluate and display univariate geochronological data using binned frequency histograms and probability density distributions. *Computers & Geosciences*, **30**, 21–31.

Sisson, T.W. & Grove, T.L. (1993). Temperatures and h_2o contents of low-mgo high-alumina basalts. *Contrib. Mineral. Petrol.*, **113**, 167–184.

Stampfli, G.M. & Borel, G.D. (2002). A plate tectonic model for the paleozoic and mesozoic constrained by dynamic plate boundaries and restored synthetic oceanic isochrons. *Earth Planet. Sci. Lett.*, **196**, 17–33.

Steiger, R.H. & Jäger, E. (1977). Subcommission on geochronology: convention on the use of decay constant in geo- and cosmochronology. *Earth Planet. Sci. Lett.*, **36**, 359–362.

Sutter, J.F. (1988). *Innovative approaches to the dating of igneous events in the Early Mesozoic basins of the eastern United States*. In A. J. Froelich and G. R. Robinson, Eds., Study of the Early Mesozoic basins of the eastern United States: U. S. Geol. Surv. Bull. 1776.

Tadili, B., Ramdani, M., Sari, B., Chapochnikov, K. & Bellot, A. (1986). Structure de la croute dans le nord du maroc. *Ann. Geophys.*, **4**, 99–104.

Takagi, D., Hiroaki, S. & Nakagawa, M. (2005). Experimental study of a low-alkali tholeite at 1-5 kbar: optimal for the crystallization of high-an plagioclase in hydrous arc tholeiite. *Contrib. Mineral. Petrol.*, **149**, 527–540.

Tanner, L.H., Lucas, S.G. & Chapman, M.G. (2004). Assessing the record and causes of late triassic extinctions. *Earth Sci. Rev.*, **65**, 103–139.

Taylor, S.R. & McLennan, S.M. (1985). *The continental crust: its composition and evolution*. Blackwell, Oxford.

Teixell, A., Arboleya, M.L., Julivert, M. & Charroud, M. (2003). Tectonic shortening and topography in the central high atlas (morocco). *Tectonics*, **22**, 1051–1056.

Torsvik, T.H. (2003). The rodinia jigsaw pattern. *Science*, **300**, 1379–1381.

Torsvik, T.H., Smethurst, M.A., Meert, J.G., der Voo, R.V., McKerrow, W.S., Sturt, B.A. & Walderhaug, H.J. (1996). Continental break-up and collision in the neoproterozoic and paleozoic: a tale of baltica and laurentia. *Earth Sci. Rev.*, **40**, 229–259.

Veevers, J.J. (1994). *Pangea: evolution of a supercontinent and its consequences for Earth's paleoclimate and sedimentary environments*. In: G. D. Klein (Ed.), Pangea: paleoclimate, tectonics and sedimentation during accretion, Zenith and break-up of a supercontinent, Vol. 228, Geological Society of America, special Paper.

Verati, C., Bertrand, H. & Féraud, G. (2005). The farthest record of the central atlantic magmatic province into west africa craton: Precise ^{40}ar/^{39}ar dating and geochemistry of taoudenni basin intrusives (northern mali). *Earth Planet. Sci. Lett.*, **235**, 391–407.

Verati, C., Rapaille, C., Féraud, G., Marzoli, A., Bertrand, H. & Youbi, N. (2007). ^{40}ar/^{39}ar ages and duration of the central atlantic magmatic province volcanism in morocco and portugal and its relation to the triassic-jurassic boundary. *Palaeogeogr. Palaeoclimatol. Palaeoecol.*, **244**, 308–325.

Villeneuve, M., Sandeman, H.A. & Davis, W.J. (2000). A method for intercalibration of u-th-pb and ^{40}ar/^{39}ar ages in the phanerozoic. *Geochim. Cosmochim. Acta*, **64**, 4017–4030.

Warrington, G. (1996). *Triassic spores and pollens*. in Jansonius, J., and McGregor, D.C., eds., Palynology: Principles and applications: American Association of Stratigraphic Palynologists Foundation, Vol. 2.

Wartiti, M.E. (1990). *Le Permien du Maroc Mésétien: etudes géologique et implication paléogéographie*. Master's thesis, Thèse d'Etat Sci., Univ. de Mohamed V, Rabat.

Whiteside, J.H., Olsen, P.E., Kent, D.V., Fowell, S.J. & Touhami, M.E. (2007).

Synchrony between the central atlantic magmatic province and the triassic-jurassic mass-extinction event? *Palaeogeog. Palaeoclim. Palaeoecol.*, **244**, 345–367.

Wigger, P., Asch, G., Giese, P., Heinsohn, W.D., Alami, S.O.E. & Ramdani, F. (1992). Crustal structure along a traverse across the middle and high atlas mountains derived from seismic reflection studies. *Intern. J. Earth Sci.*, **81**, 237–248.

Withjack, M.O., Schlische, R.W. & Olsen, P.O. (1998). Diachronous rifting, drifting and inversion on the passive margin of the central eastern north america: an analog for other passive margins. *AAPG Bulletin*, **82**, 817–835.

Yang, Z.Y., Moreau, M.G., Bucher, H., Dommergues, J.L. & Trouiller, A. (1996). Hettangian and sinemurian magnetostratigraphy from paris basin. *J. Geophys. Res.*, **101**, 8025–8042.

Youbi, N., Martins, L.T., Munha, J.M., Ibouh, H., Madeira, J., Chayeb, E.M.A. & Boukhari, A.E. (2003). *The Late Triassic-Early Jurassic volcanism of Morocco and Pourtugal in the geodynamic framework of the central Atlantic Ocean*. In: W. E. Hames, J. G. McHone, P. R. Renne, C. Ruppel (Eds.), The Central Atlantic Magmatic Province: Insights from frangments of Pangea, AGU Geophys. Mon. 136.

Ziegler, P.A. (1982). *Geological Atlas of Western and Central Europe*. The Hauge: Shell International Petroleum Mij. B. V.

Ziegler, P.A. (1989). *Evolution of Laurussia*. Dordrecht: Kluwer Academic Publishers.

Zindler, A. & Hart, S.R. (1986). Chemical geodynamics. *Ann. Rev. Earth Planet. Sci.*, **14**, 493–571.